

Once-in-a-lifetime meteorite  
bombards Costa Rican village p. 760

Roots of Huntington's disease in  
early development pp. 771 & 787

Superelastic alloys' temperature  
stretch pp. 773 & 855

# Science

\$15  
14 AUGUST 2020  
[sciencemag.org](http://sciencemag.org)

AAAS

## SOCIAL COHESION AFTER WAR

Christian and Muslim soccer in  
post-ISIS Iraq pp. 769 & 866





# CONTENTS

14 AUGUST 2020 • VOLUME 369 • ISSUE 6505



## NEWS

### IN BRIEF

**750** News at a glance

### IN DEPTH

#### **752** Antibodies may curb pandemic before vaccines

Now in efficacy trials, monoclonal antibodies promise to both prevent and treat disease  
*By J. Cohen*

#### **753** For science in Latin America, 'a fascinating challenge'

Pandemic shows benefits of investments in research but also poses grave threats  
*By R. Pérez Ortega and L. Wessel*

#### **755** Looking for the light in Haiti

For physician Marie Marcelle Deschamps, COVID-19 is just the latest challenge  
*By R. Bazell*

#### **756** Africa's pandemic puzzle: why so few cases and deaths?

Antibody surveys tell a different story than official tolls  
*By L. Nordling*

#### **757** Fed-up archaeologists aim to fix field schools' party culture

Drinking and harassment spur experiments, including local projects and student stipends, for core training course  
*By L. Wade*

#### **758** Don't crush that ant—it could plant a wildflower

New findings show how ants choose and protect the seeds they disperse  
*By E. Pennisi*

### FEATURES

#### **760** Lucky strike

Last year, an unusual meteorite crashed in a Costa Rican rainforest. Rich in the building blocks of life, it has captivated collectors and researchers  
*By J. Sokol*

## INSIGHTS

### POLICY FORUM

#### **766** Distorting science, putting water at risk

A recent rule is inconsistent with science and will compromise the integrity of U.S. waters  
*By S. M. P. Sullivan et al.*

### PERSPECTIVES

#### **769** Can playing together help us live together?

A field experiment in Iraq shows that having Muslim teammates reduced Christian soccer players' prejudice  
*By E. L. Paluck and C. S. Clark*  
REPORT p. 866

#### **770** Marine food webs destabilized

A combination of warming and acidification threaten marine biomass and productivity  
*By S. L. Chown*  
REPORT p. 829

#### **771** An early start to Huntington's disease

The huntingtin gene mutation interferes with neurogenesis in human fetal cortex  
*By M. DiFiglia*  
RESEARCH ARTICLE p. 787

#### **773** Designing a wider superelastic window

Adding chromium to an iron alloy enables shape recovery over a wide temperature range  
*By P. La Roca and M. Sade*  
REPORT p. 855

#### **774** The importins of pain

A nuclear protein importer modulates gene expression to control the persistence of neuropathic pain  
*By M. S. Yousuf and T. J. Price*  
REPORT p. 842

#### **775** A coexistence that CuO<sub>2</sub> planes can see

Antiferromagnetism and superconductivity are not at odds in a quintuple-layer cuprate  
*By I. Vishik*  
REPORT p. 833

#### **777** Michael Soulé (1936–2020)

Founder of conservation biology  
*By D. W. Inouye and P. R. Ehrlich*



## BOOKS ET AL.

### 778 How it all ends

A light-hearted exploration of the death of the Universe serves as an effective antidote for everyday worries *By P. Halpern*

### 779 Science meets politics

A passion for promoting the public good guided geneticist J. B. S. Haldane's scholarship *By P. W. Hughes*

## LETTERS

### 780 Retraction

*By S. Licht et al.*

### 780 Controlling the COVID-19 narrative

*By N. Bharti*

### 780 Dismantling systemic racism in science

*By E. A. Odekunle*

### 781 Untapped resources for medical research

*By O. A. Pérez-Escobar et al.*

# RESEARCH

## IN BRIEF

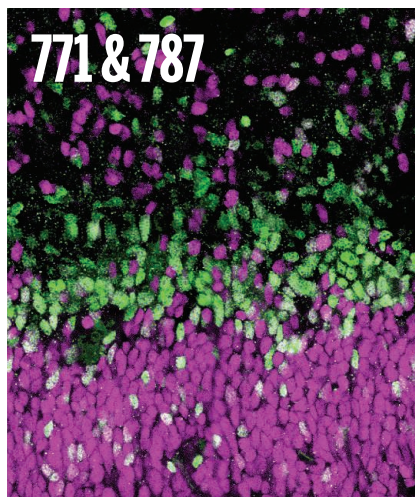
**783** From *Science* and other journals

## REVIEW

### 786 Catalysis

Using nature's blueprint to expand catalysis with Earth-abundant metals *R. M. Bullock et al.*

REVIEW SUMMARY; FOR FULL TEXT:  
DX.DOI.ORG/10.1126/SCIENCE.ABC3183



## RESEARCH ARTICLES

### 787 Neurodevelopment

Huntington's disease alters human neurodevelopment *M. Barnat et al.*  
PERSPECTIVE p. 771

### 793 Structural biology

Binding mechanisms of therapeutic antibodies to human CD20  
*A. Kumar et al.*

### 799 Organic chemistry

Divergent synthesis of complex diterpenes through a hybrid oxidative approach *X. Zhang et al.*

## Coronavirus

**806** DNA vaccine protection against SARS-CoV-2 in rhesus macaques  
*J. Yu et al.*

**812** SARS-CoV-2 infection protects against rechallenge in rhesus macaques  
*A. Chandrashekar et al.*  
REPORT p. 818

## REPORTS

### 818 Coronavirus

Primary exposure to SARS-CoV-2 protects against reinfection in rhesus macaques  
*W. Deng et al.*  
RESEARCH ARTICLES pp. 806 & 812

### 823 Immunology

BAF restricts cGAS on nuclear DNA to prevent innate immune activation *B. Guey et al.*

### 829 Trophic resilience

Trophic pyramids reorganize when food web architecture fails to adjust to ocean change *I. Nagelkerken et al.*  
PERSPECTIVE p. 770

### 833 Superconductivity

Observation of small Fermi pockets protected by clean CuO<sub>2</sub> sheets of a high-T<sub>c</sub> superconductor  
*S. Kunisada et al.*  
PERSPECTIVE p. 775

### 838 Tropical forest

Active restoration accelerates the carbon recovery of human-modified tropical forests *C. D. Philipson et al.*

### 842 Neuroscience

Importin  $\alpha$ 3 regulates chronic pain pathways in peripheral sensory neurons *L. Marvaldi et al.*  
PERSPECTIVE p. 774

## 846 Coronavirus

A mathematical model reveals the influence of population heterogeneity on herd immunity to SARS-CoV-2 *T. Britton et al.*

## 850 Electrochemistry

A molecular mediator for reductive concerted proton-electron transfers via electrocatalysis *M. J. Chalkley et al.*

## 855 Metallurgy

Iron-based superelastic alloys with near-constant critical stress temperature dependence *J. Xia et al.*  
PERSPECTIVE p. 773

## 858 Neurodevelopment

Mitochondrial dynamics in postmitotic cells regulate neurogenesis *R. Iwata et al.*

## 863 Paleoanthropology

Fire and grass-bedding construction 200 thousand years ago at Border Cave, South Africa *L. Wadley et al.*

## 866 Intergroup relations

Building social cohesion between Christians and Muslims through soccer in post-ISIS Iraq *S. Mousa*  
PERSPECTIVE p.769; PODCAST

## DEPARTMENTS

### 749 Editorial

Vaccine nationalism's politics  
*By David P. Fidler*

### 874 Working Life

Interrupted—again *By Kathy Gillen*

## ON THE COVER



A soccer game at Khazir refugee camp outside Erbil, northern Iraq. A randomized study assigned displaced Christians to a soccer team with displaced Muslims or to an all-Christian team. Playing on a mixed team improved Christians' behaviors toward Muslim peers, but not toward Muslims more broadly. The results highlight the potential and limitations of intergroup contact after war. See pages 769 and 866. *Photo: Associated Press*

Science Staff .....	746
New Products.....	871
Science Careers .....	872

SCIENCE (ISSN 0036-8075) is published weekly on Friday, except last week in December, by the American Association for the Advancement of Science, 1200 New York Avenue, NW, Washington, DC 20005. Periodicals mail postage (publication No. 484460) paid at Washington, DC, and additional mailing offices. Copyright © 2020 by the American Association for the Advancement of Science. The title SCIENCE is a registered trademark of the AAAS. Domestic individual membership, including subscription (12 months): \$165 (\$74 allocated to subscription). Domestic institutional subscription (51 issues): \$2148; Foreign postage extra: Air assist delivery: \$98. First class, airmail, student, and emeritus rates on request. Canadian rates with GST available upon request. GST #125488122. Publications Mail Agreement Number 1069624. Printed in the U.S.A.  
Change of address: Allow 4 weeks, giving old and new addresses and 8-digit account number. Postmaster: Send change of address to AAAS, P.O. Box 96178, Washington, DC 20090-6178. Single-copy sales: \$15 each plus shipping and handling available from backissues.sciencemag.org; bulk rate on request. Authorization to reproduce material for internal or personal use under circumstances not falling within the fair use provisions of the Copyright Act can be obtained through the Copyright Clearance Center (CCC), www.copyright.com. The identification code for Science is 0036-8075. Science is indexed in the Reader's Guide to Periodical Literature and in several specialized indexes.



Editor-in-Chief Holden Thorp, hthorp@aaas.org

Executive Editor Monica M. Bradford

Editors, Research Valda Vinson, Jake S. Heston Editor, Insights Lisa D. Chong

**DEPUTY EDITORS** Julia Fahrenkamp-Uppenbrink (UK), Stella M. Yurston (UK), Phillip D. Szurmi, Sacha Vignieri **SR. EDITORIAL FELLOW** Andrew M. Sugden (UK) **SR. EDITORS** Gemma Alderton (UK), Caroline Ash (UK), Brent Grocholski, Pamela J. Hines, Di Jiang, Marc S. Lavine (Canada), Ian S. Osborne (UK), Beverly A. Purnell, L. Bryan Ray, H. Jesse Smith, Keith T. Smith (UK), Jelena Stajic, Peter Stern (UK), Valerie B. Thompson, Brad Wible, Laura M. Zahn **ASSOCIATE EDITORS** Michael A. Funk, Priscilla N. Kelly, Tage S. Rai, Seth Thomas Scanlon (UK), Yury V. Suleymanov **LETTERS EDITOR** Jennifer Sills **LEAD CONTENT PRODUCTION EDITORS** Harry Jach, Lauren Kmec **CONTENT PRODUCTION EDITORS** Amelia Beyna, Jeffrey E. Cook, Chris Filatreau, Julia Katris, Nida Masulis, Suzanne M. White **SR. EDITORIAL COORDINATORS** Carolyn Kyle, Beverly Shields **EDITORIAL COORDINATORS** Aneera Dobbins, Joi S. Granger, Jeffrey Hearn, Lisa Johnson, Maryrose Madrid, Ope Martins, Shannon McMahon, Jerry Richardson, Hilary Stewart (UK), Alana Warnke, Alice Whaley (UK), Anita Wynn **PUBLICATIONS ASSISTANTS** Jeremy Dow, Alexander Kief, Ronnel Navas, Brian White **EXECUTIVE ASSISTANT** Jessica Slater **ASI DIRECTOR, OPERATIONS** Janet Clements (UK) **ASI SR. OFFICE ADMINISTRATOR** Jessica Waldoock (UK)

News Editor Tim Appenzeller

**NEWS MANAGING EDITOR** John Travis **INTERNATIONAL EDITOR** Martin Enserink **DEPUTY NEWS EDITORS** Elizabeth Culotta, Lila Guterman, David Grimm, Eric Hand (Europe), David Malakoff **SR. CORRESPONDENTS** Daniel Clerly (UK), Jon Cohen, Jeffrey Mervis, Elizabeth Pennisi **ASSOCIATE EDITORS** Jeffrey Brinard, Catherine Maticic **NEWS REPORTERS** Adrian Cho, Jennifer Couzin-Frankel, Jocelyn Kaiser, Kelly Servick, Robert F. Service, Erik Stokstad, Paul Voosen, Meredith Wadman **INTERNS** Eva Frederick, Rodrigo Perez Ortega **CONTRIBUTING CORRESPONDENTS** Warren Cornwall, Ann Gibbons, Mara Hvistendahl, Sam Kean, Eli Kintisch, Kai Kupferschmidt (Berlin), Andrew Lawler, Mitch Leslie, Eliot Marshall, Virginia Morell, Dennis Normile (Shanghai), Elisabeth Pain (Careers), Charles Piller, Michael Price, Tania Rabesandratana (Barcelona), Emily Underwood, Gretchen Vogel (Berlin), Lizzie Wade (Mexico City) **CAREERS** Donisha Adams, Rachel Bernstein (Editor), Katie Langin (Acting Editor) **COPY EDITORS** Julia Cole (Senior Copy Editor), Cyra Master (Copy Chief) **ADMINISTRATIVE SUPPORT** Meagan Welland

Creative Director Beth Rakouskas

**DESIGN MANAGING EDITOR** Marcy Atarod **GRAPHICS MANAGING EDITOR** Alberto Cuadra **PHOTOGRAPHY MANAGING EDITOR** William Douthitt **WEB CONTENT STRATEGY MANAGER** Kara Estelle-Powers **DESIGN EDITOR** Chrystal Smith **DESIGNER** Christina Aycock **GRAPHICS EDITOR** Nirja Desai **INTERACTIVE GRAPHICS EDITOR** Xing Liu **SENIOR SCIENTIFIC ILLUSTRATORS** Valerie Altounian, Chris Bickel **SCIENTIFIC ILLUSTRATOR** Alice Kitterman **SENIOR GRAPHICS SPECIALISTS** Holly Bishop, Nathalie Cary **SENIOR PHOTO EDITOR** Emily Petersen **PHOTO EDITOR** Kaitlyn Dolan **WEB DESIGNER** Jennie Pajerowski

## Chief Executive Officer and Executive Publisher Sudip Parikh

Publisher, Science Family of Journals Bill Moran

**DIRECTOR, BUSINESS SYSTEMS AND FINANCIAL ANALYSIS** Randy Yi **DIRECTOR, BUSINESS OPERATIONS & ANALYSIS** Eric Knott **DIRECTOR OF ANALYTICS** Enrique Gonzales **MANAGER, BUSINESS OPERATIONS** Jessica Tierney **SENIOR BUSINESS ANALYST** Cory Lipman, Meron Kebede **FINANCIAL ANALYST** Alexander Lee **ADVERTISING SYSTEM ADMINISTRATOR** Tina Burks **SENIOR SALES COORDINATOR** Shirley Young **DIGITAL/PRINT STRATEGY MANAGER** Jason Hillman **QUALITY TECHNICAL MANAGER** Marcus Spiegler **ASSISTANT MANAGER DIGITAL/PRINT** Rebecca Doshi **SENIOR CONTENT SPECIALISTS** Steve Forrester, Jacob Hedrick, Antoinette Hodal, Lori Murphy **PRODUCTION SPECIALIST** Kristin Wowk **DIGITAL PRODUCTION MANAGER** Lisa Stanford **CONTENT SPECIALIST** Kimberley Oster **ADVERTISING PRODUCTION OPERATIONS MANAGER** Deborah Tompkins **DESIGNER, CUSTOM PUBLISHING** Jeremy Huntsinger **SR. TRAFFIC ASSOCIATE** Christine Hall **SPECIAL PROJECTS ASSOCIATE** Sarah Dhre

**ASSOCIATE DIRECTOR, BUSINESS DEVELOPMENT** Justin Sawyers **GLOBAL MARKETING MANAGER** Allison Pritchard **DIGITAL MARKETING MANAGER** Aimee Aponte **JOURNALS MARKETING MANAGER** Shawana Arnold **MARKETING ASSOCIATES** Tori Velasquez, Mike Romano, Ashley Hylton **DIGITAL MARKETING SPECIALIST** Asleigh Rojanavongse **SENIOR DESIGNER** Kim Huynh

**DIRECTOR AND SENIOR EDITOR, CUSTOM PUBLISHING** Sean Sanders **ASSISTANT EDITOR, CUSTOM PUBLISHING** Jackie Oberst

**DIRECTOR, PRODUCT & PUBLISHING DEVELOPMENT** Chris Reid **DIRECTOR, BUSINESS STRATEGY AND PORTFOLIO MANAGEMENT** Sarah Whalen **ASSOCIATE DIRECTOR, PRODUCT MANAGEMENT** Kris Bishop **SR. PRODUCT ASSOCIATE** Robert Koepke **DIGITAL PRODUCT STRATEGIST** Michael Hardesty **SPJ ASSOCIATE** Samantha Bruno Fuller

**DIRECTOR, INSTITUTIONAL LICENSING** Iquo Edim **ASSOCIATE DIRECTOR, RESEARCH & DEVELOPMENT** Elisabeth Leonard **MARKETING MANAGER** Kess Knight **SENIOR INSTITUTIONAL LICENSING MANAGER** Ryan Rexroth **INSTITUTIONAL LICENSING MANAGER** Marco Castellani **MANAGER, AGENT RELATIONS & CUSTOMER SUCCESS** Judy Lillibridge **SENIOR OPERATIONS ANALYST** Lana Guz **FULFILLMENT COORDINATOR** Melody Stringer **SALES COORDINATOR** Josh Haverlock

**DIRECTOR, GLOBAL SALES** Tracy Holmes **EAST COAST AND MID WEST SALES** Stephanie O'Connor **US WEST COAST SALES** Lynne Stickrod **US SALES MANAGER, SCIENCE CAREERS** Claudia Paulsen-Young **US SALES REP, SCIENCE CAREERS** Tracy Anderson **ASSOCIATE DIRECTOR, ROW** Roger Gonçalves **SALES REP, ROW** Sarah Lelarge **SALES ADMIN ASSISTANT, ROW** Bryony Cousins **DIRECTOR OF GLOBAL COLLABORATION AND ACADEMIC PUBLISHING RELATIONS** Asia Xiaoying Chu **ASSOCIATE DIRECTOR, INTERNATIONAL COLLABORATION** Grace Yao **SALES MANAGER** Danny Zhao **MARKETING MANAGER** Kilo Lan **ASCA CORPORATION, JAPAN** Kaoru Sasaki (Tokyo), Miyuki Tani (Osaka) **COLLABORATION/CUSTOM PUBLICATIONS/JAPAN** Adarsh Sandhu

**DIRECTOR, COPYRIGHT, LICENSING AND SPECIAL PROJECTS** Emilie David **RIGHTS AND LICENSING COORDINATOR** Jessica Adams **RIGHTS AND PERMISSIONS ASSOCIATE** Elizabeth Sandler **CONTRACTS AND LICENSING ASSOCIATE** Lili Catlett

### MAIN HEADQUARTERS

Science/AAAS  
1200 New York Ave. NW  
Washington, DC 20005

### SCIENCE INTERNATIONAL

Clarendon House  
Clarendon Road  
Cambridge, CB2 8FH, UK

### SCIENCE CHINA

Room 1004, Culture Square  
No. 59 Zhongguancun St.  
Haidian District, Beijing, 100872

### SCIENCE JAPAN

ASCA Corporation  
Sibaura TY Bldg. 4F, 1-14-5  
Shibaura Minato-ku  
Tokyo, 108-0073 Japan

### EDITORIAL

science\_editors@aaas.org

### NEWS

science\_news@aaas.org

### INFORMATION FOR AUTHORS

sciencemag.org/authors/  
science-information-authors

### REPRINTS AND PERMISSIONS

sciencemag.org/help/  
reprints-and-permissions

### MEDIA CONTACTS

scipak@aaas.org

### MULTIMEDIA CONTACTS

SciencePodcast@aaas.org  
ScienceVideo@aaas.org

### INSTITUTIONAL SALES

science@aaas.org

### AND SITE LICENSES

sciencemag.org/librarian

### PRODUCT ADVERTISING

**& CUSTOM PUBLISHING**  
advertising.sciencemag.org/  
products-services  
science\_advertising@aaas.org

### CLASSIFIED ADVERTISING

advertising.sciencemag.org/  
science-careers  
advertise@sciencecareers.org

### JOB POSTING CUSTOMER SERVICE

employers.sciencecareers.org  
support@sciencecareers.org

### MEMBERSHIP AND INDIVIDUAL

**SUBSCRIPTIONS**  
sciencemag.org/subscriptions

### MEMBER BENEFITS

aaas.org/membercentral

### AAAS BOARD OF DIRECTORS

**CHAIR** Steven Chu  
**PRESIDENT** Claire M. Fraser  
**PRESIDENT-ELECT** Susan G. Amara  
**TREASURER** Carolyn N. Ainslie  
**CHIEF EXECUTIVE OFFICER**  
Sudip Parikh  
**BOARD** Cynthia M. Beall  
Rosina M. Bierbaum  
Ann Bostrom  
Stephen P.A. Fodor  
S. James Gates, Jr.  
Laura H. Greene  
Kaye Husbands Fealing  
Maria M. Klawe  
Robert B. Millard  
Alonda Nelson  
William D. Provine

### BOARD OF REVIEWING EDITORS (Statistics board members indicated with \$)

**Adriano Aguzzi**, U. Hospital Zürich  
**Takuzo Aida**, U. of Tokyo  
**Leslie Aiello**, Wenner-Gren Foundation  
**Judith Allen**, U. of Manchester  
**Sebastian Amigorena**, Institut Curie  
**James Analytis**, UC Berkeley  
**Trevor Archer**, NIEHS, NIH  
**Paola Arlotta**, Harvard U.  
**Johan Auwerx**, EPFL  
**David Awschalom**, U. of Chicago  
**Clare Baker**, U. of Cambridge  
**Nenad Ban**, ETH Zürich  
**Franz Bauer**, Pontificia U. Católica de Chile  
**Ray H. Baughman**, U. of Texas at Dallas  
**Carlo Beenakker**, Leiden U.  
**Yasmine Belkaid**, NIAID, NIH  
**Philip Benfey**, Duke U.  
**Gabriele Bergers**, VIB  
**Bradley Bernstein**, Mass. General Hospital  
**Joseph J. Berry**, NREL  
**Alessandra Biffi**, Harvard Med. School  
**Peer Bork**, EMBL  
**Chris Bowler**, Ecole Normale Supérieure  
**Ian Boyd**, U. of St. Andrews  
**Emily Brodsky**, UC Santa Cruz  
**Ron Brookmeyer**, UCLA (\$) **Christian Büchel**, UKE Hamburg  
**Dennis Burton**, Scripps Res.  
**Carter Tribble Butts**, U. of California, Irvine  
**György Buzsáki**, New York U. School of Med.  
**Blanche Capel**, Duke U.  
**Annmarié Carlton**, U. of California, Irvine  
**Nick Chater**, U. of Warwick  
**M. Keith Chen**, UCLA  
**Zhiqian Chen**, UT Southwestern Med. Ctr.  
**Ib Chorkendorff**, Denmark TU  
**James J. Collins**, MIT  
**Robert Cook-Deegan**, Arizona State U.  
**Alan Cowman**, Walter & Eliza Hall Inst.  
**Carolyn Coyne**, U. of Pittsburgh  
**Roberta Croce**, VU Amsterdam  
**Ismaila Dabo**, Penn State U.  
**Jeff L. Dangl**, U. of North Carolina  
**Tom Daniel**, U. of Washington  
**Chiara Darao**, Caltech  
**Nicolas Dauphas**, U. of Chicago  
**Christian Davenport**, U. of Michigan  
**Frans de Waal**, Emory U.  
**Claude Desplan**, New York U.  
**Sandra Díaz**, U. Nacional de Córdoba  
**Ulrike Diebold**, TU Wien  
**Hong Ding**, Inst. of Physics, CAS  
**Jennifer Dionne**, Stanford U.  
**Dennis Discher**, U. of Penn.  
**Gerald Dorn**, Washington U. in St. Louis  
**Jennifer A. Doudna**, UC Berkeley  
**Raissa M. D'Souza**, UC Davis  
**Bruce Dunn**, UCLA  
**William Dunphy**, Caltech  
**Christopher Dye**, U. of Oxford  
**Todd Ehlers**, U. of Tübingen  
**Jennifer Eliseff**, Johns Hopkins U.  
**Tim Elston**, U. of North Carolina  
**Andrea Encalada**, U. San Francisco de Quito  
**Nader Engheta**, U. of Penn.  
**Karen Ersche**, U. of Cambridge  
**Barry Everitt**, U. of Cambridge  
**Vanessa Ezenwa**, U. of Georgia  
**Michael Feuer**, The George Washington U.  
**Toren Finkel**, U. of Pittsburgh Med. Ctr.  
**Gwenn Flowers**, Simon Fraser U.  
**Peter Fratzl**, Max Planck Inst. Potsdam  
**Elaine Fuchs**, Rockefeller U.  
**Eileen Furlong**, EMBL  
**Jay Gallagher**, U. of Wisconsin  
**Daniel Geschwind**, UCLA  
**Karl-Heinz Glassmeier**, TU Braunschweig  
**Ramon Gonzalez**, U. of South Florida  
**Elizabeth Grove**, U. of Chicago  
**Nicolas Gruber**, ETH Zürich  
**Hua Guo**, U. of New Mexico  
**Kip Guy**, U. of Kentucky College of Pharmacy  
**Taekjip Ha**, Johns Hopkins U.  
**Christian Haass**, Ludwig Maximilians U.  
**Sharon Hammes-Schiffer**, Yale U.  
**Wolf-Dietrich Hardt**, ETH Zürich  
**Louise Harra**, U. College London  
**Jian He**, Clemson U.  
**Carl-Philipp Heisenberg**, IST Austria  
**Ykä Helariutta**, U. of Cambridge  
**Janet G. Hering**, Eawag  
**Hans Hilgenkamp**, U. of Twente  
**Kai-Uwe Hinrichs**, U. of Bremen  
**Deirdre Hollingsworth**, U. of Oxford  
**Lora Hooper**, UT Southwestern Med. Ctr.  
**Fred Hughson**, Princeton U.  
**Randall Hulet**, Rice U.  
**Auke Ijspeert**, EPFL  
**Akiko Iwasaki**, Yale U.  
**Stephen Jackson**, USGS and U. of Arizona  
**Kai Johnsson**, EPFL  
**Peter Jonas**, IST Austria  
**Matt Kaeberlein**, U. of Washington  
**William Kaelin Jr.**, Dana-Farber Cancer Inst.  
**Daniel Kammen**, UC Berkeley  
**V. Narry Kim**, Seoul Nat. U.  
**Robert Kingston**, Harvard Med. School  
**Nancy Knowlton**, Smithsonian Institution  
**Etienne Kochlin**, Ecole Normale Supérieure  
**Alex L. Kolodkin**, Johns Hopkins U.  
**Julija Krupic**, U. of Cambridge  
**Thomas Langer**, Max Planck Inst. Cologne  
**Mitchell A. Lazar**, U. of Penn.  
**Wendell Lim**, UC San Francisco  
**Jianguo Liu**, Michigan State U.  
**Luis Liz-Marzán**, CIC biomagUNE  
**Omar Lizardo**, UCLA  
**Jonathan Losos**, Washington U. in St. Louis  
**Ke Lu**, Chinese Acad. of Sciences  
**Christian Lüscher**, U. of Geneva  
**Jean Lynch-Stieglitz**, Georgia Inst. of Tech.  
**Fabienne Mackay**, QIMR Berghofer  
**Anne Magurran**, U. of St. Andrews  
**Oscar Marin**, King's College London  
**Charles Marshall**, UC Berkeley  
**Christopher Marx**, U. of Idaho  
**Geraldine Masson**, CNRS  
**C. Robertson McClung**, Dartmouth College  
**Rodrigo Medellín**, U. Nacional Autónoma de México  
**Graham Medley**, LSHTM  
**Jane Memmott**, U. of Bristol  
**C. Jessica Metcalf**, Princeton U.  
**Baoxia Mi**, UC Berkeley  
**Edward Miguel**, UC Berkeley  
**Tom Misteli**, NCI, NIH  
**Yasushi Miyashita**, U. of Tokyo  
**Allison Motsinger-Reif**, NIEHS, NIH (\$) **Danielle Navarro**, U. of New South Wales  
**Daniel Nettle**, Newcastle U.  
**Daniel Neuman**, UC Berkeley  
**Beatriz Noheda**, U. of Groningen  
**Helga Nowotny**, Vienna Sci. Res. & Tech. Fund  
**Rachel O'Reilly**, U. of Birmingham  
**Harry Orr**, U. of Minnesota  
**Pilar Ossorio**, U. of Wisconsin  
**Andrew Oswald**, U. of Warwick  
**Isabella Pagano**, Istituto Nazionale di Astrofisica  
**Margaret Palmer**, U. of Maryland  
**Elizabeth Levy Paluck**, Princeton U.  
**Jane Parker**, Max Planck Inst. Cologne  
**Giovanni Parmigiani**, Dana-Farber Cancer Inst. (\$) **Daniel Pauly**, U. of British Columbia  
**Samuel Pfaff**, Salk Inst. for Biological Studies  
**Julie Pfeiffer**, UT Southwestern Med. Ctr.  
**Philip Phillips**, UIUC  
**Matthieu Piel**, Institut Curie  
**Kathrin Plath**, UCLA  
**Martin Plenio**, Ulm U.  
**Katherine Pollard**, UC San Francisco  
**Elvira Poloczanska**, Alfred Wegener-Inst.  
**Julia Pongratz**, Ludwig Maximilians U.  
**Philippe Poulin**, CNRS  
**Jonathan Pritchard**, Stanford U.  
**Felix A. Rey**, Institut Pasteur  
**Trevor Robbins**, U. of Cambridge  
**Joeri Roelofs**, Imperial College London  
**Amy Rosenzweig**, Northwestern U.  
**Mike Ryan**, U. of Texas at Austin  
**Shimon Kaguchi**, Osaka U.  
**Miquel Salmeron**, Lawrence Berkeley Nat. Lab  
**Nitin Samarth**, Penn State U.  
**Jürgen Samadpour**, Med. U. of Vienna  
**Erica Ollmann Saphire**, La Jolla Inst.  
**Alexander Schier**, Harvard U.  
**Wolfram Schlenker**, Columbia U.  
**Susannah Scott**, UC Santa Barbara  
**Rebecca Seay**, LSHTM  
**Anuj Shah**, U. of Chicago  
**Vladimir Shalaeu**, Purdue U.  
**Jie Shan**, Cornell U.  
**Beth Shapiro**, UC Santa Cruz  
**Jay Shendure**, U. of Washington  
**Steve Sherwood**, U. of New South Wales  
**Brian Shoichet**, UC San Francisco  
**Robert Siliciano**, Johns Hopkins U. School of Med.  
**Lucia Sivilotti**, U. College London  
**Alison Smith**, John Innes Centre  
**Richard Smith**, U. of North Carolina (\$) **Mark Smyth**, QIMR Berghofer  
**Pam Solitis**, U. of Florida  
**John Speakman**, U. of Aberdeen  
**Tara Spire-Jones**, U. of Edinburgh  
**Allan C. Spradling**, Carnegie Institution for Sci.  
**V. S. Subrahmanian**, Dartmouth College  
**Ira Tabas**, Columbia U.  
**Sarah Teichmann**, Wellcome Sanger Inst.  
**Rocio Titunik**, Princeton U.  
**Shubha Tole**, Tata Inst. of Fundamental Res.  
**Wim van der Putten**, Netherlands Inst. of Ecology  
**Reinhold Veuglers**, KU Leuven  
**Bert Vogelstein**, Johns Hopkins U.  
**Kathleen Vohs**, U. of Minnesota  
**David Wallace**, Weizmann Inst. of Sci.  
**Jane-Ling Wang**, UC Davis (\$) **Jessica Ware**, Amer. Mus. of Natural Hist.  
**David Waxman**, Fudan U.  
**Jonathan Weissman**, UC San Francisco  
**Chris Wikle**, U. of Missouri (\$) **Terrie Williams**, UC Santa Cruz  
**Ian A. Wilson**, Scripps Res. (\$) **Yu Xie**, Princeton U.  
**Jan Zaenen**, Leiden U.  
**Kenneth Zaret**, U. of Penn. School of Med.  
**Jonathan Zehr**, UC Santa Cruz  
**Xiaowei Zhuang**, Harvard U.  
**Maria Zuber**, MIT



# Vaccine nationalism's politics

**B**efore coronavirus disease 2019 (COVID-19) struck, cooperation on global health—especially for pandemic preparedness and response—would, we told ourselves, enhance national security, support economic wealth, protect human rights, and facilitate humanitarian assistance around the world. However, the politics of the coronavirus catastrophe do not reflect such national interests or international solidarity. “Vaccine nationalism” is more evidence that efforts to elevate health cooperation—and the sciences that inform it—have produced more rhetoric than political roots within countries and the international community.

Concerns about vaccine nationalism were escalating even before the United States announced on 31 July its largest deal to date with pharmaceutical companies to secure COVID-19 vaccines. Other countries—including China, India, the United Kingdom, and members of the European Union—are pursuing similar strategies. To critics, this scramble to secure vaccine supplies is one of many decisions by governments that have failed to control spread of the virus, destroyed economic activity, and damaged international cooperation. Ineffective nationalistic policies appear to create a gap between science and politics that makes the pandemic worse and undermines what science and health diplomacy could achieve. In fact, vaccine nationalism reflects “business as usual” in global health.

Historically, health diplomacy has struggled with global, equitable access to drugs and vaccines during serious disease events. Countries did not achieve this goal, for example, during the 2009 H1N1 influenza pandemic. International access typically happened only after developed countries secured pharmaceuticals for use at home, as happened with vaccines for smallpox and polio and drugs for HIV/AIDS. Developing countries, such as China and India, tried to break out of this pattern by building their own pharmaceutical innovation and production capabilities. More recently, developing countries have asserted sovereignty over pathogenic samples. This approach conditions access to samples on the source country receiving benefits from research and development, including drugs and vaccines. This “viral sovereignty” strategy produced the virus-and-benefit sharing regime in the World Health Organization's Pandemic Influenza Preparedness Framework in 2011.

With COVID-19, history is repeating itself. Countries with the resources to obtain vaccines have not subordinated their needs and capacities to the objective of global, equitable access. And the worldwide spread of the coronavirus eliminates leverage that viral sovereignty might have provided countries without such means. International and nongovernmental organizations launched an ad hoc effort—the COVID-19 Vaccines Global Access (COVAX) Facility—to achieve equitable access. But with no serious participation by major states so far, COVAX lacks game-changing support. In keeping with the long-standing pattern of political behavior during pandemics, vaccines will eventually reach most populations, but only after powerful countries have protected themselves.

Further, changes in domestic and global politics have made matters worse. Domestically, the extent to which governments have ignored science, denigrated health experts, supported quack remedies and policies, peddled disinformation, and botched social distancing and other nonpharmaceutical interventions has been astonishing. This travesty flows from the traction that populist, nationalist, antiglobalist, and authoritarian attitudes have gained around the world.

Globally, balance-of-power politics has returned to world affairs. Geopolitical calculations have shaped national responses to COVID-19, with the United States and China treating the pandemic as

another front in their rivalry for power and influence. National access to coronavirus vaccines has become a priority in power politics, especially as a means to recover from the economic damage at home, in export markets, and within regions of strategic importance in the balance of power.

These changes in politics have generated ferocious headwinds against global, equitable vaccine access—an objective only approached with great difficulty when political waters were less turbulent. Reorienting health policy and diplomacy will require root-and-branch reconstruction of political interests on infectious diseases. Perhaps the mounting desperation for scientists to deliver a vaccine against COVID-19 will provide an incentive for leaders to rebuild health policies sufficiently so that, when the next pandemic hits, politicians and citizens will be less likely to drink the hydroxychloroquine.

—David P. Fidler



**David P. Fidler**

is an adjunct senior fellow at the Council on Foreign Relations, Washington, DC, USA. [dfidler@cfr.org](mailto:dfidler@cfr.org)

“...access  
to coronavirus  
vaccines  
has become  
a priority in power  
politics...”



# NEWS

## IN BRIEF

Edited by Jeffrey Brainard

Fishermen use a hose (left) to suck up netted menhaden into a ship in Virginia's portion of the Chesapeake Bay.

## CONSERVATION

### New fisheries regulation considers predators' needs

**W**hen fisheries regulators decide how many fish humans can kill, they rarely consider whether the quota affects other predators. But last week managers overseeing fisheries off the U.S. east coast took that broader view in deciding how they will set catch limits for menhaden, a small, oily fish that is the basis for the second largest fishery in the United States by weight harvested. Ending a yearslong conservation battle, the Atlantic States Marine Fisheries Commission unanimously voted to set new menhaden limits designed to leave enough

as prey for Atlantic striped bass, a species especially prized by recreational fishers. The move—one of the first like it in the world—is “a major step forward for management of marine resources and conservation science,” the Pew Charitable Trusts said in a statement. The decision should also help other fish, whales, and birds that feed heavily on menhaden, the commission said. Conservationists had long pushed for the change, arguing that menhaden, which are mostly sold for animal feed, fish oil pills, and bait, play a key role in marine food webs and needed to be managed more sustainably.

### Russia OKs COVID-19 vaccine use

**PUBLIC HEALTH** | In a move that startled and confused researchers worldwide, Russia's Ministry of Health on 11 August issued a “registration certificate” for a COVID-19 vaccine—even though it has been tested in only 76 people. The certificate allows the vaccine, made by the Gamaleya Research Institute in Moscow, to be used by “a small number of citizens from vulnerable groups,” including medical staff and older people, according to a

ministry spokesperson. (China earlier approved use of an experimental COVID-19 vaccine for its military, but it's unclear whether any troops have received it.) The certificate says the vaccine cannot be used widely until 1 January 2021, but does not explain the rationale. Vaccine researchers and public health specialists immediately denounced the certification as premature and inappropriate because the vaccine has yet to complete an efficacy trial that convincingly shows it is safe and effective in a large group of people. Critics

of Russia's move said it was politically motivated and meant to prop up the stature of its scientific community.

### A call for antibody treatments

**DRUG DEVELOPMENT** | Companies, academia, and governments should work to make monoclonal antibodies against many diseases more widely available to people across the globe, a report says. Antibody treatments have had an immense impact on treating several



types of cancer as well as autoimmune diseases and are increasingly used to fight infectious diseases like Ebola and HIV. But people in low- and middle-income countries hardly have any access to these expensive drugs, according to the report by the International AIDS Vaccine Initiative, a nonprofit research organization, and the Wellcome Trust, one of the world's biggest research funders. Academic researchers and governments can improve access, the report says, by supporting new technologies to make antibody treatments cheaper and clarifying and harmonizing regulations so that more countries can register the therapies. The report's authors also tout the potential for monoclonal antibodies to treat COVID-19 (see p. 752).

## Pollen reveals human footprint

**ECOLOGY** | Agriculture and other human activities have caused abrupt changes in North America's ecosystems more often in the past 250 years than the previous 11,000—more even than during a relatively short period of glacial advance and retreat from 13,000 to 11,000 years ago. At last week's virtual annual meeting of the Ecological Society of America, Stanford University paleoecologist M. Allison Stegner described her team's analysis of fossil pollen in 400 well-dated mud cores sampled from lakes across North America. Big shifts in pollen types

signaled major shifts in vegetation. When the last ice age ended roughly 11,000 years ago, forests and grasslands regrew across North America, creating a landscape that remained largely stable for thousands of years. But recently, humans have changed the landscape even more than melting glaciers, she reported, lending further support for the notion of a new epoch in geological history, the Anthropocene, defined by human activity.

**Number of abrupt ecosystem changes per every 250 years for every 100 sites studied**

15	10	20
13,000 to 11,000 years ago (glacial shifts)	11,000 years ago to 1700 C.E.	1700 C.E. to 1950 C.E.

## Gene renaming eases headaches

**DATA MANAGEMENT** | It was driving geneticists mad: When they entered the standardized symbols of certain human genes, such as MARCH1, into Microsoft Excel, the software program automatically converted them into dates, such as 1-Mar. Scientists could reformat columns to avoid the common problem, but many didn't, allowing errors to propagate in data sets and scholarly papers based on them. Last week, a fix was announced by an international group that manages the symbols, the Human Genome Organization's Gene Nomenclature

Committee. In *Nature Genetics*, it published revised naming guidelines that call for, among other updates, tweaking symbols known to autoconvert to dates. For example, DEC1, an abbreviation for "deleted in esophageal cancer 1," was renamed DELEC1; SEPT1 is now SEPTIN1. The committee, which considers such changes case by case, has altered 27 such symbols this year, reported The Verge, a news website.

## HIV-positive to join vaccine trials

**CLINICAL TRIALS** | In response to lobbying by AIDS activists and scientists, companies running two large clinical studies of COVID-19 vaccines have agreed to include people with HIV. Vaccine trials often exclude HIV-positive people because of concerns their infection would impair their responses to immunization. But the Infectious Diseases Society of America and AIDS activists argued that most HIV-infected people on antiviral treatment don't have suppressed immune systems and that leaving this group out would be wrong. Moderna and Pfizer, which each launched a 30,000-person U.S. phase III trial in late July, both announced last week that they plan to amend their protocols to include people with stable HIV. Lynda Dee of AIDS Action Baltimore says AstraZeneca plans to include HIV-positive people when it begins enrollment in a phase III vaccine trial at U.S. sites; a company spokesperson declined to confirm this.

## Neuroscience meeting axed

**COMMUNITY** | Organizers of one of the world's largest scientific meetings announced last week it will not take place online or in person this year because of COVID-19. Many scientific organizations have replaced in-person meetings with virtual ones this year, but the Society for Neuroscience (SfN) canceled its meeting altogether, citing risks and restrictions from the pandemic. About 30,000 neuroscientists had once planned to convene in Washington, D.C., in October. Some scientists criticized SfN's decision. "So you have \$70M [million] sitting in your bank account and you're telling us that can't organize an amazing virtual meeting with 6+ months notice?" computational neuroscientist Gunnar Blohm of Queen's University in Kingston, Canada, wrote on Twitter. Others, including neuroscientist Kay Tye of the Salk Institute for Biological Studies, said it was the right call. "It would have been a pretty sad virtual experience," she tweeted.

### ASTRONOMY

## The Milky Way's distant cousin

**A**stronomers were surprised to find that a galaxy formed just 1.4 billion years after the big bang looks remarkably like our well-ordered, disk-shaped Milky Way—a challenge to the conventional view that galaxies in the early universe were chaotic and unstructured. In *Nature* this week, a team of astronomers describes processing archival data from Chile's Atacama Large Millimeter/submillimeter Array of the distant galaxy SPT0418–47: observations captured it in its youth 12 billion years ago, when the universe was just 10% of its current age. The gravity of another galaxy between Earth and SPT0418–47 focused its rays, creating a circular image (right). But subsequent computer modeling revealed a rotating disk and central bulge, features thought to form much later in galactic evolution.

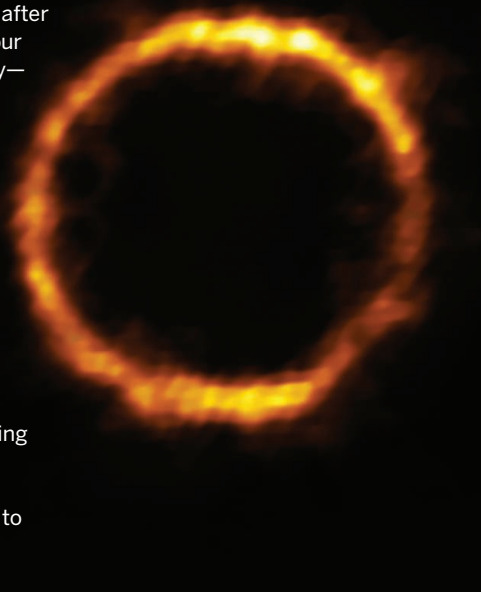
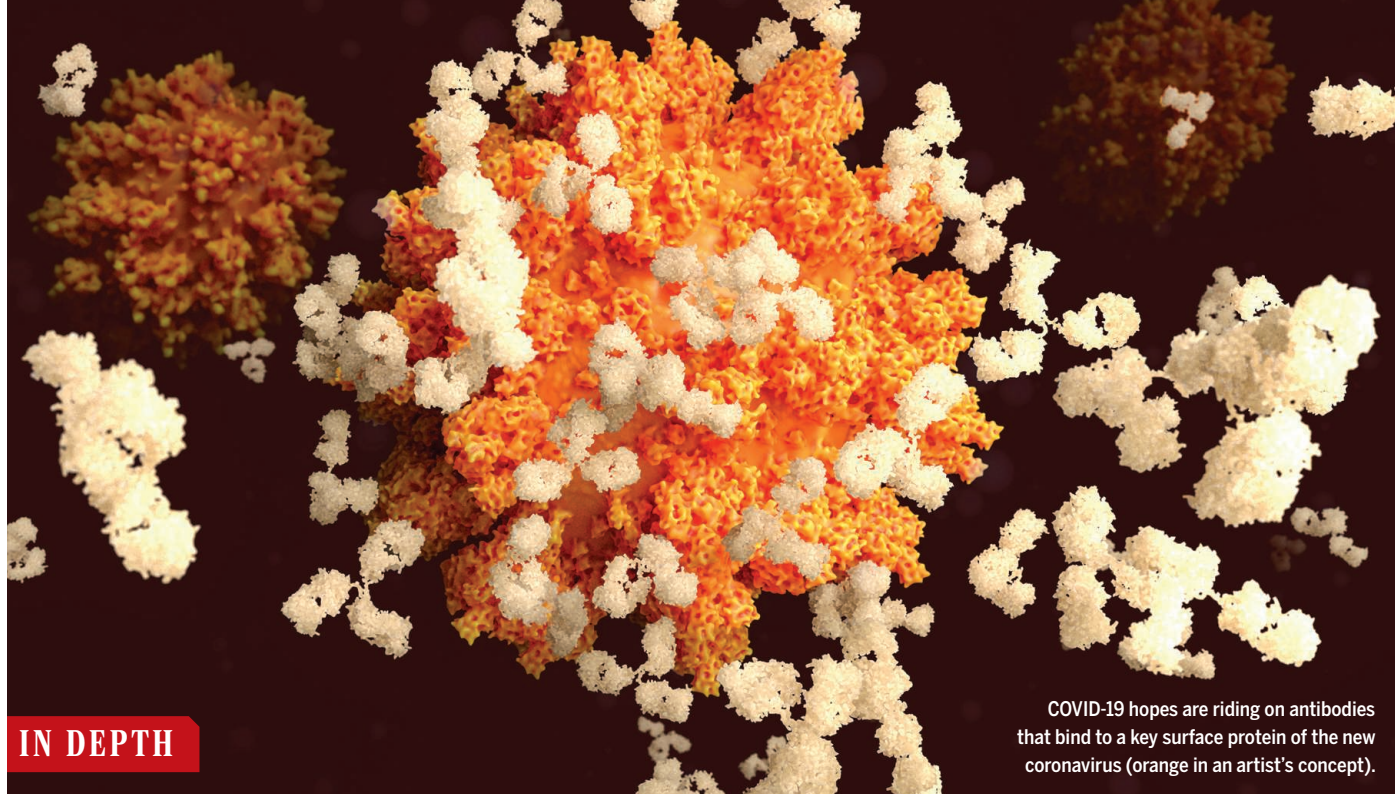


PHOTO: ALMA (ESO/NAOJ/NRAO); RIZZO ET AL.



COVID-19 hopes are riding on antibodies that bind to a key surface protein of the new coronavirus (orange in an artist's concept).

## IN DEPTH

### COVID-19

# Antibodies may curb pandemic before vaccines

Now in efficacy trials, monoclonal antibodies promise to both prevent and treat disease

By **Jon Cohen**

**W**hile the world is transfixed by the high-stakes race to develop a COVID-19 vaccine, an equally crucial competition is heating up to produce targeted antibodies that could provide an instant immune boost against the virus. Clinical trials of these monoclonal antibodies, which may both prevent and treat the disease, are already underway and could produce signs of efficacy in the next few months, perhaps ahead of vaccine trials. “If you were going to put your money down, you would bet that you get the answer with the monoclonal before you get the answer with a vaccine,” says Anthony Fauci, head of the National Institute of Allergy and Infectious Diseases (NIAID).

“Antibodies have the potential to be an important bridge until the vaccine is available,” says Ajay Nirula, a vice president at Eli Lilly, one of several large companies investing in them. Likely to be more effective than remdesivir and dexamethasone, the repurposed drugs shown to help against COVID-19, antibodies could protect the highest risk health care workers from becoming infected while also lessening the severity of the disease in hospitalized patients. But producing monoclonals involves using bioreactors to grow

lines of B cells that make the proteins, raising concerns they could be scarce and expensive. On 15 July, Lilly, AbCellera, AstraZeneca, GlaxoSmithKline, Genentech, and Amgen jointly asked the U.S. Department of Justice (DOJ) whether they could share information about manufacturing their monoclonals without violating antitrust laws “to expand and expedite production.”

Soon after the pandemic began, researchers in industry and academia began to identify, design, tweak, and conduct lab tests of monoclonal antibodies against SARS-CoV-2, the virus that causes COVID-19. Most bind to and “neutralize” the viral surface protein, or spike, that initiates an infection. On 29 May, Lilly, working with AbCellera, launched the first human study of a monoclonal antibody—a phase I trial testing its safety and tolerability in hospitalized COVID-19 patients. Other safety trials followed, from Lilly’s Chinese partner Junshi Biosciences and Regeneron, which developed a cocktail of three monoclonals that works against Ebola.

Regeneron is now testing the efficacy of its COVID-19 cocktail, which combines a spike antibody from a person who recovered and one from a mouse given the spike protein,

in three large-scale, placebo-controlled trials. A prevention trial run in coordination with NIAID’s COVID-19 Prevention Trials Network (CoVPN), an arm of the Trump administration’s Operation Warp Speed, will recruit 2000 people who live in a house with a confirmed COVID-19 case. One treatment study run by the company aims to enroll nearly 2600 hospitalized people with severe COVID-19, whereas another, about half that size, will test the antibodies in infected people

with mild or moderate symptoms. Lilly has launched its own trials, including a phase III, placebo-controlled study in 2400 residents or staff of long-term care facilities, run with the help of CoVPN.

“We should be able to see an efficacy signal very quickly” from these trials, says Amy Jenkins, who heads the Pandemic Prevention Platform

(P3) program at the Defense Advanced Research Projects Agency, which for 2 years has invested in speeding the development of monoclonal antibodies. Although Jenkins hesitates to make a firm prediction, she says the November-December time frame is “realistic and conservative.” That is likely earlier than any vaccine will prove safe and effective, researchers predict. “I would be reluctant to say [that] would be any earlier than the end

*Science’s*  
COVID-19  
reporting is  
supported by the  
Pulitzer Center  
and the  
Heising-Simons  
Foundation.



of the year,” Fauci said at a press conference about the launch of NIAID’s first COVID-19 efficacy vaccine trial on 27 July.

Regeneron’s Christos Kyratsous notes that vaccine trials must wait a few weeks for a person’s immune system to develop appropriate responses to shots and further weeks for “the event”—a chance exposure to SARS-CoV-2. This means those trials require time and many people. In contrast, for the antibody treatment trials, “your event has already happened,” Kyratsous says. And in the prevention studies, the household contacts of COVID-19 cases will be much more likely to be exposed than people who typically join a vaccine efficacy study.

Immunologist Dennis Burton, whose group at Scripps Research has isolated highly potent monoclonal antibodies against SARS-CoV-2 that it hopes to move into human studies (*Science*, 15 June, DOI: 10.1126/science.abc8511), says he is optimistic that monoclonals will protect people from infection for months with a single shot. “It’s much easier to take care of a few incoming virus particles than to try and resolve or cure an ongoing infection.” The same logic holds for treatment. “Hit the virus hard and early,” Burton says.

Kyratsous says even if monoclonal antibodies don’t beat vaccines to the finish line, they still might have a role to play against COVID-19. “We’re going to need both approaches in the long run,” Kyratsous suggests. Vaccines are rarely 100% effective, and many people may decline a vaccine or skip immunization for other reasons. What’s more, he notes, the elderly or people who are immune compromised may not mount robust immune responses after being vaccinated.

Supplies of monoclonal antibodies may be limited, however, in part because of modest investment. Operation Warp Speed, for example, has committed \$8 billion to six different COVID-19 vaccines; for monoclonals, the government has invested about \$750 million, much of it in Regeneron, which will produce somewhere between 70,000 and 300,000 doses before it even has efficacy data. Lilly says it will have 100,000 doses by the end of the year.

But no one knows how far those doses would stretch, says Janet Woodcock, who is on leave from the Food and Drug Administration to lead Warp Speed’s therapeutic effort. If the antibodies work, a study from the Duke University Margolis Center for Health Policy estimates the United States alone could require nearly 40 million doses

next year for prevention and treatment. “Unlike with vaccines, it is hard to project the number of treatment courses that will be available,” Woodcock says. Prevention, which would be a single intramuscular shot, requires less product than the intravenous infusions used in treatment, she notes, but the amount needed depends on a person’s weight.

Although how to prioritize vaccine distribution has already sparked extensive debate, no such discussion has yet taken place about monoclonal antibodies. But DOJ acknowledged the supply concerns on 23 July, giving the six companies that had petitioned it the green light to share production information.

Regeneron is not part of that group, yet Kyratsous is optimistic about meeting the need. “The good thing with some of these biologics is you can ramp up production fairly fast,” he says. Nirula agrees. “If we

have success in these clinical trials, we will have a lot of drug available,” he says.

The cost of monoclonals, especially for the higher doses needed for treatment, could split the world into the haves and have-nots. “It’s unlikely that that treatment will get down to a price point in the near future that it would be easily affordable globally,” says Seth Berkley, who leads Gavi, the Vaccine Alliance, and heads an international COVID-19 vaccine effort.

Jenkins says a key aim of the P3 project, which has provided four groups with \$96 million in seed money, has been to develop monoclonal antibodies that can be made by the body itself, instead of in large fermentation tanks. The idea, which has not yet been tested in humans for COVID-19, is to inject people with DNA or messenger RNA that encodes a desired antibody, allowing their own cells to make it. “We think we can bring down the cost of monoclonal antibodies,” Jenkins says.

Regardless of cost, evidence that monoclonals work as preventives could benefit everyone by giving vaccinemakers a clear sign that antibodies against the surface protein of SARS-CoV-2 are enough to protect a person. This, in turn, could provide a strong indicator for evaluating the worth of a candidate vaccine short of actual efficacy data. “It will be earthshaking to the vaccine field in a positive way,” says Myron Cohen of the University of North Carolina, Chapel Hill, who leads testing of monoclonal antibodies for CoVPN. “It provides a thousand opportunities to move forward faster.” ■

## COVID-19

# For science in Latin America, ‘a fascinating challenge’

Pandemic shows benefits of investments in research but also poses grave threats

By **Rodrigo Pérez Ortega** and **Lindzi Wessel**

**A**s the COVID-19 pandemic surged across the United States and Europe in February, scientists at Mexico’s Center for Research and Advanced Studies (Cinvestav) sprang into action. They quickly converted one of their research labs into a diagnostic clinic, and by mid-March, as cases began to mount in Mexico, they had launched seven other COVID-19-related projects.

Then a second crisis hit. On 2 April, Mexican President Andrés Manuel López Obrador ordered the termination of public trust funds, which pay for special and long-term projects at Cinvestav—a public institute with nine campuses that employs 7500 people—and other institutions. Three weeks later, he announced a 75% cut for some federal institutions’ operating budgets, including Cinvestav’s, that would have forced the institute to shut down, says Cinvestav Director José Mustre de León.

Another blow followed on 14 May, when the National Council of Science and Technology (Conacyt) asked scientists to donate their monthly federal supplement, a typical part of Mexican researchers’ income, to the nation’s health system to support the COVID-19 response. “Not only would we not have any money, but we’ll have to take money out of our own pockets,” says Gabriela Olmedo, a genetic engineer and director of Cinvestav’s Irapuato campus.

Mexican scientists aren’t alone in feeling conflicting pressures from the pandemic. Across Latin America, researchers have raced to contribute their expertise to the worst public health crisis in a century and demonstrate that several decades of investment in research—including the capacity to run large clinical trials—has paid off. “We basically showed that we have knowledge in the country that can be put to work for

**“Antibodies have the potential to be an important bridge until the vaccine is available.”**

Ajay Nirula, Eli Lilly



Students protest against a cut in the education budget at the Central University of Ecuador on 5 May.

the benefit of the society as a whole,” says Aisén Etcheverry, who heads Chile’s National Agency for Research and Development. At the same time, the pandemic has created deep economic and financial problems for the region, which faces a projected 5.3% contraction in gross domestic product this year. The resulting cuts are hitting science hard and threatening hard-won gains.

Latin America comprises less than 10% of the global population yet accounts for nearly one-third of reported COVID-19 deaths. In deaths and case counts, Brazil ranks second only to the United States; Colombia, Chile, Peru, and Mexico have been hard hit as well. The fallout could push an additional 16 million residents of the region into extreme poverty, according to a report from the United Nations.

Latin America’s growth in basic research, achieved through decades of investment in many countries, has put the region in a better position to fight back, says Hernando García Martínez, director of the Alexander von Humboldt Biological Resources Research Institute in Bogotá, Colombia. “We wouldn’t have had the capacity to respond to such a direct and real problem for society as COVID-19,” says García Martínez, who describes the crisis as a “fascinating challenge.”

In early April, Colombian researchers were among the first to start a clinical trial of convalescent plasma—antibody-rich serum from people who have recovered—for COVID-19 patients. More than 190 other clinical trials are ongoing in Latin America. Researchers in Brazil, Mexico, and Argentina have joined the race to develop their own vaccines and are partners in phase II and III trials of international vaccine front-runners.

In Argentina and Chile, science’s political standing has risen in the crisis. Argentine President Alberto Fernández, elected in 2019, was already taking a science-friendly approach, generally heeding his science advisers and promising more funding—a shift from his predecessor, who implemented devastating budget cuts and demoted the science ministry to a subsection of the Ministry of Education. Now, the public sees that prioritizing science helps Argentina respond to the pandemic, argues Juan Pablo Paz, secretary of scientific and technological coordination. “I think science will remain in a stronger position than before.”

In Chile, Etcheverry redirected her agency—part of a new science ministry and only 3 months old when the pandemic struck—to provide COVID-19 testing and other aid to the pandemic response and made money available to track societal impacts of the crisis, such as increases in domestic violence. Showing that science could help “generated a conversation inside the government that never had happened before,” Etcheverry says. “It’s definitely a turning point on how the sector is perceived.”

Still, the economic crisis has not spared Chilean science. Becas Chile, a scholarship program that funds international study for aspiring researchers and has boosted growth of many scientific fields in Chile, has been partly suspended. “Having that frozen or put into question just because we’re in a crisis is not the right decision because these are the kinds of things that prepare you for the next one,” says César Fuentes, an astronomer at the University of Chile.

The picture is darker in Peru, says Gisella Orjeda, former president of the country’s National Council of Science, Technology and

Technological Innovation (CONCYTEC). This year, the government paused certain funding programs; by July’s close, CONCYTEC had spent just 16% of its 2020 budget.

In neighboring Ecuador, new threats of cuts to higher education and the economic crisis have led scientists to ramp up efforts to secure funding by collaborating with researchers from the United States and the European Union, says Diego Quiroga, dean of research at San Francisco de Quito University. “If we don’t look abroad for funding, we’ll have nothing,” says Quiroga, who predicts the pandemic will cause an exodus of young scientists. As Mustre de León puts it: “We’re losing an entire generation of scientists.”

In Mexico, after an outcry from researchers, students, and the media, the president ordered Conacyt officials to drop their plea for donations. Cinvestav was allowed to keep its public trust funds for now and is negotiating a smaller budget cut. But other federal institutions will still see cuts, and the episode left scientists shaken and worried. “If we hadn’t had this budget cut environment, we could have done much more,” Mustre de León says. And the pandemic has worsened an already-tense relationship between the scientific community and Conacyt Director and developmental biologist María Elena Álvarez-Buylla Rocas, whose response to the pandemic they have criticized.

Elsewhere, too, the pandemic has deepened rifts between scientists and politicians. Brazilian President Jair Bolsonaro has repeatedly called into question scientific expertise, downplaying the severity of the pandemic and promoting treatments lacking evidence. In Venezuela, scientists’ alarms prompted threats from high-level government officials. And in Colombia, seven senators sent President Iván Duque Márquez a letter on 27 July complaining about a lack of leadership during the pandemic by Mabel Torres Torres, who leads the new Ministry of Science, Technology and Innovation and was previously engulfed in scandals over her promotion of an untested cancer treatment. “It’s an absent ministry,” says immunologist Gabriela Delgado Murcia of the National University of Colombia, Bogotá. “We feel desolate.” Two days later, the Ministry of Finance proposed a 35% cut for the country’s 2021 science budget.

Despite the challenges that the pandemic has brought, García Martínez remains hopeful. Years of scarce funding have taught Latin American researchers to do a lot with very little, he says—an especially helpful skill these days. “We are very adaptive.” ■

Rodrigo Pérez Ortega is a science journalist in Washington, D.C. Lindzi Wessel is a journalist in the San Francisco Bay Area.

PHOTO: RODRIGO BUENDIA/AFP/GETTY IMAGES



## VOICES OF THE PANDEMIC

# Looking for the light in Haiti

For physician Marie Marcelle Deschamps, COVID-19 is just the latest challenge

By Robert Bazell

**M**arie Marcelle Deschamps remembers the first patient with COVID-19 to visit a clinic she runs in Port-au-Prince, Haiti. It was late March. His blood oxygen saturation, normally above 90%, was 35%. The 45-year-old man died within 1 hour. “Oh my God,” she recalls telling her colleagues. “It’s here.”

As the director of a major health care organization in Haiti, Deschamps was already stretched thin by the struggles of providing medical help in one of the poorest nations on Earth. Her clinic was soon seeing thousands of COVID-19 cases per week, and her days became consumed with treating patients, supervising the other doctors, and dispatching teams to provide care and counseling to people in Haiti’s urban slums and countryside.

Those who have met Deschamps (including this reporter) know her as amazingly warm, bright, and charming. Clinic staff, patients, and even strangers greet her fondly as she rushes past. The need for women to take an increasing role in Haiti’s health care has long been identified as a key to economic development, and after 4 decades of practicing medicine in her native country, Deschamps is seen by many as an icon and a role model. “She is inspiring,” says Sandra Lamarque, head of mission in Haiti for Doctors Without Borders.

Jean William Pape, founding director of GHESKIO, the private nonprofit health organization Deschamps now heads, credits her for introducing multiple programs that have improved women’s health and wellbeing, including ones that care for victims of sexual assault, guide poor women in obtaining microcredit loans to start businesses, or help them get their children into schools. “When she sets out to solve a problem, it gets solved,” says Pape, who now co-directs Haiti’s response to COVID-19.

Deschamps decided on a career in medicine after witnessing her father die a slow death from kidney failure. “I had such a de-

sire to become a good doctor,” she says. The beginning of her career coincided with the huge outbreak in Haiti of the disease that came to be called HIV/AIDS, before there were meaningful treatments. She recalls telling her husband, “I am signing so many death certificates I hope that one day people won’t judge me for being a bad doctor.”

In the early days of the HIV/AIDS crisis,

a tiny building across the street from an enormous slum known as City of God into a health organization that now treats more Haitians with HIV/AIDS and tuberculosis than any other group in Haiti, as well as caring for people with myriad other maladies.

Deschamps sees COVID-19 as just the latest chapter in the Haitian saga. “Every time you make progress, finding the solutions,

you are pushed back by either a natural or political catastrophe,” she says. “You are always in a situation of crisis where you have to act rapidly.” After the devastating 2010 earthquake, Deschamps’s clinic allowed hundreds of slum dwellers whose shacks had collapsed to camp on its property. She and her colleagues circulated among the injured treating horrible fractures and other injuries.

Soon after the earthquake, U.N. troops from Nepal unknowingly brought a cholera epidemic to Haiti that sickened more than 800,000 and killed more than 10,000 over several years, putting enormous additional stress on all of Haiti’s health facilities, including Deschamps’s clinics. “The country has been very vulnerable,” Deschamps says, citing threats as diverse as political destabilization, impacts of deforestation on farmland and drinking water sources, hurricanes, and a never-ending procession of infectious diseases. “Now COVID,” she says with a laugh. “So, I said to my myself, what is it we have not seen finally?”

Until Deschamps saw her first COVID-19 patient in late March, Haiti’s poverty and isolation had kept it relatively safe from the pandemic. The government had taken precautions, closing the international airport and shutting down

businesses. Two infected travelers, one from the United States and one from Europe, had been discovered and quickly isolated.

But the patient in her clinic—and others who quickly followed—had been working at hotels in the Dominican Republic, which shares a porous border with Haiti on the island of Hispaniola. Because it is a popular winter tourist destination for people from



**“Every time you make progress ...  
you are pushed back by either a natural  
or political catastrophe.”**

Marie Marcelle Deschamps, GHESKIO

a group of senior Haitian and U.S. doctors chose Deschamps to study in the United States, where she did fellowships in Anthony Fauci’s lab at the National Institute of Allergy and Infectious Diseases, Walter Reed military hospital, and the Centers for Disease Control and Prevention. On her return to Haiti, she and Pape expanded GHESKIO. It grew from humble origins in

the northeastern United States and Europe, the Dominican Republic got hit hard and early with COVID-19. More than 30,000 Haitians lost their jobs there and were either forced out or fled home—some bringing the virus with them. Another 300,000 had commuted back and forth for occasional work.

For several weeks, Haiti saw large numbers of COVID-19 cases, often overwhelming the relatively few available hospital beds. Because many Haitians lack shelter, food, and medical care, the United Nations Economic and Social Council warned that COVID-19 could trigger a humanitarian catastrophe, a theme echoed in a letter co-authored by Deschamps and published on 16 June in *The New England Journal of Medicine* titled Facing the Monster in Haiti.

The letter warned that stigmatization—once directed against those with HIV—was now impeding care for those with COVID-19. Health care workers have endured threats and had stones thrown at them. Some patients have been driven from their homes and shunned by relatives, forcing them to live on the streets. Deschamps has directed community health workers to try to combat stigma and educate people about safety measures, but she acknowledges it isn't easy. "How can you ask someone to adopt proper distancing measures when five people are living in one room?"

So far, however, the worst predictions haven't come to pass. Although testing and surveillance is limited, the official number of confirmed cases declined from almost 300 per day in mid-June to about 100 in mid-July. As of 9 August, Haiti had reported only 183 COVID-19 deaths in its population of 11.2 million. Deschamps says that even at current levels COVID-19 represents a huge burden, but she is "hopeful and skeptical at the same time" about the future.

Some other resource-poor countries have reported similar declines in cases. Global health experts have speculated that those countries may benefit from relatively younger populations, shanties that though crowded are well-ventilated, or a more effective early immune response to COVID-19 because of the many other infections people face. "We just don't know the reasons for this but it is a very intriguing question," says immunologist Barry Bloom, former dean of the Harvard T.H. Chan School of Public Health.

Although she could live and practice medicine anywhere, Deschamps insists she'll never leave Haiti. "This is my place," she says. Haitians are resilient, she says, in spite of all they've endured. "It's not that we forget ... [but] we are always looking for the light." ■

Robert Bazell, an adjunct professor at Yale University, is a journalist based in New Haven, Connecticut.



Children run past a mural warning about COVID-19 in Nairobi. Kenya has reported relatively few cases so far.

## COVID-19

# Africa's pandemic puzzle: why so few cases and deaths?

Antibody surveys tell a different story than official tolls

By Linda Nordling

**A**lthough Africa reported its millionth official COVID-19 case last week, it seems to have weathered the pandemic relatively well so far, with fewer than one confirmed case for every thousand people and just 23,000 deaths. Yet several antibody surveys suggest far more Africans have been infected with the coronavirus—a discrepancy that is puzzling scientists around the continent. "We do not have an answer," says immunologist Sophie Uyoga of the Kenya Medical Research Institute–Wellcome Trust Research Programme.

After testing more than 3000 blood donors, Uyoga and colleagues estimated in a preprint last month that one in 20 Kenyans aged 15 to 64—or 1.6 million people—has antibodies to SARS-CoV-2, an indication of past infection. That would put Kenya on a par with Spain in mid-May, when that country had 27,000 official COVID-19 deaths. Kenya's official toll stood at 100 when the study ended. And Kenya's hospitals are not reporting huge numbers of people with COVID-19 symptoms.

Other antibody studies have yielded similarly surprising findings. From a survey of 500 asymptomatic health care workers in

Blantyre, Malawi, immunologist Kondwani Jambo of the Malawi–Liverpool Wellcome Trust Clinical Research Programme and colleagues concluded that up to 12.3% of them had been exposed to the coronavirus. Based on those findings and mortality ratios for COVID-19 elsewhere, they estimated that reported number of deaths in Blantyre at the time, 17, was eight times lower than expected.

Scientists who surveyed about 10,000 people in two cities in Mozambique, Nampula and Pemba, found antibodies to SARS-CoV-2 in 3% to 10% of participants, depending on their occupation; market vendors had the highest rates, followed by health workers. Yet in Nampula, a city of approximately 750,000, a mere 300 infections had been confirmed at the time. Mozambique only has 16 confirmed COVID-19 deaths. Yap Boum of Epicentre Africa, the research and training arm of Doctors Without Borders, says many people in Cameroon have COVID-19 antibodies as well.

So what explains the huge gap between antibody data and the official toll? Part of the reason may be that Africa misses many more cases than other parts of the world because it tests far less. Kenya tests about one in every 10,000 inhabitants daily for active SARS-CoV-2 infections, one-tenth of

PHOTO: AP PHOTO/BRIAN INGANGA



the rate in Spain or Canada. Nigeria tests one out of every 50,000 people per day. Even many people who die from COVID-19 may not get a proper diagnosis. But in that case, you would still expect an overall rise in mortality, which Kenya has not seen, says pathologist Anne Barasa of the University of Nairobi. Uyoga cautions that the pandemic has hamstrung Kenya's mortality surveillance system, however.

Marina Pollán of the Carlos III Health Institute in Madrid, who led Spain's antibody survey, says Africa's youthfulness may protect it. Spain's median age is 45; in Kenya and Malawi, it's 20 and 18, respectively. Young people around the world are far less likely to get severely ill or die from the virus. And the population in Kenya's cities, where the pandemic first took hold, skews even younger than the country as a whole, says Thumbi Mwangi, an epidemiologist at the University of Nairobi.

Jambo is exploring the hypothesis that Africans have had more exposure to other coronaviruses that cause little more than colds in humans, which may provide some defense against COVID-19. Another possibility is that regular exposure to malaria or other infectious diseases could prime the immune system to fight new pathogens, including SARS-CoV-2, Boum adds. Barasa, on the other hand, suspects genetic factors protect the Kenyan population from severe disease.

More antibody surveys may help fill out the picture. A French-funded study will test thousands for antibodies in Guinea, Senegal, Benin, Ghana, Cameroon, and the Democratic Republic of the Congo. And 13 labs in 11 African countries are participating in a global SARS-CoV-2 antibody survey coordinated by the World Health Organization.

If tens of millions of Africans have already been infected, that raises the question of whether the continent should try for "herd immunity" without a vaccine, Boum says—the controversial idea of letting the virus run its course to allow the population to become immune, perhaps while shielding the most vulnerable. That might be preferable over control measures that cripple economies and could harm public health more in the long run.

"Maybe Africa can afford it," given the apparent low death rate, he says. But Glenda Gray, president of the South African Medical Research Council, says it could be dangerous to base COVID-19 policies on antibody surveys. It's not at all clear whether antibodies actually confer immunity, and if so, how long it lasts, Gray notes—in which case, she asks, "What do these numbers really tell us?" ■

Linda Nordling is a journalist in Cape Town, South Africa.

## CAREERS

# Fed-up archaeologists aim to fix field schools' party culture

## Drinking and harassment spur experiments, including local projects and student stipends, for core training course

By **Lizzie Wade**

**E**ach year, archaeologist Carol Colaninno guides undergraduates through a consequential choice: Where should they go to field school? Every budding U.S. archaeologist must attend one to learn hands-on skills such as excavation, and to have any hope of landing a job or entering grad school for archaeology.

The undergrads can choose from hundreds of field schools, many in remote areas. But Colaninno, who teaches at Southern Illinois University, Edwardsville, knows from former students and information passed privately among others in her whisper network that some field schools have a reputation for faculty who sexually harass with impunity. Many schools are also famed for heavy drinking.

Traditional field schools foster "the archaeology cowboy mentality ... working really hard during the day but playing really hard at night—and drinking a ton," says Katrina Eichner, an archaeologist at the University of Idaho. If directors of these field schools encourage that atmosphere, she adds, "it devolves into a frat party." Over time, that cowboy culture gets perpetuated across academic generations.

Now, Colaninno, Eichner, and other archaeologists are trying to change the script. With the help of a National Science Foundation (NSF) grant, Colaninno is studying, and plans to implement, best practices for preventing sexual harassment at field schools. And some archaeologists, aware that remote summer courses can cost thousands of dollars and keep students of modest means out of the field altogether, are rethinking the whole model: They teach field skills at local sites during the regular semester. "We don't have to create the same environment that we didn't want to be in when we were students," says Jane Eva Baxter, an archaeologist at DePaul University and the author of a respected guide for field school instructors.

Although field schools are on hold this year because of the COVID-19 pandemic,

researchers say it's more important than ever for academic archaeologists to take the lead in making such schools safe. New regulations under Title IX, the U.S. federal law governing sexual harassment in higher education, no longer require universities to investigate incidents that happen in their programs abroad.

Although anecdotes of sexual harassment in field schools are plentiful, data on such episodes are limited. But studies show they are common in archaeology, as they are in other field-based disciplines. In a survey by the Southeastern Archaeological Conference, 68% of 244 respondents of all genders

reported inappropriate remarks in the field; another 13% reported unwanted sexual contact. Remote sites and field schools have been considered "an alternative space where different rules applied," Baxter says.

The current culture at such sites and schools may drive some students out of the profession, according to a paper published last month in *American Anthropologist*. An atmosphere of informality, including frequent drinking, undermined expectations of professionalism and excluded people who weren't willing or able to navigate the unspoken rules, according to the paper's analysis of archaeological field sites and an anonymous field school in Chile. "It weeds out people," says author Mary Leighton, an anthropologist at the University of Michigan, Ann Arbor. "The people who love it, stay [in archaeology]. And the people who don't like it leave."

To create a more welcoming and professional culture, Colaninno's team recently offered recommendations from the first phase of its research. The suggestions include: Create an environment that doesn't trivialize harassment, offer multiple ways to report harassment other than going to the field director, and reflect weekly on what's working and what isn't. The team, which published its guidance in May in *Advances in Archaeological Practice*, plans to implement those policies at eight U.S. field

**"The archaeology cowboy mentality ... devolves into a frat party."**

**Katrina Eichner,**  
University of Idaho

schools as part of its NSF-funded project, and study outcomes over 2 years.

In April, a study in *Advances in Archaeological Practice* addressed another way field schools weed out students: cost. Among more than 200 field schools, the average cost for 4 weeks was just over \$4000, not including airfare, the study found. Field school also interferes with summer jobs.

Archaeologists need to “think of ways to train students that are more in line with the realities of their lives,” Baxter says. Her department no longer requires anthropology majors to attend a summer field school. Instead, they take a field methods course that runs 1 day per week during the school year.

Similarly, for three recent semesters, Sarah Rowe, an archaeologist at the University of Texas, Rio Grande Valley, ran a class that trained students in archaeological survey, data collection, and community engagement as they investigated their county’s public cemetery. She also runs a field school in Ecuador, which offers several weeks of immersive training in excavation. “We need to focus on a constellation of options” for training students, she says.

Well-managed, immersive field schools can build powerful and lasting bonds, says Sara Gonzalez, an archaeologist at the University of Washington, Seattle. She co-directs a field school with the Historic Preservation Office of the Confederated Tribes of Grand Ronde Community of Oregon on their reservation. “It’s an opportunity for students to learn directly from the tribe how to do archaeology.” The school prohibits alcohol and emphasizes inclusivity and respect. Each summer begins with discussions of what students are most excited about—and

most afraid of. Together, the team comes up with principles to “minimize those fears and maximize that excitement,” Gonzalez says.

To boost access to archaeology, Eichner found grant funding so that students at the Texas field school she ran paid only for room and board. She also surveyed students so she could accommodate diverse gender identities, disabilities, and more. She estimates that 20% to 30% of students belonged to the LGBTQ+ community. “This is not extra work,” she says. “This is the work.”

Justin Dunnivant of Vanderbilt University, co-founder of the Society of Black Archaeologists, is particularly aware of how field schools shape the culture of his discipline. The society interviewed established Black archaeologists and found that attending field school together had helped them forge a strong, supportive community in a majority white discipline. (Just 0.3% of members of the Society for American Archaeology are Black, according to a 2015 survey.) “If we’re going to seriously build out a pipeline of Black archaeologists, we need to have a field school that is racially diverse and supportive,” Dunnivant says.

He keeps that in mind at the field school he co-directs, where students help study the lives of enslaved Africans on a former plantation on St. Croix in the U.S. Virgin Islands (*Science*, 8 November 2019, p. 678). A grant covers the costs of students from historically Black colleges and universities and pays them a stipend. The team could excavate faster if it focused less on training, Dunnivant says. But sprinting for results is not his goal. “If we’re not actually building capacity for people to take over in these spaces and beyond, it’s going to be a very short-term gain.” ■

## ECOLOGY

# Don’t crush that ant—it could plant a wildflower

New findings show how ants choose and protect the seeds they disperse

By Elizabeth Pennisi

**T**illiums, bloodroot, violets—many wildflowers of spring in eastern North America bloom thanks to ants. The tiny six-legged gardeners have partnered with those plants as well as about 11,000 others to disperse their seeds. The plants, in turn, “pay” for the service by attaching a calorie-laden appendage to each seed, much like fleshy fruits reward birds and mammals that discard seeds or poop them out. But there’s more to the ant-seed relationship than that exchange, researchers reported last week at the annual meeting of the Ecological Society of America, which was held online.

Far from just transporting the seeds, the ants are active gardeners, preferring some seeds over others and possibly keeping their charges safe from disease. “It’s becoming clear that it’s not a simple two-way interaction,” says Douglas Levey, an ecologist at the National Science Foundation.

The importance of this partnership is coming into focus as well. In forests disturbed by human activity, where ants can be scarce, seeds may not find their way to fertile ground, and ecosystems can suffer. “If ants are lost, then there’s a real chance that we will lose plants, as well as the other species that depend upon ants and plants,” says Judith Bronstein, an evolutionary ecologist at the University of Arizona.

Many ants eat seeds, but in deciduous forests in Europe and North America, Australian dry woodlands, and South African shrublands called fynbos, a few dozen ant species spare the seeds in favor of something better. Certain plants attach a nutritive glob called an elaiosome to their seed coats, which serves as lunch for the ants’ young and gives ants a handle on seeds that can be bigger than their head. Until now, researchers assumed the ants simply carry



Students and instructors at an archaeological field school in St. Croix forge ties for the future as they learn.

PHOTO: M. CANTWELL/SCIENCE





In return for these *Aphaenogaster* ants dispersing its seeds, bloodroot attaches a tasty “handle” that gives the ants a reward and a way to carry the seed to their nest.

the seeds to their nests, feed the elaiosome to their broods, and deposit the seed either outside or inside at the colony’s “garbage dump,” which provides a fertile environment for sprouting. But Charles Kwit, an ecologist at the University of Tennessee, Knoxville, thought ants might help seeds with more than just transportation.

The common seed-dispersing ants in the genus *Aphaenogaster*, like others, secrete antimicrobial chemicals to clean themselves and fellow ants. Kwit wondered how those disinfectants might affect the seeds’ microbial communities—and their health. He and his graduate student Chloe Lash teamed up with Melissa Cregger of Oak Ridge National Laboratory to isolate and sequence DNA from microbes on the seed coats of three common ant-dependent plants: wild ginger, bloodroot, and twinleaf. To start, each species’ seed had a complex and unique microbiome—its community of bacteria and fungi. But after an ant handled a seed, its microbiome shrank and became more similar to those of other handled seeds of different species, Lash reported at the meeting—apparently because of the antimicrobial treatment. Wild ginger and twinleaf also harbored fewer plant pathogens. The microbiome changes, Levey says, “could affect postdispersal seed predation, dormancy, seed viability, timing of germination, and health of the resulting seedlings.”

Kwit’s lab has also found that when it comes to seeds, ants have preferences that may influence the plants’ success. In both the field and the lab, his student Chelsea Miller presented ants with seeds from various trillium species and found the ants were quick to pick up some species’ seeds

while leaving others to rot, Miller told the meeting. “So being less preferred really has consequences,” Bronstein says.

To find out how ants make their choices, Miller and Susan Whitehead at the Virginia Polytechnic Institute and State University (Virginia Tech) used mass spectroscopy and other techniques to analyze the chemical makeup of elaiosomes. They found that ants pick seeds based on the specific combination and concentrations of oleic acid and other compounds made by the plant, 20 of which are unique to trilliums. The ants’ tastes may affect plant species’ distributions, says Kirsten Prior, an ecologist at Binghamton University: “Widespread trillium species [are] preferred by seed-dispersing ants compared to rare trillium species.”

Human activities, too, can influence ant-seed partnerships. Many researchers assumed ants survive disruptions such as forest clearing and quickly move back into disturbed areas. But Katie Stubble, an ecologist at the Holden Arboretum in Kirtland, Ohio, found otherwise. “Land-use history impacts ant communities,” she said at the meeting. Her arboretum covers 1416 hectares, much of it cleared for farmland at different times over the past century before the trees regrew.

Even in areas cleared decades ago, her team found higher concentrations of invasive earthworms and lower concentrations of seed-dispersing ants than in forests that were never cleared. Earthworms break down fallen leaves and organic debris, possibly leaving too little cover for ants. “This suggests that there are huge impacts of past land use that probably run deeper than we previously suspected,” Stubble says. Those impacts could explain

why secondary forests lack dense undergrowth, and why plants that rely on ants to disperse their seeds are scarce there.

At the meeting, Prior and her student Carmela Buono reported that a survey of 20 sites in northeastern North America showed a similar trend. Compared with never-cleared forests, secondary forests had fewer *Aphaenogaster* ants, which disperse up to 70% of seeds in a deciduous forest, Buono said. The secondary forests had less leaf litter and fewer decaying logs for ants to colonize. They also had more invasive slugs, which compete with ants by eating the elaiosomes—and leaving seeds behind, rather than dispersing them. The loss of seed-carrying ants “has major implications for forest communities and restoration,” Prior says. “To restore understory plant communities, we might also need to think about having to restore this important species interaction.” For example, it might help to ensure there are plenty of decaying logs and leaf litter for the ants to thrive in.

Bronstein notes that in the past, ecologists deciphered ants’ role as gardeners through painstaking observations. Now, she says, “There are exciting testable hypotheses, well-designed experiments, serious phytochemical analyses, and sophisticated statistical approaches,” as well as genome sequencing and fine-scale chemical analyses.

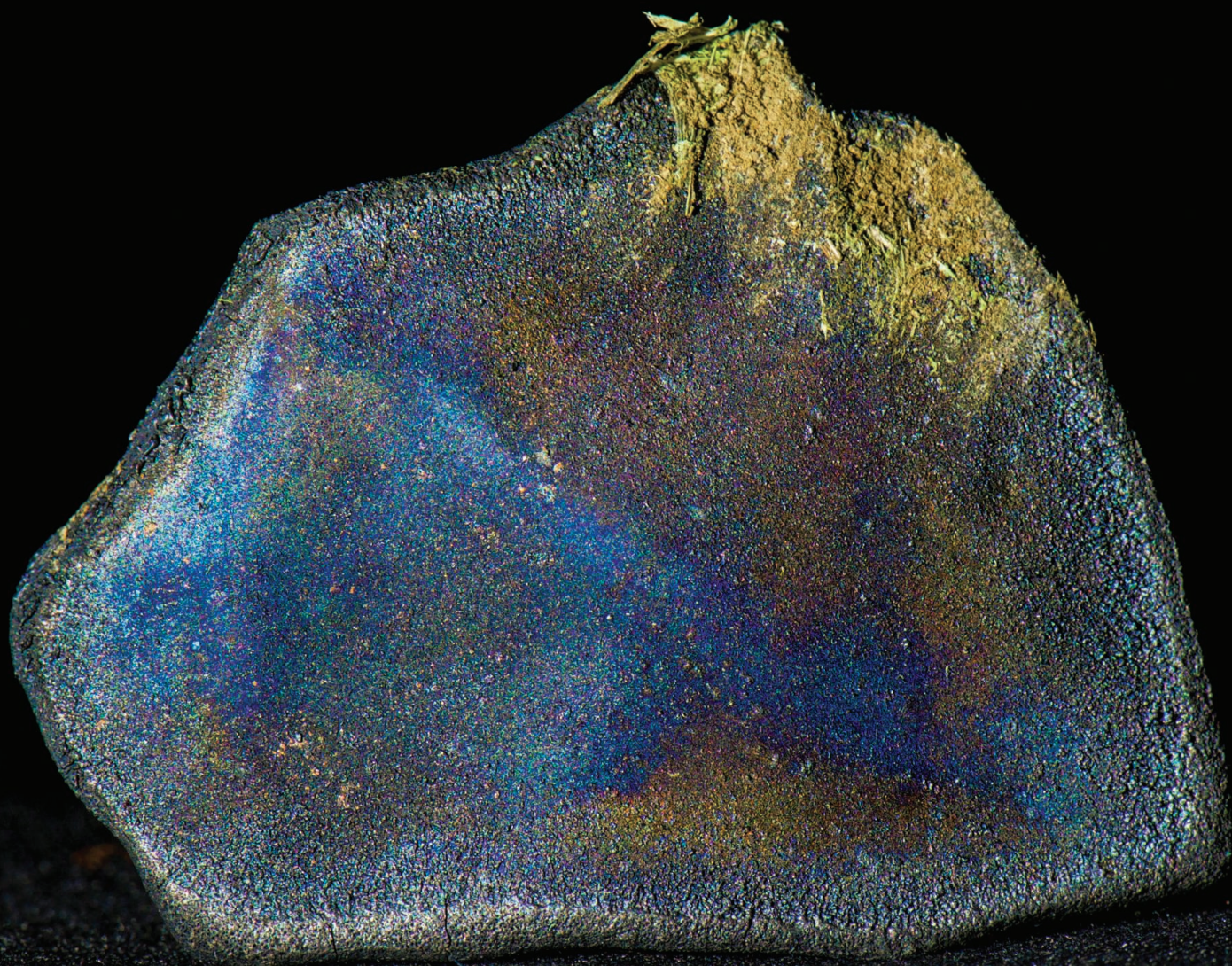
Melissa Burt, an ecologist at Virginia Tech, hopes these studies bring ants new respect. “Many people that I talk to about ants only know them as pests that are taking over their kitchens, but many ants perform important functions in ecosystems,” she says. “Seed dispersal is just one of those.” ■



# LUCKY STRIKE

Last year, an unusual meteorite crashed in a Costa Rican rainforest. Rich in the building blocks of life, it has captivated collectors and researchers

By **Joshua Sokol**





**A**s the fiery emissary streaked across the skies of Costa Rica, an unearthly mix of orange and green, Marcia Campos Muñoz was in her pajamas, watching TV on the couch. It was 23 April 2019, a bit past 9 p.m., when she heard a foreboding rumble. Heart racing, she tiptoed outside to calm her barking dog, Perry, and to check on the cow pastures ringing her small house in Aguas Zarcas, a village carved out of Costa Rica's tropical rainforest. Nothing. She ducked back inside, just before a blast on the back terrace rattled the house to its bones.

Campos Muñoz phoned her father, brother, and oldest son, who rushed to the house. On the terrace, they found a grapefruit-size hole in the corrugated zinc roof and a smashed-up plastic table, last used for the quinceañera of Campos Muñoz's daughter. The culprit was scattered on the floor, in pieces as black as coal.

She picked up the biggest fragment, still warm to the touch. Already, her phone was chiming with WhatsApp messages from friends telling of blazing fireballs and rocks raining down on farms and fields. The family added its own viral messages to the mix: photos of Campos Muñoz and her son holding the big stone that crashed through her roof. Within hours, a local journalist visited the house and streamed videos of the damage on Facebook Live.

It was only the beginning. A space rock the size of a washing machine had broken up in the skies over the village, and the excitement was about to spread globally.

Meteorites are not uncommon: Every year, tens of thousands survive the plunge through Earth's atmosphere. More than 60,000 have been found and classified by scientists. But meteorite falls, witnessed strikes that take their name from where they land, are rare—just 1196 have been documented. And even among that exclusive group, there was something extraordinary about this particular meteorite, something anyone with the right knowledge could know from the first pictures. The dull stone was, as far as rocks go, practically alive.

Aguas Zarcas, as the fragments would soon collectively be called, is a carbonaceous chondrite, a pristine remnant of the early Solar System. The vast majority of meteorites are lumps of stone or metal. But true to their name, carbonaceous chondrites are rich in carbon—and not just

boring, inorganic carbon, but also organic molecules as complex as amino acids, the building blocks of proteins. They illustrate

how chemical reactions in space give rise to complex precursors for life; some scientists even believe rocks like Aguas Zarcas gave life a nudge when they crashed into a barren Earth 4.5 billion years ago.

From the beginning, the inky Aguas Zarcas resembled a legendary carbonaceous chondrite that exploded in 1969 over Murchison, an Australian cattle town. Geology students helped collect about 100 kilograms of Murchison, and a local postmaster mailed pieces of it to labs across the world. To date, scientists have recognized nearly 100 different amino acids in it, many used by organisms on Earth and many others rare or nonexistent in known life. Hundreds more amino acids have been inferred but not yet identified.

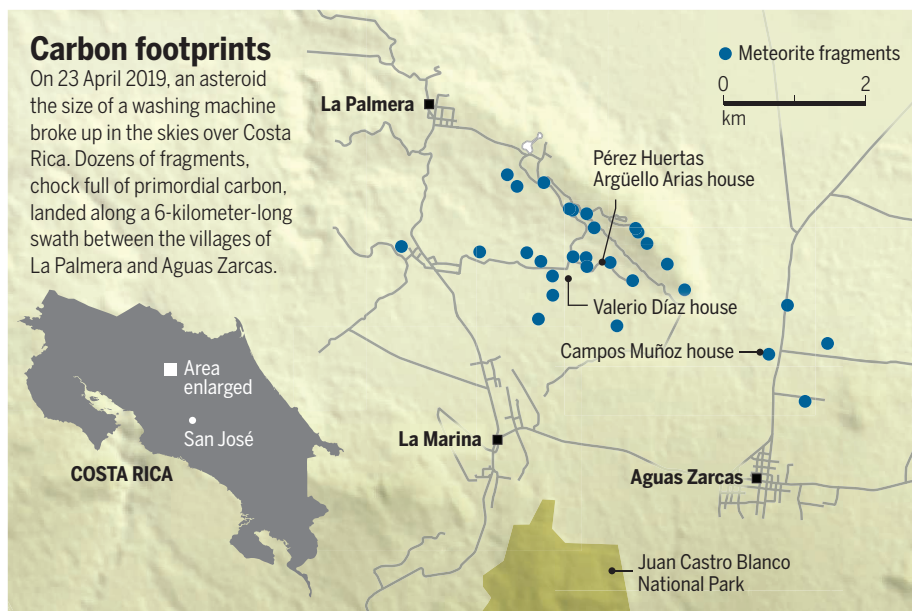
confirmed in a meteorite. And if they were clean and careful, they could hedge against a perennial criticism of the Murchison finds by ensuring the molecules discovered inside were native, and not contamination from Earth's own microbes.

"If I had to start a new museum collection for meteorites, and I could only select two, I would choose Murchison and Aguas Zarcas," says Philipp Heck, who curates the meteorite collection at Chicago's Field Museum. "If I could choose only one, I would choose Aguas Zarcas."

**FROM THE INSTANT** the rock entered the atmosphere, however, the clock began to tick. Clays—its major constituent—soak up surrounding air and water like a sponge;

## Carbon footprints

On 23 April 2019, an asteroid the size of a washing machine broke up in the skies over Costa Rica. Dozens of fragments, chock full of primordial carbon, landed along a 6-kilometer-long swath between the villages of La Palmera and Aguas Zarcas.



Murchison also contained nucleobases, the building blocks of genetic molecules such as RNA, and in November 2019, researchers found a major component of RNA's backbone: the sugar molecule ribose. This half-century parade of discoveries jump-started the now-flourishing field of astrobiology. "We're not detecting life itself, but the components are all there," says Daniel Glavin, an astrobiologist at NASA's Goddard Space Flight Center. "I wouldn't have a job without Murchison."

The 30 kilograms of primordial leftovers from Aguas Zarcas hold similar promise. But these new pieces are 50 years fresher than Murchison, allowing scientists to apply modern techniques to preserve and probe what amounts to fragile lumps of unspeakably old clay. They could sniff out delicate organic compounds long evaporated from Murchison. They could hunt not just for amino acids and sugars, but also proteins, which have long been suspected but never

earthly amino acids and other organic compounds intrude, layer by layer, followed by the microbes that produced them. Each second in contact with moist rainforest soil or human hands destroys more information. "Ideally we pluck it from the air while it's coming down," says Ashley King, a planetary scientist at London's Natural History Museum, "whilst wearing gloves."

For billions of years, Aguas Zarcas had avoided such contaminating influences. If it could stay that way just a little longer, scientists would be able to recover information from three ancient, otherwise inaccessible periods.

The first predates the Solar System. Some 7 billion or 8 billion years ago, specks of stardust were ejected from supernovae and the outer atmospheres of aging stars, some made of hardy materials such as graphite, diamond, and silicon carbide. The size of smoke particles, they drifted in space, settling in a

nameless interstellar cloud.

In the next phase, that formless cloud collapsed into a disk swirling around the newborn Sun, generating frictional heat that roasted everything but those presolar grains into a seething vapor. As the disk cooled, the first solids condensed out like frost on a window-pane: crystalline clumps of aluminum and calcium as big as poppy seeds. These fragments date back 4.56 billion years, defining the age of the Solar System. Within a few million years, molten drops of rock cooled into glassy spheres—the “chondrules” that give chondrites their name.

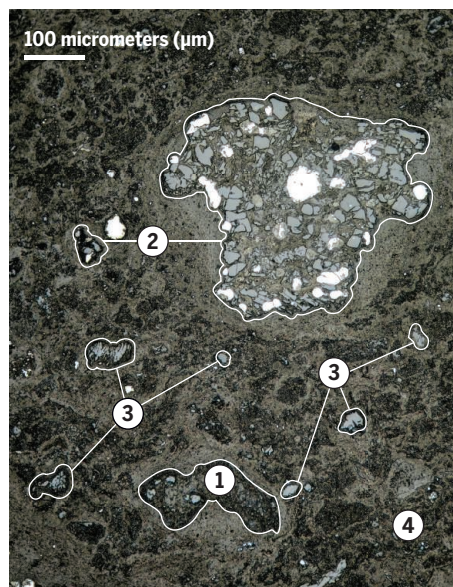
Then, in the third phase, these small particles started to stick together into boulders, among them the hodgepodge of rocks that would become Aguas Zarcas. Planets began

to sweep them up, but the future meteorite avoided that fate, remaining part of a small asteroid in the cold void beyond Jupiter. In that early home, it avoided being melted by the Sun or in the hot interior of a planet.

Instead the asteroid grew modestly, amassing specks of ice and carbon, the latter already morphing as sunlight drove chemical reactions. In its interior, the presolar stardust, the first solid minerals, the glassy spheres, and the carbon compounds all crowded together. Heat from the radioactive aluminum melted the ices. Liquid water gushed out, kicking off another wave of chemistry that would go on for a few million years more. Simple compounds such as hydrogen cyanide and ammonia dissolved and were transformed into amino acids and other complex forms.

## Heavenly messenger

Aguas Zarcas belongs to a rare class of meteorites, rich in complex organic molecules, including amino acids. Some scientists believe they gave life a nudge when they slammed into a barren Earth 4.5 billion years ago.



### Mix and match

The meteorite is a breccia—a mashup of different primordial bodies. A close-up of a cross section reveals key ingredients.

#### 1 Calcium-aluminum-rich inclusions (CAIs)

Dates from 4.56-billion-year-old CAIs, the first solids to condense from a disk of hot gas, define the age of the Solar System. Isotopes in the clumps record the early Sun's activity levels.

#### 2 Chondrules

Soon after the CAIs, glassy spheres solidified. Chondrules were first described as “droplets of fiery rain” in 1877, but theorists cannot agree on how they formed.

#### 3 Calcite

Crystals of calcite are a sign of aqueous alteration—the watery chemistry that drove the creation of complex organic molecules.

#### 4 Matrix

The dark, surrounding matrix is made of clay and holds the organic molecules. It may also contain a precious few presolar grains: hardy specks of stardust that predate the Solar System.

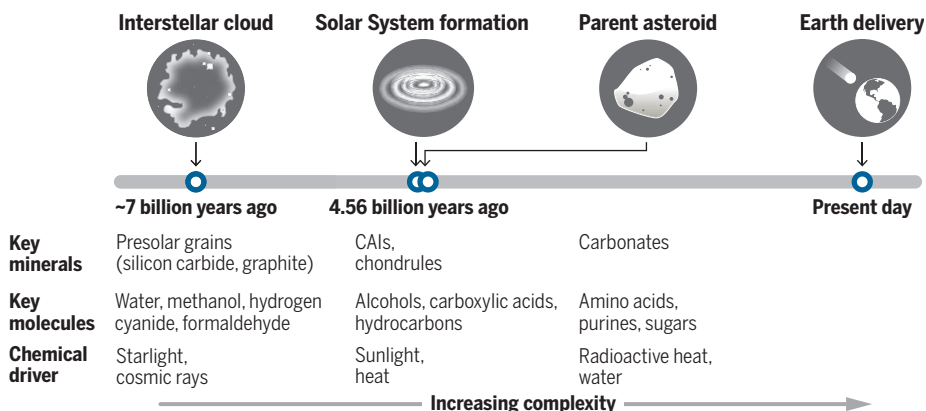
#### Presolar grain

3 μm



### Time capsule

Aguas Zarcas holds minerals and molecules forged billions of years ago in three distinct periods. Light, heat, and water drove chemical reactions that created increasingly complex organic molecules.



Many carbonaceous chondrites crashed into early Earth, perhaps delivering not just a sprinkling of organics, but also a portion of the planet's inventory of water. Aguas Zarcas itself endured several billion more years of solitude, save for occasional smashups with other wayward space rocks. Based on its fiery trajectory through Earth's atmosphere, caught on dashcams and volcano-monitoring cameras, researchers believe the unknown body ended up in the asteroid belt between Mars and Jupiter. Then one last collision splintered off a chunk, which spiraled in toward Earth, nearing the rotating globe just as Costa Rica spun into view on 23 April 2019.

Surviving its passage through the atmosphere was one test, but now another threat loomed: the country's formidable rainy season, which could erode and contaminate much of that preserved history. The most important meteorite in half a century had landed on one of the last dry nights of the year.

Nobody knew it then, but the first hard rain was 5 days away.

ON 24 APRIL 2019, the day after the Aguas Zarcas fall, meteorite dealer Mike Farmer wasn't planning on doing much, maybe relaxing with his son or doing some yardwork outside his house in a Tucson, Arizona, gated community. His bags were already packed for a flight the next day to hunt for a meteorite that fell in Cuba. But soon after he woke up, the Facebook picture from Campos Muñoz flashed across his screen. “It was like, oh, Jesus Christ,” he says. “I knew immediately what it was.” So much for Cuba.

He quickly packed \$50,000 in cash into the liner pockets of a safari vest, along with more clothes for what would now be a jungle expedition, and got on the first possible flight to Costa Rica. As the plane taxied for takeoff after a layover in Dallas, Farmer's phone dinged. It was another message from Costa Rica with a photo. Would he like to buy some meteorites? “I about had a heart attack,” Farmer says.

That message came from the family of Ronald Pérez Huertas, who lives a few kilometers from Campos Muñoz outside of the village of La Palmera. On the night of the fall, Pérez Huertas was leaving his job at a cheese factory when the fireball flashed overhead. At home, his wife, Virginia Argüello Arias, heard a sound like thunder—the sonic booms of the atmospheric breakup. When she looked outside, the neighbor's German shepherd, Rocky, was cowering and trembling. Later, they learned that a fragment had crashed through Rocky's doghouse.

The next morning, Argüello Arias walked to her front gate. She spotted a small stone coated in an iridescent sheen: the fusion





Marcia Campos Muñoz held off selling her largest meteorite chunk, even as values surpassed gold. Mike Farmer bought everything he could, including a punctured doghouse.

crust that forms in the heat of descent. That afternoon, her son and daughters joined in a family hunt through pastures and stands of mango and soursop trees. They found enough fragments to cover a table and snap a tempting photo. After Googling meteorite dealers, they sent the photo to someone they thought might be willing to pay. To their amazement, he was already en route.

The following morning Farmer showed up in person, along with Robert Ward, a competitor and sometimes collaborator in the meteorite business who had arrived on the same flight. Counting out cash, they bought those initial stones—much too cheaply, the family now realizes.

Farmer also bought the fragment that hit Rocky's doghouse. And, for good measure, the doghouse, too. For the next 4 days Farmer and Ward bunked together at a nearby coffee plantation and set up shop each day on the family's front lawn, offering to do business with anyone in town who trekked over.

A gold rush began. On the first of May, a public holiday, the village was crammed with cars as treasure hunters combed the surrounding land. Buses carrying out-of-towners parked on a nearby hill. Ronald Pérez Huertas began to patrol his property, blocking access to anyone but the Americans. His son had a friend cover his shift at the gas station one day so he could go out and search, returning with a bulky chunk weighing almost 1 kilogram.

By this time as many as 30 collectors from Russia, Germany, Belgium, and the United States had set up their own bases under the path of the fireball, which had strewn fragments across 6 kilometers. Demand grew. Prices skyrocketed from the few dollars per gram Farmer had first offered to \$50, even \$100 per gram, passing the price of gold.

Campos Muñoz, meanwhile, had called scientists at the University of Costa Rica (UCR) on the morning after the fall. Only

one meteorite is known to have landed in Costa Rica before—in 1857. For Gerardo Soto, the geologist who called her back, it was a “dream come true.” When Soto and his colleagues Pilar Madrigal and Oscar Lücke drove up from San José the next day, carrying microscopes and scales, a quick inspection eliminated their doubts. “I can die now because I saw it,” Soto says.

Madrigal, a UCR geochemist, put a piece under a magnifying glass. Her eyes sparkled when she saw the glassy, extraterrestrial chondrules. “It is really meaningful to hold a meteorite like this in one's hands: It is at least 4.5 billion years old,” she says. Campos Muñoz says she got goosebumps watching the scientists work. “It seemed like they were about to burst into tears,” she says. For hours Campos Muñoz and her family sat rapt with attention as the scientists explained what they could see within the rock.

By the time the foreign collectors arrived, the scientists had already left with photographs and a few tiny pieces of the rock. Without the institutional funding to compete, they kept out of the commercial fray. “Unfortunately, many people sold their fragments to private individuals, and they left the country,” Madrigal says.

Around the world, meteorites are subject to a patchwork of laws, often those governing antiques; Denmark, for example, classifies them as “fossil troves” that belong to the state. Australia, Canada, Chile, France, Mexico, and New Zealand consider meteorites cultural treasures that can't be exported without permission. But in many places, including Costa Rica and the United States, meteorites can be freely bought, sold, and exported.

Meteoriticists are largely content with that arrangement, because the market drives people to scour fields and deserts for rare finds, and the collectors often share samples with scientists. But attitudes are shifting, says A. J. Timothy Jull, editor-in-chief of the journal

*Meteoritics & Planetary Science*. “Some countries have lost valuable material,” he says. “I suppose over time more of these regulations will be developed.”

Costa Rica may soon restrict the trade, as well. “I consider it necessary to generate a policy regarding objects from outer space that fall into Costa Rican territory,” says Ileana Boschini López, head of the country's Directorate of Geology and Mines.

In Oman vague guidelines meant for historical artifacts snared Farmer and Ward, who were arrested there with a carful of meteorites in 2011 and sentenced, after a brief trial, to 6 months in prison. Conditions were brutal, with rioting in nearby cell blocks and meager meals. They got out halfway through after an appeal. But by then Farmer had lost almost 20 kilograms and was having recurring nightmares.

That episode and other close scrapes have cemented a strange relationship for the duo, who share a love of seat-of-the-pants adventuring—but have trouble sharing the limelight and the sums of money at stake. “Sometimes they absolutely hate each other,” says Laurence Garvie, meteorite curator at Arizona State University (ASU), Tempe. But other times they get together and laugh about it. “They are like an old married couple.”

The experience in Oman did not seem to diminish the duo's hard-charging instincts. Around Aguas Zarcas, tensions were rising, along with prices. Stones could fetch \$200, even \$400 per gram. Bidding wars ensued. “I came close to sinking a shovel in one guy's skull,” Farmer says.

That guy was Jay Piatek, a wealthy doctor and obsessive collector who runs a weight loss clinic in Indianapolis (*Science*, 28 November 2014, p. 1044). He had shown up with his girlfriend, gunning to add to his collection of rare meteorites. With a piece of Murchison already displayed at home, Piatek knew exactly what he was looking



at—and the prices it could command. “He’s screaming, ‘I’ll pay more!’” Farmer says. “I had a guy rip a bag of rocks out of my hand and rush to him.” Piatek remembers it differently. “To me, they were taking advantage of people,” he says.

As more collectors swarmed the town and fresh material kept flowing in, other conflicts erupted. Then the first rains fell. Water-logged pieces began to crumble. They emitted a sulfurous reek as the moisture liberated sulfur compounds previously trapped in pores, making remaining fragments easier to find but less precious.

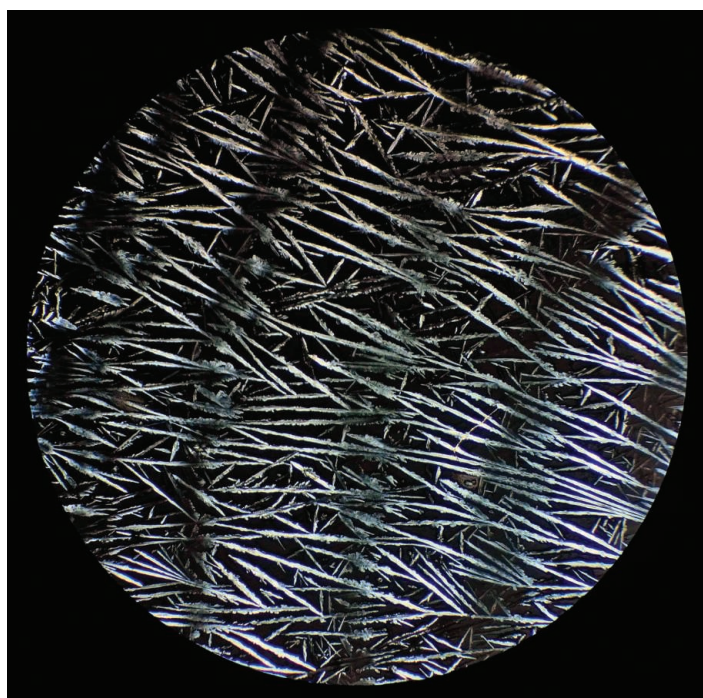
After blowing through his \$50,000 in 4 days, Farmer flew back to Tucson, and drove north toward ASU. In the desert midway between the two cities, he handed over his samples to Garvie. ASU would store some, like the doghouse smasher, on Farmer’s behalf. Others were straight donations, Garvie says, eventually totaling a few hundred grams.

Farmer was eager for Garvie to classify Aguas Zarcas scientifically, because getting an official designation was sure to buoy prices. Feeling “nerve-racking” pressure that a rival institution had obtained its own fragments, Garvie raced to combine the data obtained by Soto’s team in Costa Rica with his own mineral descriptions and an analysis of the object’s trajectory from a group in Brazil. Isotopic tests by geochemist Karen Ziegler at the University of New Mexico, Albuquerque, sealed its place in the same narrow class of carbonaceous chondrites as Murchison. Garvie submitted a write-up to the Meteoritical Society, which maintains the world’s official space rock database.

The report was accepted and published by the end of May, just 5 weeks after the fall. Now “Aguas Zarcas” was formally Aguas Zarcas, and the world’s exemplar specimens, about 40 grams worth, would reside at ASU. “Does it really matter that you got first place?” Garvie says. “No, of course not.” He pauses. “But it does matter.”

**ONE DAY** in November 2019, outside ASU’s meteorite lab, Garvie approaches me gingerly with a tiny glass beaker filled with water and powdered Aguas Zarcas, leftover from a test. He swirls the gray-black mixture like a sommelier to release its bouquet. I sniff cautiously. “You just smelled something that’s 4.5 billion years old,” he says.

I pick up the smell of moist soil, with an



In fresh samples of the Aguas Zarcas meteorite, researchers have identified salts, easily washed away by rain. Several are recrystallized on glass, including halite.

artificial edge reminiscent of permanent marker. Garvie’s official report describes a “Murchison-like” odor with “notes of compost.” Others compare it to Brussels sprouts, or describe something sweet and organic, like diesel, cooking gas, even vanilla. Farmer, who has a long-standing tradition of eating a little bit of his finds, says it’s the nastiest rock he’s ever tasted. “Laurence got mad at me,” Farmer says. “He said, ‘That’s pretty stupid, we don’t know what’s in this!’”

Few papers have been published on the meteorite so far—but they are coming. At the Field Museum, Heck is analyzing an almost 2-kilogram piece, donated by a retired health care executive, to probe the time before the Solar System took shape. He says his team has found a handful of candidate grains of silicon carbide, likely specks of dust scattered by aging giant stars that were later swept up in the protosolar disk. If confirmed and dated, those grains could add to an emerging picture of galactic conditions in the distant past.

A few similar grains from the Murchison meteorite are as much as 7.5 billion years old. But most of its grains were forged just a few hundred million years before the Solar System. If Heck finds a similar age clustering in Aguas Zarcas grains, it could point to a generation of stars all born about 7 billion years ago, giving them a few billion years to grow old and seed the Solar System with dust. Some astronomers believe the Milky Way went through a wave of starbirth at that earlier epoch, perhaps triggered by a galactic

merger or a deluge of fresh gas.

The Field Museum team has also been combing through Aguas Zarcas for the calcium- and aluminum-rich inclusions, the earliest minerals to condense out of the protosolar disk. Drifting around the disk, they gathered a record of the young Sun’s unruly outbursts, as surges of particle radiation left telltale signatures of helium and neon in each grain. “They are like flight recorders,” Heck says. “We can just count those elements that form and learn about the activity of the Sun.”

Several other teams are going after the meteorite’s complex organic compounds. They formed millions of years later, as basic carbon molecules reacted in the warm, wet interior of Aguas Zarcas’s parent asteroid. Some of the products of that early chemistry are volatiles—compounds, frozen

in pockets when the meteorite floated in cold space, that are unstable at room temperature on Earth and escape with their telltale smells. Using electronic “noses” designed for the purpose, researchers at Brown University and ASU are hoping to capture the fleeting chemicals before they fade.

Other carbon compounds are sturdier. At NASA Goddard, for example, Glavin’s team ground up bits of Aguas Zarcas with a mortar and pestle, mixed them in pure water, heated the mixture to almost boiling, and, using a mass spectrometer, analyzed the compounds rising off.

The process spat out a graph crowded with unknown organic molecules of different weights. “It’s like, oh my God, there’s likely hundreds of different amino acids in this meteorite,” Glavin says. “Murchison, for 50 years, has been the gold standard. Aguas is comparable.” The team is now working on a lower temperature technique to hunt for peptides: multiple amino acids bound together. If found, they would illustrate another level of prebiological space chemistry, suspected but never seen.

In a recent twist, though, ASU researchers report they’ve struggled to find any amino acids in their fragments. “It’s strange,” says Maitrayee Bose, an ASU cosmochemist. Bose suggests one explanation for the contradictory results: Each piece samples a different bit of a heterogeneous rock, which may have experienced different levels of alteration by water and heat. “It’s like the human body,” she says. “Every part is slightly different.”



Looking close at isovaline, an amino acid that occurs in space but is almost never found in earthly life, the NASA team has uncovered hints of a deeper pattern. Amino acids can occur in two mirror-image molecular forms, differing like right and left hands. Chemical reactions have no preference for either form, so left alone, nature should produce half-and-half mixtures. But organisms on Earth seem to build themselves out of only left-handed amino acids.

That bias could reflect a roll of the dice by the first life, a random choice that descendants preserved. Another theory, published in May, suggests the left-hand bias arose on Earth: After life emerged in a mix of mirror-image forms, the radiation of cosmic ray showers in the atmosphere, which has its own inherent handedness, offered an evolutionary advantage to organisms with left-handed proteins.

But Aguas Zarcas has up to 15% more left-handed than right-handed isovaline, underscoring similar findings from Murchison and other carbonaceous chondrites. The persistent pattern suggests the lefty bias may have arisen in space. Perhaps, another camp argues, the polarized light from nearby stars imparted a slight bias to meteoritic organic molecules that was incorporated by life. “I think the meteorites are telling us the story that we were destined to evolve left hand-based protein life,” Glavin says.

Other labs are examining Aguas Zarcas for clues to a later stage of Earth’s evolution. Models predict carbonaceous asteroids crashing down on early Earth would have produced an ancient atmosphere rich in water vapor and carbon dioxide. At the University of California, Santa Cruz, cosmochemist Myriam Telus wanted to test the idea with real data. She reached out to a dealer for samples, which she then would destroy by baking them to dust and measuring the emitted gases. “It can be very hard to convince people this is worthwhile for something that is precious,” she says. But soon she had 2 grams—enough to proceed with the experiment.

For still other scientists, Aguas Zarcas landed at a fortuitous moment.

Right now, Japan’s Hayabusa2 spacecraft is hurtling back toward Earth bearing dust from Ryugu, an asteroid with asphalt-black patches that resemble carbonaceous chondrites. Those samples are scheduled to parachute down to Australia on 6 December. And in 2023, NASA’s OSIRIS-REx mission will deliver about 60 grams of material from the carbon-rich asteroid Bennu, also thought to be a close relative of Aguas Zarcas.

These asteroid scraps will be truly pristine, having never touched the atmosphere or sat atop rainforest soil. Aguas Zarcas—precious but not space-mission precious—is a good material for trial runs: The OSIRIS-REx team bought 60 grams of it to refine its analysis pipeline in advance of the Bennu material.

Expecting two chunks of prehistoric carbon, scientists find themselves with three. “It wasn’t a million- or a billion-dollar mission to go collect it. It just fell,” says Jessica Barnes, a team member at the University of Arizona. “So, thank you to the cosmos for that.”

**ONE DAY IN MAY**, once again on the cusp of Costa Rica’s rainy season, Ruddy Valerio Díaz sat enjoying the open air at his restaurant next to a freshwater tank teeming with tilapia. Butterflies fluttered through



With the money from meteorite stones he sold, Ruddy Valerio Díaz paid off his debts, built a butterfly farm, and started a restaurant.

an adjacent breeding garden. COVID-19 had cleared the place of customers, leaving an empty patio, but at least he had a financial cushion. When the rocks rained down, Valerio Díaz had been skipping between temp jobs, dreaming of opening a business. No bank would give him a loan. “Our economic situation was so tough,” he says. “This money literally rained from the sky.”

Valerio Díaz waited 2 months to sell the 300 grams of stones he found along roads, under electrical towers, and on his own land. Farmer wouldn’t pay enough. But someone else agreed to \$50 per gram, enough to pay off all his debts, build his wife, Rosibel, the butterfly farm, and start the restaurant. The only problem was what to call the place. They came up with a long list of punning titles: Manna from Heaven, Cosmos Restaurant, Black Stones. Now, it’s Tilapias Rancho El Meteorito—Meteorite Tilapia Ranch.

Nearby, Pérez Huertas and his family used

meteorite proceeds to repaint the house, replace the roof, expand their dairy barn, and buy new furniture and a car. Once prices started to climb, Farmer—now a family friend—gave them more money to compensate for his initial lowball purchases, plus bonuses for acting as his fixers. For Argüello Arias’s 50th birthday, the women of the family all took a trip to Panama.

Having sold all the putrid fragments harvested after the rains, Farmer said he’s hoarding five intact kilograms, out of seven total kilograms he obtained. Some are at home, in the same Ziploc bags they went into the instant he bought them; other pieces are being stored on his behalf at ASU in sealed boxes filled with nitrogen instead of air. Right now, there’s still too much available online and at rock and mineral exhibitions for him to sell his collection. “I have the majority of it in the world, and all pristine,” Farmer says. “Ten, 20 years down the road, when me or my son or somebody opens that box, you’ve got a very important asset there.”

Little of Aguas Zarcas remains in Aguas Zarcas—or in Costa Rica. UCR is now home to a few fragments, each weighing a few tenths of a gram. San José’s National Museum has a little more. Madrigal says she hopes some of the pieces sold overseas might eventually be donated back to Costa Rican institutions.

Campos Muñoz is still a holdout, maybe the last. She still has the big chunk that fell through her roof, which she hopes will end up in an exhibition. She wants more for it—she won’t say exactly how much—than dealers have offered.

The hole in the roof remains. She had meant to fix it, but first came the meteorite hunting frenzy, then the rainy season, and now the pandemic. Plus, she knows these bits of collateral damage are valuable to collectors, too. “This hole in the roof and the damaged tables are part of our family now,” she says.

Neighbors suspect her family are all millionaires, winners of a cosmic lottery, she says. Strangers still show up from time to time and dawdle out front, looking for the “house of the meteorite.” She stays in touch with the Costa Rican scientists to follow their research and reads every paper they send her way.

“I feel very proud that such an important event for history and science took place in my country,” she says, “and in my house.” ■

Joshua Sokol is a journalist in Raleigh, North Carolina. Andrea Solano Benavides, a journalist in San José, Costa Rica, contributed reporting.



Ephemeral streams, such as this one in western South Dakota, have lost federal protection under the Navigable Waters Protection Rule.



## POLICY FORUM

### WATER

# Distorting science, putting water at risk

A recent rule is inconsistent with science and will compromise the integrity of U.S. waters.

By **S. Mažeika Patricio Sullivan**<sup>1</sup>,  
**Mark C. Rains**<sup>2</sup>, **Amanda D. Rodewald**<sup>3,4</sup>,  
**William W. Buzbee**<sup>5</sup>, **Amy D. Rosemond**<sup>6</sup>

**T**he Navigable Waters Protection Rule (NWPR) (1), which was published in April by the U.S. Environmental Protection Agency (EPA) and the Department of the Army (“the Agencies”), has redefined “waters of the U.S.” (WOTUS) to restrict federal protection of vulnerable waters (2). With its emphasis on “continuous surface connections” and “permanen[ce]”, the NWPR removes or reduces protection for U.S. waters, including millions of miles of streams and acres of wetlands, many of which comprise headwaters that are critical for sustain-

ing water quality and healthy watersheds (3) (see the figure). Although the Agencies claim to have “looked to scientific principles to inform” the NWPR, science has been largely ignored and oversimplified. These new exclusions are based on selective parsing of statutory language and earlier case law, rather than on previously established, science-based interpretations of the U.S. Federal Water Pollution Control Act, commonly known as the Clean Water Act (CWA) (4). The EPA’s own Science Advisory Board (SAB) found sufficient evidence to conclude that “...the proposed Rule lacks a scientific justification, while potentially introducing new risks to human and environmental health” (5). Responding to this unprecedented distortion of science and rollback

in water protections, which went into effect nationwide on 22 June, will require coordinated efforts among scientists, lawmakers, and resource managers.

Clearly articulated in the CWA is the intention “to restore and maintain the chemical, physical, and biological integrity of the Nation’s waters” (4). The CWA was explicit in protecting “navigable waters,” which Congress defined broadly as WOTUS; however, the extent to which waters other than navigable rivers, lakes, and territorial seas [traditional navigable waters (TNWs)] are protected has repeatedly provoked legal skirmishing. Particularly contentious are determinations about which nontraditional waters, such as wetlands and small tributary streams, contribute to the integrity of TNWs.



The NWPR functionally ends the debate by elevating state over federal regulatory authority. Without federal law as a protective regulatory floor, states can and often do choose to leave waterbodies unprotected, making waters vulnerable to unregulated pollution, dredging, filling, and other activities that may profoundly erode water quality (3).

The NWPR downplays science by redefining protected “waters” and explicitly states that “science cannot dictate where to draw the line between Federal and State waters.” The NWPR relies overwhelmingly (and arguably arbitrarily) upon the 2006 Supreme Court opinion by Justice Scalia in *Rapanos v. United States*, *Carabell v. United States Army Corps of Engineers* that lacked majority support. A more scientifically nuanced position was articulated by Justice Kennedy on the same case; the four dissenting Justices agreed with Kennedy’s rationales for protecting waters, but would have protected even more.

The realized impacts are likely to be worse than projected, as ephemeral streams and nonfloodplain wetlands are usually underestimated by remotely sensed data (3). The economic analysis filed with the NWPR was largely silent about impacts, simply acknowledging that “the [A]gencies are unable to quantify [the scope] of these changes with any reliable accuracy” owing to geospatial data issues and uncertainty about government responses (6). Yet, in spite of this uncertainty and the potential for harm, the Agencies proceeded with a restrictive and risky rule.

## CONNECTIVITY AND QUALITY

Connectivity is a cornerstone in understanding how freshwater ecosystem functions are sustained. In 2015, the Obama administration promulgated the Clean Water Rule (CWR) that included all tributaries and most wetlands as WOTUS (7). The scientific rationale for the CWR was reviewed in the EPA Connectivity Report (8), which synthesized >1200 peer-reviewed scientific publications and input from 49 technical experts. After a public review process, the 25-member EPA SAB confirmed the scientific underpinnings of both the Connectivity Report and the CWR.

Since then, the body of supporting evidence has grown (3, 9), enhancing our understanding of how the integrity of freshwater ecosystems within a watershed relates to the biological, chemical, and hydrological connectivity among waterbodies, including wetlands and ephemeral streams. This un-

derstanding recognizes as critical to services derived from freshwater ecosystems gradients of connectivity (versus a binary property: connected, not connected) that operate as a function of frequency, magnitude, timing, and duration of biological, chemical, and physical connections among waterbodies (10). By disregarding or misinterpreting the science of waterbody connectivity, the NWPR draws scientifically unsupported boundaries to distinguish WOTUS, reaches conclusions contrary to current science, and asserts legal and scientific views substantially different from those of the Agencies under previous administrations of both political parties going back to the 1970s. The NWPR promotes regulations contrary to what science shows about effective water protection. Although agencies often have latitude to adjust regulatory choices when implementing longstanding statutes, they cannot do so arbitrarily and without reasoned justification and rationales in light of relevant law, facts, and science.

In contrast to the CWR’s recognition of biological, chemical, and physical connectivity, the NWPR relies solely on direct hydrologic surface connectivity to determine wetland jurisdiction. Nonfloodplain wetlands and ephemeral streams are categorically excluded on the basis of lack of hydrological connectivity irrespective of their degree of biological or chemical connectivity. Also excluded are floodplain wetlands lacking a direct surface water connection to TNWs “in a typical year,” and intermittent tributaries lacking relatively permanent surface flows.

Such exclusions are inconsistent with evidence demonstrating that these waters are functionally connected to and support the integrity of downstream waters. Removal of federal protection is likely to diminish numerous ecosystem services, such as safeguarding water quality and quantity, reducing or mitigating flood risk, conserving biodiversity, and maintaining recreationally and commercially valuable fisheries (3).

## EPHEMERAL, ISOLATED

Just as tiny capillaries play critical roles in the human body, nonfloodplain wetlands (so-called “isolated”) and ephemeral streams (that flow only after precipitation events) support an extensive suite of ecosystem services. Because nonfloodplain wetlands and ephemeral streams are connected to one another and downstream waters along a gradient of connectivity, they also provide substantial cumulative or aggregate ecosystem services (10).

Because these wetlands and streams will summarily lose federal protection, they will be vulnerable to outright destruction, fill, or unpermitted industrial pollution discharges that risk transporting pollutants throughout watersheds. Losses of nonfloodplain wetlands could include particularly vulnerable and often valuable waters (2), including some playa lakes, prairie potholes, Carolina and Delmarva Bays, pocosins, and vernal pools. A preliminary analysis predicts widespread losses of wetland functions, with particularly high impacts on wetlands in arid and semi-arid regions. For example, the CWR protected 72%, whereas the NWPR will only protect 28% of wetland acres, in New Mexico’s Río Peñasco watershed (11).

The NWPR also categorically excludes subsurface hydrologic connectivity. To disregard groundwater connectivity is to disregard the scientific understanding of how natural waters function. The Agencies justify this exclusion by claiming that “A groundwater or subsurface connection could also be confusing and difficult to implement.” Although implementation may be challenging in some cases, claimed implementation ease under the NWPR should not supersede an evidence-based determination of connectivity given the potential for economic and environmental harm.

## A PATH FORWARD IN UNCERTAIN TIMES

The NWPR directly conflicts with a growing body of scientific evidence and with input and review by federal and nonfederal scientists. The rule narrows WOTUS in ways that are inconsistent with longstanding views about the CWA’s mandate to safeguard access to clean water. The NWPR opens previously protected waters to filling, impairment, and industrial pollution, and will undermine decades of investments restoring water quality across the United States and lead to profound loss or impairment of ecosystems and the services they provide. For context, the economic value of ecosystem services provisioned by nonfloodplain wetlands alone has been estimated at \$673 billion per year (2).

Congress has the power to strengthen the CWA by enacting new legislation to replace or repeal the NWPR. Future administrations can reassess and act to restore protections through new rulemaking, without the need for new legislation. Toward these ends, the scientific community has already spoken on the matter, proposing three frameworks for the development of renewed protections based on sound scientific merits (2).

<sup>1</sup>Schiermeier Olentangy River Wetland Research Park, School of Environment and Natural Resources, The Ohio State University, Columbus, OH, USA. <sup>2</sup>School of Geosciences, University of South Florida, Tampa, FL, USA. <sup>3</sup>Cornell Lab of Ornithology, Cornell University, Ithaca, NY, USA. <sup>4</sup>Department of Natural Resources, Cornell University, Ithaca, NY, USA. <sup>5</sup>Georgetown University Law Center, Georgetown University, Washington, DC, USA. <sup>6</sup>Odom School of Ecology, University of Georgia, Athens, GA, USA. Email: sullivan.191@osu.edu

Meanwhile, litigation may present challenges to and perhaps enjoin implementation of the NWPR. The April 2020 *County of Maui v. Hawaii Wildlife Fund* may help. In that case, the U.S. Supreme Court rejected an argument that would have eliminated federal CWA protections. The Court instead called for a functional and context-sensitive analysis of the disputed activities and their effects to determine federal jurisdiction over intentional pollution discharges into groundwater that predictably flows into WOTUS. In that 6 to 3 decision, the Court laid out a clear scientific basis for closing a loophole in the CWA, affirming for the first time that pollutants that travel through groundwater and

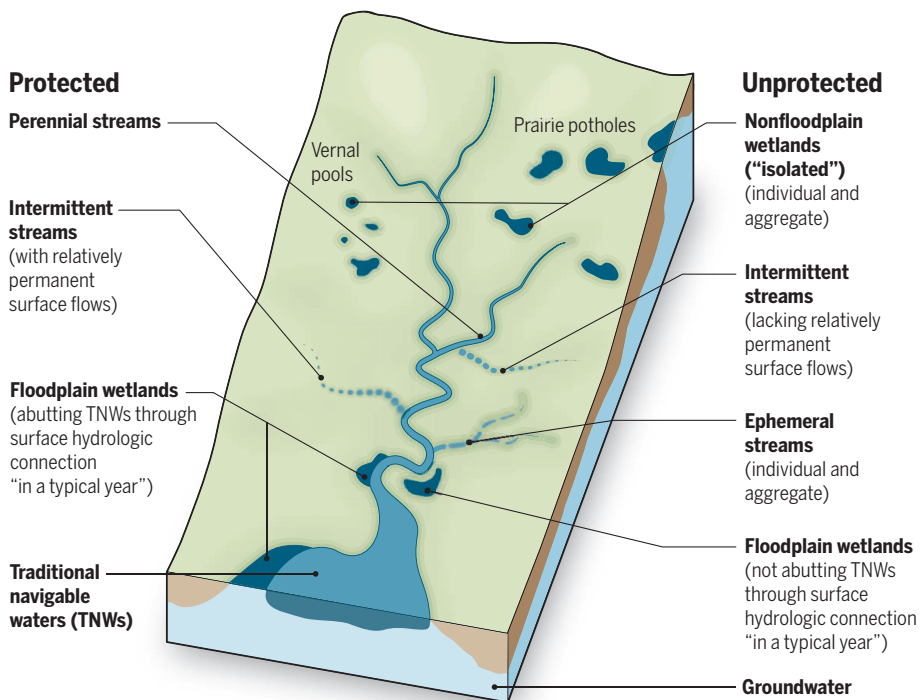
Research-based evidence on the impacts of climate change were notably absent in the NWPR and will also be critical in challenging the rule. Under current human-use and water-management schemes, many stream flows are declining, such that intermittent and perennial streams are increasingly being replaced with ephemeral streams that will lose protection. For example, the Upper Kansas River Basin lost 558 km (21%) of stream length between 1950 and 1980, presumably as a result of groundwater pumping exacerbated by climate change, with a cumulative loss of 844 km (32%) predicted by 2060 (12). Reduced mountain snowpack and increased evaporation have been implicated

exploitation of water resources. Although federal statutes grant latitude to state, tribal, and local governments to provide additional, more protective regulation, many states do not do so, and many even prohibit regulations more stringent than federally required (2, 14). Thus, absent federal protections, many waterbodies will go unprotected.

If the NWPR remains in place, local and grassroots approaches to water conservation, including watershed councils and coalitions, information and educational plans to reduce pollution, and university extension programs, will need to further mobilize to fill the vacuum created by the new rule. Such efforts would require additional resources and heightened stakeholder coordination. ■

## Protected versus unprotected waters

Multiple waterbody types were initially under consideration for protection as “waters of the United States” under the Navigable Waters Protection Rule. Ephemeral streams flow only after precipitation events, intermittent streams flow periodically or seasonally, and perennial streams flow continuously. There are many types of nonfloodplain, or “isolated” wetlands, including prairie potholes and vernal pools, as illustrated here.



then emerge into surface waters are in fact covered by the CWA.

Redoubled research efforts also can help address knowledge gaps critical for effective water policy. Quantifying the potential “harm” to clean water that will be caused by the NWPR is critical for both litigation and future rulemaking. Thus, the scientific community will be challenged to further demonstrate the consequences of changes to physical, chemical, and biological connectivity on water quality—especially in the context of nonperennial streams and non-floodplain wetlands.

in the ~20% decline in the Colorado River’s mean annual flow in comparison to the previous century; the Upper Colorado River basin supplies water to around 40 million people and supports ~16 million jobs (13).

Adoption of the NWPR is an indicator that the federal government is at least in part shedding the use of science and responsibility for water protection. Additional federal roll-backs of environmental protection, such as the Update to the Regulations Implementing the Procedural Provisions of the National Environmental Policy Act, a rule finalized on 15 July, could create a perfect storm for

## REFERENCES AND NOTES

1. U.S. Environmental Protection Agency and Department of Defense, Department of the Army, Corps of Engineers, The Navigable Waters Protection Rule: Definition of “Waters of the United States,” 85 Fed. Reg. 22250 (A2020).
2. I. F. Creed *et al.*, *Nat. Geosci.* **10**, 809 (2017).
3. S. A. R. Colvin *et al.*, *Fisheries* (Bethesda, MD) **44**, 73 (2019).
4. Federal Water Pollution Control Act, 33 U.S.C. 1251 *et seq.*, Sec. 101, p. 3 (1972).
5. U.S. EPA, Letter to Andrew Wheeler, 27 February 2020, SAB commentary on the proposed rule defining the scope of waters federally regulated under the Clean Water Act, EPA-SAB-20-002 (Environmental Protection Agency, 2020).
6. U.S. Environmental Protection Agency and Department of the Army, Economic analysis for the Navigable Waters Protection Rule: Definition of “Waters of the United States” (EPA, 2020).
7. U.S. Environmental Protection Agency and Department of Defense, Department of the Army, Corps of Engineers, Clean Water Rule: Definition of “Waters of the United States” 80 Fed. Reg. 37054 (EPA, 2015).
8. U.S. Environmental Protection Agency, Connectivity of streams and wetlands to downstream waters: a review and synthesis of the scientific evidence technical report, EPA/600/R-14/475F (EPA, 2015).
9. S. M. P. Sullivan, M. C. Rains, A. D. Rodewald, *Proc. Natl. Acad. Sci. U.S.A.* **116**, 11558 (2019).
10. U.S. Environmental Protection Agency, Letter to Gina McCarthy, 17 October 2014. SAB review of the draft EPA report Connectivity of streams and wetlands to downstream waters: A review and synthesis of the scientific evidence (EPA, 2014).
11. R. Meyer, A. Robertson, Navigable Waters Protection Rule spatial analysis: A GIS based scenario model for comparative analysis of the potential spatial extent of jurisdictional and non-jurisdictional waters and wetlands (Saint Mary’s University of Minnesota, Winona, MN, 2020).
12. J. S. Perkins *et al.*, *Proc. Natl. Acad. Sci. U.S.A.* **114**, 7373 (2017).
13. P. C. D. Milly, K. A. Dunne, *Science* **367**, 1252 (2020).
14. State constraints: State-imposed limitations on the authority of agencies to regulate waters beyond the scope of the federal Clean Water Act (Environmental Law Institute, 2013).

## ACKNOWLEDGMENTS

We thank the many individuals who contributed to previous and related documents concerning the proposed replacement rule that helped inform this paper, including letters to the Federal Register (Docket ID No. EPAHQ-OW-2018-0149) and Public Input on the SAB Commentary on the Proposed Rule Defining the Scope of Waters Federally Regulated under the Clean Water Act (84 FR 4154). We also thank L. Poff, W. Kleindl, and three anonymous reviewers for their critiques and suggestions in earlier drafts. R. B. Keast and S.M.P.S. developed the figure. S.M.P.S. is currently providing advisory and expert consulting services to ongoing litigation regarding the NWPR.

10.1126/science.abb6899





Displaced Iraqis play soccer. Christian players' prejudice decreased toward Muslim teammates but not toward Muslim strangers.

## PERSPECTIVES

### INTERGROUP RELATIONS

# Can playing together help us live together?

A field experiment in Iraq shows that having Muslim teammates reduced Christian soccer players' prejudice

By Elizabeth Levy Paluck and Chelsey S. Clark

**T**he contact hypothesis in psychology predicts that prejudice can be reduced when rival groups come together under optimal circumstances of cooperation and equal status. To date, the weight of real-world evidence for this hypothesis comes from self-reported attitudes after self-initiated contact, not from preregistered randomized trials that take intergroup contact as seriously as one would take a potential vaccine for conflict (1, 2). Consequently, on page 866 of this issue, the results of Mousa's (3) new field experiment are breaking news. Mousa intervened in amateur Christian soccer leagues across Northern Iraqi cities affected by ISIS violence. To assess the impact of this ambitious real-world intervention, she randomly assigned Muslim players to half of the teams, measured players' behavior up to 6 months later, and posted her preregistered analysis plan and data alongside the report. Mousa finds that having Muslim teammates causes Christian players to change their behavior for the better toward Muslim players, by including them, working with them, and awarding them material signs of respect. Team-based contact with minority group members reduced prejudiced behavior toward other minority group players.

Given its relevance for policy (Mousa notes that \$877 million was allocated in 2020 toward "social cohesion" programming by the U.S. Agency for International Development) and that the contact hypothesis has been studied for many years, some may classify this research as an application of a well-known finding. This would be inaccurate. Previous research has not demonstrated cause and effect with real-world interventions or measured behaviors or otherwise leveraged the most robust research methodologies. These methods are crucial, given that the anticipated effects of contact range from positive change to backlash, in which contact stirs latent resentments. This makes Mousa's research more similar to basic science that makes progress toward fundamental evidence than to applied research that tests policy interventions based on a robust foundation of scientific evidence. Work in the field, which is often mistaken for applied research because of its location outside the laboratory, performs the function of basic science when it comes to the question of whether intergroup contact increases social cohesion.

The study presents a fundamental theoretical puzzle: Why don't the positive behavioral effects generalize out of context, or to positive intergroup attitudes? The first piece of the puzzle is that the observed changes are limited to behaviors and not attitudes. A growing number of field experiments on prejudice reduction uncover this pattern (4,

5), which counters both lay and scientific notions that attitudes guide behavior. One could argue that between attitudes and behaviors, it is better to change behavior because prejudicial action is worse than harboring prejudicial attitudes. Additionally, public behaviors may cause more downstream change because they are more easily observable than private attitudes (6). More work is needed to measure these kinds of spillover effects, following on Mousa's finding that community members who attended more games were more likely to view religious and ethnic divisions as arbitrary. Future work can also disentangle whether attitudes are simply more difficult to change or whether current research is not measuring the correct attitudes.

Perhaps the nature of intergroup contact is useful for changing a more limited range of attitudes than those measured in the present study. Mousa observes one instance of attitude change among players: the item regarding arbitrary religious and ethnic divisions. She points out that it represents a change in "abstract attitudes rather than concrete policy positions." As it was originally conceived, the contact hypothesis was a salve for prejudice or animus, not for antagonistic political opinion or behavior (7). Since then, psychological evidence has grown, suggesting that prejudice-reduction interventions have inconsistent and even unintended effects on related political attitudes (8). Mousa defines and measures the target of her intervention, social cohesion, as a more compound concept than prejudice, involving intergroup cooperation and policy attitudes. Interventions such as contact that are intended to soften attitudes toward outgroups may need to be combined with additional activities to channel newfound goodwill into a political or policy position. Early work on interracial contact in the United States recognized this point. For example, in addition to creating ideal contact conditions for Black and White individuals working in teams, one study using Black actors to mention instances of discrimination and race-based hardship helped White participants connect their experience to larger societal issues (9).

The second piece of the theoretical puzzle is that changes in behavior toward other Muslim players in the league did not generalize to changes in behavior toward Muslim strangers. Mousa offers possible explanations, including ongoing threat from recent anti-Christian violence, the fragile quality of the contact with other players, and the possibility that behavior change takes longer to manifest. Another

Department of Psychology and Policy, School of Public and International Affairs, Princeton University, Princeton, NJ, USA. Email: epaluck@princeton.edu

PHOTO: SPENCER PLATT/GETTY IMAGES

possibility rests in the basic math of the league's intergroup contact: Christian leaders allowed a maximum of three Muslim players on treatment teams. This limitation represents a hard-won insight about the difficulty of implementing intergroup contact interventions in post-conflict settings but may have limited the generalizability of behavioral effects.

Psychological theory predicts that individuals can make positive generalizations from one prototypical group member to the rest of the group (10). The handful of Muslim players may have been seen as exceptional, not prototypical, in the eyes of the Christian players, similar to other contexts with a token number of outgroup individuals. If the Muslim players were considered an exception to the rule, psychological theory would not predict that positive impressions of Muslim players would generalize to their group.

Another consequence of the small number of Muslim players is that it inhibits the research from exploring effects on both sides of the intergroup contact. Mousa's data suggest that Muslim players' prejudice did not change over time, but there are too few Muslims and no Muslim control group to rigorously test this claim. Leaving out the perspectives of minority group members, who are often instrumentalized for the purpose of attitude change among the majority, is a pattern in intergroup contact research. There is much to learn by studying reactions to intergroup contact among minority group participants.

This landmark study cuts a clear path for future scholarship. Generalized answers will only emerge after more experimental work that may seem like policy application but is actually basic science, working systematically toward robust conclusions. Mousa is one of a cohort (2) of young scientists who are leading the way. ■

#### REFERENCES AND NOTES

1. E. L. Paluck, S. A. Green, D. P. Green, *Behav. Pub. Pol.* **3**, 129 (2019).
2. E. L. Paluck, Harvard Dataverse (2020); doi:10.7910/DVN/ODACR5.
3. S. Mousa, *Science* **369**, 866 (2020).
4. A. Scacco, S. S. Warren, *Am. Polit. Sci. Rev.* **112**, 654 (2018).
5. E. L. Paluck, *J. Pers. Soc. Psychol.* **96**, 574 (2009).
6. T. Kuran, *Private Truths, Public Lies* (Harvard Univ. Press, 1997).
7. G. Allport, *The Nature of Prejudice* (Addison Wesley, 1954).
8. J. Dixon, M. Levine, S. Reicher, K. Durrheim, *Behav. Brain Sci.* **35**, 411 (2012).
9. S. W. Cook, *J. Res. Dev. Educ.* **55**, 647 (1978).
10. J. C. Turner, M. A. Hogg, P. J. Oakes, S. D. Reicher, M. S. Wetherell, *Rediscovering the Social Group, A Self-Categorization Theory* (Basil Blackwell, 1987).

#### ACKNOWLEDGMENTS

The authors thank the Rita Allen Foundation for funding and R. Porat and D. Green for comments.

10/1126.science.abb9990

#### MARINE ECOLOGY

# Marine food webs destabilized

## A combination of warming and acidification threaten marine biomass and productivity

By **Steven L. Chown**

**F**orecasting the ecological consequences of climate change requires both observations and experiments. Among the most informative experiments are manipulations of ecosystems, either through large outdoor interventions or through the construction of mesocosms (1)—replicas of the natural world that enable conditions to be carefully controlled. Mesocosms typically mimic the complexity of natural ecosystems, enabling researchers to disentangle how these systems work now and what path they might follow as future conditions change. They can also be replicated, enabling signal to be distinguished from the variability that is an inherent feature of natural systems. On page 829 of this issue, Nagelkerken *et al.* (2) report on their use of mesocosms to better understand the future of marine systems and the ecological services they deliver. They find that marine benthic ecosystems have limited capacity to respond to a future combination of warming and acidification, with considerable degradation a potential outcome.

Nagelkerken *et al.* address several key questions. Their experiments explore the way that ecological interactions will play out under end-of-century temperature and ocean acidification conditions compared with those now. They assess how species with similar functions, but different responses to changing physical conditions, replace each other, thus preserving the form of ecological interactions (especially feeding) among community members. They also aim to determine whether the trophic structure of present-day marine systems (see the figure, left)—with a high biomass of primary producers and lower biomasses of primary and secondary consumers—will be maintained as physical conditions change.

Nagelkerken *et al.* constructed replicas of Australian marine benthic systems, including all of the major groups of organisms that might be expected: cyanobacteria, algae, copepods, shrimps, crabs, molluscs, polychaetes, brittle stars, sponges, and fish. Primary producers (such as algae) and both primary (molluscs) and secondary

(fish, crabs) consumers were represented by the species included in the mesocosms, as were typical feeding interactions among species and trophic levels. The 1800-liter mesocosms were then either exposed to conditions typical of those along the South Australian coast (a control setting) or exposed to increased temperature, simulated acidification, or a combination of the two, as expected at the end of this century under the Intergovernmental Panel on Climate Change's Representative Concentration Pathway 8.5 (RCP8.5) scenario. RCP8.5 is based on an extreme anthropogenic greenhouse gas emissions scenario, but one that continues to be plausible (3). Nagelkerken *et al.* then investigated food web structure in the form of feeding interactions and the way in which biomass and productivity change among trophic groups.

Simulated ocean acidification had little effect, except for a benefit from bottom-up resource enrichment. By contrast, although food web structure was relatively insensitive to temperature and to the combination of temperature and acidification, both biomass and productivity were greatly reorganized among trophic groups (see the figure, center). In effect, and especially under combined warming and acidification, primary producer and secondary consumer biomass and productivity increased, whereas substantial declines occurred among primary consumers. As Nagelkerken *et al.* point out, such trophic imbalance is unlikely to be stable in the long term. Rather, it represents a transitory state, with one likely outcome the collapse of the system such that primary producers dominate and secondary consumers, such as fish, are largely lost (see the figure, right). Less extreme outcomes might result if species are capable of adapting to the combination of warmer temperatures and higher acidity.

The outcomes from these mesocosm experiments are worrying. Secondary marine consumers, such as fish and larger invertebrates, are an important nutritional source for people (4). Indeed, demersal and small pelagic fish now dominate global fisheries catch (5). Yet these important marine resources are under pressure because of fishing for human consumption (6) or the production of fish meal for aquaculture (7). These mesocosm trials suggest that this direct

School of Biological Sciences, Monash University, Victoria 3800, Australia. Email: steven.chown@monash.edu



pressure, which includes increased benthic trawling (5), will further be compounded by the combination of warming and acidification. These local-scale conclusions are well aligned with global models forecasting continual declines in global ocean animal biomass, especially at higher trophic levels, as climates change (8). Beyond the end of this century, these impacts are expected to be especially severe in some regions (9).

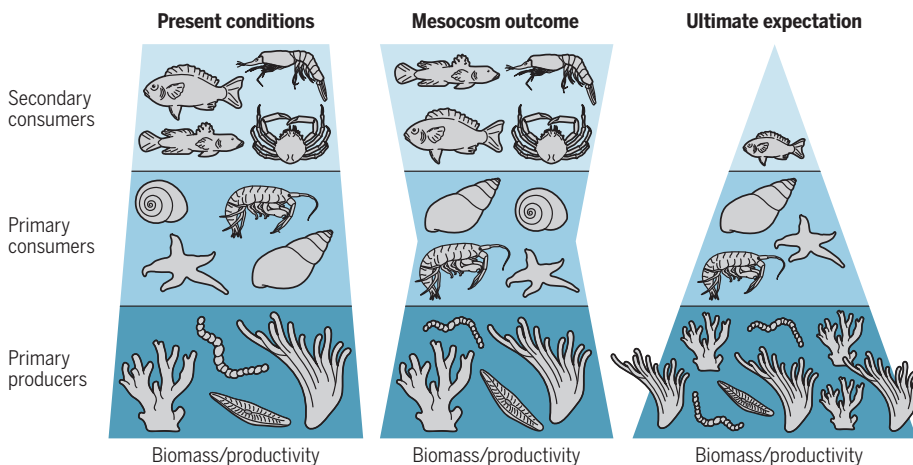
Human futures are not the only ones that are at stake. Other species, and ecosystems, also depend on what's happening in the sea. Marine secondary consumers, such as fish, are not the end of the trophic line. Rather, they are also food for seabird and marine mammal species, which are themselves now

results, which show an absence under future conditions of important stabilizing processes that include species substitution, functional redundancy, and trophic compensation, apply as much to other settings as they do to the system they investigated is far from clear. Indeed, replication in other ways and other settings of this work is critical because mesocosm outcomes can be quite variable (1).

If the trajectory documented by Nagelkerken *et al.* is found elsewhere, additional early warning indicators, such as initial declines in primary consumer biomass and productivity, will have been made available. These are indicators that could help detect and perhaps prevent the transition of marine systems to states that are

## Expected changes to future marine trophic structure

Currently, marine nearshore systems have high primary producer biomass and productivity, which declines moderately with increasing trophic level. Mesocosm experiments reveal a sharp decline in primary—but not secondary—consumer biomass and productivity in response to expected end-of-century temperature and acidification conditions. Such trophic structure is unstable. In the absence of adaptation, systems are expected to collapse to those with few secondary consumers and a dominance of primary producers.



under pressure from changing climates and human activity (10). Moreover, these vertebrates play a role in the transfer of marine nutrients to terrestrial areas, thus contributing to the functioning of coastal margin and island ecosystems (11).

One finding from Nagelkerken *et al.*'s experiments that might seem unusual is the limited impact of acidification alone. Acidification's effects on animals—such as influences on embryonic development, adult reproduction, and energetics—are now proving in many cases to be less severe than feared (12). But the effects of interactions between stressors are not yet well characterized. Rich opportunity exists to determine just how general Nagelkerken *et al.*'s findings are, by exploring the outcomes of interactions among multiple stressors such as increased temperature, increased carbon dioxide, and changing salinity. Whether their

much less rich and productive than they are now. Overall, the message from these marine mesocosm trials is clear: Destabilization of marine food webs can only be mitigated if further concerted action is taken to reduce greenhouse gas emissions. ■

## REFERENCES AND NOTES

1. R. I. A. Stewart *et al.*, *Adv. Ecol. Res.* **48**, 71 (2013).
2. I. Nagelkerken, S. U. Goldenberg, C. M. Ferreira, H. Ullah, S. D. Connell, *Science* **369**, 829 (2020).
3. Z. Hausfather, G. P. Peters, *Nature* **577**, 618 (2020).
4. C. C. Hicks *et al.*, *Nature* **574**, 95 (2019).
5. R. A. Watson, A. Tidd, *Mar. Policy* **93**, 171 (2018).
6. D. A. Kroodsma *et al.*, *Science* **359**, 904 (2018).
7. D. Pauly, *Nature* **574**, 41 (2019).
8. H. K. Lotze *et al.*, *Proc. Natl. Acad. Sci. U.S.A.* **116**, 12907 (2019).
9. J. K. Moore *et al.*, *Science* **359**, 1139 (2018).
10. M. A. Hindell *et al.*, *Nature* **580**, 87 (2020).
11. B. Moss, *J. Exp. Mar. Biol. Ecol.* **492**, 63 (2017).
12. L. S. Peck, *Oceanogr. Mar. Biol. Annu. Rev.* **56**, 105 (2018).

10.1126/science.abd5739

## NEUROSCIENCE

# An early start to Huntington's disease

The huntingtin gene mutation interferes with neurogenesis in human fetal cortex

By Marian DiFiglia

**H**untington's disease (HD) is a rare, inherited brain disorder that causes progressive degeneration of neurons, impaired movement and cognition, and death ~15 years after onset. Most carriers of the pathogenic mutation in the huntingtin (*HTT*) gene develop symptoms in midlife, but abnormalities in the brain can occur a decade earlier. On page 787 of this issue, Barnat *et al.* (1) describe anomalies in neuronal precursors destined for the cortex of human fetal brain and embryonic mouse brain harboring HD-associated mutations in the *HTT* gene. These findings prompt questions about the impact of these events on early development, the emergence of disease, and the timing of therapeutic interventions.

The genetic mutation in *HTT* causes an increase in the number of consecutive DNA triplets of CAG, which encodes glutamine. This results in 39 or more glutamine residues in the mutant huntingtin protein (mHTT) (2). Most of the affected individuals are heterozygous for the mutation, have an average of 42 CAG repeats in the mutant *HTT* allele, and experience onset of the disease in midlife. Human embryos studied by Barnat *et al.* had CAG repeat numbers in this range. Ten percent of *HTT* carriers have 55 or more CAG repeats and suffer juvenile onset with progressive cognitive decline but more rigid postures instead of the choreiform (rapid, jerky) movements that are typical of adult onset HD. Thus, CAG repeat length inversely correlates with the age of disease onset. The CAG repeat is also unstable and continues to expand in postmitotic neurons, likely instigating greater harm.

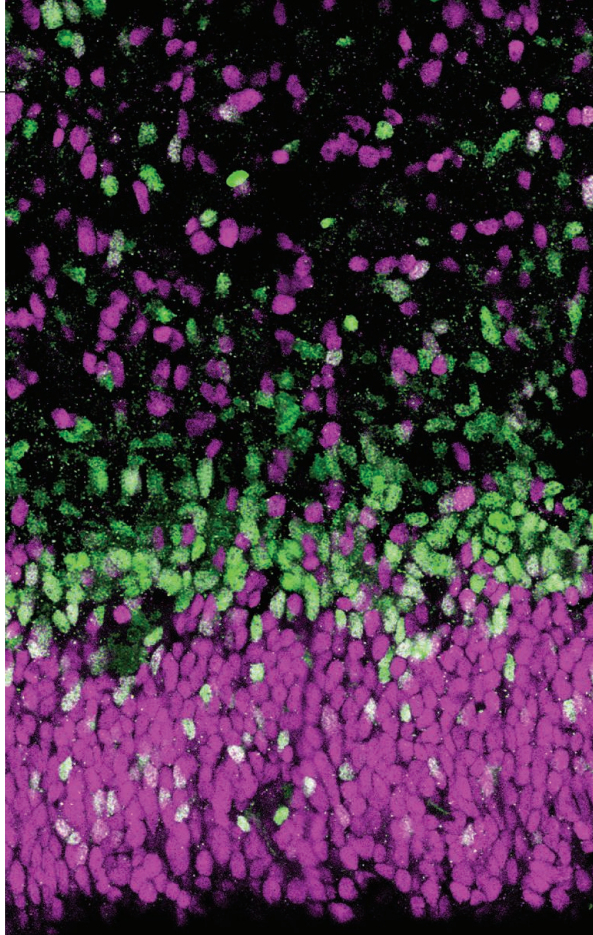
In the postmortem brain of *HTT* gene

Laboratory of Cellular Neurobiology, Department of Neurology, Massachusetts General Hospital and Harvard Medical School, Charlestown MA, USA.  
Email: difiglia@helix.mgh.harvard.edu

carriers, there is marked atrophy of the cortex and the neostriatum (which comprises the caudate nucleus and putamen in the human brain); the neostriatum is a region heavily innervated by the cortex (3). Thinning of the cortex can be detected by brain imaging a decade before disease onset (4). The loss of projections from neurons in the cortex to neurons in the neostriatum contributes to early signs of disease, including slight involuntary movements, decreased executive functions, and emotional changes. Most HD mouse models, including the one studied by Barnat *et al.*, are engineered with an expanded CAG repeat (Q111) in the mouse *Htt* gene; as these mice become adults, they do not develop the severe neuropathological features and motor deficits seen in the human disorder (3). One neuropathological feature shared between human and mouse HD is the presence of aggregates of mHTT that form in the nucleus and cytoplasm of cortical and neostriatal neurons (3, 5).

Barnat *et al.* found that mHTT in 13-week-old human fetal brain and 13.5-day-old mouse embryonic brain had impaired the processes that regulate interkinetic nuclear migration of progenitors and caused premature commitment of neuronal precursors to their differentiated cell fate. mHTT and other proteins were mislocalized and engaged in abnormal protein interactions that led to dysfunction. Cultured embryonic stem cells derived from the same HD mouse model (Q111) also exhibit “premature” neurogenesis caused by imbalance between progenitor and neural induction states (6). If this occurred throughout neurogenesis in individuals with HD, it could affect neuron density and distribution and cause smaller brain size. However, knowledge of other events in the embryonic and early postnatal periods—including generation of astrocytes, synapse formation and pruning, and programmed cell death—is necessary to discern the impact of the mutant HD gene on human cortex formation.

Wild-type HTT is expressed throughout the developing and adult mouse brain, and it is highly expressed in neurons (7). The protein reaches its highest expression levels in the developing mouse brain between postnatal days 2 and 7, when astrocytes populate the cortex and neurons start to extend branches and form synaptic connections. In this period, aberrant interactions by mHTT with other proteins are known



The developing human fetal brain is produced from apical progenitors (magenta) and basal progenitors (green) that generate neurons and are altered in carriers of the huntingtin gene mutation.

to interfere with many functions including membrane trafficking, cytoskeleton-dependent transport of synaptic vesicles, and synaptic activation. These altered functions can in turn disrupt synaptic connections between the cortex and other regions, thereby contributing to disease.

Studies support an influence of mHTT on cortical neurodevelopment. HD gene carriers have a subtle reduction in head circumference and lower body mass index decades before predicted onset (8). Moreover, human cortical neurons derived from stem cells of juvenile-onset HD patients are delayed in neurite growth and firing action potentials, and they express lower levels of genes involved in synaptic functions (9). In the same HD model (Q111) used by Barnat *et al.*, young mice had altered electrophysiological properties in neurons of the neostriatum, and older mice displayed subtle reductions in cortical volume and thickness (10).

The lasting effects of mHTT on neurogenesis and on postnatal and early adult brain development could be forestalled for decades by compensatory homeostatic processes. For example, molecular pathways are activated in human and mouse HD to cope with the oxidative stress and altered energy metabolism that occur in neurons

of HD patients (11). In HD mice, the expression of genes involved in synaptic function decreases early, whereas the expression of genes involved in responses to DNA damage and cell death increases later (12). Stem cells seem to accumulate in the subependymal region, adjacent to the caudate nucleus, of HD postmortem human brain, suggesting increased neurogenesis (13). Moreover, medium spiny neurons in the neostriatum of HD postmortem human brain can grow longer processes and sprout more spines, indicative of neuronal plasticity (14). The aggregates of mHTT formed in nuclei of cortical and neostriatal neurons are not linked to neuron death and may even facilitate neuron survival by sequestering the mutant protein and limiting abnormal protein interactions (5, 15).

The unequivocal evidence offered by Barnat *et al.* that the mutation in HD has effects on cortical neurogenesis in the human fetal brain stirs the question of how much this contributes to cortical changes that affect dysfunction. Identifying targets for therapy that specifically address neurodevelopmental milestones could be challenging.

The primary therapeutic approach today is to reduce the expression of *HTT* and the mutant protein it encodes. With these new findings in hand, it will be important to consider when treatment to lower expression of the mutant *HTT* gene should begin and whether such a therapy can attenuate potential deficits arising at an early stage in neurodevelopment. ■

#### REFERENCES AND NOTES

1. M. Barnat *et al.*, *Science* **369**, 787 (2020).
2. Huntington's Disease Collaborative Research Group, *Cell* **72**, 971 (1993).
3. J.-P. G. Vonsattel, *Acta Neuropathol.* **115**, 55 (2008).
4. H. D. Rosas *et al.*, *Brain* **131**, 1057 (2008).
5. M. DiFiglia *et al.*, *Science* **277**, 1990 (1997).
6. G. D. Nguyen, S. Gokhan, A. E. Molero, M. F. Mehler, *PLOS ONE* **8**, e64368 (2013).
7. P. G. Bhide *et al.*, *J. Neurosci.* **16**, 5523 (1996).
8. J. K. Lee *et al.*, *Neurology* **79**, 668 (2012).
9. S. R. Mehta *et al.*, *Cell Rep.* **25**, 1081 (2018).
10. M. Kovalenko *et al.*, *J. Huntingtons Dis.* **7**, 17 (2018).
11. J. M. Dubinsky, *J. Huntingtons Dis.* **6**, 267 (2017).
12. S. A. Ament *et al.*, *Mol. Syst. Biol.* **14**, e7435 (2018).
13. M. A. Curtis *et al.*, *Proc. Natl. Acad. Sci. U.S.A.* **100**, 9023 (2003).
14. G. A. Graveland, R. S. Williams, M. DiFiglia, *Science* **227**, 770 (1985).
15. F. Saudou, S. Finkbeiner, D. Devys, M. E. Greenberg, *Cell* **95**, 55 (1998).

#### ACKNOWLEDGMENTS

The author is supported by NINDS 1U01NS114098, CHDI Foundation, and Duke Family Fund.

10.1126/science.abd6215



# Designing a wider superelastic window

Adding chromium to an iron alloy enables shape recovery over a wide temperature range

By **Paulo La Roca**<sup>1</sup> and **Marcos Sade**<sup>2</sup>

**C**onventional metal alloys can only recover their original shape if subjected to very small elastic deformations. Superelastic alloys (also named pseudoelastic alloys) can recover their shape after deformations as great as 20% (1) just by unloading the force on the material. They are part of the larger group of shape-memory alloys but do not require a temperature change for recovery, and they have found applications in areas including robotics, structural engineering of buildings, and aerospace engineering (2, 3). A superelastic alloy usually exhibits this property only over a well-determined and often small temperature range normally called a “superelastic window.” On page 855 of this issue, Xia *et al.* (4) describe superelastic “invar” alloys with functional properties that

are independent of temperature over the largest superelastic window reported, from 10 to 473 K.

Superelasticity is explained by the presence of a stress-induced martensitic transformation. In this solid-solid displacive transition between two crystal structures, usually named austenite and martensite after the phases originally described in steel, much harder martensite forms by rapid quenching of austenite. This transition does not require diffusion because the atoms move over distances much smaller than the interatomic distance. The structure of these phases depends on the specific material (5). A schematic plot of a stress-deformation cycle corresponding to a martensitic stress-induced transition obtained at constant temperature (see the figure, left) is accompanied by a schematic of the evolution of a material sample as the transformation cycle goes on. The sample is initially fully austenitic (shown in gray). After a tensile stress is applied, the sample is elastically deformed; when the applied stress reaches

a critical value  $\sigma_T$ , a first martensitic plate forms (shown in blue).

A constant-stress plateau in the curve characterizes both the direct and inverse transitions, usually named transformation and retransformation, respectively. The end of the transformation plateau corresponds to the sample completely transformed to martensite. The inverse path is also shown until the material recovers the form when it reaches the original austenitic state. The functional properties of a superelastic alloy that determine its performance are the critical stress to induce the martensitic transformation  $\sigma_T$ , the retransformation stress  $\sigma_R$ , the hysteresis width  $H_\sigma$ , and the maximum recoverable strain  $\epsilon_{\max}$ . The dissipated energy in each transformation cycle, determined by the enclosed area of the cycle, increases as the hysteresis width and maximum recoverable deformation enlarge. This energy dissipation makes these alloys potential candidates as damping materials in devices to be used in buildings or aerospace structures (2, 3).

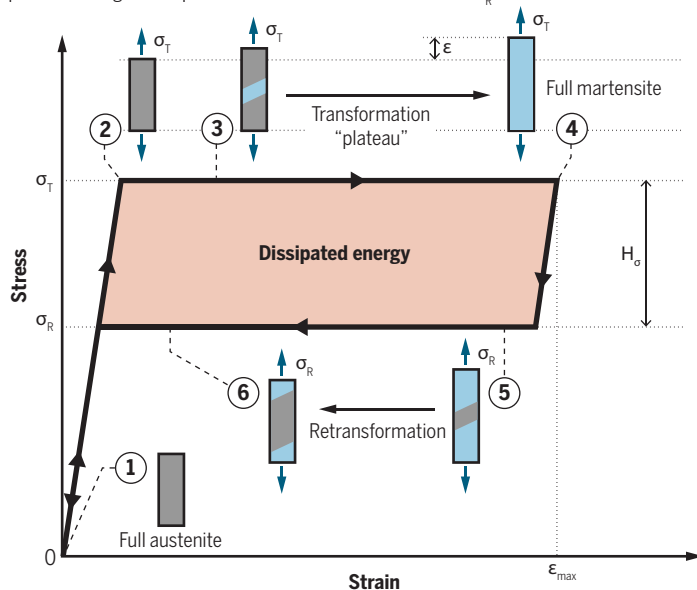
<sup>1</sup>Centro Atómico Bariloche (CNEA), 8400 Bariloche, Argentina. <sup>2</sup>Instituto Balseiro (Universidad Nacional de Cuyo–CNEA), CONICET, Bariloche, Argentina. Email: paulo.laroca@cab.cnea.gov.ar

## Widening the superelastic window

Superelastic alloys can recover their shape after deformation over a small temperature range. Xia *et al.* now report an almost temperature-independent response for a superelastic iron alloy.

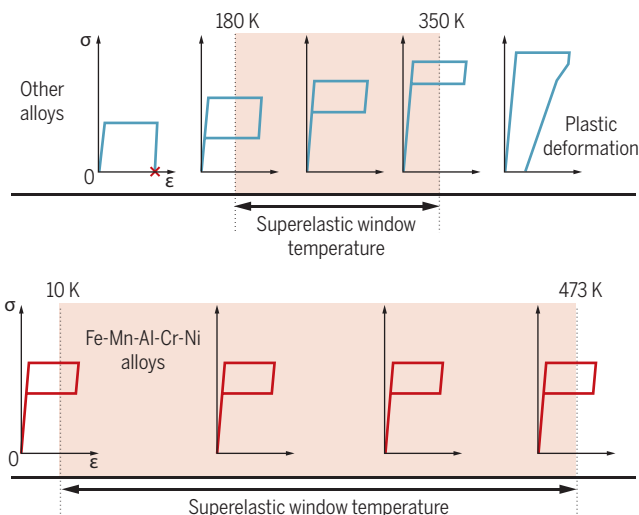
### Snapping back from strain

Pulling on an austenite sample transforms it to martensite at a constant stress  $\sigma_T$  and reaches a maximum elongation at a strain  $\epsilon_{\max}$ . When strain is released, the austenite phase and original shape are recovered but at a lower stress  $\sigma_R$ .



### A wider temperature range

Stress-induced transformations for a conventional superelastic material (blue curves) are limited at hysteresis (red cross) and by plastic deformation. The temperature range is for a Cu-Mn-Al shape-memory alloy (7). A very large superelastic window was reported by Xia *et al.* for a Fe-Mn-Al-Cr-Ni alloy (red curves).



The variation of functional properties with temperature can be strongly detrimental for several types of applications, such as damping devices in platforms that operate over a wide temperature range. Finding new alloys with functional properties independent of temperature variations would strongly increase the benefit of using superelastic alloys. For example, devices in space applications must function over a wide range of temperature variations (2, 6). Unlike a more conventional shape-memory alloy (7), the superelastic response of the Fe-Mn-Al-Cr-Ni alloy reported by Xia *et al.* can be considered independent of temperature (see the figure, right). The family of iron-nickel-based invar alloys already exhibits very low thermal expansion. The addition of Cr led to superelastic alloys in which this mechanical response was independent of temperature.

It is known from thermodynamic concepts related to martensitic transformations (first-order transitions) that the variation with temperature of the critical transformation stress needed to induce the martensite phase linearly depends on the entropy change between the involved phases. Thus, there is a thermodynamic magnitude that controls the effect of temperature on the most important parameter that characterizes the superelastic effect—that is,  $\sigma_p$ . If a specific superelastic alloy is designed to have a negligible amount of entropy change between the austenite and martensite phases, superelasticity independent of temperature should result.

Xia *et al.* showed that it is possible to control the entropy change with the addition of Cr to an Fe-Mn-Al-Ni alloy, and in this way, a composition was found where the entropy change was nearly zero. This remarkable result may be connected with magnetic order transitions that are present in both austenite and martensite phases, and this aspect deserves more attention in future research. Finally, Xia *et al.* show that the search for superelastic alloys with tunable entropy changes between austenite and martensite phases—for example, by varying composition—constitutes a powerful tool for designing alloys with remarkable properties. ■

#### REFERENCES AND NOTES

1. F. C. Bubbani, M. Sade, F. Lovey, *Mater. Sci. Eng. A* **543**, 88 (2012).
2. J. Mohd Jani *et al.*, *Mater. Des.* **56**, 1078 (2014).
3. P. La Roca, A. Baruj, M. Sade, *Shape Memory Superelasticity* **3**, 37 (2016).
4. J. Xia *et al.*, *Science* **369**, 855 (2020).
5. K. Otsuka, C. M. Wayman, *Shape Memory Materials* (Cambridge Univ. Press, rev. ed., 1999).
6. T. Omori *et al.*, *Science* **333**, 68 (2011).
7. Y. Sutou, N. Koeda, T. Omori, R. Kainuma, K. Ishida, *Acta Mater.* **57**, 5759 (2009).

#### ACKNOWLEDGMENTS

Supported by ANPCyT (PICT 2017-2198 and PICT 2017-4518), CONICET (PIP 2017-0634), and U.N.Cuyo (06/C588).

10.1126/science.abc8244

## NEUROSCIENCE

# The importins of pain

A nuclear protein importer modulates gene expression to control the persistence of neuropathic pain

By Muhammad Saad Yousuf and Theodore J. Price

Neuropathic pain, which is pain that arises from injury or disease affecting the somatosensory nervous system, affects millions of people with devastating consequences to their well-being. Available therapeutics have limited efficacy, and the underlying mechanisms governing the persistence of this disorder are mysterious. On page 842 of this issue, Marvaldi *et al.* (1) reveal that the nuclear import protein, importin  $\alpha 3$ , plays a crucial role in maintaining neuropathic pain months after a peripheral nerve injury in mice. Their findings demonstrate that activator protein 1 (AP1) family transcription factors require this nuclear transport complex for entrance to the sensory neuronal nucleus, pointing to a defined set of drug targets for the potential disruption of persistent neuropathic pain. An implication of the findings is that even very long-lasting neuropathic pain can be disrupted with disease-modifying therapeutics.

An important advance in the work of Marvaldi *et al.* is the demonstration of a mechanism that may be responsible for the transition to chronic neuropathic pain. The idea of an acute-to-chronic pain transition has received a lot of attention because clinical trials and clinical experience suggest that drugs used for acute pain are rarely effective for chronic pain (2). Acute pain typically has a clear cause, and the amount of pain is usually proportional to the injury or the stimulus. Chronic pain does not always have a clear cause, often persists after an injury has healed, and may be disproportionate to the original injury or to the apparent stimulus. These properties of chronic pain are particularly relevant in chronic neuropathic pain, which is often not recognized until it is chronic, because diagnostics to identify peripheral nerve damage are lacking, and treatment options are ineffective and limited. The neurons that are most commonly affected in neuropathic pain are sensory neurons in the dorsal root ganglion (DRG, which connects to the spinal cord); injury to these sensory DRG neurons was studied by Marvaldi *et al.*

Typically, researchers follow neuropathic pain in animal models for 20 to 30 days after induction with an injury to DRG neurons. The phenotype identified by Marvaldi *et al.* in mice lacking importin  $\alpha 3$  does not emerge until 60 days after peripheral nerve injury, a time point that is rarely explored in such studies. Specifically, reducing importin  $\alpha 3$  expression in sensory neurons also resolved neuropathic pain 60 days after nerve injury, as did interfering with AP1 transcription factor signaling using a variety of drugs. Notably, the authors demonstrate that reduction of AP1 signaling in sensory neurons of the DRG is the locus of this effect, in agreement with their importin  $\alpha 3$  findings. This strongly supports the conclusion that a late wave of importin  $\alpha 3$ -facilitated, AP1-driven gene expression in DRG neurons is responsible for persistent neuropathic pain (see the figure). One such gene that appears to be regulated by this late wave of AP1 activity is *Synap1*, which encodes a synaptic protein that might increase the strength of connections between the injured peripheral neurons and the first synapses in the pain pathway in the dorsal horn of the spinal cord in the central nervous system (CNS). This importin  $\alpha 3$ -driven facilitation of gene expression could presynaptically enhance signaling efficacy between DRG neurons and their targets in the CNS in neuropathic pain, representing an exciting candidate mechanism to explain the transition from acute to chronic neuropathic pain.

A critical insight from this work is a reconceptualization of the acute-to-chronic neuropathic pain transition. It is broadly accepted that neuropathic pain is initially driven by the emergence of spontaneous or ectopic activity in DRG sensory neurons, including pain-sensing neurons called nociceptors (3–5). However, once neuropathic pain becomes chronic, it is widely thought that there is a shift from changes in the peripheral nervous system toward independent CNS-mediated mechanisms, suggesting a “centralization” of neuropathic pain when it becomes chronic. The study of Marvaldi *et al.* does not upend this concept, but it places focus back on DRG neurons in the peripheral nervous system as the key drivers of chronic neuropathic pain.

This work persuasively demonstrates that there are likely distinct transcriptional programs in DRG sensory neurons that are responsible for different phases of neuropathic

University of Texas at Dallas, Center for Advanced Pain Studies, Richardson, TX, USA. Email: theodore.price@utdallas.edu; yousuf.muhammadsaad@utdallas.edu



pain. This complexity may contribute to why the disease is so challenging to treat, especially because most researchers have focused on the acute phase of injury. The work also parallels recent clinical findings demonstrating that peripheral nerve block with regional injection of lidocaine or lidocaine derivatives is almost always effective for alleviating neuropathic pain, even in people who have suffered for long periods of time (6, 7). Bringing our understanding of mechanisms in line with clinical observations is promising from the view of developing better therapeutics.

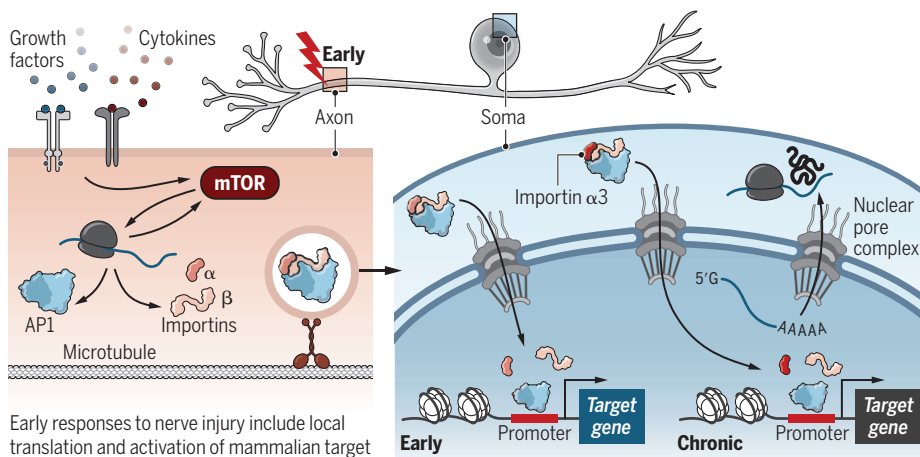
Injury to peripheral nerves turns on a regeneration program that is frequently accompanied by emergence of neuropathic pain. One of the earliest signaling events at the

importin  $\alpha 3$  and AP1 transcription factors, FOS and JUN. Sequencing of DRGs taken from humans with neuropathic pain demonstrate up-regulation in the expression of *FOS* and *JUN* in a subset of male neuropathic pain patients (5). This clinical parallel emphasizes the translational value of these findings.

Marvaldi *et al.* lay a new foundation for thinking about neuropathic pain. Focusing on the therapeutic potential of these mechanistic insights has potential for development of long sought-after disease-modifying therapeutics in this clinical space. The work demonstrates that drugs targeting AP1 transcription factors can be effective in reducing neuropathic pain in mice. Some of these drugs are already

## Importin $\alpha 3$ regulates persistent pain following nerve injury

Different combinations of activator protein 1 (AP1) transcription factors and importins are likely responsible for early versus chronic phases of neuropathic pain.



Early responses to nerve injury include local translation and activation of mammalian target of rapamycin (mTOR), which induces local translation of transcription factors, such as AP1 family members, and nuclear transporters, such as importins. These proteins then undergo retrograde transport to the nucleus.

In chronic neuropathic pain, importin  $\alpha 3$  selectively mediates nuclear translocation of AP1 transcription factors. Once in the nucleus, they regulate gene transcription and subsequent changes in protein synthesis that maintain the chronic pain state.

site of DRG axon injury is the local translation of the protein kinase mammalian target of rapamycin (mTOR), which then drives reprogramming of translational capacity in the axon (8). These events are critical for regeneration, but they also lead to local synthesis of transcription factors, such as cyclic adenosine monophosphate response element-binding protein (CREB) (9), and nuclear import factors, such as importin  $\beta 1$  (10), which then act as positive, retrograde signals linking axonal injury to transcriptional changes in the neuronal nucleus, paving the way for neuropathic pain. The study of Marvaldi *et al.* suggests that these transcriptional changes may be coordinated in temporal waves that are ultimately controlled by a nuclear membrane gatekeeper (importin  $\alpha 3$ ). Early signals may be mediated by CREB or other transcription factors, whereas late signals are controlled by

in existence and could be repurposed for pain treatment. Indeed, Marvaldi *et al.* intentionally considered drug repurposing when choosing AP1 inhibitors to study. Therefore, Marvaldi *et al.* have identified some excellent candidates for future study, namely sulmazole and sulfamethizole. ■

### REFERENCES AND NOTES

1. L. Marvaldi *et al.*, *Science* **369**, 842 (2020).
2. T. J. Price *et al.*, *Nat. Rev. Neurosci.* **19**, 383 (2018).
3. L. Djouhri *et al.*, *J. Neurosci.* **26**, 1281 (2006).
4. J. Serra *et al.*, *Pain* **153**, 42 (2012).
5. R. Y. North *et al.*, *Brain* **142**, 1215 (2019).
6. A. Vaso *et al.*, *Pain* **155**, 1384 (2014).
7. S. Haroutounian *et al.*, *Pain* **155**, 1272 (2014).
8. M. Terenzio *et al.*, *Science* **359**, 1416 (2018).
9. O. K. Melemedjian *et al.*, *Mol. Pain* **15**, S45 (2014).
10. S. Hanz *et al.*, *Neuron* **40**, 1095 (2003).

### ACKNOWLEDGMENTS

The authors are supported by NIH grant NS065926.

10.1126/science.abd4196

## SUPERCONDUCTIVITY

# A coexistence that $\text{CuO}_2$ planes can see

## Antiferromagnetism and superconductivity are not at odds in a quintuple-layer cuprate

By Inna Vishik

Superconductivity is a zero-resistance quantum-coherent state with applications to sensing, powerful electromagnets, and computing. Some materials have mysterious reasons for becoming superconducting, which continues to drive interest in the topic. Cuprates exhibit the highest superconducting transition temperature ( $T_c$ ) of known materials under ambient pressure, exceeding the boiling point of liquid nitrogen in many compounds. On page 833 of this issue, Kunisada *et al.* (1) show how a seldom-studied quintuple-layer cuprate,  $\text{Ba}_2\text{Ca}_4\text{Cu}_5\text{O}_{10}(\text{F},\text{O})_z$ , can help uncover the elusive superconductivity mechanism in these high-temperature superconductors.

Superconductivity is not found by itself in cuprates. Instead, interrelationships between multiple competing, coexisting, and intertwined electronic phases may be key to formulating a mechanism for cuprate superconductivity (2, 3). Despite this complexity, most experimental studies on cuprates have focused on a small handful of compounds (4, 5), even though hundreds of different cuprate superconductors have been identified. Key insights can be overlooked by studying compounds that manifest a particular phenomenon only weakly. In this context, seldom-studied cuprate compounds give a fresh perspective on a long-standing problem, especially if they are compatible with both surface spectroscopies and bulk transport measurements.

Cuprate properties can be tuned by modifying the number of charge carriers with a process called doping. Hole-doped cuprates involve introducing positive charge and achieve the highest  $T_c$ . The parent compound with no doping is an electrical insu-

Department of Physics, University of California Davis, Davis, CA 95616, USA. Email: ivishik@ucdavis.edu

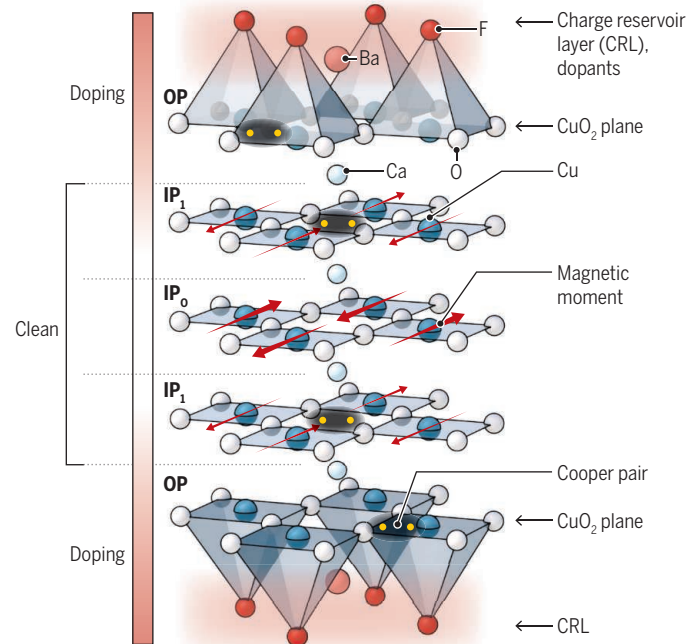
lator, owing to strong electron-electron repulsion, and the spins on adjacent copper sites point in opposite directions, making it an antiferromagnet. The antiferromagnetism is diminished by hole-doping, allowing superconductivity to emerge. The relationship between the antiferromagnetic electronic phase and the mechanism of superconductivity has driven cuprate research. Moreover, other families of unconventional superconductors—including heavy fermion materials, organic superconductors, and iron-based superconductors—have similar phenomenology in which superconductivity appears proximate to the demise of antiferromagnetic order. This has led to proposals of a common mechanism of superconductivity between these different superconductors, invoking dynamic excitations related to antiferromagnetism in joining electrons into Cooper pairs (6). Despite this, the electronic and superconducting properties inherent to lightly hole-doped cuprates are still poorly understood.

$\text{Ba}_2\text{Ca}_4\text{Cu}_5\text{O}_{10}(\text{F},\text{O})_2$  offers a distinct perspective by permitting access to the doping regime where superconductivity is in closest proximity to long-range antiferromagnetism while minimizing disorder. All cuprates share a structural unit of copper oxide ( $\text{CuO}_2$ ) planes, which participate most heavily in superconductivity. Doped electrons or holes are transferred to the  $\text{CuO}_2$  planes, but the elemental substitution actually happens in the portion of the crystal structure between blocks of  $\text{CuO}_2$  planes called the charge-reservoir layers (CRLs). The composition of the CRLs distinguishes different cuprate compounds. Cuprates can have one or more  $\text{CuO}_2$  planes in a structural block close to one another, separated by intervening CRLs.

The highest  $T_c$  is typically found in compounds with three or more adjacent  $\text{CuO}_2$  planes (7), making such materials highly promising for understanding factors that enhance  $T_c$ . In such compounds, one or more inner  $\text{CuO}_2$  planes (IPs) are not directly adjacent to the CRL. Because of this distance, IPs tend to have smaller doping and less disorder.  $\text{Ba}_2\text{Ca}_4\text{Cu}_5\text{O}_{10}(\text{F},\text{O})_2$  is a quintuple-layer cuprate, meaning

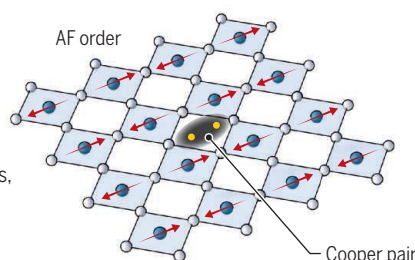
## Superconducting five-layer cuprate

The  $\text{Ba}_2\text{Ca}_4\text{Cu}_5\text{O}_{10}(\text{F},\text{O})_2$  superconductor has two outer  $\text{CuO}_2$  planes (OP), and two inner  $\text{CuO}_2$  planes (IP<sub>1</sub>) that sandwich a fifth  $\text{CuO}_2$  layer (IP<sub>0</sub>). Each layer has properties that combine to allow the compound to have both antiferromagnetism and superconductivity.



### A look inside

A top-down view of IP<sub>1</sub> shows the antiferromagnetic (AF) order and creation of a Cooper pair, which is needed for superconducting behavior. Unlike other cuprates, the AF order is retained when the material becomes superconducting.



that there are two types of IPs: one in the middle of the stack and two equivalently in the second and fourth positions. In  $\text{Ba}_2\text{Ca}_4\text{Cu}_5\text{O}_{10}(\text{F},\text{O})_2$ , each of the structurally inequivalent  $\text{CuO}_2$  planes tells a distinct story (see the figure). The outer planes yield information consistent with commonly studied single- and double-layer cuprates, whereas the two types of IPs reveal two  $\text{CuO}_2$  planes that are lightly hole-doped and still superconducting and one IP which is very lightly hole-doped and not superconducting.

Kunisada *et al.* first confirmed long-range antiferromagnetism in the IPs using two techniques: quantum oscillations and angle-resolved photoemission spectroscopy (ARPES). This multitechnique approach indicated a common ground state in high magnetic field and zero magnetic field. Evidence for antiferromagnetism was observed using the size and location of the Fermi surface, which is the locus of zero-

energy electronic excitations. This surface is also important for circumscribing the origin of superconductivity.

The superconducting gap is an excitation tied to the Fermi surface and reflects the energy required to break a Cooper pair, the bound pair of electrons that forms the charge carrier unit in a superconductor. In  $\text{Ba}_2\text{Ca}_4\text{Cu}_5\text{O}_{10}(\text{F},\text{O})_2$ , Kunisada *et al.* observed a superconducting gap on the outer IPs. The magnitude of the superconducting gap is large enough to suggest that superconductivity on these IPs is not a consequence of simply being near to the superconducting outer planes but instead that the IPs themselves are favorable for superconductivity while simultaneously hosting antiferromagnetism. Moreover, the IP superconducting gap does not extend to the antinodal regions of the Brillouin zone, where the superconducting gap is at a maximum in other cuprates, disputing proposals that superconductivity originates there. These results indicate that cuprate superconductivity can robustly coexist with long-range antiferromagnetism. Further, this study helps disentangle doping from chemical disorder to highlight how the latter may play a greater role in more commonly studied cuprates.

Understanding how superconductivity develops from an antiferromagnetic insulator may be key to uncovering the elusive mechanism of superconductivity in cuprate high-temperature superconductors. The high-quality surface-sensitive ARPES and bulk-sensitive quantum oscillation observations on  $\text{Ba}_2\text{Ca}_4\text{Cu}_5\text{O}_{10}(\text{F},\text{O})_2$  move the field closer to this goal while highlighting the importance of continued investigation of cuprates with three or more adjacent  $\text{CuO}_2$  layers. ■

### REFERENCES AND NOTES

1. S. Kunisada *et al.*, *Science* **369**, 833 (2020).
2. M. Hashimoto, I. M. Vishik, R.-H. He, T. P. Devereaux, Z.-X. Shen, *Nat. Phys.* **10**, 483 (2014).
3. E. Fradkin, S. A. Kivelson, J. M. Tranquada, *Rev. Mod. Phys.* **87**, 457 (2015).
4. S. Hufner, M. A. Hossain, A. Damascelli, G. A. Sawatzky, *Rep. Prog. Phys.* **71**, 062501 (2008).
5. C. C. Homes *et al.*, *Nature* **430**, 539 (2004).
6. D. J. Scalapino, *Rev. Mod. Phys.* **84**, 1383 (2012).
7. A. Iyo *et al.*, *J. Phys. Soc. Jpn.* **76**, 094711 (2007).

10.1126/science.aba9482



RETROSPECTIVE

# Michael Soulé (1936–2020)

Founder of conservation biology

By David W. Inouye<sup>1,2</sup> and Paul R. Ehrlich<sup>3</sup>

**M**ichael Soulé, widely credited with starting the field of conservation biology, died on 17 June at age 84. Michael's research laid the intellectual groundwork for a new avenue of study, and he cofounded the Society for Conservation Biology in 1985 to ensure that the nascent field had the resources and organization to address the critical environmental issues we face today. Michael's vision of a better world, in which nature holds a central place, has inspired scientists and nature enthusiasts across the globe.

Born on 28 May 1936, Michael grew up in San Diego, California. His free-ranging childhood, spent exploring tide pools and collecting abalones and lobsters, sparked his lifelong love of natural history and helped shape his interest in ecosystems. Michael obtained his undergraduate degree in biology at San Diego State College and his Ph.D. in biology in 1964 from Stanford University in Stanford, California.

After joining the biology faculty at the University of California (UC) San Diego in 1967, Michael became troubled by the rapid loss of natural habitats in Southern California. He resigned from the university in 1979 to become director of the Kuroda Institute for the Study of Buddhism at the Zen Center of Los Angeles. In 1984, he returned to academia, first teaching at the University of Michigan and then, in 1989, moving to UC Santa Cruz, where he served as chair of the environmental studies department and helped start the environmental studies Ph.D. program, one of the first in the United States.

Michael's research spanned conservation, evolutionary biology, population genetics, island biogeography, environmental studies, biodiversity policy, and ethics. His work helped distinguish conservation biology as a field with a mission (conserving biodiversity), an urgency (species are going extinct), and a need for a broad focus (including economics, policy, and ecology). Although his fieldwork provided new insights, Michael's greatest contribution was to introduce, and argue for, big ideas in developing the field.

In 1978, Michael helped convene the First International Conference on Research in Conservation Biology, and in 1980, he coauthored with Bruce Wilcox the field's first textbook. He was a cofounder and president of the Wildlands Network, co-chair of the science council for Australia's WildCountry Project, and a council member of RewildingEarth. In 1998, he and conservation biologist Reed Noss wrote the first paper about restoring habitat at a continental scale, a strategy they called "rewilding," which is now an international movement.

Another example of Michael's characteristic foresight was his decision to begin sampling insect populations at the Rocky Mountain Biological Laboratory in 1984. This ongoing project recently served as the source for reports that climate change has caused substantial insect decline in that undisturbed habitat. Michael's childhood familiarity with the chaparral canyons of San Diego contributed to his insights about the effects of coyotes as predators and the consequences of their disappearance. In their groundbreaking 1999 *Nature* paper, he and his graduate student Kevin Crooks introduced the idea that coyotes flourish in the absence of larger predators and in turn reduce small-predator populations, allowing prey populations to increase.

I (P.R.E.) met Michael when he became one of my first grad students in 1959. He showed his independence and humor from the very start. At the end of a seminar, eminent biologist Ernst Mayr—our invited guest—said, "I always instruct my grad students to tell me if they think I'm mistaken." Michael quipped, "Does that go for grad students at other universities, too?" Ernst laughed, but our department chair, sitting next to me, thought it a terrible insult and whispered that I should get rid of Michael. I disagreed, and Michael and I became lifelong friends and colleagues.

The recent appearance of a wolf pack in Colorado cheered Michael, who hoped he might also see the return of grizzly bears to

the state. His love of nature was profound, and he was always willing to share his knowledge of natural history. He was eager to participate in river trips, including an 18-day raft trip I (D.W.I.) led through the Grand Canyon, where Michael rowed his own raft and shared his expertise about local amphibians and reptiles.

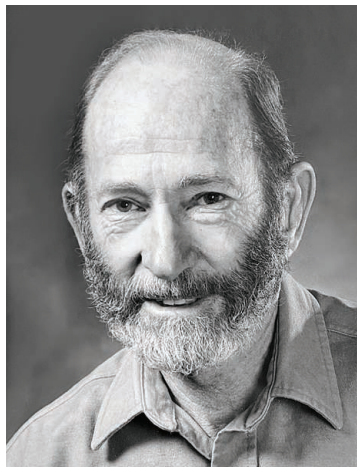
Michael was an inspiring speaker. At the 2000 meeting of the Society for Conservation Biology, he ended his talk with a plea for contributions to fund the society's programs. In response, many hundreds of dollar bills fluttered down from the balcony into the audience below, as Michael watched with surprise and delight.

After retiring in 1998, Michael contributed his expertise to local nongovernmental environmental organizations and promoted biological mosquito control. He consulted on wildlands conservation for governments in Romania, Australia, and the Republic of

Georgia, as well as the United States. In the rural town of Paonia, Colorado, located in an agricultural valley flush with small farms, orchards, and vineyards, Michael and June, his wife, enjoyed kayaking and rafting. Despite his Buddhist bent, Michael was an occasional carnivore and hunter of big game, especially species numerous enough to cause overgrazing, such as introduced caribou in Alaska.

A fellow of the American Academy of Arts and Sciences, Michael was also awarded a Guggenheim Fellowship, the Archie Carr Medal, and the Edward O. Wilson Biodiversity Technology Pioneer Award. *Audubon* magazine named him as one of the 100 Champions of Conservation of the 20th Century. He received the National Wildlife Federation's National Conservation Achievement Award for Science in 1998 and the Zoological Society of San Diego's Conservation Medal in 2007.

His gentle demeanor, sense of humor, scientific expertise, and visionary leadership, tempered by a Buddhist perspective, made Michael approachable, collegial, and memorable. Leading the development of a field in which science must be combined with policy and economics to produce successful outcomes required foresight and commitment, which will be carried on by the generations of conservation biologists inspired by Michael's example. ■



<sup>1</sup>Department of Biology, University of Maryland, College Park, MD 20742, USA. <sup>2</sup>Rocky Mountain Biological Laboratory, Crested Butte, CO 81224, USA. <sup>3</sup>Department of Biology, Stanford University, Stanford, CA 94305, USA. Email: inouye@umd.edu



An artistic rendering shows the predicted merger of the Milky Way and Andromeda galaxies.

## ASTROPHYSICS

## How it all ends

A light-hearted exploration of the death of the Universe serves as an effective antidote for everyday worries

By **Paul Halpern**

In these challenging times for Earth, the notion of exploring and inhabiting other worlds is enticing. After all, if someday humanity's existence on this planet appears threatened, we might continue civilization elsewhere—assuming we have the technology to do so. Yet, as astrophysicist and popular science communicator Katie Mack shows in her excellent, far-reaching debut book, *The End of Everything* (*Astrophysically Speaking*), at some point the entire Universe's luck will run out.

In clear, succinct prose, Mack details five different ways the cosmos might end. For the first possibility, “the Big Crunch,” she posits that the Universe's expansion will reverse itself into a lethal crush that manifests as collisions between neighboring galaxies. In this scenario, she argues, the Milky Way will crash together with Andromeda, and old stars will suddenly be jolted from their orbits, while, elsewhere, hydrogen gas coalesces and ignites to form new stars. The Sun, by then a swollen red giant, will have subsumed our mother planet. Meanwhile,

many such collisions will occur between numerous other galaxies, until all of space has been condensed back down to a single highly compressed, potentially infinitely dense glob. Scary? Very much so. She reassures us, however, that mounting astronomical evidence indicates that cosmic collapse is very unlikely.

Before we can breathe a sigh of relief, Mack reveals a second scenario that might be even worse for the Universe than the first: the space-stretching effect of dark energy. An abundance of observational data indicates that an unknown agent is accelerating the expansion of the Universe, driving distant galaxies farther away from our own at a faster and faster rate. What is not known yet is how that dark energy behaves over time. Some models endow it with greater potency than others.

Albert Einstein once added a fudge factor, known as the cosmological constant, to the equations of general relativity to artificially induce stable solutions. At that time, he did not believe in cosmic growth or shrinkage. Once Edwin Hubble revealed evidence of the recession of galaxies, which was in agreement with Georges Lemaître's theory

of an expanding Universe, Einstein decided to eliminate the term. However, Einstein may have been right to include such a constant after all. Although dark energy could well be volatile, most astronomical observations indicate that it is relatively steady, conveying a rate of accelerated expansion that is comparable to what is predicted when a cosmological constant is retained in the relativity equations.

If the Universe were to succumb to dark energy-induced expansion, an increasingly rapid stretching of space would eventually isolate us from the bulk of the Universe. Over the eons, all stars would burn out, resulting in a lack of usable energy, a scenario called “heat death.” But what if dark energy turns out to be even more potent than a cosmological constant, overcoming every possible form of attraction and rendering everything unstable? Mack devotes perhaps the most frightening chapter of all to this scenario, known as “the Big Rip,” in which everything—including space itself—is torn into shreds.

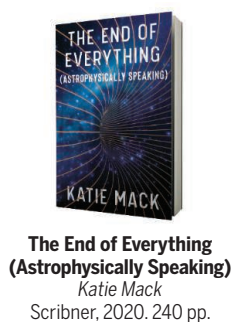
In the chapter that follows, she explores yet another kind of cosmic catastrophe, this one triggered by changes, on the quantum level, of the vacuum state of the Universe. Like a frozen river that permits skaters to frolic on its surface, the vacuum state supports the particle dynamics that make life possible. But, just as rising temperatures might cause chunks of ice to break off and melt, unexpected cosmic conditions might suddenly disrupt the vacuum state, alter the masses of elementary particles, and sink the particle world.

The final and presumably most optimistic scenario that Mack describes is a “cosmic bounce,” which at least permits the prospect of new worlds after an interval of universal destruction. The basic idea is that the cosmos would experience endless cycles of devastation and rebirth. Having completed her Ph.D. thesis under Paul Stein-

hardt, the co-originator of one such model (called the ekpyrotic universe), she is the ideal writer to convey this theory's premise. And describe it well she does, drawing upon a clever analogy that involves hands clapping together and drawing apart.

All in all, *The End of Everything* serves as an outstanding, levelheaded guide to a horrific medley of ways the Universe might expire. The book is the perfect antidote to the malaise of mundane worries. ■

10.1126/science.abb9026



**The End of Everything**  
(*Astrophysically Speaking*)  
Katie Mack  
Scribner, 2020. 240 pp.

The reviewer is at the Department of Mathematics, Physics, and Statistics, University of the Sciences, Philadelphia, PA 19104, USA. Email: p.halpern@uscience.edu



## SCIENCE LIVES

# Science meets politics

A passion for promoting the public good guided geneticist J. B. S. Haldane's scholarship

By P. William Hughes

In 1906, 13-year-old Jack Haldane stood on the floor of Loch Striven, 40 meters under the sea. His father had sent him down to test whether decompression sickness—caused by nitrogen bubble formation in divers' blood—could be avoided by controlling the rate of ascent. In his leaky suit, Jack knew that each dive carried a risk of drowning. Still, the data they collected was invaluable. A risk-chasing and industrious scientist, his father was developing protocols that would benefit many people. It would be absurd—even immoral, Jack believed—to refuse to be his guinea pig.

Despite holding no formal science degree, the younger Haldane would himself go on to have an extraordinary scientific career, becoming one of the founders of modern evolutionary synthesis and a famous writer of popular science books. In a new biography, *A Dominant Character*, Samanth Subramanian highlights Haldane's many accomplishments and considers how his strong moral and political beliefs influenced his scientific work.

After recounting his early experiments with his father, the book follows young John Burdon Sanderson Haldane (nicknamed “Jack” or “JBS”) from his aristocratic origins in North Oxford to Eton College and then Oxford University, where he graduated in 1912 with first-class honors in classics and mathematics. His first great scientific success, we learn, was a 1915 paper on genetic linkage in mice, coauthored with his sister, Naomi. Although Haldane had always been interested in genetics, the positive reception of this paper, which Haldane completed while serving in the British Army during World War I, intensified his focus.

Between World Wars I and II, Haldane constructed mathematical formalizations of the laws of Mendelian inheritance and their impact on evolution by natural selection, culminating in his best-known work, a series of 10 papers written between 1924 and 1934 called *A Mathematical Theory of Natural and*

*Artificial Selection*. During this time, he also formulated two eponymous hypotheses: Haldane's rule, which predicted that the heterogametic sex (i.e., the XY male or ZW female) of a species hybrid is more likely to be sterile than the homogametic sex; and Haldane's dilemma, which asserted that the rate of adaptive evolution is limited because advantageous alleles rarely cosegregate efficiently.

Haldane wrote prolifically. He published one of the first textbooks on enzyme function; discussed chemical warfare, religious

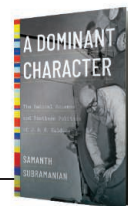


Haldane, shown holding a model air raid shelter, never lost the sense of public duty he learned as a young aristocrat.

faith, and air raid precautions in newspapers; argued with racist propagandists in eugenics journals; and even authored a futuristic manifesto (“Daedalus; or, Science and the Future”) that argued that advancements in biology would permit the abolition of disease and the self-direction of human evolution.

Haldane never lost the sense of public duty that he had learned as a young aristocrat, and in 1942, he joined the Communist Party of Great Britain (CPGB) and the editorial board of its newspaper, the *Daily Worker*. This came at a cost: MI5 kept a file on him for more than 30 years, and he was barred from speaking at certain American universities.

**A Dominant Character:**  
The Radical Science  
and Restless Politics  
of J. B. S. Haldane  
Samanth Subramanian  
Norton, 2020. 400 pp.



Subramanian explains that Haldane viewed science as the most effective tool for promoting the public good. He designed safer bomb shelters for Blitz-affected London and better mineshaft ventilation, and, like many others of this era, he advocated methods of eugenic family planning. Haldane's interest in genetics was motivated by a similar concern for human welfare. He wrote, for example, that “a satisfactory theory of natural selection must be quantitative,” but he also felt that it should be useful: Accurate quantification of artificial selection could assist plant breeders throughout the world.

Haldane's tempestuous relationship with authority led him to leave England for India in 1956. There, Haldane spent the twilight of his career, first at the Indian Statistical Institute (ISI) in Kolkata and later at a special research unit in Bhubaneswar. He explained that this move was his way of protesting the United Kingdom's repressive actions during the Suez crisis, and he argued that Jawaharlal Nehru's newly established Indian state was more conducive to scientific freedom. Nearing retirement, Haldane confined himself to simple but insightful breeding and biometry experiments and continued to write about science in the popular press.

Subramanian admonishes Haldane's belated rejection of Lysenkoism, suggesting that he demurred because he was reluctant to criticize fellow communists. This criticism lands awkwardly, mostly because Haldane did disown Lysenko—although not as quickly as his anticommunist peers—and eventually left the CPGB, disillusioned by its rejection of “bourgeois genetics.” However, Haldane clearly admired Stalin and tried to reconcile Darwinian evolution with Soviet dialectical materialism (“diamat”) pseudoscience. Subramanian suggests that these mistakes were the predictable result of the political views that motivated Haldane's best work.

Ultimately, Subramanian's depiction of Haldane is balanced and modern and should prove engaging to readers interested in the birth of genetics and in the intersection of science and political belief. ■

The reviewer is at the Department of Ecology, Environment, and Plant Sciences, Stockholm University, Stockholm, Sweden, and the Science for Life Laboratory, Stockholm, Sweden. Email: william.hughes@su.se

10.1126/science.abc6371

## LETTERS

Edited by Jennifer Sills

## Retraction

We have obtained new evidence, 6 years after the publication of our Report “Ammonia synthesis by  $N_2$  and steam electrolysis in molten hydroxide suspensions of nanoscale  $Fe_2O_3$ ” (1), that there is a trace  $NO_x^-$  impurity in the nanoscale  $Fe_2O_3$  that was unknown at the time. We no longer have the original nanoscale  $Fe_2O_3$ , and manufacturers’ content levels of impurities in chemicals may vary over time. However, recently purchased nanoscale  $Fe_2O_3$  per gram contains 0.0005 g N as  $NO_x^-$ , and an  $^{15}N_2$  isotopic tracer analysis conducted by Wenzhen Li, Yifu Chen, and Hengzhou Liu at Iowa State University; Shuang Gu at Wichita State University; and author S.L. suggests that this trace impurity, rather than  $N_2$ , is the major nitrogen reactant in the observed ammonia synthesis. We are retracting the original Report, and we encourage exploration of an  $N_2$  to  $NO_x^-$  intermediate to ammonia pathway, rather than direct elemental nitrogen pathway, to ammonia synthesis. All observed stimulation of ammonia generation with these (likely  $NO_x^-$ -containing) nanoscale  $Fe_2O_3$  materials, as well as all thermodynamic calculation results, remain accurate as documented in the original Report.

Stuart Licht<sup>1\*</sup>, Baochen Cui<sup>1</sup>, Baohui Wang<sup>1</sup>, Fang-Fang Li<sup>1</sup>, Jason Lau<sup>2</sup>, Shuzhi Liu<sup>1</sup>

<sup>1</sup>Department of Chemistry, George Washington University, Washington, DC 20502, USA.

<sup>2</sup>Department of Chemistry, Contra Costa College, San Pablo, CA 94806, USA.

\*Corresponding author. Email: slicht@gwu.edu

## REFERENCES AND NOTES

1. S. Licht *et al.*, *Science* **345**, 637 (2014).

10.1126/science.abe0412

## Controlling the coronavirus narrative

The corruption of scientific results has serious consequences for human health. Climate change deniers (1, 2) and people who amplify anti-vaccine messages (3) have created dangerous, enduring myths, giving rise to new problems for which scientists must now find solutions. Now, politicians are undermining the response to coronavirus disease 2019 (COVID-19) by disregarding scientific facts and the guidance of epidemiologists (4). Simultaneously, nonscientists have asserted that Black Lives Matter protests caused increases in COVID-19 cases,



when preliminary evidence suggests they were not a substantial factor (5). To combat this new misinformation, scientists must communicate clearly and dispute inaccurate, politically motivated narratives.

Black, Native, and Latinx Americans have shouldered the greatest burden of the unscientific COVID-19 mismanagement in the United States (6). Protests against police brutality have been dismissed as nonurgent or unnecessary, despite evidence that systemic racial injustice disproportionately kills Black Americans (7). Scientific evidence, which should be at the forefront of public discussions and policy on health and civil rights, has been drowned out by political arguments.

Scientists cautiously explain uncertainties while politicians and politically motivated media outlets emphatically cast blame and misappropriate scientific evidence. Scientists cannot allow propagandists to spread lies that dismantle a reasoned response to COVID-19 or urgently needed progress toward health equity and social justice for Black Americans. Informed scientists must take a strong public stance on complex issues, emphasizing evidence to clearly communicate and contextualize scientific results to the public, not just to other scientists. Institutions must recognize that the current system of promotion and tenure devalues such communication, at a huge societal cost.

Irresponsible, unscientific voices have killed too many because of their reach and efficacy. Academic incentives must be updated to meaningfully reward outreach efforts, and scientific training should prepare scientists to discuss their findings

with the public. In the meantime, scientists who have the capacity, seniority, and job security should help value and amplify the messages and motivations of those who are willing to participate in public engagement, often at the expense of career advancement. It is essential for scientists to work across disciplines and integrate multiple communication strategies to make scientific evidence understandable, engaging, and approachable.

Nita Bharti

Biology Department, Center for Infectious Disease Dynamics, The Pennsylvania State University, University Park, PA 16802, USA. Email: nita@psu.edu

## REFERENCES AND NOTES

1. B. Deese, R. A. Klain, “Another deadly consequence of climate change: The spread of dangerous diseases,” *The Washington Post* (2017).
2. W. C. Tucker, *Ecol. Law Quart.* **39**, 831 (2012).
3. O. Bencke, S. E. DeYoung, *Glob. Pediatr. Health* **6**, 2333794X19862949 (2019).
4. E. Lipton *et al.*, “He could have seen what was coming: Behind Trump’s failure on the virus,” *The New York Times* (2020).
5. D. M. Dave, A. I. Friedson, K. Matsuzawa, J. J. Sabia, S. Safford, “Black Lives Matter protests, social distancing, and COVID-19,” National Bureau of Economic Research Working Paper No. 27408 (2020); <https://www.nber.org/papers/w27408>.
6. “Health equity considerations and racial and ethnic minority groups” (Centers for Disease Control and Prevention, 2020).
7. L. Peoples, *Nature* **573**, 24 (2019).

10.1126/science.abd3662

## Dismantling systemic racism in science

In his Editorial “Time to look in the mirror” (12 June, p. 1161), H. H. Thorp calls on scientists to recognize systemic racism





Preliminary evidence indicates that protests demanding justice for Black Americans, such as this one, have not caused a spike in COVID-19 infections.

within the science community. As part of this self-reflection, scientists should consider the many ways that inequality manifests in science, including science's historical contributions to discrimination, the lack of representation in science, and the extra burden placed on minority scientists to fix issues relating to diversity and inclusion. Understanding the scope of systemic inequality in science will enable genuine and sustainable efforts to make scientific institutions fair for all.

Racial categories historically developed and endorsed by scientists led to a hierarchy of groups seen as superior or inferior. Although unsupported by biological evidence, these categories have had devastating effects on non-white communities throughout history. The myth that racial groups were fundamentally different was used to justify colonialism, slavery, genocide, and eugenics (1), and it still governs policies today. The intersectionality of racism and modern society has left a legacy of racial disparities in socioeconomic status (2), education (3), and health (4, 5).

The lack of diversity in scientific institutions reveals ongoing systemic racism in the field. As of 2019, less than 1% of UK professors were Black (6). Black female professors in the United Kingdom experience bullying, racial discrimination, and institutional neglect (7). Systemic racism has also contributed to the lack of diverse representation. Even textbooks currently lack representation of Black female scientists (8). According to a recent report, leadership positions such as CEO or executive in the biotech industry are largely occupied by white professionals

(9). A majority of these leaders claimed to be committed to diversity and inclusion, but diversity and inclusion training or programs existed in only half of the organizations surveyed, and 41% of organizations did not monitor diversity (such as employee demographics) or discrepancies in performance rankings, pay, and promotion (9).

Unfortunately, scientists from underrepresented groups are often the ones who take on the responsibility (often coupled with additional labor and minimal recognition) of trying to change a racist system (10). To lighten their burden, white colleagues should also take responsibility for dismantling systemic racism in the science community. Although there is no single "one size fits all" approach to addressing inequality, there are common themes and actions that can be implemented in scientific institutions.

Scientists involved in hiring should implement advertising strategies, especially at leadership levels, that attract diverse applicant pools, and they should facilitate fair decisions by forming diverse recruitment panels. To retain diverse individuals, leaders should promote an inclusive environment. To do so, they must develop training material on understanding and tackling bias and create safe spaces for professionals to speak freely and honestly. All departments should develop zero-tolerance, anti-racism policies and put procedures in place that effectively handle complaints about racism and race-related aggression. Mentoring schemes should be embedded into departments to address the neglect that Black, Indigenous, and people of color often experience when navigating their career. Underrepresented individuals (many of whom are already used as unpaid consultants) should be given the power to make important decisions.

All scientists should recognize the achievements of diverse individuals. Recognition includes citing their work, referring them for opportunities, nominating them for awards, and teaching their work in classes. Appropriately recognizing the work of underrepresented individuals will enable them (rightly) to be as competitive as their white counterparts when looking to progress professionally. By taking these steps, scientists of all backgrounds can help create a more inclusive, diverse, and fair community.

**Esther A. Odekunle**

GlaxoSmithKline, Stevenage, Hertfordshire SG1 2NY, UK. Email: e.a.odekunle@gmail.com

#### REFERENCES AND NOTES

1. R. J. Cottrol, *J. Social Hist.* **49**, 740 (2015).
2. D. R. Williams et al., *Health Psychol.* **35**, 407 (2016).
3. K. Weir, *Monitor Psychol.* **47**, 42 (2016).

4. Petersen et al., *MMWR Morb. Mortal. Wkly. Rep.* **68**, 423 (2019).
5. S. Yaya, *BMJ Glob. Health* **5**, e002913 (2020).
6. Higher Education Statistics Agency, "Who's working in HE?: Personal characteristics" (2019); [www.hesa.ac.uk/data-and-analysis/staff/working-in-he/characteristics](http://www.hesa.ac.uk/data-and-analysis/staff/working-in-he/characteristics). To view the number of Black professors compared with the total number of professors, in the "Personal characteristics by occupational classification" table, select "Show: Ethnicity" and "Contract levels: Professor."
7. N. Rollock, "Staying Power" (University and College Union, 2019); [www.ucu.org.uk/media/10075/Staying-Power/pdf/UCU\\_Rollock\\_February\\_2019.pdf](http://www.ucu.org.uk/media/10075/Staying-Power/pdf/UCU_Rollock_February_2019.pdf).
8. S. Wood et al., *Proc. R. Soc. Ser. B Biol. Sci.* **287**, 20200877 (2020).
9. Biotechnology Innovation Organization, "Measuring diversity in the biotech industry: Building an inclusive workforce" (Center for Talent Innovation and BIO, 2020); [http://go.bio.org/rs/490-EHZ-999/images/Measuring\\_Diversity\\_in\\_the\\_Biotech\\_Industry\\_Building\\_an\\_Inclusive\\_Workforce.pdf](http://go.bio.org/rs/490-EHZ-999/images/Measuring_Diversity_in_the_Biotech_Industry_Building_an_Inclusive_Workforce.pdf).
10. M. F. Jimenez et al., *Nat. Ecol. Evol.* **3**, 1030 (2019).

10.1126/science.abd7531

## Untapped resources for medical research

A therapeutic solution to the coronavirus disease 2019 (COVID-19) pandemic is urgently needed, but new drug discovery and development are lengthy processes. Pharmaceuticals derived from plants and fungi remain important in our armory against numerous diseases (1, 2), yet much of plant and fungal biodiversity remains unexplored for drug discovery (3). Of about 350,000 known plant species, 7% have medicinal uses (1, 4), and the wider potential of the world's flora to yield new medicines has been discussed by conservation biologists for decades (5). We urgently need a comprehensive scientific study of biodiversity to inspire, accelerate, and innovate medicinal discovery.

Acquiring usable plant and fungal material is resource-consuming, but a partial solution lies in specimens already housed in herbaria, botanic gardens (6), and fungal biological resource centers. Herbaria host about 380 million specimens from all described plant species (7), and botanic gardens maintain about one-third of all known land plant species (8). Fungal collections currently host about 860,000 strains worldwide (9). These collections are invaluable resources representing unparalleled chemical diversity.

Evolutionary relationships inferred from DNA could be used to guide selection of species with medicinal potential. Just a few milligrams from specimens enable comprehensive chemical profiling, uncovering new chemical entities that share chemical or physical characteristics with drug molecules, potentially with novel modes of action (1). Artificial intelligence and emerging technologies could reveal

# Where Science Gets Social.

## AAAS.ORG/COMMUNITY



AAAS' Member Community is a one-stop destination for scientists and STEM enthusiasts alike. It's "Where Science Gets Social": a community where facts matter, ideas are big and there's always a reason to come hang out, share, discuss and explore.

**Member  
COMMUNITY**  
AAAS

AMERICAN ASSOCIATION FOR THE ADVANCEMENT OF SCIENCE

compounds with mechanistic effects relevant to diseases threatening humanity (1, 10). Furthermore, collections are increasingly used to generate genomic data, which could be used to identify members of gene families known to be involved in the synthesis of useful compounds (11).

Investing in a new era of large-scale exploration of therapeutic candidates from nature could help humanity prepare for future health challenges. Scientists, governments, and other stakeholders must establish functional and equitable agreements to ensure that this work complies with the Nagoya Protocol and associated access and benefit sharing legislation and reflects the value and origins of specimens collected during the colonial era (12). It is also critical that benefits are shared with the nations and Indigenous peoples from where these resources derive.

Oscar A. Pérez-Escobar<sup>1</sup>, James E. Richardson<sup>2,3</sup>, Melanie-Jayne R. Howes<sup>1,4\*</sup>, Eve Lucas<sup>1</sup>, Noelia Álvarez de Roman<sup>5</sup>, Jérôme Collemare<sup>6</sup>, Ian A. Graham<sup>7</sup>, Joachim Gratzfeld<sup>5</sup>, Paul J. Kersey<sup>1</sup>, Ilia J. Leitch<sup>1</sup>, Alan Paton<sup>1</sup>, Peter M. Hollingsworth<sup>3</sup>, Alexandre Antonelli<sup>1,8</sup>

<sup>1</sup>Royal Botanic Gardens, Kew, TW9 3AE, UK. <sup>2</sup>Department of Biology, Faculty of Natural Sciences, Universidad del Rosario, Bogotá, Colombia. <sup>3</sup>Royal Botanic Garden Edinburgh, Edinburgh, EH3 5LR, UK. <sup>4</sup>Institute of Pharmaceutical Science, Faculty of Life Sciences & Medicine, King's College London, SE1 9NH, UK. <sup>5</sup>Botanic Gardens Conservation International, Richmond, TW9 3BW, UK. <sup>6</sup>Westerdijk Fungal Biodiversity Institute, Utrecht, Netherlands. <sup>7</sup>Department of Biology, Centre for Novel Agricultural Products, University of York, York, YO10 5DD, UK. <sup>8</sup>Gothenburg Global Biodiversity Centre and University of Gothenburg, Gothenburg, Sweden.

\*Corresponding author: Email: m.howes@kew.org

### REFERENCES AND NOTES

1. M.-J. R. Howes *et al.*, *Plants, People, Planet*. 10.1002/ppp3.10138 (2020).
2. D. J. Newman, G. M. Cragg, *J. Natural Prod.* **83**, 770 (2020).
3. J. W. H. Li, J. C. Vederas, *Science* **325**, 161 (2009).
4. K. J. Willis, Ed., "State of the World's Plants 2017" (Royal Botanic Gardens, Kew, UK, 2017); <https://stateoftheworldsplants.org>.
5. W. F. Laurance *et al.*, *Science* **278**, 1117 (1997).
6. E. K. Meineke *et al.*, *Ecol. Monographs* **88**, 505 (2018).
7. A. James *et al.*, *Appl. Plant. Sci.* **6**, e1024 (2018).
8. R. Mounce *et al.*, *Nat. Plants* **3**, 795 (2017).
9. World Data Centre for Microorganisms (WDCM) Culture Collections Information Worldwide ([www.wdcm.org/](http://www.wdcm.org/)).
10. J. M. Stokes *et al.*, *Cell* **180**, 688 (2020).
11. R. D. Kersten, J.-K. Wenig, *Proc. Natl. Acad. Sci. U.S.A.* **115**, E10961 (2018).
12. S. Das, M. Lowe, *J. Natural Sci. Collect.* **6**, 4 (2018).

### COMPETING INTERESTS

O.A.P.-E. receives financial support from the Swiss Orchid Foundation and the Sainsbury Orchid Trust. I.A.G. is Director of the United Kingdom Research and Innovation–Biotechnology and Biological Sciences Research Council (UKRI-BBRSC) High Value Biorenewables Network. A.A. receives financial support from the Swedish Research Council, the Swedish Foundation for Strategic Research, the Knut and Alice Wallenberg Foundation, and the Royal Botanic Gardens, Kew.

10.1126/science.abc8085

sciencemag.org **SCIENCE**



# RESEARCH

## IN SCIENCE JOURNALS

Edited by Michael Funk

### TROPICAL FOREST

#### The carbon gain in restored logged forest

**T**here is currently great interest in the capacity of global forest to store carbon and hence contribute to the mitigation of climate change in the coming decades. In a study of Southeast Asian tropical forest, Philipson *et al.* show that active restoration of logged forests generates higher rates of carbon accumulation than naturally regenerating forest. To estimate the economic feasibility of restoration treatments, they modeled the carbon price required to offset the cost of restoration, finding that the highest prices seen in recent years would be needed to approach those that could offset restoration costs. These results are important for tropical forest policy, establishing the importance of restoration for the carbon recovery potential of tropical forests. —AMS *Science*, this issue p. 838

Efforts to restore tropical forests in Sabah, Malaysia, can accelerate carbon storage but require high prices on carbon.

### ORGANIC CHEMISTRY

#### Trio of enzymes power divergent synthesis

Diterpene natural products are built from a 20-carbon building block, with a huge range of possible structures and modifications. Chemical synthesis of specific molecules, some of which have valuable biological activities, is tricky because of the need for selective oxidations and rearrangements when starting from widely available scaffolds. Zhang *et al.* characterized selectivities for three oxidative enzymes that each attack different positions on a common scaffold. They then seamlessly combined chemical transformations with the enzymatic oxidations to produce nine distinct compounds across three families of diterpenes. These results highlight the potential of hybrid organic-biocatalytic

synthetic schemes for divergent synthesis. —MAF

*Science*, this issue p. 799

### IMMUNOLOGY

#### A loose BAF puts its foot on the cGAS

A signaling pathway in vertebrates called cGAS-STING detects the presence of intracellular DNA as a surrogate for both cellular damage and viral infection. At the same time, sensing of self-DNA must be suppressed to prevent the development of autoimmune responses. Guey *et al.* identify barrier-to-autointegration factor 1 (BAF) as a protein that intrinsically competes with the cGAS component of this pathway for binding to genomic self-DNA. When there is a breakdown in nuclear compartmentalization, cytosolic cGAS enzymatic activity is prevented because

of BAF. This work suggests that the regulation of DNA detection by the innate immune system relies on more complex mechanisms than simple physical separation alone. —STS

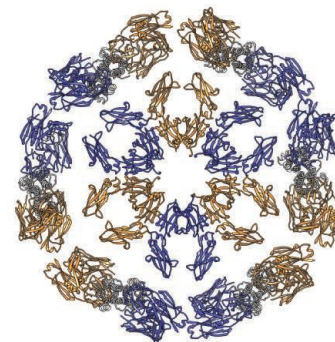
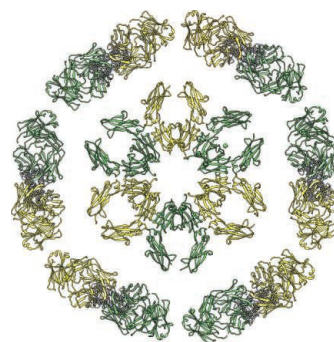
*Science*, this issue p. 823

### STRUCTURAL BIOLOGY

#### Strength in numbers

Human cluster of differentiation 20 (CD20) is expressed

on malignant B cells and is the target of therapeutic antibodies used in cancer immunotherapy. Kumar *et al.* now present structures that explain why so-called type I antibodies efficiently activate the complement pathway to kill cells, whereas type II antibodies do not. Type I antibodies each bind to two CD20 dimers and form clusters that facilitate binding to a



Hexameric assembly models illustrate potential differences in compactness between therapeutic antibodies (rituximab, left; ofatumumab, right).

component of the complement pathway. The second-generation type I antibody ofatumumab has molecular features that make it more efficient at clustering than first-generation rituximab. By contrast, the type II antibody obinutuzumab interacts with just one CD20 dimer and cannot form higher-order assemblies. Understanding these mechanisms will inform the design of next-generation immunotherapies. —VV

*Science*, this issue p. 793

## NEURODEVELOPMENT Mitochondrial dynamics and cell fate

Radial ganglia cells, the stem cells of early brain development, can generate more of themselves or generate differentiating neurons. Iwata *et al.* now show that these fate decisions involve the mitochondria. Cells that have fragmented mitochondria shortly after mitosis are more likely to become neurons, whereas cells that are undergoing mitochondrial fusion are likely to continue being stem cells. —PJH

*Science*, this issue p. 858

## METALLURGY Temperature-stable superelasticity

Shape memory alloys are superelastic, which means that they can recover their original shape after a large amount of strain. However, in most alloys, this behavior tends to only work well for a small range of temperatures. Xia *et al.* identified an iron-manganese-aluminum-chromium-nickel alloy for which superelasticity is virtually temperature independent (see the Perspective by La Roca and Sade). This distinctive property is attractive for a variety of applications in which large temperature variations are normal, such as in space exploration. —BG

*Science*, this issue p. 855;  
see also p. 773

## ECOLOGY Ozone pollution threatens biodiversity

Terrestrial ecosystem composition and biodiversity are tightly linked to environmental factors, and there are concerns that they may be at risk from anthropogenic ozone pollution. In a Review, Agathokleous *et al.* synthesize widespread evidence that ozone pollution can affect key ecological processes and functions of terrestrial ecosystems and alter the diversity of plants, insects, and soil microorganisms. They also identify areas of high endemic richness throughout the world that will also be at high ozone risk by the end of the century. These advances in our understanding of ozone pollution and its effects present new challenges for the preservation of terrestrial biodiversity. —YL

*Sci. Adv.* 10.1126/  
sciadv.abc1176 (2020).

## CELL TRANSPLANTATION A second transplant for intestinal disease

Allogeneic hematopoietic cell transplantation (HCT) is a beneficial treatment for blood and bone marrow cancers. However, HCT can lead to graft-versus-host disease (GvHD), which affects various organs, including the gut. Fecal microbial transplantation (FMT) from a healthy donor has successfully treated intestinal disorders such as *Clostridium difficile* infection and ulcerative colitis. Van Lier *et al.* conducted a single-arm clinical trial to investigate whether such FMTs could ameliorate symptoms of intestinal GvHD in 15 HCT recipients. Within a month of treatment, intestinal GvHD resolved and gut microbial diversity was restored in 10 of 15 study participants. Although confirmation is required in larger trials, FMT may be a promising treatment for intestinal GvHD. —MN

*Sci. Transl. Med.* 12,  
eaaz8926 (2020).

## IN OTHER JOURNALS

Edited by **Caroline Ash**  
and **Jesse Smith**



Mare's milk has a high lactose content and rapidly ferments into products that are digestible by lactose intolerant Central Asian herdspeople.

## SIGNAL TRANSDUCTION Plants take the splice to the fight

Plants transiently activate immune responses using layers of diverse regulatory mechanisms. This strategy minimizes any potential damage from an overly active protective response. Dressano *et al.* discovered in the model plant *Arabidopsis* that when an immune response was activated, the plant's immunoregulatory RNA binding protein (IRR) became dephosphorylated. Dephosphorylation altered IRR's interaction with messenger RNA transcripts, including that of calcium-dependent protein kinase 28 (CPK28), a key negative regulator of pattern recognition receptor signaling complexes. CPK28 is acutely regulated by changes in calcium concentration and its own phosphorylation state. However, altered splicing results in the expression of a truncated CPK28 protein that

cannot bind calcium, and thus an enhanced immune response can be triggered. —LBR

*Nat. Plants* 6, 1008 (2020).

## IMMUNOLOGY The thymus X factor

The thymus is an organ that facilitates the maturation of thymocytes into T cells and is notable for its variable size and composition. It is largest during early life, then it shrinks with age and in response to injury and infection. Thymic development also affects T cell output but remains poorly understood. Chan *et al.* report that liver X receptors (LXRs), nuclear receptors important for immunity and metabolism, play an important role in thymus dynamics. In mice, thymic epithelial cells use LXR $\alpha\beta$  for self-renewal and thymic regeneration. Meanwhile, LXR $\alpha\beta$  makes thymocytes more resistant to negative selection, thereby boosting the production

PHOTO: PAUL&39;S LADY/SHUTTERSTOCK



## HUMAN GENETICS

### Fermenting coevolution

**T**he dogma is that lactase persistence is a recent human adaptation to the domestication of dairy animals. Paradoxically, retaining the ability to digest lactose beyond infancy is not universal among pastoralists. Questioning the fitness advantage of lactase persistence, Segurel *et al.* genotyped more than 900 people from 13 ethnic groups and confirmed a low frequency of the persistence allele among Central Asians. Since the emergence of the mutation in modern-day Ukraine almost 6000 years ago, and after extensive migrations across the steppes, the persistence mutation became strongly represented in European populations but was lost among Central Asians. The authors suggest that Central Asian herdspeople adapted to milk consumption either by fermenting it, which was accompanied by the ingestion of helpful lactobacilli, or as a result of the selection of lactose-digesting bifidobacteria in their gut microbiota. The question is why these exogenous strategies are more advantageous to Central Asians than the mutation is to Europeans. —CA  
*PLoS Biol.* **18**, e3000742 (2020).

## FOLLOW THE MONEY

### Philanthropy—or tax-exempt lobbying?

Major corporations appear to fund their charitable foundations in part to cater to politicians who are important to the firm's profitability. Integrating corporate tax returns, lobbying data, and data on U.S. congressional committee assignments, Bertrand *et al.* show that donations from a given corporate-funded foundation to charities in a particular congressional representative's district, or for which a congressional representative is a board member, ebb and flow according to whether the representative sits on a committee that is of interest to the corporation. The patterns parallel spending by political action committees (PACs). Around 7% of charitable giving (~\$1.2 billion annually) appears to be politically motivated, amounting to about 2.5 times the annual PAC spending and one-third of the total federal lobbying spending—and it is tax exempt and thus subsidized by taxpayers. —BW

*Am. Econ. Rev.* **110**, 2065 (2020).

## NEURODEVELOPMENT

### Early vision matures

Prior to eye opening, neurons in the visual cortex of certain mammals respond to orientation of a visual stimulus but cannot parse its direction of

motion. In the weeks after the eyes open, the visual cortex acquires this ability. Roy *et al.* studied the newborn ferret to determine how synaptic and cell-intrinsic properties enable the development of direction selectivity. Receptive fields of mature neurons were more elongated along the temporal axis and narrower along the space-time axis compared with the receptive fields for neurons before visual stimulus. With visual experience, neurons improved their short-latency responses but also became more selective in their responses. —PJH

*eLife* **9**, e58509 (2020).

## MATERIALS SCIENCE

### An uncuttable foam

Designing structures across many different length scales provides flexibility in optimizing for certain properties. Szyniszewski *et al.* created a new material, called Proteus, that is highly deformable yet resistant to cutting. Proteus consists of ceramic spheres embedded in aluminum foam to accomplish this unique property pairing. The authors show that this multiscale material is resistant to the extreme loads of angle grinders, power drills, and even water jet cutters. The underlying design principles should be useful for developing other architected materials for a range of applications. —BG

*Sci. Rep.* **10**, 11539 (2020).

of autoreactive T cells. This work therefore cautions that LXR-focused thymic regeneration therapies may need to be cell specific to prevent unwanted autoimmunity. —STS

*J. Exp. Med.* **217**, e20200318 (2020).

## ENERGY STORAGE

### Advancing Li-air batteries

Lithium (Li)-air batteries demonstrate ultrahigh theoretical energy densities, but their practical realization is subject to various technical limitations because of the poor chemical stability of their components under exposure to air. Chen *et al.* showed that CO<sub>2</sub>, which is traditionally considered one of the chemical mediators that facilitate parasitic chemical reactions, could in fact improve battery stability. When introduced into the feeding gas, CO<sub>2</sub> facilitates the formation of a passivated, protective Li<sub>2</sub>CO<sub>3</sub> film on the Li anode and captures O<sub>2</sub><sup>-</sup>, thus suppressing side

reactions involving electrolyte and cathode. Using Pd/CNT as cathode that effectively catalyzes Li<sub>2</sub>CO<sub>3</sub> decomposition, the authors developed a rechargeable Li-O<sub>2</sub>/CO<sub>2</sub> battery with high energy capacity and long storage life. —YS

*Angew. Chem. Int. Ed.* **10.1002/anie.202006303** (2020).



Newborn ferret pups' eyes can discern light despite being closed, but they cannot follow its direction of motion until they open.

ALSO IN *SCIENCE* JOURNALS

Edited by Michael Funk

## CATALYSIS

**Making chemistry less precious**

Much of modern chemistry relies on catalysis by precious metals such as platinum, palladium, and rhodium. By contrast, more abundant metals such as iron and copper suffice in biochemistry. Bullock *et al.* review the opportunities presented from the study of enzymes to shift the balance in synthetic catalysts further toward the use of these abundant metals. Whether by modifying the enzymes themselves or by designing ligand and support architectures that take advantage of the cheaper metals' characteristic electron transfer properties, recent work points toward substantial progress. —JSY

*Science*, this issue p. 786

## NEURODEVELOPMENT

**Neural progenitors disrupted**

Symptoms of Huntington's disease (HD) manifest in adulthood despite the aberrant protein being present much earlier in persons carrying the disease-causing mutation. Barnat *et al.* studied the cellular effects of the HD mutation on human and mouse fetal brain development (see the Perspective by DiFiglia). The authors found that neural progenitor cells at the brain's ventricular zone reach out to both the apical and basal surfaces of the neuroepithelial wall, and their cellular nuclei shuttle back and forth as the cell cycle progresses. With the aberrant protein, these epithelial junctions are disrupted, epithelial polarity is disturbed, and the cell cycle favors premature neuronal differentiation. —PJH

*Science*, this issue p. 787;  
see also p. 771

## CORONAVIRUS

**Prototype DNA vaccines for SARS-CoV-2**

The development of a vaccine to protect against severe acute respiratory syndrome coronavirus 2 (SARS-CoV-2) is an urgent biomedical need. Yu *et al.* designed a series of prototype DNA vaccines against the SARS-CoV-2 spike protein, which is used by the virus to bind and invade human cells. Analysis of the vaccine candidates in rhesus macaques showed that animals developed protective humoral and cellular immune responses when challenged with the virus. Neutralizing antibody titers were also observed at levels similar to those seen in humans who have recovered from SARS-CoV-2 infection. —PNK

*Science*, this issue p. 806

## CORONAVIRUS

**Immunity from reinfection**

One of the many open questions about severe acute respiratory syndrome coronavirus 2 (SARS-CoV-2) infection is whether an individual who has cleared the virus can be infected a second time and get sick. Chandrashekar *et al.* and Deng *et al.* generated rhesus macaque models of SARS-CoV-2 infection and tested whether natural SARS-CoV-2 infection could result in immunity to viral challenge. They found that animals indeed developed immune responses that protected against a second infection. Although there are differences between SARS-CoV-2 infection in macaques and in humans, these findings have key implications for public health and economic initiatives if validated in human studies. —PNK

*Science*, this issue p. 812, p. 818

## NEUROSCIENCE

**Nuclear transport controls chronic pain**

Chronic neuropathic pain is debilitating and difficult to treat. Marvaldi *et al.* now show that chronic pain is regulated by a specific nuclear import factor in peripheral sensory neurons (see the Perspective by Yousuf and Price). Importin  $\alpha 3$  is required for nuclear import of the transcription factor c-Fos in sensory neurons, and perturbation of this pathway ameliorates sustained neuropathic pain in mice. Candidate drugs were identified that mimic this pathway and alleviate neuropathic pain in mouse models. Identification of a nuclear transport factor that regulates pain mechanisms offers opportunities for future analgesic development. —SMH

*Science*, this issue p. 842;  
see also p. 774

## ELECTROCHEMISTRY

**Delivering protons with electrons**

Many chemical reactions involve concurrent transfer of a proton and an electron. In electrochemical synthesis, this mechanism could prove useful in lowering the energy necessary for cathodic electron transfer alone, but it is hindered by competing direct coupling of the protons and electrons to make hydrogen instead. Chalkley *et al.* now report a molecular mediator consisting of a dimethylaniline base tethered to a cobaltoxide electron acceptor. This construct can deliver both a proton and an electron to a substrate from an acid and a cathode while skirting the hydrogen pathway. —JSY

*Science*, this issue p. 850

## CORONAVIRUS

**Heterogeneity and herd immunity**

In response to severe acute respiratory syndrome coronavirus 2 (SARS-CoV-2), some politicians have been keen to exploit the idea of achieving herd immunity. Countering this possibility are estimates derived from work on historical vaccination studies, which suggest that herd immunity may only be achieved at an unacceptable cost of lives. Because human populations are far from homogeneous, Britton *et al.* show that by introducing age and activity heterogeneities into population models for SARS-CoV-2, herd immunity can be achieved at a population-wide infection rate of ~40%, considerably lower than previous estimates. This shift is because transmission and immunity are concentrated among the most active members of a population, who are often younger and less vulnerable. If nonpharmaceutical interventions are very strict, no herd immunity is achieved, and infections will then resurge if they are eased too quickly. —CA

*Science*, this issue p. 846

## SUPERCONDUCTIVITY

**An elusive pocket**

Superconductivity in copper oxide materials emerges by doping a special kind of correlated state called the Mott insulator. However, studying what happens when a small concentration of charge carriers—holes or electrons—is added to a Mott insulator is experimentally challenging. It has been predicted that the so-called “Fermi pockets” should become visible during experimentation, but such pockets have not been unambiguously observed. Kunisada *et al.* studied the unusual cuprate  $\text{Ba}_2\text{Ca}_4\text{Cu}_5\text{O}_{10}(\text{F},\text{O})_2$ , which has five copper oxide planes in a unit cell, whereas most cuprates have one or two (see



the Perspective by Vishik). They observed two Fermi pockets in both photoemission and quantum oscillations data, with the innermost copper oxide planes playing a crucial role. —JS

*Science*, this issue p. 833;  
see also p. 775

## INTERGROUP RELATIONS

### Social contact and reconciliation

It has been theorized that positive intergroup relations can reduce prejudice and facilitate peace. However, supporting empirical evidence is weak, particularly in the context of real-world conflict. Mousa randomized Christian Iraqi refugees to soccer teams that were composed of either all Christian players or a mixture of Christian and Muslim players (see the Perspective by Paluck and Clark). Playing on the same team as Muslims had positive effects on Christian players' attitudes and behaviors toward Muslims within the context of soccer, but these effects did not generalize to non-soccer contexts. These findings have implications for the potential benefits and limits of positive intergroup contact for achieving peace between groups. —TSR

*Science*, this issue p. 866;  
see also p. 769

## TROPHIC RESILIENCE

### Inflexible webs

It is clear that human activities are negatively affecting current ecosystems. Predicting how our activities will affect future systems is more challenging because it involves estimating the unknown. Nagelkerken *et al.* overcame some of these unknowns by constructing small versions, or mesocosms, of a marine ecosystem that included species representing all trophic levels (see the Perspective by Chown). They then exposed these systems to predicted future levels of carbon dioxide and acidification. The trophic structure was relatively resistant to acidification but not

to warming. Warmed systems experienced a reorganization of trophic structure that was not rescued by functional redundancy or other stabilizing responses. Such inflexibility may be a precursor of ecosystem collapse. —SNV

*Science*, this issue p. 829;  
see also p. 770

## PALEOANTHROPOLOGY

### Bedding of grass and ashes

The Border Cave site in the KwaZulu-Natal region of South Africa has been a rich source of archaeological knowledge about Stone Age humans because of its well-preserved stratigraphic record. Wadley *et al.* now report the discovery of grass bedding in Border Cave, dated to approximately 200,000 years ago. The bedding, identified with a range of microscopic and spectroscopic techniques, was mingled with layers of ash. It also incorporated debris from lithics, burned bone, and rounded ochre grains, all of which were of clear anthropogenic origin. The authors speculate that the ash may have been deliberately used in bedding to inhibit the movement of ticks and other arthropod irritants. These discoveries extend the record of deliberate construction of plant bedding by at least 100,000 years. —AMS

*Science*, this issue p. 863

## NEUROSCIENCE

### PERKing up neurons without toxicity

Chronic activity of the unfolded protein response in some neurodegenerative diseases suppresses the protein synthesis that is necessary for neuronal function and survival and for cognition. Hughes *et al.* found that the phosphorylation of a threonine residue in the stress response kinase PERK reduced its interaction with the translation initiation factor eIF2 $\alpha$  but left the kinase activity of PERK intact. This partial inhibition

approach reduced neuronal loss and increased survival in a mouse model of prion disease without the pancreatic damage seen with catalytic inhibitors of PERK. —LKF

*Sci. Signal.* **13**, eabb4749 (2020).

## AUTOIMMUNITY

### Autoimmunity promotor

Tissue-resident memory T (Trm) cells are involved in peripheral immunity against reinfection, but their role in autoimmunity is unclear. Krebs *et al.* examined the contribution of Trm cells in patients with antineutrophil cytoplasmic antibody-dependent glomerulonephritis (ANCA-GN). They identified multiple T cell subsets in healthy kidney tissue biopsies, but a marked increase in CD4<sup>+</sup> Trm cells was seen in kidney biopsies from patients with ANCA-GN. They infected mice with *Staphylococcus aureus*, which induced renal T helper 17 cells with a Trm cell phenotype and persisted in kidney tissue. In a mouse model of this disease, *S. aureus* infection aggravated kidney pathology and appeared to drive localized renal autoimmune responses. These findings provide critical insight into the role of CD4<sup>+</sup> Trm cells in contributing to autoimmune disease. —CNF

*Sci. Immunol.* **5**, eaba4163 (2020=0).

## REVIEW SUMMARY

## CATALYSIS

## Using nature's blueprint to expand catalysis with Earth-abundant metals

R. Morris Bullock\*, Jingguang G. Chen\*, Laura Gagliardi\*, Paul J. Chirik, Omar K. Farha, Christopher H. Hendon, Christopher W. Jones, John A. Keith, Jerzy Klosin, Shelley D. Minteer, Robert H. Morris, Alexander T. Radosevich, Thomas B. Rauchfuss, Neil A. Strotman, Aleksandra Vojvodic, Thomas R. Ward, Jenny Y. Yang, Yogesh Surendranath\*

**BACKGROUND:** Catalysis has had a transformative impact on society, playing a crucial role in the production of modern materials, medicines, fuels, and chemicals. Precious metals have been the cornerstone of many industrial catalytic processes for decades, providing high activity, stability, and tolerance to poisons. In stark contrast, redox catalysis essential to life is carried out by metalloenzymes that feature exclusively Earth-abundant metals (EAMs). The terrestrial abundance of some EAMs is  $10^4$  times that of precious metals, and thus their increased use would lead to reduced cost and environmental footprint. In addition to these practical considerations, EAMs display distinct reactivity profiles that originate from their characteristic electronic structure, thermochemistry, and kinetics. The behavior of EAMs provides compelling scientific opportunities for catalyst design. We assert that nature's blueprint provides essential principles for vastly expanding the use of EAMs in sustainable catalysis.

**ADVANCES:** Exquisite tuning of the local environment around EAM active sites is key to enabling their use in catalysis. Such control

is achieved in enzymatic catalysis by directed evolution of the amino acid environment, resulting in engineered enzymes with extraordinary catalytic performance. Similarly in molecular catalysis, modifying the steric and electronic properties of ligands can lead to some EAM catalysts with performance superior to that obtained from precious metal catalysts. In addition, for heterogeneous catalysts, the local environment and electronic structure of active sites can be modified by bonding to other metals or main-group elements, facilitating reaction pathways distinct from those involving precious metals. Innovations in the design of EAM catalysts demonstrate their potential to catalyze many of the reactions that traditionally relied on precious metals, although further improvements are needed in activity, selectivity, lifetime, or energy efficiency. The characteristics of EAMs point to an overarching need for improved theories and computational methods that accurately treat their multiconfigurational electronic structure.

**OUTLOOK:** The remarkable ability of enzymes to catalyze a variety of reactions under mild

conditions, using only EAMs, highlights compelling opportunities for the discovery of new catalysis. Although enzymes are versatile platforms for harnessing the properties of EAMs, they are insufficiently robust under the harsh pH, temperature, pressure, and solvent conditions required for some industrial catalytic processes. Thus, systematic strategies are needed for directed evolution to extend the reactivity and persistence of engineered enzymes. For molecular catalysts, the tunability of the ligands provides opportunities for systematically varying the activities of EAMs. Key challenges include enhancing metal-ligand cooperativity, controlling transport to EAM active sites, and mastering the interactions of EAM centers with both metal-based and organic-based redox-active ligands. In heterogeneous catalysis, tuning the lattice environment of EAMs offers new opportunities for catalyst discovery, but for practical applications EAM catalysts should exhibit long-term stability and high active-site density. Thus, advances are needed in the synthesis of materials with tunable phase and nanostructure, as well as insights into how EAM catalysts undergo electronic and structural changes under sustained catalytic turnover. Strategies for controlling EAM reactivity patterns, coupled with advances in synthetic methods and spectroscopic and computational techniques, are critical for the systematic use of EAMs in sustainable catalysis. ■

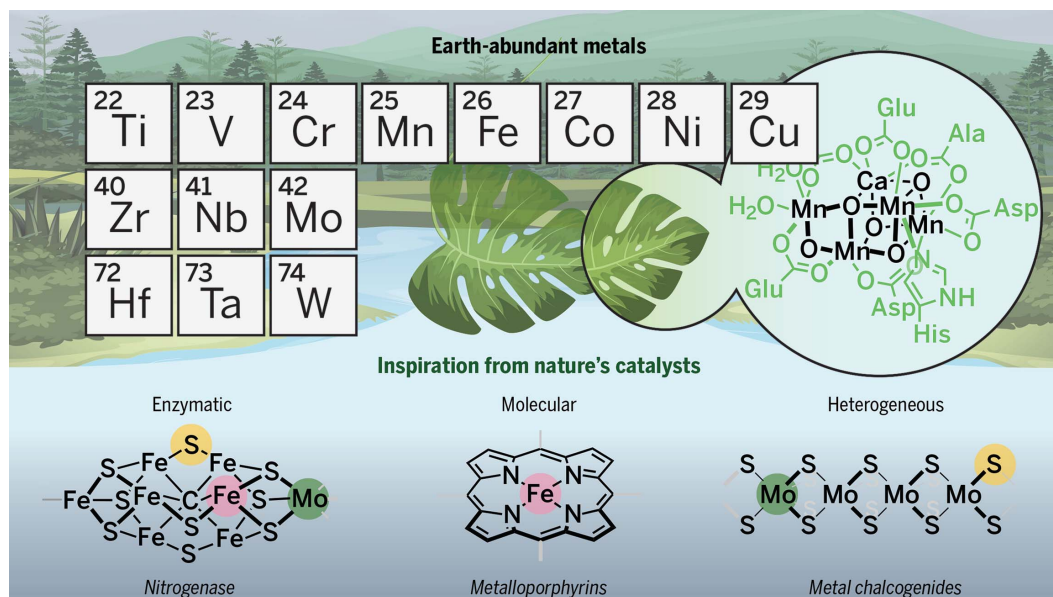
The list of author affiliations is available in the full article online.

\*Corresponding author. Email: morris.bullock@pnnl.gov (R.M.B.); jgchen@columbia.edu (J.G.C.); gagliardi@umn.edu (L.G.); yogi@mit.edu (Y.S.)

Cite this article as R. M. Bullock *et al.*, *Science* **369**, eabc3183 (2020). DOI: 10.1126/science.abc3183

**S READ THE FULL ARTICLE AT**  
<https://doi.org/10.1126/science.abc3183>

**Catalysis by Earth-abundant metals.** Nature's blueprint provides the fundamental principles for expanding the use of abundant metals in catalysis by controlling the local environment and electronic structure of metal centers. Examples include nitrogenase-based enzymatic catalysts for  $N_2$  reduction, metalloporphyrin-based molecular catalysts for reduction of oxygen and carbon dioxide, and metal chalcogenides in heterogeneous catalysis for hydrodesulfurization and hydrogen evolution reactions.





## REVIEW

## CATALYSIS

## Using nature's blueprint to expand catalysis with Earth-abundant metals

R. Morris Bullock<sup>1\*</sup>, Jingguang G. Chen<sup>2,3\*</sup>, Laura Gagliardi<sup>4\*</sup>, Paul J. Chirik<sup>5</sup>, Omar K. Farha<sup>6</sup>, Christopher H. Hendon<sup>7</sup>, Christopher W. Jones<sup>8</sup>, John A. Keith<sup>9</sup>, Jerzy Klosin<sup>10</sup>, Shelley D. Minter<sup>11</sup>, Robert H. Morris<sup>12</sup>, Alexander T. Radosevich<sup>13</sup>, Thomas B. Rauchfuss<sup>14</sup>, Neil A. Strotman<sup>15</sup>, Aleksandra Vojvodic<sup>16</sup>, Thomas R. Ward<sup>17</sup>, Jenny Y. Yang<sup>18</sup>, Yogesh Surendranath<sup>13\*</sup>

Numerous redox transformations that are essential to life are catalyzed by metalloenzymes that feature Earth-abundant metals. In contrast, platinum-group metals have been the cornerstone of many industrial catalytic reactions for decades, providing high activity, thermal stability, and tolerance to chemical poisons. We assert that nature's blueprint provides the fundamental principles for vastly expanding the use of abundant metals in catalysis. We highlight the key physical properties of abundant metals that distinguish them from precious metals, and we look to nature to understand how the inherent attributes of abundant metals can be embraced to produce highly efficient catalysts for reactions crucial to the sustainable production and transformation of fuels and chemicals.

Catalysis has had a transformative impact on society, playing a decisive role in the production of modern materials we use daily, medicines to keep us healthy, and fuels for transportation. Most of the key chemical reactions essential to our contemporary lifestyle are catalyzed by transition metals (TMs). The terrestrial abundance of TMs varies over a remarkable range. The first-row (3d) metals of the transition series in the periodic table, as well as the early second-row (4d) and third-row (5d) metals, are relatively abundant, whereas the platinum group metals (PGMs)

that constitute the mid- to late portion of the second and third rows have substantially lower crustal abundance (Fig. 1) (1). Here, we highlight frontier opportunities for designing and enabling new catalysts based on Earth-abundant metals (EAMs), with an emphasis on redox reactions crucial to the sustainable production and transformation of fuels and chemicals.

Many redox transformations (2) that are essential to life are catalyzed by EAMs in nature. Because biological organisms must accumulate metals from their surroundings, evolution selected the EAMs exclusively in biological catalysis. Indeed, there are no known native biological catalysts that use a PGM. Consequently, metalloenzymes provide an expansive existence proof that EAMs catalyze complex redox transformations. A tri-Cu active site in the laccase enzyme (3, 4) reduces O<sub>2</sub> to H<sub>2</sub>O, a key cathodic reaction in fuel cells. A cluster containing Fe and Mo reduces N<sub>2</sub> to NH<sub>3</sub> in nitrogenase (5). A dinuclear Ni active site catalyzes the CO insertion reaction in acetyl-coenzyme A (CoA) synthase (Fig. 2, top left). Enzymes containing Ni-Fe organometallic complexes carry out the reversible interconversion of H<sub>2</sub> and H<sup>+</sup> in hydrogenase (6) (Fig. 2, middle left). A Mn-Ca cluster catalyzes the oxidation of water to O<sub>2</sub> in photosystem II (7) (Fig. 2, bottom left). The selective oxidation of methane to methanol occurs at the dinuclear Fe active site in methane monooxygenase (8). Diverse C-H functionalization reactions are catalyzed by Fe-S cluster active sites in radical S-adenosylmethionine (SAM) enzymes (9). All of these transformations involve multielectron redox reactions, and most require precise control of the delivery or removal of protons.

In contrast to the extensive use of EAMs in nature, PGMs have historically been the corner-

stone of many industrial catalytic reactions for decades, owing to their high catalytic activity, thermal stability, and tolerance to chemical poisons. Pd-catalyzed cross-coupling reactions that form C-C bonds (10) have broad utility and tremendous versatility in pharmaceutical, electronic, and materials applications. A second wave of Pd-catalyzed cross-coupling chemistry has given rise to powerful methods for C-N, C-S, and C-O bond-forming reactions that are widely used (11). Rh-based complexes catalyze the CO insertion reaction, hydroformylation (12) (Fig. 2, top right). Pt is the prototypical catalyst for hydrogen production (13) and oxidation (Fig. 2, middle right). Ir oxide catalyzes the oxidation of water to O<sub>2</sub> (14) in polymer electrolyte membrane (PEM) electrolyzers (Fig. 2, bottom right). C-H oxidation and functionalization reactions have been extensively developed using Pd catalysts (15). Selective hydrogenation reactions required in oil refining and fine chemical synthesis routinely use PGM catalysts. The three-way catalyst in catalytic converters used daily in hundreds of millions of cars requires Pt, Rh, and Pd.

EAM catalysts are attractive for many reasons. The "terawatt challenge" (16) for global energy demand highlights the need to consider the scalability of catalytic materials for sustainable energy conversions. The crustal abundance of EAMs exceeds that of PGMs by a factor of 10<sup>4</sup> or greater (Fig. 1), leading to costs that differ by similar ratios. Costs are influenced both by abundance and production rate (17). The price of a mole of Rh reached >\$15,000 (USD) as of November 2019, whereas the cost of most EAMs is typically <\$2 per mole (although for many catalytic reactions, the metal cost constitutes only a small fraction of the overall process cost; in the synthesis of pharmaceutical products, the cost of chiral ligands can substantially exceed that of the metal). Prices of PGMs are much more volatile than those of EAMs. Moreover, EAMs generally have lower biological toxicity (18), permitting higher levels of residual EAMs than of PGMs in pharmaceutical products (19). Lastly, the high abundance of EAMs generally leads to a lower environmental footprint associated with their mining and purification relative to PGMs. For example, the production of 1 kg of Rh generates >35,000 kg of CO<sub>2</sub> equivalent, whereas 1 kg of Ni produces only 6.5 kg of CO<sub>2</sub> equivalent (Fig. 1, black bars) (20).

Given the appealing attributes of EAMs noted above, one can ask why PGMs continue to be so prevalent in many industrial catalytic processes. The specific reasons vary according to catalytic application. In general, the requirement for effective integration of a catalyst into an overall process often places stringent constraints on the choice of catalyst. For example, in a fuel cell, the use of fast ion conductivity in Nafion (separating charge transfer between

<sup>1</sup>Center for Molecular Electrocatalysis, Pacific Northwest National Laboratory, Richland, WA 99352, USA. <sup>2</sup>Department of Chemical Engineering, Columbia University, New York, NY 10027, USA. <sup>3</sup>Chemistry Division, Brookhaven National Laboratory, Upton, NY 11973, USA. <sup>4</sup>Department of Chemistry, Minnesota Supercomputing Institute, and Chemical Theory Center, University of Minnesota, Minneapolis, MN 55455, USA. <sup>5</sup>Department of Chemistry, Princeton University, Princeton, NJ 08544, USA. <sup>6</sup>Department of Chemistry and Chemical and Biological Engineering, Northwestern University, Evanston, IL 60208, USA. <sup>7</sup>Department of Chemistry and Biochemistry, University of Oregon, Eugene, OR 97403, USA. <sup>8</sup>School of Chemical and Biomolecular Engineering, Georgia Institute of Technology, Atlanta, GA 30332, USA. <sup>9</sup>Department of Chemical and Petroleum Engineering, University of Pittsburgh, Pittsburgh, PA 15261, USA. <sup>10</sup>Core R&D, Dow Chemical Co., Midland, MI 48674, USA. <sup>11</sup>Department of Chemistry, University of Utah, Salt Lake City, UT 84112, USA. <sup>12</sup>Department of Chemistry, University of Toronto, Toronto, Ontario M5S 3H6, Canada. <sup>13</sup>Department of Chemistry, Massachusetts Institute of Technology, Cambridge, MA 02139, USA. <sup>14</sup>School of Chemical Sciences, University of Illinois, Urbana, IL 61801, USA. <sup>15</sup>Process Research and Development, Merck & Co. Inc., Rahway, NJ 07065, USA. <sup>16</sup>Department of Chemical and Biomolecular Engineering, University of Pennsylvania, Philadelphia, PA 19104, USA. <sup>17</sup>Department of Chemistry, University of Basel, CH-4058 Basel, Switzerland. <sup>18</sup>Department of Chemistry, University of California, Irvine, CA 92697, USA.

\*Corresponding author. Email: morris.bullock@pnnl.gov (R.M.B.); jgchen@columbia.edu (J.G.C.); gagliardi@umn.edu (L.G.); yogi@mit.edu (Y.S.)

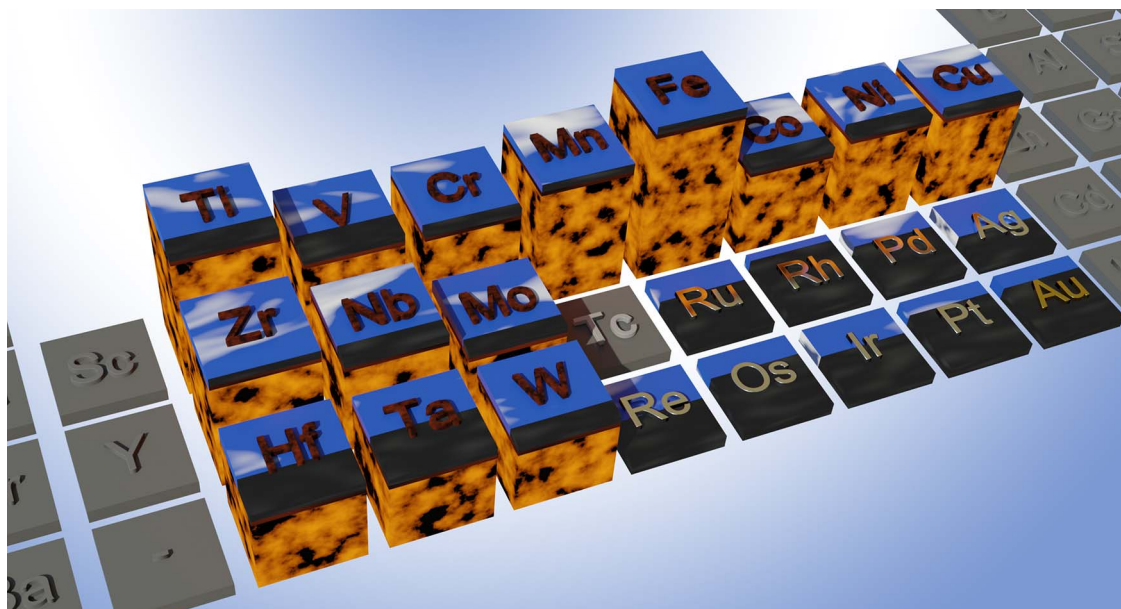


**Fig. 1. Definition of different groups of transition metals.** Platinum group metals (PGMs) include Ru, Rh, Pd, Os, Ir, and Pt. The broader term, precious metals, includes PGMs along with Re, Au, and Ag. Earth-abundant metals (EAMs), sometimes referred to as base metals, include all other transition metals. (Tc is shown but is radioactive and unstable.) The height of the pillar for each metal indicates its crustal abundance on a log scale; the values range from 5.6% (Fe) to ~0.001 ppm (Rh, Ir). The black bar on each metal shows (also on a log scale) the relative amount of CO<sub>2</sub> produced through mining and purification for each metal (20), which is markedly larger for PGMs than for EAMs.

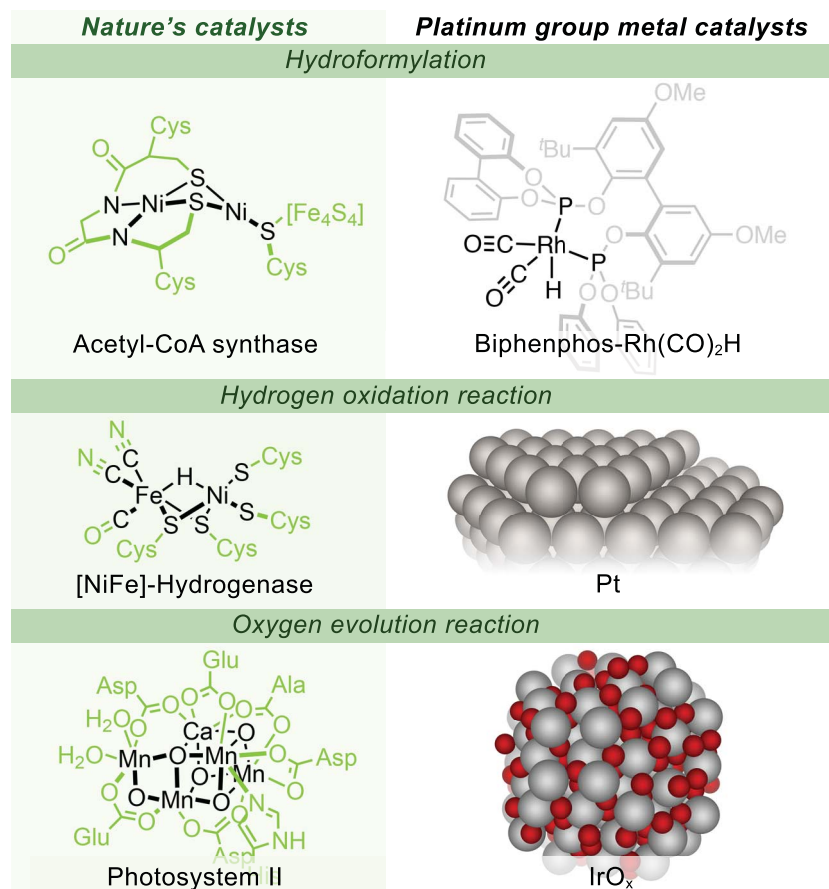


**Fig. 2. Many of the transformations carried out by enzymatic EAM catalysts are replicated in the chemical industry by means of PGM catalysts.**

anodes and cathodes) requires an acidic pH, thereby constraining the choice of catalysts to corrosion-resistant PGMs. Likewise, the requirement for high-temperature operations in catalytic converters places stringent requirements on durability, constraining viable replacement of PGMs. In addition, the high capital and energy cost of complex downstream separations imposes a constraint on the minimum selectivity of catalytic processes, and this consideration may dominate relative to the cost and environmental footprint of the metal catalyst itself. These factors motivate the emphasis on the development of EAM catalysts in tandem with new processes that can circumvent the constraints of current catalytic technologies.

EAM catalysts are currently successfully used in several major industrial processes. The Haber-Bosch reaction, which converts N<sub>2</sub> to ammonia, uses an Fe-based catalyst, despite the higher performance of a Ru-based analog (27). Hydrogenation of CO to methanol is carried out using a Cu/Zn-based catalyst. Hydrogen is produced from water in commercial electrolyzers under basic conditions using Ni/Fe-based catalysts. Olefin oligomerization and polymerizations are carried out worldwide on a tremendous scale using EAMs, dominated by Ti, Zr, and Cr catalysts. Terephthalic acid is produced on a large scale through oxidation of *p*-xylene using Co and Mn catalysts. Some industrial processes are catalyzed by both PGMs and EAMs. For example, hydroformylation is conducted using either Co- or Rh-based catalysts



(12), and propane dehydrogenation is carried out on either Pt- or Cr-based catalysts (22). Despite these examples, it remains clear that the scope of EAM catalysis is limited relative to the remarkable diversity of transformations catalyzed by EAMs in nature.

Whereas biology provides an invaluable (although sometimes inscrutable) guide to the broadened implementation of EAMs, industrial catalysis often requires substrates, reactions, and reaction conditions quite different from those in biology; PGM catalysts proliferate in this arena. For example, alkenes, which are derived from petroleum, are processed quite differently by enzymes than by industrial catalysts. With the notable exception of Cu-based ethylene-sensor proteins (23), metal-alkene complexes are unknown in nature, although transfer hydrogenations of C=C bonds are catalyzed by a family of biocatalysts, ene reductases (24). In stark contrast, industrial catalytic transformations of alkenes include polymerization, carbonylation, and metathesis; analogs of these processes are absent from the biocatalysis repertoire. Instead, alkenes are often processed in natural systems by attacking weakened allylic C-H bonds using iron-oxo-based radicals (25).

Considering the diversity of catalysis performed by biological systems, a central challenge revolves around coaxing biological macromolecules into displaying entirely abiotic reactivity/selectivity/stability characteristics that have traditionally been the domain of PGM-based catalysts. A daunting challenge in designing bio-inspired catalysts is to identify and replicate only the parts of the metalloenzyme structure (first, second, or outer coordination sphere) that are thought to be required for catalytic activity, recognizing that while biological reaction networks must maintain life, their catalytic functionality may be accessible from synthetically simpler structures. Replicating the active site is necessary but not sufficient for achieving catalysis comparable to that found in enzymes, as dynamics and conformational changes often exert a large influence on enzymatic catalysis (26).

The considerations discussed above have fueled burgeoning interest in developing new EAM-based catalysts. We assert that this endeavor is best advanced by establishing the fundamental science of EAMs that embraces their particular physical properties and resultant catalytic activities. Herein, we put forward the premise that nature's blueprint provides the fundamental principles for vastly expanding the use of EAMs in catalysis. We highlight the key physical properties of EAMs that distinguish their reactivity from those of PGMs, and then seek to understand how the inherent attributes of EAMs can be embraced, leading to highly efficient catalysis. Building on that foundation, we identify compelling opportunities

for the increased use of EAMs in enzymatic, molecular, and heterogeneous catalysis.

### The origins of divergent reactivity between EAMs and PGMs

#### Electronic structure

The distinctive reactivity profiles of EAMs relative to PGMs originate from fundamental differences arising from periodic trends of the elements (27). In particular, 3d orbitals extend to a lesser extent beyond the 3s and 3p orbitals (28), leading to attenuated orbital overlap with bonding partners, relative to the corresponding 4d and 5d counterparts. This overlap deficit has a considerable impact on the electronic structure of 3d metal-based catalysts. For molecular

TM complexes, the overlap deficit leads to more ionic character in metal-ligand bonds and a small frontier d-orbital splitting (Fig. 3, top), stabilizing high-spin electronic configurations. High spin configurations are extremely rare (29, 30) among 4d and 5d TM complexes owing to their much higher frontier orbital splitting energies (Fig. 3, top). Similar phenomena are observed for extended solids: Attenuated orbital overlap between 3d metal atoms leads to a diminished spread in the d-band energies and a corresponding increase in the d-band center of 3d metals relative to the 4d and 5d counterparts (Fig. 3, top). The prevalence of high-spin electronic configurations among 3d TMs has important implications for reactivity (31).

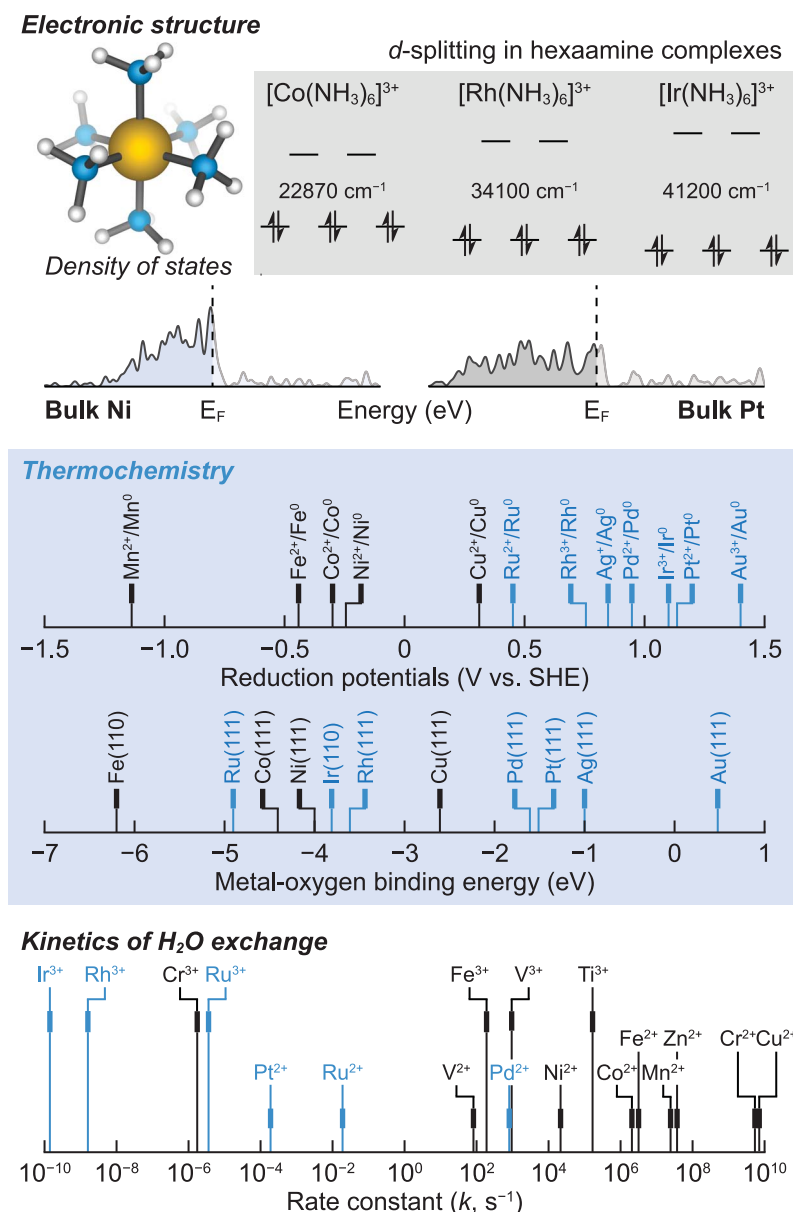
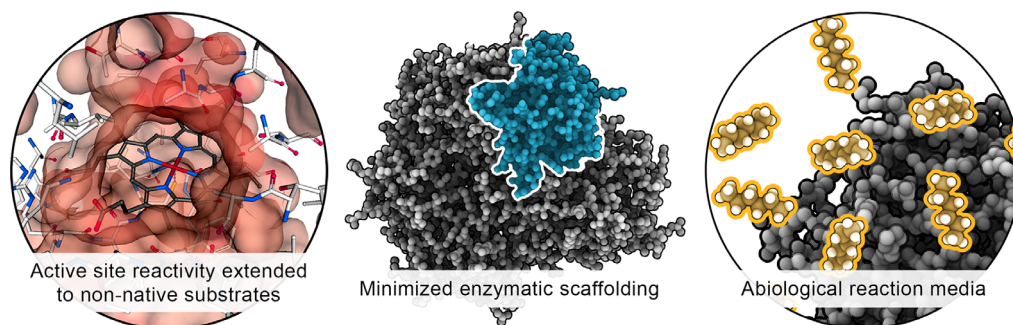


**Fig. 3. Physical properties of EAMs versus PGMs, illustrating substantial differences that lead to divergent reactivity that can be exploited in catalysis.** Data are from (1, 38, 124).

**Fig. 4. The utility of enzymatic catalysis can be enhanced by expanding active-site reactivity to abiotic substrates, minimizing the enzymatic scaffolding, and enabling operation in nonphysiological reaction environments.** Images were obtained from PDB code 1W0E, cytochrome P450.



Homogeneous PGM catalysts typically cycle through two-electron processes, including familiar examples of oxidative addition/reductive elimination of  $\text{Rh}^{\text{I}}/\text{Rh}^{\text{III}}$  and  $\text{Pd}^0/\text{Pd}^{\text{II}}$ . In contrast, 3d TM complexes more readily engage in single-electron bond activation reactions, including M-X bond homolysis. Additionally, the availability of multiple spin states among EAMs can lead to multistate acceleration of certain reactions.

### Thermochemistry

The differences in the electronic structures of EAMs and PGMs are manifested in the thermochemistry of interactions of metals with ligands, reactants, products, and intermediates. The classical Sabatier principle states that an optimal catalyst should bind intermediates neither too strongly nor too weakly, essentially a “Goldilocks” effect (21). In general, bonding to 3d TMs in molecular complexes is weaker relative to 4d/5d TM centers with the same ancillary ligand environment. For example, the bond dissociation energies of the M-H bond in  $\text{MH}(\eta^5\text{-C}_5\text{H}_5)(\text{CO})_2$  are 68 kcal/mol (32), 77 kcal/mol (32), and  $\geq 82$  kcal/mol (33) for Fe, Ru, and Os, respectively; for  $\text{MH}(\text{CO})_5$ , the values are 68 kcal/mol and 75 kcal/mol for Mn and Re, respectively (34). Additionally, the greater extension of the d-orbitals of the second and third TMs also provides for stronger back-bonding interactions with  $\pi$ -accepting ligands, such as CO and olefins, increasing their binding strength. Intermediates bearing such ligands are critical in a number of industrially important processes such as hydroformylation.

The differences in metal bonding thermochemistry are also mirrored in changes in the reduction potentials of metal ions. PGMs are commonly referred to as noble because of their resistance to oxidation, a reflection of their much higher reduction potentials and of the lower O-atom affinities of 4d and 5d metals (Fig. 3, middle, black) relative to 3d TMs (Fig. 3, middle, blue). For example, whereas the  $\text{Pt}^{\text{II}/0}$  and  $\text{Pd}^{\text{II}/0}$  reduction potentials are 1.18 and 0.951 V, respectively, versus the standard hydrogen electrode (SHE), the corresponding  $\text{Ni}^{\text{II}/0}$  reduction potential,  $-0.26$  V, is lower by more

than 1 V. Likewise, Pt (III) and Pd (III) surfaces have an O-atom affinity of  $\sim 0.5$  eV (12 kcal/mol), whereas Ni (III) surfaces have an O-atom affinity of  $\sim 4$  eV (92 kcal/mol) (Fig. 3). Because these baseline reduction potentials correspond to interconversion of the metallic solid and aquated metal ions, they are influenced by the coordination, electrostatic, and hydrogen-bonding environment of the metal center (35). Because of these effects, the active-site EAMs in metalloenzymes span a wide range of potentials (2) that differ substantially from their baseline values. Similar potential ranges can be accessible through changes in the coordination environment of synthetic coordination compounds (36).

The differences in reduction potential between EAMs and PGMs are of central importance in electrocatalysis, where electron flow drives the conversion of reactants to products. For example, the very positive potential for oxidizing Pt allows it to avoid corrosion at the oxidizing potentials of the  $\text{O}_2/\text{H}_2\text{O}$  couple in fuel cells, making it the only currently viable corrosion-resistant cathode catalyst for PEM fuel cells. To achieve similar feats, enzymes such as multi-copper oxidases, laccases (3, 4), and cytochrome c oxidase (37) use an ensemble of metal centers organized within the protein environment that markedly alters their redox properties and oxophilicities.

### Kinetics

Owing to their weaker metal-ligand bonds, complexes of the 3d metals are much more labile than their 4d and 5d counterparts (Fig. 3, bottom). The rate accelerations can be extraordinary: Exchange of a water ligand on a high-spin Fe(III) center is faster than on Ru(III) by a factor of  $10^8$  (38). We emphasize that lability is a kinetic phenomenon; many labile complexes are thermodynamically stable. Although typically viewed as an impediment to understanding catalytic reactivity, the higher lability of EAMs can, in principle, be beneficial for catalysis. Turnover frequencies are often strongly influenced by the rates of association and dissociation of reactants and products, a manifestation of the Sabatier principle (27). Thus, the inherently higher rate of ligand ex-

change on the 3d TMs offers the opportunity for rapid catalysis. Two key properties sought are kinetic stability of the metal-supporting ligand ensemble and labile coordination sites with appropriate affinities for substrates. The challenge arises from the fact that lability of EAMs can also lead to the rapid exchange of supporting ligands that tune the local electronic structure and reaction environment of the metal center. To circumvent problems with lability in molecular complexes, polydentate ligands are often used to strongly sequester the metal ion while preserving one or more coordination sites for catalysis. Consequently, tridentate or tetradentate ligands are ubiquitous in catalysis by synthetic 3d TMs relative to PGMs, so as to overcome the inherent differences in lability relative to PGMs. The premier examples of multidentate ligands in biocatalysis are porphyrins, where four metal-nitrogen bonds confer substantial kinetic inertness.

In extended solids, the kinetics of substitution at EAMs also play a central role in the longevity of catalysts. The weaker M-lattice bonding in mid- to late 3d metal and metal oxide materials contributes to their high propensity to sinter, restructure, become amorphous, and corrode under catalytic conditions, relative to 4d and 5d analogs. A richer understanding of how to control metal lability in extended solids is essential for creating robust EAM catalysts, particularly for harsh reaction environments.

### Computational insights

Much of our physical understanding of EAMs has been enhanced through consistent benchmarking between experiment and theory. A comprehensive understanding of EAM reactivity will require a refined understanding of electronic structure, thermochemistry, and kinetics. Yet current theoretical tools that are effective at modeling multiconfigurational electronic structure commonplace among EAMs are often ineffective for predicting thermochemical and kinetic properties (39). This impasse results from the enormous computational expense required to calculate the properties of EAMs that reside in shallow potential



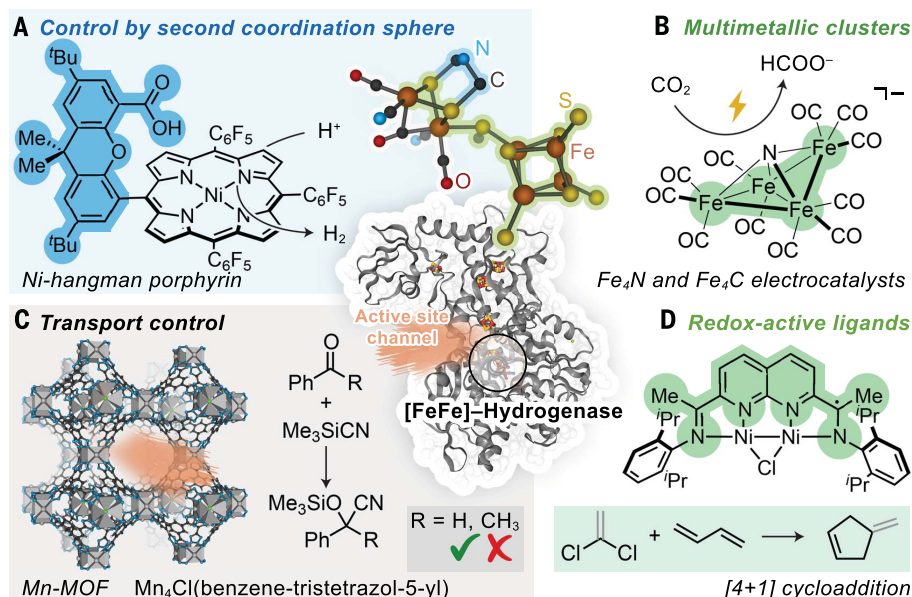


**Fig. 5. EAM enzymes provide the blueprint for molecular EAM catalyst design.** The example shown is  $[\text{Fe-Fe}]$ -hydrogenase (center; PDB code 5LA3). (A) Proton relays positioned proximate to EAM active sites (blue highlight) are deployed in molecular catalysts for hydrogen production (125). (B) Multimetallic cluster active sites catalyze energy conversion reactions (95). (C) Transport to active sites via enzyme channels can be mimicked in porous molecular materials (126). (D) The density of available electronic states is increased through redox-active ligands that can steer reactivity in synthetic systems (90). Me, methyl;  $t\text{-Bu}$ , *tert*-butyl;  $i\text{-Pr}$ , isopropyl; Ph, phenyl.

energy wells with a diversity of available spin configurations.

The widely used density functional theory (DFT) has strengths and weaknesses, and both are highlighted in modeling catalysis by EAMs. In some cases, trends can be identified readily using simple basis sets and commonly used functionals. Often complementing experimental results, theoretical studies can identify rate-determining steps, assign vibrational bands, and determine redox potentials. Useful thermochemical predictions of energies can often be obtained, even if specific spin states may not be easily determined reliably. Spin transitions and d-orbital splitting of EAMs are difficult to treat because states that are very similar in energy occur frequently with EAMs.

Machine learning (ML)-based methods have generated enormous recent interest in the computational analysis of catalysis (40). In a typical application of ML, large datasets (often resulting from thousands of DFT calculations) are used for statistical regression analyses with ML methods to identify the most accurately parametrized model for the dataset. A well-trained ML model should successfully interpolate within the chemical/materials space of the training data and be useful for screening molecular/material properties for hypothetical homogeneous (41, 42) and/or heterogeneous (43, 44) catalyst active sites across larger regions of chemical and materials space than are accessible with DFT calculations alone. Complementary

to ML approaches, theoretical schemes such as alchemical perturbation DFT allow rapid screening of adsorbate binding energies (45) with minimal precalculated reference data and low computational cost.

### Emerging opportunities for catalytic reactivity of EAMs

Recent progress in the design of EAM catalysts demonstrates their potential in many reactions that traditionally use PGMs, although they often fall short of the performance of PGM catalysts on one or more benchmarks (46): activity, selectivity, lifetime, or energy efficiency. Yet EAM-based enzymes have evolved in nature to facilitate an impressively diverse array of reactions. We assert that nature's blueprint provides invaluable guidance for frontier areas of exploration in EAM catalysis that takes advantage of the inherent electronic structure, thermodynamic, and kinetic characteristics of EAMs. We discuss below how to use biologically inspired approaches to design EAM catalysts with enhanced performance in the context of enzymatic, molecular, and heterogeneous reactivity.

### Enzymatic catalysis

Biological catalysts with TM active sites feature exclusively EAMs; a central challenge revolves around modifying enzymes to display abiotic functions (Fig. 4). Many metalloenzymes display promiscuous activities (47), a feature that

provides a diversity of reactivity for the discovery of abiotic enzymatic catalysis. There has been increasing recognition that biological cofactors featuring EAMs are active, albeit at a low level, for a wide array of abiotic transformations that are commonly carried out by synthetic PGM-based catalysts. For example, carbene insertion reactions, which enable the rapid elaboration of simple organic feedstocks into fine and pharmaceutical chemicals, are catalyzed efficiently by synthetic Rh-based catalysts (48). Remarkably, many native hemo-proteins also display low-level activity for these same reactions, and directed evolution of these enzymes has led to a family of biocatalysts (49) with excellent activity and selectivity for carbene insertion into C-H, N-H, and Si-H bonds. The activity and selectivity of these evolved metalloproteins now rival and even exceed those of Rh-based catalysts. One recent study (50) showed that hemoproteins can be repurposed to catalyze carbon-carbon bond formation by insertion of a carbene, rather than oxygen, into a C-H bond—a reaction traditionally dominated by PGMs (51). Implementing the blueprint from nature requires precise control of the local environment by modifying the active site to bind an abiotic reactant, such as a carbene, while minimizing the binding of the native substrate (i.e.,  $\text{O}_2$ ) with exquisite selectivity (52). The fundamental workflow of protein engineering—identifying promiscuous reactivity for abiotic substrates, then using protein-engineering tools to maximize performance—serves as a valuable blueprint for further advances in catalysis of abiotic reactions. Continued progress to expand the palette of enzymatic catalysis will benefit from the development of new methods for identifying enzyme candidates and strategies for accelerating directed evolution and selection of high-performance mutant enzymes.

The macromolecular scaffolds that house EAM active sites in enzymes are critical to their function but invariably afford high-molecular weight catalysts. For commodity-scale catalysis, the density of active sites is a critical determinant of space-time yield, imposing constraints on overall performance. In some cases, subunits of enzymes can be discarded without greatly lowering catalytic efficiency; this suggests that there is ample opportunity for enhancing active-site density without necessarily decreasing the turnover frequency or selectivity of each site. In other cases, mutation of a single amino acid remote from the active site can appreciably alter catalytic performance (53). Reliable methods for discriminating the portions of the enzyme scaffold that are essential for catalysis from those that are not necessary will facilitate the wider use of enzymatic EAM catalysis for large-scale industrial processes.

Many abiotic reactions of critical importance are ideally performed under conditions

(temperature, pressure, pH) that are far removed from the mild conditions of biology. For example, catalysts in fuel cells and electrolyzers often operate at the extremes of pH to facilitate ion conduction, and many heterogeneous catalysts operate at elevated temperatures to enhance the reaction rate and facilitate heat integration. Biological systems offer opportunities for adapting enzyme catalysis to extreme reaction conditions. In particular, thermophilic archaea sustain life processes at temperatures exceeding 100°C and at extremes of pH (54). It has long been recognized that some enzymes display enhanced catalytic activity in organic solvents (55), yet there remains limited fundamental understanding of the characteristics of enzymes that engender persistent activity under these conditions. Additionally, whereas abiotic reactivity modes can be screened using abiotic reagents, screening for enzymatic performance under abiotic reaction conditions is more difficult because the biological replication machinery operates within a narrow domain of conditions. Strategies for driving directed evolution within extremophile hosts, and a deeper understanding of the factors that contribute to protein stability, provide plentiful opportunities for extending the rich EAM catalytic reactivity of enzymes toward the harsher conditions often required for thermal and electrochemical catalysis.

### Molecular catalysis

The modern molecular synthetic toolkit affords virtually unlimited scope for tailoring the primary, secondary, and outer coordination spheres around a molecular EAM active site. Several areas of exploration leverage this synthetic capability to embrace the distinctive physical properties of EAMs (Fig. 5).

EAM active sites in nature are subject to exquisite tuning by the arrangement of proximal amino acid residues and cofactors, as well as by the enzyme channels that gate the transport of reactants and products in and out. Similarly, achieving precise control over the local environment and transport in synthetic molecular EAM catalysts is critical for realizing their full potential. The ability to synthesize increasingly sophisticated ligands provides control of steric and electronic attributes, as demonstrated by remarkable progress in asymmetric hydrogenations, which are used extensively to achieve the enantioselectivity required in the preparation of pharmaceuticals and agrochemicals. This field has been dominated by Rh- and Ru-based catalysts with chiral diphosphines (56), but recent examples show that EAM catalysts can offer outstanding selectivity. For example, an Fe complex catalyzes the asymmetric transfer hydrogenation of ketones with performance superior to that of Ru catalysts (57), and a Co complex catalyzes the asymmetric hydrogenation of the C=C bond of enamides (58).

In addition to modifications of the ligands bound directly to the metal (primary coordination sphere), the environment of molecular catalysts can be tuned by positioning secondary coordination sphere substituents, such as Lewis acids (59), positively charged groups (60–62), hydrogen bond donors (63), and pendant amines functioning as proton relays (64–68) (Fig. 5A) proximal to the EAM center. These strategies have enhanced the rates of molecular EAM catalysis of electrochemical H<sub>2</sub> evolution (64–66), H<sub>2</sub> oxidation (65, 66, 68), CO<sub>2</sub> reduction (60), and O<sub>2</sub> reduction (69). Because the redox reactivity involves coupling of electron flow and bond rearrangement, the secondary coordination sphere substituents must be precisely positioned to foster optimal cooperativity. For example, the rates of proton-coupled electron transfer (70, 71) can be sensitive to sub-angstrom-level changes in the distance between proton donor and acceptor (72). Cooperativity between the primary and secondary coordination spheres in enzymes is achieved through the dynamic flexibility of the protein scaffold (26), a property that is difficult to recreate systematically in synthetic EAM catalysts. Strong electric fields can influence enzyme catalysis (73) by manipulating the energies of intermediates or transition states, thereby changing the rates and selectivity. Computations offer the opportunity to prescreen the impact of positioning of the secondary coordination sphere moieties; such studies could motivate synthetic efforts toward optimized secondary coordination sphere control in EAM catalysis.

Controlling transport to EAM active sites is difficult to achieve with freely diffusing small molecules, but improved transport environments can be created by anchoring molecular EAM active sites on the surfaces of, or within the pores of, extended solid host materials including, for example, graphitic carbon, microporous silica, and metal-organic frameworks (MOFs) (74). Solid-supported site-isolated EAMs have been used to catalyze a wide array of reactions; they benefit from structural constraints that prevent inhibitory bimolecular reactivity between metal centers while facilitating catalyst separation and recycling. For these molecular materials, the extended lattice can serve as scaffolding to incorporate secondary coordination sphere elements proximate to the embedded active site, and the pore structure and dimensions can be used to gate the transport of reactants and products to and from the active site. MOFs with EAM active sites have been deployed to carry out, for example, photocatalytic CO<sub>2</sub> reduction (75), ethylene hydrogenation (76), oxidation of alcohols (77), olefin cyclopropanation (78), arene C-H borylation (79), tandem oxidation and functionalization of styrene (80), and selective oxidation of methane to methanol (81). Enzymes often feature disparate channels that transport each

reactant and product molecule in different directions, with the EAM active sites precisely positioned at the junction of these conduits. Similar precision has been difficult to achieve in synthetic systems, and efforts toward constructing molecular materials with active sites at the intersection of multiple transport conduits could substantially advance selectivity in EAM catalysis.

Because of their low field strengths, EAM complexes have a propensity to undergo single-electron transfer pathways (82). The control levers noted above are particularly important for embracing and controlling radical reactivity. Because of their smaller d-orbital splitting and weaker spin-pairing energy, EAMs tend to react in enzymes through radical intermediates. Controlled radical reactions are central to biological detoxification by heme centers in cytochrome P450 enzymes, the synthesis of DNA precursors mediated by ribonucleotide reductase, and many other critical transformations mediated by cobalamins and radical SAM enzymes (9). By controlling the reactivity of Co(III) carbon-centered radicals generated from Co(II) porphyrin complexes, eight-membered rings have been produced from ring-closing reactions; this strategy provides attractive synthetic methods for reactions that traditionally required precious metal catalysts (83). Cooperative catalysis using EAM complexes of two metals, Ti and Cr, has provided a highly selective route to anti-Markovnikov alcohols through ring-opening of epoxides (84). This hydrogenation of epoxides is unusual because at different steps of the mechanism, a chromium complex transfers an electron, a hydrogen atom, and a proton.

Aerobic oxidation of primary alcohols to aldehydes and H<sub>2</sub>O<sub>2</sub> is catalyzed in natural systems by galactose oxidase, a copper-containing enzyme. A bio-inspired synthetic binuclear copper complex exhibiting metal-ligand cooperative reactivity catalyzes the oxidation of primary alcohols using O<sub>2</sub> from air (85). Similar to the accepted mechanism for galactose oxidase, the rate-determining step of the synthetic system is proposed to involve hydrogen atom transfer from a C-H bond of the alcohol to the oxygen-centered radical bound to Cu.

Many of the EAM active sites that occur naturally, particularly those carrying out multi-electron redox transformations, feature multiple metal centers linked to each other in cluster active sites or metal centers coupled to redox-active cofactor ligands. The presence of these additional metals and redox-active ligands expands the number of available redox states accessible over a range of potentials. This increased density of electron states serves to buffer redox changes at the metal center that binds and activates the reactant, thereby lowering the energy barrier to multi-electron transformations. Harnessing the full power of EAMs



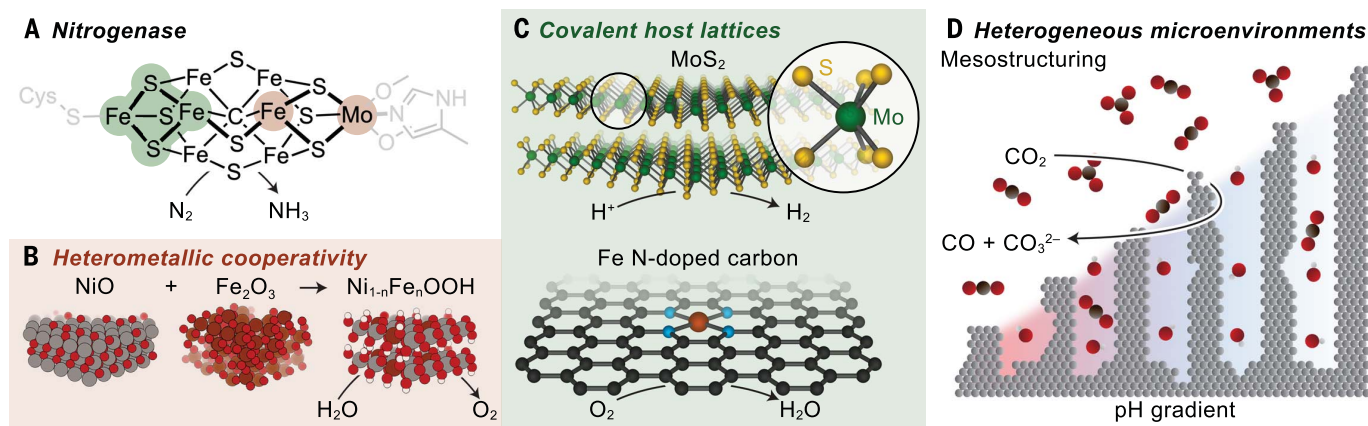


**Fig. 6. EAM sites in enzymes such as nitrogenase provide the blueprint for heterogeneous EAM catalyst design.** (A and B) Multimetallic cooperativity in nature [green in (A)] can guide the design of mixed metal-oxide oxygen evolution catalysts (B) (106). (C) The more covalent metal-ligand bonding in natural systems [Fe/Mo in (A)] parallels the more covalent chalcogenide (108) and graphitic carbon host lattices (127) in synthetic catalysts. (D) The function of the fine-tuned catalyst microenvironments in enzymes can be replicated in synthetic catalysts through micro- and mesostructuring (128).

in synthetic catalysts will require mastering the interactions of EAM centers with both metal-based and organic-based redox active ligands.

EAMs with redox-active ligands (86–88) catalyze a wide variety of reactions, including cleavage of C–C bonds (89), cycloadditions (90), oxidation of alcohols (91), and aminations (92). Further systematic deployment of redox-active ligands in EAM catalysis will benefit from general design rules for independently tuning metal-based and ligand-based redox levels to control the thermochemistry of elementary reaction steps. These ligands also play a key role in electrocatalysis at molecular active sites by providing a reservoir for accumulating redox equivalents that are cumulatively discharged to promote multielectron reactions including, for example,  $\text{CO}_2$  reduction (93) and  $\text{O}_2$  reduction (94). An improved understanding of how to design systems with enhanced metal/ligand redox cooperativity would facilitate the design of more efficient (electro)catalysts.

Coupling between the metal binding site and one or more metals can also increase the density of electronic states available for a multielectron transformation. Bimetallic and multimetallic EAM catalysts have been used for  $\text{CO}_2$  reduction (Fig. 5B) (95, 96), cycloadditions (Fig. 5D) (90), dehydrogenation of formic acid (97), and reduction of  $\text{NO}_2$  (67) or  $\text{O}_2$  (98). Further systematic development of multimetallic systems in EAM catalysis will benefit from a better understanding of how to stabilize the cluster against irreversible fragmentation while retaining the capacity to rapidly break and regenerate M–M or M–E–M (E = S, O) bonds during a catalytic cycle.

Understanding molecular EAM catalysts in systems with an increased density of states requires new spectroscopic tools and computational methods (99). Whereas current com-

putational methods effectively model weakly correlated closed-shell singlets, new methods are needed for accurately modeling open-shell species, and deconvolution of spin-state populations is required to accurately model the multiconfigurational electronic structure of metal clusters and metal complexes involving redox-active ligands (100). Open-shell systems are often paramagnetic and intractable to characterize by routine nuclear magnetic resonance methods; emerging improved spectroscopic tools for characterizing paramagnetic species are advancing mechanistic understanding of these systems (101–103).

#### Heterogeneous catalysis

Heterogeneous catalysis occurs on the surfaces of extended solids. Although these extended solids may bear little direct structural resemblance to active sites in nature, the principles that define EAM catalysis in enzymes provide valuable leads toward their greater utility in heterogeneous catalysis.

Similar to the catalytic cooperativity in nature, enhanced catalytic performance can emerge from extended solids that incorporate multiple EAMs acting cooperatively. For example, by combining the different binding strengths of Ti and Cu toward hydrogen, alloying Ti and Cu leads to hydrogen evolution reactivity similar to that of PGMs (104). Analogously, mixed oxyhydroxides containing Fe, Co, and W catalyze oxygen evolution in an alkaline environment (105); the cooperative interactions of even trace amounts of Fe can profoundly promote oxygen evolution activity on  $\text{NiOOH}$  (Fig. 6B) (106). Considering the inherent lability of EAMs, improved characterization tools are needed to track the time dependence of surface restructuring in multimetallic EAM catalysts. Additionally, multimetallic EAM oxide-based catalytic materials are challenging to model

with conventional computational methods (107); detailed mechanistic understanding of these systems would benefit from new computational tools that effectively model compositional heterogeneity and extend multiconfigurational methods to periodic solids. Given the enormous compositional diversity available in multimetallic solids, machine learning tools offer the potential to explore multidimensional reaction landscapes rapidly.

Historically, EAM heterogeneous catalysis focused predominantly on the reactivity of metal or metal oxide phases, the two endpoint thermodynamic sinks under reducing or oxidizing conditions, respectively. In contrast, many EAM active sites in nature are hosted within highly evolved combinations of sulfur, nitrogen, and carbon in the primary coordination environments, suggesting an appealing opportunity to exploit new types of heterogeneous catalysts. Relative to the O atoms in oxide host lattices, the greater orbital extension and/or energetic match of the p-orbitals in C, N, P, and S with the d-orbitals of EAMs leads to substantial changes in the band structures of chalcogenides (108, 109), pnictides (110–112), and carbides (110, 113), potentially endowing these EAM catalysts with enhanced activity relative to the corresponding metal or oxide phases. For example, metal sulfide and phosphide materials have emerged as potent catalysts for electrochemical hydrogen evolution (109), and EAM carbides have been shown to be highly selective for hydrodeoxygenation of biomass-derived molecules (114). Considering the vast phase space available among chalcogenides, pnictides, and carbides, there is ample opportunity to discover new EAM catalysts that take advantage of environments akin to those found in nature. Progress toward these goals will require advances in the synthesis of materials with tunable phase and nanostructure at sufficient scales for

catalytic applications. In addition, because these materials are typically metastable relative to their corresponding metal or oxide phases, fundamental insights are needed to understand how the surfaces of these materials undergo reconstruction under sustained catalytic turnover (115). Surface-sensitive operando spectroscopic characterization (116) revealing the chemical stability of these materials is critical for the design of optimal catalysis.

EAM active sites can also be hosted within graphitic carbon host lattices. For many decades, it has been recognized that the high-temperature pyrolysis of nitrogen and carbon precursors bound to EAMs such as Fe and Co can lead to the generation of relatively high-performance electrocatalysts for the oxygen reduction reaction in fuel cells (117, 118). These materials, often referred to as M-N-C catalysts, are postulated to contain metal nanoparticles and mononuclear metal sites embedded in the graphitic framework, with varying ratios depending on the synthetic conditions (119). Fe-N-C materials are leading EAM candidates to replace Pt in fuel cells, and this class of materials presents an opportunity to create emergent reactivity from EAMs through strong interaction between the EAM orbitals and the electronic states of graphitic carbons. Despite decades of work in this area, the local structure of the active sites remains poorly understood, and the synthetic toolkit for tuning the population of active sites remains limited. Thus, continued progress in this area will hinge on new strategies for better understanding and controlling the inherent distribution of active-site structures present in these materials.

The microenvironment around the active site in natural systems is precisely controlled by preorganizing reactants, imposing a local electric field, and controlling transport to and from active sites. The dynamic nature of EAMs affords opportunities to implement these concepts within heterogeneous catalysts. Many strategies have been used for imposing a particular microenvironment at the catalyst surface: For catalysis at solid-liquid interfaces, the composition of the solvent or electrolyte can be varied; the catalyst can be designed with appropriate meso/microstructure to create diffusional gradients at the surface; and the catalyst surface can be chemically modified (120). Electrolyte choice, catalyst mesostructuring, and chemical modification have all been applied to tune the selectivity of Cu-based CO<sub>2</sub>/CO reduction catalysts (121). The solution environment can also be used to favor mechanisms for dynamic self-repair of catalysts; for example, Co ions in solution promote dynamic stability and self-repair of Co-based oxygen evolution catalysts that would otherwise undergo corrosion (122). Additionally, thin gas-permeable layers of ionic liquids (123) and/or molecular promoters could create specific microenvironments that contain substrate-

binding units proximate to active sites. This strategy enhances the stability of EAMs prone to irreversible reconstruction/oxidation, and may also foster improved selectivity. Despite the enormous synthetic opportunities in this area, mechanistic insights into how local microenvironments tune heterogeneous catalysis are rare. Although there are many tools for operando characterization of catalysts, these tools often only shed light on the primary coordination environments of EAM active sites. Thus, improved tools are needed for characterizing longer-range interactions in the secondary and outer coordination spheres that define the microenvironment of the catalyst. Notwithstanding these formidable challenges, the tantalizing prospect of creating enzyme-like three-dimensional active sites on surfaces has enormous appeal for emerging EAM catalysis.

## Outlook

Recent years have seen tremendous growth in the development and application of EAM catalysts; however, the fundamental understanding of reactivity patterns of these metals has lagged behind that of PGMs. This disparity in both understanding and use of EAMs is attributed to the broader landscape of reactivity available to EAMs and the smaller historical investment devoted to the study of them. The gaps in fundamental scientific knowledge highlighted here are intended as a “call to action” to identify and overcome scientific barriers to EAM catalysis, based on compelling opportunities that embrace and exploit the characteristic reactivity of EAMs. Examples of recent discoveries of EAM catalysts that rival, or even exceed, the performance of PGM catalysts document the value of identifying design principles for new classes of catalysts. In addition to catalytic activity, EAM catalysts should possess long-term stability and high active-site density for practical applications. The quest to develop efficient, sustainable catalysts based on EAMs benefits from cohesive efforts in synthesis, operando characterization, mechanistic inquiry, materials design, and theoretical modeling. Spurred by recent advances, the collective efforts of the catalysis community can bring the full potential of EAM catalysts to realization.

## REFERENCES AND NOTES

1. CRC Handbook of Chemistry and Physics, 97th Edition (CRC Press, 2016).
2. J. Liu et al., Metalloproteins containing cytochrome, iron-sulfur, or copper redox centers. *Chem. Rev.* **114**, 4366–4469 (2014). doi: [10.1021/cr400479b](https://doi.org/10.1021/cr400479b); pmid: 24758379
3. M. A. Thorseth, C. E. Tornow, E. C. M. Tse, A. A. Gewirth, Cu complexes that catalyze the oxygen reduction reaction. *Coord. Chem. Rev.* **257**, 130–139 (2013). doi: [10.1016/j.ccr.2012.03.033](https://doi.org/10.1016/j.ccr.2012.03.033)
4. E. I. Solomon et al., Copper active sites in biology. *Chem. Rev.* **114**, 3659–3853 (2014). doi: [10.1021/cr400327t](https://doi.org/10.1021/cr400327t); pmid: 24588098
5. L. C. Seefeldt et al., Energy Transduction in Nitrogenase. *Acc. Chem. Res.* **51**, 2179–2186 (2018). doi: [10.1021/acs.accounts.8b00112](https://doi.org/10.1021/acs.accounts.8b00112); pmid: 30095253
6. W. Lubitz, H. Ogata, O. Rüdiger, E. Reijerse, Hydrogenases. *Chem. Rev.* **114**, 4081–4148 (2014). doi: [10.1021/cr4005814](https://doi.org/10.1021/cr4005814); pmid: 24655035
7. J. P. McEvoy, G. W. Brudvig, Water-splitting chemistry of photosystem II. *Chem. Rev.* **106**, 4455–4483 (2006). doi: [10.1021/cr0204294](https://doi.org/10.1021/cr0204294); pmid: 17091926
8. V. C. C. Wang et al., Alkane Oxidation: Methane Monooxygenases, Related Enzymes, and Their Biomimetics. *Chem. Rev.* **117**, 8574–8621 (2017). doi: [10.1021/acs.chemrev.6b00624](https://doi.org/10.1021/acs.chemrev.6b00624); pmid: 28206744
9. J. B. Broderick, B. R. Duffus, K. S. Duschene, E. M. Shepard, Radical S-adenosylmethionine enzymes. *Chem. Rev.* **114**, 4229–4317 (2014). doi: [10.1021/cr4004709](https://doi.org/10.1021/cr4004709); pmid: 24476342
10. C. C. C. Johansson Seechurn, M. O. Kitching, T. J. Colacot, V. Snieckus, Palladium-catalyzed cross-coupling: A historical contextual perspective to the 2010 Nobel Prize. *Angew. Chem. Int. Ed.* **51**, 5062–5085 (2012). doi: [10.1002/anie.201107017](https://doi.org/10.1002/anie.201107017); pmid: 22573393
11. R. Dorel, C. P. Grugel, A. M. Haydl, The Buchwald-Hartwig Amination After 25 Years. *Angew. Chem. Int. Ed.* **58**, 17118–17129 (2019). doi: [10.1002/anie.201904795](https://doi.org/10.1002/anie.201904795); pmid: 31166642
12. R. Franke, D. Selent, A. Börner, Applied hydroformylation. *Chem. Rev.* **112**, 5675–5732 (2012). doi: [10.1021/cr3001803](https://doi.org/10.1021/cr3001803); pmid: 22937803
13. J. K. Nørskov et al., Trends in the Exchange Current for Hydrogen Evolution. *J. Electrochem. Soc.* **152**, J23–J26 (2005). doi: [10.1149/1.1856888](https://doi.org/10.1149/1.1856888)
14. C. C. L. McCrory, S. Jung, J. C. Peters, T. F. Jaramillo, Benchmarking heterogeneous electrocatalysts for the oxygen evolution reaction. *J. Am. Chem. Soc.* **135**, 16977–16987 (2013). doi: [10.1021/ja407115p](https://doi.org/10.1021/ja407115p); pmid: 24171402
15. J. F. Hartwig, Evolution of C-H Bond Functionalization from Methane to Methodology. *J. Am. Chem. Soc.* **138**, 2–24 (2016). doi: [10.1021/jacs.5b08707](https://doi.org/10.1021/jacs.5b08707); pmid: 26566092
16. R. E. Smalley, Future Global Energy Prosperity: The Terawatt Challenge. *MRS Bull.* **30**, 412–417 (2005). doi: [10.1557/mrs2005.124](https://doi.org/10.1557/mrs2005.124)
17. P. C. K. Vesborg, T. F. Jaramillo, Addressing the terawatt challenge: Scalability in the supply of chemical elements for renewable energy. *RSC Adv.* **2**, 7933–7947 (2012). doi: [10.1039/c2ra20839c](https://doi.org/10.1039/c2ra20839c)
18. K. S. Egorova, V. P. Ananikov, Toxicity of Metal Compounds: Knowledge and Myths. *Organometallics* **36**, 4071–4090 (2017). doi: [10.1021/acs.organomet.7b00605](https://doi.org/10.1021/acs.organomet.7b00605)
19. J. D. Hayler, D. K. Leahy, E. M. Simmons, A Pharmaceutical Industry Perspective on Sustainable Metal Catalysis. *Organometallics* **38**, 36–46 (2019). doi: [10.1021/acs.organomet.8b00566](https://doi.org/10.1021/acs.organomet.8b00566)
20. P. Nuss, M. J. Eckelman, Life cycle assessment of metals: A scientific synthesis. *PLOS ONE* **9**, e101298 (2014). doi: [10.1371/journal.pone.0101298](https://doi.org/10.1371/journal.pone.0101298); pmid: 24999810
21. A. J. Medford et al., From the Sabatier principle to a predictive theory of transition-metal heterogeneous catalysis. *J. Catal.* **328**, 36–42 (2015). doi: [10.1016/j.jcat.2014.12.033](https://doi.org/10.1016/j.jcat.2014.12.033)
22. J. H. B. Sattler, J. Ruiz-Martinez, E. Santillan-Jimenez, B. M. Weckhuysen, Catalytic dehydrogenation of light alkanes on metals and metal oxides. *Chem. Rev.* **114**, 10613–10653 (2014). doi: [10.1021/cr5002436](https://doi.org/10.1021/cr5002436); pmid: 25163050
23. K. M. Light, J. A. Wisniewski, W. A. Vinyard, M. T. Kieber-Emmons, Perception of the plant hormone ethylene: Known-knowns and known-unknowns. *J. Biol. Inorg. Chem.* **21**, 715–728 (2016). doi: [10.1007/s00775-016-1378-3](https://doi.org/10.1007/s00775-016-1378-3); pmid: 27456611
24. H. S. Toogood, N. S. Scrutton, Discovery, Characterisation, Engineering and Applications of Ene Reductases for Industrial Biocatalysis. *ACS Catal.* **8**, 3532–3549 (2019). doi: [10.1021/acscatal.8b00624](https://doi.org/10.1021/acscatal.8b00624); pmid: 31157123
25. M. Costas, M. P. Mehn, M. P. Jensen, L. Que Jr., Dioxygen activation at mononuclear nonheme iron active sites: Enzymes, models, and intermediates. *Chem. Rev.* **104**, 939–986 (2004). doi: [10.1021/cr020628n](https://doi.org/10.1021/cr020628n); pmid: 14871146
26. G. G. Hammes, S. J. Benkovic, S. Hammes-Schiffer, Flexibility, diversity, and cooperativity: Pillars of enzyme catalysis. *Biochemistry* **50**, 10422–10430 (2011). doi: [10.1021/bi201486f](https://doi.org/10.1021/bi201486f); pmid: 22029278
27. J. K. McCusker, Electronic structure in the transition metal block and its implications for light harvesting. *Science* **363**, 484–488 (2019). doi: [10.1126/science.aav9104](https://doi.org/10.1126/science.aav9104); pmid: 30705184
28. P. Pykkö, Relativistic Effects in Structural Chemistry. *Chem. Rev.* **88**, 563–594 (1988). doi: [10.1021/cr00085a006](https://doi.org/10.1021/cr00085a006)
29. L. A. Watson, O. V. Ozerov, M. Pink, K. G. Caulton, Four-coordinate, planar Rull. A triplet state as a response to a



- 14-valence electron configuration. *J. Am. Chem. Soc.* **125**, 8426–8427 (2003). doi: [10.1021/ja035166p](https://doi.org/10.1021/ja035166p); pmid: [12848535](https://pubmed.ncbi.nlm.nih.gov/12848535/)
30. M. Kinauer *et al.*, An iridium(III/IV) redox series featuring a terminal imido complex with triplet ground state. *Chem. Sci.* **9**, 4325–4332 (2018). doi: [10.1039/C8SC01113C](https://doi.org/10.1039/C8SC01113C); pmid: [29780564](https://pubmed.ncbi.nlm.nih.gov/29780564/)
  31. M. Swart, M. Costas, Eds., *Spin States in Biochemistry and Inorganic Chemistry: Influence on Structure and Reactivity* (Wiley, 2016).
  32. D. P. Estes, A. K. Vannucci, A. R. Hall, D. L. Lichtenberger, J. R. Norton, Thermodynamics of the Metal-Hydrogen Bonds in ( $\eta^5$ -C<sub>5</sub>H<sub>5</sub>)M (CO)<sub>2</sub>H (M = Fe, Ru, Os). *Organometallics* **30**, 3444–3447 (2011). doi: [10.1021/om2001519](https://doi.org/10.1021/om2001519)
  33. J. Zhang, D. C. Grills, K.-W. Huang, E. Fujita, R. M. Bullock, Carbon-to-metal hydrogen atom transfer: Direct observation using time-resolved infrared spectroscopy. *J. Am. Chem. Soc.* **127**, 15684–15685 (2005). doi: [10.1021/ja0555724](https://doi.org/10.1021/ja0555724); pmid: [16277493](https://pubmed.ncbi.nlm.nih.gov/16277493/)
  34. V. D. Parker, K. L. Handoo, F. Roness, M. Tilset, Electrode Potentials and Thermodynamics of Isodesmic Reactions. *J. Am. Chem. Soc.* **113**, 7493–7498 (1991). doi: [10.1021/ja00020a007](https://doi.org/10.1021/ja00020a007)
  35. N. M. Marshall *et al.*, Rationally tuning the reduction potential of a single cupredoxin beyond the natural range. *Nature* **462**, 113–116 (2009). doi: [10.1038/nature08551](https://doi.org/10.1038/nature08551); pmid: [19890331](https://pubmed.ncbi.nlm.nih.gov/19890331/)
  36. A. B. P. Lever, Electrochemical Parametrization of Metal Complex Redox Potentials, Using the Ruthenium(III)/ruthenium(II) Couple to Generate a Ligand Electrochemical Series. *Inorg. Chem.* **29**, 1271–1285 (1990). doi: [10.1021/ic00331a030](https://doi.org/10.1021/ic00331a030)
  37. M. Wikström, K. Krab, V. Sharma, Oxygen Activation and Energy Conservation by Cytochrome c Oxidase. *Chem. Rev.* **118**, 2469–2490 (2018). doi: [10.1021/acs.chemrev.7b00664](https://doi.org/10.1021/acs.chemrev.7b00664); pmid: [29350917](https://pubmed.ncbi.nlm.nih.gov/29350917/)
  38. L. Helm, A. E. Merbach, Inorganic and bioinorganic solvent exchange mechanisms. *Chem. Rev.* **105**, 1923–1959 (2005). doi: [10.1021/cr030726o](https://doi.org/10.1021/cr030726o); pmid: [15941206](https://pubmed.ncbi.nlm.nih.gov/15941206/)
  39. C. A. Gaglioli, S. J. Stoneburner, C. J. Cramer, L. Gagliardi, Beyond Density Functional Theory: The Multiconfigurational Approach To Model Heterogeneous Catalysis. *ACS Catal.* **9**, 8481–8502 (2019). doi: [10.1021/acscatal.9b01775](https://doi.org/10.1021/acscatal.9b01775)
  40. P. Schlexer Lamoureux *et al.*, Machine Learning for Computational Heterogeneous Catalysis. *ChemCatChem* **11**, 3581–3601 (2019). doi: [10.1002/cctc.201900595](https://doi.org/10.1002/cctc.201900595)
  41. J. P. Janet, S. Ramesh, C. Duan, H. J. Kulik, Accurate Multiobjective Design in a Space of Millions of Transition Metal Complexes with Neural-Network-Driven Efficient Global Optimization. *ACS Cent. Sci.* **6**, 513–524 (2020). doi: [10.1021/acscentsci.0c00026](https://doi.org/10.1021/acscentsci.0c00026); pmid: [32342001](https://pubmed.ncbi.nlm.nih.gov/32342001/)
  42. B. Meyer, B. Sawatlon, S. Heinen, O. A. von Lilienfeld, C. Corminboeuf, Machine learning meets volcano plots: Computational discovery of cross-coupling catalysts. *Chem. Sci.* **9**, 7069–7077 (2018). doi: [10.1039/C8SC01949E](https://doi.org/10.1039/C8SC01949E); pmid: [30310627](https://pubmed.ncbi.nlm.nih.gov/30310627/)
  43. Z. W. Ulissi *et al.*, Machine-Learning Methods Enable Exhaustive Searches for Active Bimetallic Facets and Reveal Active Site Motifs for CO<sub>2</sub> Reduction. *ACS Catal.* **7**, 6600–6608 (2017). doi: [10.1021/acscatal.7b01648](https://doi.org/10.1021/acscatal.7b01648)
  44. M. Zhong *et al.*, Accelerated discovery of CO<sub>2</sub> electrocatalysts using active machine learning. *Nature* **581**, 178–183 (2020). doi: [10.1038/s41586-020-2242-8](https://doi.org/10.1038/s41586-020-2242-8); pmid: [32405017](https://pubmed.ncbi.nlm.nih.gov/32405017/)
  45. K. Saravanan, J. R. Kitchin, O. A. von Lilienfeld, J. A. Keith, Alchemical Predictions for Computational Catalysis: Potential and Limitations. *J. Phys. Chem. Lett.* **8**, 5002–5007 (2017). doi: [10.1021/acs.jpclett.7b01974](https://doi.org/10.1021/acs.jpclett.7b01974); pmid: [28938798](https://pubmed.ncbi.nlm.nih.gov/28938798/)
  46. T. Bligaard *et al.*, Toward Benchmarking in Catalysis Science: Best Practices, Challenges, and Opportunities. *ACS Catal.* **6**, 2590–2602 (2016). doi: [10.1021/acscatal.6b00183](https://doi.org/10.1021/acscatal.6b00183)
  47. O. Khersonsky, D. S. Tawfik, Enzyme promiscuity: A mechanistic and evolutionary perspective. *Annu. Rev. Biochem.* **79**, 471–505 (2010). doi: [10.1146/annurev-biochem-030409-143718](https://doi.org/10.1146/annurev-biochem-030409-143718); pmid: [20235827](https://pubmed.ncbi.nlm.nih.gov/20235827/)
  48. H. M. L. Davies, D. Morton, Guiding principles for site selective and stereoselective intermolecular C-H functionalization by donor/acceptor rhodium carbenes. *Chem. Soc. Rev.* **40**, 1857–1869 (2011). doi: [10.1039/c0cs00217h](https://doi.org/10.1039/c0cs00217h); pmid: [21359404](https://pubmed.ncbi.nlm.nih.gov/21359404/)
  49. O. F. Brandenberg, K. Chen, F. H. Arnold, Directed Evolution of a Cytochrome P450 Carbene Transferase for Selective Functionalization of Cyclic Compounds. *J. Am. Chem. Soc.* **141**, 8989–8995 (2019). doi: [10.1021/jacs.9b02931](https://doi.org/10.1021/jacs.9b02931); pmid: [31070908](https://pubmed.ncbi.nlm.nih.gov/31070908/)
  50. R. K. Zhang *et al.*, Enzymatic assembly of carbon-carbon bonds via iron-catalyzed sp<sup>3</sup> C-H functionalization. *Nature* **565**, 67–72 (2019). doi: [10.1038/s41586-018-0808-5](https://doi.org/10.1038/s41586-018-0808-5); pmid: [30568304](https://pubmed.ncbi.nlm.nih.gov/30568304/)
  51. J. F. Hartwig, M. A. Larsen, Undirected, Homogeneous C-H Bond Functionalization: Challenges and Opportunities. *ACS Cent. Sci.* **2**, 281–292 (2016). doi: [10.1021/acscentsci.6b00032](https://doi.org/10.1021/acscentsci.6b00032); pmid: [27294201](https://pubmed.ncbi.nlm.nih.gov/27294201/)
  52. O. F. Brandenberg, R. Fasan, F. H. Arnold, Exploiting and engineering hemoproteins for abiological carbene and nitrene transfer reactions. *Curr. Opin. Biotechnol.* **47**, 102–111 (2017). doi: [10.1016/j.copbio.2017.06.005](https://doi.org/10.1016/j.copbio.2017.06.005); pmid: [28711855](https://pubmed.ncbi.nlm.nih.gov/28711855/)
  53. G. Jiménez-Osés *et al.*, The role of distant mutations and allosteric regulation on LovD active site dynamics. *Nat. Chem. Biol.* **10**, 431–436 (2014). doi: [10.1038/nchembio.1503](https://doi.org/10.1038/nchembio.1503); pmid: [24727900](https://pubmed.ncbi.nlm.nih.gov/24727900/)
  54. F. Niehaus, C. Bertoldo, M. Kähler, G. Antranikian, Extremophiles as a source of novel enzymes for industrial application. *Appl. Microbiol. Biotechnol.* **51**, 711–729 (1999). doi: [10.1007/s002530051456](https://doi.org/10.1007/s002530051456); pmid: [10422220](https://pubmed.ncbi.nlm.nih.gov/10422220/)
  55. A. M. Kilbanov, Improving enzymes by using them in organic solvents. *Nature* **409**, 241–246 (2001). doi: [10.1038/35051719](https://doi.org/10.1038/35051719); pmid: [11196652](https://pubmed.ncbi.nlm.nih.gov/11196652/)
  56. R. Noyori, Asymmetric catalysis: Science and opportunities (Nobel lecture). *Angew. Chem. Int. Ed.* **41**, 2008–2022 (2002). doi: [10.1002/1521-3773\(20020617\)41:12<2008:AID-ANGE2008>3.0.CO;2-4](https://doi.org/10.1002/1521-3773(20020617)41:12<2008:AID-ANGE2008>3.0.CO;2-4); pmid: [19746595](https://pubmed.ncbi.nlm.nih.gov/19746595/)
  57. W. Zuo, A. J. Lough, Y. F. Li, R. H. Morris, Amine(imine) diphosphine iron catalysts for asymmetric transfer hydrogenation of ketones and imines. *Science* **342**, 1080–1083 (2013). doi: [10.1126/science.1244466](https://doi.org/10.1126/science.1244466); pmid: [24288329](https://pubmed.ncbi.nlm.nih.gov/24288329/)
  58. M. R. Friedfeld, H. Zhong, R. T. Ruck, M. Shevlin, P. J. Chirik, Cobalt-catalyzed asymmetric hydrogenation of enamides enabled by single-electron reduction. *Science* **360**, 888–893 (2018). doi: [10.1126/science.aar6117](https://doi.org/10.1126/science.aar6117); pmid: [29798879](https://pubmed.ncbi.nlm.nih.gov/29798879/)
  59. J. J. Kiernicki, M. Zeller, N. K. Szymczak, Hydrazine Capture and N-N Bond Cleavage at Iron Enabled by Flexible Appended Lewis Acids. *J. Am. Chem. Soc.* **139**, 18194–18197 (2017). doi: [10.1021/jacs.7b11465](https://doi.org/10.1021/jacs.7b11465); pmid: [29227655](https://pubmed.ncbi.nlm.nih.gov/29227655/)
  60. I. Azcarate, C. Costentin, M. Robert, J.-M. Savéant, Through-Space Charge Interaction Substituent Effects in Molecular Catalysis Leading to the Design of the Most Efficient Catalyst of CO<sub>2</sub>-to-CO Electrochemical Conversion. *J. Am. Chem. Soc.* **138**, 16639–16644 (2016). doi: [10.1021/jacs.6b07014](https://doi.org/10.1021/jacs.6b07014); pmid: [27976580](https://pubmed.ncbi.nlm.nih.gov/27976580/)
  61. T. Chantarojsiri, J. W. Ziller, J. Y. Yang, Incorporation of redox-inactive cations promotes iron catalyzed aerobic C-H oxidation at mild potentials. *Chem. Sci.* **9**, 2567–2574 (2018). doi: [10.1039/C7SC04486K](https://doi.org/10.1039/C7SC04486K); pmid: [29732136](https://pubmed.ncbi.nlm.nih.gov/29732136/)
  62. D. J. Martin, B. Q. Mercado, J. M. Mayer, Combining scaling relationships overcomes rate versus overpotential trade-offs in O<sub>2</sub> molecular electrocatalysis. *Sci. Adv.* **6**, eaaz3318 (2020). doi: [10.1126/sciadv.aaz3318](https://doi.org/10.1126/sciadv.aaz3318); pmid: [32201730](https://pubmed.ncbi.nlm.nih.gov/32201730/)
  63. C. L. Ford, Y. J. Park, E. M. Matson, Z. Gordon, A. R. Fout, A bioinspired iron catalyst for nitrate and perchlorate reduction. *Science* **354**, 741–743 (2016). doi: [10.1126/science.aah6886](https://doi.org/10.1126/science.aah6886); pmid: [27846604](https://pubmed.ncbi.nlm.nih.gov/27846604/)
  64. C. M. Klug, A. Cardenas, R. M. Bullock, M. O'Hagan, E. S. Wiedner, Reversing the Tradeoff Between Rate and Overpotential in Molecular Electrocatalysts for H<sub>2</sub> Production. *ACS Catal.* **8**, 3286–3296 (2018). doi: [10.1021/acscatal.7b04379](https://doi.org/10.1021/acscatal.7b04379)
  65. A. Le Goff *et al.*, From hydrogenases to noble metal-free catalytic nanomaterials for H<sub>2</sub> production and uptake. *Science* **326**, 1384–1387 (2009). doi: [10.1126/science.1179773](https://doi.org/10.1126/science.1179773); pmid: [19965754](https://pubmed.ncbi.nlm.nih.gov/19965754/)
  66. T. N. Huan *et al.*, Biol.-inspired noble metal-free nanomaterials approaching platinum performances for H<sub>2</sub> evolution and uptake. *Energy Environ. Sci.* **9**, 940–947 (2016). doi: [10.1039/C5EE02739J](https://doi.org/10.1039/C5EE02739J)
  67. C.-W. Hsu, S. C. Rathnayaka, S. M. Islam, S. N. MacMillan, N. P. Mankad, N<sub>2</sub>O Reductase Activity of a [Cu<sub>4</sub>S] Cluster in the 4Cu<sup>+</sup> Redox State Modulated by Hydrogen Bond Donors and Proton Relays in the Secondary Coordination Sphere. *Angew. Chem. Int. Ed.* **59**, 627–631 (2020). doi: [10.1002/anie.201906327](https://doi.org/10.1002/anie.201906327); pmid: [31661177](https://pubmed.ncbi.nlm.nih.gov/31661177/)
  68. T. Liu, D. L. Dubois, R. M. Bullock, An iron complex with pendent amines as a molecular electrocatalyst for oxidation of hydrogen. *Nat. Chem.* **5**, 228–233 (2013). doi: [10.1038/nchem.1571](https://doi.org/10.1038/nchem.1571); pmid: [23422565](https://pubmed.ncbi.nlm.nih.gov/23422565/)
  69. D. J. Martin, B. Q. Mercado, J. M. Mayer, Combining scaling relationships overcomes rate versus overpotential trade-offs in O<sub>2</sub> molecular electrocatalysis. *Sci. Adv.* **6**, eaaz3318 (2020). doi: [10.1126/sciadv.aaz3318](https://doi.org/10.1126/sciadv.aaz3318)
  70. J. J. Warren, T. A. Tronic, J. M. Mayer, Thermochemistry of proton-coupled electron transfer reagents and its implications. *Chem. Rev.* **110**, 6961–7001 (2010). doi: [10.1021/cr100085k](https://doi.org/10.1021/cr100085k); pmid: [20925411](https://pubmed.ncbi.nlm.nih.gov/20925411/)
  71. D. R. Weinberg *et al.*, Proton-coupled electron transfer. *Chem. Rev.* **112**, 4016–4093 (2012). doi: [10.1021/cr200177j](https://doi.org/10.1021/cr200177j); pmid: [22702235](https://pubmed.ncbi.nlm.nih.gov/22702235/)
  72. S. Horvath, L. E. Fernandez, A. V. Soudakov, S. Hammes-Schiffer, Insights into proton-coupled electron transfer mechanisms of electrocatalytic H<sub>2</sub> oxidation and production. *Proc. Natl. Acad. Sci. U.S.A.* **109**, 15663–15668 (2012). doi: [10.1073/pnas.1118333109](https://doi.org/10.1073/pnas.1118333109); pmid: [22529352](https://pubmed.ncbi.nlm.nih.gov/22529352/)
  73. S. D. Fried, S. Bagchi, S. G. Boxer, Extreme electric fields power catalysis in the active site of ketosteroid isomerase. *Science* **346**, 1510–1514 (2014). doi: [10.1126/science.1259802](https://doi.org/10.1126/science.1259802); pmid: [25525245](https://pubmed.ncbi.nlm.nih.gov/25525245/)
  74. Q. Wang, D. Astruc, State of the Art and Prospects in Metal-Organic Framework (MOF)-Based and MOF-Derived Nanocatalysis. *Chem. Rev.* **120**, 1438–1511 (2020). doi: [10.1021/acs.chemrev.9b00223](https://doi.org/10.1021/acs.chemrev.9b00223); pmid: [31246430](https://pubmed.ncbi.nlm.nih.gov/31246430/)
  75. X. Feng *et al.*, Metal-Organic Frameworks Significantly Enhance Photocatalytic Hydrogen Evolution and CO<sub>2</sub> Reduction with Earth-Abundant Copper Photosensitizers. *J. Am. Chem. Soc.* **142**, 690–695 (2020). doi: [10.1021/jacs.9b12229](https://doi.org/10.1021/jacs.9b12229); pmid: [31895984](https://pubmed.ncbi.nlm.nih.gov/31895984/)
  76. J. Liu *et al.*, Introducing Nonstructural Ligands to Zirconia-like Metal-Organic Framework Nodes To Tune the Activity of Node-Supported Nickel Catalysts for Ethylene Hydrogenation. *ACS Catal.* **9**, 3198–3207 (2019). doi: [10.1021/acscatal.8b04828](https://doi.org/10.1021/acscatal.8b04828)
  77. K. I. Otake *et al.*, Single-Atom-Based Vanadium Oxide Catalysts Supported on Metal-Organic Frameworks: Selective Alcohol Oxidation and Structure-Activity Relationship. *J. Am. Chem. Soc.* **140**, 8652–8656 (2018). doi: [10.1021/jacs.8b05107](https://doi.org/10.1021/jacs.8b05107); pmid: [29950097](https://pubmed.ncbi.nlm.nih.gov/29950097/)
  78. C. Sun, G. Skorpouski, J.-H. Dou, A. M. Wright, M. Dincă, Reversible Metalation and Catalysis with a Scorpionate-like Metallo-ligand in a Metal-Organic Framework. *J. Am. Chem. Soc.* **140**, 17394–17398 (2018). doi: [10.1021/jacs.8b11085](https://doi.org/10.1021/jacs.8b11085); pmid: [30497263](https://pubmed.ncbi.nlm.nih.gov/30497263/)
  79. T. Zhang, K. Manna, W. Lin, Metal-Organic Frameworks Stabilize Solution-Inaccessible Cobalt Catalysts for Highly Efficient Broad-Scope Organic Transformations. *J. Am. Chem. Soc.* **138**, 3241–3249 (2016). doi: [10.1021/jacs.6b00849](https://doi.org/10.1021/jacs.6b00849); pmid: [26864496](https://pubmed.ncbi.nlm.nih.gov/26864496/)
  80. M. H. Beyzavi *et al.*, A Hafnium-Based Metal-Organic Framework as a Nature-Inspired Tandem Reaction Catalyst. *J. Am. Chem. Soc.* **137**, 13624–13631 (2015). doi: [10.1021/jacs.5b08440](https://doi.org/10.1021/jacs.5b08440); pmid: [26434603](https://pubmed.ncbi.nlm.nih.gov/26434603/)
  81. J. Baek *et al.*, Bioinspired Metal-Organic Framework Catalysts for Selective Methane Oxidation to Methanol. *J. Am. Chem. Soc.* **140**, 18208–18216 (2018). doi: [10.1021/jacs.8b11525](https://doi.org/10.1021/jacs.8b11525); pmid: [30525562](https://pubmed.ncbi.nlm.nih.gov/30525562/)
  82. N. P. van Leest *et al.*, Single-Electron Elementary Steps in Homogeneous Organometallic Catalysis. *Adv. Organomet. Chem.* **70**, 71–180 (2018). doi: [10.1016/bs.adomc.2018.07.002](https://doi.org/10.1016/bs.adomc.2018.07.002); pmid: [29155465](https://pubmed.ncbi.nlm.nih.gov/29155465/)
  83. C. te Grotenhuis, N. van den Heuvel, J. I. van der Vlugt, B. de Bruin, Catalytic Dibenzylocyclohexene Synthesis via Cobalt(III)-Carbene Radical and ortho-Quinodimethane Intermediates. *Angew. Chem. Int. Ed.* **57**, 140–145 (2018). doi: [10.1002/anie.201711028](https://doi.org/10.1002/anie.201711028); pmid: [29155465](https://pubmed.ncbi.nlm.nih.gov/29155465/)
  84. C. Yao, T. Dahmen, A. Gansäuer, J. Norton, Anti-Markovnikov alcohols via epoxide hydrogenation through cooperative catalysis. *Science* **364**, 764–767 (2019). doi: [10.1126/science.aaw3913](https://doi.org/10.1126/science.aaw3913); pmid: [31123133](https://pubmed.ncbi.nlm.nih.gov/31123133/)
  85. P. Chaudhuri, M. Hess, U. Florke, K. Wiegardt, From Structural Models of Galactose Oxidase to Homogeneous Catalysis: Efficient Aerobic Oxidation of Alcohols. *Angew. Chem. Int. Ed.* **37**, 2217–2220 (1998). doi: [10.1002/\(SICI\)1521-3773\(19980904\)37:16<2217:AID-ANGE2217>3.0.CO;2-D](https://doi.org/10.1002/(SICI)1521-3773(19980904)37:16<2217:AID-ANGE2217>3.0.CO;2-D); pmid: [29711456](https://pubmed.ncbi.nlm.nih.gov/29711456/)
  86. P. J. Chirik, K. Wiegardt, Radical ligands confer nobility on base-metal catalysts. *Science* **327**, 794–795 (2010). doi: [10.1126/science.1183281](https://doi.org/10.1126/science.1183281); pmid: [20150476](https://pubmed.ncbi.nlm.nih.gov/20150476/)
  87. V. K. K. Praneth, M. R. Ringenberg, T. R. Ward, Redox-active ligands in catalysis. *Angew. Chem. Int. Ed.* **51**, 10228–10234 (2012). doi: [10.1002/anie.201204100](https://doi.org/10.1002/anie.201204100); pmid: [22996755](https://pubmed.ncbi.nlm.nih.gov/22996755/)
  88. V. Lyaskovskyy, B. de Bruin, Redox Non-Innocent Ligands: Versatile New Tools to Control Catalytic Reactions. *ACS Catal.* **2**, 270–279 (2012). doi: [10.1021/cs200660v](https://doi.org/10.1021/cs200660v)
  89. J. M. Darmon *et al.*, Oxidative addition of carbon-carbon bonds with a redox-active bis(imino)pyridine iron complex. *J. Am. Chem. Soc.* **134**, 17125–17137 (2012). doi: [10.1021/ja306526d](https://doi.org/10.1021/ja306526d); pmid: [23043331](https://pubmed.ncbi.nlm.nih.gov/23043331/)

90. Y.-Y. Zhou, C. Uyeda, Catalytic reductive [4 + 1]-cycloadditions of vinylidenes and dienes. *Science* **363**, 857–862 (2019). doi: [10.1126/science.aau0364](https://doi.org/10.1126/science.aau0364); pmid: 30792299
91. L. Que Jr., W. B. Tolman, Biologically inspired oxidation catalysis. *Nature* **455**, 333–340 (2008). doi: [10.1038/nature07371](https://doi.org/10.1038/nature07371); pmid: 18800132
92. K. M. Carsch *et al.*, Synthesis of a copper-supported triplet nitrene complex pertinent to copper-catalyzed amination. *Science* **365**, 1138–1143 (2019). doi: [10.1126/science.aax4423](https://doi.org/10.1126/science.aax4423); pmid: 31515388
93. C. Rörmelt *et al.*, Electronic Structure of a Formal Iron(0) Porphyrin Complex Relevant to CO<sub>2</sub> Reduction. *Inorg. Chem.* **56**, 4746–4751 (2017). doi: [10.1021/acs.inorgchem.7b00401](https://doi.org/10.1021/acs.inorgchem.7b00401); pmid: 28379689
94. C. J. Kaminsky, J. Wright, Y. Surendranath, Graphite-Conjugation Enhances Porphyrin Electrocatalysis. *ACS Catal.* **9**, 3667–3671 (2019). doi: [10.1021/acscatal.9b00404](https://doi.org/10.1021/acscatal.9b00404)
95. N. D. Loewen, T. V. Neelakantan, L. A. Berben, Renewable Formate from C-H Bond Formation with CO<sub>2</sub>: Using Iron Carbonyl Clusters as Electrocatalysts. *Acc. Chem. Res.* **50**, 2362–2370 (2017). doi: [10.1021/acs.accounts.7b00302](https://doi.org/10.1021/acs.accounts.7b00302); pmid: 28836757
96. R. B. Ferreira, L. J. Murray, Cyclophanes as Platforms for Reactive Multimetallic Complexes. *Acc. Chem. Res.* **52**, 447–455 (2019). doi: [10.1021/acs.accounts.8b00559](https://doi.org/10.1021/acs.accounts.8b00559); pmid: 30668108
97. T. Nakajima *et al.*, Synergistic Cu<sub>2</sub> Catalysts for Formic Acid Dehydrogenation. *J. Am. Chem. Soc.* **141**, 8732–8736 (2019). doi: [10.1021/jacs.9b03532](https://doi.org/10.1021/jacs.9b03532); pmid: 31083993
98. S. Dey *et al.*, Electrocatalytic O<sub>2</sub> reduction by [Fe-Fe]-hydrogenase active site models. *J. Am. Chem. Soc.* **136**, 8847–8850 (2014). doi: [10.1021/ja5021684](https://doi.org/10.1021/ja5021684); pmid: 24846692
99. S. Sharma, K. Sivalingam, F. Neese, G. K.-L. Chan, Low-energy spectrum of iron-sulfur clusters directly from many-particle quantum mechanics. *Nat. Chem.* **6**, 927–933 (2014). doi: [10.1038/nchem.2041](https://doi.org/10.1038/nchem.2041); pmid: 25242489
100. L. Gagliardi *et al.*, Multiconfiguration Pair-Density Functional Theory: A New Way To Treat Strongly Correlated Systems. *Acc. Chem. Res.* **50**, 66–73 (2017). doi: [10.1021/acs.accounts.6b00471](https://doi.org/10.1021/acs.accounts.6b00471); pmid: 28001359
101. J. C. Ott, H. Wadepohl, M. Enders, L. H. Gade, Taking Solution Proton NMR to Its Extreme: Prediction and Detection of a Hydride Resonance in an Intermediate-Spin Iron Complex. *J. Am. Chem. Soc.* **140**, 17413–17417 (2018). doi: [10.1021/jacs.8b11330](https://doi.org/10.1021/jacs.8b11330); pmid: 30486649
102. P. L. Holland, Distinctive Reaction Pathways at Base Metals in High-Spin Organometallic Catalysts. *Acc. Chem. Res.* **48**, 1696–1702 (2015). doi: [10.1021/acs.accounts.5b00036](https://doi.org/10.1021/acs.accounts.5b00036); pmid: 25989357
103. M. P. Crockett, H. Zhang, C. M. Thomas, J. A. Byers, Adding diffusion ordered NMR spectroscopy (DOSY) to the arsenal for characterizing paramagnetic complexes. *Chem. Commun.* **55**, 14426–14429 (2019). doi: [10.1039/C9CC08229H](https://doi.org/10.1039/C9CC08229H); pmid: 31730148
104. Q. Lu *et al.*, Highly porous non-precious bimetallic electrocatalysts for efficient hydrogen evolution. *Nat. Commun.* **6**, 6567 (2015). doi: [10.1038/ncomms7567](https://doi.org/10.1038/ncomms7567); pmid: 25910892
105. B. Zhang *et al.*, Homogeneously dispersed multimetal oxygen-evolving catalysts. *Science* **352**, 333–337 (2016). doi: [10.1126/science.aaf1525](https://doi.org/10.1126/science.aaf1525); pmid: 27013427
106. L. Trotochaud, S. L. Young, J. K. Ranney, S. W. Boettcher, Nickel-iron oxyhydroxide oxygen-evolution electrocatalysts: The role of intentional and incidental iron incorporation. *J. Am. Chem. Soc.* **136**, 6744–6753 (2014). doi: [10.1021/ja502379c](https://doi.org/10.1021/ja502379c); pmid: 24779732
107. E. A. Carter, Challenges in modeling materials properties without experimental input. *Science* **321**, 800–803 (2008). doi: [10.1126/science.1158009](https://doi.org/10.1126/science.1158009); pmid: 18687955
108. T. F. Jaramillo *et al.*, Identification of active edge sites for electrochemical H<sub>2</sub> evolution from MoS<sub>2</sub> nanocatalysts. *Science* **317**, 100–102 (2007). doi: [10.1126/science.1141483](https://doi.org/10.1126/science.1141483); pmid: 17615351
109. Z. W. Seh *et al.*, Combining theory and experiment in electrocatalysis: Insights into materials design. *Science* **355**, eaad4998 (2017). doi: [10.1126/science.aad4998](https://doi.org/10.1126/science.aad4998); pmid: 28082532
110. J. G. Chen, Carbide and Nitride Overlayers on Early Transition Metal Surfaces: Preparation, Characterization, and Reactivities. *Chem. Rev.* **96**, 1477–1498 (1996). doi: [10.1021/cr950232u](https://doi.org/10.1021/cr950232u); pmid: 11848799
111. Z. W. Seh *et al.*, Two-Dimensional Molybdenum Carbide (MXene) as an Efficient Electrocatalyst for Hydrogen Evolution. *ACS Energy Lett.* **1**, 589–594 (2016). doi: [10.1021/acsenenergylett.6b00247](https://doi.org/10.1021/acsenenergylett.6b00247)
112. J. Kibsgaard *et al.*, Designing an improved transition metal phosphide catalyst for hydrogen evolution using experimental and theoretical trends. *Energy Environ. Sci.* **8**, 3022–3029 (2015). doi: [10.1039/C5EE02179K](https://doi.org/10.1039/C5EE02179K)
113. R. B. Levy, M. Boudart, Platinum-like behavior of tungsten carbide in surface catalysis. *Science* **181**, 547–549 (1973). doi: [10.1126/science.181.4099.547](https://doi.org/10.1126/science.181.4099.547); pmid: 17777803
114. Z. Lin, R. Chen, Z. Qu, J. G. Chen, Hydrodeoxygenation of biomass-derived oxygenates over metal carbides: From model surfaces to powder catalysts. *Green Chem.* **20**, 2679–2696 (2018). doi: [10.1039/C8CG00239H](https://doi.org/10.1039/C8CG00239H)
115. B. Yan *et al.*, Surface Restructuring of Nickel Sulfide Generates Optimally Coordinated Active Sites for Oxygen Reduction Catalysis. *Joule* **1**, 600–612 (2017). doi: [10.1016/j.joule.2017.08.020](https://doi.org/10.1016/j.joule.2017.08.020)
116. J. Dou *et al.*, Operando chemistry of catalyst surfaces during catalysis. *Chem. Soc. Rev.* **46**, 2001–2027 (2017). doi: [10.1039/C6CS00931J](https://doi.org/10.1039/C6CS00931J); pmid: 28358410
117. G. Wu, P. Zelenay, Nanostructured nonprecious metal catalysts for oxygen reduction reaction. *Acc. Chem. Res.* **46**, 1878–1889 (2013). doi: [10.1021/ar400011z](https://doi.org/10.1021/ar400011z); pmid: 23815084
118. Y. P. Zhu, C. Guo, Y. Zheng, S.-Z. Qiao, Surface and Interface Engineering of Noble-Metal-Free Electrocatalysts for Efficient Energy Conversion Processes. *Acc. Chem. Res.* **50**, 915–923 (2017). doi: [10.1021/acs.accounts.6b00635](https://doi.org/10.1021/acs.accounts.6b00635); pmid: 28205437
119. T. Asset, P. Atanassov, Iron-Nitrogen-Carbon Catalysts for Proton Exchange Membrane Fuel Cells. *Joule* **4**, 33–44 (2020). doi: [10.1016/j.joule.2019.12.002](https://doi.org/10.1016/j.joule.2019.12.002)
120. J. D. A. Pelletier, J.-M. Basset, Catalysis by Design: Well-Defined Single-Site Heterogeneous Catalysts. *Acc. Chem. Res.* **49**, 664–677 (2016). doi: [10.1021/acs.accounts.5b00518](https://doi.org/10.1021/acs.accounts.5b00518); pmid: 26959689
121. S. Nitopi *et al.*, Progress and Perspectives of Electrochemical CO<sub>2</sub> Reduction on Copper in Aqueous Electrolyte. *Chem. Rev.* **119**, 7610–7672 (2019). doi: [10.1021/acs.chemrev.8b00705](https://doi.org/10.1021/acs.chemrev.8b00705); pmid: 31117420
122. Y. Surendranath, D. A. Lutterman, Y. Liu, D. G. Nocera, Nucleation, growth, and repair of a cobalt-based oxygen evolving catalyst. *J. Am. Chem. Soc.* **134**, 6326–6336 (2012). doi: [10.1021/ja3000084](https://doi.org/10.1021/ja3000084); pmid: 22394103
123. J. M. Marinkovic, A. Rissager, R. Franke, P. Wasserscheid, M. Haumann, Fifteen Years of Supported Ionic Liquid Phase-Catalyzed Hydroformylation: Material and Process Developments. *Ind. Eng. Chem. Res.* **58**, 2409–2420 (2019). doi: [10.1021/acs.iecr.8b04010](https://doi.org/10.1021/acs.iecr.8b04010)
124. H. Falsig *et al.*, Trends in the catalytic CO oxidation activity of nanoparticles. *Angew. Chem. Int. Ed.* **47**, 4835–4839 (2008). doi: [10.1002/anie.200801479](https://doi.org/10.1002/anie.200801479); pmid: 18496809
125. B. H. Solis, A. G. Maher, D. K. Dogutan, D. G. Nocera, S. Hammes-Schiffer, Nickel phlorin intermediate formed by proton-coupled electron transfer in hydrogen evolution mechanism. *Proc. Natl. Acad. Sci. U.S.A.* **113**, 485–492 (2016). doi: [10.1073/pnas.1521834112](https://doi.org/10.1073/pnas.1521834112); pmid: 26655344
126. S. Horike, M. Dincă, K. Tamaki, J. R. Long, Size-selective Lewis acid catalysis in a microporous metal-organic framework with exposed Mn<sup>2+</sup> coordination sites. *J. Am. Chem. Soc.* **130**, 5854–5855 (2008). doi: [10.1021/ja800669j](https://doi.org/10.1021/ja800669j); pmid: 18399629
127. F. Jaouen *et al.*, Recent advances in non-precious metal catalysis for oxygen-reduction reaction in polymer electrolyte fuel cells. *Energy Environ. Sci.* **4**, 114–130 (2011). doi: [10.1039/C0EE00011F](https://doi.org/10.1039/C0EE00011F)
128. R. Kas *et al.*, Electrochemical CO<sub>2</sub> reduction on nanostructured metal electrodes: Fact or defect? *Chem. Sci.* **11**, 1738–1749 (2020). doi: [10.1039/C9SC05375A](https://doi.org/10.1039/C9SC05375A)

## ACKNOWLEDGMENTS

We gratefully acknowledge the Division of Chemical Sciences, Geosciences and Biosciences of the U.S. Department of Energy, Office of Science, Office of Basic Energy Sciences. This article evolved from presentations and discussions at the workshop “Earth-Abundant Metal Catalysis” held in April 2019 in Gaithersburg, Maryland. **Competing interests:** The authors have no competing interests relevant to this publication.

10.1126/science.abc3183



## RESEARCH ARTICLE

## NEURODEVELOPMENT

## Huntington's disease alters human neurodevelopment

Monia Barnat<sup>1</sup>, Mariacristina Capizzi<sup>1\*</sup>, Esther Aparicio<sup>1\*</sup>, Susana Boluda<sup>2</sup>, Doris Wennagel<sup>1</sup>, Radhia Kacher<sup>1</sup>, Rayane Kassem<sup>1</sup>, Sophie Lenoir<sup>1</sup>, Fabienne Agasse<sup>1</sup>, Barbara Y. Braz<sup>1</sup>, Jeh-Ping Liu<sup>3</sup>, Julien Ighil<sup>4</sup>, Aude Tessier<sup>5</sup>, Scott O. Zeitlin<sup>3</sup>, Charles Duyckaerts<sup>2</sup>, Marc Dommergues<sup>4</sup>, Alexandra Durr<sup>6†</sup>, Sandrine Humbert<sup>1†</sup>

Although Huntington's disease is a late-manifesting neurodegenerative disorder, both mouse studies and neuroimaging studies of presymptomatic mutation carriers suggest that Huntington's disease might affect neurodevelopment. To determine whether this is actually the case, we examined tissue from human fetuses (13 weeks gestation) that carried the Huntington's disease mutation. These tissues showed clear abnormalities in the developing cortex, including mislocalization of mutant huntingtin and junctional complex proteins, defects in neuroprogenitor cell polarity and differentiation, abnormal ciliogenesis, and changes in mitosis and cell cycle progression. We observed the same phenomena in Huntington's disease mouse embryos, where we linked these abnormalities to defects in interkinetic nuclear migration of progenitor cells. Huntington's disease thus has a neurodevelopmental component and is not solely a degenerative disease.

**H**untington's disease (HD) is a neurodegenerative disease that is part of the larger family of "proteopathies," which includes the polyglutamine diseases, amyotrophic lateral sclerosis, and Alzheimer's and Parkinson's diseases. These diverse disorders share a delayed onset in mid-adulthood or later despite the expression, at least in hereditary cases, of the disease-driving protein from the first days of life. This raises the question of whether early events might set the stage for later disease. For example, huntingtin (HTT), the protein mutated in HD, is essential for development, at least in mice (1–3). The mutant HTT (mHTT) impairs neural progenitor cell division and neuronal migration and maturation (4–6), giving HD mice a thinner cortex (7). The fact that expression of either mHTT or hypomorphic HTT solely during early life is sufficient to produce HD features in adult mice strongly suggests that there is a developmental component to the disease (8, 9).

In support of this notion, human neuroimaging studies have revealed smaller intracranial volume in HD mutation carriers as young as 7 years of age (10, 11). Loss of cortical volume takes place long before any symptoms appear, and defects in the corticostriatal net-

work lead to striatal dysfunction and degeneration (12–15). Studies in neurons derived from HD human induced pluripotent stem cells (iPSCs) have identified changes in gene expression that support an altered developmental program (16, 17), and mHTT alters neuronal identity in cortical populations of HD brain organoids (18). But does mHTT affect early human development? And if so, how early? To answer these questions, we recruited HD mutation carriers who sought prenatal testing in order to determine whether the fetus carried an HD-causing mutation.

#### Mutant huntingtin mislocalizes in human and mouse embryos

We were able to procure rare intact cortical tissues from four HD mutation carrier fetuses and four healthy controls at gestation week 13 (GW13) (table S1). At this developmental stage, the cortical neurons that project to the striatum and later deteriorate in HD are arising from the division of progenitor cells at the ventricular zone. These apical progenitors extend processes toward both the apical and basal surfaces of the neuroepithelial wall, and their nuclei move back and forth between surfaces in concert with cell cycle progression in a process known as interkinetic nuclear migration. This process, common to all developing pseudostratified neuroepithelia (19, 20), maintains the balance between progenitor renewal and differentiation by controlling when apical progenitor nuclei are exposed to proliferative versus neurogenic signals, and in what proportions.

To examine the expression pattern of HTT at the ventricular zone of the GW13 cortex, we used an antibody that recognizes both HTT and mHTT (4C8; Fig. 1, A and B, and fig. S1A). In wild-type tissues, HTT staining demarcated

the apical surface of the ventricular zone and spread diffusely throughout the basal region. In cortical tissue of HD mutation carriers, however, HTT staining concentrated at the apical endfeet (the apical surface of the processes).

Given the preciousness of the human tissue, we turned to mice to further investigate these observations, using embryonic day 13.5 (E13.5) mouse embryos, which correspond to GW13 in human neurodevelopment. We studied an HD knock-in mouse model in which the first exon of the *HTT* gene is replaced by human exon 1 carrying 111 CAG repeats (Hdh<sup>Q111/Q111</sup>) (21). Immunostaining coronal sections revealed a pattern of HTT expression that paralleled our observations in human fetuses (fig. S1B). To determine the distribution of mHTT specifically, we used another HD knock-in mouse model in which Flag tags are inserted in the N terminus of wild-type HTT (Hdh<sup>F7Q/+</sup>) or mutant HTT carrying 140 CAG repeats (Hdh<sup>F140Q/+</sup>) (22) (fig. S1C). The Flag labeling showed that mHTT localized to the apical surface and was decreased in the basal region.

#### Mutant huntingtin impairs endosome secretion and recycling

Apical progenitors maintain their polarity through endocytosis and the trafficking of proteins from the trans-Golgi network to the plasma membrane at the apical endfeet (19). In HD, both endocytosis and Golgi-membrane trafficking are dysregulated (23). Because one of HTT's main functions is to transport vesicles, we used markers of the endosomal pathway to map the subcellular localization of HTT in HD and to gauge whether transport is affected this early in HD.

We stained for calnexin (a marker of the endoplasmic reticulum), GRASP65 (Golgi assembly stacking protein of 65 kDa to mark the cis-Golgi network), TGN38 (trans-Golgi network integral membrane protein 38), EEA1 (early endosome antigen 1), and transferrin receptor (recycling endosomes). In control samples, HTT colocalized partially with these markers (figs. S2 and S3). In both human and mouse HD samples, however, HTT strongly colocalized with TGN38, EEA1, and transferrin receptor, and to a lesser extent with calnexin and GRASP65. These results suggest that mHTT hinders endosomal trafficking in apical progenitors, even at this very early stage of development.

#### Mutant huntingtin disrupts neuroepithelial junctional complexes

Apical endfeet contain junctional complexes (19, 24) composed of tight-junction and adherens-junction proteins, including ZO1, PAR3, NCAD, and  $\beta$ -catenin (25), that link neighboring progenitors to each other, thereby sealing the neuroepithelium. Because HTT regulates the trafficking of these proteins,

<sup>1</sup>Univ. Grenoble Alpes, INSERM, U1216, Grenoble Institut Neurosciences, Grenoble, France. <sup>2</sup>Department of Neuropathology Raymond Escourolle, AP-HP, Pitié-Salpêtrière University Hospital, Paris, France. <sup>3</sup>Department of Neuroscience, University of Virginia School of Medicine, Charlottesville, VA 22908, USA. <sup>4</sup>AP-HP, Sorbonne University, Service de Gynécologie Obstétrique, Pitié-Salpêtrière Hospital, Paris, France. <sup>5</sup>AP-HP, Unité d'Embryofœtopathologie, Necker Hospital, Paris, France. <sup>6</sup>Sorbonne University, Paris Brain Institute, APHP, INSERM U1127, CNRS UMR7225, Pitié-Salpêtrière Hospital, Paris, France

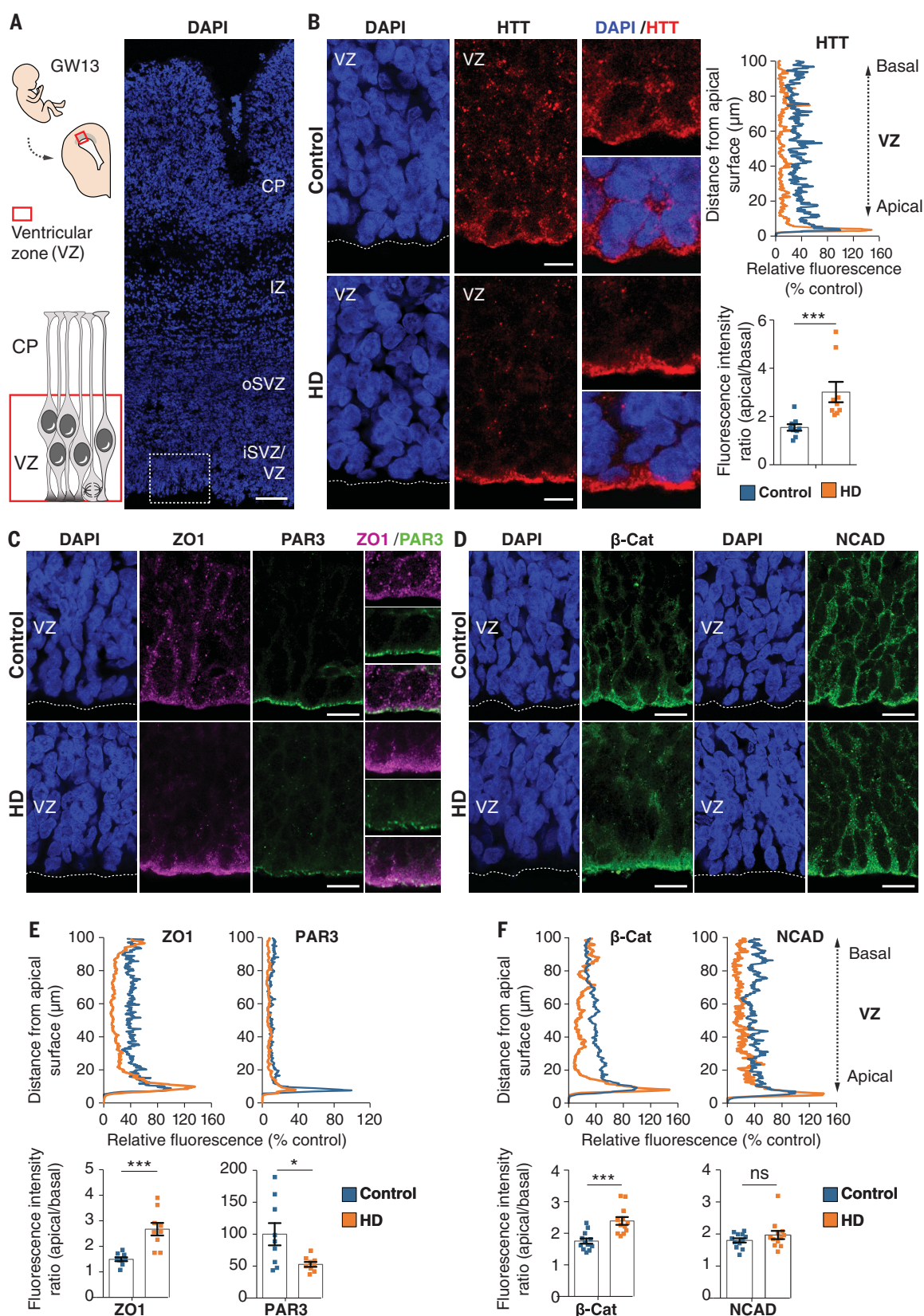
\*These authors contributed equally to this work.

†Corresponding author. Email: alexandra.durr@upmc.fr (A.D.); sandrine.humbert@inserm.fr (S.H.)

**Fig. 1. Huntingtin and junctional complex proteins mislocalize in the ventricular zone of human fetuses carrying HD-causing mutations.** (A) Left: Diagram showing the position of the fetal ventricular zone relative to the cortical plate (CP). Right: Coronal brain sections of GW13 control human cortex were counterstained with 4',6-diamidino-2-phenylindole (DAPI). The dotted square shows the region imaged in (B). Scale bar, 100  $\mu$ m.

(B) Left: Coronal GW13 brain sections from control fetus and fetus carrying HD-causing mutation were immunostained for HTT. Scale bars, 10  $\mu$ m. Right: Representative line-scan analysis (relative fluorescence intensity) of HTT immunostaining and quantification of apical/basal human HTT fluorescence intensity in the ventricular zone. For each condition,  $n = 3$  fetuses from different mothers;  $***P = 0.0044$  (unpaired  $t$  test).

(C and D) Coronal GW13 fetal brain sections were immunostained for ZO1 and PAR3 (C) and  $\beta$ -catenin and NCAD (D). Scale bars, 15  $\mu$ m. (E and F) Representative line-scan analysis (relative fluorescence intensity) of indicated immunostainings (top) and quantification of indicated fluorescence intensities in the ventricular zone (bottom graphs). For each condition,  $n = 3$  fetuses from different mothers. ZO1:  $***P = 0.0003$  (unpaired  $t$  test); PAR3:  $*P = 0.0177$  (unpaired  $t$  test);  $\beta$ -cat:  $***P = 0.0003$  (unpaired  $t$  test); NCAD:  $P = 0.4682$  (Mann-Whitney U test), ns (not significant). Results are means  $\pm$  SEM. VZ, ventricular zone; iSVZ, inner subventricular zone; oSVZ, outer subventricular zone; IZ, intermediate zone; CP, cortical plate. Nuclei were counterstained with DAPI.





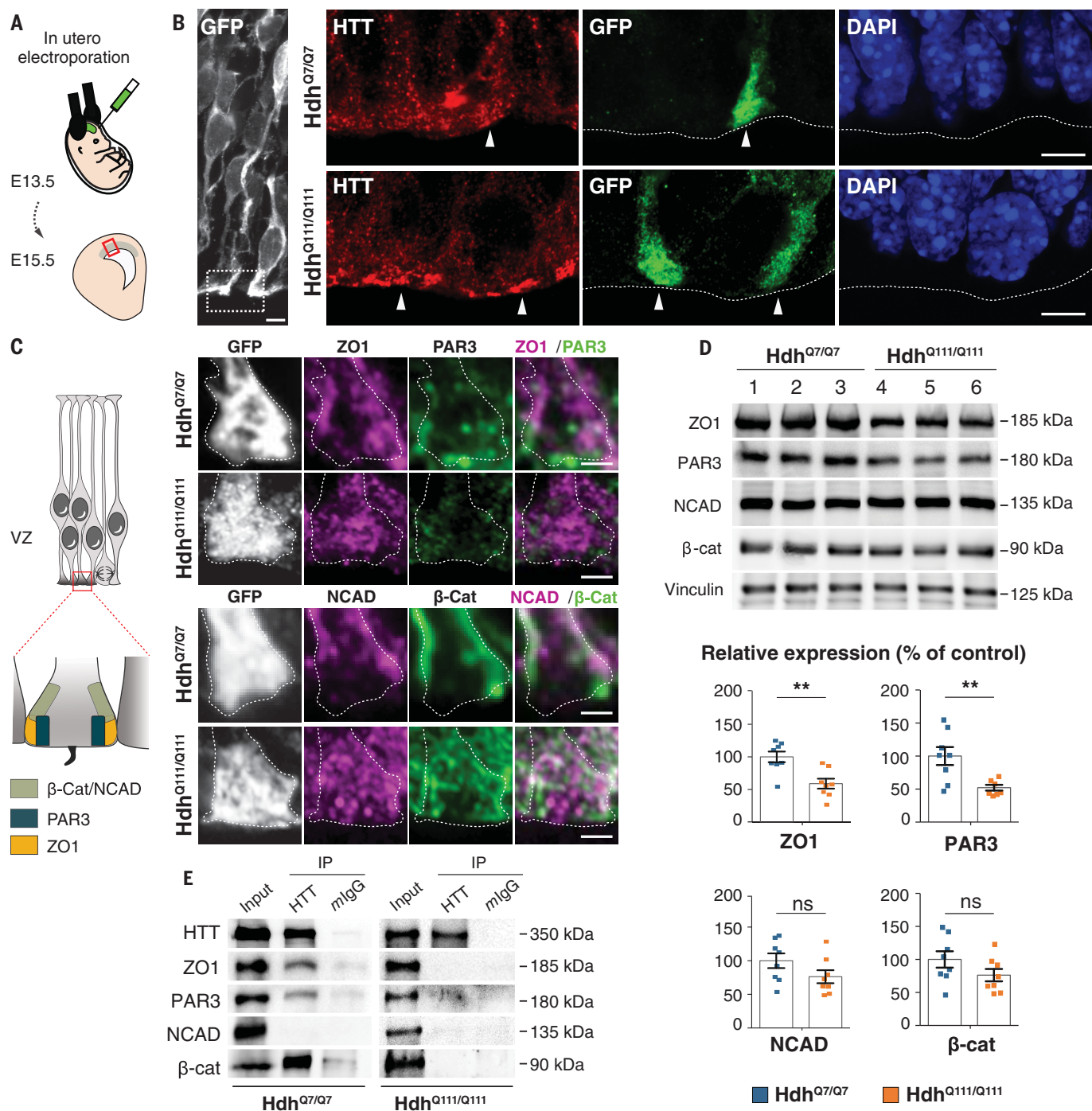


**Fig. 2. Junctional protein complexes are disrupted in the apical endfeet of HD mouse embryos.** (A) Schematic of the in utero electroporation experiment. (B and C) Mouse embryos were electroporated at E13.5 with a pCAG-GFP construct to delineate the apical endfoot in E15.5 cortices. (B) Hdh<sup>Q7/Q7</sup> and Hdh<sup>Q111/Q111</sup> cortical sections were immunostained for GFP (left) and for HTT and GFP (right). White arrowheads point to apical endfeet. Nuclei were counterstained with DAPI. (C) Left: Diagram indicating the position of junctional complexes at the apical endfeet. Right: Cortical sections were immunostained for GFP, ZO1, and PAR3 (upper panel) and GFP,

NCAD, and β-Cat (lower panel). Scale bars, 5 μm (B), 2 μm (C). (D) ZO1, PAR3, NCAD, β-catenin, and vinculin immunoblotting analyses of lysates from E15.5 Hdh<sup>Q7/Q7</sup> and Hdh<sup>Q111/Q111</sup> cortices. Bar graphs correspond to the quantitative evaluation of the indicated proteins. For each condition,  $n =$  at least 7 embryos from different mothers. ZO1:  $**P = 0.0026$ ; PAR3:  $**P = 0.0075$ ; NCAD:  $P = 0.1255$ ; β-cat:  $P = 0.1476$  (unpaired  $t$  tests). Results are means  $\pm$  SEM. (E) HTT-associated complexes were immunoprecipitated with the 4C8 antibody from E15.5 Hdh<sup>Q7/Q7</sup> and Hdh<sup>Q111/Q111</sup> cortical extracts. Mouse IgG (mlgG) was used as a negative control.

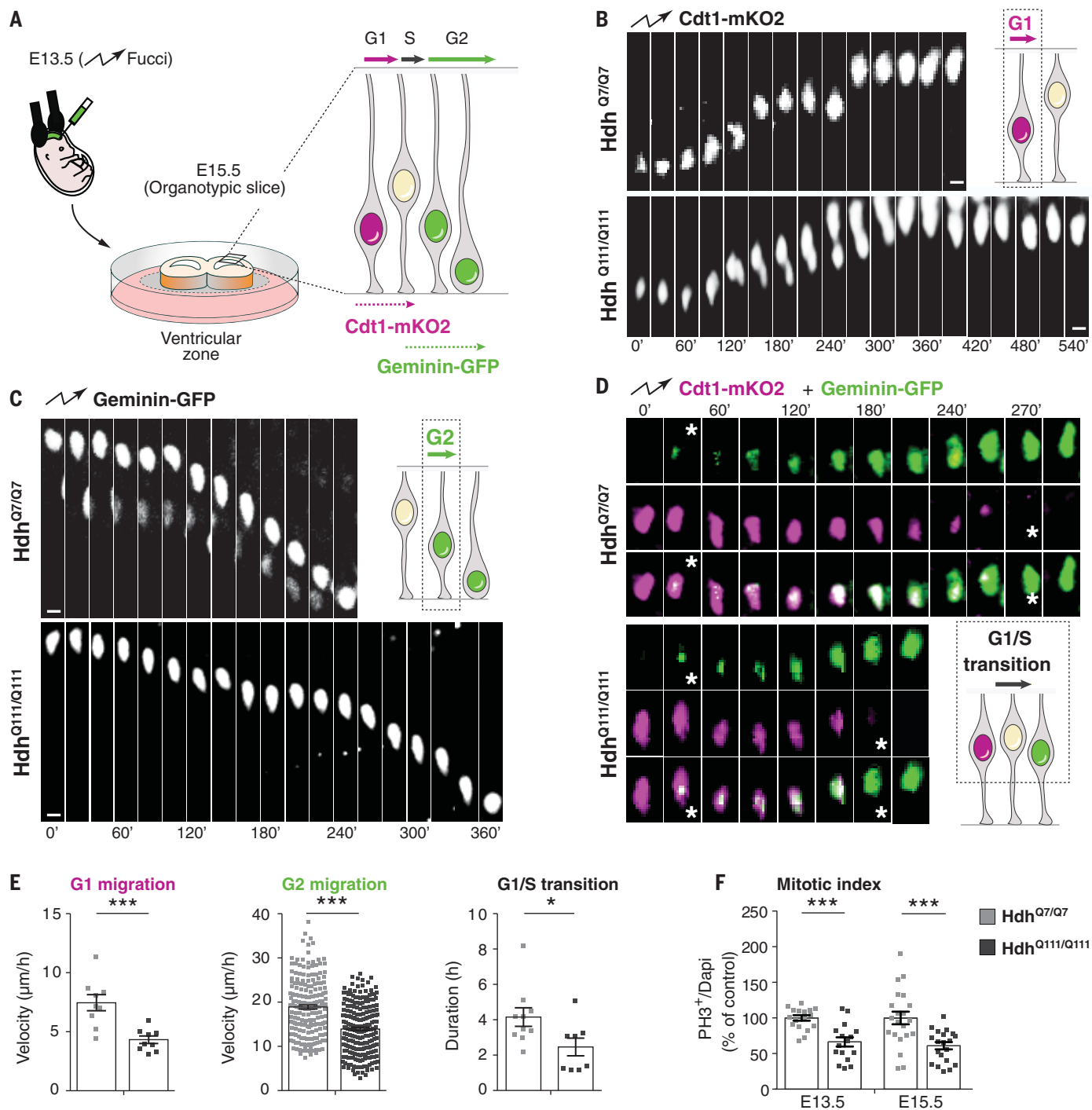


**Fig. 3. Interkinetic nuclear migration and mitosis of cortical apical progenitors are impaired in HD mouse embryos.** (A) Schematic of the experiment for analysis of interkinetic nuclear migration. E13.5  $\text{Hdh}^{\text{Q7/Q7}}$  and  $\text{Hdh}^{\text{Q111/Q111}}$  embryos were electroporated with Cdt1-mKO2 and geminin-GFP constructs. After 48 hours, the movement of the GFP- and mKO2-labeled nuclei was followed by spinning disc microscopy, taking one image every 10 or 15 min for 10 hours. (B to D) Representative images showing the movement of nuclei in G<sub>1</sub>, G<sub>2</sub>, and G<sub>1</sub>/S transition phases as indicated. (D) Stars indicate the beginning and ending of the G<sub>1</sub>/S transition. Scale bars, 5  $\mu\text{m}$ . (E) Quantitative differences in the velocity of G<sub>1</sub>-phase nuclei [for each condition,  $n = 9$  cells from three

embryos from different mothers; \*\*\* $P = 0.0008$  (unpaired  $t$  test)], velocity of G<sub>2</sub>-phase nuclei [for each condition,  $n =$  at least 202 cells from four embryos from different mothers; \*\*\* $P < 0.0001$  (Mann-Whitney U test)], and length of G<sub>1</sub>/S transition [for each condition,  $n =$  at least 8 cells from three embryos from different mothers; \* $P = 0.0356$  (unpaired  $t$  test)]. (F) Bar graphs show the percentage of phospho-histone 3 (PH3) cells (mitotic index) of dividing progenitors [E13.5: for each condition,  $n =$  at least 2151 cells from four embryos from different mothers, \*\*\* $P < 0.0001$  (unpaired  $t$  test); E15.5: for each condition,  $n =$  at least 1801 cells from three embryos from different mothers, \*\*\* $P = 0.0005$  (unpaired  $t$  test)]. Results are means  $\pm$  SEM.



which are dysregulated in HD (6, 26–30), we hypothesized that mHTT hinders the correct positioning of these junctions, which would diminish the integrity of the neuroepithelium. As predicted, HTT partially codistributed with

ZO1, PAR3,  $\beta$ -catenin, and NCAD at the apical endfeet of human GW13 control and mouse E13.5 neuroepithelium (figs. S4 and S5A). The levels of ZO1, NCAD, and  $\beta$ -catenin were high at the apical surface of the human and

mouse control ventricular zone and even higher in HD tissues, with a concomitant reduction in these proteins in the basal region (Fig. 1, C to F, and fig. S5, B to E). PAR3 was also misregulated in HD but in a different pattern

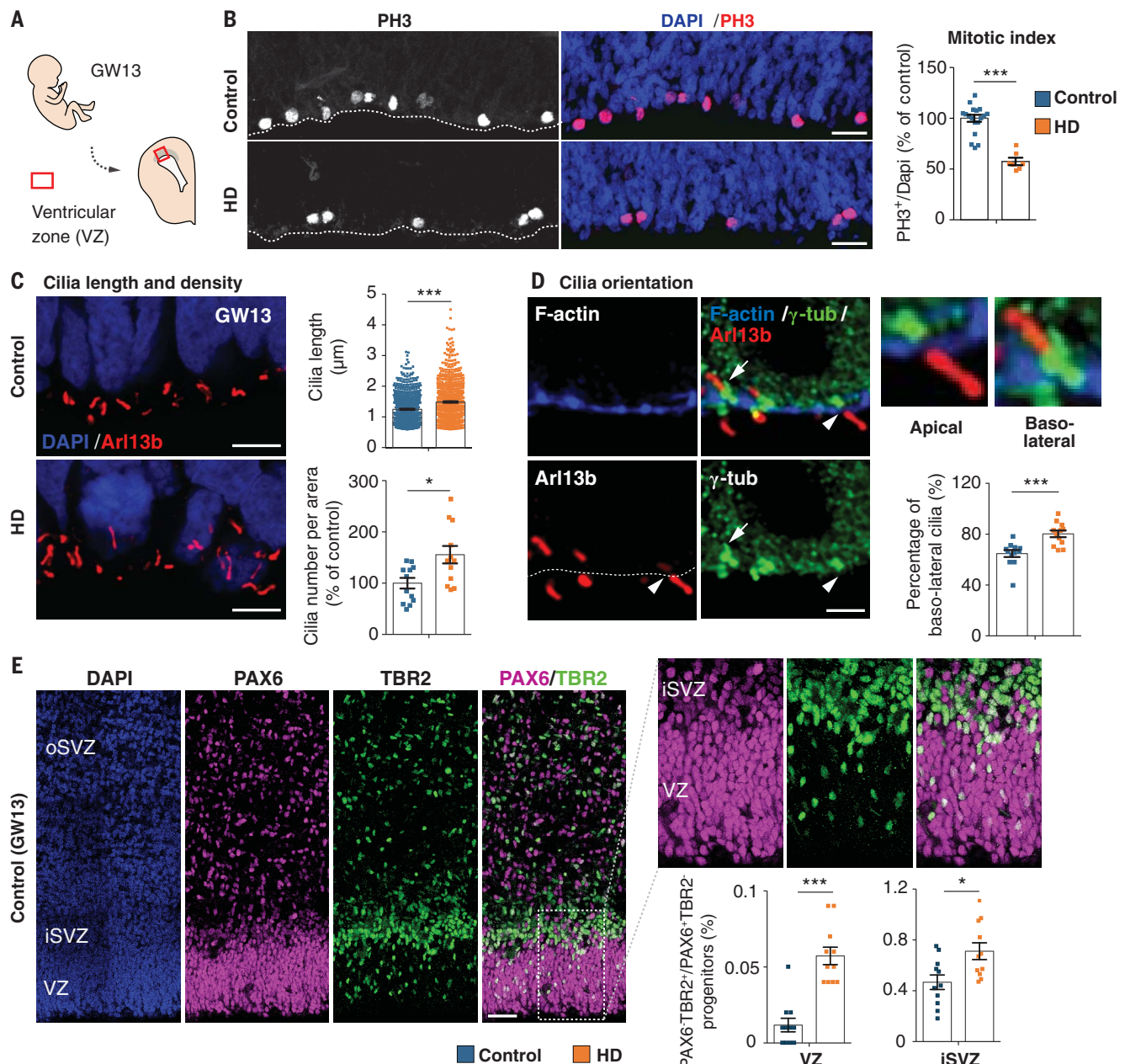


**Fig. 4. Mutant huntingtin shifts neurogenesis toward neuronal lineage.**

(A) Diagram showing the position of the fetal ventricular zone. (B) Cortical sections of GW13 fetuses were immunostained with antibody against phospho-histone 3 (PH3) and the mitotic index was quantified. For each condition,  $n =$  at least 1146 cells from three fetuses from different mothers;  $***P < 0.0001$  (Mann-Whitney U test). Scale bars, 25  $\mu\text{m}$ . (C) Coronal GW13 brain sections from control fetus and fetus carrying HD-causing mutation (HD) were immunostained for the cilia marker Arl13b. Scale bars, 5  $\mu\text{m}$ . Bar graphs show cilia length [for each condition,  $n =$  at least 770 cilia from four fetuses from different mothers;  $***P < 0.0001$  (Mann-Whitney U test)] and cilia density [for each condition,  $n = 4$  fetuses from different mothers;  $*P = 0.0104$  (unpaired  $t$  test)] at the apical surface. (D) Coronal brain sections of GW13

human cortex were immunostained for F-actin,  $\gamma$ -tubulin ( $\gamma$ -tub), and Arl13b. Scale bars, 2  $\mu\text{m}$ . White arrowheads and white arrows show apical and basolateral cilia, respectively. Bar graph shows the percentage of basolateral cilia at the apical surface. For each condition,  $n =$  at least 260 cilia from four fetuses from different mothers;  $***P = 0.0003$  (Mann-Whitney U test). (E) Typical PAX6 and TBR2 staining of a GW13 human fetal sample analyzed. Scale bars, 50  $\mu\text{m}$ . Bar graphs show the percentage of PAX6/TBR2-positive cells (PAX6 $^{+}$ /TBR2 $^{+}$ ) over PAX6-positive, TBR2-negative (PAX6 $^{+}$ /TBR2 $^{-}$ ) progenitors [for each condition, three fetuses from different mothers were analyzed; VZ,  $n =$  at least 2447 cells,  $***P < 0.0001$  (Mann-Whitney U test); iSVZ,  $n =$  at least 1580 cells,  $*P = 0.011$  (unpaired  $t$  test)]. Results are means  $\pm$  SEM. Nuclei were counterstained with DAPI.

from these other proteins: Its expression levels were down-regulated, so its demarcation of the apical surface in control samples was diminished, rather than intensified, in HD.

To better understand how junctional complexes in individual apical endfeet are affected in HD, we electroporated E13.5 control and HD mouse embryos in utero with a pCAG-GFP (green fluorescent protein) construct and performed immunohistochemistry on E15.5 coronal sections (Fig. 2, A and B). At this stage in mice and at the corresponding stage GW16 in humans (table S1), the mislocalization of HTT and junction proteins in HD apical progenitors persisted (figs. S6 and S7). Indeed, GFP-expressing knock-in HD progenitors, but not controls, showed a bright line of HTT along the apical surface (Fig. 2B). In control embryos, ZO1, NCAD, and  $\beta$ -catenin immunostaining marked the sides of the apical endfeet; PAR3 staining was more apical (Fig. 2C). In Hdh<sup>Q111/Q111</sup> embryos, ZO1, NCAD, and  $\beta$ -catenin spread throughout the apical endfeet and PAR3 staining was diminished. These observations were corroborated by immunoblotting protein extracts from Hdh<sup>Q7/Q7</sup> and Hdh<sup>Q111/Q111</sup> E15.5 cortices (Fig. 2D). The levels of NCAD and  $\beta$ -catenin were similar in control and HD conditions, but ZO1 and PAR3 protein levels were lower in the mutant mice. Coimmunoprecipitation showed that HTT associates with ZO1, PAR3, and  $\beta$ -catenin, but these interactions were disrupted in HD (Fig. 2E and fig. S8).

### Mutant HTT alters progression through the cell cycle

The integrity of the apical junctional complexes is essential for progression through interkinetic nuclear migration, when the nuclei of progenitor cells born at the apical surface move toward the basal side during the G<sub>1</sub> phase of the cell cycle, enter and complete the S phase, then return to the apical surface, where they undergo division (19, 20, 31, 32). Given that the junctional complexes do not form properly with mHTT, we examined cell cycle progression in the apical progenitors.

To measure apical (G<sub>1</sub> phase) and basal (G<sub>2</sub> phase) movements in vivo, we used the fluorescent ubiquitination-based cell cycle indicator (FUCCI), which tracks the expression of markers of the different phases of the cell cycle (33). We electroporated wild-type E13.5 embryos with plasmids encoding CDT1 (chromatin licensing and DNA replication factor 1)-mKO2 and geminin-GFP, then carried out time-lapse imaging on acute cortical slices 2 days after in utero electroporation (Fig. 3A) so that we could distinguish cycling progenitors in G<sub>1</sub> from neurons exiting the cell cycle and migrating away from the ventricular zone (fig. S9A and movie S1). As expected, CDT1 levels peaked during G<sub>1</sub> and fell upon entry into S phase, whereas geminin levels were high during S phase and

G<sub>2</sub> (fig. S9B and movie S2). The velocities of nuclear movement in G<sub>1</sub> and G<sub>2</sub> in control cells were as previously reported (34) (Fig. 3, B, C, and E, and movies S3 to S6), but in Hdh<sup>Q111/Q111</sup> embryos, migrating nuclei moved more slowly in both G<sub>1</sub> and G<sub>2</sub>, causing these phases to lengthen while the G<sub>1</sub>/S phase transition was shortened (Fig. 3, D and E, and movies S7 and S8). We next immunostained cortical sections of Hdh<sup>Q111/Q111</sup> embryos and GW13 HD carrier fetuses with antibody against phospho-histone 3 (PH3), a marker of mitosis, and evaluated the mitotic index (Fig. 3F and Fig. 4, A and B). HD mice and human mutation carriers had roughly half the mitotic index of controls. In HD, therefore, the pool of proliferating cells is diminished.

### Mutant HTT biases neurogenesis toward the neuronal lineage

The cell cycle correlates with the assembly (during G<sub>0</sub>) and disassembly (at the onset of M phase) of the primary cilium at the apical progenitor endfeet (19, 32). Immunostaining with the cilia marker Arl13b, a member of the adenosine diphosphate ribosylation factor-like family, revealed that both the length and density of the cilia were greater at the apical area of the developing cortex in HD human and mouse samples than in controls (Fig. 4C and fig. S10A), which confirms that the cells were not progressing through the cell cycle properly (20). Because a longer G<sub>1</sub> phase and a shorter G<sub>1</sub>/S transition characterize progenitors committed toward the neuronal lineage (32, 35), we asked whether mHTT favors the production of apical over basal progenitors.

We evaluated cilia orientation by labeling brain sections with F-actin (to delineate the apical surface) and Arl13b and  $\gamma$ -tubulin (to label the basal body) (Fig. 4D and fig. S10B). The proportion of basolateral cilia, which signal the generation of basal progenitors (36), was greater in HD human and mouse samples than in controls. To discriminate between apical progenitors and basal progenitors, which are more engaged in the neuronal lineage (37), we labeled for the transcription factors PAX6 and TBR2, respectively. HD human and mouse samples showed a greater proportion of basal progenitors at the ventricular zone, subventricular zone, and inner subventricular zone than did controls (Fig. 4E and fig. S10C).

### Discussion

Our data show that mHTT mislocalizes at junctional complexes, disrupts the polarity of human and mouse neuroepithelium, and interferes with the cell cycle of apical progenitors, leading to fewer proliferating cells and more neural progenitors prematurely entering lineage specification. This is consistent with previous evidence that HTT regulates

cellular adhesion, polarity, and epithelial organization (27). In the presence of mHTT, the epithelial-mesenchymal transition is accelerated (28). It is possible that mHTT contributes to cellular disorganization through other means as well, such as by interfering with the orientation of the mitotic spindle (7). Given that HTT also establishes apical polarity in the mammary epithelium, where it forms a complex with PAR3, aPKC, and RAB11A and ensures the apical translocation of PAR3-aPKC through RAB11A (29), we speculate that HTT may act to maintain epithelial cell polarity throughout the body.

A recent neuroimaging study found that the posterior Sylvian fissure, normally asymmetrical between the right and left hemispheres, lacks asymmetry in the HD population studied (38). Because the Sylvian fissure appears early in utero, the authors concluded that this abnormal symmetry arises during fetal development. Our results show that mHTT does alter very early stages of brain development in human HD, even though the samples we analyzed were from mutation carriers with small pathological expansions (39, 40, and 42 repeats) that would typically cause later manifestations of HD. The defects we observed likely render the corticostriatal circuitry more vulnerable to the later dysfunctions characteristic of HD (23), as proposed for another polyglutamine disease, spinocerebellar ataxia type 1 (39). The path to degeneration is complex, however, and weaves together both pathogenic and compensatory mechanisms. For example, a recent study found that HD mutation carriers as young as 6 years of age show compensatory hyperconnectivity between the striatum and cerebellum; this initially enlarges the striatum but the metabolic load soon overwhelms it, the connections are rapidly lost, and the striatum atrophies well before the onset of motor symptoms (40).

It is now beyond doubt that neurodegenerative diseases can have a developmental component. For HD, this discovery opens the door for future studies to identify molecular treatments. For example, the HD iPSC Consortium characterized isoxazole-9 after finding that it reverts abnormal neuronal differentiation in HD-derived pluripotent stem cells (17). It may be that treatment should be given very early in life; it remains to be seen whether reducing mHTT levels in adulthood, even in the prodromal stage, would be sufficient to forestall symptom progression, because the brain circuitry is already altered.

### REFERENCES AND NOTES

1. M. P. Duyao et al., *Science* **269**, 407–410 (1995).
2. S. Zeitlin, J. P. Liu, D. L. Chapman, V. E. Papaioannou, A. Efstratiadis, *Nat. Genet.* **11**, 155–163 (1995).
3. A. Reiner, I. Dragatsis, S. Zeitlin, D. Goldowitz, *Mol. Neurobiol.* **28**, 259–276 (2003).
4. J. D. Godin et al., *Neuron* **67**, 392–406 (2010).



5. S. U. McKinstry *et al.*, *J. Neurosci.* **34**, 9455–9472 (2014).
6. M. Barnat, J. Le Friec, C. Benstaali, S. Humbert, *Neuron* **93**, 99–114 (2017).
7. M. Molina-Calavita *et al.*, *J. Neurosci.* **34**, 10034–10040 (2014).
8. E. E. Arteaga-Bracho *et al.*, *Neurobiol. Dis.* **96**, 144–155 (2016).
9. A. E. Molero *et al.*, *Proc. Natl. Acad. Sci. U.S.A.* **113**, 5736–5741 (2016).
10. J. K. Lee *et al.*, *Neurology* **79**, 668–674 (2012).
11. P. C. Nopoulos *et al.*, *Brain* **134**, 137–142 (2011).
12. S. J. Tabrizi *et al.*, *Lancet Neurol.* **10**, 31–42 (2011).
13. C. C. Tang *et al.*, *J. Clin. Invest.* **123**, 4076–4088 (2013).
14. A. Virlogeux *et al.*, *Cell Rep.* **22**, 110–122 (2018).
15. X. Zhao *et al.*, *Proc. Natl. Acad. Sci. U.S.A.* **113**, E5655–E5664 (2016).
16. K. L. Ring *et al.*, *Stem Cell Rep.* **5**, 1023–1038 (2015).
17. HD iPSC Consortium, *Nat. Neurosci.* **20**, 648–660 (2017).
18. P. Conforti *et al.*, *Proc. Natl. Acad. Sci. U.S.A.* **115**, E762–E771 (2018).
19. Y. Arai, E. Taverna, *Front. Cell. Neurosci.* **11**, 384 (2017).
20. T. Miyata, M. Okamoto, T. Shinoda, A. Kawaguchi, *Front. Cell. Neurosci.* **8**, 473 (2015).
21. V. C. Wheeler *et al.*, *Hum. Mol. Genet.* **11**, 633–640 (2002).
22. S. Zheng, N. Ghitani, J. S. Blackburn, J. P. Liu, S. O. Zeitlin, *Mol. Brain* **5**, 28 (2012).
23. F. Saudou, S. Humbert, *Neuron* **89**, 910–926 (2016).
24. F. S. Chou, R. Li, P. S. Wang, *Cell. Mol. Life Sci.* **75**, 1027–1041 (2018).
25. R. S. Bultje *et al.*, *Neuron* **63**, 189–202 (2009).
26. J. D. Godin, G. Poizat, M. A. Hickey, F. Maschat, S. Humbert, *EMBO J.* **29**, 2433–2445 (2010).
27. V. Lo Sardo *et al.*, *Nat. Neurosci.* **15**, 713–721 (2012).
28. C. Moreira Sousa *et al.*, *EMBO Mol. Med.* **5**, 309–325 (2013).
29. S. Elias, J. R. McGuire, H. Yu, S. Humbert, *PLOS Biol.* **13**, e1002142 (2015).
30. M. S. Thion *et al.*, *J. Natl. Cancer Inst.* **107**, djv208 (2015).
31. E. Taverna, M. Götz, W. B. Huttner, *Annu. Rev. Cell Dev. Biol.* **30**, 465–502 (2014).
32. C. Norden, *J. Cell Sci.* **130**, 1859–1863 (2017).
33. A. Sakaue-Sawano *et al.*, *Cell* **132**, 487–498 (2008).
34. Y. Kosodo *et al.*, *EMBO J.* **30**, 1690–1704 (2011).
35. Y. Arai *et al.*, *Nat. Commun.* **2**, 154–165 (2011).
36. M. Wilsch-Bräuninger, J. Peters, J. T. Paridaen, W. B. Huttner, *Development* **139**, 95–105 (2012).
37. M. N. Manuel, D. Mi, J. O. Mason, D. J. Price, *Front. Cell. Neurosci.* **9**, 70 (2015).
38. J. F. Mangin *et al.*, *Neuroimage Clin.* **26**, 102211 (2020).
39. C. R. Edamakanti, J. Do, A. Didonna, M. Martina, P. Opal, *J. Clin. Invest.* **128**, 2252–2265 (2018).
40. A. V. Tereshchenko *et al.*, *Neurology* **94**, e1908–e1915 (2020).

# ACKNOWLEDGMENTS

We are grateful to the patients and their families. We thank L. Benammar and M. Biet for their logistical help; midwife O. Philippon for her support; C. Benstaali and E. Martin for help with experiments; staff of the animal facility and of the Photonic Imaging Center (part of the ISdV core facility and certified by the *IBiSA* label) of GIN for technical help; F. Saudou, members of the Humbert laboratory, and V. L. Brandt for helpful discussions; and the Association Huntington France (AHF) for continuous support.

**Funding:** Supported by grants from Agence Nationale pour la

Recherche (ANR-15-IDEX-02 NeuroCoG, S.H.; Network of centers of excellence in neurodegeneration COEN, A.D. and S.H.); Fondation pour la Recherche Médicale (DEQ 20170336752, S.H.); Fondation pour la Recherche sur le Cerveau (S.H.); and the AGEMED program from INSERM (S.H.). M.B. and S.H. are INSERM investigators. E.A. was supported by a CIFRE (2012-0401) doctoral fellowship. M.C. is supported by a La ligue contre le cancer post-doctoral fellowship. J.-P.L. and S.O.Z. are supported by NIH NS077926. **Author contributions:** M.B., A.D., and S.H. designed the study; M.B. and S.H. wrote the manuscript, which was commented on by all authors; M.B. performed most of the experiments; M.C. performed biochemical experiments and immunohistochemistry; E.A. performed interkinetic nuclear migration experiments; D.W., R.Kac., R.Kas., and F.A. performed immunohistochemistry; S.L. and B.Y.B. provided mouse embryonic brains; J.L., A.T., A.D., and M.D. collected human data; S.B. and C.D. performed fetopathological examinations; and J.-P.L. and S.O.Z. provided embryonic brains from Flag-tagged Hdh mice. **Competing interests:** None declared. **Data and materials availability:** All data are available in the manuscript or the supplementary materials.

# SUPPLEMENTARY MATERIALS

science.sciencemag.org/content//369/6505/787/suppl/DC1  
Materials and Methods  
Figs. S1 to S10  
Table S1  
Movies S1 to S8

15 March 2019; resubmitted 27 April 2020  
Accepted 29 June 2020  
Published online 16 July 2020  
10.1126/science.aax3338

## STRUCTURAL BIOLOGY

# Binding mechanisms of therapeutic antibodies to human CD20

Anand Kumar<sup>1,2,3</sup>, Cyril Planchais<sup>4,5</sup>, Rémi Fronzes<sup>3,6</sup>, Hugo Mouquet<sup>4,5</sup>, Nicolas Reyes<sup>1,2,3\*</sup>

Monoclonal antibodies (mAbs) targeting human antigen CD20 (cluster of differentiation 20) constitute important immunotherapies for the treatment of B cell malignancies and autoimmune diseases. Type I and II therapeutic mAbs differ in B cell binding properties and cytotoxic effects, reflecting differential interaction mechanisms with CD20. Here we present 3.7- to 4.7-angstrom cryo-electron microscopy structures of full-length CD20 in complexes with prototypical type I rituximab and ofatumumab and type II obinutuzumab. The structures and binding thermodynamics demonstrate that upon binding to CD20, type II mAbs form terminal complexes that preclude recruitment of additional mAbs and complement components, whereas type I complexes act as molecular seeds to increase mAb local concentration for efficient complement activation. Among type I mAbs, ofatumumab complexes display optimal geometry for complement recruitment. The uncovered mechanisms should aid rational design of next-generation immunotherapies targeting CD20.

**H**uman cluster of differentiation 20 (CD20) (1, 2) is an integral membrane protein expressed during B lymphocyte development (3). Its cellular function is poorly understood, and it is involved in intracellular calcium signaling associated with the B cell receptor (4). CD20 is also expressed in malignant B cells and is the target of approved therapeutic monoclonal antibodies (mAbs), which are divided into two groups, type I and type II, on the basis of two signature differences (5–8): Type I mAbs recruit complement more potently than type II mAbs and therefore induce robust complement-dependent cytotoxicity (CDC); type I mAbs bind twice as many type II mAbs to a given B cell type. These properties are likely related, because complement activation requires oligomerization of the mAb fragment crystallizable region (Fc) to increase the binding avidity of complement component 1q (C1q), which is a hexa-headed molecule that optimally binds Fc hexameric arrangements (9–11).

Type I rituximab (RTX) is a recombinant mAb bearing murine antigen-binding domains linked to human immunoglobulin G (IgG) constant domains. RTX is recommended for the treatment of non-Hodgkin's lymphomas (12) and certain autoimmune diseases (13) and was the first approved cancer immunotherapy (14). Despite the widespread use of RTX, its immunogenicity and patient polymorphisms stimulated the development of second-generation mAbs that replaced the murine domains with

humanized or human antigen-binding domains, as with the type II mAb obinutuzumab (OBZ) (15) and the type I mAb ofatumumab (OFA) (16), respectively, which are approved for the treatment of chronic lymphocytic leukemia (CLL) (8, 17). Although OFA is a type I mAb, it shows more potent complement recruitment than RTX, particularly in cells with low CD20 expression levels, as occurs in CLL (18, 19).

Binding studies (20, 21) and crystal structures of monovalent antigen-binding fragments (Fabs) of RTX (Fab<sub>RTX</sub>) (22) and OBZ (Fab<sub>OBZ</sub>) (23) in complex with CD20 cyclic peptides revealed a critical antigenic determinant region (<sup>170</sup>ANPS<sup>173</sup>) on the large extracellular loop of CD20, as well as 1:1 Fab:CD20 peptide binding stoichiometry (24). Recently, the cryo-electron microscopy (cryo-EM) structure determination of N-terminally truncated CD20 in complex with Fab<sub>RTX</sub> ( $\Delta$ 41CD20-Fab<sub>RTX</sub>) showed two Fab<sub>RTX</sub> molecules bound to composite epitopes on the surface of dimeric CD20 and revealed extensive Fab-Fab homotypic interactions (25).

Despite the wealth of available functional and structural data, the molecular bases underlying the differential binding mechanisms of murine versus human type I mAbs, as well as those for type I versus type II mAbs, remain elusive. We set out to unravel these mechanisms using *in vitro* approaches to determine the three-dimensional (3D) structures and binding mechanisms of full-length human CD20 in complex with Fab fragments from three major therapeutic mAbs: RTX (murine type I), OFA (human type I), and OBZ (humanized type II).

## Results

### Antibody binding and complement recruitment

Full-length human CD20 in nondenaturing detergent solutions exists as a single and stable oligomeric state corresponding to homodimers (fig. S1). To probe the ability of purified CD20 to

reconstitute the properties of type I and type II mAbs, we analyzed their binding thermodynamics and kinetics by using isothermal titration calorimetry (26, 27), as well as the mAbs' abilities to recruit complement.

Isothermal titrations of full-length Ig molecules bearing identical IgG1 Fc regions and corresponding Fab fragments from either RTX (IgG<sub>RTX</sub>) or OBZ (IgG<sub>OBZ</sub>) into purified CD20 yielded dissociation constant ( $K_d$ ) values in the low nanomolar range, as observed in B cells (15), and binding stoichiometries of 1:1 and 1:2 for IgG<sub>RTX</sub> and IgG<sub>OBZ</sub>, respectively, providing the thermodynamic basis to understand the half-maximal values of type II compared to type I mAb binding to B cells.

Further calorimetric analysis of both divalent [F(ab')<sub>2</sub>] and monovalent (Fab) mAb fragments from RTX, OBZ, and OFA (Fig. 1, A to D, and table S1) yielded conserved thermodynamic binding parameters, compared to full-length IgGs. Moreover, molecules bearing Fab<sub>RTX</sub> showed higher binding enthalpy values ( $-27.4 \pm 0.6$  kcal/mol) than those bearing Fab<sub>OBZ</sub> ( $-19.0 \pm 0.8$  kcal/mol) or Fab<sub>OFA</sub> ( $-23.0 \pm 0.8$  kcal/mol), although the large excess of binding enthalpy translates to a small change in binding energy ( $\sim 1$  kcal/mol) due to entropic compensations. From a kinetic viewpoint, we observed similar association rate ( $k_{on}$ ) values for the three F(ab')<sub>2</sub> molecules but significantly slower dissociation rates of F(ab')<sub>2-RTX</sub> than for both F(ab')<sub>2-OBZ</sub> and F(ab')<sub>2-OFA</sub> (table S2).

We next probed the ability of IgG<sub>RTX</sub> and IgG<sub>OBZ</sub> bound to purified CD20 to recruit complement (Fig. 1E). As a proxy for complement recruitment, we quantified the deposition of fluorescently labeled C1q complex on synthetic liposomes with CD20 incorporated on their surface, as well as on HEK293 cells expressing CD20, as a control. Indeed, C1q deposition was much higher in both cells and liposomes opsonized with IgG<sub>RTX</sub> than those opsonized with IgG<sub>OBZ</sub>, demonstrating that dimeric CD20 reconstituted in a synthetic membrane is sufficient to promote Fc oligomerization and complement recruitment.

Overall, the above results demonstrate that binding of mAbs to purified dimeric CD20 recapitulates accurately the signature differences between type I and type II anti-CD20 antibodies observed in B lymphocytes.

### Cryo-EM structural analysis of CD20 in complex with divalent antibody fragments

For cryo-EM structure determination, we focused on CD20 complexes with divalent F(ab')<sub>2</sub> molecules from RTX, OFA, and OBZ, because they structurally resemble full-length mAbs more closely than monovalent fragments and lack flexible Fc domains that might complicate single-particle reconstructions. Cryo-EM imaging showed that the majority of the CD20

<sup>1</sup>Membrane Protein Mechanisms Unit, Institut Pasteur, 75015 Paris, France. <sup>2</sup>Membrane Protein Mechanisms Group, European Institute of Chemistry and Biology, University of Bordeaux, 33607 Pessac, France. <sup>3</sup>CNRS UMR 5234 Fundamental Microbiology and Pathogenicity, Bordeaux, France. <sup>4</sup>Laboratory of Humoral Immunology, Department of Immunology, Institut Pasteur, Paris, France. <sup>5</sup>INSERM U1222, Paris, France. <sup>6</sup>Structure and Function of Bacterial Nanomachines Group, European Institute of Chemistry and Biology, University of Bordeaux, 33607 Pessac, France. \*Corresponding author. Email: nicolas.reyes@u-bordeaux.fr



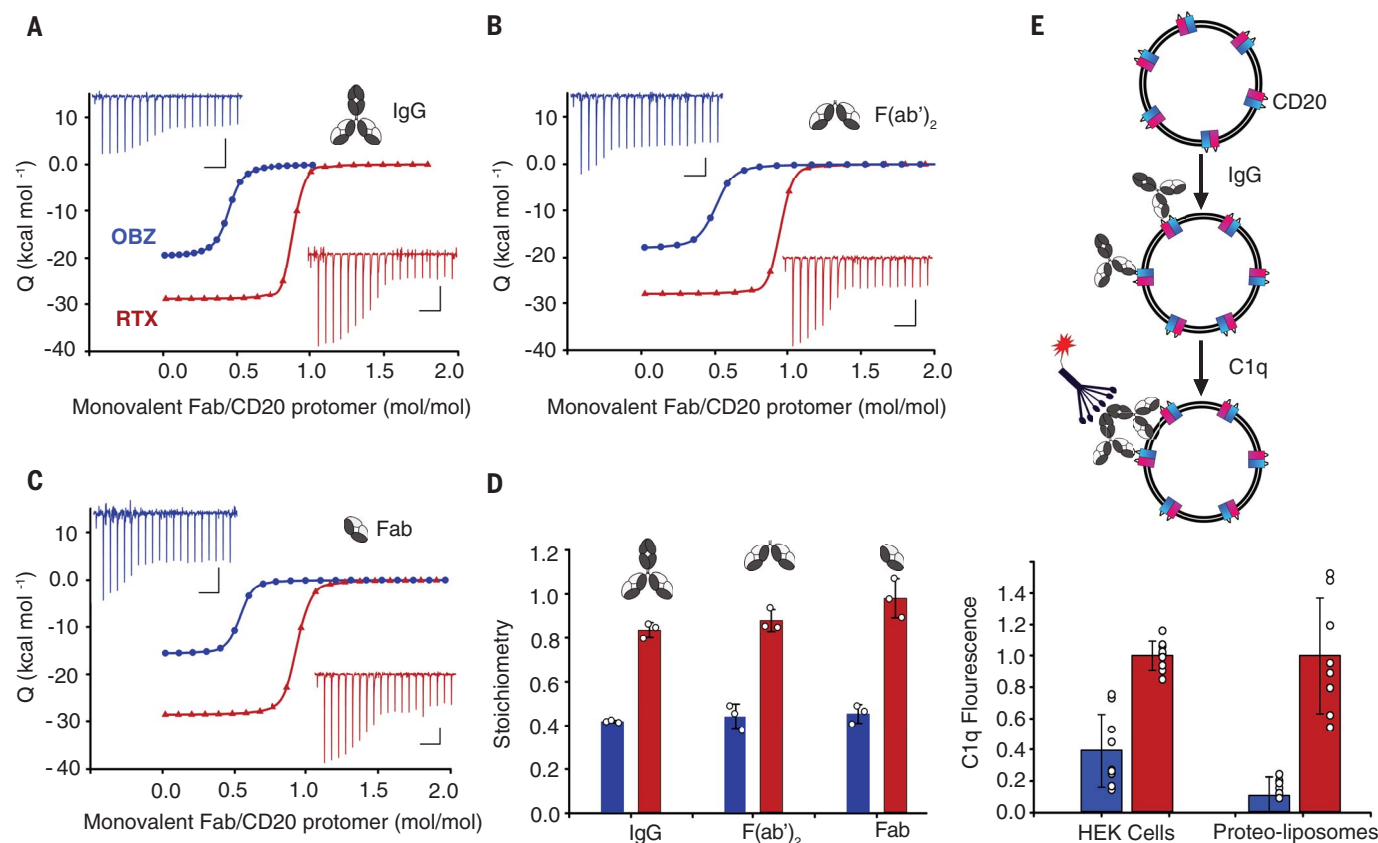


**Fig. 1. Antibody binding and complement recruitment.** (A to C) Isothermal titrations of IgG (A), F(ab')<sub>2</sub> (B), and Fab (C) molecules into purified CD20. Thermal powers are shown, with scale bars indicating 0.1  $\mu$ cal s<sup>-1</sup> and 500 s. Throughout the figure, RTX and OBZ data are colored red and blue, respectively.  $Q$ , binding heat. (D) Averaged binding stoichiometry of monovalent and divalent molecules to CD20. Stoichiometry is plotted as moles of monovalent

Fab per mole of CD20 protomer for comparison. (E) Fluorescently labeled C1q deposition upon IgG opsonization of liposomes and cells with CD20 on their surface. Plots depict an average of three independent experiment measurements (D) or three independent experiment measurements performed in triplicates (E), and error bars represent SEM. Empty circles represent values from individual experiments.

complexes with type I F(ab')<sub>2</sub> molecules formed 2:2 F(ab')<sub>2</sub>:CD20 cyclic arrangements; we also observed 3:3 and 4:4 arrangements, but not 1:1 complexes (Fig. 2, A and B). In contrast, CD20 complexes with type II F(ab')<sub>2</sub>OBZ showed exclusively 1:2 arrangements (Fig. 2C). A feature common to all of these macromolecular assemblies is that the two Fab arms from one F(ab')<sub>2</sub> molecule bind two CD20 molecules. However, we observed that the CD20 dimer binds two type I Fab molecules, but only one type II Fab molecule. These structural data are in excellent agreement with our thermodynamic analysis and further show that the two type I Fabs bound to CD20 come from different F(ab')<sub>2</sub> molecules.

The large flexibility of F(ab')<sub>2</sub> fragments around the hinge region connecting the Fab arms precluded high-resolution 3D reconstructions. To alleviate this problem, we decreased the particle box size to extract only one copy of CD20 from the macromolecular assemblies with either two type I (Fig. 2, D and E) or one type II (Fig. 2F) Fab molecule bound, respectively. This “single-copy approach” effectively increased the number of particles and decreased particle het-

erogeneity, and as a consequence it improved the quality of 2D classes and 3D reconstructions substantially, yielding cryo-EM maps with global resolutions between 3.7 and 4.7 Å that enabled structure determinations of CD20 in complex with Fab<sub>RTX</sub>, Fab<sub>OFA</sub>, and Fab<sub>OBZ</sub>, respectively (figs. S2 to S7 and table S3).

#### Cryo-EM structures of CD20 in complexes with type I Fab

The cryo-EM structures of full-length CD20 in complexes with murine Fab<sub>RTX</sub> (CD20-Fab<sub>RTX</sub>) and human Fab<sub>OFA</sub> (CD20-Fab<sub>OFA</sub>) showed two CD20 subunits (here, CD20<sub>A</sub> and CD20<sub>B</sub>) arranged in a symmetric dimer with two Fab-bound molecules (Fig. 3, A to D).

Each CD20 subunit contains four trans-membrane helices (TM1 to -4) (Fig. 3E). TM1 barely spans the width of the membrane core, while TM2 unwinds close to the midpoint of the membrane, dividing the helix into TM2a and TM2b. TM1 and TM2a are connected by extracellular loop 1 (ECL1), which positions Gly<sup>75</sup>, Ile<sup>76</sup>, and Tyr<sup>77</sup> outside the membrane plane. The region including TM2b and the in-

tracellular loop that connects it to TM3 (ICL1), and also TM4, differs significantly in the CD20-Fab<sub>RTX</sub> and CD20-Fab<sub>OFA</sub> structures compared to the reported  $\Delta$ 41CD20-Fab<sub>RTX</sub> structure (25). In the former, TM2b is a canonical  $\alpha$  helix including residues Leu<sup>88</sup>-Ala<sup>103</sup>, while in the latter TM2b was modeled as a 3-10  $\alpha$  helix between Ile<sup>96</sup> and Ile<sup>101</sup> with an extended ICL1. Additionally, in our structures TM4 is three helix turns longer than in  $\Delta$ 41CD20-Fab<sub>RTX</sub> and protrudes outside the membrane plane on the intracellular side. The observed differences are most likely due to low molecular detail around those regions in the reported  $\Delta$ 41CD20-Fab<sub>RTX</sub> cryo-EM map (EMD-21212), or partial unfolding of the truncated construct.

TM3 and TM4 are connected by ECL2: Its N-terminal residues form an amphipathic loop (ECL2a) that partitions in the lipid-detergent micelle with hydrophobic side chains buried in the membrane core, next to extra density corresponding to lipid or detergent molecules arranged in a bilayer fashion. The C-terminal part of ECL2 (ECL2b) is flanked by two extracellular helices (EH),  $\alpha$  helix EH1 and 3-10  $\alpha$

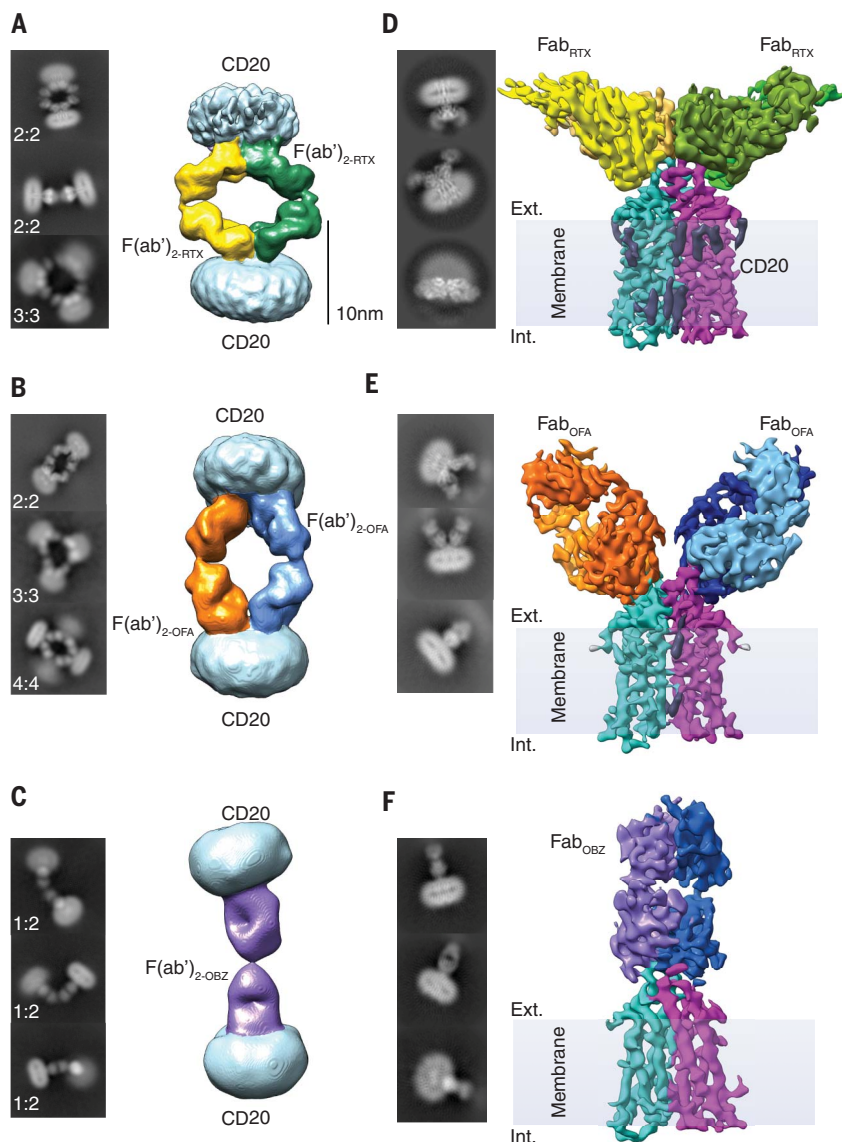


**Fig. 2. Cryo-EM analysis of CD20-F(ab')<sub>2</sub> complexes.** (A to C) 3D reconstructions of 2:2 F(ab')<sub>2</sub>:CD20 assemblies, with lipid-detergent micelles colored light blue and individual F(ab')<sub>2</sub> molecules color coded. 2D classes are also shown for 2:2, 3:3, and 4:4 assemblies. (D to F) Cryo-EM maps of a single copy of CD20 bound to Fab (individual CD20 subunits in cyan and pink, respectively) within the CD20-F(ab')<sub>2</sub> assemblies with Fab (heavy and light chains in dark and light colors, respectively) and lipid (gray) molecules bound. Examples of 2D classes in different orientations are shown. Ext., exterior; Int., interior.

helix EH2, and is linked to TM4 through a disulfide between Cys<sup>167</sup> and Cys<sup>184</sup>, which is strictly conserved among CD20 orthologs.

The two Fab-bound molecules in CD20-Fab<sub>RTX</sub> and CD20-Fab<sub>OFA</sub> structures are arranged head-to-head with their Fab constant domains oriented in opposite directions (Fig. 3, A and B). Notably, Fab<sub>OFA</sub> binds at a sharper angle to the membrane plane (~60°) than Fab<sub>RTX</sub> (~36°) and is rotated ~180° along the long axis of the Fab. As a consequence, the variable domains of the two bound Fab<sub>OFA</sub> molecules separate, with their closest atoms at ~7 Å, and do not establish any homotypic

contacts, while the constant domains come in closer proximity by as much as ~9 Å, compared to RTX.

RTX and OFA bind overlapping and extensive 3D epitopes that bury ~890 and ~720 Å<sup>2</sup> on the extracellular surface of CD20, respectively (Fig. 3, C and D), mostly through amino acid interactions with their heavy-chain complementary determinant regions (HC-CDR) (table S4). However, the orientations of RTX and OFA HC-CDRs are opposite, with the former crossing the CD20 dimeric interface and establishing Fab-Fab homotypic interactions and the latter lying ~40 Å apart from

each other and pointing to the membrane. As a consequence, RTX interacts mainly with residues <sup>170</sup>ANPS<sup>173</sup> in EH2, while OFA interacts with residues Tyr<sup>161</sup>, Asn<sup>166</sup>, and Glu<sup>168</sup> in ECL2b, as well as Ala<sup>170</sup> and Asn<sup>171</sup> in the tip of CD20 (Fig. 3, C and D, and table S4). The more N-terminal location of CD20 determinant residues for OFA, in comparison with RTX binding, is in excellent agreement with reported binding studies (28).

Overall, our structural comparison showed that the OFA epitope is restricted to one CD20 subunit and its core interactions localize to ELC2b and EH2, while Fab<sub>RTX</sub> recognizes both CD20 subunits and its core epitope localizes to EH2. OFA orients its Fab constant domains closer to each other than RTX while separating its variable domains that lack homotypic interactions.

### RTX homotypic Fab-Fab interactions

CD20-bound Fab<sub>RTX</sub> molecules establish unexpected Fab-Fab homotypic interactions (25) (fig. S8). These interactions occur at germline-encoded positions that are not the product of affinity maturation (25), raising an important question about the strength of the interactions and the extent of the thermodynamic coupling at the homotypic interface. To shed light on this problem, we built a double mutant thermodynamic cycle (29), introducing amino acid exchanges on opposite sides of the CD20-Fab<sub>RTX</sub> homotypic interface, and tested if the effect on IgG<sub>RTX</sub> binding of mutating residues on one side depends on whether residues on the other side are mutated. Four tyrosine residues play critical roles at this interface (fig. S8A): Tyr<sup>101</sup>(HC-CDR3) forms an aromatic stack with symmetry-related Tyr<sup>101</sup>; Tyr<sup>102</sup>(HC-CDR3) makes contacts with Thr<sup>28</sup>(HC-CDR1), Ser<sup>31</sup>(HC-CDR1), and Tyr<sup>32</sup>(HC-CDR1) and is hydrogen-bonded to Thr<sup>28</sup>(HC-CDR1); Tyr<sup>52</sup>(HC-CDR2) and Tyr<sup>48</sup>(LC-CDR2) are hydrogen-bonded to Gly<sup>103</sup>(HC-CDR3) and Ser<sup>31</sup>(HC-CDR1), respectively. To build the cycle, we exchanged amino acid side chains to impair their ability to form H-bonds using the following IgG<sub>RTX</sub> constructs (fig. S8C): (i) wild type (WT), (ii) Thr<sup>28</sup>→Ala Ser<sup>31</sup>→Ala (T28A-S31A), (iii) Tyr<sup>102</sup>→Phe Tyr<sup>48</sup>→Phe (Y102F-Y48F), and (iv) T28A-S31A-Y102F-Y48F. Isothermal titrations showed that all IgG<sub>RTX</sub> constructs bind CD20 with 1:1 stoichiometry and similar *K<sub>d</sub>* values (fig. S8C and table S5). Notably, we observed a significant increase in favorable binding enthalpy when mutations T28A-S31A were introduced in WT IgG (ΔΔ*H* = -5.5 kcal/mol) compared to those mutations introduced in the background of Y102F-Y48F (ΔΔ*H* = -0.93 kcal/mol), showing that there is detectable thermodynamic coupling at the homotypic interface. However, the observed enthalpic changes are not translated into significant changes in IgG<sub>RTX</sub> affinity due to entropic compensations,



**Fig. 3. Structures of CD20 complexes with type I Fab fragments.**

(A and B) Structures of CD20 in complexes with two Fab<sub>RTX</sub>-bound (A) and Fab<sub>OFA</sub>-bound (B) molecules, color coded as in Fig. 2, D to F. Insets show extracellular views of the Fab variable domains bound to CD20. (C and D) The most important CD20 residues interacting with single Fab<sub>RTX-A</sub> (yellow; C) or Fab<sub>OFA-A</sub> (orange; D) molecules are highlighted. Residues in ball-and-stick representation establish the majority of H-bonds and contacts with the Fab molecule. Single-letter abbreviations for the amino acid residues are as follows: A, Ala; C, Cys; D, Asp; E, Glu; F, Phe; G, Gly; H, His; I, Ile; K, Lys; L, Leu; M, Met; N, Asn; P, Pro; Q, Gln; R, Arg; S, Ser; T, Thr; V, Val; W, Trp; and Y, Tyr. (E) Membrane view of CD20<sub>A</sub> subunit from the CD20-Fab<sub>RTX</sub> complex.

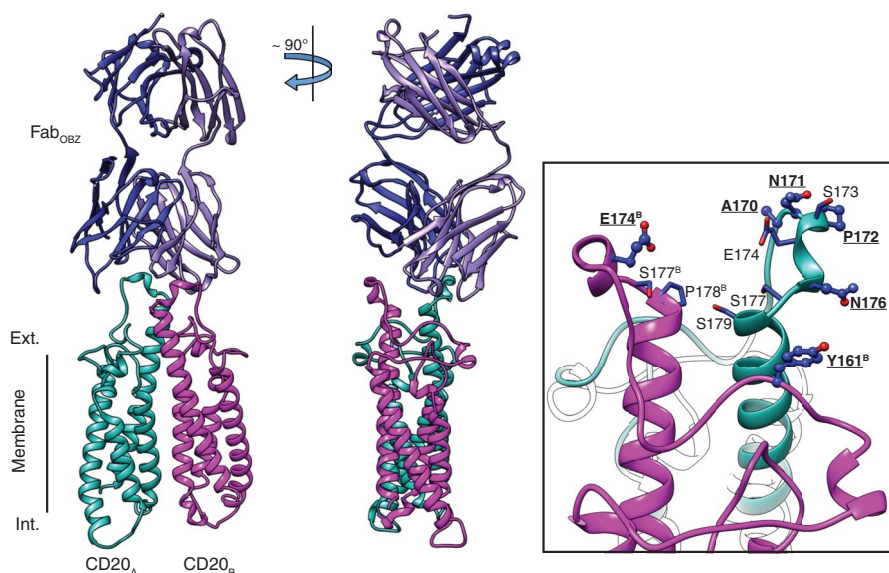
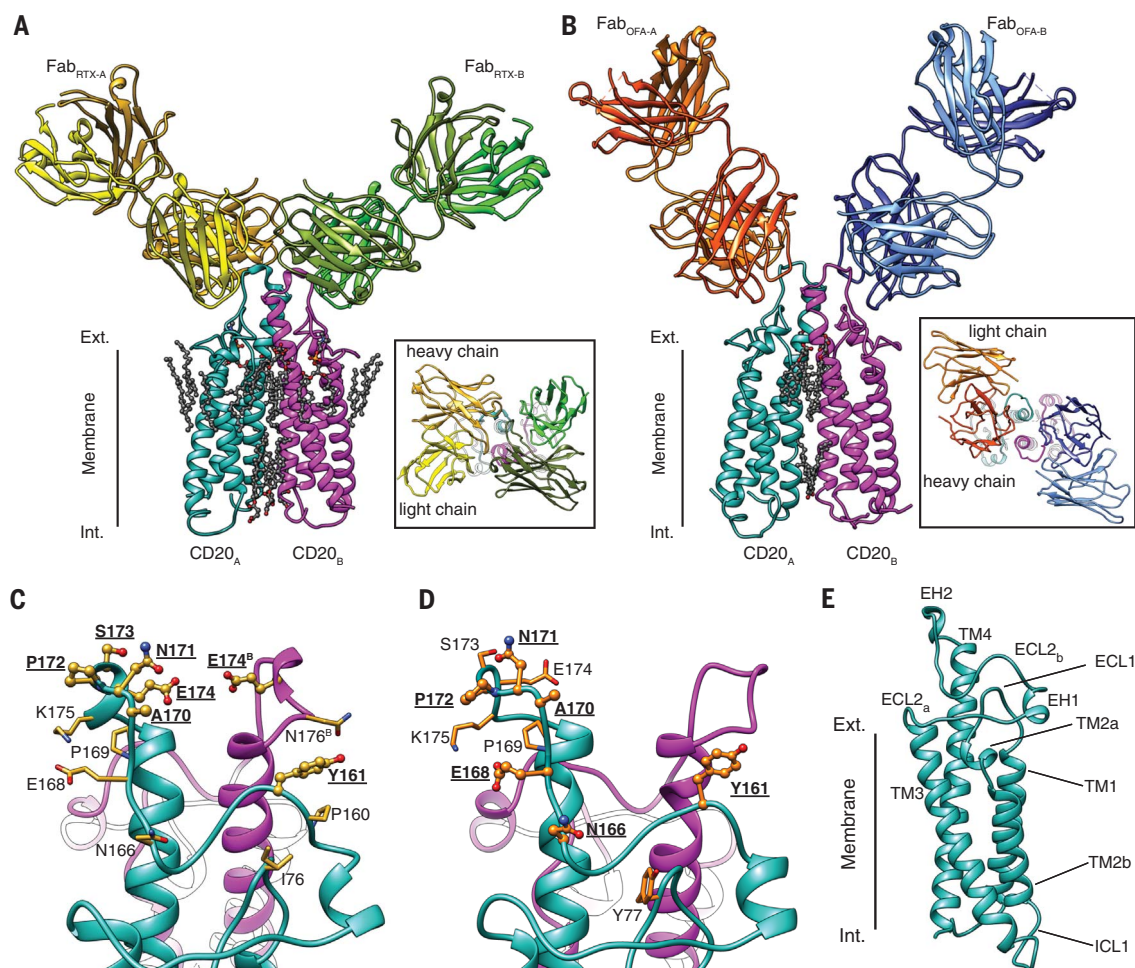


**Fig. 4. Structure of CD20 in complex with type II Fab<sub>OBZ</sub>.** Structure of CD20 with one Fab<sub>OBZ</sub>-bound molecule. Fab<sub>OBZ</sub> interacts more extensively with CD20<sub>A</sub> subunit (cyan), but it also interacts with CD20<sub>B</sub> (pink). Inset shows the most important CD20 residues interacting with Fab<sub>OBZ</sub>. Residues in ball-and-stick representation establish the majority of H-bonds and contacts with the Fab molecule.

demonstrating that the H-bond network at the core of the homotypic interface contributes weakly to the overall binding energy.

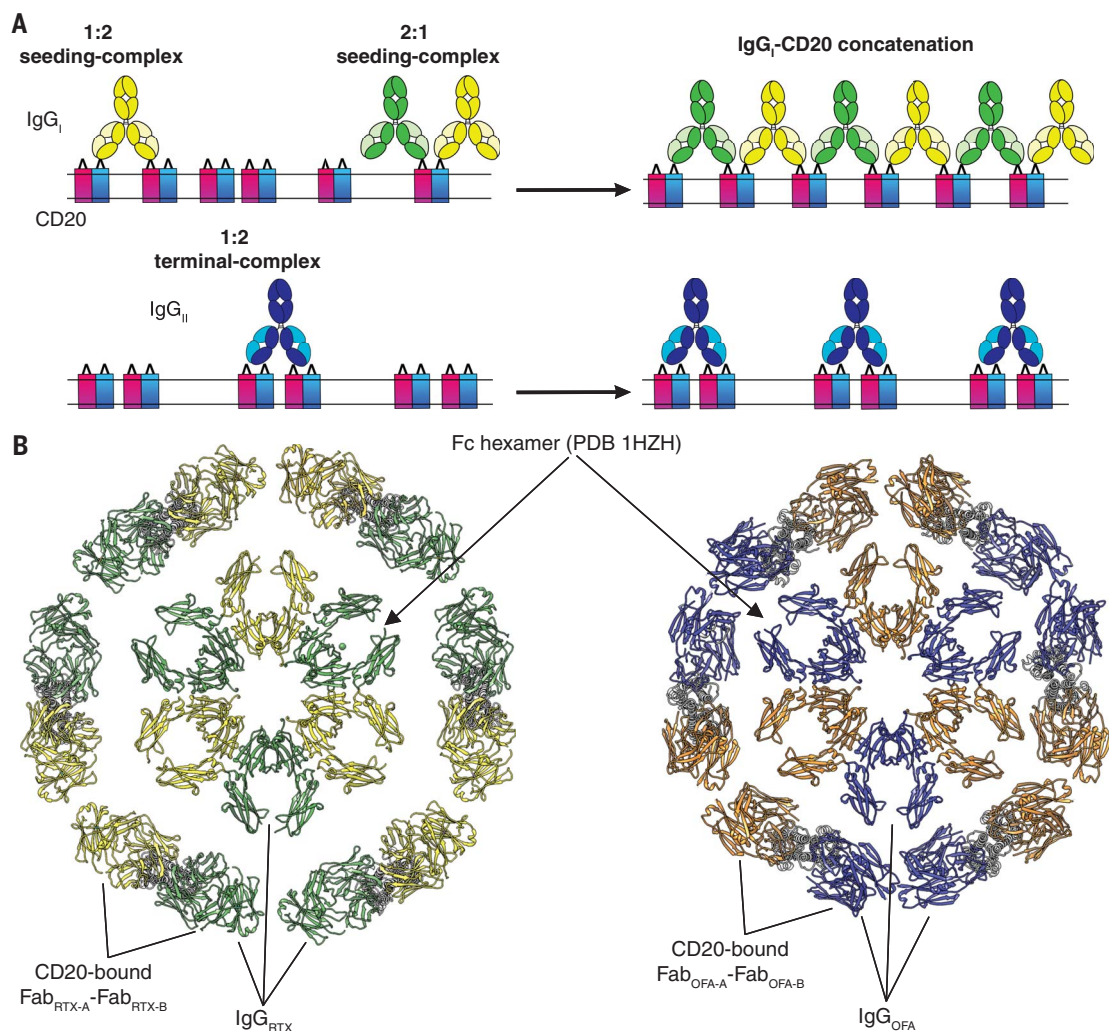
#### CD20 complex with type II OBZ fragments

To gain insights into the differential binding mechanisms of type I and II anti-CD20 mAbs, we determined the structure of CD20 in complex with type II Fab<sub>OBZ</sub> (Fig. 4). The structure showed a single Fab<sub>OBZ</sub> molecule bound to the tip of CD20, with pseudosymmetric CD20 subunits in a conformation similar to those in the CD20-Fab<sub>RTX</sub> structure. In contrast to type I Fab molecules, Fab<sub>OBZ</sub> binds nearly normally to the membrane plane, with its constant domain protruding far into the extracellular solution.

Fab<sub>OBZ</sub> forms a wide and rather shallow binding pocket involving all CDR loops, with the exception of CDR-L2, to bind extensive areas on the surface of both CD20<sub>A</sub> (~566 Å<sup>2</sup>) and CD20<sub>B</sub> (~226 Å<sup>2</sup>). Binding to CD20<sub>A</sub> occurs at an extended <sup>170</sup>ANPSEKNSP<sup>178</sup> motif, with key interacting residues <sup>170</sup>ANP<sup>172</sup> and EH2 C-terminal Glu<sup>174</sup> and Asn<sup>176</sup> residues (table S4). The C-terminal shift of the OBZ

**Fig. 5. Binding mechanism and hexameric CD20-IgG model.**

**(A)** IgG:CD20 seeding and terminal complex mechanisms for type I and II mAbs, respectively. **(B)** Extracellular view of a structural model built with the symmetric Fc hexamer from PDB 1HZH and six copies of CD20-Fab<sub>RTX</sub> (left) or CD20-Fab<sub>OFA</sub> (right) structures (determined in this work), arranged symmetrically and concentric to the Fc ring. The space between CD20-Fab complexes was minimized to avoid clashes between Fab domains bound to different CD20 molecules. Fc domains and the two corresponding Fab domains are shown in the same color.



epitope compared to RTX is in good agreement with previous binding and structural studies (23). Other residues in CD20<sub>A</sub> establish contacts mostly with the light chain, while heavy-chain Arg<sup>52</sup>(CDR-H2) and Trp<sup>33</sup>(CDR-H1) are H-bonded to Pro<sup>172</sup> and Ser<sup>173</sup>, respectively. The Fab<sub>OBS</sub> heavy chain also establishes two contact points on CD20<sub>B</sub>, one with Tyr<sup>161</sup>(ECL2b) that packs against Ser<sup>30</sup>(CDR-H1), Tyr<sup>31</sup>(CDR-H1), Gly<sup>54</sup>(CDR-H2), and Asp<sup>55</sup>(CDR-H2) and another with Glu<sup>174</sup>, Ser<sup>177</sup>, and Pro<sup>178</sup> on the C-terminal end of EH2 that interact extensively with CDR-H3 residues Asp<sup>102</sup>, Gly<sup>103</sup>, and Tyr<sup>104</sup>.

The structure of the CD20-Fab<sub>OBS</sub> complex demonstrates that bound Fab<sub>OBS</sub> precludes binding of a second molecule on the surface of CD20, because it interacts with the <sup>174</sup>EKN<sup>178</sup> motif in both CD20<sub>A</sub> and CD20<sub>B</sub> and would generate extensive steric clashes with a second symmetrical Fab<sub>OBS</sub> molecule, rotated around the pseudo two-fold symmetry axis of CD20. These structures provide the structural basis underlying the differential binding stoichiometry of OBS and in general type II mAbs, compared to type I.

entry of OBS and in general type II mAbs, compared to type I.

### Discussion

Our structural and thermodynamic analyses unravel the differential binding mechanisms of major therapeutic anti-CD20 antibodies used in the clinic for the treatment of lymphomas and autoimmune diseases.

The CD20 oligomeric state is important to the mAb binding mechanisms, and we provide strong experimental evidence that the dimer represents a native oligomeric state: the structure of CD20-Fab<sub>OFA</sub> demonstrated that the CD20 dimer is stabilized by extensive intersubunit contacts that are conserved in the absence of both extensive Fab-Fab homotypic interactions and binding of a single Fab molecule to two CD20 subunits (Fig. 3B). Moreover, in our structures, we observed cholesterol-like lipids bound to the outer and inner halves of the intersubunit interface in a bilayer-like arrangement (Fig. 3A), suggesting that cellular cholesterol further stabilizes the CD20 dimer.

Finally, purified dimeric CD20 both in detergent solution and in lipid membrane recapitulates well the signature properties of type I and type II mAbs observed in B cells.

RTX, OFA, and OBS bind extensive 3D epitopes that extend beyond the core <sup>170</sup>ANPSEKNSP<sup>178</sup> motif. Notably, Fab<sub>RTX</sub> (22) and Fab<sub>OBS</sub> (23) bind CD20 cyclic peptides encompassing this motif with similar coordination as in the cryo-EM structures, but with nearly three orders of magnitude weaker affinity (23) compared to full-length CD20 (table S1). This difference highlights the importance of the epitopic expansion observed in the cryo-EM structures and predicts that secondary epitopes outside the above-mentioned motif contribute ~30% to the total mAb binding energy. Moreover, there is ~1 kcal excess binding energy of RTX, over that of OBS and OFA, arguing that the homotypic interface contributes weakly (~10%) to that energy, due to the entropic penalty associated with tightly packing two Fab molecules. However, this interface might play a significant kinetic role by slowing down RTX



dissociation from CD20. The crystal structure of ocrelizumab (OCR) Fab—a murine type I mAb approved for multiple sclerosis treatment (30)—in complex with CD20 peptide (31) shows a Fab-Fab interface within the crystal lattice nearly identical to that of RTX (fig. S8B), suggesting that Fab<sub>OCR</sub> molecules bound to full-length CD20 also form extensive homotypic interactions.

The key mechanistic difference between IgG type I (IgG<sub>I</sub>) and type II (IgG<sub>II</sub>) molecules is that upon binding to CD20, IgG<sub>II</sub> forms 1:2 (IgG<sub>II</sub>:CD20) “terminal” complexes that preclude binding of additional IgG<sub>II</sub> molecules, while IgG<sub>I</sub> forms 1:2 or 2:1 (IgG<sub>I</sub>:CD20) “seeding” complexes that enable subsequent concatenation of IgG or CD20 molecules, respectively (Fig. 5A). Hence, seeding and terminal complexes explain the half-maximal saturation values of IgG<sub>II</sub> compared to IgG<sub>I</sub> reported in cells (6).

Both IgG<sub>I</sub> and IgG<sub>II</sub> are able to recruit complement to similar levels, although IgG<sub>I</sub> does so with half-saturation values 10- to 1000-fold lower than IgG<sub>II</sub>, depending on whether CD20 expression levels are high (~10<sup>6</sup> copies per cell) or low (~10<sup>4</sup> copies per cell), respectively (32). Indeed, concatenation of IgG<sub>I</sub> molecules upon binding to CD20 would increase locally the concentration of Fc domains and promote their oligomerization for C1q recruitment. In turn, IgG<sub>II</sub> terminal complexes—unable to concatenate additional molecules—would require higher antigen densities for Fc oligomerization, explaining why the difference in IgG<sub>I</sub> and IgG<sub>II</sub> complement recruitment potency strongly depends on CD20 expression levels.

The above arguments raise the important question of why OFA activates complement more potently than RTX, considering that both are able to form seeding complexes. The sharper binding angle of Fab<sub>OFA</sub> compared to Fab<sub>RTX</sub> suggests that concatenation of IgG<sub>OFA</sub> seeding complexes would bring their Fc domains in closer proximity, further facilitating their oligomerization. To visualize this effect, we built symmetrical and circular arrangements of six CD20-Fab<sub>RTX</sub> and CD20-Fab<sub>OFA</sub> copies, respectively, around a hexameric Fc ring as the one required for optimal complex

recruitment (9, 11, 33) (Fig. 5B). This speculative model showed that CD20-bound Fab<sub>OFA</sub> molecules localize ~15 Å closer to the corresponding Fc domain than Fab<sub>RTX</sub>, supporting the idea that concatenation of CD20-IgG<sub>OFA</sub> complexes upon binding to CD20 in the membrane forms more compact assemblies and brings Fc in closer proximity for oligomerization. Finally, it is also likely that the lack of homotypic interactions between bound Fab<sub>OFA</sub> molecules confers a higher degree of freedom to the 2:1 seeding complexes for further facilitation of Fc oligomerization. From all the above, we conclude that IgG binding stoichiometry is a key determinant of the mAb potency to recruit complement, but the angle and flexibility of CD20-bound Fab molecules in seeding complexes also contribute to it.

The molecular mechanisms presented here should facilitate the rational design of new generations of mAbs and biosimilar molecules to fine-tune treatments of different B cell malignancies and autoimmune diseases, as well as to make these more affordable to health care systems.

## REFERENCES AND NOTES

- K. Ishibashi, M. Suzuki, S. Sasaki, M. Imai, *Gene* **264**, 87–93 (2001).
- Y. Liang, T. F. Tedder, *Genomics* **72**, 119–127 (2001).
- D. A. Einfeld, J. P. Brown, M. A. Valentine, E. A. Clark, J. A. Ledbetter, *EMBO J.* **7**, 711–717 (1988).
- R. J. Petrie, J. P. Deans, *J. Immunol.* **169**, 2886–2891 (2002).
- J. P. Deans, S. M. Robbins, M. J. Polyak, J. A. Savage, *J. Biol. Chem.* **273**, 344–348 (1998).
- M. S. Cragg *et al.*, *Blood* **101**, 1045–1052 (2003).
- M. S. Cragg, M. J. Glennie, *Blood* **103**, 2738–2743 (2004).
- M. J. E. Marshall, R. J. Stopforth, M. S. Cragg, *Front. Immunol.* **8**, 1245 (2017).
- C. A. Diebold *et al.*, *Science* **343**, 1260–1263 (2014).
- G. Wang *et al.*, *Mol. Cell* **63**, 135–145 (2016).
- D. Ugurlar *et al.*, *Science* **359**, 794–797 (2018).
- T. M. Pierpont, C. B. Limper, K. L. Richards, *Front. Oncol.* **8**, 163 (2018).
- F. H. Du, E. A. Mills, Y. Mao-Draayer, *Auto Immun. Highlights* **8**, 12 (2017).
- D. G. Maloney *et al.*, *Blood* **84**, 2457–2466 (1994).
- E. Mössner *et al.*, *Blood* **115**, 4393–4402 (2010).
- J. L. Teeling *et al.*, *Blood* **104**, 1793–1800 (2004).
- G. Cartron, H. Watier, *Blood* **130**, 581–589 (2017).
- A. W. Pawluczuk *et al.*, *J. Immunol.* **183**, 749–758 (2009).
- S. O'Brien, A. Osterborg, *Clin. Lymphoma Myeloma Leuk.* **10**, 361–368 (2010).
- M. J. Polyak, J. P. Deans, *Blood* **99**, 3256–3262 (2002).
- M. Binder, F. Otto, R. Mertelsmann, H. Veelken, M. Trepel, *Blood* **108**, 1975–1978 (2006).
- J. Du *et al.*, *J. Biol. Chem.* **282**, 15073–15080 (2007).
- G. Niederfellner *et al.*, *Blood* **118**, 358–367 (2011).
- C. Klein *et al.*, *mAbs* **5**, 22–33 (2013).
- L. Rougé *et al.*, *Science* **367**, 1224–1230 (2020).
- T. Wiseman, S. Williston, J. F. Brandts, L. N. Lin, *Anal. Biochem.* **179**, 131–137 (1989).
- D. Burnouf *et al.*, *J. Am. Chem. Soc.* **134**, 559–565 (2012).
- J. L. Teeling *et al.*, *J. Immunol.* **177**, 362–371 (2006).
- A. Horovitz, *Fold. Des.* **1**, R121–R126 (1996).
- S. Faissner, J. R. Plemel, R. Gold, V. W. Yong, *Nat. Rev. Drug Discov.* **18**, 905–922 (2019).
- J. Du *et al.*, *Mol. Immunol.* **45**, 2861–2868 (2008).
- S. Herter *et al.*, *Mol. Cancer Ther.* **12**, 2031–2042 (2013).
- Y. Wu *et al.*, *Cell Rep.* **5**, 1443–1455 (2013).

## ACKNOWLEDGMENTS

We thank P. V. Krasteva (IECB, Bordeaux) for help with negative-stained EM imaging and discussion; J. Prigent and A. Kok (Humoral Immunology Lab) for help with production of recombinant antibodies and fragments; and C. Velours (I2BC, Paris-Saclay) for SEC-MALS analysis. We acknowledge the IECB cryo-EM imaging facility for support in cryo-EM sample screening and initial data acquisition, the EMBL-Heidelberg Cryo-Electron Microscopy Service Platform for support in image acquisition of CD20-Fab<sub>RTX</sub> and CD20-Fab<sub>OFA</sub> complexes, and the Institut Pasteur cryo-EM Nanoimaging Facility for image acquisition of the CD20-Fab<sub>OFA</sub> complex. **Funding:** This research was supported by ERC Grant 309657 and Institut Pasteur funds to N.R.; CNRS funds to N.R. and R.F.; G5 Institut Pasteur, *Milieu Interieur* (ANR-10-LABX-69-01) Programs, and INSERM funds to H.M. Anand Kumar was supported by fellowships from the Pasteur-Paris University (PPU) international PhD program and Fondation-ARC. CACSICE grant (ANR-11-EQPX-008) supported access to the Institut Pasteur cryo-EM Nanoimaging Facility. **Author contributions:** A.K. optimized and performed protein expression, purification, cryo-EM sample preparation, and functional assays; C.P. and H.M. cloned CD20 and anti-CD20 molecules and produced and purified recombinant antibodies and fragments. A.K. collected cryo-EM data, and A.K., R.F., and N.R. analyzed cryo-EM data. A.K. and N.R. built structural models, analyzed structures, and prepared the manuscript with comments and edits from R.F. and H.M.; N.R. conceived and supervised the project. **Competing interests:** The authors declare no competing interests. **Data and materials availability:** Structural models of CD20-Fab<sub>RTX</sub>, CD20-Fab<sub>OFA</sub>, CD20-Fab<sub>OFA</sub>, and CD20-Fv<sub>OFA</sub> have been deposited in Protein Data Bank (PDB) with accession codes 6Y90, 6Y92, 6Y97, and 6Y9A, respectively. The corresponding cryo-EM maps were deposited in the Electron Microscopy Data Bank (EMDB) under accession numbers EMD-10731, EMD-10732, EMD-10733, and EMD-10734. All data are available in the main text or the supplementary materials. Materials are available upon reasonable request.

## SUPPLEMENTARY MATERIALS

science.sciencemag.org/content/369/6505/793/suppl/DC1  
Materials and Methods  
Figs. S1 to S8  
Tables S1 to S5  
References (34–44)  
MDAR Reproducibility Checklist

[View/request a protocol for this paper from Bio-protocol.](#)

19 March 2020; accepted 22 June 2020  
10.1126/science.abb8008

## ORGANIC CHEMISTRY

## Divergent synthesis of complex diterpenes through a hybrid oxidative approach

Xiao Zhang<sup>1</sup>, Emma King-Smith<sup>1</sup>, Liao-Bin Dong<sup>1\*</sup>, Li-Cheng Yang<sup>1</sup>, Jeffrey D. Rudolf<sup>1‡</sup>, Ben Shen<sup>1,2</sup>, Hans Renata<sup>1‡</sup>

Polycyclic diterpenes exhibit many important biological activities, but de novo synthetic access to these molecules is highly challenging because of their structural complexity. Semisynthetic access has also been limited by the lack of chemical tools for scaffold modifications. We report a chemoenzymatic platform to access highly oxidized diterpenes by a hybrid oxidative approach that strategically combines chemical and enzymatic oxidation methods. This approach allows for selective oxidations of previously inaccessible sites on the parent carbocycles and enables abiotic skeletal rearrangements to additional underlying architectures. We synthesized a total of nine complex natural products with rich oxygenation patterns and skeletal diversity in 10 steps or less from *ent*-steviol.

The *ent*-kauranes, *ent*-atisanes, and *ent*-trachylobanes (Fig. 1A) are biosynthetically related families of diterpene natural products with wide-ranging biological activities (1). These activities include inhibition of ion channels, signal transduction cascades, and the inflammasome (2–4). The main structural difference between the three natural product families lies in the carbocyclic architecture of their C and D rings: *ent*-kauranes share a common [3.2.1] bicyclic ring system, whereas *ent*-atisanes and *ent*-trachylobanes are characterized by the presence of a [2.2.2] bicycle and [3.2.1.0] tricycle, respectively. These three distinct ring systems are thought to arise from a common precursor (5), *ent*-copalyl pyrophosphate, through several Wagner-Meerwein shifts after initial formation of *ent*-pimaranyl cation (fig. S1). Oxidative tailoring and oxidation-enabled rearrangements could then take place on the minimally oxidized carbocyclic skeleton, contributing to the enormous diversity found in the three natural product families. Despite recent discoveries on terpene syntheses involved in the production of these families (6–8), most of the oxygenases that are responsible for the subsequent tailoring events have yet to be identified. Such limitations have rendered synthetic biology access to these privileged structures difficult.

Owing to their intriguing architectures and promising biological activities, *ent*-kauranes, *ent*-atisanes, and *ent*-trachylobanes have been the subject of many synthetic studies, more commonly through the use of de novo approaches [see (9, 10) for recent reviews and fig. S2 for a full graphical summary]. Semi-

synthetic efforts, although not as popular, have also been pursued, including Mander's pioneering synthesis of 6,7-*seco-ent*-kauranes from gibberellic acid (11) and recent syntheses (12, 13) of atisane-type diterpene alkaloids (e.g., 10, Fig. 1B) and neotripterifordin from steviol. These examples suggest the possibility of developing a more systematic pursuit of highly oxidized *ent*-kauranes from stevioside, which, at \$0.65/g, represents an attractive starting point for synthesis. However, the realization of this concept has been hampered by the lack of useful methods for scaffold modification. As steviol (stevioside aglycone, 9) lacks any appropriate functional handles in its A, B, or C ring, semisynthetic elaborations of the framework have mostly relied on the use of C19 functionality in Hofmann-Löffler-Freytag or Suarez hypiodite reactions (12, 13), which currently only allow modification of the C20 methyl group. Remote chemical oxidation of steviol has remained unexplored, likely because of the incompatibility of its C16–C17 *exo* olefin with C–H oxidation conditions. To the best of our knowledge, such oxidation has only been performed electrochemically (14) on isosteviol ethyl ester (11), an *ent*-beyerane compound lacking any olefin, producing the corresponding C2-keto product. An efficient, remote, and site-selective C–H functionalization toolkit that can act on *ent*-kaurane skeleton would overcome a major roadblock in converting steviol to *ent*-kauranes containing multiple oxidations on their A, B, and/or C rings (e.g., auricuoid I, Fig. 1B). Furthermore, oxidized *ent*-atisanes and *ent*-trachylobanes remain hard to access using semisynthetic approaches because of the need to convert the C and D rings of *ent*-kaurane to those of *ent*-atisane and *ent*-trachylobane in a facile manner (less than five steps).

We have developed a chemoenzymatic synthetic strategy to access a wide array of oxidized *ent*-kauranes, *ent*-atisanes, and *ent*-trachylobanes. A key feature of this strategy is the application

of a hybrid oxidative approach featuring a combination of remote biocatalytic hydroxylations and “guided” C–H oxidation methods (15) to access a variety of oxidation patterns previously unattainable using purely chemical means. In prior applications of C–H functionalization in natural product synthesis, each of these oxidation strategies has been employed independently (16, 17), and our approach illustrates the value in combining them in a synergistic fashion. We also designed a skeletal reorganization sequence toward *ent*-atisane and *ent*-trachylobane frameworks starting from steviol (Fig. 1C), which can enter analogous oxidation series to afford highly decorated members of these families. A total of nine natural product targets were synthesized with high synthetic ideality, as well as redox and step economy, highlighting the enabling nature of our strategy.

## Enzymatic tool development for scaffold modifications

The overarching premise of our synthetic strategy is to identify biocatalytic oxidation methods to address the methodology gap in the selective functionalization of the A, B, and C rings of minimally oxidized *ent*-kaurane, *ent*-atisane, and *ent*-trachylobane skeletons. Each of the newly introduced hydroxyl groups is viewed as a gateway for further manipulations to access many members of these diterpene families through a combination of functional group interconversions and chemical C–H oxidation methods (Fig. 1C). To access the *ent*-atisane and *ent*-trachylobane frameworks, we drew inspiration from the postulated biogenetic relationship between the two and the *ent*-kaurane framework. One hypothesis proposed that they arise from a common carbocation through divergent alkyl/H shifts (5). As such rearrangements could potentially be reversible in nature, we hypothesized that under suitable conditions, an *ent*-beyerane skeleton could be converted to an *ent*-atisane or *ent*-trachylobane product. Synthetic entry into this sequence could be achieved readily through the well-precedented conversion of the *ent*-kaurene stevioside to the *ent*-beyerane isosteviol (18). We postulated that further carbocation generation at C12 would trigger a Wagner-Meerwein rearrangement to an *ent*-atisane product, from which access to the *ent*-trachylobane framework could be realized by C–C bond formation between C13 and C16. After such skeletal reorganization, an array of oxidative transformations on minimally oxidized *ent*-atisane and *ent*-trachylobane skeleton would provide rapid access to targets such as spiramylactone C (5) and the mitrephorones (7, 8).

Successful execution of the aforementioned strategy would thus hinge on the identification of the appropriate enzymes for selective and practical oxidations of the A, B, and C rings of

<sup>1</sup>Department of Chemistry, The Scripps Research Institute, Jupiter, FL 33458, USA. <sup>2</sup>Department of Molecular Medicine, Natural Products Discovery Center at Scripps Research, Jupiter, FL 33458, USA.

\*Present address: School of Traditional Chinese Pharmacy, China Pharmaceutical University, Nanjing, 211198, China.

†Present address: Department of Chemistry, University of Florida, Gainesville, FL 32611, USA.

‡Corresponding author. Email: hrenata@scripps.edu



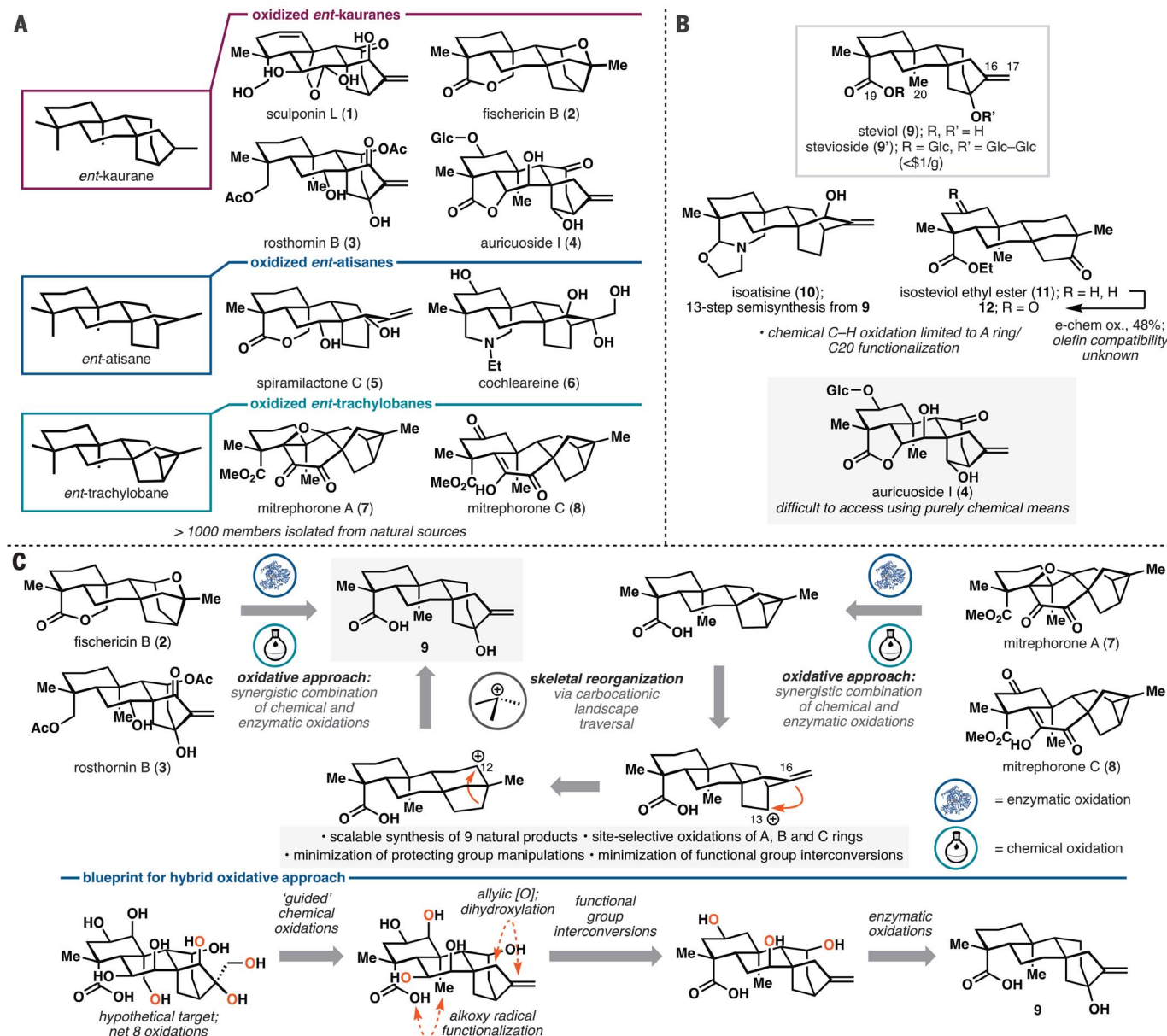


**Fig. 1. Complex *ent*-kaurane, *ent*-atisane, and *ent*-trachylobane diterpenoids.** (A) Selected examples of oxidized *ent*-kauranes, *ent*-atisanes, and *ent*-trachylobanes. Ac, acetyl; Et, ethyl; Glc,  $\beta$ -D-glucopyranosyl; Me, methyl. (B) Limitations of purely chemical C–H oxidation approaches in

steviol-based semisynthesis. e-chem ox., electrochemical oxidation. (C) Retrosynthetic analysis of oxidized *ent*-kauranes, *ent*-atisanes, and *ent*-trachylobanes using a hybrid oxidative approach that combines chemical and enzymatic C–H oxidations.

steviol. Prior investigations in this area (fig. S3) have not resulted in the development of synthetically useful methods. Recent characterization of the platensimycin biosynthesis pathway has revealed the presence of several dedicated *ent*-kaurane hydroxylases for selective C–H oxidations (19, 20). Early in the pathway, a P450 monooxygenase, PtmO5, catalyzes a remote C–H hydroxylation at the C11 position of *ent*-kauranol, followed by an intramolecular cyclization to form the ether bridge. Next, two functionally redundant  $\alpha$ -ketoglutarate-dependent dioxygenases (Fe/ $\alpha$ KGs), PtmO3 and PtmO6, hy-

droxylate the C7 carbon from the  $\beta$  face en route to the construction of the enone functionality of platensimycin. If these enzymes have sufficient substrate promiscuity to accept steviol or *ent*-kaurenoic acid as substrate and could do so with high reaction efficiency, they would comprise ideal biocatalysts for use in our synthetic campaign. PtmO3 and PtmO6 are highly homologous (99% identical). However, the latter was better overproduced upon expression in *Escherichia coli* and was used exclusively in this work. Selective C7 hydroxylation of **9** and **13** could be observed with high total turnover num-

bers (Fig. 2), suggesting this enzyme could be useful for preparative-scale B-ring oxidation of *ent*-kauranes.

Annotated as a class I P450, PtmO5 requires a separate reductase partner to support its function. We have previously employed the CamA and CamB reductase system for the functional characterization of PtmO5 (19) but found that this system gave very low reaction conversion in whole-cell and lysate reactions. This observation prompted us to examine alternative reductase partners. Given prior successes (21, 22), artificial fusion with a reductase

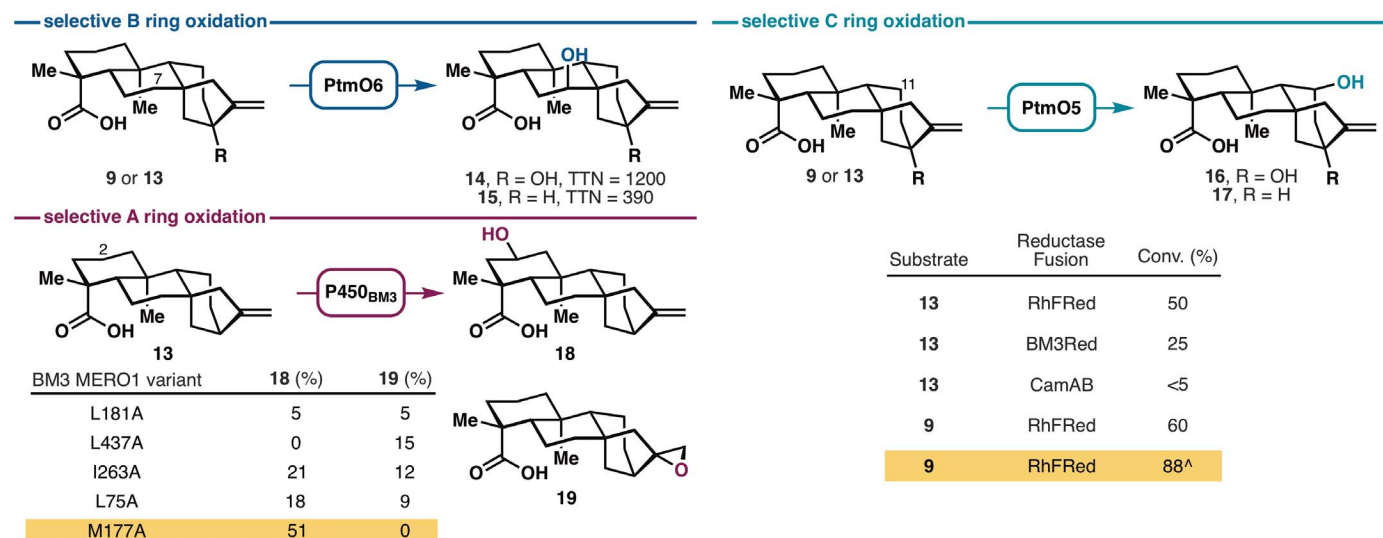


**Fig. 2. Discovery of three enzymes, PtmO6, PtmO5-RhFRed, and BM3 MERO1 M177A, for site-selective oxidations at C7, C11, and C2, respectively.** Plasmid construction (fig. S4) and reaction conditions are in the supplementary materials. <sup>A</sup>Performed by coexpressing PtmO5-RhFRed, Opt13, and GroES and GroEL in a single *E. coli* C41(DE3) strain.

partner were deemed as a particularly viable solution. Among the chimeras tested, PtmO5-RhFRed, generated by linking PtmO5 with the reductase domain of P450<sub>RhF</sub>, provided the most promising outcome in the hydroxylation of **9** and **13**. Further coexpression of PtmO5-RhFRed, GroES and GroEL chaperone, and the phosphite dehydrogenase Opt13 for NADPH (reduced form of nicotinamide adenine dinucleotide phosphate) regeneration in a single *E. coli* C41(DE3) strain allowed selective C11 hydroxylation of **9** to be attained with 88% isolated yield on a preparative scale.

Variants of P450<sub>BM3</sub> have proven to be highly effective biocatalysts for selective oxidations of readily available terpene scaffolds (fig. S5) (**23**), including the A-ring oxidation of decalin-containing terpenes (**24–27**). Furthermore, they have been shown to exhibit exceptional substrate promiscuity and excellent evolvability for new reactions. On the basis of these precedents, we postulated that some of these variants would be capable of performing similar oxidation on **9** or **13**. To test this hypothesis, we conducted preliminary screening of P450<sub>BM3</sub> alanine-scanning variants in our enzyme library (**27**) for the hydroxylation of **9** or **13**. No hydroxylation activity could be observed with **9**, but oxidized product(s) were formed from **13** with some of the variants tested. Variant BM3 MERO1 M177A in particular produced the C2-hydroxylated product **18** selectively without any overoxidation or formation of C16–C17 epoxide side product. These results demonstrate the ready tunability of these oxidation biocatalysts to achieve selective reaction in the presence of other reactive functional group(s), a notable advantage over chemical oxidation methods. This discov-

ery identified a solution for the A-ring oxidation problem.

#### Chemoenzymatic synthesis of oxidized *ent*-kauranes

Preliminary substrate scope examination of PtmO6, PtmO5-RhFRed, and BM3 MERO1 M177A (fig. S6) suggested that they can accept other *ent*-kaurane and *ent*-atisane substrates bearing alternative functional group arrangements. This observation, in combination with the promiscuity of many other bacterial oxygenases (**17, 28**), suggested that they could be useful for divergent synthesis. We initially targeted three *ent*-kauranes that would require the use of only remote B-ring oxidation (Fig. 3): mitrekaurenone (**21**), fujenoic acid (**23**), and pharboside aglycone (**25**). These three molecules contain different oxidation states and stereochemical configurations at C6 and C7, and their divergent synthesis would provide an ideal test bed for the synthetic versatility of biocatalytic oxidation with PtmO6. Steviol (**9**) was first converted to *ent*-kaurenoic acid (**13**) through a two-step protocol involving brominative displacement of the 3° alcohol and radical dehalogenation. The use of PtmO6 on **13** allowed selective installation of a 2° alcohol at C7, delivering the product as a single diastereomer with good conversion and yield. This transformation could be carried out routinely on gram scale using clarified lysate of *E. coli* cells expressing PtmO6. Conversion of alcohol **15** to the corresponding ketone (**20**) was accomplished by treatment with DMP. Introduction of the C6 α-OH of mitrekaurenone would require oxidation from the more hindered face of the skeleton. Thus, a strategy featuring an S<sub>N</sub>2-type displacement of

a β-disposed leaving group at C6 by the C19 acid was pursued. α-Oxidation with pyridinium tribromide was found to elicit simultaneous intramolecular lactonization by the C19 acid, thereby completing the synthesis of **21** in five steps.

To access fujenoic acid (**23**), a net 10-electron oxidation needed to be carried out on the B ring of the scaffold. Chemical methods for α-hydroxy ketone synthesis were initially attempted on **20**, but we found that PtmO6 can install the C6 alcohol with superior yield. Oxidative cleavage of the C6–C7 bond with NaIO<sub>4</sub>, followed by hemiketal oxidation with Dess-Martin Periodinane (DMP), furnished **23** in seven steps from **9**. Pharboside aglycone (**25**), by contrast, contains a β-disposed *syn*-diol motif at C6 and C7. Although **22** could potentially be a viable synthetic intermediate, the conversion of its α-hydroxy ketone functionality to the desired diol motif would require a difficult reduction from the more hindered face. As an alternative, the 2° alcohol of methyl ester **24** was dehydrated to the corresponding olefin with Burgess reagent, thereby allowing the C6,C7 *syn*-diol motif to be introduced by dihydroxylation. The use of OsO<sub>4</sub> and *N*-methylmorpholine *N*-oxide (NMO) simultaneously converted the two olefins to the corresponding *syn*-diol units and completed the synthesis of **25** in six steps from steviol.

Next, we sought to demonstrate the utility of our strategy in the preparation of *ent*-kauranes that contain oxidations on multiple rings (Fig. 4), such as rosthornins B (**3**) and C (**30**) and fischericin B (**2**). These targets were chosen to highlight how multiple enzymatic hydroxylation reactions could be combined together or used strategically in combination with the concept of innate and guided C–H



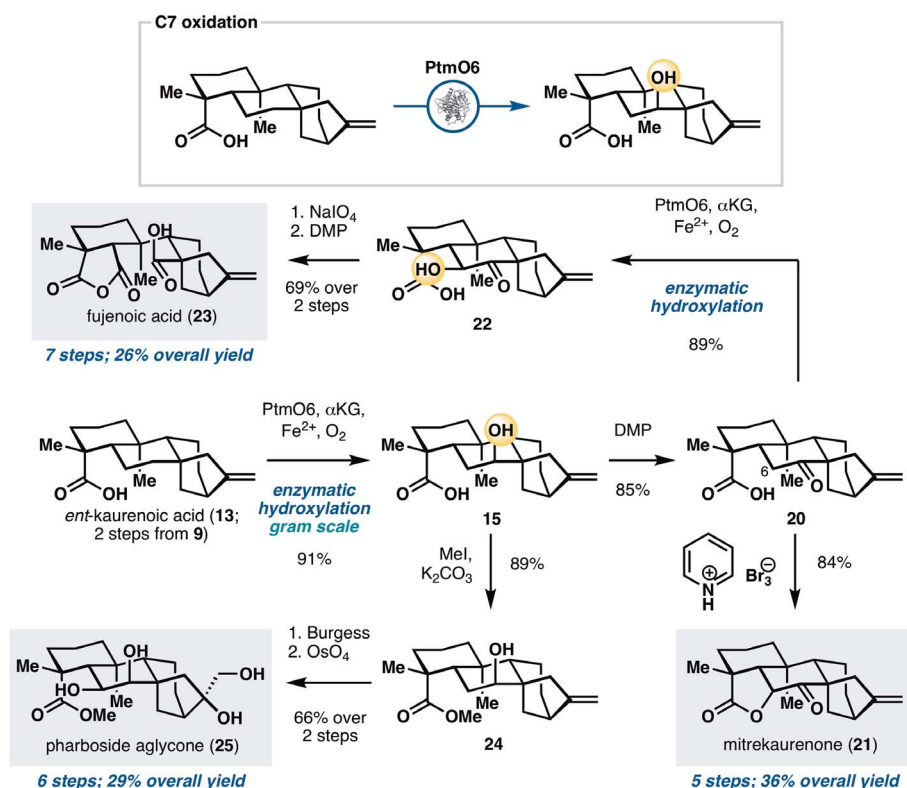


**Fig. 3.** Application of PtmO6 in the chemoenzymatic total synthesis of mitrekaurenone (**21**), fujenoic acid (**23**), and pharposide aglycone (**25**). Reaction conditions are in the supplementary materials.  $\alpha$ KG,  $\alpha$ -ketoglutaric acid; DMP, Dess-Martin Periodinane; MeI, iodomethane; Burgess, methyl *N*-(triethylammoniumsulfonyl)carbamate.

functionalization logic (**15**). Access to **3** and **30** from steviol would require hydroxylation at C7 and C11 with PtmO6 and PtmO5-RhFRed, reduction of the carboxylic acid at C19, and introduction of a carbonyl group at C15. To install the two alcohols at C7 and C11, a strategic decision had to be made in terms of the ordering of the two enzymatic hydroxylation steps. Performing C11 hydroxylation before C7 hydroxylation would necessitate nontrivial differentiation between the two alcohols for subsequent acetylation at C11 and stereochemical inversion at C7. Conversely, oxidation at C7 before that at C11 would allow the use of a carbonyl motif at C7 as a “masking” group for the C7  $\alpha$ -OH and minimize potential chemoselectivity issues in subsequent manipulations. We found that ketone **26**, accessed in two steps from **9** by PtmO6 hydroxylation and pyridinium dichromate (PDC) oxidation, could undergo a regioselective hydroxylation at C11 with PtmO5-RhFRed, albeit with only moderate conversion. Using lysates of *E. coli* expressing PtmO5-RhFRed and OptI3, C11 hydroxylation of **26** could be carried out with 65% isolated yield. The use of  $\text{Ac}_2\text{O}$  and 4-dimethylaminopyridine (DMAP) allowed selective acetylation of the C11 alcohol without any undesired side reaction with the 3° alcohol at C13. At this stage, the C19

carboxylic acid needed to be reduced to the alcohol without concomitant removal of the acetate group at C11. This was achieved by first converting the acid to the corresponding acyl imidazole (**28**), followed by treatment with  $\text{NaBH}_4$ , which also led to concomitant reduction of the C7 ketone to the  $\alpha$ -disposed alcohol. Installation of the enone unit on the D ring by selective C15–OH oxidation with  $\text{SeO}_2$  and 2-iodoxybenzoic acid (IBX) completed the synthesis of rosthornin C (**30**) in seven steps overall. Finally, conversion of **30** to rosthornin B (**3**) could be effected by selective acetylation of the primary alcohol at C19.

Fischericin B (**2**) contains a caged ether motif that is reminiscent of platensimycin and a bridging lactone ring between C19 and C20. Synthesis of **2** would thus provide an opportunity to develop a hybrid strategy that combines enzymatic hydroxylation at C11 and alkoxy radical-based C–H functionalization at C20. Our synthesis commenced with PtmO5-catalyzed C11 hydroxylation of **9**. Using information gleaned from prior biosynthetic studies of platensimycin (**19**), the hydroxylated product could be treated with strong acidic conditions to construct the desired caged ether motif. In the presence of this motif, the C13 tertiary alcohol proved inert to conversion to the cor-

responding bromide for subsequent radical debromination. As a workaround, the free acid of **31** was first methylated and a Barton deoxygenation was performed on its C13 tertiary alcohol. The key hypiodite-mediated C20 functionalization under Suarez conditions (**13**, **29**) cleanly delivered iodoaldehyde **35**, which could be further oxidized and subjected to intramolecular ring closure to complete our synthesis of fischericin B (**2**) in just nine steps.

### Oxidation-enabled skeletal rearrangement to *ent*-atisane and *ent*-trachylobane

Access to minimally oxidized *ent*-atisane and *ent*-trachylobane skeletons commenced from isosteviol (**36**), an *ent*-beyerane available in one step through acid-catalyzed degradation and rearrangement of stevioside (Fig. 5A). Execution of our synthetic blueprint required the installation of a functional group at C12 that is suited for subsequent carbocation generation. We envisioned first C11 hydroxylation of **36** with PtmO5-RhFRed, followed by a C11-to-C12 transposition of the resulting alcohol. Hydroxylation of isosteviol with PtmO5-RhFRed unexpectedly proceeded at its C12 carbon instead of C11, thereby obviating the need for any further functional group interconversions. Furthermore, this reaction proceeded with high conversion and yield and could be carried out routinely on a multigram scale in a single pass. The unexpected switch in regioselectivity could be rationalized by the difference in C-ring conformation of *ent*-kaurane and *ent*-beyerane. PtmO5 oxidizes the axial C11  $\beta$ -H of its native substrate. By contrast, the equivalent C11  $\beta$ -H on **36** adopts an equatorial configuration and is therefore inaccessible for abstraction by the active Fe(IV)-oxo species. Instead, C–H abstraction takes place at the adjacent axial C12  $\beta$ -H. Treatment of **37** with trifluoromethanesulfonic acid ( $\text{TfOH}$ ) initiated the intended Wagner–Meerwein rearrangement, delivering **38**, which contains the requisite *ent*-atisane [2.2.2] C- and D-ring bicycle. Access to *ent*-trachylobane skeleton from **38** required the formation of a new C–C bond between C13 and C16. Examination of several different methods (**30**) to forge this bond led to the discovery of a reductive rearrangement in the presence of boron trifluoride diethyl etherate ( $\text{BF}_3 \cdot \text{Et}_2\text{O}$ ) and triethylsilane ( $\text{Et}_3\text{SiH}$ ), which afforded an *ent*-trachylobane product **40** from **39** in 61% yield after recycling three times. We propose that this rearrangement proceeds by means of ionization of C13 alcohol, followed by formation of a nonclassical carbocation and selective reductive quenching at C15. Overall, this synthetic sequence provides rapid and controlled access to *ent*-atisane and *ent*-trachylobane frameworks from isosteviol in two and four steps, respectively, and is made possible by the use of PtmO5-catalyzed hydroxylation of **36**.

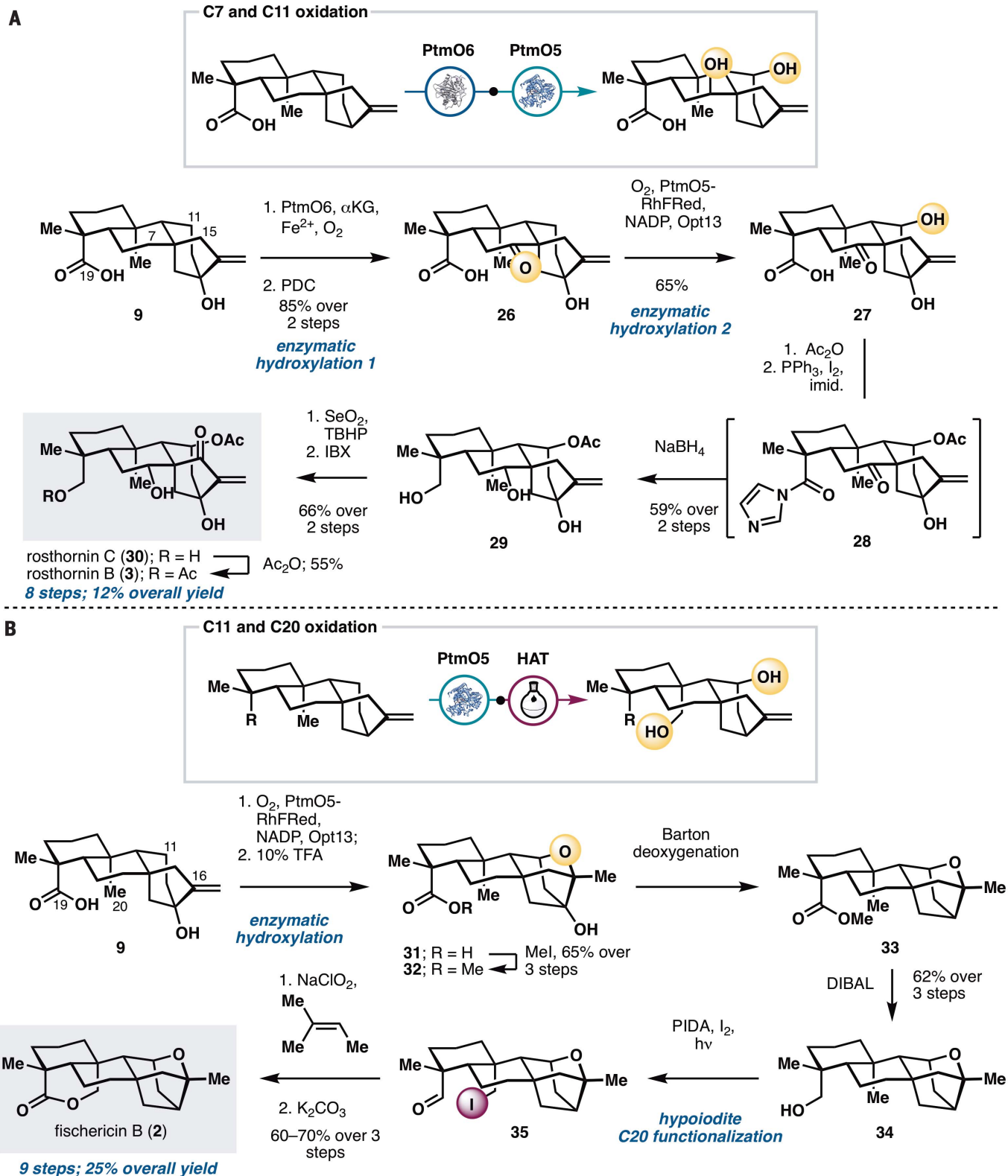


**Fig. 4. Application of PtmO5-RhFRed in the chemoenzymatic total synthesis of rosthornins B (3) and C (30) and fischericin B (2).**

(A and B) Reaction conditions are in the supplementary materials. PDC, pyridinium dichromate; Ac<sub>2</sub>O, acetic anhydride; PPh<sub>3</sub>,

triphenylphosphine; imid., imidazole; TBHP, *tert*-butyl hydrogen peroxide; IBX, 2-iodoxybenzoic acid; HAT, hydrogen atom transfer; TFA, trifluoroacetic acid; DIBAL, diisobutyl aluminum hydride; PIDA, phenyliodine(III) diacetate.



Preliminary investigation suggests that **38**, bearing high structural resemblance to the native *ent*-atiserenoic acid precursor of plantensin (**6**, **20**), is a useful intermediate for accessing more oxidized *ent*-atisanes through

enzymatic hydroxylation (Fig. 5B). It can undergo oxidation at C7 with PtmO6 and is hydroxylated in a more efficient fashion than its C13-deoxy counterpart. Wolff-Kishner deoxygenation of C13 ketone and PDC oxidation of

C7-OH afforded ketone **42**, which represents a potential intermediate toward spiramylactone C (**5**). In an alternative sequence, **38** could first be oxidized at C2 with BM3 MERO1 M177A to acid **43** without any observable epoxidation

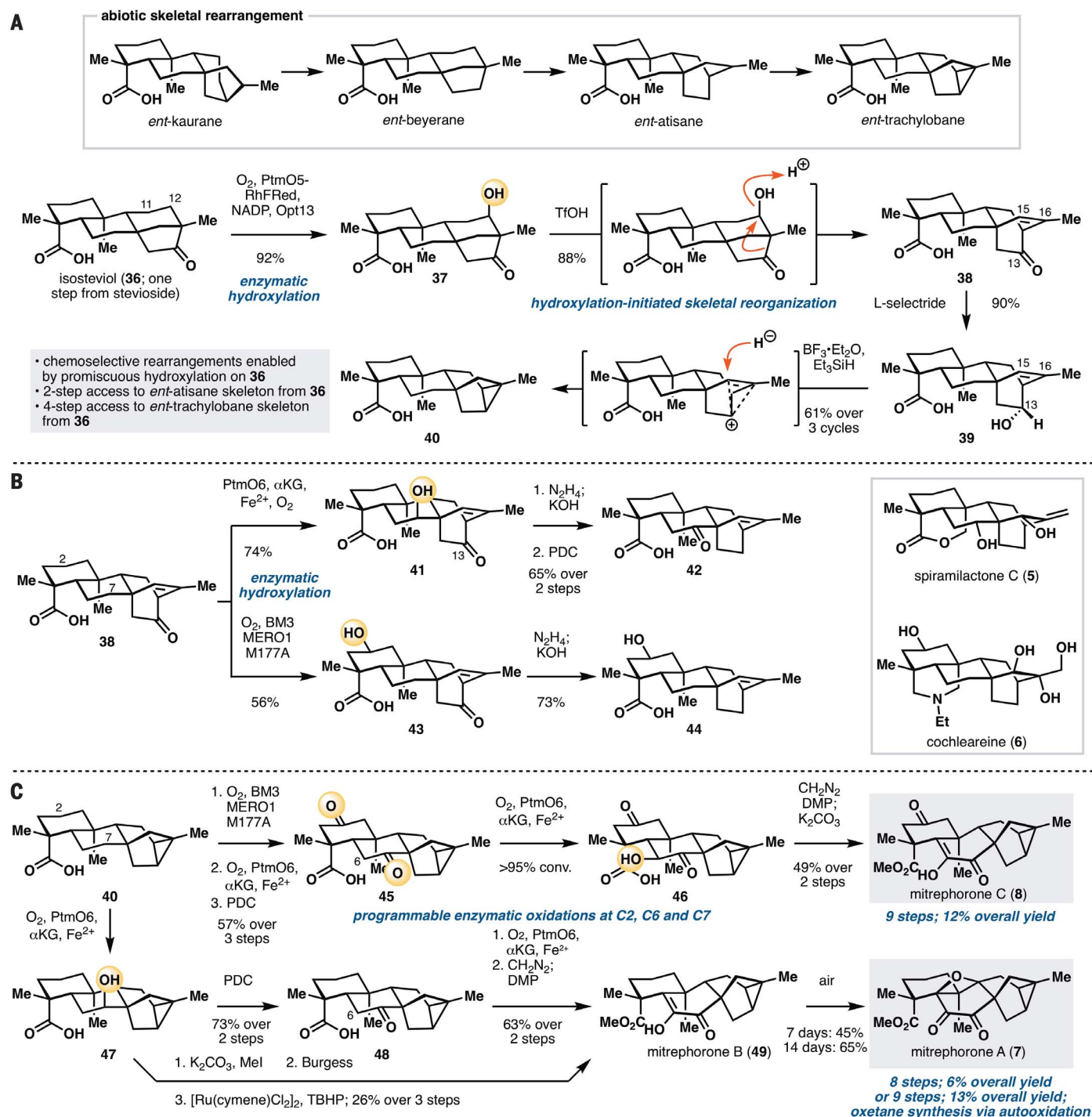


**Fig. 5. Chemoenzymatic synthesis of complex *ent*-atisanes and *ent*-trachylobanes through abiotic skeletal rearrangement and hybrid oxidative approach.**

(A) Conversion of isosteviol (**36**) to *ent*-atisane and *ent*-trachylobane products by site-selective C12 hydroxylation and carbocationic rearrangements. (B) Further

site-selective oxidations of **38** using PtmO6 and BM3 MERO1 M177A. **(C)** Divergent chemoenzymatic total synthesis of the mitrephorones starting from **40**. Reaction conditions are in the supplementary materials. TfoH, trifluoromethanesulfonic acid; BF<sub>3</sub>•Et<sub>2</sub>O, boron trifluoride diethyl etherate; Et<sub>3</sub>SiH, triethylsilane.

of its C15–C16 olefin. Wolff–Kishner reduction delivered **44**, which has the appropriate functionalities to be converted to the diterpenoid alkaloid cochleareine (**6**).

### Chemoenzymatic synthesis of the mitrephorones

Intermediate **40** could be used to divergently prepare mitrephorones A, B, and C (**7**, **49**, **8**) (Fig. 5C). In accord with its structural similarity to **9** or **13**, C2 oxidation of **40** with BM3 MERO1 M177A proceeded very efficiently. At high enough enzyme-to-substrate ratio, this process also led to iterative oxidation to install a ketone moiety at C2. Enzymatic oxidation with PtmO6, followed by PDC oxidation, furnished diketone **45**. As is the case with fujenoic acid (**27**), PtmO6 was capable of installing C6-OH on **45**. Intermediate **46** proved to be unstable, requiring rapid methylation of the C19 acid and mild oxidation at C6. Thus, the synthesis of mitrephorone C (**8**) was completed by methylation of the C19 acid with CH<sub>2</sub>N<sub>2</sub> and by further oxidation at C6 with DMP, followed by keto-enol tautomerization.

Synthesis of mitrephorone B (**49**) from **40** commenced by C7 enzymatic oxidation with PtmO6. Initial attempts focused on the dehydration of the C7-OH to the corresponding olefin, followed by a ruthenium-catalyzed direct oxidation (**31**) to install the C6–C7 dione moiety. However, this sequence was found to be low yielding and accompanied by formation of side-products, even at low conversion. Moreover, this sequence provided no desired product at all when the C2 carbon exists in the ketone oxidation state (for the mitrephorone C series). As a workaround, **40** was oxidized to the corresponding ketone (**48**), enzymatically hydroxylated at C6 with PtmO6, and then methylated and oxidized with PDC. Although this route led to one more step than the dehydration and oxidation sequence, it provided a superior overall yield. According to Magauer's report (**32**), conversion of **49** to mitrephorone A (**7**) could be achieved through the use of electrochemical oxidation or White-Chen catalyst. We found serendipitously that **49** is capable of undergoing a slow autooxidation to form **7** (45% yield after 7 days or 65% yield after 14 days). Such autooxidation did not take place with **8**, suggesting that distal substituents are capable of modulating the reactivity of the diosphenol motif of **49**. This discovery allowed us to divergently prepare the entire known family members of the mitrephorones from **40**. The use of enzymatic oxidations with PtmO5–RhFRed, PtmO6, and BM3 MERO1 M177A proved to be highly enabling, as all three members of the family could be prepared in less than 10 steps, a marked

improvement over previous routes to the mitrephorones (**32**, **33**).

### Conclusion

Using this chemoenzymatic strategy, we prepared nine highly oxidized *ent*-kaurane and *ent*-trachylobane natural products in less than 10 steps each. Central to this strategy is the use of three selective and scalable biocatalytic processes that are able to hydroxylate the A, B, and C rings of the parent carbocyclic structures with site selectivity and functional group compatibility unmatched by any known small-molecule reagents or catalysts. Leveraging the newly introduced hydroxyl groups in a series of carbocationic rearrangements enables rapid traversal of the diterpene landscape spanning the *ent*-kaurane, *ent*-atisane, and *ent*-trachylobane families. By virtue of the substrate promiscuity of the enzymes, the biocatalytic oxidations can also be carefully permuted and used in conjunction with chemical C–H oxidations in multistep synthetic sequences for streamlined access to complex natural products with minimal functional group interconversions and protecting group manipulations (**34**). The marriage of chemical and enzymatic C–H oxidations, in particular, constitutes a powerful means to streamline access to highly oxidized terpenes and avoids circuitous oxidative transformations, which are at times necessary in the “two-phase” strategy for terpene synthesis (**35**) owing to the exclusive use of small-molecule reagents or catalysts. The strategy outlined here not only opens the door for rapid access to a wide array of *ent*-kauranes, *ent*-atisanes, and *ent*-trachylobanes but also provides a blueprint for combining emerging synthetic paradigms with biocatalysis in the preparation of privileged molecular scaffolds. Generalization of this hybrid oxidative approach to other complex terpene families can be readily envisioned by way of identifying and profiling new oxygenases for site-selective modifications of building blocks (**36**) or late-stage functionalization (**37**). Finally, continued advancement in enzyme engineering strategies (**38**) and the development of new-to-nature transformations (**39**) will further expand the pool of reactions available for use and ultimately encourage broader adoption of this strategy in multistep synthesis.

### REFERENCES AND NOTES

- M. Liu, W.-G. Wang, H.-D. Sun, J.-X. Pu, *Nat. Prod. Rep.* **34**, 1090–1140 (2017).
- J. Friese et al., *Eur. J. Pharmacol.* **337**, 165–174 (1997).
- Y.-J. Liao et al., *Cell Death Dis.* **5**, e1137 (2014).
- H. He et al., *Nat. Commun.* **9**, 2550 (2018).
- Y. J. Hong, D. J. Tantillo, *J. Am. Chem. Soc.* **132**, 5375–5386 (2010).
- M. J. Smanski et al., *Proc. Natl. Acad. Sci. U.S.A.* **108**, 13498–13503 (2011).

- A. J. Jackson, D. M. Hershey, T. Chesnut, M. Xu, R. J. Peters, *Phytochemistry* **103**, 13–21 (2014).
- B. Jin et al., *Plant Physiol.* **174**, 943–955 (2017).
- P. S. Riehl, Y. C. DePorre, A. M. Armaly, E. J. Groso, C. S. Schindler, *Tetrahedron* **71**, 6629–6650 (2015).
- K. E. Lazarski, B. J. Moritz, R. J. Thomson, *Angew. Chem. Int. Ed.* **53**, 10588–10599 (2014).
- M. J. Kenny, L. N. Mander, S. P. Sethi, *Tetrahedron Lett.* **27**, 3927–3930 (1986).
- E. C. Cherney, J. M. Lopchuk, J. C. Green, P. S. Baran, *J. Am. Chem. Soc.* **136**, 12592–12595 (2014).
- S. Kobayashi et al., *J. Org. Chem.* **83**, 1606–1613 (2018).
- Y. Kawamata et al., *J. Am. Chem. Soc.* **139**, 7448–7451 (2017).
- T. Brückl, R. D. Baxter, Y. Ishihara, P. S. Baran, *Acc. Chem. Res.* **45**, 826–839 (2012).
- K. Hung et al., *J. Am. Chem. Soc.* **141**, 3083–3099 (2019).
- A. N. Lowell et al., *J. Am. Chem. Soc.* **139**, 7913–7920 (2017).
- O. E. Hutt, T. L. Doan, G. I. Georg, *Org. Lett.* **15**, 1602–1605 (2013).
- J. D. Rudolf, L.-B. Dong, X. Zhang, H. Renata, B. Shen, *J. Am. Chem. Soc.* **140**, 12349–12353 (2018).
- L.-B. Dong et al., *J. Am. Chem. Soc.* **141**, 4043–4050 (2019).
- S. Li, L. M. Podust, D. H. Sherman, *J. Am. Chem. Soc.* **129**, 12940–12941 (2007).
- C. Lu et al., *ACS Catal.* **8**, 5794–5798 (2018).
- C. J. C. Whitehouse, S. G. Bell, L.-L. Wong, *Chem. Soc. Rev.* **41**, 1218–1260 (2012).
- J. C. Lewis et al., *ChemBioChem* **11**, 2502–2505 (2010).
- S. Kille, F. E. Zilly, J. P. Acevedo, M. T. Reetz, *Nat. Chem.* **3**, 738–743 (2011).
- K. Zhang, S. El Damaty, R. Fasan, *J. Am. Chem. Soc.* **133**, 3242–3245 (2011).
- J. Li, F. Li, E. King-Smith, H. Renata, *Nat. Chem.* **12**, 173–179 (2020).
- J. J. Schmidt et al., *ACS Chem. Biol.* **15**, 524–532 (2020).
- W. Yu, P. Hjerrild, J. Overgaard, T. B. Poulsen, *Angew. Chem. Int. Ed.* **55**, 8294–8298 (2016).
- R. B. Kelly, B. A. Beckett, J. Eber, H.-K. Hung, J. Zamecnik, *Can. J. Chem.* **53**, 143–147 (1975).
- S. Kawamura, H. Chu, J. Felding, P. S. Baran, *Nature* **532**, 90–93 (2016).
- L. A. Wein, K. Wurst, P. Angyal, L. Weisheit, T. Magauer, *J. Am. Chem. Soc.* **141**, 19589–19593 (2019).
- M. J. R. Richter, M. Schneider, M. Brandstätter, S. Krautwald, E. M. Carreira, *J. Am. Chem. Soc.* **140**, 16704–16710 (2018).
- T. Gaich, P. S. Baran, *J. Org. Chem.* **75**, 4657–4673 (2010).
- Y. Kanda et al., *J. Am. Chem. Soc.* **142**, 10526–10533 (2020).
- A. Hernandez-Ortega, M. Vinaixa, Z. Zebec, E. Takano, N. S. Scrutton, *Sci. Rep.* **8**, 14396 (2018).
- B. Hong, T. Luo, X. Lei, *ACS Cent. Sci.* **6**, 622–635 (2020).
- S. Galanie, D. Entwistle, J. Lalonde, *Nat. Prod. Rep.* (2020).
- K. Chen, F. H. Arnold, *Nat. Catal.* **3**, 203–213 (2020).

### ACKNOWLEDGMENTS

We thank P. S. Baran, R. A. Shenivi, T. J. Maimone, and K. M. Engle for useful discussions. **Funding:** This work is supported, in part, by the National Institutes of Health Grant GM134954 (B.S.), GM128895 (H.R.), and GM124461 (J.D.R.). **Author contributions:** X.Z. and H.R. conceived of the work. X.Z., E.K.-S., L.-B.D., L.-C.Y., and J.D.R. designed and executed experiments. B.S. and H.R. provided insight and direction for experimental design. **Competing interests:** PtmO3, PtmO5, and PtmO6 are gene products of the platensimycin and platencin biosynthetic gene cluster included in U.S. patent no. 8,652,838, for which B.S. is a patent holder. **Data and materials availability:** All data are available in the main text or the supplementary materials.

### SUPPLEMENTARY MATERIALS

science.sciencemag.org/content/369/6505/799/suppl/DC1  
Materials and Methods  
Figs. S1 to S7  
Tables S1 to S19  
References (40–59)  
MDAR Reproducibility Checklist  
Spectral Data

20 March 2020; accepted 19 June 2020  
10.1126/science.abb8271



## CORONAVIRUS

# DNA vaccine protection against SARS-CoV-2 in rhesus macaques

Jingyou Yu<sup>1\*</sup>, Lisa H. Tostanoski<sup>1\*</sup>, Lauren Peter<sup>1\*</sup>, Noe B. Mercado<sup>1\*</sup>, Katherine McMahan<sup>1\*</sup>, Shant H. Mahrokhian<sup>1\*</sup>, Joseph P. Nkolola<sup>1\*</sup>, Jinyan Liu<sup>1\*</sup>, Zhenfeng Li<sup>1\*</sup>, Abishek Chandrashekar<sup>1\*</sup>, David R. Martinez<sup>2</sup>, Carolin Loos<sup>3</sup>, Caroline Atyeo<sup>3</sup>, Stephanie Fischinger<sup>3</sup>, John S. Burke<sup>3</sup>, Matthew D. Slein<sup>3</sup>, Yuezhou Chen<sup>4</sup>, Adam Zuiani<sup>4</sup>, Felipe J. N. Lelis<sup>4</sup>, Meghan Travers<sup>4</sup>, Shaghayegh Habibi<sup>4</sup>, Laurent Pessaint<sup>5</sup>, Alex Van Ry<sup>5</sup>, Kelvin Blade<sup>5</sup>, Renita Brown<sup>5</sup>, Anthony Cook<sup>5</sup>, Brad Finneyrock<sup>5</sup>, Alan Dodson<sup>5</sup>, Elyse Teow<sup>5</sup>, Jason Velasco<sup>5</sup>, Roland Zahn<sup>6</sup>, Frank Wegmann<sup>6</sup>, Esther A. Bondzie<sup>1</sup>, Gabriel Dagotto<sup>1</sup>, Makda S. Gebre<sup>1</sup>, Xuan He<sup>1</sup>, Catherine Jacob-Dolan<sup>1</sup>, Maritela Kirilova<sup>1</sup>, Nicole Kordana<sup>1</sup>, Zijin Lin<sup>1</sup>, Lori F. Maxfield<sup>1</sup>, Felix Nampunya<sup>1</sup>, Ramya Nityanandam<sup>1</sup>, John D. Ventura<sup>1</sup>, Huahua Wan<sup>1</sup>, Yongfei Cai<sup>7</sup>, Bing Chen<sup>7,8</sup>, Aaron G. Schmidt<sup>3,8</sup>, Duane R. Wesemann<sup>4,8</sup>, Ralph S. Baric<sup>2</sup>, Galit Alter<sup>3,8</sup>, Hanne Andersen<sup>5</sup>, Mark G. Lewis<sup>5</sup>, Dan H. Barouch<sup>1,3,8†</sup>

The global coronavirus disease 2019 (COVID-19) pandemic caused by severe acute respiratory syndrome coronavirus 2 (SARS-CoV-2) has made the development of a vaccine a top biomedical priority. In this study, we developed a series of DNA vaccine candidates expressing different forms of the SARS-CoV-2 spike (S) protein and evaluated them in 35 rhesus macaques. Vaccinated animals developed humoral and cellular immune responses, including neutralizing antibody titers at levels comparable to those found in convalescent humans and macaques infected with SARS-CoV-2. After vaccination, all animals were challenged with SARS-CoV-2, and the vaccine encoding the full-length S protein resulted in >3.1 and >3.7 log<sub>10</sub> reductions in median viral loads in bronchoalveolar lavage and nasal mucosa, respectively, as compared with viral loads in sham controls. Vaccine-elicited neutralizing antibody titers correlated with protective efficacy, suggesting an immune correlate of protection. These data demonstrate vaccine protection against SARS-CoV-2 in nonhuman primates.

**T**he coronavirus disease 2019 (COVID-19) pandemic has made the development of a safe, effective, and deployable vaccine to protect against infection with severe acute respiratory syndrome coronavirus 2

(SARS-CoV-2) a critical global priority (1–8). Our current understanding of immune correlates of protection against SARS-CoV-2 is limited but will be essential to enable the development of SARS-CoV-2 vaccines and

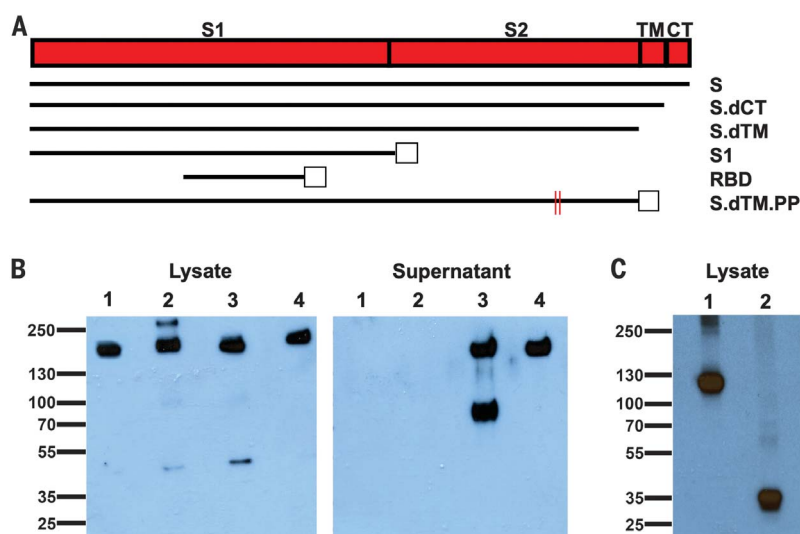
other immunotherapeutic interventions. To facilitate the preclinical evaluation of vaccine candidates, we recently developed a rhesus macaque model of SARS-CoV-2 infection (9). In the present study, we constructed a set of prototype DNA vaccines expressing various forms of the SARS-CoV-2 spike (S) protein and assessed their immunogenicity and protective efficacy against SARS-CoV-2 viral challenge in rhesus macaques.

## Construction and immunogenicity of DNA vaccine candidates

We produced a series of prototype DNA vaccines expressing six variants of the SARS-CoV-2 S protein: (i) full length (S), (ii) deletion of the cytoplasmic tail (S.dCT) (10), (iii) deletion of the transmembrane domain and cytoplasmic tail reflecting the soluble ectodomain (S.dTM) (10), (iv) S1 domain with a foldon trimerization tag (S1), (v) receptor-binding domain with a foldon trimerization tag (RBD), and (vi) a prefusion-stabilized soluble ectodomain with deletion of the furin cleavage site, two proline mutations, and a foldon trimerization tag (S.dTM.PP) (11–13) (Fig. 1A). Western blot analyses confirmed expression in cell lysates for all constructs and in culture supernatants for the soluble S.dTM and S.dTM.PP constructs (Fig. 1, B and C). Proteolytic cleavage of the secreted protein was noted for S.dTM but not S.dTM.PP, presumably as a result of mutation of the furin cleavage site in S.dTM.PP.

We immunized 35 adult rhesus macaques (6 to 12 years old) with DNA vaccines in the following groups: S (N = 4), S.dCT (N = 4), S.dTM (N = 4), S1 (N = 4), RBD (N = 4), S.dTM.

**Fig. 1. Construction of candidate DNA vaccines against SARS-CoV-2.** (A) Six DNA vaccines were produced expressing different SARS-CoV-2 spike (S) variants: (i) full length (S), (ii) deletion of the cytoplasmic tail (S.dCT), (iii) deletion of the transmembrane (TM) domain and cytoplasmic tail (CT) reflecting the soluble ectodomain (S.dTM), (iv) S1 domain with a foldon trimerization tag (S1), (v) receptor-binding domain with a foldon trimerization tag (RBD), and (vi) prefusion-stabilized soluble ectodomain with deletion of the furin cleavage site, two proline mutations, and a foldon trimerization tag (S.dTM.PP). Open squares depict foldon trimerization tags; red lines depict proline mutations. (B) Western blot analyses for expression from DNA vaccines encoding S (lane 1), S.dCT (lane 2), S.dTM (lane 3), and S.dTM.PP (lane 4) in cell lysates and culture supernatants using an anti-SARS polyclonal antibody (BEI Resources). (C) Western blot analyses for expression from DNA vaccines encoding S1 (lane 1) and RBD (lane 2) in cell lysates using an anti-SARS-CoV-2 RBD polyclonal antibody (Sino Biological).



<sup>1</sup>Center for Virology and Vaccine Research, Beth Israel Deaconess Medical Center, Harvard Medical School, Boston, MA 02215, USA. <sup>2</sup>Department of Epidemiology, University of North Carolina at Chapel Hill, Chapel Hill, NC 27599, USA. <sup>3</sup>Ragon Institute of MGH, MIT, and Harvard, Cambridge, MA 02139, USA. <sup>4</sup>Brigham and Women's Hospital, Harvard Medical School, Boston, MA 02115, USA. <sup>5</sup>Bioqual, Rockville, MD 20852, USA. <sup>6</sup>Janssen Vaccines & Prevention BV, Leiden, Netherlands. <sup>7</sup>Children's Hospital, Boston, MA 02115, USA. <sup>8</sup>Massachusetts Consortium on Pathogen Readiness, Boston, MA 02215, USA.

\*These authors contributed equally to this work.

†Corresponding author. Email: dbarouch@bidmc.harvard.edu

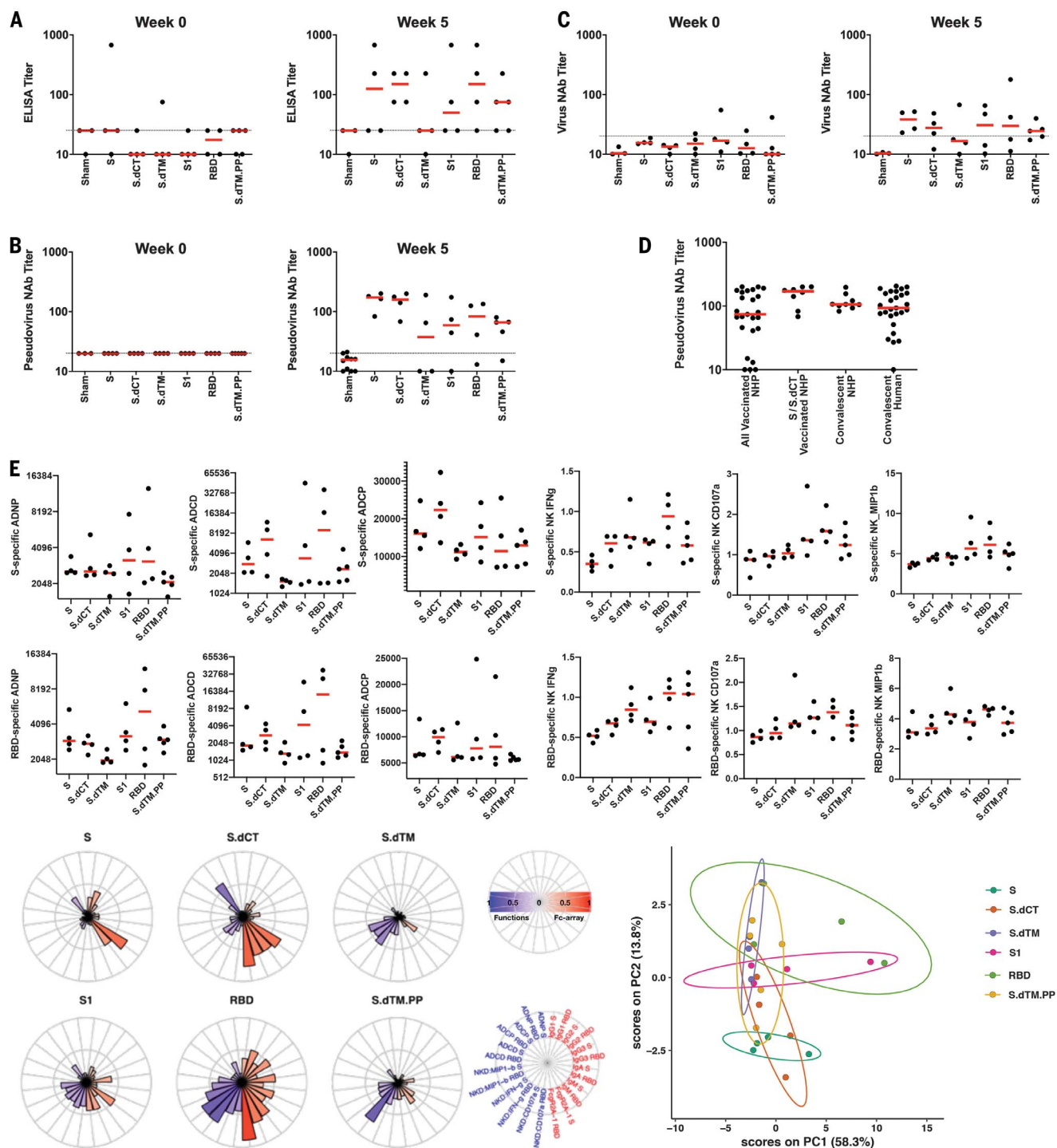


**Fig. 2. Humoral immune responses in vaccinated rhesus macaques.** (A to C) Humoral immune responses were assessed after immunization by (A) binding antibody ELISA, (B) pseudovirus neutralization assays, and (C) live virus neutralization assays. (D) Comparison of pseudovirus neutralization titers in vaccinated macaques (all animals as well as the S and S.dCT groups), a cohort of 9 convalescent macaques, and a cohort of 27 convalescent humans from Boston, United States, who had recovered from SARS-CoV-2 infection. NHP, nonhuman primates. (E) S- and RBD-specific antibody-dependent neutrophil phagocytosis (ADNP), antibody-dependent complement deposition (ADCD), antibody-dependent monocyte cellular phagocytosis (ADPCP), and antibody-

dependent NK cell activation (IFN- $\gamma$  secretion, CD107a degranulation, and MIP-1b expression) are shown. Radar plots show the distribution of antibody features across the vaccine groups. The size and color intensity of the wedges indicate the median of the feature for the corresponding group (blue depicts antibody functions; red depicts antibody isotype, subclass, and Fc $\gamma$ R binding). The principal components analysis (PCA) plot shows the multivariate antibody profiles across groups. Each dot represents an animal, the color of the dot denotes the group, and the ellipses show the distribution of the groups as 70% confidence levels assuming a multivariate normal distribution. In the dot plots above, red bars reflect median responses, and dotted lines reflect assay limits of quantitation.



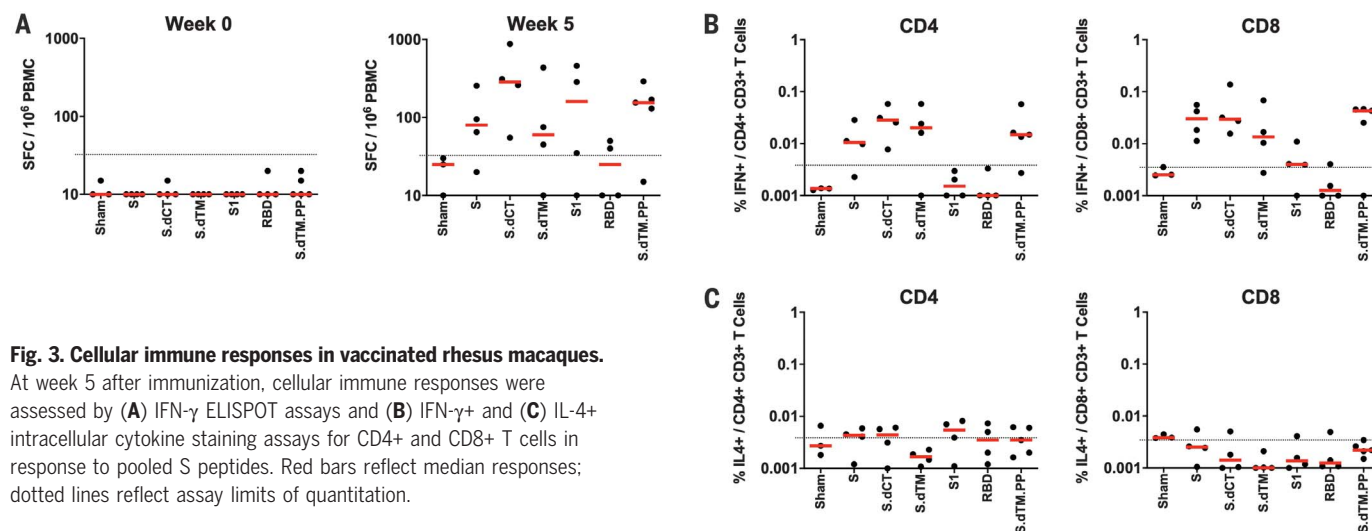


**Fig. 3. Cellular immune responses in vaccinated rhesus macaques.**

At week 5 after immunization, cellular immune responses were assessed by (A) IFN-γ ELISPOT assays and (B) IFN-γ+ and (C) IL-4+ intracellular cytokine staining assays for CD4+ and CD8+ T cells in response to pooled S peptides. Red bars reflect median responses; dotted lines reflect assay limits of quantitation.

PP ( $N = 5$ ), and sham controls ( $N = 10$ ). Animals received 5-mg DNA vaccines by the intramuscular route without adjuvant at weeks 0 and 3. After the boost immunization at week 5, we observed S-specific binding antibodies by enzyme-linked immunosorbent assay (ELISA) (Fig. 2A) and neutralizing antibodies (NABs) by both a pseudovirus neutralization assay (10) (Fig. 2B) and a live virus neutralization assay (14, 15) (Fig. 2C). As determined by ELISA, two animals had binding antibodies at baseline, which might reflect cross-reactivity of other natural primate coronaviruses. NAb titers measured by the pseudovirus neutralization assay correlated with NAb titers measured by the live virus neutralization assay ( $P < 0.0001$ ,  $R = 0.8052$ , two-sided Spearman rank-correlation test; fig. S1). Moreover, NAb titers in the vaccinated macaques (median titer = 74; median titer in the S and S.dCT groups = 170) were comparable in magnitude to NAb titers in a cohort of 9 convalescent macaques (median titer = 106) and a cohort of 27 convalescent humans (median titer = 93) who had recovered from SARS-CoV-2 infection (Fig. 2D).

S-specific and RBD-specific antibodies in the vaccinated macaques included diverse subclasses and effector functions, including antibody-dependent neutrophil phagocytosis (ADNP), antibody-dependent complement deposition (ADCD), antibody-dependent monocyte cellular phagocytosis (ADCP), and antibody-dependent natural killer (NK) cell activation [interferon-γ (IFN-γ) secretion, CD107a degranulation, and MIP-1β expression] (16) (Fig. 2E). A trend toward higher ADCD responses was observed in the S and S.dCT groups, whereas higher NK cell activation was observed in the RBD and S.dTM.PP groups. A principal components analysis of the functional and biophysical antibody features showed overlap of the different vaccine groups,

with more distinct profiles in the S and RBD groups (Fig. 2E).

We also observed cellular immune responses to pooled S peptides in most vaccinated animals by IFN-γ enzyme-linked immunosorbent spot (ELISPOT) assays at week 5 (Fig. 3A). Intracellular cytokine staining assays at week 5 demonstrated induction of S-specific IFN-γ+ CD4+ and CD8+ T cell responses, with lower responses induced by the shorter S1 and RBD immunogens (Fig. 3B). S-specific IL-4+ CD4+ and CD8+ T cell responses were marginal (Fig. 3C), suggesting induction of T helper 1 ( $T_H1$ )-biased cellular immune responses.

### Protective efficacy against SARS-CoV-2 challenge

At week 6, which was 3 weeks after the boost immunization, all animals were challenged with  $1.2 \times 10^8$  virus particles (VPs) [ $1.1 \times 10^4$  plaque-forming units (PFUs)] of SARS-CoV-2, administered as 1 ml by the intranasal route and 1 ml by the intratracheal route. After challenge, we assessed viral RNA levels by reverse transcription polymerase chain reaction (17) in bronchoalveolar lavage (BAL) and nasal swabs (NS). Viral RNA was negative in plasma, and animals exhibited only mild clinical symptoms. High levels of viral RNA were observed in the sham controls, with a median peak of 6.46 (range = 4.81 to 7.99)  $\log_{10}$  RNA copies/ml in BAL and a median peak of 6.82 (range = 5.96 to 7.96)  $\log_{10}$  RNA copies/swab in NS (fig. S2). Lower levels of viral RNA were observed in the vaccine groups (figs. S3 and S4), including 1.92 and 2.16  $\log_{10}$  reductions of median peak viral RNA in BAL and NS, respectively, in S-vaccinated animals compared with sham controls ( $P = 0.02$  and  $0.04$ , two-sided Mann-Whitney tests) (fig. S5). Viral RNA assays were confirmed by PFU assays, which similarly showed lower infectious virus titers

in S-vaccinated animals compared with sham controls ( $P = 0.04$ , two-sided Mann-Whitney test) (fig. S5).

We speculated that a substantial fraction of viral RNA in BAL and NS after challenge represented input challenge virus. Therefore, we also assessed levels of subgenomic mRNA (sgmRNA), which are believed to reflect viral replication cellular intermediates that are not packaged into virions, and thus putative replicating virus in cells (18). High levels of sgmRNA were observed in the sham controls (Fig. 4A) with a median peak of 5.35 (range = 3.97 to 6.95)  $\log_{10}$  sgmRNA copies/ml in BAL and 6.40 (range = 4.91 to 7.01)  $\log_{10}$  sgmRNA copies per swab in NS. Peak viral loads occurred variably on days 1 to 4 after challenge. Markedly lower levels of sgmRNA were observed in the vaccine groups (Fig. 4, B and C), including  $>3.1$  and  $>3.7$   $\log_{10}$  decreases of median peak sgmRNA in BAL and NS, respectively, in S-vaccinated animals compared with sham controls ( $P = 0.03$  and  $0.01$ , two-sided Mann-Whitney tests) (Fig. 4D). Reduced levels of sgmRNA were also observed in other vaccine groups, including S.dCT, S1, RBD, and S.dTM.PP, although minimal to no protection was seen in the S.dTM group, confirming the importance of prefusion ectodomain stabilization, as reported previously (13). Protection was generally more robust in BAL compared with NS, particularly for the less immunogenic constructs. A total of 8 of 25 vaccinated animals exhibited no detectable sgmRNA in BAL and NS at any time point after challenge.

### Immune correlates of vaccine-induced protection

The variability in protective efficacy in this study facilitated an analysis of immune correlates of protection. The  $\log_{10}$  pseudovirus NAb titer at week 5 inversely correlated with peak

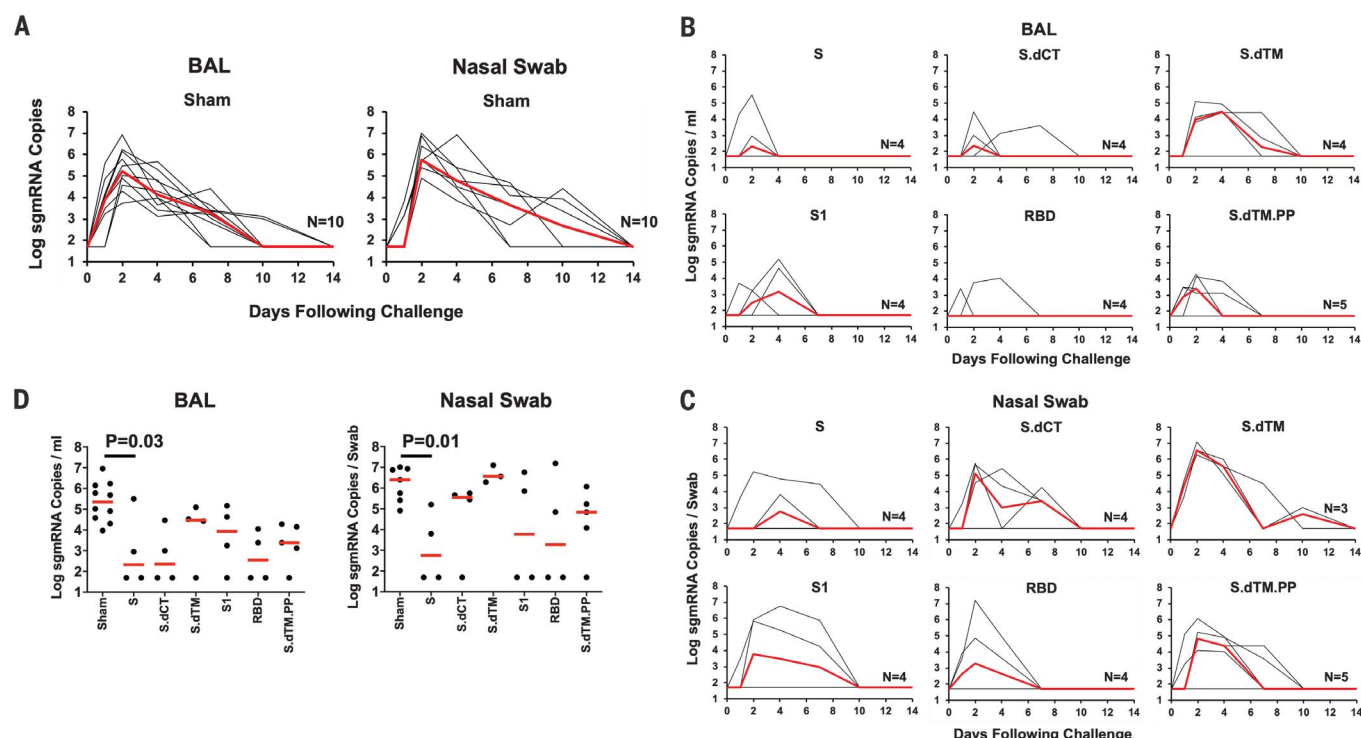


**Fig. 4. Viral loads in rhesus macaques challenged with SARS-CoV-2 virus.** Rhesus macaques were challenged via the intranasal and intratracheal routes with  $1.2 \times 10^8$  VPs ( $1.1 \times 10^4$  PFUs) of SARS-CoV-2. (A) Log<sub>10</sub> sgRNA copies per milliliter or copies per swab (limit 50 copies) were assessed in bronchoalveolar lavage (BAL) and nasal swabs (NS) in sham controls at multiple

time points after challenge. (B) Log<sub>10</sub> sgRNA copies per milliliter in BAL and (C) log<sub>10</sub> sgRNA copies per swab in NS in vaccinated animals at multiple time points after challenge. (D) Summary of peak viral loads in BAL and NS after challenge. Peak viral loads occurred variably on days 1 to 4 after challenge. Red lines reflect median viral loads. *P* values indicate two-sided Mann-Whitney tests.

log<sub>10</sub> sgRNA in both BAL ( $P < 0.0001$ ,  $R = -0.6877$ , two-sided Spearman rank-correlation test) and NS ( $P = 0.0199$ ,  $R = -0.4162$ ) (Fig. 5A). Similarly, the log<sub>10</sub> live virus NAb titer at week 5 inversely correlated with peak log<sub>10</sub> sgRNA levels in both BAL ( $P < 0.0001$ ,  $R = -0.7702$ ) and NS ( $P = 0.1006$ ,  $R = -0.3360$ ) (Fig. 5B). These data suggest that vaccine-elicited serum NAb titers may be immune correlates of protection against SARS-CoV-2 challenge. We speculate that correlations were more robust with viral loads in BAL compared with viral loads in NS, due to intrinsic variability of collecting swabs. The log<sub>10</sub> ELISA titer at week 5 also inversely correlated with peak log<sub>10</sub> sgRNA levels in BAL ( $P = 0.0041$ ,  $R = -0.4733$ ) (fig. S6). Vaccine-elicited ELISPOT responses (fig. S7), CD4<sup>+</sup> intracellular cytokine staining (ICS) responses (fig. S8), and CD8<sup>+</sup> ICS responses (fig. S9) did not correlate with protection.

We next explored the potential contribution of other antibody effector functions to immune correlates of protection. In addition to NAb titers, S- and RBD-specific ADCD responses inversely correlated with peak log<sub>10</sub> sgRNA levels in BAL (Fig. 5C, top). Two orthogonal unbiased machine learning approaches were then used to define minimal combined correlates of protection. A nonlinear random forest regression analysis and a linear partial least

squares regression analysis showed that using two features improved the correlations with protection, such as RBD-specific FcγR2a-1 binding with ADCD responses or NAb titers with RBD-specific IgG2 responses (Fig. 5C, bottom left). Moreover, NAb titers correlated with most antibody effector functions, except for antibody-mediated NK cell activation (Fig. 5C, bottom right). Taken together, these data suggest that NAb titers have a primary role in protecting against SARS-CoV-2, supported by certain innate immune effector functions such as ADCD.

Finally, we compared antibody parameters in vaccinated animals that were completely protected (defined as no detectable sgRNA after challenge) with those in vaccinated animals that were partially protected (defined as detectable sgRNA after challenge). Log<sub>10</sub> NAb titers ( $P = 0.0004$ , two-sided Mann-Whitney test), RBD-specific ADCD responses ( $P = 0.0001$ ), S-specific RBD responses ( $P = 0.0010$ ), and RBD-specific ADCP responses ( $P = 0.0005$ ) were higher in completely protected animals than in partially protected animals (Fig. 5D).

#### Anamnestic immune responses after challenge

All animals exhibited anamnestic humoral and cellular immune responses after challenge, in-

cluding increased ELISA titers (fig. S10), pseudovirus NAb titers (fig. S11), live virus NAb titers (fig. S12), and IFN-γ ELISPOT responses (fig. S13) on day 14 after challenge. These data suggest that vaccine protection was probably not sterilizing (including in the 8 of 25 animals that had no detectable sgRNA in BAL and NS at any time point after challenge) but rather was likely mediated by rapid virologic control after challenge.

#### Discussion

A safe and effective SARS-CoV-2 vaccine may be required to end the global COVID-19 pandemic. Several vaccine candidates have initiated clinical testing, and many others are in preclinical development (19, 20). However, very little is currently known about immune correlates of protection and protective efficacy of candidate SARS-CoV-2 vaccines in animal models. In this study, we generated a series of prototype DNA vaccines expressing various S immunogens and assessed protective efficacy against intranasal and intratracheal SARS-CoV-2 challenge in rhesus macaques. We demonstrated vaccine protection with substantial  $>3.1$  and  $>3.7$  log<sub>10</sub> reductions in median viral loads in BAL and NS, respectively, in S-immunized animals compared with sham controls. Protection was likely



not sterilizing but instead appeared to be mediated by rapid immunologic control after challenge.

Our data extend the findings of previous studies on SARS and Middle East respira-

tory syndrome (MERS) vaccine protection in mice, ferrets, and macaques (10, 21–24). Phase 1 clinical studies for SARS and MERS vaccine candidates have also been conducted (25), but these vaccines have not been tested

for efficacy in humans. Our data suggest that vaccine protection against SARS-CoV-2 in macaques is feasible. We observed a marked reduction of viral replication in both the upper respiratory tract and the lower respiratory

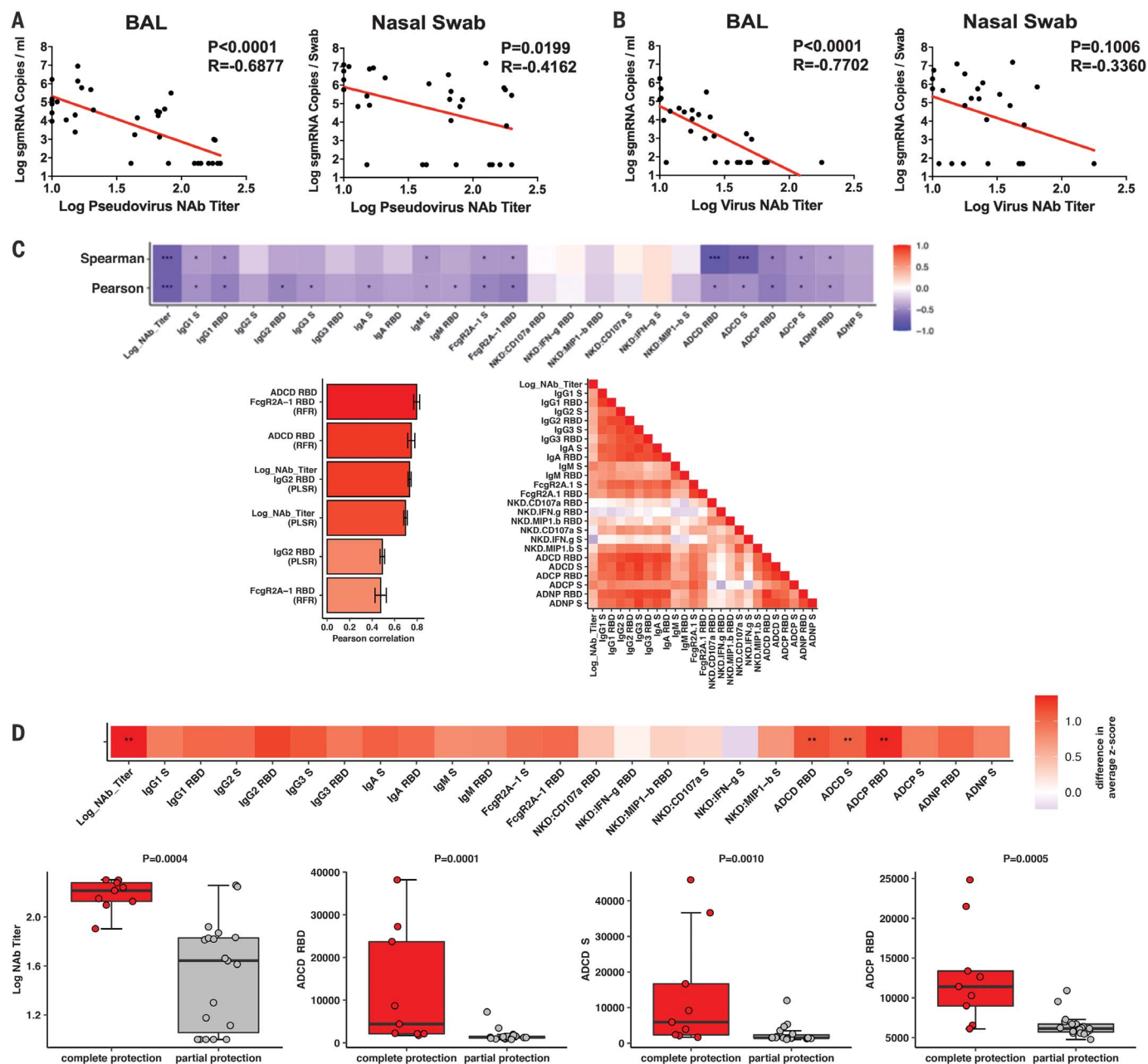


**Fig. 5. Immune correlates of protection.** (A and B) Correlations of (A) pseudovirus NAb titers and (B) live NAb titers before challenge with log peak sgRNA copies per milliliter in BAL or log peak sgRNA copies per swab in nasal swabs after challenge. Red lines reflect the best-fit relationship between these variables.  $P$  and  $R$  values reflect two-sided Spearman rank-correlation tests. (C) The heatmap (top) shows the Spearman and Pearson correlations between antibody features and  $\log_{10}$  peak sgRNA copies per milliliter in BAL ( $*q < 0.05$ ,  $**q < 0.01$ ,  $***q < 0.001$  with Benjamini-Hochberg correction for multiple testing). The bar graph (bottom left) shows the rank of the Pearson correlation between cross-validated model predictions and data using the most

predictive combination or individual antibody features for partial least squares regression (PLSR) and random forest regression (RFR). Error bars indicate SEs. The correlation heatmap (bottom right) represents pairwise Pearson correlations between features across all animals. (D) The heatmap (top) shows the difference in the means of the z-scored features between the completely protected and partially protected animals ( $**q < 0.01$  with Benjamini-Hochberg correction for multiple testing). The dot plots show differences in  $\log_{10}$  NAb titers, RBD-specific ADICD responses, S-specific ADICD responses, and RBD-specific ADICP responses between the completely protected and partially protected animals.  $P$  values indicate two-sided Mann-Whitney tests.

tract with the optimal vaccines. By contrast, the less immunogenic vaccines, such as S.dTM, showed partial protection in BAL but essentially no protection in NS. These data suggest that it may be easier to protect against lower respiratory tract disease than against upper respiratory tract disease. In the present study, optimal protection was achieved with the full-length S immunogen in both the upper and lower respiratory tracts, and reduced protection was observed with soluble constructs and smaller fragments. Our study did not address the question of whether emerging mutations in the SARS-CoV-2 S sequence mediate escape from NAb responses induced by immunogens designed from the Wuhan/WIV04/2019 sequence.

Further research will need to address the durability of protective immunity and the optimal platforms for a SARS-CoV-2 vaccine for humans (26). Although our data are restricted to DNA vaccines, our findings may be generalizable to other gene-based vaccines as well, including RNA vaccines and recombinant vector-based vaccines. Additional research should also evaluate vaccine immunogenicity and protective efficacy in older animals. Future studies should also address the question of enhanced respiratory disease, which may result from antibody-dependent enhancement (27–29). Although our study was not designed to examine safety issues, it is worth noting that the DNA vaccines induced T<sub>H</sub>1 rather than T<sub>H</sub>2 responses, and we did not observe enhanced clinical disease even with the suboptimal vaccine constructs that failed to protect against infection.

We identified serum NAb titers, as measured by two independent assays (pseudovirus neutralization and live virus neutralization), as a significant correlate of protection against disease of both the lower and upper respiratory tracts. It is likely that protection in both

anatomic compartments will be necessary for pandemic control, although protection in the upper respiratory tract may be more difficult to achieve. If this NAb correlate proves generalizable across multiple vaccine studies in both nonhuman primates and humans, then this parameter would be a simple and useful benchmark for clinical development of SARS-CoV-2 vaccines. Innate immune effector functions such as ADCD may also contribute to protective efficacy. In summary, we demonstrate effective vaccine protection against SARS-CoV-2 in rhesus macaques and define NAb titers as an immune correlate of protection, which will accelerate the development of SARS-CoV-2 vaccines for humans.

## REFERENCES AND NOTES

1. F. Wu *et al.*, *Nature* **579**, 265–269 (2020).
2. P. Zhou *et al.*, *Nature* **579**, 270–273 (2020).
3. M. L. Holshue *et al.*, *N. Engl. J. Med.* **382**, 929–936 (2020).
4. Q. Li *et al.*, *N. Engl. J. Med.* **382**, 1199–1207 (2020).
5. N. Zhu *et al.*, *N. Engl. J. Med.* **382**, 727–733 (2020).
6. N. Chen *et al.*, *Lancet* **395**, 507–513 (2020).
7. C. Huang *et al.*, *Lancet* **395**, 497–506 (2020).
8. J. F. Chan *et al.*, *Lancet* **395**, 514–523 (2020).
9. A. Chandrasekar *et al.*, *Science* **369**, 812–817 (2020).
10. Z. Y. Yang *et al.*, *Nature* **428**, 561–564 (2004).
11. R. N. Kirchdoerfer *et al.*, *Nature* **531**, 118–121 (2016).
12. J. Pallesen *et al.*, *Proc. Natl. Acad. Sci. U.S.A.* **114**, E7348–E7357 (2017).
13. D. Wrapp *et al.*, *Science* **367**, 1260–1263 (2020).
14. T. Scobey *et al.*, *Proc. Natl. Acad. Sci. U.S.A.* **110**, 16157–16162 (2013).
15. B. Yount *et al.*, *Proc. Natl. Acad. Sci. U.S.A.* **100**, 12995–13000 (2003).
16. A. W. Chung *et al.*, *Cell* **163**, 988–998 (2015).
17. P. Abbink *et al.*, *Science* **365**, 1029–1033 (2019).
18. R. Wolfel *et al.*, *Nature* **581**, 465–469 (2020).
19. Q. Gao *et al.*, *Science* **369**, 77–81 (2020).
20. B. L. Corey, J. R. Mascola, A. S. Fauci, F. S. Collins, *Science* **368**, 948–950 (2020).
21. L. Liu *et al.*, *Antiviral Res.* **150**, 30–38 (2018).
22. K. Muthumani *et al.*, *Sci. Transl. Med.* **7**, 301ra132 (2015).
23. G. P. Kobinger *et al.*, *Vaccine* **25**, 5220–5231 (2007).
24. J. Zhou *et al.*, *Vaccine* **23**, 3202–3209 (2005).
25. J. E. Martin *et al.*, *Vaccine* **26**, 6338–6343 (2008).
26. P. Abbink *et al.*, *Sci. Transl. Med.* **9**, eaao4163 (2017).
27. C. T. Tseng *et al.*, *PLOS ONE* **7**, e35421 (2012).

28. L. Liu *et al.*, *JCI Insight* **4**, e123158 (2019).

29. B. S. Graham, *Science* **368**, 945–946 (2020).

## ACKNOWLEDGMENTS

We thank D. Lauffenburger, T. Orekov, A. Thomas, M. Porto, N. Thornburg, P. Abbink, E. Borducchi, M. Silva, A. Richardson, C. Caron, and J. Cwiak for advice, assistance, and reagents. **Funding:** We acknowledge support from the Ragon Institute of MGH, MIT, and Harvard; the Mark and Lisa Schwartz Foundation; Beth Israel Deaconess Medical Center; the Massachusetts Consortium on Pathogen Readiness (MassCPR); Janssen Vaccines & Prevention BV; and the National Institutes of Health (OD024917, AI129797, AI124377, AI128751, and AI126603 to D.H.B.; AI007151 to D.R.M.; AI146779 to A.G.S.; AI121394 and AI139538 to D.R.W.; and 2722017000361-0-759301900131-1, AI100625, AI107000, AI132178, AI149644, and AI108197 to R.S.B.). We also acknowledge a Burroughs Wellcome Fund Postdoctoral Enrichment Program Award to D.R.M. **Author contributions:** D.H.B. designed the study. J.Y., L.H.T., L.P., N.B.M., K.M., S.H.M., J.P.N., J.L., Z.Li, A.C., E.A.B., G.D., M.S.G., X.H., C.J.-D., M.K., N.K., Z.Li, L.F.M., F.N., R.N., J.V., and H.W. performed the immunologic and virologic assays. D.R.M. and R.S.B. performed the live virus neutralization assays. C.L., C.A., S.F., J.S.B., M.D.S., and G.A. performed the systems serology. Y.C., A.Z., F.J.N.L., M.T., S.H., and D.R.W. provided the convalescent human specimens. L.P., A.V.R., K.B., R.B., A.C., B.F., A.D., E.T., J.D.V., H.A., and M.G.L. led the clinical care of the animals. R.Z. and F.W. participated in study design and interpretation of data. Y.C., B.C., and A.G.S. provided purified proteins. D.H.B., J.L., Z.Li, and B.C. designed the immunogens. D.H.B. wrote the paper with all coauthors. **Competing interests:** D.H.B. is a co-inventor on related vaccine patents. R.Z. and F.W. are employees of Janssen Vaccines & Prevention BV. The other authors declare no competing interests. **Data and materials availability:** All data are available in the manuscript or the supplementary materials. This work is licensed under a Creative Commons Attribution 4.0 International (CC BY 4.0) license, which permits unrestricted use, distribution, and reproduction in any medium, provided the original work is properly cited. To view a copy of this license, visit <https://creativecommons.org/licenses/by/4.0/>. This license does not apply to figures/photos/artwork or other content included in the article that is credited to a third party; obtain authorization from the rights holder before using such material.

## SUPPLEMENTARY MATERIALS

[science.sciencemag.org/content/369/6505/806/suppl/DC1](https://science.sciencemag.org/content/369/6505/806/suppl/DC1)  
Materials and Methods  
Figs. S1 to S13  
References

[View/request a protocol for this paper from Bio-protocol.](#)

5 May 2020; accepted 16 May 2020

Published online 20 May 2020

10.1126/science.abc6284



## CORONAVIRUS

# SARS-CoV-2 infection protects against rechallenge in rhesus macaques

Abishek Chandrashekar<sup>1\*</sup>, Jinyan Liu<sup>1\*</sup>, Amanda J. Martinot<sup>1,2\*</sup>, Katherine McMahan<sup>1\*</sup>, Noe B. Mercado<sup>1\*</sup>, Lauren Peter<sup>1\*</sup>, Lisa H. Tostanoski<sup>1\*</sup>, Jingyou Yu<sup>1\*</sup>, Zoltan Maliga<sup>3</sup>, Michael Nekorchuk<sup>4</sup>, Kathleen Busman-Sahay<sup>4</sup>, Margaret Terry<sup>4</sup>, Linda M. Wrijil<sup>2</sup>, Sarah Ducat<sup>2</sup>, David R. Martinez<sup>5</sup>, Caroline Atyeo<sup>3,6</sup>, Stephanie Fischinger<sup>6</sup>, John S. Burke<sup>6</sup>, Matthew D. Slein<sup>6</sup>, Laurent Pessaint<sup>7</sup>, Alex Van Ry<sup>7</sup>, Jack Greenhouse<sup>7</sup>, Tammy Taylor<sup>7</sup>, Kelvin Blade<sup>7</sup>, Anthony Cook<sup>7</sup>, Brad Finneyrock<sup>7</sup>, Renita Brown<sup>7</sup>, Elyse Teow<sup>7</sup>, Jason Velasco<sup>7</sup>, Roland Zahn<sup>8</sup>, Frank Wegmann<sup>8</sup>, Peter Abbink<sup>1</sup>, Esther A. Bondzie<sup>1</sup>, Gabriel Dagotto<sup>1,3</sup>, Makda S. Gebre<sup>1,3</sup>, Xuan He<sup>1</sup>, Catherine Jacob-Dolan<sup>1,3</sup>, Nicole Kordana<sup>1</sup>, Zhenfeng Li<sup>1</sup>, Michelle A. Lifton<sup>1</sup>, Shant H. Mahrokhian<sup>1</sup>, Lori F. Maxfield<sup>1</sup>, Ramya Nityanandam<sup>1</sup>, Joseph P. Nkolola<sup>1</sup>, Aaron G. Schmidt<sup>6,9</sup>, Andrew D. Miller<sup>10</sup>, Ralph S. Baric<sup>5</sup>, Galit Alter<sup>6,9</sup>, Peter K. Sorger<sup>3</sup>, Jacob D. Estes<sup>4</sup>, Hanne Andersen<sup>7</sup>, Mark G. Lewis<sup>7</sup>, Dan H. Barouch<sup>1,6,9†</sup>

An understanding of protective immunity to severe acute respiratory syndrome coronavirus 2 (SARS-CoV-2) is critical for vaccine and public health strategies aimed at ending the global coronavirus disease 2019 (COVID-19) pandemic. A key unanswered question is whether infection with SARS-CoV-2 results in protective immunity against reexposure. We developed a rhesus macaque model of SARS-CoV-2 infection and observed that macaques had high viral loads in the upper and lower respiratory tract, humoral and cellular immune responses, and pathologic evidence of viral pneumonia. After the initial viral clearance, animals were rechallenged with SARS-CoV-2 and showed 5 log<sub>10</sub> reductions in median viral loads in bronchoalveolar lavage and nasal mucosa compared with after the primary infection. Anamnestic immune responses after rechallenge suggested that protection was mediated by immunologic control. These data show that SARS-CoV-2 infection induced protective immunity against reexposure in nonhuman primates.

**T**he explosive spread of the coronavirus disease 2019 (COVID-19) pandemic has made the development of countermeasures an urgent global priority (1–8). However, our understanding of the immunopathogenesis of severe acute respiratory syndrome coronavirus 2 (SARS-CoV-2) is currently very

limited. In particular, it is not yet known whether SARS-CoV-2 infection induces natural immunity that protects against reexposure in humans. Such information is critical for vaccine strategies, epidemiologic modeling, and public health approaches. To explore this question, we developed a rhesus macaque mod-

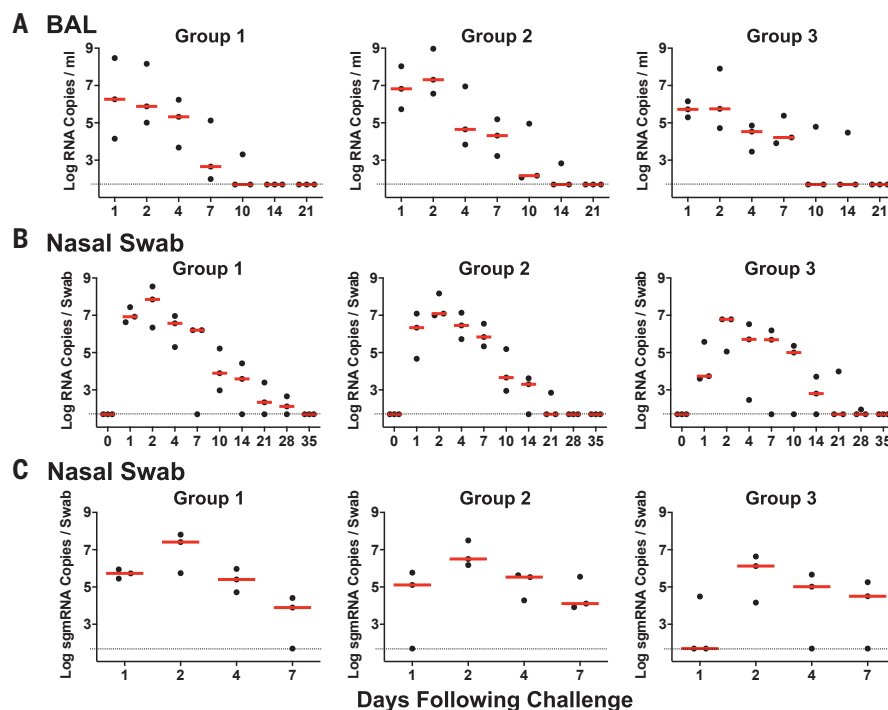
el of SARS-CoV-2 infection and assessed virologic, immunologic, and pathologic features of infection, as well as protective immunity against rechallenge.

## Virology and immunology of SARS-CoV-2 infection in rhesus macaques

We inoculated nine adult rhesus macaques (6 to 12 years of age) with a total of  $1.1 \times 10^6$  plaque-forming units (PFU) (Group 1;  $N = 3$ ),  $1.1 \times 10^5$  PFU (Group 2;  $N = 3$ ), or  $1.1 \times 10^4$  PFU (Group 3;  $N = 3$ ) of SARS-CoV-2 administered as 1 ml by the intranasal (IN) route and 1 ml by the intratracheal (IT) route. After viral challenge, we assessed viral RNA levels by reverse transcription polymerase chain reaction (RT-PCR) in multiple anatomic compartments. We observed high levels of viral RNA in bronchoalveolar lavage (BAL) (Fig. 1A) and nasal swabs (NS) (Fig. 1B), with a median peak of 6.56 (range 5.32 to 8.97) log<sub>10</sub> RNA copies/ml in BAL and a median peak of 7.00 (range 5.06 to 8.55) log<sub>10</sub> RNA copies/swab in NS. Viral RNA in NS increased in all animals from day 1 to day 2, suggesting viral replication. Viral RNA peaked on day 2 and typically resolved by day 10 to day 14 in BAL and by day 21 to day 28 in NS. After day 2, viral loads in BAL and NS appeared comparable in all groups regardless of dose. Viral RNA was undetectable in plasma (fig. S1). Animals exhibited modestly decreased appetite and responsiveness suggestive of mild clinical disease (fig. S2), as well as mild transient neutropenia and lymphopenia in the high-dose group (fig. S3), but fever, weight loss, respiratory distress, and mortality were not observed.

### Fig. 1. Viral loads in SARS-CoV-2-challenged rhesus macaques.

Rhesus macaques were inoculated by the IN and IT routes with  $1.1 \times 10^6$  PFU (Group 1;  $N = 3$ ),  $1.1 \times 10^5$  PFU (Group 2;  $N = 3$ ), or  $1.1 \times 10^4$  PFU (Group 3;  $N = 3$ ) of SARS-CoV-2. (A) Log<sub>10</sub> viral RNA copies/ml (limit 50 copies/ml) were assessed in BAL at multiple time points after challenge. (B and C) Log<sub>10</sub> viral RNA copies/swab (B) and log<sub>10</sub> sgRNA copies/swab (C) (limit 50 copies/swab) were assessed in NS at multiple time points after challenge. Red horizontal bars reflect median viral loads.



To help differentiate input challenge virus from newly replicating virus, we developed an RT-PCR assay to assess E gene subgenomic mRNA (sgmRNA), which reflects viral replication cellular intermediates that are not packaged into virions and thus represent putative replicat-

ing virus in cells (9). Compared with total viral RNA (Fig. 1B), sgmRNA levels were lower in NS on day 1, with a median of 5.11 (range <1.70 to 5.94)  $\log_{10}$  sgmRNA copies/swab, but then increased by day 2 to a median of 6.50 (range 4.16 to 7.81)  $\log_{10}$  sgmRNA copies/swab (Fig. 1C).

We next evaluated SARS-CoV-2-specific humoral and cellular immune responses in these animals. All nine macaques developed binding antibody responses to the SARS-CoV-2 spike (S) protein by ELISA (Fig. 2A) and neutralizing antibody (NAb) responses using both a pseu-

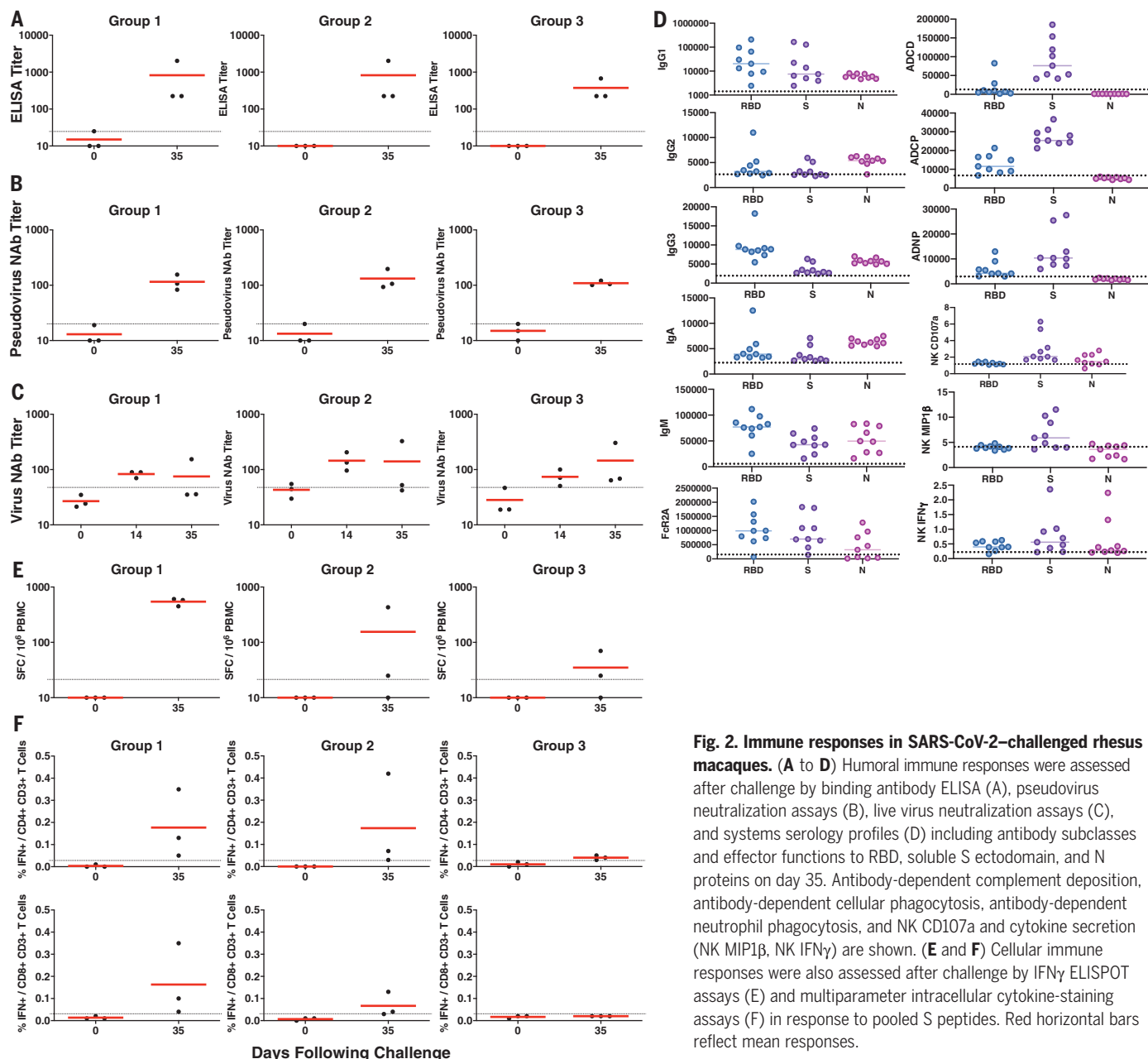


**Fig. 2. Immune responses in SARS-CoV-2-challenged rhesus macaques.** (A to D) Humoral immune responses were assessed after challenge by binding antibody ELISA (A), pseudovirus neutralization assays (B), live virus neutralization assays (C), and systems serology profiles (D) including antibody subclasses and effector functions to RBD, soluble S ectodomain, and N proteins on day 35. Antibody-dependent complement deposition, antibody-dependent cellular phagocytosis, antibody-dependent neutrophil phagocytosis, and NK CD107a and cytokine secretion (NK MIP1β, NK IFNγ) are shown. (E and F) Cellular immune responses were also assessed after challenge by IFNγ ELISPOT assays (E) and multiparameter intracellular cytokine-staining assays (F) in response to pooled S peptides. Red horizontal bars reflect mean responses.

<sup>1</sup>Center for Virology and Vaccine Research, Beth Israel Deaconess Medical Center, Harvard Medical School, Boston, MA 02215, USA. <sup>2</sup>Tufts University Cummings School of Veterinary Medicine, North Grafton, MA 01536, USA. <sup>3</sup>Harvard Medical School, Boston, MA 02115, USA. <sup>4</sup>Oregon Health & Sciences University, Beaverton, OR 97006, USA. <sup>5</sup>University of North Carolina, Chapel Hill, NC 27599, USA. <sup>6</sup>Ragon Institute of MGH, MIT, and Harvard, Cambridge, MA 02139, USA. <sup>7</sup>Bioqual, Rockville, MD 20852, USA. <sup>8</sup>Janssen Vaccines & Prevention BV, Leiden, Netherlands. <sup>9</sup>Massachusetts Consortium on Pathogen Readiness, Boston, MA 02215, USA. <sup>10</sup>Cornell University College of Veterinary Medicine, Ithaca, NY 14853, USA.

\*These authors contributed equally to this work.

†Corresponding author. Email: dbarouch@bidmc.harvard.edu



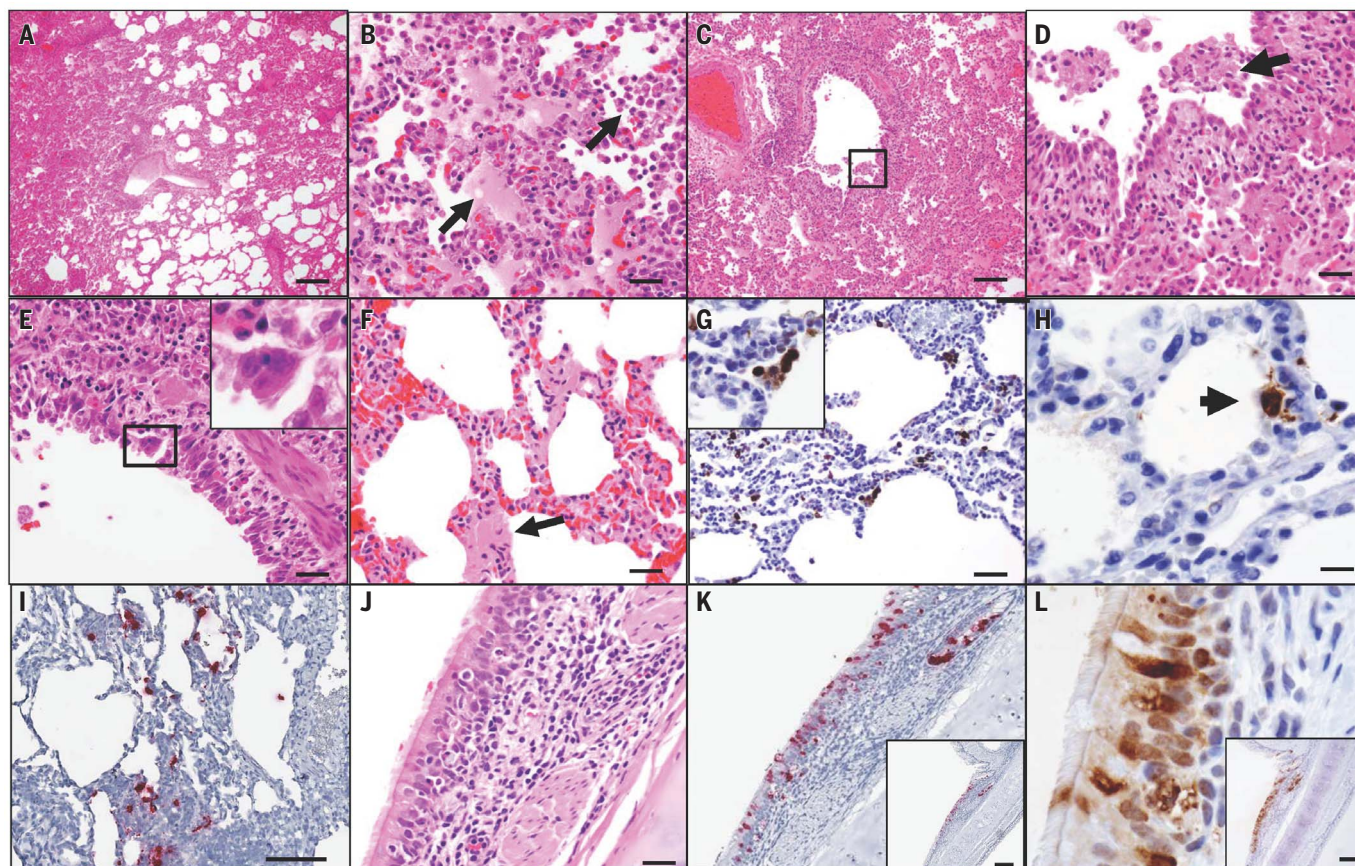


**Fig. 3. SARS-CoV-2 induces acute viral interstitial pneumonia.** (A to F) Hematoxylin and eosin–stained sections of fixed lung tissue from SARS-CoV-2–infected rhesus macaques 2 days after challenge showing interstitial edema and regional lung consolidation (A), intra-alveolar edema and infiltrates of neutrophils (B), bronchiolar epithelial sloughing and necrosis [(C) and (D)], bronchiolar epithelial syncytial cell formation (E), and hyaline membranes within alveolar septa (F). (G and H) Immunohistochemistry for SARS-N showing virus-infected cells within

interstitial spaces, including a viral syncytial cell within the lumen (G) and virus-infected alveolar lining cells (H). (I) Inflammatory infiltrate showing multiple cells containing SARS-CoV-2 RNA by RNAscope in situ hybridization. (J to L) Bronchial respiratory epithelium showing inflammation within the submucosa and transmigration of inflammatory cells into the ciliated columnar respiratory epithelium of a bronchus (J), SARS-CoV-2 RNA (K), and SARS-N (L). Scale bars: (A), 200  $\mu$ m; (C), (I), (K), and (L), 100  $\mu$ m; (G), 50  $\mu$ m; (B), (D), (E), (F), and (J), 20  $\mu$ m; (H), 10  $\mu$ m.

dovirus neutralization assay (10) (Fig. 2B) and a live virus neutralization assay (11, 12) (Fig. 2C). NAb titers of ~100 were observed in all animals on day 35 regardless of dose group (range 83 to 197 by the pseudovirus neutralization assay and 35 to 326 by the live virus neutralization assay). Antibody responses of multiple subclasses were observed against the receptor binding domain (RBD), the prefusion S ectodomain (S), and the nucleocapsid (N), and antibodies exhibited diverse effector functions, including antibody-dependent complement deposition, antibody-dependent cellular phagocytosis, antibody-dependent neutrophil phagocytosis, and antibody-dependent natural killer (NK) cell degranulation (NK CD107a) and cytokine secretion [NK macrophage inflammatory protein 1 $\beta$  (MIP1 $\beta$ ), NK interferon  $\gamma$  (IFN $\gamma$ )] (13) (Fig. 2D). Cellular immune responses to pooled S peptides were observed in most animals by IFN $\gamma$  ELISPOT assays on day 35, with a trend toward lower responses in the lower-dose groups (Fig. 2E). Intracellular cytokine-staining as-

says demonstrated induction of both S-specific CD8 $^{+}$  and CD4 $^{+}$  T cell responses (Fig. 2F).

#### SARS CoV-2 infection induces acute viral interstitial pneumonia in rhesus macaques

Only limited pathology data from SARS-CoV-2–infected humans are currently available. To assess the pathologic characteristics of SARS-CoV-2 infection in rhesus macaques, we inoculated four animals with  $1.1 \times 10^5$  PFU of virus by the IN and IT routes as above and necropsied them on day 2 ( $N = 2$ ) and day 4 ( $N = 2$ ) after challenge. Multiple regions of the upper respiratory tract, lower respiratory tract, gastrointestinal tract, lymph nodes, and other organs were harvested for virologic and pathologic analyses. High levels of viral RNA were observed in all nasal mucosa, pharynx, trachea, and lung tissues, and lower levels of virus were found in the gastrointestinal tract, liver, and kidney (fig. S4). Viral RNA was readily detected in paratracheal lymph nodes but was only sporadically found in distal lymph nodes and spleen (fig. S4).

Upper airway mucosae, trachea, and lungs were paraformaldehyde fixed, paraffin embedded, and evaluated by histopathology. On day 2 after challenge, both necropsied animals demonstrated multifocal regions of inflammation and evidence of viral pneumonia, including expansion of alveolar septae with mononuclear cell infiltrates, consolidation, and edema (Fig. 3, A and B). Regions with edema also contained numerous polymorphonuclear cells, predominantly neutrophils. Terminal bronchiolar epithelium was necrotic and sloughed with clumps of epithelial cells detected within airways and distally within alveolar spaces (Fig. 3, C and D), with formation of occasional bronchiolar epithelial syncytial cells (Fig. 3E). Hyaline membranes were occasionally observed within alveolar septa, consistent with damage to type I and type II pneumocytes (Fig. 3F). Diffusely reactive alveolar macrophages filled alveoli, and some were multinucleated and labeled positive for nucleocapsid by immunohistochemistry (Fig. 3G). Alveolar lining cells (pneumocytes)



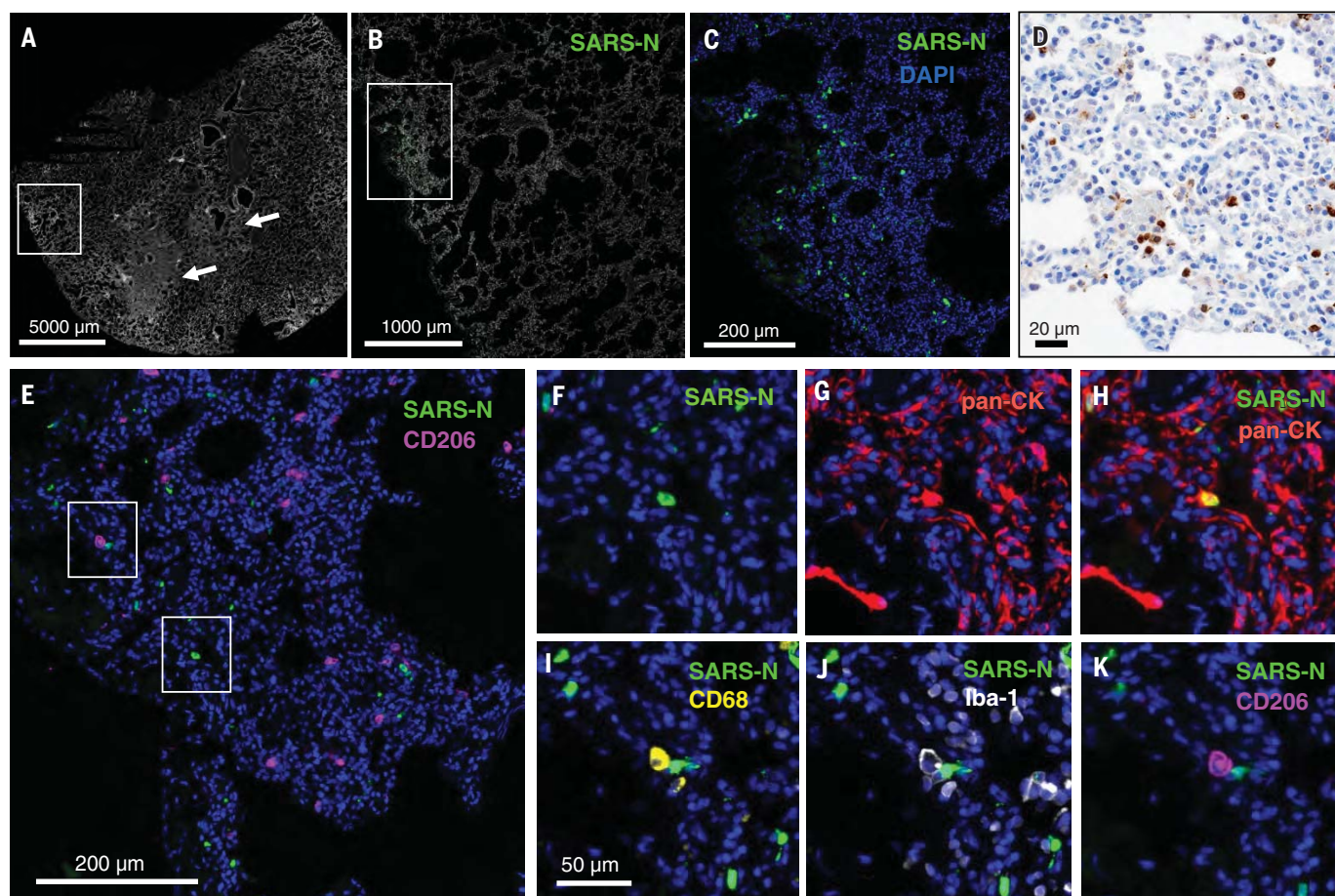


**Fig. 4. SARS-CoV-2 infects alveolar epithelial cells in rhesus macaques.** Shown is CyCIF staining of fixed lung tissue from SARS-CoV-2–infected rhesus macaques 2 days after challenge. **(A)** Whole-slide image of a lung stained with Hoechst 33342 to visualize cell nuclei (grayscale); regions of nuclear consolidation (arrows) and foci of viral replication (box) are highlighted. **(B)** Higher-magnification image of inset box in (A) showing staining for SARS-N (green) and cell nuclei (grayscale). **(C)** Higher-

magnification image of inset box in (B) showing SARS-N (green) and cell nuclei (blue). **(D)** Bright-field immunohistochemistry for SARS-N from corresponding lung region depicted in (C). **(E to K)** CyCIF staining for DNA (all panels, blue) and SARS-N [(E), (F), and (H) to (K), green], CD206 [(E) and (K), magenta], pan-CK [(G) and (H), red], CD68 [(I), yellow], or Iba-1 [(J), grayscale] showing virus-infected epithelial cells and macrophages near an infected epithelial cell. Scale bar for (F) to (K), 50 μm.

also prominently labeled positive for nucleocapsid (Fig. 3H).

Multifocal clusters of virus-infected cells were present throughout the lung parenchyma, as detected by immunohistochemistry and in situ RNA hybridization (RNAscope) (14, 15) (Fig. 3I). Both positive-sense and negative-sense viral RNA were observed by RNAscope (fig. S5), suggesting viral replication in lung tissue. The dense inflammatory infiltrates included polymorphonuclear cells detected by endogenous myeloperoxidase staining, CD68<sup>+</sup> and CD163<sup>+</sup> macrophages, CD4<sup>+</sup> and CD8<sup>+</sup> T lymphocytes, and diffuse up-regulation of the type 1 IFN gene MX1 (fig. S6). SARS-CoV-2 infection led to a significant increase in polymorphonuclear cell infiltration of lung alveoli compared with uninfected animals ( $P = 0.0286$ ), as well as extensive MX1 staining in ~30% of total lung tissue ( $P = 0.0286$ ) (fig. S7). Inflammatory infiltrates were also detected in the respiratory epithelial submucosa of larger airways, with

transmigration of inflammatory cells into bronchiole lumen (Fig. 3J). Ciliated epithelial cells also stained positive for both SARS-CoV-2 RNA (Fig. 3K) and SARS nucleocapsid (SARS-N) (Fig. 3L). By day 4 after infection, the extent of inflammation and viral pneumonia had diminished, but virus was still detected in lung parenchyma, and neutrophil infiltration and type 1 IFN responses persisted (fig. S7).

To further characterize infected tissues, we performed cyclic immunofluorescence (CyCIF) imaging, a method for multiplex immunophenotyping of paraformaldehyde-fixed tissue specimens (16). Tissues were stained for SARS-N, pan-cytokeratin (to identify epithelial cells), Iba-1 (ionized calcium-binding adaptor as a pan-macrophage marker), CD68 (monocyte and macrophage marker), and CD206 (macrophage marker), in addition to a panel of markers to identify other immune cells and anatomical structures (table S1) and counterstaining for DNA to label all nuclei. Foci of virus-infected

cells were randomly dispersed throughout the lung and were variably associated with inflammatory infiltrates (Fig. 4, A to D). Some areas of parenchymal consolidation and inflammation contained little to no virus (Fig. 4A, arrows, and fig. S8). Virus-infected cells frequently costained with pan-cytokeratin (Fig. 4, E to H), suggesting that they were alveolar epithelial cells (pneumocytes). Uninfected Iba-1<sup>+</sup> CD68<sup>+</sup> CD206<sup>+</sup> activated macrophages were also frequently detected adjacent to virally infected epithelial cells (Fig. 4, E and I to K). These data demonstrate that SARS-CoV-2 induced multifocal areas of acute inflammation and viral pneumonia involving infected pneumocytes, ciliated bronchial epithelial cells, and likely other cell types.

#### Protective efficacy against rechallenge with SARS-CoV-2 in rhesus macaques

On day 35 after initial viral infection (Figs. 1 and 2), all nine rhesus macaques were rechallenged



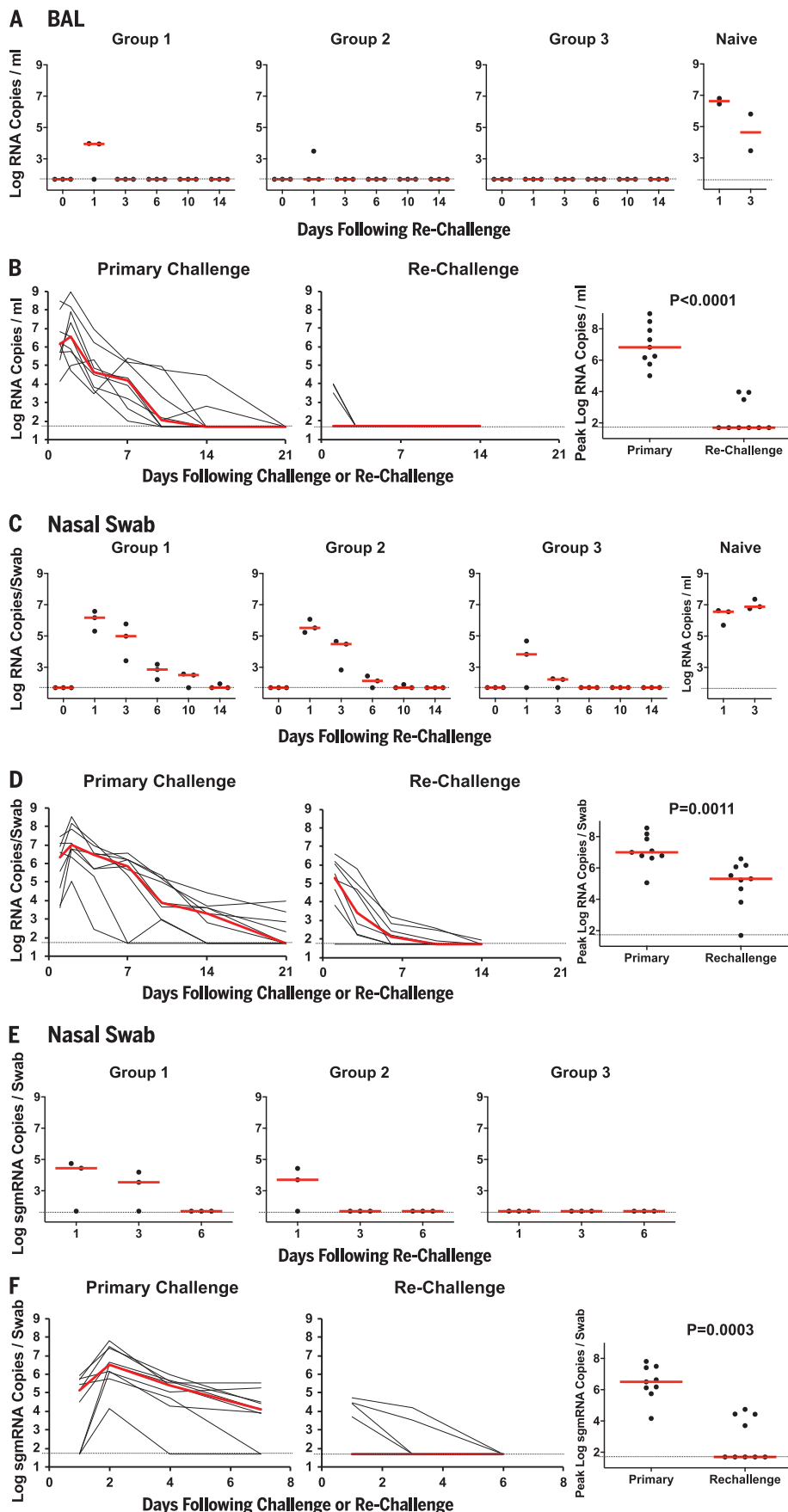


**Fig. 5. Viral loads after SARS-CoV-2 rechallenge in rhesus macaques.** On day 35 after the initial infection (Fig. 1), rhesus macaques were rechallenged by the IN and IT routes with  $1.1 \times 10^6$  PFU (Group 1;  $N = 3$ ),  $1.1 \times 10^5$  PFU (Group 2;  $N = 3$ ), or  $1.1 \times 10^4$  PFU (Group 3;  $N = 3$ ) of SARS-CoV-2. Three naïve animals were included as a positive control in the rechallenge experiment. **(A)**  $\text{Log}_{10}$  viral RNA copies/ml (limit 50 copies/ml) were assessed in BAL at multiple time points after rechallenge. One of the naïve animals could not be lavaged. **(B)** Comparison of viral RNA in BAL after primary challenge and rechallenge. **(C and E)**  $\text{Log}_{10}$  viral RNA copies/ml (C) and  $\text{log}_{10}$  sgRNA copies/swab (limit 50 copies/ml) (E) were assessed in NS at multiple time points after rechallenge. **(D and F)** Comparison of viral RNA (D) and sgRNA (F) in NS after primary challenge and rechallenge. Red horizontal bars reflect median viral loads.  $P$  values reflect two-sided Mann-Whitney tests.

with the same doses of SARS-CoV-2 that were used for the primary infection, namely  $1.1 \times 10^6$  PFU (Group 1;  $N = 3$ ),  $1.1 \times 10^5$  PFU (Group 2;  $N = 3$ ), or  $1.1 \times 10^4$  PFU (Group 3;  $N = 3$ ). Three naïve animals were included as positive controls in the rechallenge experiment. Very limited viral RNA was observed in BAL on day 1 after rechallenge in two Group 1 animals and in one Group 2 animal, with no viral RNA detected at subsequent time points (Fig. 5A). By contrast, high levels of viral RNA were observed in the concurrently challenged naïve animals (Fig. 5A), as expected. Median peak viral loads in BAL were  $>5.1 \log_{10}$  lower after rechallenge compared with after the primary challenge ( $P < 0.0001$ , two-sided Mann-Whitney test; Fig. 5B). After rechallenge, viral RNA was higher in NS compared with BAL but exhibited dose dependence and rapid decline (Fig. 5C), and median peak viral loads in NS were still  $>1.7 \log_{10}$  compared with after the primary challenge ( $P = 0.0011$ , two-sided Mann-Whitney test; Fig. 5D).

We speculated that most of the virus detected in NS after rechallenge was input challenge virus, so sgRNA levels in NS were assessed. Low but detectable levels of sgRNA were still observed in four of nine animals in NS on day 1 after rechallenge, but sgRNA levels declined quickly (Fig. 5E) and median peak sgRNA levels in NS were  $>4.8 \log_{10}$  lower after rechallenge compared with after the primary challenge ( $P = 0.0003$ , two-sided Mann-Whitney test; Fig. 5F). Consistent with these data, plaque assays in BAL and NS samples after rechallenge showed no recoverable virus and plaque levels were lower than those after the primary infection ( $P = 0.009$  and  $P = 0.002$ , respectively, two-sided Mann-Whitney tests; fig. S9). Moreover, little or no clinical

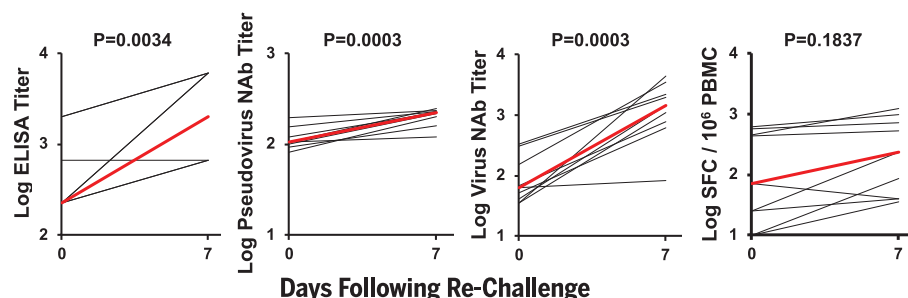


**Fig. 6. Anamnestic immune responses after SARS-CoV-2 rechallenge in rhesus macaques.** Results of binding antibody ELISAs, pseudovirus neutralization assays, live virus neutralization assays, and IFN $\gamma$  ELISPOT assays are depicted before and 7 days after SARS-CoV-2 rechallenge. Red lines reflect mean responses. *P* values reflect two-sided Mann-Whitney tests.

disease was observed in the animals after rechallenge (fig. S10).

After SARS-CoV-2 rechallenge, animals exhibited rapid anamnestic immune responses, including increased virus-specific ELISA titers ( $P = 0.0034$ , two-sided Mann-Whitney test), pseudovirus NAb titers ( $P = 0.0003$ ), and live virus NAb titers ( $P = 0.0003$ ), as well as a trend toward increased IFN- $\gamma$  ELISPOT responses ( $P = 0.1837$ ) by day 7 after rechallenge (Fig. 6). In particular, NAb titers were markedly higher on day 14 after rechallenge compared with day 14 after the primary challenge ( $P < 0.0001$ , two-sided Mann-Whitney test) (fig. S11). All animals developed anamnestic antibody responses after rechallenge regardless of the presence or absence of residual viral RNA or sgRNA in BAL or NS, so we speculate that the protective efficacy against rechallenge was mediated by rapid immunologic control.

## Discussion

Individuals who recover from certain viral infections typically develop virus-specific antibody responses that provide robust protective immunity against reexposure, but some viruses, such as HIV-1 (17), do not generate protective natural immunity. Human challenge studies for the common cold coronavirus 229E have suggested that there may be partial natural immunity (18). However, there are currently no data on whether humans who have recovered from SARS-CoV-2 infection are protected from reexposure (19). This is a critical issue with profound implications for vaccine development, public health strategies, antibody-based therapeutics, and epidemiologic modeling of herd immunity. In this study, we have demonstrated that SARS-CoV-2 infection in rhesus macaques provides protective efficacy against SARS-CoV-2 rechallenge.

We developed a rhesus macaque model of SARS-CoV-2 infection that recapitulates many aspects of human SARS-CoV-2 infection, including high levels of viral replication in the

upper and lower respiratory tract (Fig. 1) and clear pathologic evidence of viral pneumonia (Figs. 3 and 4). Histopathology, immunohistochemistry, RNAscope, and CycIF imaging demonstrated multifocal clusters of virus-infected cells in areas of acute inflammation, with evidence for virus infection of alveolar pneumocytes and ciliated bronchial epithelial cells. These data suggest the utility of rhesus macaques as a model for testing vaccines and therapeutics and for studying the immunopathogenesis of SARS-CoV-2 infection, and our findings complement and extend recently published data in cynomolgus macaques (20). However, neither nonhuman primate model led to respiratory failure or mortality, so further research will be required to develop a model of severe COVID-19 disease.

SARS-CoV-2 infection in rhesus macaques led to humoral and cellular immune responses (Fig. 2) and provided protection against rechallenge (Fig. 5). Residual low levels of subgenomic mRNA in nasal swabs in a subset of animals (Fig. 5) and anamnestic immune responses in all animals (Fig. 6) after SARS-CoV-2 rechallenge suggest that protection was mediated by immunologic control and likely was not sterilizing.

Given the near-complete protection in all animals after SARS-CoV-2 rechallenge, we were unable to determine immune correlates of protection in this study. SARS-CoV-2 infection in rhesus monkeys resulted in the induction of neutralizing antibody titers of  $\sim 100$  as measured by both a pseudovirus neutralization assay and a live virus neutralization assay, but the relative importance of neutralizing antibodies, other functional antibodies, cellular immunity, and innate immunity to protective efficacy against SARS-CoV-2 remains to be determined. Moreover, additional research will be required to define the durability of natural immunity.

In summary, SARS-CoV-2 infection in rhesus macaques induced humoral and cellular immune responses and provided protective ef-

ficacy against SARS-CoV-2 rechallenge. These data raise the possibility that immunologic approaches to the prevention and treatment of SARS-CoV-2 infection may in fact be possible. However, it is critical to emphasize that there are important differences between SARS-CoV-2 infection in macaques and humans, with many parameters still yet to be defined in both species, so our data should be interpreted cautiously. Rigorous clinical studies will be required to determine whether SARS-CoV-2 infection effectively protects against SARS-CoV-2 reexposure in humans.

## REFERENCES AND NOTES

1. F. Wu et al., *Nature* **579**, 265–269 (2020).
2. P. Zhou et al., *Nature* **579**, 270–273 (2020).
3. M. L. Holshue et al., *N. Engl. J. Med.* **382**, 929–936 (2020).
4. Q. Li et al., *N. Engl. J. Med.* **382**, 1199–1207 (2020).
5. N. Zhu et al., *N. Engl. J. Med.* **382**, 727–733 (2020).
6. N. Chen et al., *Lancet* **395**, 507–513 (2020).
7. C. Huang et al., *Lancet* **395**, 497–506 (2020).
8. J. F. Chan et al., *Lancet* **395**, 514–523 (2020).
9. R. Wölfel et al., *Nature* **581**, 465–469 (2020).
10. Z. Y. Yang et al., *Nature* **428**, 561–564 (2004).
11. T. Scobey et al., *Proc. Natl. Acad. Sci. U.S.A.* **110**, 16157–16162 (2013).
12. B. Yount et al., *Proc. Natl. Acad. Sci. U.S.A.* **100**, 12995–13000 (2003).
13. A. W. Chung et al., *Cell* **163**, 988–998 (2015).
14. C. Deleage et al., *JCI Insight* **1**, e87065 (2016).
15. C. Deleage et al., *Pathog. Immun.* **1**, 68–106 (2016).
16. J. R. Lin et al., *eLife* **7**, e31657 (2018).
17. M. Altfeld et al., *Nature* **420**, 434–439 (2002).
18. K. A. Callow, H. F. Parry, M. Sergeant, D. A. Tyrrell, *Epidemiol. Infect.* **105**, 435–446 (1990).
19. World Health Organization, “Immunity passports” in the context of COVID-19, Scientific Brief, 24 April 2020; <https://www.who.int/news-room/commentaries/detail/immunity-passports-in-the-context-of-covid-19>.
20. B. Rockx et al., *Science* **368**, 1012–1015 (2020).

## ACKNOWLEDGMENTS

We thank B. Walker, A. Chakraborty, K. Reeves, B. Chen, J. Feldman, B. Hauser, T. Caradonna, S. Bondoc, C. Starke, C. Jacobson, D. O'Connor, S. O'Connor, N. Thornburg, E. Borducchi, M. Silva, A. Richardson, C. Caron, and J. Cwiak for generous advice, assistance, and reagents. **Funding:** We acknowledge support from the Ragon Institute of MGH, MIT, and Harvard, Mark and Lisa Schwartz Foundation, Beth Israel Deaconess Medical Center, Massachusetts Consortium on Pathogen Readiness (MassCPR), Bill & Melinda Gates Foundation (INV-006131), Janssen Vaccines & Prevention BV, and the National Institutes of Health (OD024917, AI129797, AI124377, AI128751, AI126603 to D.H.B.; AI135098 to A.J.M.; AI007387 to L.H.T.; AI007151 to D.R.M.; AI146779 to A.G.S.; 2722017000361-0-759301900131-1, AI100625, AI110700, AI132178, AI149644, AI108197 to R.S.B.; CA225088 to P.K.S.; and OD011092, OD025002 to J.D.E.). We also acknowledge a Fast Grant, Emergent Ventures, from the Mercatus Center at George Mason University, to A.J.M. and a Burroughs Wellcome Fund Postdoctoral Enrichment Program Award to D.R.M. **Author contributions:** D.H.B., H.A., and M.G.L. designed the study. A.C., J.L., K.M., N.B.M., L.P., L.H.T., J.Y., P.A., E.A.B., G.D., M.S.G., X.H., C.J.-D., N.K., Z.L., M.A.L., L.F.M., and J.P.N. performed the immunologic and virologic assays. A.J.M., Z.M., M.N., K.B.-S., M.T. L.M.W., S.D., A.D.M., P.K.S., and J.D.E. performed the pathology studies. D.R.M. and R.S.B. performed the live virus neutralization assays. C.A., S.F., J.S.B., M.D.S., and G.A. performed the antibody phenotyping. L.P., A.V.R., J.G., T.T., K.B., A.C., B.F., R.B., E.T., J.V., H.A., and M.G.L. led the clinical care of the animals and performed the virologic assays. R.Z. and F.W. participated in study design and interpretation of data. A.G.S. provided purified proteins. D.H.B. wrote the paper with input from all authors. **Competing interests:** The authors declare no competing financial interests. G.A. is an inventor on patent application WO 2017/184733 A1 submitted by Massachusetts General Hospital that covers systems serology. R.Z. and F.W. are employees of Janssen Vaccines & Prevention BV. **Data and materials availability:** All data are available in the manuscript



or the supplementary material. Virus stocks are available from D.H.B. under a material transfer agreement with Beth Israel Deaconess Medical Center. This work is licensed under a Creative Commons Attribution 4.0 International (CC BY 4.0) license, which permits unrestricted use, distribution, and reproduction in any medium, provided the original work is properly cited. To view a copy of this license, visit <https://creativecommons.org/licenses/by/4.0/>. This license does not apply to figures, photos, artwork, or

other content included in the article that is credited to a third party; obtain authorization from the rights holder before using such material.

**SUPPLEMENTARY MATERIALS**

[science.sciencemag.org/content/369/6505/812/suppl/DC1](https://science.sciencemag.org/content/369/6505/812/suppl/DC1)  
Materials and Methods

Table S1  
Figs. S1 to S11  
References

[View/request a protocol for this paper from Bio-protocol.](#)

26 April 2020; accepted 16 May 2020  
Published online 20 May 2020  
10.1126/science.abc4776

## REPORT

## CORONAVIRUS

# Primary exposure to SARS-CoV-2 protects against reinfection in rhesus macaques

Wei Deng<sup>1\*</sup>, Linlin Bao<sup>1\*</sup>, Jiangning Liu<sup>1\*</sup>, Chong Xiao<sup>1\*</sup>, Jiayi Liu<sup>2\*</sup>, Jing Xue<sup>1\*</sup>, Qi Lv<sup>1\*</sup>, Feifei Qi<sup>1</sup>, Hong Gao<sup>1</sup>, Pin Yu<sup>1</sup>, Yanfeng Xu<sup>1</sup>, Yajin Qu<sup>1</sup>, Fengdi Li<sup>1</sup>, Zhiguang Xiang<sup>1</sup>, Haisheng Yu<sup>1</sup>, Shuran Gong<sup>1</sup>, Mingya Liu<sup>1</sup>, Guanpeng Wang<sup>1</sup>, Shunyi Wang<sup>1</sup>, Zhiqi Song<sup>1</sup>, Ying Liu<sup>1</sup>, Wenjie Zhao<sup>1</sup>, Yunlin Han<sup>1</sup>, Linna Zhao<sup>1</sup>, Xing Liu<sup>1</sup>, Qiang Wei<sup>1</sup>, Chuan Qin<sup>1†</sup>

Coronavirus disease 2019 (COVID-19), which is caused by infection with the severe acute respiratory syndrome coronavirus 2 (SARS-CoV-2), has become a global pandemic. It is unclear whether convalescing patients have a risk of reinfection. We generated a rhesus macaque model of SARS-CoV-2 infection that was characterized by interstitial pneumonia and systemic viral dissemination mainly in the respiratory and gastrointestinal tracts. Rhesus macaques reinfected with the identical SARS-CoV-2 strain during the early recovery phase of the initial SARS-CoV-2 infection did not show detectable viral dissemination, clinical manifestations of viral disease, or histopathological changes. Comparing the humoral and cellular immunity between primary infection and rechallenge revealed notably enhanced neutralizing antibody and immune responses. Our results suggest that primary SARS-CoV-2 exposure protects against subsequent reinfection in rhesus macaques.

Coronavirus disease 2019 (COVID-19), which is caused by the severe acute respiratory syndrome coronavirus 2 (SARS-CoV-2), emerged in China and spread throughout the world, causing a global pandemic (1, 2). Some patients who were discharged with undetectable SARS-CoV-2 have reportedly had a positive result upon subsequent tests (3–5). Recently, SARS-CoV-2-specific neutralizing antibodies (NAbs) were detected around 10 to 15 days after the onset of COVID-19 (6–8). The possibility that patients have a risk of “relapse” or “reinfection” after recovery from the initial infection has raised concern. In this study, we therefore used nonhuman primates to longitudinally track the short-term infectious status from primary SARS-CoV-2 infection to reinfection by the same viral strain.

Seven adult Chinese-origin rhesus macaques (M0 to M6, 3 to 5 kg, 3 to 5 years of age) were modeled for challenge–rechallenge observations. Six monkeys (M1 to M6) were intratracheally challenged with SARS-CoV-2 at  $1 \times 10^6$  50% tissue-culture infectious doses (TCID<sub>50</sub>). After undergoing a mild-to-moderate course of SARS-CoV-2 infection, and transitioning into the recovery stage from the primary infection, four monkeys (M3 to M6) were rechallenged intratracheally with the same dose of

the SARS-CoV-2 strain at 28 days post-initial challenge (dpi). The remaining two monkeys (M1 and M2) with primary infection were not rechallenged and were used as the negative control of the rechallenge group. A healthy monkey (M0) was given an initial challenge as a model control of the second challenge. The pathological changes with viral-dependent distribution were compared using necropsy specimens between two monkeys that underwent only the initial challenge (M0 at 5 dpi and M1 at 7 dpi) and two monkeys that underwent challenge–rechallenge (M3 and M5) at 5 days post-rechallenge (dpr, 33 dpi). Body weight, rectal temperature, nasal/throat/anal swabs, hematological measurement, chest x-ray, virus distribution, pathological changes, and the analysis of immunocytes and binding and neutralizing antibodies were examined at the designated time points (Fig. 1). Weight loss ranging from 200 to 400 g was found in four monkeys that underwent the initial challenge (4 of 7: M0, M1, M2, and M4) (Fig. 2A), whereas the rectal temperature was not increased in any of the monkeys (0 of 7) (Fig. 2B). Reduced appetite and/or increased respiration were common (6 of 7, with the exception of M4) but emerged transiently and exhibited a very short duration. Regarding viral dissemination, the peak viral load ( $6.5 \log_{10}$  RNA copies/ml) in nasal swabs and pharyngeal swabs was detected at 3 dpi, followed by a gradual decline (Fig. 2, C and D). The peak viral load ( $5 \log_{10}$  RNA copies/ml) in anal swabs was observed at 3 dpi, followed by a linear decline to reach undetectable amounts at 14 dpi (Fig. 2E). In all monkeys that received the initial challenge, white blood cell count

[WBC,  $(3.5 \text{ to } 9.5) \times 10^9/\text{liter}$ ], lymphocyte counts [LYMP,  $(1.1 \text{ to } 3.4) \times 10^9/\text{liter}$ ], and neutrophil counts [NEUT,  $(1.8 \text{ to } 6.4) \times 10^9/\text{liter}$ ] fluctuated within normal ranges. Compared with the baseline, a slight but significant reduction in WBC and LYMP was observed after the primary infection (Fig. 2F). On radiological examination, bilateral obscured diaphragmatic surface and decreased transparency of lung fields with a small patch shadow in the left lower lobe were detected, indicating mild-to-moderate interstitial infiltration in monkeys with pneumonia (represented by M4 and M6, Fig. 2G). Using necropsy specimens, we detected viral RNA copies in the M0 monkey at 5 dpi and the M1 monkey at 7 dpi in the nose ( $10^6$  to  $10^8$  copies/ml), pharynx ( $10^4$  to  $10^6$  copies/ml), lung ( $10^3$  to  $10^7$  copies/ml), and gut ( $10^4$  to  $10^6$  copies/ml) (Fig. 3A, left panel). Hematoxylin and eosin (H&E) staining revealed a mild-to-moderate interstitial pneumonia characterized by widened alveolar septa, increased alveolar macrophages and lymphocytes in the alveolar interstitium, and degenerated alveolar epithelia; moreover, infiltrated inflammatory cells were detected in the lungs of monkeys with primary infection. Collagen fiber could also be observed in the thickened alveolar interstitium in M0 and M1 monkeys using modified Masson’s trichrome stain at 5 or 7 dpi (Fig. 3B). Furthermore, the trachea, tonsils, pulmonary lymph nodes, jejunum, and colon of the M0 and M1 monkeys exhibited inflammatory cell infiltrations (fig. S1, left panel), as well as infiltration with abundant CD4<sup>+</sup> T cells, CD8<sup>+</sup> T cells, B cells, macrophages, and plasma cells in lungs, as assessed using immunohistochemistry (IHC) (fig. S2). Viral-infected cells were mainly found in alveolar epithelia and macrophages by IHC on sequential sections (Fig. 3C), as well as in the trachea, tonsils, pulmonary lymph nodes, jejunum, and colon (fig. S1), confirming that SARS-CoV-2 caused COVID-19 in rhesus monkeys. Collectively, these data demonstrated that all seven monkeys were successfully infected with SARS-CoV-2 and that the pathogenicity in monkeys is similar to that reported in recent studies (9–14).

By 15 dpi, the body weight of infected monkeys (M2 to M6) had gradually increased into the normal range (4 of 5, with the exception of M4, Fig. 2A), and their rectal temperature was maintained within the normal range (Fig. 2B). Moreover, the viral loads were negative in all nasopharyngeal and anal swabs (5 of 5, Fig. 2, C to E). As shown in Fig. 2F, the hematological changes remained relatively stable within the normal range. Chest x-rays returned to normal manifestation at 28 dpi (represented by M4 and M6, Fig. 2G). These traits were similar to the hospital discharge criteria used for patients with COVID-19, including absence of clinical symptoms, radiological

<sup>1</sup>Beijing Key Laboratory for Animal Models of Emerging and Remerging Infectious Diseases, NHC Key Laboratory of Human Disease Comparative Medicine, Institute of Laboratory Animal Science, Chinese Academy of Medical Sciences and Comparative Medicine Center, Peking Union Medical College, Beijing, China. <sup>2</sup>Department of Radiology, Beijing Anzhen Hospital, Capital Medical University, Beijing, China.

\*These authors contributed equally to this work.  
†Corresponding author. Email: qinchuan@pumc.edu.cn



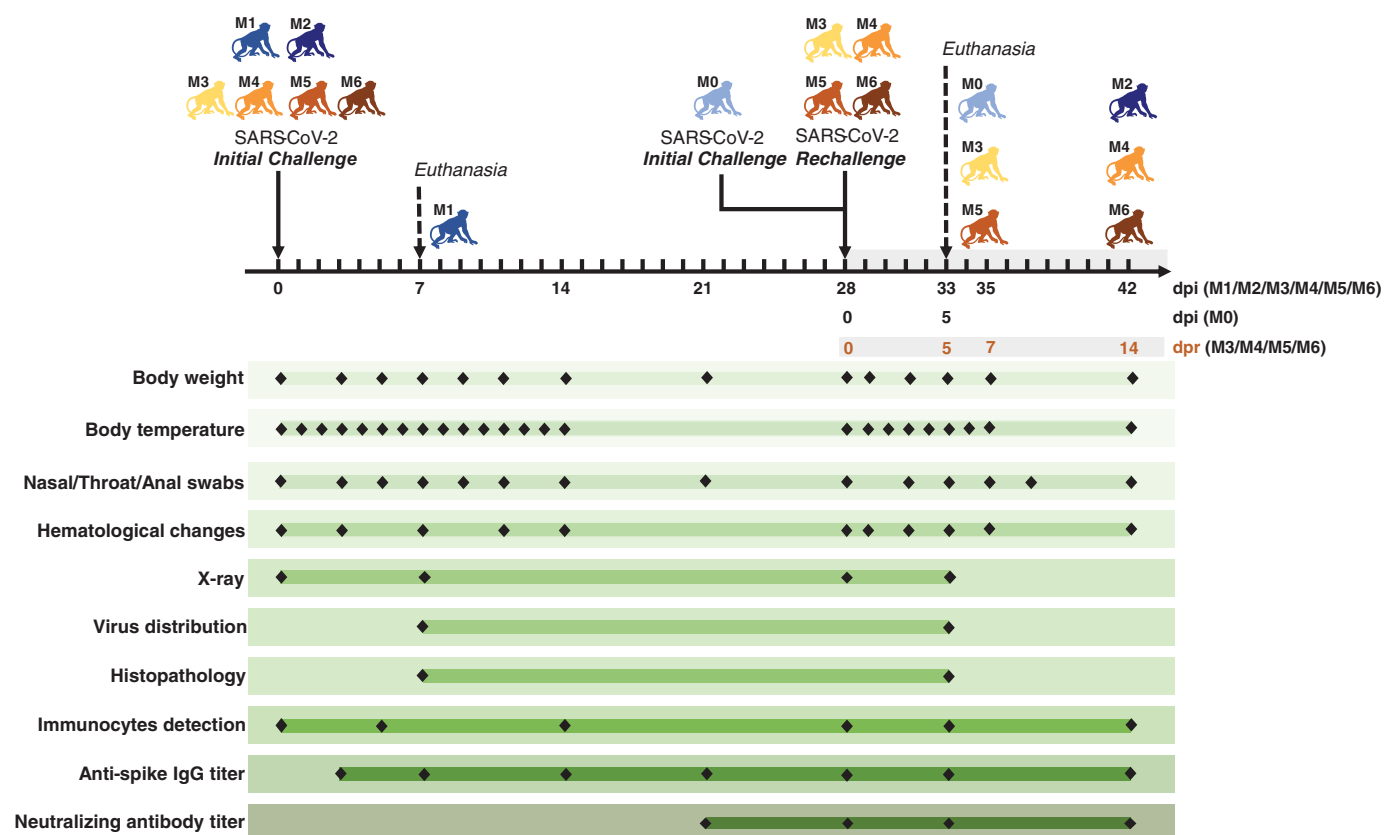


**Fig. 1. Experimental design and sample collection.** Seven adult Chinese-origin rhesus macaques (M0 to M6) were enrolled in the current study. At the outset of this experiment, six monkeys (M1 to M6) were challenged intratracheally with SARS-CoV-2 at  $1 \times 10^6$  TCID<sub>50</sub>. After all the experimentally infected monkeys had recovered from the primary infection, four infected monkeys (M3 to M6) were intratracheally rechallenged at 28 days post-initial challenge (dpi) with the same dose of the SARS-CoV-2 strain, to ascertain the possibility of reinfection. In addition, an uninfected monkey (M0) was also treated with SARS-CoV-2 as the model control of the second challenge, and a previously infected monkey (M2) was untreated in the rechallenge experiment and was continuously monitored as the control animal. To compare the virus

distribution and histopathological changes between the initially infected monkeys and the reinfected monkeys, two monkeys per group (M0 and M1 in the initial infection group, M3 and M5 in the reinfection group) were euthanized and necropsied at 5 dpi (M0), 7 dpi (M1), and 5 days post-rechallenge (dpr) (M3 and M5), respectively. Body weight, body temperature, nasal/throat/anal swabs, hematological changes, immunocytes, and specific antibodies were measured over the short-term observation period. Two measurements of virus distribution and histopathology (H&E and IHC staining) were carried out at 5 dpi (M0), 7 dpi (M1), and 5 dpr (M3 and M5). Chest x-ray and neutralizing antibody titers against SARS-CoV-2 were examined at the indicated time points.

abnormalities, and twice-negative reverse transcription-quantitative polymerase chain reaction (RT-qPCR) results (15). Taken together, our results suggest that monkeys that underwent initial SARS-CoV-2 infection required about 2 weeks to transition into the recovery stage (10, 16).

At 28 dpi, four monkeys (M3 to M6) that underwent primary infection and recovery were rechallenged intratracheally with the same dose of an identical SARS-CoV-2 strain. The clinical tracking of the reinfection included examination of weight loss (Fig. 2A) and rectal temperature (Fig. 2B). The rechallenged monkeys exhibited a transient increase in temperature, which was not observed during the primary infection. Viral loads remained negative over a 2-week intensive detection of the virus in nasopharyngeal and anal swabs after rechallenge with SARS-CoV-2 (Fig. 2, C to

E). Peripheral blood measurements revealed no significant fluctuation during the rechallenge stage (Fig. 2F). Moreover, we did not detect abnormalities by x-ray in the M4 and M6 monkeys at 33 dpi (5 dpr, Fig. 2G). In necropsy specimens of the lungs and extrapulmonary tissues of rechallenged monkeys (M3 and M5 at 5 dpr), we found no detectable viral RNA (Fig. 3A, right panel), no notable pathological lesions (Fig. 3B and fig. S1, right panel), no viral-infected cells (Fig. 3C and fig. S1, right panel), and no immune cell infiltration (fig. S2). Therefore, the rhesus monkeys that initially developed primary SARS-CoV-2 infection did not appear to be reinfected with the identical SARS-CoV-2 strain during their early recovery stage.

To interpret the challenge-rechallenge disparity, we performed a comparison of the clinical, pathological, viral, and immunological

traits that comprehensively reflected the virus-host interaction between the primary-challenge stage and the rechallenge stage in four monkeys (M3 to M6). First, the viral loads in nasopharyngeal and anal swabs were much higher at 5 or 7 dpi than they were at 5 or 7 dpr (Fig. 2, C to E, right panels). An increased WBC and neutrophils were observed at 14 dpr compared with 14 dpi (Fig. 2F, right panel). Second, T and B cells from peripheral blood, including CD4<sup>+</sup> T subsets [naïve CD4<sup>+</sup> T cells (CD4<sup>+</sup> T<sub>Naïve</sub>), central memory CD4<sup>+</sup> T cells (CD4<sup>+</sup> T<sub>CM</sub>), and effective memory CD4<sup>+</sup> T cells (CD4<sup>+</sup> T<sub>EM</sub>)], CD8<sup>+</sup> T subsets (CD8<sup>+</sup> T<sub>Naïve</sub>, CD8<sup>+</sup> T<sub>CM</sub>, and CD8<sup>+</sup> T<sub>EM</sub>), memory B cells, and plasma cells were relatively stable during the challenge-rechallenge infectious stage. However, an increased percentage of activated CD8<sup>+</sup> T cells from peripheral blood was observed at 14 dpi, which was also found at 0 dpr compared with





**Fig. 2. Longitudinal tracking of clinical signs, viral replication, hematological changes, and radiological changes.** (A and B) Clinical signs in each monkey. Monkeys were examined daily for changes in body weight and rectal temperature over the observation period after the initial infection, followed by virus rechallenge. The changes in weight are expressed as body weight loss after primary infection. (C to E) Detection of viral RNA in nasal, throat, and anal swabs. The SARS-CoV-2 RNA was detected by quantitative RT-PCR in the swabs from seven monkeys at the indicated time points. (F) Hematological changes, including WBC, LYMP, and NEUT counts in the peripheral blood, were monitored. (G) Chest x-rays of animals at 0, 7, 28, and 33 dpi (5 dpr) were examined, and representative images of M4 and M6 are shown

(red circles, areas of interstitial infiltration and exudative lesion; red arrows, obscured diaphragmatic surface; blue circles and arrows, areas that have recovered from pneumonia). Four monkeys (M3 to M6) were rechallenged at 28 dpi (dotted line and shaded areas), and the results of the initial infection and rechallenge were compared in bar graphs. The bars represent the average of four rechallenged animals at the indicated time points. The viral RNA loads in nasal, throat, and anal swabs of rechallenged animals were significantly lower than those of the initial infection, and significant hematological changes were observed between the primary and second challenges (unpaired *t* test, dpi versus dpr, \**P* < 0.05; \*\**P* < 0.01; \*\*\**P* < 0.001; #*P* < 0.05 0 dpi versus 7 dpi). ns, not significant.

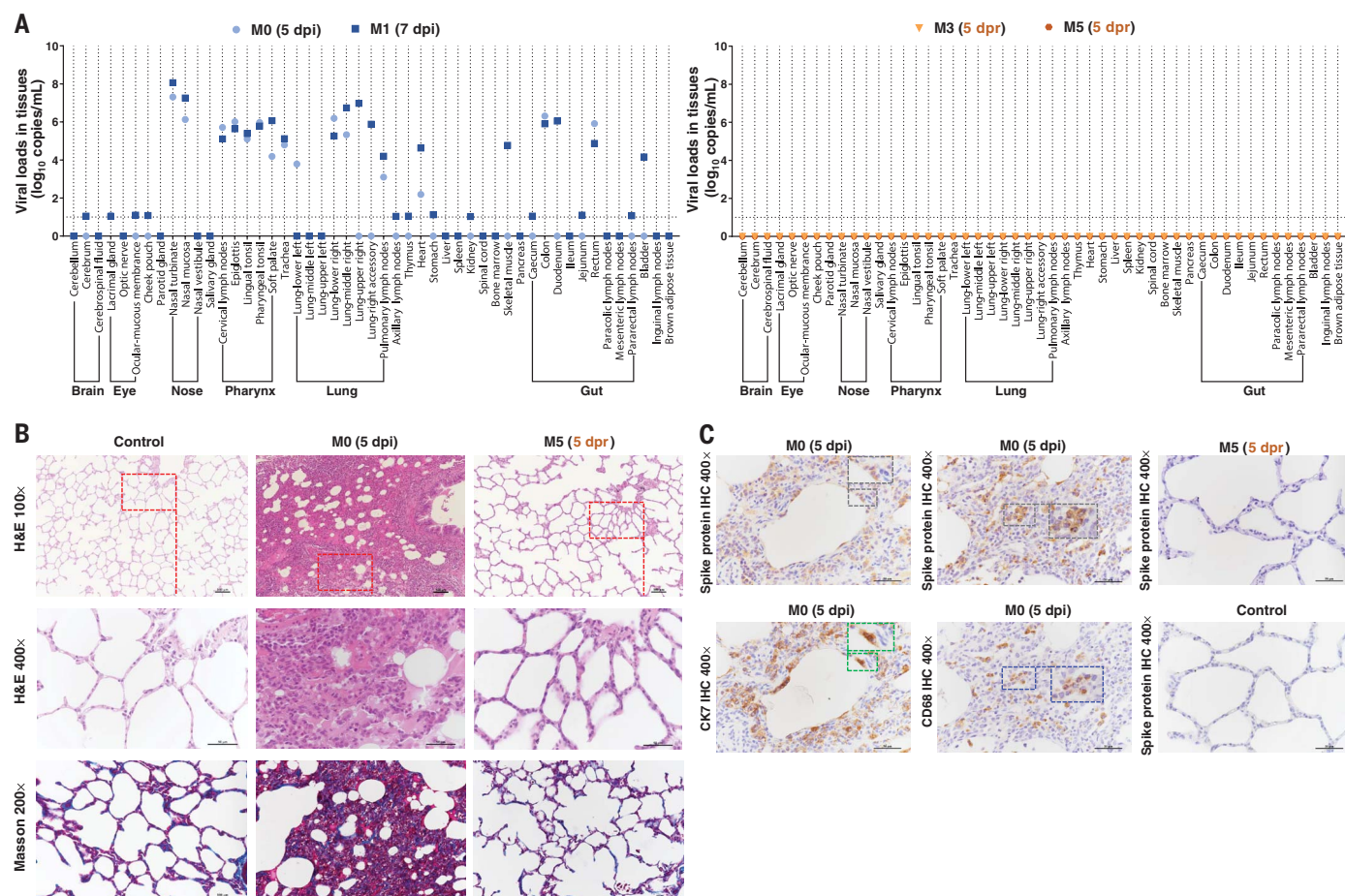


**Fig. 3. Comparison of virus distribution and pathological changes between the primary challenge and rechallenge stages.** (A) Detection of viral RNA in the indicated organs (brain, eye, nose, pharynx, lung, and gut. Compared with M0 and M1 (at 5 or 7 dpi; primary infection stage), viral replication tested negative in the indicated tissues from M3 and M5 (at 5 dpr; virus rechallenge stage). Using 10 copy equivalents of viral RNA as the limits of detection for SARS-CoV-2, we detected tissues from 49 anatomical parts for qualifying virus-infected positivity. Fourteen tissues from the respiratory tract, three tissues from the gut, and heart exhibited SARS-CoV-2-positive cells in both M0 and M1. SARS-CoV-2-positive cells were only observed in the left lower lung from M0 or in the right upper lung, upper accessory lung, skeletal muscle, duodenum, and bladder from M1. The remaining tissues from 29 anatomical parts did not show SARS-CoV-2-positive cells, indicating that these tissues were intact from viral invasion. (B) In M0 (5 dpi), an interstitial

lesion including markedly widened alveolar septa and massive infiltrated inflammatory cells was observed using H&E staining. A mild fibrosis was clearly detected within widened alveolar septa using Masson staining. (C) IHC against the spike protein of SARS-CoV-2 (7D2, gray frame), macrophages (CD68, blue frame), or alveolar epithelial cells (CK7, green frame) are visualized in parallel. The spike-positive cells overlapped with either alveolar epithelial cells or macrophages showing diffused interstitial pneumonia affected by SARS-CoV-2 invasion. In M5 (5 dpr), no marked pathological changes and virus distribution were detected by H&E staining, Masson staining, or IHC, indicating that the interstitial lesions had completely recovered from the SARS-CoV-2 primary infection and were intact to reinfection. The red rectangles indicate the areas of magnification. Scale bar at 100× or 200× indicates 100 μm. Scale bar at 400× indicates 50 μm. Data are representative of three independent experiments.

0 dpi (Fig. 4A, rightmost panel). Regarding the immune responses from lymph nodes, an increased percentage of CD4<sup>+</sup> T<sub>CM</sub> cells and decreased percentage of CD4<sup>+</sup> T<sub>Naive</sub> cells and memory B cells from lymph nodes were observed at 5 dpr compared with 5 dpi (Fig. 4B). Third, the specific antibody titers against the SARS-CoV-2 spike increased gradually, leading to a significantly higher titer at 21 dpi than at 3 dpi and 42 dpi (14 dpr) compared with

28 dpi or 0 dpr (Fig. 4C). Moreover, the specific antibody titers were much higher at 14 dpr compared to 14 dpi (Fig. 4C, right panel). As shown in Fig. 4D, the average titers of neutralizing antibodies exhibited a linear enhancement at the time of rechallenge (28 dpi; range, 1:8 to 1:20 in all monkeys). We observed an enhanced activation of CD8<sup>+</sup> T cells from peripheral blood, and changes in CD4<sup>+</sup> T<sub>CM</sub> cells and memory B cells from lymph nodes. It ap-

peared that an increased number of neutralizing antibodies against SARS-CoV-2 were induced by cellular or humoral immunity facilitated by the primary infection, which might have protected the same nonhuman primates against reinfection in the short term. However, factors that are directly correlated to protection are yet to be fully elucidated. Further studies of passive transfer of convalescent sera from this model to a naïve macaque, or CD8<sup>+</sup> T cell

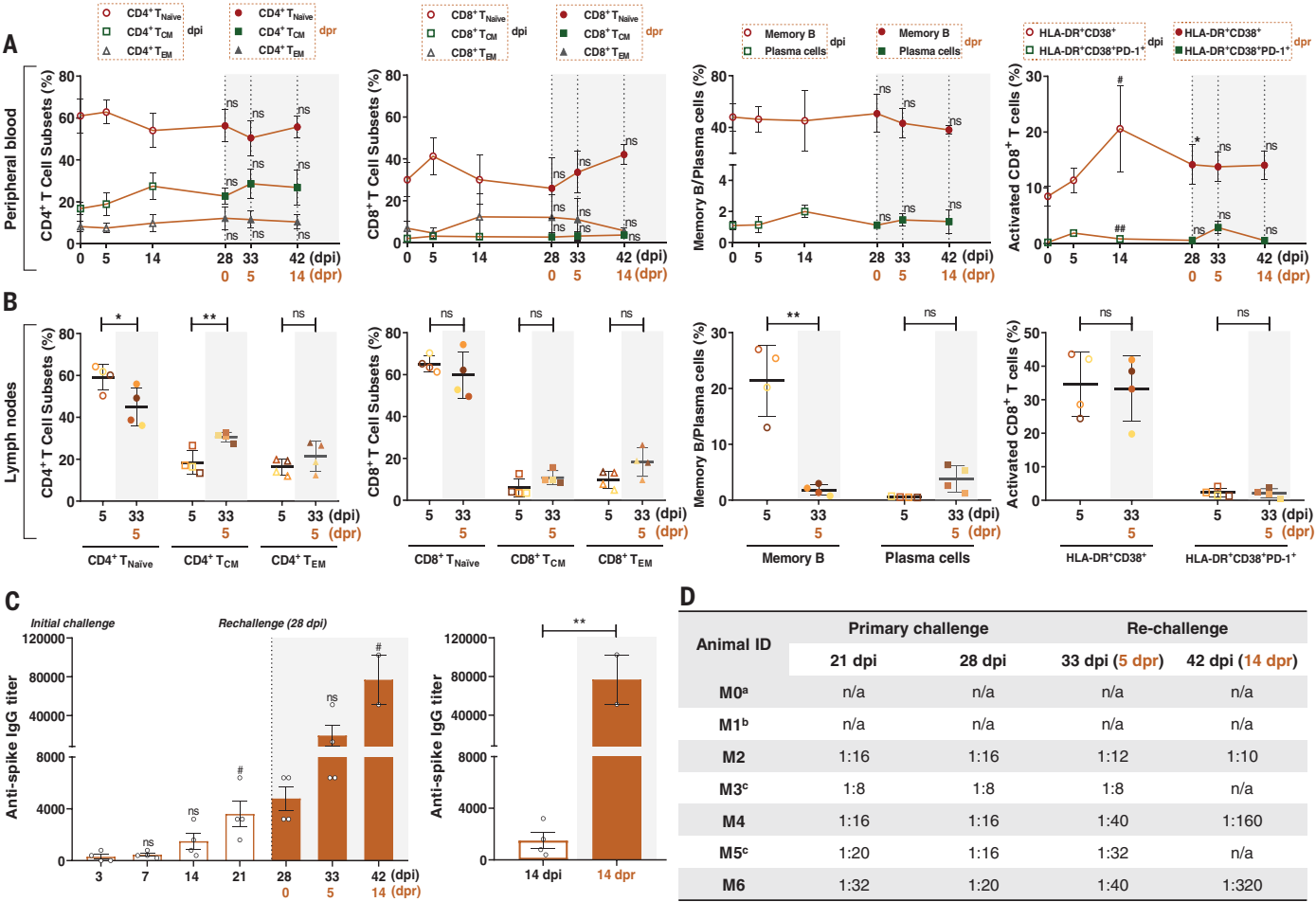


**Fig. 4. Comparison of cellular and humoral immunity between primary challenge and rechallenge stages in macaques.** Four macaques (M3 to M6) were rechallenged at 28 dpi (dotted line and shaded areas), and the results of the initial infection and rechallenge were compared at the same time points after the challenge and after the rechallenge. **(A)** Percentages of memory CD4<sup>+</sup>/CD8<sup>+</sup> T cell subsets, memory B cells, plasma cells, or activated CD8<sup>+</sup> T cells from peripheral blood for the challenge–rechallenge experiments. Compared with 0, 5, or 14 dpi, there were no significant differences on the percentage of naïve CD4<sup>+</sup>/CD8<sup>+</sup> T cells (CD4<sup>+</sup>/CD8<sup>+</sup> T<sub>Naive</sub>, CD3<sup>+</sup> CD4<sup>+</sup>/CD8<sup>+</sup> CCR7<sup>+</sup> CD45RA<sup>+</sup>), central memory CD4<sup>+</sup>/CD8<sup>+</sup> T cells (CD4<sup>+</sup>/CD8<sup>+</sup> T<sub>CM</sub>, CD3<sup>+</sup> CD4<sup>+</sup>/CD8<sup>+</sup> CCR7<sup>+</sup> CD45RA<sup>+</sup>), effective memory T cells (CD4<sup>+</sup>/CD8<sup>+</sup> T<sub>EM</sub>, CD3<sup>+</sup> CD4<sup>+</sup>/CD8<sup>+</sup> CCR7<sup>+</sup> CD45RA<sup>+</sup>), memory B cells (CD3<sup>+</sup> CD20<sup>+</sup> CD27<sup>+</sup>), and plasma cells (CD3<sup>+</sup> CD20<sup>+</sup> CD43<sup>+</sup>) from peripheral blood at 0, 5, and 14 dpr (unpaired *t* test, *ns*, *P* > 0.05). The activation of CD8<sup>+</sup> T cells (CD8<sup>+</sup> CD38<sup>+</sup> HLA-DR<sup>+</sup> or CD8<sup>+</sup> CD38<sup>+</sup> HLA-DR<sup>+</sup> PD-1<sup>+</sup>) at 14 dpi was

increased compared with the baseline (unpaired *t* test, <sup>#</sup>*P* < 0.05, <sup>##</sup>*P* < 0.01), and increased numbers of CD8<sup>+</sup> CD38<sup>+</sup> HLA-DR<sup>+</sup> T cells were also observed at 28 dpi (unpaired *t* test, 0 dpi versus 0 dpr, <sup>\*</sup>*P* < 0.05). **(B)** Percentages of memory CD4<sup>+</sup>/CD8<sup>+</sup> T cell subsets, memory B cells, plasma cells, or activated CD8<sup>+</sup> T cells from lymph nodes between 5 dpi and 5 dpr. An increased percentage of CD4<sup>+</sup> T<sub>CM</sub> cells and decreased percentage of CD4<sup>+</sup> T<sub>Naive</sub> cells and memory B cells from lymph nodes were found in the dot plots (unpaired *t* test, <sup>\*</sup>*P* < 0.05, <sup>\*\*</sup>*P* < 0.01). **(C)** Specific IgG titers against the spike protein of SARS-CoV-2 in four rechallenged monkeys. The titers of antigen-specific IgG from each monkey were detected at 3, 7, 14, 21, 28, 33, and 42 dpi. Significantly increased titers of IgG were observed between the primary and second challenges (unpaired *t* test, <sup>\*\*</sup>*P* < 0.01, 14 dpi versus 14 dpr; <sup>#</sup>*P* < 0.05, 3 dpi versus 21 dpi, 28 dpi versus 42 dpi). **(D)** Neutralizing antibody titers for protection of SARS-CoV-2-infected monkeys against reinfection.



depletion in the recovered monkeys prior to rechallenge, would be required to define the mechanisms underlying the pathogenicity of SARS-CoV-2.

In the present challenge-rechallenge infection of rhesus monkeys with SARS-CoV-2, observations and detections were carried out within the relative short time window in which neutralizing antibodies plateaued after the primary infection. A longer interval (longer than 6 months) between the primary challenge and the rechallenge is needed to track longitudinally the host-virus interaction and elucidate the protective mechanism against SARS-CoV-2 in primates. Moreover, all infected monkeys exhibited relative mild-to-moderate pneumonia, which is similar to the mild or common clinical characteristics of COVID-19 in infected human individuals; however, a COVID-19 monkey or transgenic mouse model with severe clinical symptoms or lethality should be explored according to increasing challenge dose, exposed tissues, or other treatments. Although we observed macrophages in association with SARS-CoV-2 infection, rapid rechallenge in the absence of potent serology relieved some level of concern regarding the occurrence of antibody-dependent enhancement (ADE). In addition, mucosal immunity, which is triggered by primary infection and includes both the respiratory and intestinal mucosa and local lymph nodes, might contribute substantially to the viral rechallenge response. Thus, future studies are required to examine experimentally the mucosal antibody responses, such as bronchoalveolar lavage im-

munoglobulin G (IgG) concentrations and serum IgA or IgM concentrations.

Taken together, our results suggest that rhesus macaques that have undergone an initial infection with SARS-CoV-2 mount protection against rechallenge during the early recovery days. However, it remains necessary to elucidate the protective mechanism against SARS-CoV-2 regarding neutralizing antibodies or other immunological roles. This short-term infection rechallenge macaque model provides insightful information for vaccination research, therapy of convalescent sera, and prognosis of COVID-19.

## REFERENCES AND NOTES

1. N. Zhu et al., *N. Engl. J. Med.* **382**, 727–733 (2020).
2. "Coronavirus disease (COVID-2019) Situation Reports," WHO (2020). <https://www.who.int/emergencies/diseases/novel-coronavirus-2019/situation-reports/>
3. L. Lan et al., *JAMA* **323**, 1502–1503 (2020).
4. L. Zhou, K. Liu, H. G. Liu, *Zhonghua Jie He He Hu Xi Za Zhi* **43**, 281–284 (2020).
5. J. An et al., Clinical characteristics of the recovered COVID-19 patients with re-detectable positive RNA test. medRxiv 2020.03.26.20044222 [Preprint]. 30 March 2020; <https://doi.org/10.1101/2020.03.26.20044222>.
6. F. Wu et al., Neutralizing antibody responses to SARS-CoV-2 in a COVID-19 recovered patient cohort and their implications. medRxiv 2020.03.30.20047365 [Preprint]. 20 April 2020; <https://doi.org/10.1101/2020.03.30.20047365>
7. N. M. A. Okba et al., *Emerg. Infect. Dis.* **26**, 1478–1488 (2020).
8. K. K. To et al., *Lancet Infect. Dis.* **20**, 565–574 (2020).
9. S. Lu et al., Comparison of SARS-CoV-2 infections among 3 species of non-human primate. bioRxiv 2020.04.08.031807 [Preprint]. 12 April 2020; <https://doi.org/10.1101/2020.04.08.031807>.
10. V. J. Munster et al., Respiratory disease and virus shedding in rhesus macaques inoculated with SARS-CoV-2. bioRxiv 2020.03.21.001628 [Preprint]. 21 March 2020; <https://doi.org/10.1101/2020.03.21.001628>.
11. B. Rockx et al., *Science* **368**, 1012–1015 (2020).
12. B. N. Williamson et al., Clinical benefit of remdesivir in rhesus macaques infected with SARS-CoV-2.

bioRxiv 2020.04.15.043166 [Preprint]. 22 April 2020; <https://doi.org/10.1101/2020.04.15.043166>.

13. P. Yu et al., *Animal Model. Exp. Med.* **3**, 93–97 (2020).
14. A. Chandrasekar et al., *Science* 10.1126/science.abc4776 (2020).
15. "Diagnostic and treatment protocol for Novel Coronavirus Pneumonia (Trial version 6)," National Health Commission of the People's Republic of China, (2020). <http://www.nhc.gov.cn/yzygj/s7652m/202002/54e1ad5c2aac45c19eb541799bf637e9.shtml>
16. S. F. Wang et al., *Biochem. Biophys. Res. Commun.* **451**, 208–214 (2014).

## ACKNOWLEDGMENTS

**Funding:** This work was supported by the CAMS initiative for Innovative Medicine of China (grant No. 2016-I2M-2-006), National Mega projects of China for Major Infectious Diseases (2017ZX10304402), and National Key Research and Development Project of China (grant no. 2016YFD0500304). **Author**

**contributions:** Conceptualization: C.Q.; Methodology: W.D., L.B., Jiangning Liu, C.X., Jiayi Liu, J.X., and Q.L.; Investigation: W.D., L.B., Jiangning Liu, C.X., Jiayi Liu, J.X., Q.L., F.Q., H.G., P.Y., Y.X., Y.Q., F.L., Z.X., H.Y., S.G., M.L., G.W., S.W., Z.S., Y.L., W.Z., Y.H., L.Z., X.L., and Q.W.; Writing – Original Draft: J.X.; Writing –Review and Editing: J.X. and C.Q.; Funding Acquisition: L.B. and C.Q.; Resources: C.Q.; Supervision: C.Q. **Competing interests:** The authors declare no competing interests. **Data and materials availability:** All data are available in the main text or the supplementary materials. This work is licensed under a Creative Commons Attribution 4.0 International (CC BY 4.0) license, which permits unrestricted use, distribution, and reproduction in any medium, provided the original work is properly cited. To view a copy of this license, visit <https://creativecommons.org/licenses/by/4.0/>. This license does not apply to figures/photos/artwork or other content included in the article that is credited to a third party; obtain authorization from the rights holder before using such material.

## SUPPLEMENTARY MATERIALS

[science.sciencemag.org/content/369/6505/818/suppl/DC1](https://science.sciencemag.org/content/369/6505/818/suppl/DC1)  
Materials and Methods  
Figs. S1 and S2  
Reference (17)

[View/request a protocol for this paper from Bio-protocol.](#)

29 April 2020; accepted 24 June 2020  
Published online 2 July 2020  
10.1126/science.abc5343

## IMMUNOLOGY

# BAF restricts cGAS on nuclear DNA to prevent innate immune activation

Baptiste Guey<sup>1\*</sup>, Marilena Wischnewski<sup>1\*</sup>, Alexiane Decout<sup>1</sup>, Kristina Makasheva<sup>2</sup>, Murat Kaynak<sup>3</sup>, Mahmut S. Sakar<sup>3</sup>, Beat Fierz<sup>2</sup>, Andrea Ablasser<sup>1†</sup>

The appearance of DNA in the cytosol is perceived as a danger signal that stimulates potent immune responses through cyclic guanosine monophosphate–adenosine monophosphate synthase (cGAS). How cells regulate the activity of cGAS toward self-DNA and guard against potentially damaging autoinflammatory responses is a fundamental biological question. Here, we identify barrier-to-autointegration factor 1 (BAF) as a natural opponent of cGAS activity on genomic self-DNA. We show that BAF dynamically outcompetes cGAS for DNA binding, hence prohibiting the formation of DNA–cGAS complexes that are essential for enzymatic activity. Upon acute loss of nuclear membrane integrity, BAF is necessary to restrict cGAS activity on exposed DNA. Our observations reveal a safeguard mechanism, distinct from physical separation, by which cells protect themselves against aberrant immune responses toward genomic DNA.

**T**he enzyme cGAS is a universal innate sensor for double-stranded DNA (dsDNA) (1, 2). On binding dsDNA, cGAS synthesizes the second messenger cyclic guanosine monophosphate (GMP)–adenosine monophosphate (AMP) (cGAMP) (3–7). cGAMP, in turn, activates STING (Stimulator of interferon genes) to initiate a downstream signaling cascade that culminates in the production of type I interferons and other inflammatory mediators (8).

The physical separation between nuclear DNA and cytoplasmic cGAS by the nuclear envelope (NE) is viewed as a crucial regulatory strategy to avoid aberrant innate immune activation (9). However, transient loss of nuclear integrity can occur during normal physiological processes, likely requiring an “immunologically silent” resolution and repair process (10–12). At present, it remains unclear how cGAS is controlled during transient openings of the NE.

To investigate cGAS responses toward disrupted nucleo-cytoplasmic compartmentalization, we reduced the levels of key factors known to support NE assembly at the end of mitosis with short interfering RNAs (siRNAs) and monitored levels of interferon-stimulated genes (ISGs) as a surrogate readout for cGAS activity in HeLa cells (13). We found that down-regulation of barrier-to-autointegration factor 1 (BAF), encoded by *BANFI*, triggered a robust ISG response, whereas suppression of other relevant genes had no effect (Fig. 1A and fig. S1A). The induction of ISGs was completely abrogated in cGAS-deficient cells

(Fig. 1A). Furthermore, suppression of *BAF* resulted in cGAMP production and activation of TBK1 (Fig. 1, B and C). Similar results were obtained in mouse embryonic fibroblasts and human fibroblasts (fig. S1, B to F). Thus, BAF appears to exert an important regulatory function over cGAS, and defects in BAF can trigger innate immune activation.

BAF is a chromatin-binding protein that is essential for nuclear membrane reformation at the end of mitosis (13–16). However, arresting cells in which *BAF* was knocked down (*BAF*-KD cells) in S phase of the cell cycle had no effect on the induced ISG response (fig. S2A). Moreover, ISG up-regulation was not accompanied by a detectable increase in micronuclei or by the appearance of cytosolic chromatin fragments (fig. S2, B to E). Instead, *BAF*-KD cells showed repetitive NE rupture events, which were strongly correlated with the accumulation of cGAS within discrete intranuclear foci (Fig. 1, D to F, and fig. S3, A to D). Live-cell imaging confirmed that cytosolic cGAS was recruited toward the nucleus interior after loss of NE integrity (Fig. 1G and movie S1). Stabilizing the NE with the myosin II inhibitor blebbistatin not only prevented NE ruptures after *BAF* suppression but also completely abrogated cGAS activity (Fig. 1H and fig. S3E). NE integrity could also be disrupted through either alterations in the nuclear lamina by suppressing lamin A (*LMNA*) or through mechanical compression (17–19). Despite cGAS nuclear translocation, neither approach induced an ISG response in wild-type (WT) cells (Fig. 2, A and B, and figs. S4 and S5). By contrast, in *BAF*-KD cells, mechanical compression elicited cGAS-STING pathway activation, as revealed by robust IRF3 activation (Fig. 2, C and D). Thus, the control of cGAS activity against nuclear self-DNA depends on more than just the nuclear

membrane and appears to critically rely on the function of BAF.

To explore the mechanism by which BAF restricts cGAS activity, we considered BAF's functional properties to bind dsDNA and to interact with inner nuclear membrane proteins through its LEM (Lap2/Emerin/Man1) domain (16). Reconstitution of *BAF*-KD cells with a mutant defective in LEM-domain binding, *BAF L58R* (16), or the combined depletion of LEM-domain proteins had no effect. By contrast, reconstitution with a *BAF* mutant compromised in DNA binding, *BAF G47E* (20), induced ISG up-regulation (Fig. 3A and fig. S6, A to D). We therefore hypothesized that BAF may prevent cGAS activity by competing for DNA binding. Using purified components, we determined that WT BAF, but not *BAF G47E*, reduced cGAS binding to both chromatin and dsDNA in a dose-dependent manner (Fig. 3B and fig. S6, E and F). Moreover, BAF robustly inhibited DNA-dependent cGAMP synthesis in vitro, whereas *BAF G47E* had no such effect (Fig. 3, C and D). We next used single-molecule total internal reflection fluorescence (smTIRF) microscopy to visualize in real time the binding of individual cGAS molecules to dsDNA (fig. S7, A to C). Single-molecule traces revealed that cGAS engaged in very transient [dwell time ( $\tau_{\text{off},1}$ ) =  $1.4 \pm 0.5$  s] and occasionally longer ( $\tau_{\text{off},2}$  =  $15 \pm 5$  s) interactions with dsDNA (Fig. 3, E and H, and fig. S7D). When BAF was added, there was no change in the binding rate ( $k_{\text{on}}$ ) of cGAS on dsDNA. Instead, WT BAF, but not *BAF G47E*, led to the rapid dissociation of cGAS from dsDNA, as indicated by a marked reduction of the average dwell times ( $\tau_{\text{off},1}$ ,  $\tau_{\text{off},2}$ ) (Fig. 3, F to H, and fig. S7D). Thus, rather than passively interfering with cGAS activity by blocking DNA binding sites, BAF dynamically displaces transiently bound cGAS monomers from dsDNA.

The above data suggest a model in which BAF outcompetes cGAS on DNA, preventing the formation of oligomeric DNA–cGAS assemblies, which is required for enzymatic activity (21). Under this model, cGAS should form larger and more stable complexes, with DNA exposed at the site of NE rupture if BAF was absent. Monitoring cGAS intracellular localization at a given moment in time revealed that a large fraction of *BAF*-KD cells accumulated cytosolic cGAS in the nucleus (Fig. 4A). By contrast, only few *LMNA*-KD cells showed intranuclear cGAS accumulation (Fig. 4A). In addition, for those nuclei that accumulated cGAS, the intranuclear volume covered by cGAS was larger when *BAF* was down-regulated (Fig. 4, A inset, B, and C). Using fluorescence recovery after photobleaching (FRAP), we also found that cGAS was less mobile on chromatin in *BAF*-KD cells versus *LMNA*-KD cells or control cells, respectively

<sup>1</sup>Global Health Institute, Swiss Federal Institute of Technology Lausanne (EPFL), Switzerland. <sup>2</sup>Institute of Chemical Sciences and Engineering, EPFL, Switzerland.

<sup>3</sup>Institute of Mechanical Engineering, EPFL, Switzerland.

\*These authors contributed equally to this work.

†Corresponding author. Email: andrea.ablasser@epfl.ch



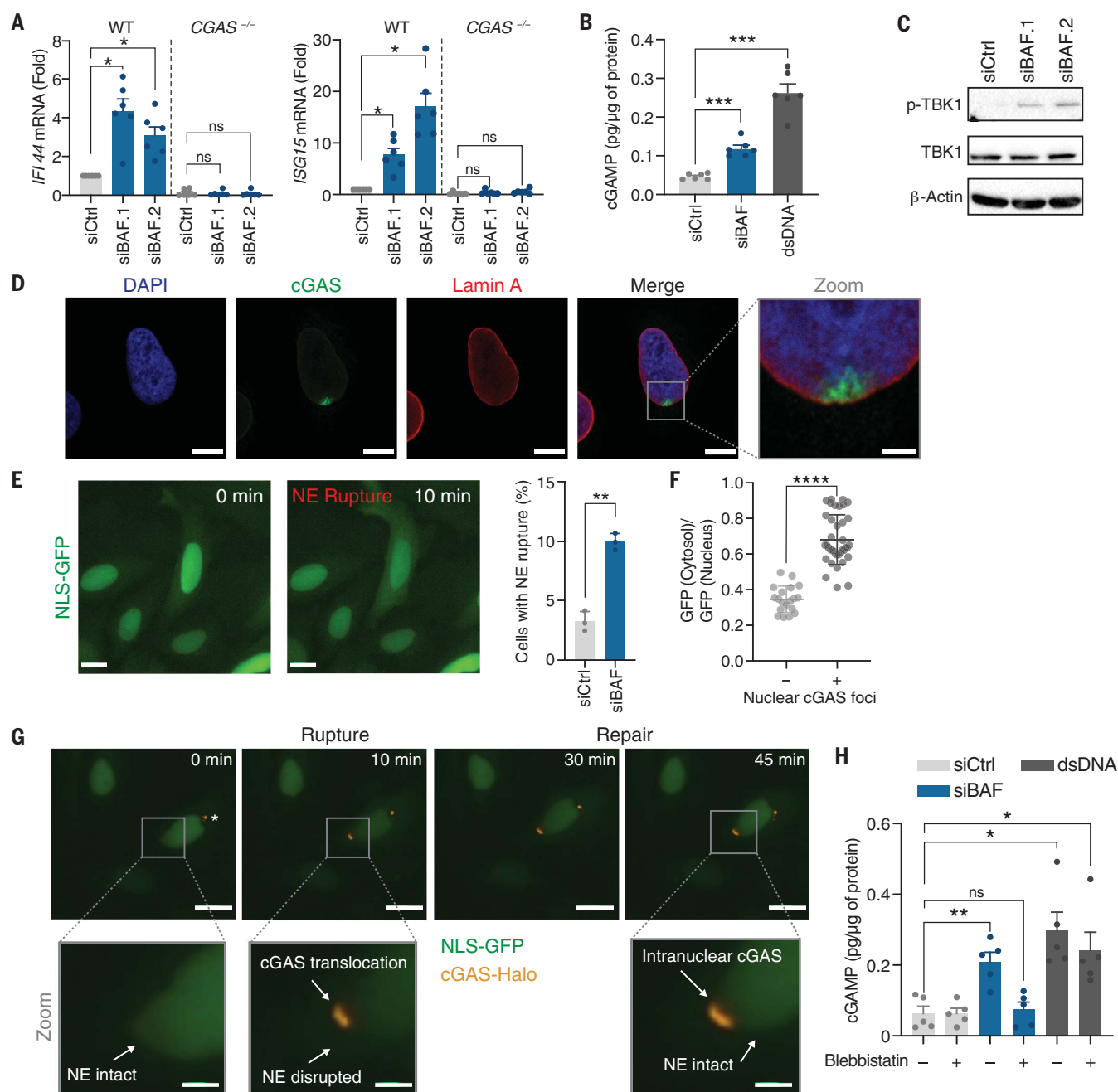


**Fig. 1. BAF depletion causes NE rupture and cGAS activation on chromatin.**

(A) ISG (*ISG15*, *IFI44*) induction in WT and *CGAS*<sup>-/-</sup> HeLa cells treated with a control siRNA (siCtrl) or siRNAs against BAF (siBAF.1 and siBAF.2) ( $n = 6$  independent experiments). One-way analysis of variance (ANOVA) with post hoc Tukey multiple comparison test was used. (B) 2'3'-cGAMP quantification in HeLa cells treated with siCtrl or siBAF or transfected with 90-nucleotide oligomer dsDNA (dsDNA) ( $n = 6$  independent experiments). One-way ANOVA with post hoc Dunnett multiple comparison test was used. (C) Phosphorylation of TBK1 in HeLa cells after BAF knockdown (representative of three independent experiments). (D) Representative confocal fluorescence microscopy images of BAF-KD HeLa cells stained with antibodies against cGAS (green) and lamin A (red). 4',6-diamidino-2-phenylindole (DAPI) is shown in blue (representative of three independent experiments). Scale bar, 20 μm or (inset) 5 μm. (E) (Left) Representative fluorescence microscopy images showing a NE rupture event (NLS-GFP escape; green). (Right) Incidence of NE ruptures in HeLa cells upon

treatment with a control siRNA or one targeting BAF ( $n = 3$  independent experiments). A complete image sequence is available in fig. S3B. Scale bar, 20 μm. Student's  $t$  test was used. (F) NLS-GFP fluorescence ratio cytosol/nucleus in BAF-depleted HeLa cells exhibiting or not cGAS nuclear foci [ $n = 19$  cells without cGAS nuclear foci (-),  $n = 38$  cells with cGAS nuclear foci (+)]. Student's  $t$  test was used. (G) Representative image sequence of a BAF-depleted HeLa cell exhibiting a NE rupture event (NLS-GFP escape; green) accompanied by cGAS-Halo (orange) intranuclear accumulation (representative of three independent experiments) (movie S1). Asterisk indicates cGAS in a micronucleus. Scale bar, 20 μm or (inset) 5 μm. (H) 2'3'-cGAMP quantification in HeLa cells pretreated or not with blebbistatin and treated with siCtrl or siBAF or transfected with 90-nucleotide oligomer DNA (dsDNA) ( $n = 5$  independent experiments). One-way ANOVA with post hoc Dunnett multiple comparison test was used. Error bars indicate SEM. \* $P < 0.05$ ; \*\* $P < 0.01$ ; \*\*\* $P < 0.001$ ; \*\*\*\* $P < 0.0001$ ; ns, not significant.

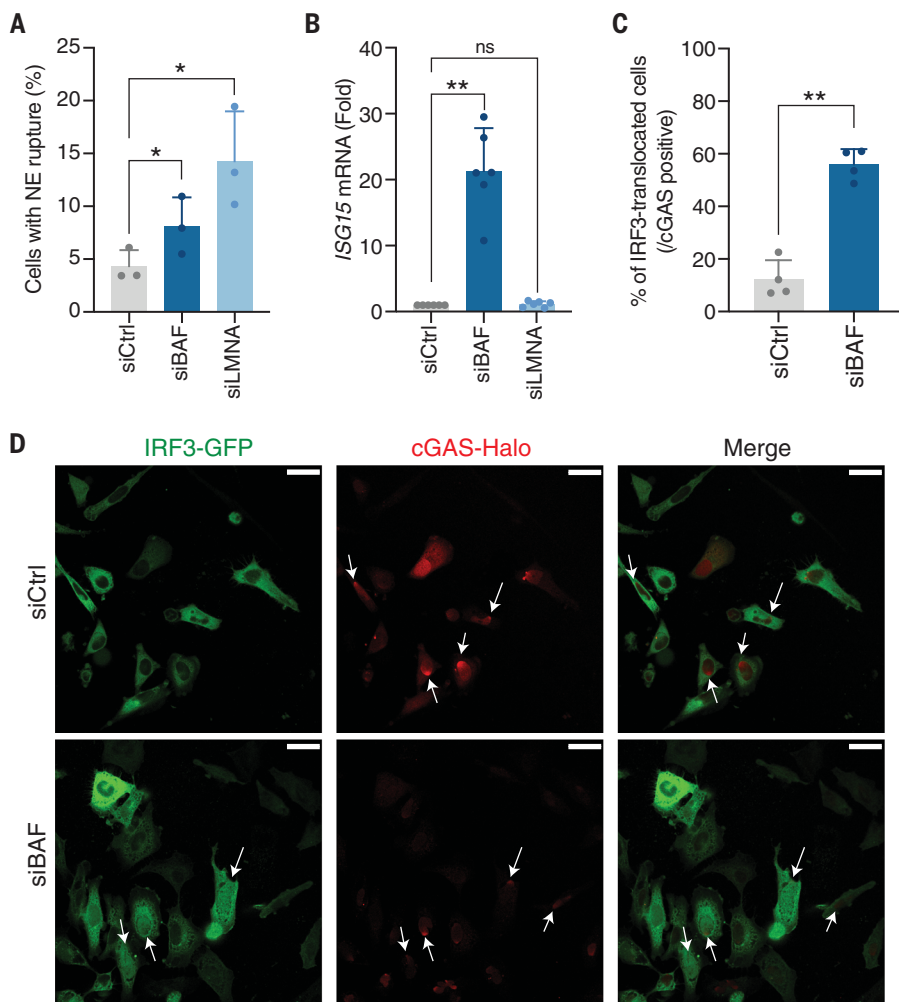


**Fig. 2. Loss of nuclear integrity is not uniformly linked to cGAS activity.**

(**A**) Incidence of NE ruptures in HeLa cells treated with siCtrl, siBAF, or siLMNA ( $n = 3$  independent experiments). Multiple  $t$  test was used. (**B**) ISG15 mRNA expression levels in HeLa cells treated with siCtrl, siBAF, or siLMNA ( $n = 6$  independent experiments). One-way ANOVA with post hoc Dunnett multiple comparison test was used. (**C**) Quantification of cells with cGAS-positive nuclei showing GFP-IRF3 nuclear translocation after confinement of HeLa treated with blebbistatin (20  $\mu$ M) and siCtrl or siBAF, respectively ( $n = 4$  independent experiments). Student's  $t$  test was used. (**D**) Representative image of HeLa cells stably expressing GFP-IRF3 (green) and cGAS-Halo (red), treated with blebbistatin (20  $\mu$ M) and siCtrl or siBAF and subjected to 3- $\mu$ m confinement for 1 min. Image was acquired 5 hours after confinement (representative of three independent experiments). Scale bar, 40  $\mu$ m. Error bars indicate SEM. \* $P < 0.05$ ; \*\* $P < 0.01$ ; \*\*\*\* $P < 0.0001$ ; ns, not significant.

(Fig. 4D; fig. S8, A, B and C; and movie S2). Critically, the frequency of rupture events as well as the overall rate of NE repair was similar between *BAF*-KD and *LMNA*-KD cells (fig. S8D). Thus, in living cells, BAF limits cGAS associations with chromatin after NE rupture, which is consistent with the competition for DNA binding.

BAF has been implicated in the recognition of exogenous dsDNA in the cytosol (22). Visualizing the recruitment of BAF and cGAS to transfected DNA revealed a negative correlation between DNA foci that were targeted by cGAS versus BAF, and overexpression of BAF enhanced this effect (fig. S9A). We also measured cGAMP production and ISG transcripts and found that *BAF* overexpression resulted in compromised cGAS activation at least in part (fig. S9B). Competition for DNA binding between cGAS and BAF can therefore also occur in the cytosol, albeit with lower overall efficacy.

Although the activation of cGAS by DNA typically occurs within the cytosol, a considerable fraction of cGAS resides within the nucleus at steady state (19, 23). However,

the nuclear pool of cGAS appears functionally inactive through strong binding to chromatin and is considered to not participate in DNA sensing and activation (23, 24). To understand the relationship between the inhibitory effect of chromatin versus BAF for cGAS regulation, we used two distinct *CGAS* mutants, *CGAS R236A* and *R255A*, that are defective in nuclear tethering (23). Consistent with prior work (23), cells expressing either mutant showed spontaneous cGAMP synthesis, presumably as a result of nuclear DNA sensing. Suppression of *BAF* markedly enhanced the overall level of cGAMP production from both *CGAS*-mutant cells, whereas overexpression of *BAF* reduced cGAMP synthesis (fig. S10, A and B). We also generated cells that selectively express cGAS inside the nucleus (*GFP-NLS-CGAS*) to lower the threshold of intranuclear cGAS activation (19). Suppression of *BAF* in this experimental system led to prominent cGAS activity, even in the absence of NE ruptures (Fig. 4E). Last, we investigated whether other chromatin organizing factors exert similar regulatory function over cGAS (25).

Using the cGAS-nuclear localization signal (NLS) experimental system, we found that compared with several other architectural chromatin proteins, the suppression of *BAF* had by far the strongest effect on both cGAMP production and ISG up-regulation (fig. S11, A to C). Moreover, the decondensation of chromatin by treating cells with the histone deacetylase inhibitors valproic acid (VA) and trichostatin A (TSA) did not trigger cGAS-NLS activity. Chromatin decompaction through overexpression of *HMGN5* in HeLa cells similarly had no effect on this pathway (fig. S11, D and E) (26). Thus, although the precise role of chromatin architecture and chromatin itself requires further study, our experimental findings provide strong evidence that BAF acts as a critical regulatory factor over cGAS on nuclear DNA.

This study identifies a safeguard mechanism that restricts cGAS activity on genomic self-DNA: Upon loss of nuclear compartmentalization, cytosolic cGAS accumulates on chromatin at the nuclear periphery. Its enzymatic activity is prevented, however, by BAF, which dynamically outcompetes cGAS



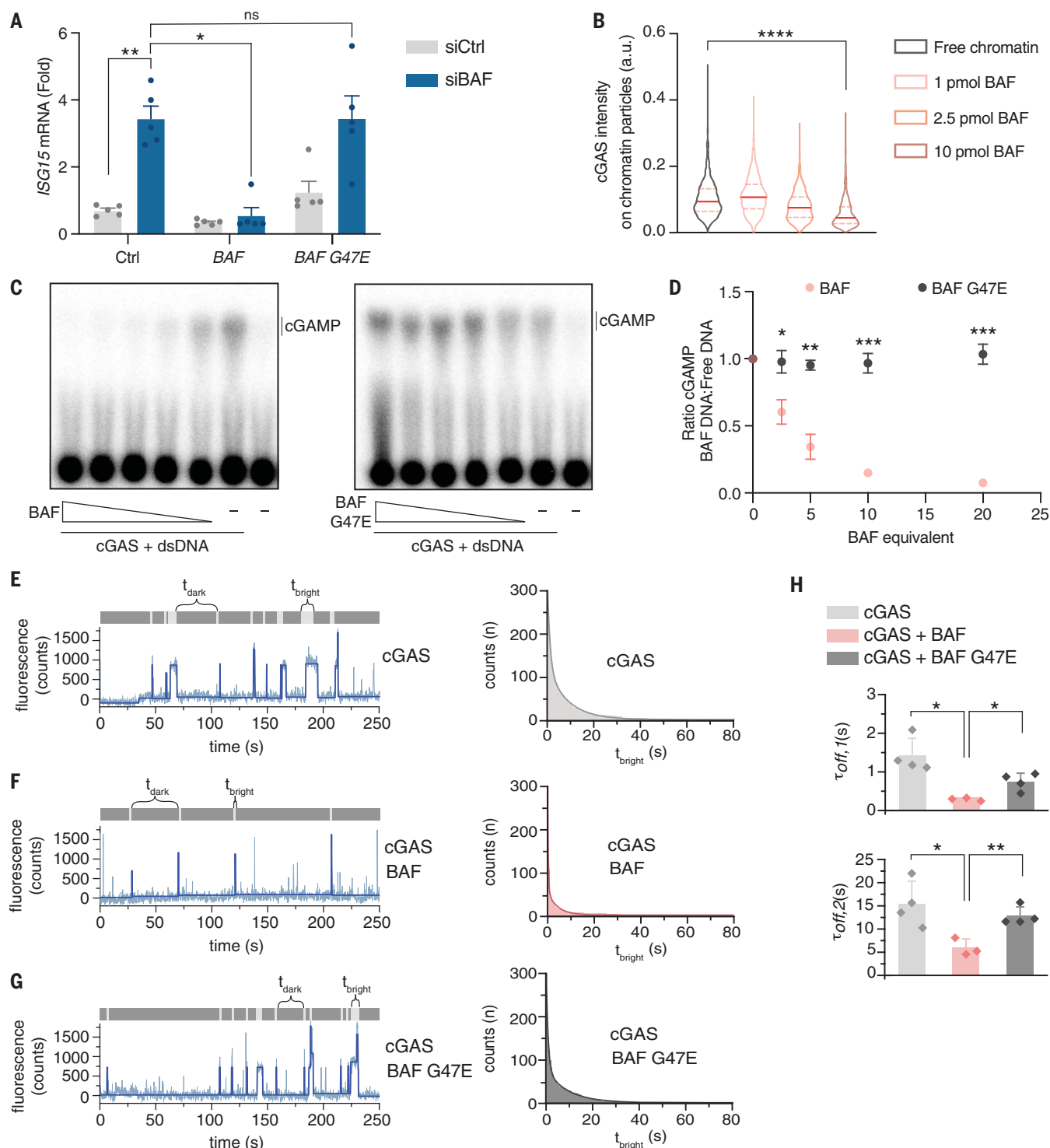


**Fig. 3. Molecular mechanism of cGAS inhibition by BAF.** (A) *ISG15* mRNA expression levels of HeLa cells (Ctrl) and siRNA-resistant WT BAF- and BAF G47E-expressing HeLa cells depleted or not for BAF ( $n = 5$  independent experiments). One-way ANOVA with post hoc Dunnett multiple comparison test was used. (B) Labeled-cGAS intensity obtained by means of confocal microscopy of chromatin particles preincubated or not with BAF ( $n = 3$  independent experiments). One-way ANOVA with post hoc Dunnett multiple comparison test was used. (C) In vitro analysis of 2'3'-cGAMP synthesis by means of dsDNA-stimulated cGAS and addition of (left) WT BAF or (right) BAF G47E (representative of three independent experiments). (D) Ratio of

in vitro 2'3'-cGAMP synthesis between cGAS stimulated with dsDNA precomplexed with WT BAF or BAF G47E, and free dsDNA ( $n = 3$  independent experiments). Multiple  $t$  test was used. (E to G) Extracted single-molecule (sm) fluorescence time trace (left) and corresponding dwell-time histograms for (E) cGAS in the absence of BAF, (F) cGAS in the presence of WT BAF, and (G) cGAS in the presence of BAF G47E, showing stochastic binding events. (H) Dwell times ( $\tau_{off,1}$ ;  $\tau_{off,2}$ ) for cGAS, cGAS + WT BAF, and cGAS + BAF G47E.  $n = 4$  (cGAS),  $n = 3$  (cGAS + BAF WT), and  $n = 4$  (cGAS + BAF G47E) independent experiments. Two-tailed Student's  $t$  test was used. Error bars indicate SEM. \* $P < 0.05$ ; \*\* $P < 0.01$ ; \*\*\* $P < 0.001$ ; \*\*\*\* $P < 0.0001$ ; ns, not significant.

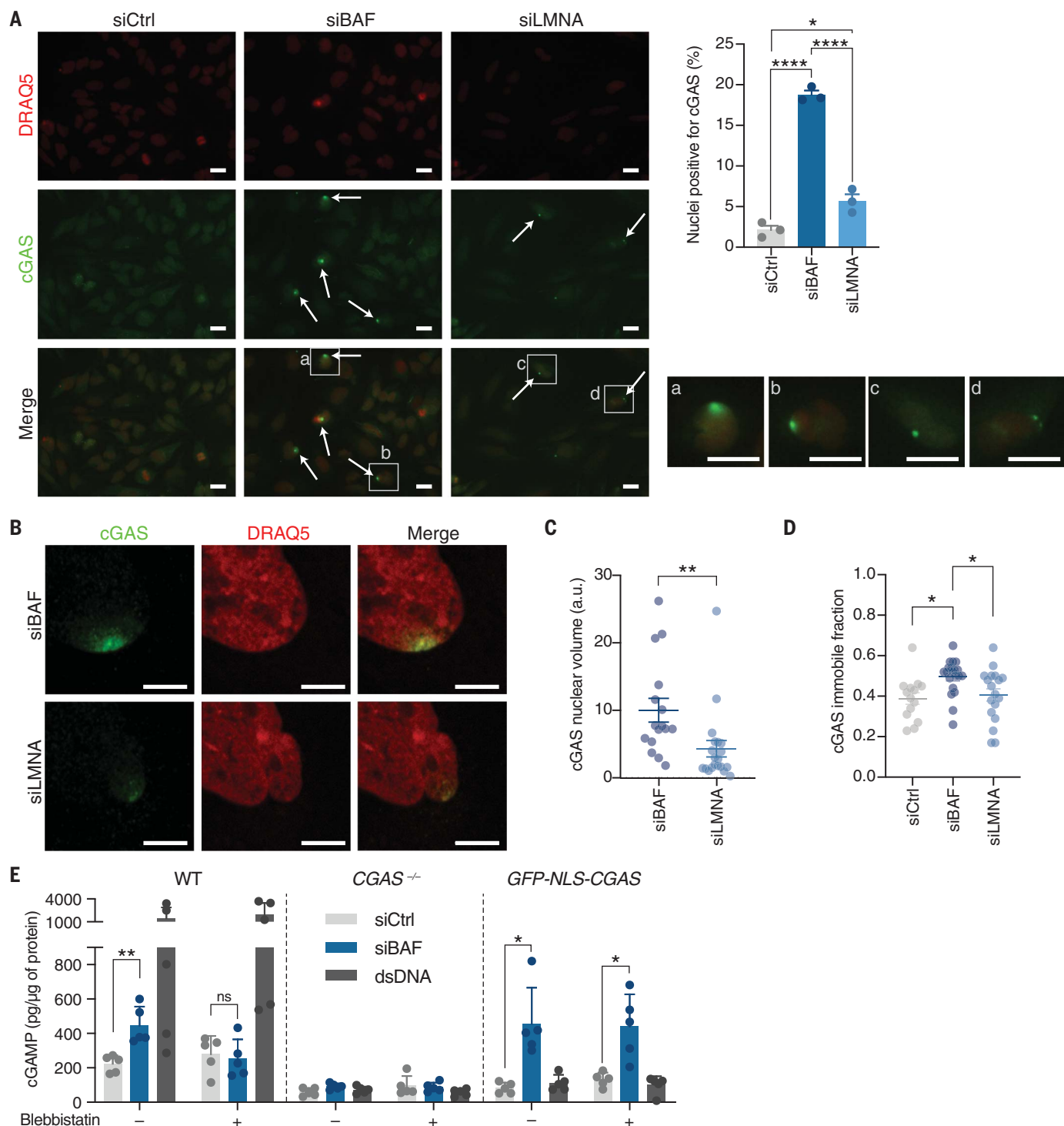


**Fig. 4. BAF outcompetes cGAS from DNA in living cells.** (A) (Left) Representative fluorescence microscopy images of HeLa cells treated with siCtrl, siBAF, or siLMNA for 3 days and stained for cGAS (green) and DNA (DRAQ5, red). Scale bar, 20  $\mu$ m. (Top right) Quantification of nuclei exhibiting cGAS nuclear foci for each condition as indicated ( $n = 3$  independent experiments). One-way ANOVA with post hoc Dunnett multiple comparison test. (Bottom right) Enlargement of indicated nuclei. (B and C) Representative high-resolution confocal fluorescence microscopy images of cGAS nuclear foci and measurement of cGAS nuclear volume in HeLa cells treated for 3 days with siBAF or siLMNA. Cells were stained for cGAS (green) and DNA (DRAQ5, red) (representative of

three independent experiments). Scale bar, 5  $\mu$ m. (D) cGAS-GFP immobile fraction obtained after photobleaching of cGAS-GFP nuclear foci in HeLa cells treated with siCtrl, siBAF, or siLMNA (representative of three independent experiments). One-way ANOVA with post hoc Dunnett multiple comparison test was used. (E) 2'3'-cGAMP levels from WT HeLa,  $CGAS^{-/-}$  HeLa, or  $CGAS^{-/-}$  HeLa cells overexpressing NLS-cGAS (GFP-NLS- $CGAS$ ) and treated with siCtrl or siBAF or transfected with 90-nucleotide oligomer DNA (dsDNA) ( $n = 5$  independent experiments). Two-way ANOVA with post hoc Dunnett multiple comparison test was used. Error bars indicate SEM. \* $P < 0.05$ ; \*\* $P < 0.01$ ; \*\*\* $P < 0.001$ ; ns, not significant.



for DNA binding. Although limiting cGAS activity against self-DNA depends on compartmentalization in certain situations (such as mitochondria, micronuclei, and cytosolic chromatin fragments) (2, 9), our work implicates that regulation of nuclear DNA sensing requires more complex mechanisms than simple physical separation. We propose that dynamic competition with BAF at the nuclear periphery is a critical strategy used by the host to reconcile the advantages of maintaining a universal DNA recognition machinery with routine operations occurring within a living cell.

## REFERENCES AND NOTES

1. L. Sun, J. Wu, F. Du, X. Chen, Z. J. Chen, *Science* **339**, 786–791 (2013).
2. A. Ablasser, Z. J. Chen, *Science* **363**, eaat8657 (2019).
3. A. Ablasser *et al.*, *Nature* **498**, 380–384 (2013).
4. E. J. Diner *et al.*, *Cell Rep.* **3**, 1355–1361 (2013).
5. P. Gao *et al.*, *Cell* **153**, 1094–1107 (2013).
6. J. Wu *et al.*, *Science* **339**, 826–830 (2013).
7. X. Zhang *et al.*, *Mol. Cell* **51**, 226–235 (2013).
8. G. N. Barber, *Nat. Rev. Immunol.* **15**, 760–770 (2015).
9. A. Ablasser, S. Hur, *Nat. Immunol.* **21**, 17–29 (2020).
10. C. M. Denais *et al.*, *Science* **352**, 353–358 (2016).
11. M. Raab *et al.*, *Science* **352**, 359–362 (2016).
12. R. Ungricht, U. Kutay, *Nat. Rev. Mol. Cell Biol.* **18**, 229–245 (2017).
13. T. Haraguchi *et al.*, *J. Cell Sci.* **121**, 2540–2554 (2008).
14. T. Haraguchi *et al.*, *J. Cell Sci.* **114**, 4575–4585 (2001).
15. A. Margalit, M. Segura-Totten, Y. Gruenbaum, K. L. Wilson, *Proc. Natl. Acad. Sci. U.S.A.* **102**, 3290–3295 (2005).
16. M. Samwer *et al.*, *Cell* **170**, 956–972.e23 (2017).
17. W. H. De Vos *et al.*, *Hum. Mol. Genet.* **20**, 4175–4186 (2011).
18. M. Le Berre, E. Zlotek-Zlotkiewicz, D. Bonazzi, F. Lautenschlaeger, M. Piel, *Methods Cell Biol.* **121**, 213–229 (2014).
19. M. Gentili *et al.*, *Cell Rep.* **26**, 3798 (2019).
20. T. C. Umland, S. Q. Wei, R. Craigie, D. R. Davies, *Biochemistry* **39**, 9130–9138 (2000).
21. L. Andreeva *et al.*, *Nature* **549**, 394–398 (2017).
22. S. Kobayashi *et al.*, *Proc. Natl. Acad. Sci. U.S.A.* **112**, 7027–7032 (2015).
23. H. E. Volkman, S. Cambier, E. E. Gray, D. B. Stetson, *eLife* **8**, e47491 (2019).
24. C. Zierhut *et al.*, *Cell* **178**, 302–315.e23 (2019).
25. S. J. McBryant, V. H. Adams, J. C. Hansen, *Chromosome Res.* **14**, 39–51 (2006).
26. T. Furusawa *et al.*, *Nat. Commun.* **6**, 6138 (2015).

## ACKNOWLEDGMENTS

We thank N. Jordan and J. Ricci for technical assistance and members of the Ablasser laboratory for discussions. We thank

T. Laroche, R. Guiet, O. Burri, and A. Seitz of the Bioimaging and Optics Platform (BIOP) at EPFL. **Funding:** This work was supported by the SNF (BSSGI0-155984, 31003A\_159836), the Gebert R f Foundation (GRS-059\_14), the NCCR Chemical Biology, and the ERC (804933, ImAgine) to A.A. B.G. has been awarded a Long-Term EMBO Fellowship (ALTF 203-2016). B.F. is supported by the ERC (724022, chromo-SUMMIT) and the NCCR Chemical Biology. M.S.S. is supported by the ERC (714609, ROBOCHIP). **Author contributions:** B.G. and A.A. designed the study. B.G., M.W., A.D., K.M., and M.K. performed experiments, and all authors analyzed the data. A.A. wrote the manuscript, with input from all authors, and supervised the study. **Competing interests:** A.A. is a member of the scientific advisory board of IFM Therapeutics and scientific cofounder of IFM Due. All other authors declare no conflicts of interest. **Data and materials availability:** All data are available in the main text or the supplementary materials.

## SUPPLEMENTARY MATERIALS

[science.sciencemag.org/content/369/6505/823/suppl/DC1](https://science.sciencemag.org/content/369/6505/823/suppl/DC1)

Materials and Methods

Figs. S1 to S11

References (27–29)

Movies S1 and S2

[View/request a protocol for this paper from Bio-protocol.](#)

18 January 2019; resubmitted 18 November 2019

Accepted 12 June 2020

10.1126/science.aaw6421

## TROPIC RESILIENCE

# Trophic pyramids reorganize when food web architecture fails to adjust to ocean change

Ivan Nagelkerken<sup>1\*†</sup>, Silvan U. Goldenberg<sup>1,2†</sup>, Camilo M. Ferreira<sup>1</sup>, Hadayet Ullah<sup>1</sup>, Sean D. Connell<sup>1</sup>

As human activities intensify, the structures of ecosystems and their food webs often reorganize. Through the study of mesocosms harboring a diverse benthic coastal community, we reveal that food web architecture can be inflexible under ocean warming and acidification and unable to compensate for the decline or proliferation of taxa. Key stabilizing processes, including functional redundancy, trophic compensation, and species substitution, were largely absent under future climate conditions. A trophic pyramid emerged in which biomass expanded at the base and top but contracted in the center. This structure may characterize a transitional state before collapse into shortened, bottom-heavy food webs that characterize ecosystems subject to persistent abiotic stress. We show that where food web architecture lacks adjustability, the adaptive capacity of ecosystems to global change is weak and ecosystem degradation likely.

Humanity is sustained by complex and inherently adaptive systems that can provide goods and services in a continuously changing world (1). These self-organizing networks are recognized in medicine and economics. Immune systems maintain health against novel pathogens via millions of specialized cells that communicate and rearrange. Economies meet an ever-changing demand as individual businesses constantly emerge, fail, or adjust. Although similar adaptive principles have been applied to ecosystems (2), the preservation of their services into the future is threatened by the overwhelming pressure of human activities (3–6).

As humans alter the environment, ecological processes can accelerate or counter ecosystem degradation (7). Degradation may be accelerated by the unrestrained expansion of species whose modified functions destabilize food webs (8) and cascade through the ecosystem (9, 10). Degradation may be buffered, though, by the complex network of consumer interactions (i.e., trophic architecture) that maintain the functioning of food webs (11). Food web modifications are commonly studied using trophic pyramids, as they convey information on food web health as well as underlying ecological processes (12). For example, trophic pyramids can reveal the inverted state of coral reefs due to overfishing (13), forecast primary consumer dominance through species invasions (5), and explain the stepwise re-

covery of life on Earth after mass extinctions (14). Revealing the internal dynamics of food webs is a critical step toward understanding ecosystem vulnerability.

The adaptive capacity of trophic architecture is embedded in the flexible behavior of consumers (15) (Fig. 1). Consumers tend to forage for resources that are plentiful (16) and therefore play a critical role in the regulation of proliferating resources and the recovery of rare resources (17). Adaptive capacity is further enhanced through redundancy among functionally similar consumers (17); for instance, the loss of sensitive species can be compensated for through niche expansion and density substitution by less sensitive species now liberated from competition (18). Such adaptive capacity may be limited and highly variable (19) but is considered key to the resistance and resilience of ecosystems because it

reinforces prey population control and maintains energy flow (15, 20).

Rising CO<sub>2</sub> levels challenge the adaptability of ecosystems (21). Although ocean acidification can threaten calcifiers (22) and impair animal behaviors (7), primary producers may use the excess CO<sub>2</sub> as a nutrient to fuel growth (23). Similarly, climate warming causes metabolic stress in species near their upper thermal limits (24), whereas others may gain from the increased scope for physiological performance (6, 25) and expand their populations (26, 27). However, it is not species richness or community structure but ecosystem functions that provide natural resources and services (17, 19, 28). We must therefore ask whether fundamental ecosystem properties can persist into the future via stabilizing processes in the face of community reorganization.

In this study, we tested whether food web architecture can adjust to climatic stress by countering shifts in community composition and productivity (Fig. 1). Because climate change often advantages weedy primary producers, we anticipate that food webs will adjust in three ways: (i) functional replacement of sensitive herbivores by those more resilient to climate change, (ii) greater reliance of secondary consumers on omnivory as primary production increases but secondary production decreases (6), and (iii) loss of secondary consumers that cannot switch to omnivory.

In 1800-liter mesocosms, we exposed a benthic community to simulated ocean acidification (elevated partial pressure of CO<sub>2</sub>: 910  $\mu$ atm) and ocean warming (elevated temperature: +2.8°C) for 4.5 months, according to end-of-century projections under a high-emission scenario (Representative Concentration Pathway 8.5). We assessed the performance of functional groups at different trophic levels

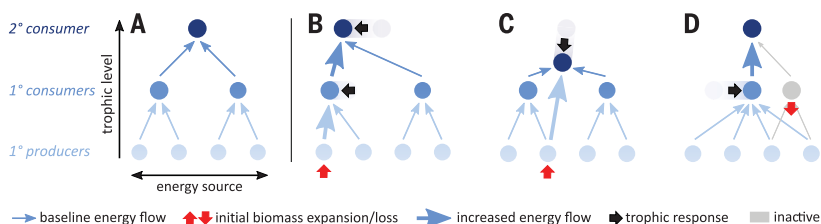


**Fig. 1. Adaptive trophic architecture.** (A) We define trophic architecture as a network of feeding interactions (blue arrows) between organisms (nodes) that propagate energy through food webs (11). The trophic niches of consumers (position within the architecture) reflect the origin of energy (horizontal axis;  $\delta^{13}\text{C}$  used as a proxy) and the number of trophic levels (vertical axis;  $\delta^{15}\text{N}$  used as a proxy). Flexibility in these links may allow trophic architecture to adjust to changes in community composition driven by abiotic change (11, 15, 16). (B to D) Potential consumer responses (black arrows) and modified energy flows (thick blue arrows) resulting from altered biomass of other community members (red arrows), leading to a shift in the trophic position of consumers. (B) Overexpansion of a 1° producer is buffered by higher consumption throughout the food web. (C) Overexpansion of a 1° producer is buffered by a 2° consumer that switches to omnivory, shortening the architecture. (D) A lost 1° consumer is replaced by a competitor (functional redundancy).

<sup>1</sup>Southern Seas Ecology Laboratories, School of Biological Sciences and The Environment Institute, DX 650 418, The University of Adelaide, Adelaide, SA 5005, Australia.

<sup>2</sup>GEOMAR Helmholtz Centre for Ocean Research Kiel, Düsternbrooker Weg 20, Kiel 24105, Germany.

\*Corresponding author. Email: [ivan.nagelkerken@adelaide.edu.au](mailto:ivan.nagelkerken@adelaide.edu.au)

†These authors contributed equally to this work.

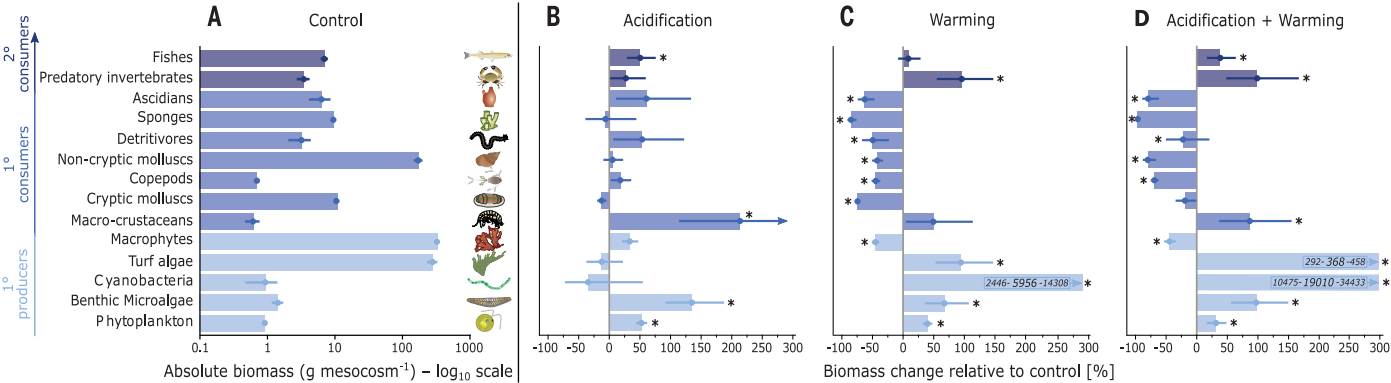


through standing biomass and productivity rates and evaluated the response of the trophic architecture by using stable isotope analysis and by modeling trophic interaction strengths and energy flows (29). Stable isotope ratios provide time-integrated estimates of feeding interactions on the basis of energy flow, in which the trophic position of a consumer is approximated by  $\delta^{15}\text{N}$  ( $^{15}\text{N}$ : $^{14}\text{N}$ ) and the basal resources that support it by  $\delta^{13}\text{C}$  ( $^{13}\text{C}$ : $^{12}\text{C}$ ).

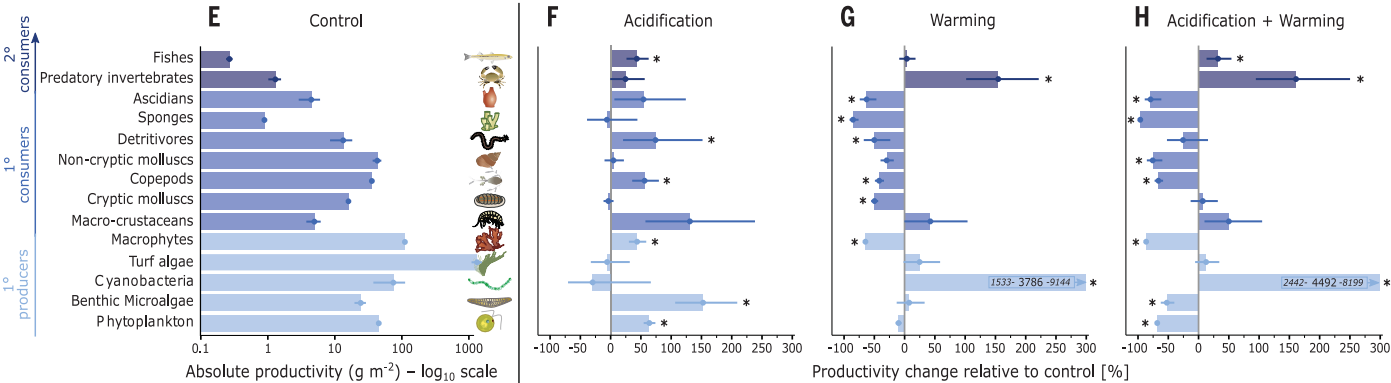
Trophic pyramids, in terms of both biomass and productivity, shifted as a function of strong but opposing responses of trophic levels to warming but not to ocean acidification (Fig. 2, A to H, and table S1). Under acidification alone, consumers across all trophic levels benefited from a boosted bottom-up forcing (Fig. 2, B and F; fig. S1A; and table S2), and communities maintained a functional composition close to that of present-day con-

ditions (figs. S1B and S2). Warming, by contrast, altered the community structure (figs. S1B and S2), with biomass and productivity of primary producers (particularly cyanobacteria and turf algae) and secondary consumers increasing but that of primary consumers declining by >40%, on average (Fig. 2, C, D, G, and H). The expansion of the bottom of the food web was particularly pronounced under the combined stressor effect (Fig. 2, D

COMMUNITY COMPOSITION



PRODUCTIVITY



TROPHIC ARCHITECTURE

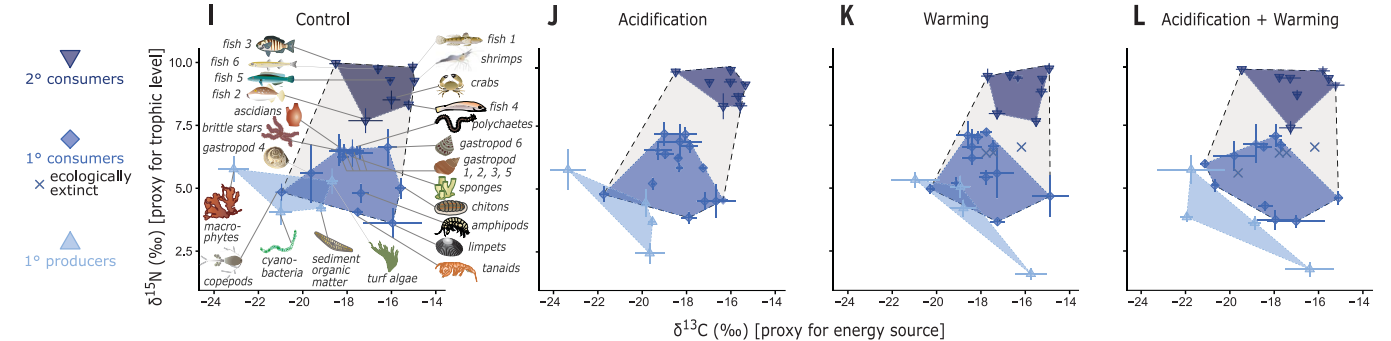


**Fig. 2. Response of food web composition, productivity, and trophic architecture to climatic stress.** Mean ( $\pm$  SE) standing biomass (A) and modeled productivity (E) of functional groups under control conditions and their relative change in response to climate treatments (B to D and F to H).  $n = 3$  mesocosms per treatment;  $*P < 0.05$  (table S1). (I to L) Position of taxa in bivariate trophic space (mean  $\pm$  SE stable

isotope ratios). Dashed polygons represent the trophic niche of the entire consumer community (which has the capacity for trophic adjustment). See fig. S13 and table S9 for taxon labels and sample sizes. Taxon symbols were created by S.U.G. and the Integration and Application Network, University of Maryland Center for Environmental Science (ian.umces.edu/symbols/).

and H), causing a 10-fold increase in dominance of autotrophic over heterotrophic organisms (fig. S1B). The excess and unconsumed primary production driven by warming accumulated as detrital biomass and was partly exported from the system (fig. S3).

The trophic architecture of the consumer community was maintained among climate treatments (Fig. 2, I to L). We focused solely on the consumers, as they have the adaptive capacity to alter their resource use under changing food conditions (30). The trophic niche of the consumer community (i.e., the overall architecture) retained its shape and size, as shown by measures of trophic level range, basal resource range, niche breadth, centroid position, and overlap in consumer niche space (fig. S4 and table S3). Likewise, the trophic positioning of consumer taxa relative to one another—measured through trophic diversity, redundancy, and evenness—remained unaltered (fig. S4). Even niche breadth of taxa (i.e., the within-taxa architecture that represents between-individual diet specialization) showed no general trend toward expansion or collapse (fig. S5).

Although each taxon was able to maintain its specific position in trophic space and hence trophic function (fig. S6), quantitative network analyses suggest that warming (alone or combined with acidification) strengthened many trophic interactions, especially at lower levels (fig. S7). Despite this strengthening, energy flow through the food web was largely reduced under warming (Fig. 3). By contrast, acidification alone drove smaller changes in trophic interaction strengths (fig. S7) with boosted energy flow through most of the food web (Fig. 3B).

Functional redundancy (Fig. 1D) was absent, as illustrated using herbivory. Key herbivores (such as noncryptic mollusks and copepods) declined markedly under both warming treatments (Fig. 2). However, none of the less-sensitive herbivore groups reoccupied the vacated trophic space (fig. S8 and table S4), implying a loss of consumer control over the respective primary producers. Trophic compensation can also be triggered through increased omnivory, resulting in a shortened architecture (Fig. 1C). However, we observed no decrease in trophic level of higher-order consumers across climate treatments, neither for their community nor for individual taxa (fig. S9 and table S5).

We show that trophic architecture of consumers can remain invariant under ocean warming, whereas biomass and productivity reorganize among trophic groups. This absence of architectural flexibility implies the lack or loss of compensatory processes that can buffer change (11, 15, 18, 20, 30). Under warming, biomass and productivity increased substantially at the base of the food web and mod-

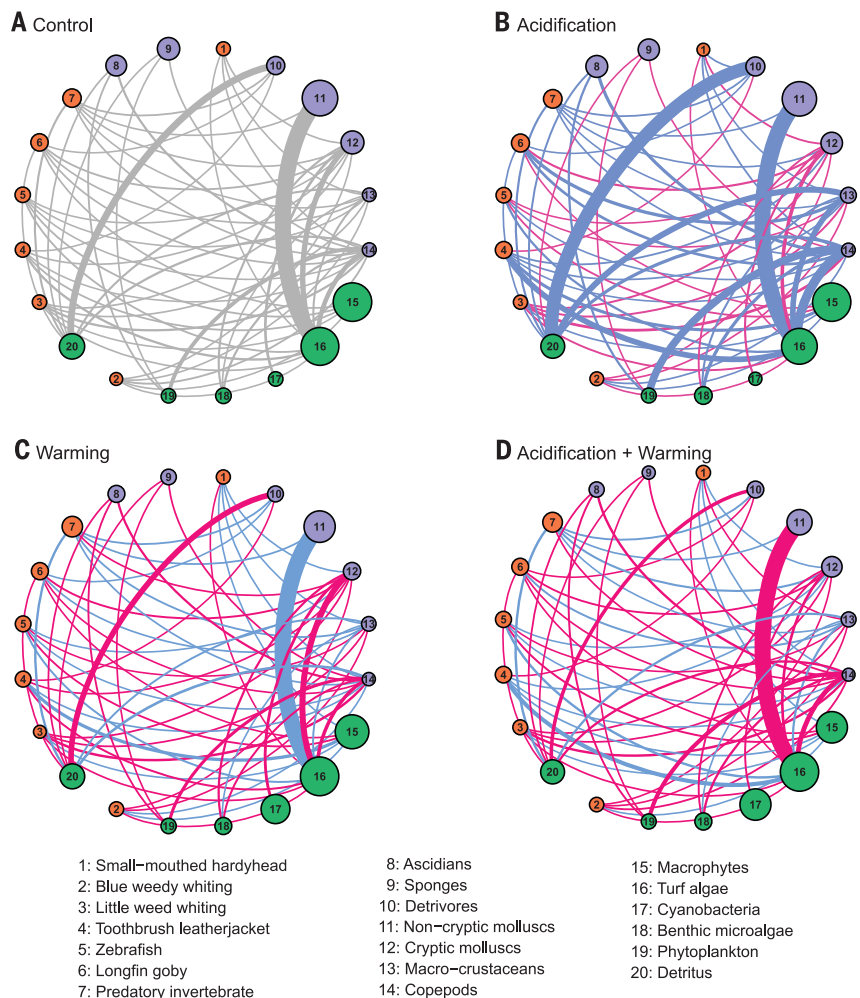


**Fig. 3. Alteration of trophic flows within a marine food web under ocean warming and acidification.**

Modeled flows under control conditions (A) and their relative change under climate treatments (B to D). Trophic levels are represented by node colors (green, 1° producers; purple, 1° consumers; orange, 2° consumers) and biomass by node size (log-transformed). Flows that increase compared with those in the control model are blue and those that decrease are magenta. Line thickness of flow scales with the magnitude of change.

erately at the top but contracted in the center (Fig. 4, B and D). This pattern was exaggerated under future climate conditions (warming and acidification). As a principal driver of physiological processes (25), warming may unbalance ecological interactions across the trophic pyramid. This unbalancing includes (i) expansion of the base [(23, 26) and this study] through dominance of “weedy” primary producers (i.e., increased turf), increase of less-palatable primary producers (i.e., increased cyanobacteria), or increased detrital production (i.e., increased flow to detritus); (ii) expansion of the base and contraction of the center [(31) and this study] through ingestion inefficiency in primary consumers (i.e., reduced energy flow to higher trophic levels); and (iii) contraction of the center and expansion of the top [(6, 32) and this study] through overconsumption of re-

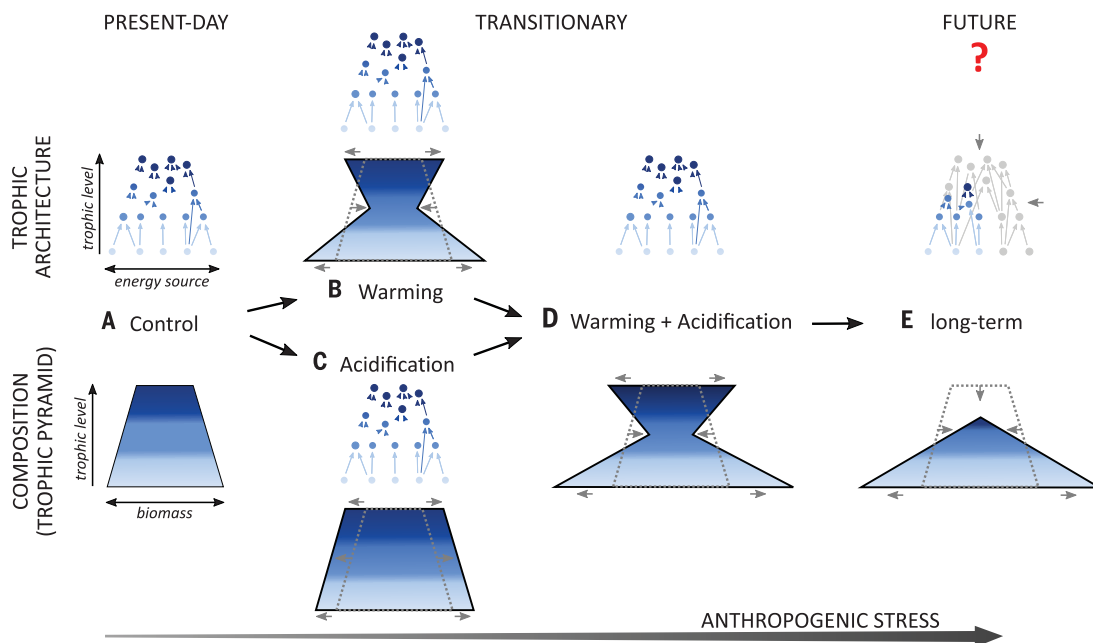
sources by consumers that face elevated metabolic demand (i.e., increased negative interaction strengths). Consequently, warming was a key driver of altering energy flow through the food web and the structure of the trophic pyramid.

Ocean acidification, by contrast, had a moderately positive influence at all food web levels. Enhanced bottom-up forcing and energy flows propagated to higher trophic levels, maintaining the shape of the trophic pyramid (Fig. 4C). This behavior is consistent with trophic theory on resource enrichment (10) and is also observed at natural CO<sub>2</sub> vents (33). Because the surplus energy could be channeled upward via the same feeding interactions, without increased losses to the detrital pool or export from the system, a change in trophic architecture was neither expected nor observed.



**Fig. 4. Conceptual diagram of alterations to trophic pyramids under climate stress.**

Inflexible trophic architecture (see Fig. 1) under anthropogenic stress can drive fundamental changes to food webs, including the creation of bottom-heavy trophic pyramids (**B** to **D**). Further stress may lead to the loss of higher-order consumers, as commonly reported in ecosystem-level studies (**E**). Shifts relative to the baseline pyramid and architecture (**A**) are highlighted by the gray dotted outlines and gray arrows [(B) to (E)].



The top of food webs may eventually become depleted under future climate conditions or additional human disturbances. Although predators in our study resisted the effects of warming, the community of primary consumers (their prey) became impoverished. Such an imbalance in predator-prey interactions (6) may undermine the viability of predator populations over time. Our model food web of 4.5-month exposure to future climate may therefore represent a transitional state (Fig. 4), with several possible scenarios over the longer term.

In the future, an ecological tipping point may be surpassed (8, 21, 27), beyond which the top of the food web can no longer be supported, with an ensuing collapse into shorter, bottom-heavy trophic pyramids (Fig. 4E). Such states characterize natural ecosystems enduring intense and long-term pressure of overfishing (3, 13), species invasions (5), nutrient enrichment (4), and environmental instability (34). Trophic architecture could ultimately be simplified through species extinction (loss of nodes and interactions) (Fig. 4E), as experienced during extreme changes in climate over Earth's history (9, 14).

Alternatively, given sufficient time, species may adapt genetically (35) or may be functionally replaced by range-shifting species from warmer regions (27, 36). In environments with a larger number of species or populations, sensitive species might be replaced with more-resilient species (9), or populations harboring preadapted phenotypes (traits favored under climate change) might sustain species persistence (28). Without adaptation or phenotypic plasticity over time, imbalanced trophic pyramids—with an adjustment of biomass

and productivity contrasting a stable trophic architecture—may have little capacity to resist further disturbances.

#### REFERENCES AND NOTES

- J. S. Lansing, *Annu. Rev. Anthropol.* **32**, 183–204 (2003).
- S. A. Levin, *Ecosystems* **1**, 431–436 (1998).
- D. Pauly, V. Christensen, J. Dalsgaard, R. Froese, F. Torres Jr., *Science* **279**, 860–863 (1998).
- V. H. Smith, *Environ. Sci. Pollut. Res. Int.* **10**, 126–139 (2003).
- J. E. Byrnes, P. L. Reynolds, J. J. Stachowicz, *PLOS ONE* **2**, e295 (2007).
- I. Nagelkerken, S. D. Connell, *Proc. Natl. Acad. Sci. U.S.A.* **112**, 13272–13277 (2015).
- S. U. Goldenberg et al., *Nat. Clim. Change* **8**, 229–233 (2018).
- M. Scheffer, S. Carpenter, J. A. Foley, C. Folke, B. Walker, *Nature* **413**, 591–596 (2001).
- J. L. Blois, P. L. Zarnetske, M. C. Fitzpatrick, S. Finnegan, *Science* **341**, 499–504 (2013).
- M. R. Heath, D. C. Speirs, J. H. Steele, *Ecol. Lett.* **17**, 101–114 (2014).
- B. C. McMeans et al., *Ecol. Monogr.* **86**, 4–19 (2016).
- R. Trebilco, J. K. Baum, A. K. Salomon, N. K. Dulvy, *Trends Ecol. Evol.* **28**, 423–431 (2013).
- S. A. Sandin et al., *PLOS ONE* **3**, e1548 (2008).
- Z. Q. Chen, M. J. Benton, *Nat. Geosci.* **5**, 375–383 (2012).
- F. S. Valdovinos, R. Ramos-Jiliberto, L. Garay-Narváez, P. Urbani, J. A. Dunne, *Ecol. Lett.* **13**, 1546–1559 (2010).
- G. H. Pyke, *Annu. Rev. Ecol. Syst.* **15**, 523–575 (1984).
- J. S. Rosenfeld, *Oikos* **98**, 156–162 (2002).
- A. R. Ives, B. J. Cardinale, *Nature* **429**, 174–177 (2004).
- D. Mouillot et al., *Proc. Natl. Acad. Sci. U.S.A.* **111**, 13757–13762 (2014).
- S. D. Connell, G. Ghedini, *Trends Ecol. Evol.* **30**, 513–515 (2015).
- C. D. G. Harley et al., *Ecol. Evol.* **7**, 6035–6045 (2017).
- K. J. Kroeker et al., *Glob. Change Biol.* **19**, 1884–1896 (2013).
- S. D. Connell, K. J. Kroeker, K. E. Fabricius, D. I. Kline, B. D. Russell, *Philos. Trans. R. Soc. B* **368**, 20120442 (2013).
- H. O. Pörtner, A. P. Farrell, *Science* **322**, 690–692 (2008).
- A. Clarke, *Principles of Thermal Ecology: Temperature, Energy and Life* (Oxford Univ. Press, 2017).
- J. M. O'Neil, T. W. Davis, M. A. Burford, C. J. Gobler, *Harmful Algae* **14**, 313–334 (2012).

- T. Wernberg et al., *Science* **353**, 169–172 (2016).
- D. Mouillot, N. A. J. Graham, S. Villéger, N. W. H. Mason, D. R. Bellwood, *Trends Ecol. Evol.* **28**, 167–177 (2013).
- See supplementary materials.
- G. Ghedini, B. D. Russell, S. D. Connell, *Ecol. Lett.* **18**, 182–187 (2015).
- N. P. Lemoine, D. E. Burkepile, *Ecology* **93**, 2483–2489 (2012).
- S. U. Goldenberg, I. Nagelkerken, C. M. Ferreira, H. Ullah, S. D. Connell, *Glob. Change Biol.* **23**, 4177–4184 (2017).
- I. Nagelkerken, S. U. Goldenberg, C. M. Ferreira, B. D. Russell, S. D. Connell, *Curr. Biol.* **27**, 2177–2184.e4 (2017).
- J. L. Sabo, J. C. Finlay, T. Kennedy, D. M. Post, *Science* **330**, 965–967 (2010).
- J. Merilä, A. P. Hendry, *Evol. Appl.* **7**, 1–14 (2014).
- J. M. Sunday, A. E. Bates, N. K. Dulvy, *Nat. Clim. Change* **2**, 686–690 (2012).

#### ACKNOWLEDGMENTS

We thank W. Hutchinson, M. Gluis, T. Kildea, M. Brustolin, G. Walden, M. Rollog, and all students involved in the mesocosm maintenance. **Funding:** The study was financially supported by an Australian Research Council (ARC) Future Fellowship (FT120100183) to I.N. and a grant from the Environment Institute (University of Adelaide) to I.N. I.N. was also supported by an ARC Discovery Project (DP170101722), S.D.C. by Future Fellowship grant FT0991953, and C.M.F. by a Science without Borders Ph.D. scholarship (CAPES scholarship 13058134). **Author contributions:** S.U.G., I.N., C.M.F., and S.D.C. designed the study; I.N. coordinated the project; S.U.G., C.M.F., and H.U. maintained the mesocosms; S.U.G. conducted the isotope analyses; S.U.G. and H.U. analyzed the data; S.U.G., I.N., and S.D.C. wrote the manuscript; all authors reviewed the manuscript; and I.N. revised the manuscript. **Competing interests:** The authors declare no competing interests. **Data and materials availability:** All data supporting the results can be found in the supplementary materials.

#### SUPPLEMENTARY MATERIALS

science.sciencemag.org/content/369/6505/829/suppl/DC1  
Materials and Methods  
Figs. S1 to S14  
Tables S1 to S18  
References (37–105)  
MDAR Reproducibility Checklist  
Data S1 to S3

19 February 2019; resubmitted 31 March 2020  
Accepted 23 June 2020  
10.1126/science.aax0621

## SUPERCONDUCTIVITY

# Observation of small Fermi pockets protected by clean CuO<sub>2</sub> sheets of a high-*T<sub>c</sub>* superconductor

So Kunisada<sup>1</sup>, Shunsuke Isono<sup>2</sup>, Yoshimitsu Kohama<sup>1,3</sup>, Shiro Sakai<sup>4</sup>, Cédric Baille<sup>1</sup>, Shunsuke Sakuragi<sup>1</sup>, Ryo Noguchi<sup>1</sup>, Kifu Kurokawa<sup>1</sup>, Kenta Kuroda<sup>1</sup>, Yukiaki Ishida<sup>1</sup>, Shintaro Adachi<sup>5</sup>, Ryotaro Sekine<sup>2</sup>, Timur K. Kim<sup>6</sup>, Cephise Cacho<sup>6</sup>, Shik Shin<sup>1,7</sup>, Takami Tohyama<sup>8</sup>, Kazuyasu Tokiwa<sup>2\*</sup>, Takeshi Kondo<sup>1,3\*</sup>

In cuprate superconductors with high critical transition temperature (*T<sub>c</sub>*), light hole-doping to the parent compound, which is an antiferromagnetic Mott insulator, has been predicted to lead to the formation of small Fermi pockets. These pockets, however, have not been observed. Here, we investigate the electronic structure of the five-layered Ba<sub>2</sub>Ca<sub>4</sub>Cu<sub>5</sub>O<sub>10</sub>(F,O)<sub>2</sub>, which has inner copper oxide (CuO<sub>2</sub>) planes with extremely low disorder, and find small Fermi pockets centered at ( $\pi/2$ ,  $\pi/2$ ) of the Brillouin zone by angle-resolved photoemission spectroscopy and quantum oscillation measurements. The d-wave superconducting gap opens along the pocket, revealing the coexistence between superconductivity and antiferromagnetic ordering in the same CuO<sub>2</sub> sheet. These data further indicate that superconductivity can occur without contribution from the antinodal region around ( $\pi$ , 0), which is shared by other competing excitations.

The superconductivity in cuprates emerges with carrier doping to an antiferromagnetic (AF) Mott insulator (1, 2). In the half-filled insulating state, the top of the occupied band with convex upward is located at the ( $\pi/2$ ,  $\pi/2$ ) point of the Brillouin zone (3, 4). Hole-doping is expected to shift the Fermi energy so that it crosses the lower Hubbard band (or charge transfer band), turning the state metallic (5, 6). The observation of a small Fermi surface (FS) pocket by angle-resolved photoemission spectroscopy (ARPES) has been reported for single-layered Bi<sub>2</sub>Sr<sub>2</sub>CuO<sub>6+ $\delta$</sub>  (Bi2201) (7). However, this pocket was detected considerably off ( $\pi/2$ ,  $\pi/2$ ) and only for a narrow region in the electronic phase diagram relatively close to the optimal doping. The pocket was later ascribed to an artifact coming from the distorted crystal structure inherent in Bi2201 (8), which generates replicas of the main band in photoemission (9). Moreover, the Fermi pocket in Bi2201 has not been detected by the bulk-sensitive quantum oscillation measurements.

Quantum oscillations have been measured to identify Fermi pockets in three hole-doped cuprates: double-layered YBa<sub>2</sub>Cu<sub>3</sub>O<sub>6.5</sub> (Y123) (10) and YBa<sub>2</sub>Cu<sub>4</sub>O<sub>8</sub> (Y124) (11) and single-layered HgBa<sub>2</sub>CuO<sub>4+ $\delta$</sub>  (Hg1201) (12). However, the corresponding structures have not been detected by ARPES. The pockets soon turned

out to be negative in charge, and it has since been widely acknowledged that they are not due to the genuine ground state but rather to FSs reconstructed under an external magnetic field, which eliminates superconductivity and instead leads to a competing charge density wave (13). Thus, the experimental observation of a small hole pocket in a lightly doped cuprate has been lacking to date, even though it could be a key element in relating high-critical temperature (*T<sub>c</sub>*) superconductivity to Mott physics.

In single- and double-layered prototype materials, the superconducting CuO<sub>2</sub> sheet is adjacent to dopant layers with random vacancies, which cause a spatially inhomogeneous state, as revealed by scanning tunneling microscopy (14). This undesirable situation is resolved in systems with three or more layers, where the inner CuO<sub>2</sub> planes are screened from the disorder of the outermost dopant layers (15, 16). The nuclear magnetic resonance (NMR) data indicate that the protected inner planes are not only structurally flatter but also more homogeneously carrier-doped than the outer planes, and those in five-layered cuprates are much cleaner than the CuO<sub>2</sub> planes in Y123 and Hg1201 (15, 16).

Here, we studied the five-layered Ba<sub>2</sub>Ca<sub>4</sub>Cu<sub>5</sub>O<sub>10</sub>(F,O)<sub>2</sub> (*T<sub>c</sub>* = 65 K) with lightly doped inner planes (Fig. 1C and fig. S1), which is easy to cleave and hence suitable for ARPES. Importantly, the crystal is free from structural distortion and therefore from the observation of artificial Fermi pockets. Moreover, the AF-ordered phase extends inside the superconducting region, which is a common property of cuprates with three or more layers with interlayer magnetic coupling (15, 16); this would be desirable for the formation of Fermi pockets. This material, therefore, is well suited to unveiling the electronic structure inherent to the lightly doped Mott insulator. Additionally, the

protected inner plane of cuprates deserves careful investigation, because it may be a key platform for increasing the *T<sub>c</sub>* as demonstrated by the trilayer HgBa<sub>2</sub>Ca<sub>2</sub>Cu<sub>3</sub>O<sub>8+ $\delta$</sub>  (17), where  $\delta$  is excess oxygen, with the highest *T<sub>c</sub>* among the existing substances.

Figure 1A plots the ARPES intensities integrated close to the Fermi level (*E<sub>F</sub>*) measured at the lowest temperature (*T* = 5 K) by a laser-ARPES with high energy and momentum resolutions. Surprisingly, we find two hole pockets centered at ( $\pi/2$ ,  $\pi/2$ ), in addition to a Fermi arc typical for underdoped cuprates (18). These are also confirmed in band dispersions (Fig. 1, K to M); the back side of the Fermi pockets becomes clear by changing the color scale of ARPES images (Fig. 1, H to J). The corresponding peaks are also clearly seen in momentum distribution curves (MDCs) at *E<sub>F</sub>* (Fig. 1, E to G), whereas there is no such signature for the Fermi arc.

We identify the observed pockets as intrinsic FSs and rule out other possibilities as follows. The pockets (Fig. 1B) and occupied dispersions (Fig. 1N) both perpendicularly cross the AF zone boundary (AFZB); these structures are exactly what is expected for one band folded about AFZB and are not compatible with two artificially overlapped bands (fig. S2, A and B). Moreover, the band dispersion along the AFZB line exhibits MDCs with very sharp peaks (Fig. 1, O and P) comparable to those along the nodal cut, which is not expected for overlapped bands (fig. S2A). The scenario of surface reconstruction can also be ruled out from the fact that there is no folding back for the Fermi arc (dashed green arrows in Fig. 1, E to G). Although the signature of AF order has been detected not only from the inner planes but also from the outer planes by NMR measurements, the NMR signal from the inner planes is much stronger, which is compatible with our ARPES results showing apparent Fermi pockets only for the inner planes.

Because the hole carriers are doped by the O substitution for the F sites (Fig. 1C), the outer CuO<sub>2</sub> layers close to the BaF dopant layer are more doped than the inner layers (19, 20). Thus, the smallest pocket, larger pocket, and Fermi arc should be predominantly formed by the innermost plane (IP<sub>0</sub>), the second inner planes (IP<sub>1</sub>), and the outermost planes (OP), respectively (arrows in Fig. 1A). Typically, the spectral peaks get broader with fewer carriers owing to stronger correlation effects, as demonstrated for Bi<sub>2</sub>Sr<sub>2</sub>CaCu<sub>2</sub>O<sub>8+ $\delta$</sub>  (Bi2212) (fig. S3); with underdoping, the nodal Fermi wave number (*k<sub>F</sub>*) gets closer to the AFZB, forming a hot spot where the AF fluctuations with a ( $\pi$ ,  $\pi$ ) vector cause considerable electron scattering. Interestingly, we find the opposite trend here (Fig. 1D): The peak of the nodal spectrum is sharper for the pockets than for the Fermi arc, and it becomes sharpest for the smallest pocket (even sharper than that in optimally doped

<sup>1</sup>ISSP, University of Tokyo, Kashiwa, Chiba 277-8581, Japan.

<sup>2</sup>Department of Applied Electronics, Tokyo University of Science, Tokyo 125-8585, Japan. <sup>3</sup>Trans-scale Quantum Science Institute, University of Tokyo, Bunkyo-ku, Tokyo 113-0033, Japan. <sup>4</sup>RIKEN Center for Emergent Matter Science (CEMS), Wako, Saitama 351-0198, Japan. <sup>5</sup>MANA, National Institute for Materials Science, Tsukuba, Ibaraki 305-0047, Japan. <sup>6</sup>Diamond Light Source, Harwell Campus, Didcot OX11 0DE, UK. <sup>7</sup>Office of University Professor, The University of Tokyo, Kashiwa, Chiba 277-8568, Japan. <sup>8</sup>Department of Applied Physics, Tokyo University of Science, Tokyo 125-8585, Japan.

\*Corresponding author. Email: tokiwa@rs.tus.ac.jp (K.T.); kondo1215@issp.u-tokyo.ac.jp (T.K.)



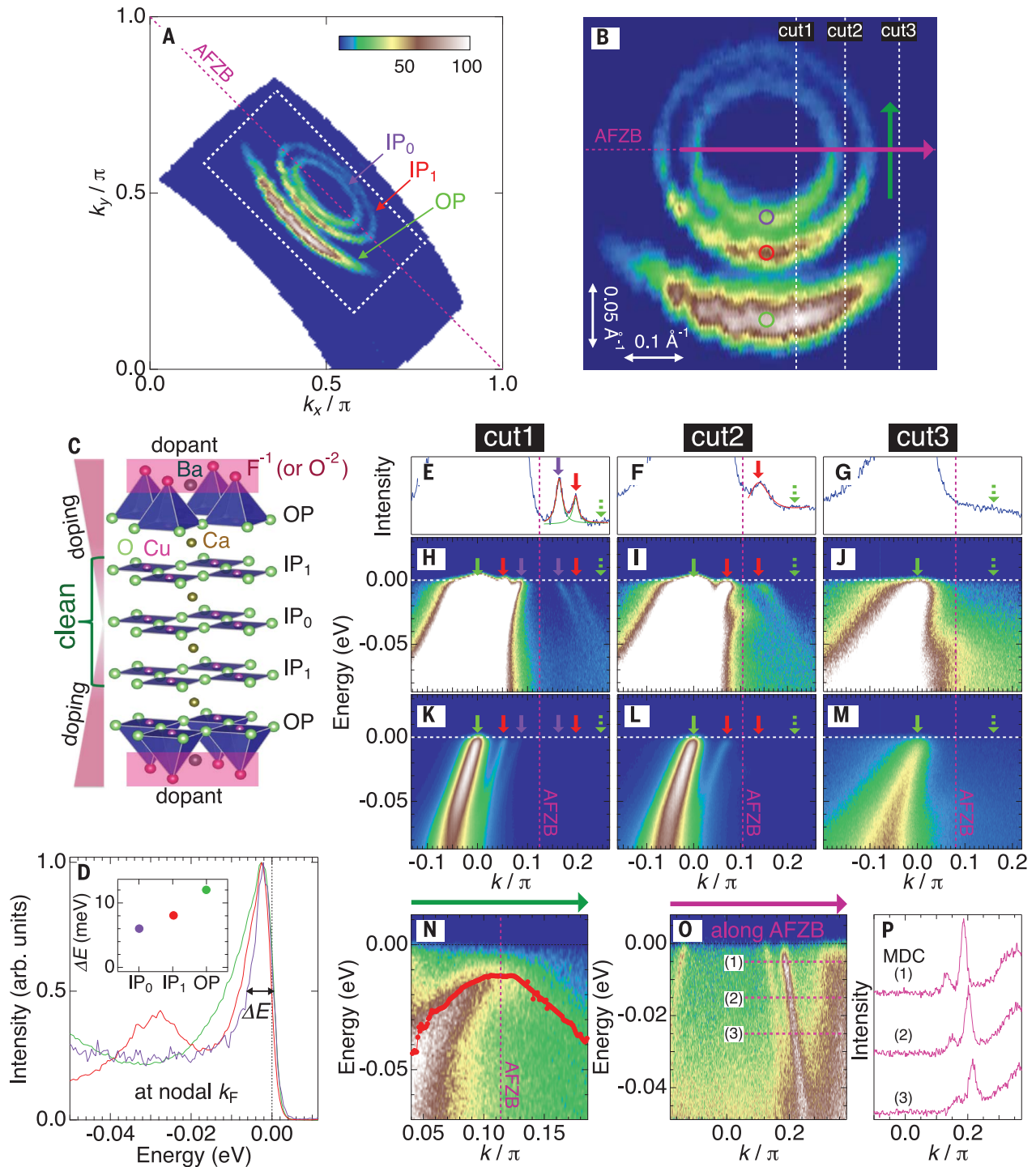
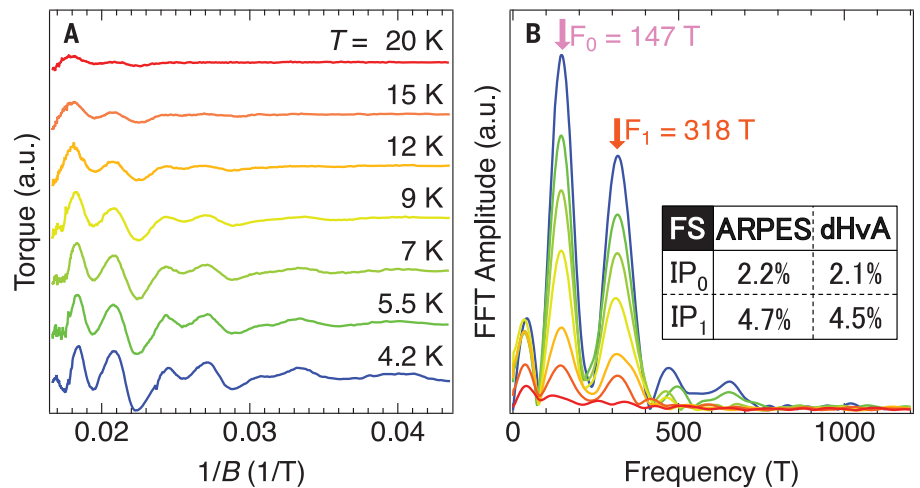


**Fig. 1. Small Fermi pockets revealed by laser-ARPES.** (A) FS mapping obtained by integrating ARPES intensities within an energy window of 10 meV about  $E_F$ . The arrows point to FSs dominated by the innermost plane ( $IP_0$ ), the second inner planes ( $IP_1$ ), and the outermost planes ( $OP$ ), which are depicted in (C). (B) Magnified image of the area enclosed by a white dashed rectangle in (A). The scales for the horizontal and vertical axes are noted with white double-headed arrows. (C) Five  $CuO_2$  sheets in the crystal structure of  $Ba_2Ca_4Cu_5O_{10}(F,O)_2$ . (D) The EDCs at the nodes [marked by colored circles in (B)] for the smaller and larger Fermi pockets ( $IP_0$  and  $IP_1$ , respectively) and Fermi arc ( $OP$ ). The inset plots the energy width of the spectral peaks ( $\Delta E$ ) for each FS (or each  $CuO_2$  sheet). The broad peak around  $-0.03$  eV in the red spectrum comes from the energy state of the band for  $IP_0$ , which stays

energetically below the band of  $IP_1$  [for example, see (H) and (K)]. (E to G) MDCs at  $IP_1$  for (H) to (J). The vertical axis values are decreased to clearly exhibit peaks for the back sides of Fermi pockets; the peaks for the pockets (fitted by Lorentzian curves) are clearly visible, whereas the one corresponding to the Fermi arc is missing (green dashed arrow). (H to J) The same images as in (K) to (M), but the color scale is changed to emphasize the folded bands; the white color is displayed at intensities greater than 0.019, 0.031, and 0.160 times those in (H), (I), and (J), respectively. (K to M) ARPES dispersions obtained along the momentum cuts indicated in (B) by white dashed lines (cut1, cut2, and cut3). (N and O) ARPES dispersions extracted along the momentum cuts indicated in (B) by green and purple arrows, respectively. (P) MDCs along the dashed lines in (O). All the data presented here were measured at 5 K.

**Fig. 2. Small Fermi pockets revealed by quantum oscillations.**

**(A)** Magnetic torque signals (dHvA) at several temperatures where smooth backgrounds are subtracted (21). The angle between the field direction and the crystallographic  $c$  axis was set to be  $7^\circ$  during the measurements. a.u., arbitrary units. **(B)** The FFT spectra of the observed quantum oscillations in (A). Arrows mark the two main peaks ( $F_0$  and  $F_1$ ). The inset shows the area of the two Fermi pockets, estimated by means of dHvA and ARPES, as a percentage of the Brillouin zone area. The small peaks other than  $F_0$  and  $F_1$  arise owing to trivial reasons. For frequencies higher than  $F_1$ , the small peaks could represent higher harmonics of  $F_0$  and  $F_1$ ; however, the peak positions change with temperature, indicating that these peaks must be affected by or might even just be artifacts of noise in the raw data. The small peaks below  $F_0$  are stable with temperature but are sensitive to the method of background subtraction and thus are not intrinsic (see the raw data before background subtraction in fig. S4B); we assumed a polynomial curve as the background for each quantum oscillation spectrum. Hence, artificial intensities of a wave-like structure with a low frequency are inevitably left after background subtraction. Most importantly, we have confirmed that the frequencies of the two main peaks ( $F_0$  and  $F_1$ ) are robust against both the noise in data and the method of background subtraction.



Bi2212; see fig. S3L). This indicates that the inner planes are indeed very clean and have carriers with long lifetimes; the suppression of AF fluctuations may be another factor that causes less scattering in the inner planes.

To confirm the same Fermi pockets by bulk sensitive probes, we measured the de Haas–van Alphen effect (dHvA) (Fig. 2A and fig. S4B) and the Shubnikov–de Haas effect (SdH) (fig. S4A) through torque and contactless resistivity measurements, respectively; both experiments detected quantum oscillations, indicating two-dimensional pockets (fig. S5). In the fast Fourier transformation (FFT) spectra for dHvA (Fig. 2B), we find mainly two peaks at frequencies  $F_0 = 147$  T and  $F_1 = 318$  T, which correspond to the FS area covering 2.1 and 4.5% of the Brillouin zone, respectively. Importantly, these values almost perfectly agree with the ARPES results (2.2 and 4.7%). The charge carriers are found to always be hole type regardless of temperature, with no sign inversion even at high magnetic fields, as confirmed by the behavior of Hall resistance against the magnetic field [see fig. S6 and related discussion (21)]. Therefore, the Fermi pockets captured by quantum oscillations are the same as those detected by ARPES, rather than the reconstructed FSs with electron-type carriers as reported for Y123 and Y124 (13).

We have also confirmed a good agreement in the mass of conduction electrons:  $0.69 m_0$  for IP<sub>0</sub> and  $0.74 m_0$  for IP<sub>1</sub> by dHvA (fig. S4C) and  $\sim 0.7 m_0$  for the two pockets by ARPES. Another consistency is seen in the Dingle temperature ( $T_D$ ), proportional to the scattering rate (fig. S4D), and the inverse of the mean free path ( $l$ ); the  $T_D$  and  $l$  values are estimated to be lower and longer, respectively, for the smaller pocket ( $T_D = 6.5$  K,  $l = 210$  Å) than those for the larger pocket ( $T_D = 11.8$  K,  $l = 160$  Å), which

is consistent with ARPES spectra showing sharper peaks for the smaller pocket (Fig. 1D) and with the argument that IP<sub>0</sub> is cleaner than IP<sub>1</sub>. We also note that these values are comparable to those of Y123 ( $T_D = 6.2$  K,  $l = 200$  Å) (10, 22) and lower and longer, respectively, than those of Hg1201 ( $T_D = 18$  K,  $l = 85$  Å) (12, 22), which further verifies that the carriers of protected inner planes have an exceptionally high mobility even in such a lightly doped regime.

Laser-ARPES with low-energy photons cannot access the momentum region close to the Brillouin zone boundary. Therefore, we have used synchrotron light to determine the whole band structure. Moreover, the photon energies ( $h\nu$ ) are tunable in this setup, and thus the band-selective measurement becomes available with the matrix element effect in photoemission, which can selectively enhance or suppress ARPES intensities of a particular band dispersion by choosing a proper photon energy (23). We have fine-tuned the photon energy in reference to previous research on a Mott insulator  $\text{Ca}_2\text{CuO}_2\text{Cl}_2$  (CCOC), which demonstrated that the spectral intensities for the folded band are sensitive to the used photon energy because of the matrix element effect and could become even stronger than those of the main band (4, 24). We find that  $h\nu$  of 70 eV is best suited not only to observe the Fermi pockets selectively by suppressing the Fermi arc signal but also to enhance the ARPES intensity for the back side of the pockets (Fig. 3, A and C). Our data clearly exhibit a pocket around  $(\pi/2, \pi/2)$ ; the two pockets observed by laser-ARPES cannot be resolved separately because of limited resolutions in the synchrotron ARPES.

The energy dispersion along  $(-\pi, \pi)$  to  $(\pi, -\pi)$  crossing the pocket (Fig. 3B) can be contrasted with the large parabolic dispersion seen at

$h\nu = 100$  eV (fig. S7B), which selectively observes the Fermi arc band (fig. S7, A to G). To unveil the whole band shape for the Fermi pockets, we also extracted the ARPES dispersion along AFZB over multiple Brillouin zones (Fig. 3D); a periodic pattern has been obtained. The band determined by a tight-binding fit to our ARPES data is plotted in Fig. 3E. We find that the saddle point at the zone edge (25), a famous feature in cuprates, is missing. Instead, a parabola disperses down below  $-1$  eV at  $(\pi, 0)$  (see Fig. 3D). Therefore, the CDW and pseudogap states known to emerge around  $(\pi, 0)$  with the energy scale of  $\sim 100$  meV (26–29) cannot develop in the inner planes, which lack electrons required to generate these excitations in the band structure; this is in stark contrast to the situation in the outer planes, where the pseudogap opens around  $(\pi, 0)$  as in other underdoped cuprates, and thus the CDW state is likewise expected to occur (30–32).

The band shape we observed is compatible with that of Mott insulating CCOC (33) and  $\text{Sr}_2\text{CuO}_2\text{Cl}_2$  (SCOC) (3); however, our sample is metallic, and hence the chemical potential crosses the lower Hubbard band (Fig. 3F). In our sample, the bandwidth ( $W$ ) is about 1.5 eV, and a kink structure is observable around  $-0.5$  eV in the band dispersion (see Fig. 3, B and D). Such a waterfall-like dispersion with a large energy width of 1.3 to 2.0 eV has been commonly observed in many cuprate compounds (34), including the insulating CCOC ( $W \sim 1.8$  eV) with the lower Hubbard band fully occupied (35). The Fermi pockets in the carrier-doped Mott band of our sample seem to persist above the Neel temperature  $T_N$  ( $\sim 135$  K), given that the temperature dependence of the Hall coefficient (fig. S6C) exhibits no notable variation across  $T_N$ . This agrees



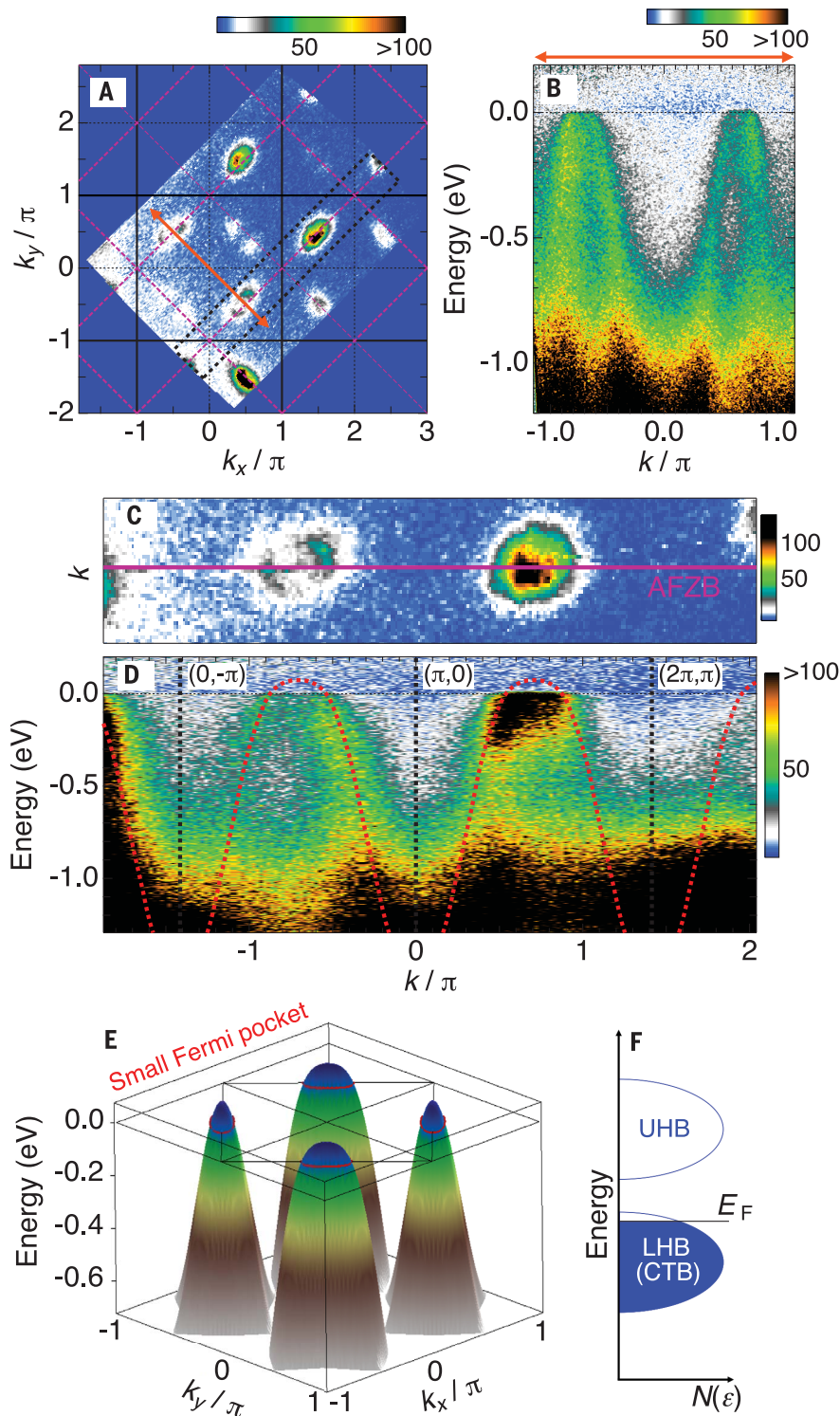


**Fig. 3. Overall band structure with Fermi pocket revealed by synchrotron-ARPES.** (A) ARPES intensity map about  $E_F$  over multiple Brillouin zones measured at  $T = 10$  K. The data were taken at  $\hbar\nu = 70$  eV, which selectively observes the Fermi pocket (fig. S7). (B) ARPES dispersion along a diagonal momentum cut [red double-headed arrow in (A)]. (C) Magnified image of the area enclosed by a black dashed rectangle in (A). (D) ARPES dispersion along AFZB indicated in (C). Band dispersion is traced by dashed red curves, which are extracted from the band shape in (E). (E) Band dispersion determined by tight-binding fitting to our ARPES data (table S1) (21). (F) Schematic for the density of states in the lightly hole-doped Mott state.  $N(\epsilon)$ , density of states; UHB, upper Hubbard band; LHB, lower Hubbard band; CTB, charge transfer band.

with the ARPES studies of Mott-insulating CCOC ( $T_N = 245$  K) and SCOC ( $T_N = 256$  K), where the band folding has been clearly observed at room temperature (24) or even 100 K higher than  $T_N$  (3).

To investigate the superconducting gap (36–39), we used a high-resolution laser-ARPES apparatus. In Fig. 4A, we plot the energy distribution curves (EDCs) along the Fermi pocket for  $IP_1$  (red oval in Fig. 4F), especially for the main side of the Brillouin zone (green circles in Fig. 4G). As expected for a d-wave gap structure, the spectral edge reaches  $E_F$  with no gap in the diagonal direction ( $\phi = 0^\circ$ ;  $\phi$  is defined in Fig. 4G), and it shifts to higher binding energies with a gap opening off the node. This gap behavior is visualized in Fig. 4B with the EDCs symmetrized across  $E_F$ . The nodal spectrum with one peak changes to a two-peak structure off the node, and the gap increases up to the tip of the ellipsoidal Fermi pocket ( $\phi = 90^\circ$ ). Notably, we have obtained almost the same results (Fig. 4, C and D) for the folded side of the Brillouin zone (purple circles in Fig. 4G); the results are summarized in Fig. 4E.

These results suggest that the superconductivity occurs in the inner  $\text{CuO}_2$  plane ( $IP_1$ ), rather than as a consequence of the proximity effect from the superconducting outer planes with the Fermi arc. We demonstrate this with a model calculation (fig. S8) by comparing the spectra calculated with and without a superconducting order in  $IP_1$ . In the latter case, the EDC at the larger Fermi pocket (mainly contributed by  $IP_1$ ) never shows a finite superconducting gap unlike the experiment; the spectral gap is reproduced only when  $IP_1$  itself is superconducting. In the model, the Fermi pockets are formed by band folding stemming from the AF order in the inner planes, so that the results also demonstrate a microscopic coexistence of the AF order and superconductivity in  $IP_1$ . We also note that the coexistence of the AF order and superconductivity in the lightly doped  $\text{CuO}_2$  plane has been confirmed by numerical calculations for the Hubbard model (40–42).

To validate the relationship between the different layers more directly, we compared the superconducting gaps on the Fermi pocket and arc measured by ARPES (fig. S9, A to D) and found that the gap size in the pocket for  $IP_1$  is slightly larger than that in the Fermi arc for OP (fig. S9H). The trend is opposite to what is expected from the proximity scenario, which can therefore be ruled out. Because the Fermi pocket emerges in the doped Mott band with AF ordering (Fig. 3F), the observation of a superconducting gap along the pocket (Fig. 4E) directly demonstrates the coexistence of superconductivity and AF order in a  $\text{CuO}_2$  sheet (Fig. 4H) (15, 16). It is notable that such a small amount of carriers ( $p \sim 0.04$ ) form superconducting pairs under the majority background of the AF-ordered state.

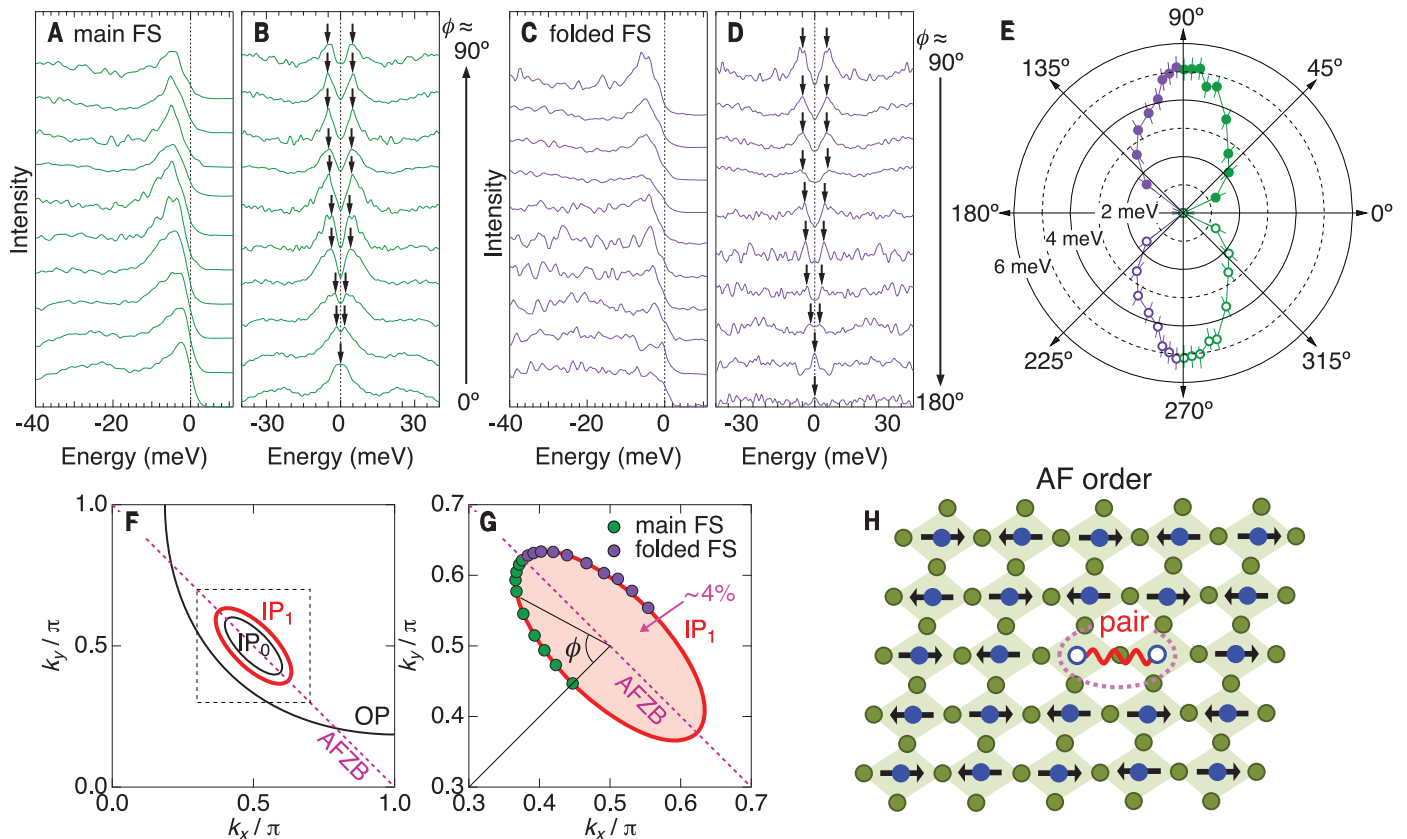


**Fig. 4. Superconducting gap along the Fermi pocket observed by high-resolution laser-ARPES.** (A and C) EDCs measured far below  $T_c$  ( $T = 5$  K) at  $k_F$ 's along the Fermi pocket for the second inner plane [ $IP_1$ ; see (F)] on the main side (A) and the folded side (C) of the Brillouin zone; the measured  $k_F$ 's are marked by green and purple circles in (G). (B and D) Symmetrized EDCs of (A) and (C), respectively, which visualize the gap opening. (E) The magnitude of the superconducting

gaps [arrows in (B) and (D)] plotted in polar coordinates. The angle  $\phi$  is defined in (G). (F) FSs determined by our ARPES data; the dominant CuO<sub>2</sub> plane for each FS is labeled by  $IP_0$ ,  $IP_1$ , and OP. (G) Magnified FS for  $IP_1$  [the region marked by the dashed square in (F)] with the  $k_F$  points at which high-resolution measurements for the gap estimation in (A) to (D) were performed. (H) Schematic real-space showing the coexistence between the AF order and electron pairs.

Along the smallest Fermi pocket, the superconducting gap is found to be almost zero within the experimental resolution (fig. S9, F and H). This extreme difference in the superconductivity between the two pockets has two notable implications. First, the two pockets are almost separately contributed by  $IP_0$  and  $IP_1$ , respectively, because otherwise the mixing of layers would produce superconducting gaps of similar magnitudes for both pockets. Second, the electronic state of  $IP_0$ , less doped than  $IP_1$ , should be situated outside of the  $T_c$  dome in the phase diagram.

The data showing the larger superconducting gap in the Fermi pocket than in the Fermi arc (fig. S9H) imply that the electron pairing gets more stabilized in the former despite smaller doping by avoiding the competition with other ordered states, which could develop around the zone edge ( $\pi, 0$ ). This may be the main reason why superconductivity persists down to dopings in the close vicinity of the half-filled Mott state in the five-layered cuprates, in contrast to single-layered cuprates with disordered CuO<sub>2</sub> layers, which are insulating up to about 10% carrier doping (29). None-

theless, further investigations will be necessary to clarify which layer actually triggers the superconductivity in bulk because the relationship between the value of  $T_c$  and the superconducting gap magnitude in cuprates is still under debate; in the context of the pairing mechanism, it is particularly intriguing that larger pairing gaps open in the CuO<sub>2</sub> sheet with the AF-fluctuations suppressed. Our results will contribute to solving the long-standing puzzle of the Fermi arc phenomena and urge the need for revisiting the Mott physics leading to the electron pairing in cuprates, which, up to now, has been based mainly on the research on single- and double-layered compounds with inhomogeneous electronic states.

#### REFERENCES AND NOTES

1. E. Dagotto, *Rev. Mod. Phys.* **66**, 763–840 (1994).
2. M. Imada, A. Fujimori, Y. Tokura, *Rev. Mod. Phys.* **70**, 1039–1263 (1998).
3. B. O. Wells et al., *Phys. Rev. Lett.* **74**, 964–967 (1995).
4. F. Ronning et al., *Phys. Rev. B* **67**, 035113 (2003).
5. F. Ronning et al., *Phys. Rev. B* **67**, 165101 (2003).
6. T. Tohyama, *Phys. Rev. B* **70**, 174517 (2004).
7. J. Meng et al., *Nature* **462**, 335–338 (2009).
8. Y. Matsui, H. Maeda, Y. Tanaka, S. Horiuchi, *Jpn. J. Appl. Phys.* **27**, L372–L375 (1988).

9. P. D. C. King et al., *Phys. Rev. Lett.* **106**, 127005 (2011).
10. N. Doiron-Leyraud et al., *Nature* **447**, 565–568 (2007).
11. E. A. Yelland et al., *Phys. Rev. Lett.* **100**, 047003 (2008).
12. N. Barišić et al., *Nat. Phys.* **9**, 761–764 (2013).
13. D. LeBoeuf et al., *Nature* **450**, 533–536 (2007).
14. K. McElroy et al., *Science* **309**, 1048–1052 (2005).
15. H. Mukuda, S. Shimizu, A. Iyo, Y. Kitaoka, *J. Phys. Soc. Jpn.* **81**, 011008 (2012).
16. S. Shimizu et al., *Phys. Rev. B* **85**, 024528 (2012).
17. A. Schilling, M. Cantoni, J. D. Guo, H. R. Ott, *Nature* **363**, 56–58 (1993).
18. M. R. Norman et al., *Nature* **392**, 157–160 (1998).
19. A. Iyo et al., *J. Phys. Conf. Ser.* **43**, 333–336 (2006).
20. H. Koteagawa et al., *J. Phys. Chem. Solids* **62**, 171–175 (2001).
21. See materials and methods and supplementary text in the supplementary materials.
22. M. K. Chan et al., *Nat. Commun.* **7**, 12244 (2016).
23. S. Iideta et al., *Phys. Rev. Lett.* **104**, 227001 (2010).
24. S. Haffner, D. M. Brammeier, C. G. Olson, L. L. Miller, D. W. Lynch, *Phys. Rev. B* **63**, 212501 (2001).
25. A. Damascelli, Z. Hussain, Z.-X. Shen, *Rev. Mod. Phys.* **75**, 473–541 (2003).
26. T. Kondo, R. Khasanov, T. Takeuchi, J. Schmalian, A. Kaminski, *Nature* **457**, 296–300 (2009).
27. W. D. Wise et al., *Nat. Phys.* **5**, 213–216 (2009).
28. M. Hashimoto et al., *Nat. Mater.* **14**, 37–42 (2015).
29. Y. Peng et al., *Nat. Commun.* **4**, 2459 (2013).
30. J. Chang et al., *Nat. Phys.* **8**, 871–876 (2012).
31. R. Comin et al., *Science* **343**, 390–392 (2014).
32. G. Ghiringhelli et al., *Science* **337**, 821–825 (2012).
33. F. Ronning et al., *Science* **282**, 2067–2072 (1998).
34. K. P. Kramer et al., *Phys. Rev. B* **99**, 224509 (2019).
35. F. Ronning et al., *Phys. Rev. B* **71**, 094518 (2005).
36. J. W. Harter et al., *Phys. Rev. Lett.* **109**, 267001 (2012).
37. A. Sugimoto et al., *Phys. Procedia* **58**, 78–81 (2014).



38. T. Yoshida *et al.*, *Phys. Rev. Lett.* **103**, 037004 (2009).
39. H. Matsui *et al.*, *Phys. Rev. Lett.* **95**, 017003 (2005).
40. M. Capone, G. Kotliar, *Phys. Rev. B* **74**, 054513 (2006).
41. K. Kobayashi, H. Yokoyama, *Phys. Procedia* **45**, 17–20 (2013).
42. H.-K. Wu, T.-K. Lee, *Phys. Rev. B* **95**, 035133 (2017).
43. S. Kunisada, The dataset for “Observation of small Fermi pocket protected in a clean CuO<sub>2</sub> sheet of high-T<sub>c</sub> superconductor” by So Kunisada *et al.*, Version 2, Harvard Dataverse (2020); <https://doi.org/10.7910/DVN/YWYOLQ>.

#### ACKNOWLEDGMENTS

We thank K. Akiba for supporting the analysis of quantum oscillation, T. Kiss for useful discussions, and T. Yajima for technical assistance in the x-ray measurements, performed using facilities of the Institute for Solid State Physics, University of Tokyo. **Funding:** We thank

Diamond Light Source for access to beamline I05 under proposals SI20445 and SI20446 that contributed to the results presented here. This work was supported by the JSPS KAKENHI (grants nos. JP19H05825, JP19H00651, JP19K03722, JP18H01163, JP18H01165, JP16H06345, JP19H01829, JP19H02594, and JP19H02683), and by MEXT Q-LEAP (grant no. JPMXS0118068681). **Author contributions:** T.K. conceived and designed the project. S.K. performed the ARPES experiments with help from C.B., S.Saku., R.N., K.Kurok., K.Kurod., Y.I., T.K.K., C.C., and T.K., and S.K. and T.K. analyzed the data. S.I., R.S., and K.T. grew the crystals, and S.K., S.I., R.S., and K.T. conducted the sample characterization. S.K., Y.K., K.Kurok., S.I., and K.T. measured the Hall effect. S.K., S.A., and Y.K. performed the quantum oscillations experiments, and S.K. and Y.K. analyzed the data. S.Saka. carried out the model calculations. S.K., Y.K., S.Saka., T.T., K.T., and T.K. interpreted the data. All authors discussed the results, and S.K., Y.K., S.Saka., K.T.,

and T.K. wrote the manuscript. T.K. and K.T. supervised the overall project. **Competing interests:** The authors declare that they have no competing interests. **Data and materials availability:** All data are shown in the main text and supplementary materials and are available at (43).

#### SUPPLEMENTARY MATERIALS

[science.sciencemag.org/content/369/6505/833/suppl/DC1](https://science.sciencemag.org/content/369/6505/833/suppl/DC1)  
Materials and Methods  
Supplementary Text  
Figs. S1 to S9  
Table S1  
References (44–49)

14 July 2019; accepted 29 June 2020  
10.1126/science.aay7311

## TROPICAL FOREST

# Active restoration accelerates the carbon recovery of human-modified tropical forests

Christopher D. Philipson<sup>1,2\*</sup>, Mark E. J. Cutler<sup>1\*</sup>, Philip G. Brodrick<sup>3</sup>, Gregory P. Asner<sup>3</sup>, Doreen S. Boyd<sup>4</sup>, Pedro Moura Costa<sup>5</sup>, Joel Fiddes<sup>6,7</sup>, Giles M. Foody<sup>4</sup>, Geertje M. F. van der Heijden<sup>4</sup>, Alicia Ledo<sup>8</sup>, Philippa R. Lincoln<sup>9</sup>, James A. Margrove<sup>2</sup>, Roberta E. Martin<sup>3</sup>, Sol Milne<sup>8</sup>, Michelle A. Pinard<sup>8</sup>, Glen Reynolds<sup>10</sup>, Martijn Snoep<sup>11</sup>, Hamzah Tangki<sup>12</sup>, Yap Sau Wai<sup>12</sup>, Charlotte E. Wheeler<sup>13</sup>, David F. R. P. Burslem<sup>8</sup>

More than half of all tropical forests are degraded by human impacts, leaving them threatened with conversion to agricultural plantations and risking substantial biodiversity and carbon losses. Restoration could accelerate recovery of aboveground carbon density (ACD), but adoption of restoration is constrained by cost and uncertainties over effectiveness. We report a long-term comparison of ACD recovery rates between naturally regenerating and actively restored logged tropical forests. Restoration enhanced decadal ACD recovery by more than 50%, from 2.9 to 4.4 megagrams per hectare per year. This magnitude of response, coupled with modal values of restoration costs globally, would require higher carbon prices to justify investment in restoration. However, carbon prices required to fulfill the 2016 Paris climate agreement [\$40 to \$80 (USD) per tonne carbon dioxide equivalent] would provide an economic justification for tropical forest restoration.

**T**ropical forests contain 55% of global stores of aboveground forest carbon (1), but the size of these stocks is declining rapidly because of forest loss and degradation (2). Across the tropics, primary forests continue to be degraded by numerous human impacts, such as timber harvesting, agriculture, and fire. Consequently, more than half of all tropical forests have some human impact, even though many disturbed sites retain high tree cover (3). Loss of tropical forest cover is particularly acute in Southeast Asia, which has the highest deforestation rate in the tropics and where the intensity of logging is increased by the high densities of commercially important dipterocarp trees (4). These forests, which are no longer pristine, may still support numerous ecosystem services, including timber production, sequestration of carbon, maintenance of biodiversity, and hydrological services (5–8).

Despite their ecological value, degraded forests remain vulnerable to conversion to agroecosystems possessing substantially lower carbon stocks and biodiversity (5, 9, 10). Alternatively, carbon stocks in degraded tropical forests can recover, particularly if accelerated by active restoration and if financial compensation mechanisms encourage avoided deforestation projects. However, these mechanisms require verification of aboveground carbon density (ACD) baseline values and recovery rates (11), which are currently lacking. Mean

and maximum ACD values are higher in Southeast Asian forests than in other tropical forests, and the highest values occur in Malaysia (12). For example, in the Malaysian state of Sabah, where selective logging has been one of the main forms of habitat degradation, unlogged lowland forests show consistently high ACD values averaging over 200 Mg C ha<sup>-1</sup>, whereas in logged forests, ACD varies from 60 to 140 Mg C ha<sup>-1</sup> (10). The difference in ACD between logged and unlogged forests in Sabah shows the potential carbon gain if logged forests were allowed to recover, which is estimated at 362.5 Tg C (10). At current carbon prices [typically between \$2 and \$10 (USD) per tonne carbon dioxide equivalent (tCO<sub>2</sub> e)], the potential value of this sequestered carbon would total between \$0.725 billion and \$3.625 billion for Sabah alone (13–15). Similar values could be calculated for any territory that has a comprehensive map of forest carbon and information on land-use history, but such data are not widely available across the globe.

Carbon sequestration rates in degraded tropical forests are highly variable. Long-term studies indicate that postlogging carbon recovery rates are between 0.30 and 4.3 Mg C ha<sup>-1</sup> year<sup>-1</sup> in Southeast Asia (17) and 0.04 and 2.96 Mg C ha<sup>-1</sup> year<sup>-1</sup> in Amazonia (16), whereas naturally regenerating pasture and abandoned agricultural land accumulate ACD at a mean rate of 3.05 Mg C ha<sup>-1</sup> year<sup>-1</sup> in the Neotropics

(17). These rates could be enhanced by implementing active restoration measures, which include tree planting, cutting of climbers such as lianas, and liberation of sapling trees from competing vegetation by thinning. Enrichment planting is especially important in the logged forests of Southeast Asia because selective logging affects the ecologically and economically important dipterocarp trees that are dispersal limited and mast fruit at irregular intervals (18, 19). Such measures are, however, expensive to implement; for example, enrichment planting of lowland forest in Sabah costs ~\$1500 to \$2500 ha<sup>-1</sup> over the implementation period, consistent with estimates of restoration costs for other tropical forests globally (table S1). Carbon offset schemes could provide a potential financing mechanism for these restoration costs, but evidence of restoration treatment efficacy with respect to ACD recovery in degraded forests exists for very few sites globally (table S1). The likelihood that such measures will be adopted is critically dependent on the operational costs over the lifetime of the stand relative to the additional value in terms of enhanced ACD accumulation.

Here, we report estimates of the response of ACD accumulation rates to active restoration using a combination of climber cutting and enrichment planting in a logged tropical forest over decadal time scales. We compare the fiscal benefits of this restoration across a range of potential carbon prices. Using detailed information on logging history and repeated in situ measurements from 257 forest plots from three different plot networks in Sabah, Malaysia, we compared recovery rates for naturally regenerating forest with recovery rates for areas that had been actively restored (20). During the 30 to 35 years after logging, naturally regenerating forest accumulated aboveground carbon at a rate of 2.9 Mg ha<sup>-1</sup> year<sup>-1</sup> (Fig. 1 and fig. S2) [confidence interval (CI): 2.1 to 3.7], whereas those areas with active restoration recovered at the considerably higher rate of 4.4 Mg ha<sup>-1</sup> year<sup>-1</sup> (Fig. 1 and fig. S2) (CI: 3.6 to 5.2). These values suggest that the reduction in ACD associated with a single logging event would be recovered to the ACD of unlogged forest (mean of 203 Mg ha<sup>-1</sup>) (Fig. 1 and fig. S2) (95% CI: 157 to 247) through natural regeneration after ~60 years, but that this could be reduced to 40 years if restoration treatments are applied.

We validated the distribution of ACD spanned by our plots using a fine-spatial-resolution ACD

<sup>1</sup>School of Social Sciences, University of Dundee, Dundee DD1 4HN, UK. <sup>2</sup>Department of Environmental Systems Science, ETH Zürich, 8092 Zürich, Switzerland. <sup>3</sup>Center for Global Discovery and Conservation Science, Arizona State University, Tempe, AZ 85287, USA. <sup>4</sup>School of Geography, University of Nottingham, Nottingham NG7 2RD, UK. <sup>5</sup>Smith School of Enterprise and the Environment, University of Oxford, Oxford OX1 3QY, UK. <sup>6</sup>Mountainsense Consulting, 7249 Serneus, Switzerland. <sup>7</sup>WSL Institute for Snow and Avalanche Research, CH-7260 Davos Dorf, Switzerland. <sup>8</sup>School of Biological Sciences, University of Aberdeen, Aberdeen AB24 3FX, UK. <sup>9</sup>LTS International, Pentland Science Park, Penicuik EH26 0PL, UK. <sup>10</sup>South East Asia Rainforest Research Partnership, Danum Valley Field Centre, Lahad Datu, Sabah, Malaysia. <sup>11</sup>Face the Future, 6706 KN Wageningen, Netherlands. <sup>12</sup>Conservation & Environmental Management Division, Yayasan Sabah Group, 88817 Kota Kinabalu, Sabah, Malaysia. <sup>13</sup>School of Geosciences, University of Edinburgh, Edinburgh EH9 3FF, UK.

\*Corresponding author. Email: christopher.philipson@usys.ethz.ch (C.D.P.); m.e.j.cutler@dundee.ac.uk (M.E.J.C.)



**Fig. 1. ACD as a function of time**

**since logging.** (A and B) The recovery of ACD in (A) naturally regenerating logged forest and (B) forest with active restoration using climber cutting and enrichment planting. Blue solid lines represent the mean recovery rate, and blue dotted lines represent the 95% CI. Each gray line represents the recovery for an individual plot between measurement intervals. The plot on the far right displays the mean ( $\pm 95\%$  CI) ACD of unlogged forest and therefore highlights the potential for ACD recovery. The green arrow represents the time frame in which restoration activities took place.

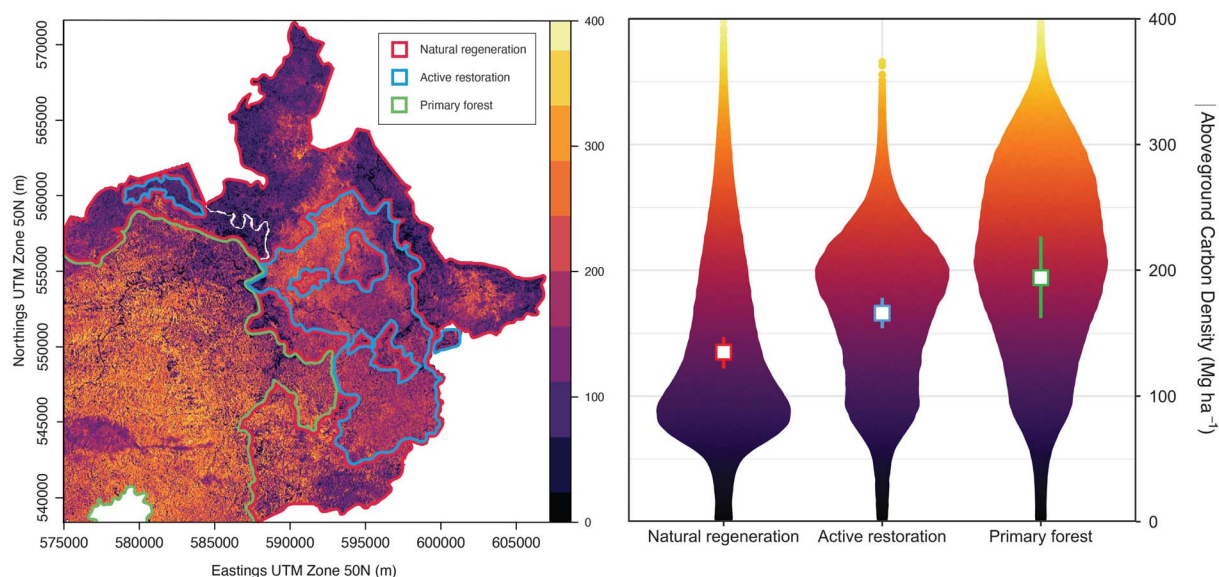
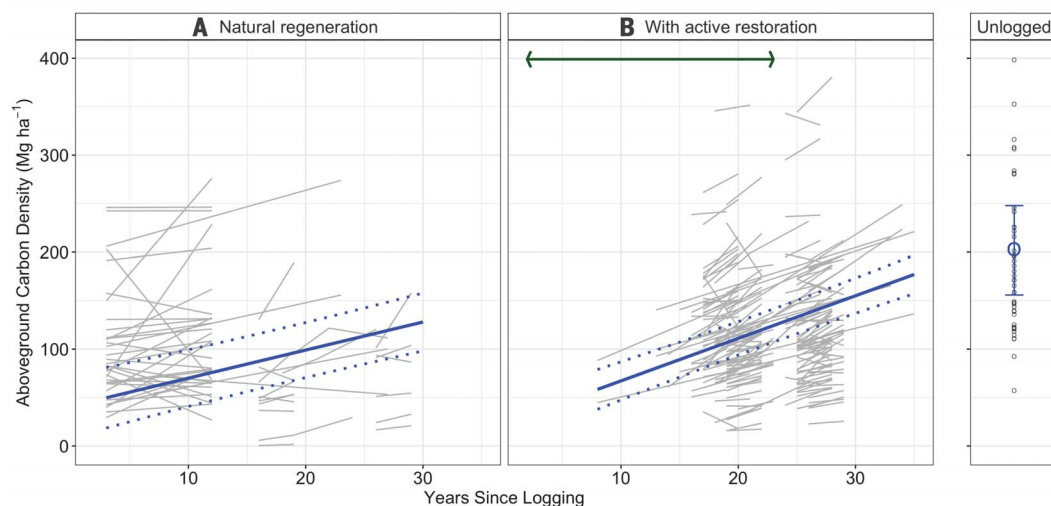


**Fig. 2. ACD across the entire study area.** (Left) ACD ( $\text{Mg ha}^{-1}$ ) across the study landscape in 2016 derived from an airborne LIDAR-derived carbon map (30-m resolution). Naturally regenerating logged forest ( $225 \text{ km}^2$ ) is outlined in red, logged forest that underwent active restoration ( $124 \text{ km}^2$ ) is outlined in blue, and the primary forest ( $449 \text{ km}^2$ ) is outlined in green. The color bar indicates low (dark) to high (light) values of ACD. UTM, Universal

Transverse Mercator (in meters). (Right) Violin plots indicating the distribution of ACD ( $\text{Mg ha}^{-1}$ ) from logged forest allowed to regenerate naturally (left, red outline), actively restored (middle, blue outline), and from primary unlogged forest (right, green outline). The data presented on the right correspond to the full study area shown on the left and are independent of those used in the analysis of forest regrowth (Fig. 1).

map of the study landscape that was generated using an airborne LIDAR (light detection and ranging) survey in 2016 and calibrated with independent ground surveys (10, 21). Remote estimates showed a mean ACD of naturally regenerating forests in 2016 to be  $135 \text{ Mg ha}^{-1}$  (Fig. 2) (CI: 123 to 148), whereas that of forest that had been subjected to restoration treatments was  $166 \text{ Mg ha}^{-1}$  (Fig. 2) (CI: 152 to 176), confirming a substantial difference in ACD in response to restoration (Fig. 2). We inferred remote estimates of ACD accumulation rates

based on the 2016 LIDAR-derived carbon map and baseline ACD values derived from plot data (the intercepts in Fig. 1), which gave values of  $3.5$  and  $4.8 \text{ Mg C ha}^{-1} \text{ year}^{-1}$  without and with restoration treatments, respectively, consistent with the results from ground surveys alone. Together, these results suggest that our estimates of carbon recovery are robust and scalable across the whole study area.

To estimate the economic feasibility of applying restoration treatments, we modeled the carbon price required to offset the cost of res-

toration, assuming carbon credits are released every 5 years for a project life span of 30 years and adjusting for the time value of money through nominal discount rates of 1, 5, and 10% (Fig. 3 and fig. S3). Carbon prices on the voluntary market fluctuate widely, and our analyses suggest that only values close to the top of those seen in recent years (around  $\$10$  per  $\text{tCO}_2 \text{ e}$ ) approach the minimum value required to offset the cost of restoration by tree planting and maintenance (13–15). Accounting for variation in ACD recovery rates

suggests that implementing restoration uniformly across the logged forest landscape would require carbon prices 2- to 10-fold greater than those that currently exist in the

voluntary carbon market (Fig. 3). Independent reports suggest that carbon prices in the range of \$40 to \$80 per tCO<sub>2</sub> e by 2020 are required to fulfill the obligations of signatories to the

**Fig. 3. Carbon price breakeven point as a function of restoration costs.**

Estimates of carbon price breakeven point for the increase of 1.5 Mg ha<sup>-1</sup> year<sup>-1</sup> (CI: 0.4 to 2.6) in ACD recovery attributed to restoration over a 30-year period with discounted revenues accrued at 5-year intervals, assuming a nominal 5% discount rate. The envelope shows a CI propagated from the ACD recovery model. The break-even carbon price represents the threshold price required to offset restoration costs. Dark green lines highlight the typical range of enrichment planting costs in Malaysia at the present time. The red region within the confidence envelope highlights the current (2017 to 2019) range in the voluntary carbon market prices (\$2 to \$10 per tCO<sub>2</sub> e), and the blue region highlights the estimated range in carbon price required to fulfill the Paris Agreement and limit global temperature increases to less than 2°C (\$40 to \$80 per tCO<sub>2</sub> e).

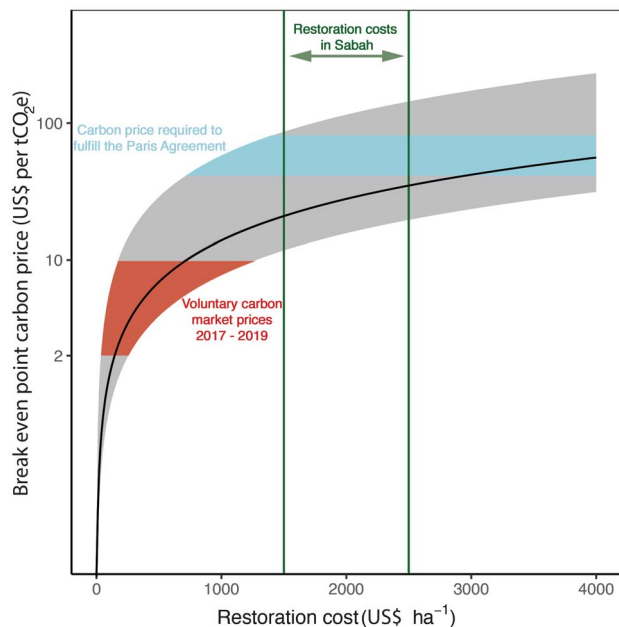
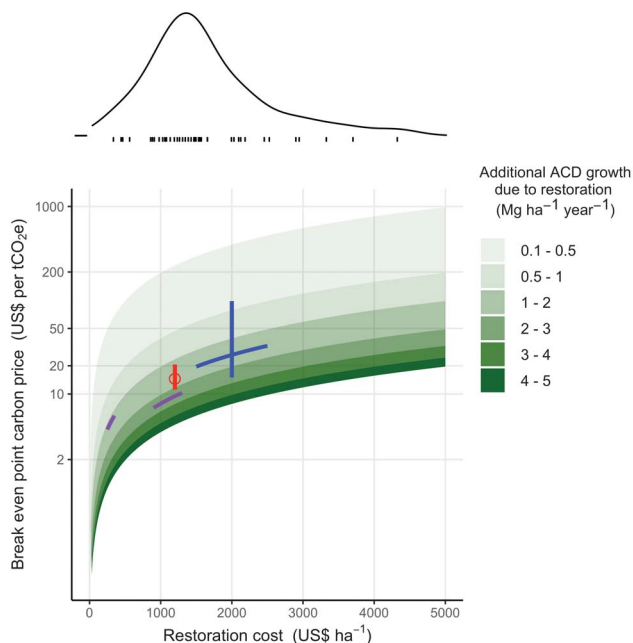


**Fig. 4. Carbon price breakeven point estimated for multiple scenarios. (Bottom)**

Estimates of carbon price breakeven point are calculated over a 30-year period with revenues accrued every 5 years, with a 5% nominal discount rate. Shading represents bins in which the additional ACD accumulation attributable to restoration is 0.1 to 0.5 (lightest green), 0.5 to 1.0, 1.0 to 2.0, 2.0 to 3.0, 3.0 to 4.0, and 4.0 to 5.0 Mg ha<sup>-1</sup> year<sup>-1</sup> (dark green). Data from two case studies are superimposed relating to fire protection and native seedling planting in Uganda (red circle) (30), two approaches to restoration of planting tree islands (at a lower cost) and larger-scale restoration in Costa Rica (purple lines) (32), and this study (blue line). The vertical red and blue lines represent 95% CIs for predicted breakeven carbon price based on variation in ACD accumulation rates in response to restoration. **(Top)** Density plot of published restoration costs based on values indicated by the tick marks on the horizontal axis (see table S1 for data and details).



Paris Climate Agreement for maintaining a global temperature rise of less than 2°C (22), and a value in this range would be sufficient to offset the costs of tropical forest restoration in our model (Fig. 3).

We report the long-term gains in tropical forest ACD after restoration of logged forest using interventions such as enrichment planting, climber cutting, and liberation thinning. These methods contribute differentially to ACD recovery. Climber cutting is likely effective because lianas compete with trees and substantially reduce carbon accumulation in tropical secondary forests (23–25). Enrichment planting eliminates the constraints of dispersal limitation for large canopy trees and may have resulted in a more uniform distribution of trees than in areas regenerating naturally, thus filling canopy gaps more quickly and reducing light competition from other species (18). The tree species that were planted, mostly in the Dipterocarpaceae family, have a potential for rapid growth rates (26, 27) and include the tallest trees recorded in the tropics (28), yielding high biomass when mature. Our findings support previous claims that rates of ACD accumulation in formerly logged Southeast Asian tropical forests are among the highest in the tropics [e.g., (11)] and reinforce the value of logged forests with respect to carbon storage potential in addition to maintenance of biodiversity and other ecosystem functions and services (5–8, 10, 29). We also show that targeted restoration treatments, initiated an average of 9 years after logging, generate substantially higher rates of ACD over the following two decades, which has important implications for the conservation and management of logged forests.

The breakeven carbon price can be estimated for any combination of ACD accumulation rate attributable to restoration and restoration costs for a specific set of economic assumptions (Fig. 4). Restoration programs have a lower breakeven carbon price if they achieve a higher additional ACD accumulation rate (over and above natural regeneration) or if the costs are reduced (Fig. 4). To our knowledge, only two other studies have reported both the costs and additional carbon benefits of tropical forest restoration (30–32). In Uganda, for lands dominated by grasses that were degraded by agricultural encroachment, an additional ACD gain of 1.62 Mg ha<sup>-1</sup> year<sup>-1</sup> was achieved through protection from fire and tree planting at a cost of \$1200 ha<sup>-1</sup>, and abandoned pastures in Costa Rica gained an additional ACD of 1.17 or 2.48 Mg ha<sup>-1</sup> year<sup>-1</sup> through tree planting at costs of \$297 or \$1100 ha<sup>-1</sup>, respectively, depending on planting strategy. The mean cost of tropical forest restoration (except Australia) across more than 50 published examples was \$1596 ha<sup>-1</sup> (95% CI: \$1338 to \$1854 ha<sup>-1</sup>) (Fig. 4 and table S1). Most



of these examples were derived from projects in tropical developing countries where restoration costs are less than \$5000 ha<sup>-1</sup>, whereas restoration costs of Australian forests are in the range of \$6000 to \$15,000 ha<sup>-1</sup> (table S1).

This review of previously published costs suggests that the range of carbon prices available on the voluntary market during 2017 and 2019 would be sufficient to incentivize investment in widespread active restoration in about half the settings where restoration costs have been reported, as long as the additional ACD gains from this investment are equivalent to those achieved by the three case studies in Fig. 4. Conversely, current carbon prices may be insufficient to support restoration in the logged forests of Southeast Asia despite the high rates of recovery reported in this study, unless financing to accept a low (1 to 3%) nominal discount rate is available (fig. S3). An additional constraint is that the infrastructure and labor force required to implement this large-scale restoration across the global tropics are lacking in many sites, particularly in Southeast Asia, where mast fruiting necessitates greater investment in seedling nurseries (33). Under these circumstances, an alternative approach is to implement generic low-cost measures such as climber cutting, combined with selective tree planting in accessible parts of the degraded forest landscapes where the density of mature trees is insufficient to ensure adequate natural regeneration. This strategy may be attractive to investors in the carbon market, even at current carbon prices, and would leverage recent investments in a new generation of space-borne sensors designed to deliver global high-resolution maps of forest biomass (34–36). Varying the type and intensity of restoration treatments according to the residual ACD of the stand has the potential to reduce the net costs of implementation, help bridge the gap to financial sustainability, and therefore enable much larger areas of forest to be restored.

Carbon stocks and future carbon sequestration are not the only valuable services provided by forest ecosystems (37), and climate change mitigation is not the single goal of restoration, particularly for local stakeholders. The multiple

co-benefits of restoration, such as biodiversity conservation (8, 38), flood protection, provision of clean drinking water, and support for the livelihoods of local communities and stakeholders, provide additional justification for legislation and financing mechanisms that incentivize tropical forest restoration.

## REFERENCES AND NOTES

1. Y. Pan *et al.*, *Science* **333**, 988–993 (2011).
2. A. Baccini *et al.*, *Science* **358**, 230–234 (2017).
3. A. P. Jacobson, J. Riggio, A. M. Tait, J. E. M. Baillie, *Sci. Rep.* **9**, 14179–13 (2019).
4. W. Laurance, D. P. Edwards, *Front. Ecol. Environ.* **12**, 147–147 (2014).
5. N. J. Berry *et al.*, *Biodivers. Conserv.* **19**, 985–997 (2010).
6. F. E. Putz *et al.*, *Conserv. Lett.* **5**, 296–303 (2012).
7. A. H. Rozak, E. Rutishauser, K. Raulund-Rasmussen, P. Sist, *For. Ecol. Manage.* **417**, 154–166 (2018).
8. E. Dinerstein *et al.*, *Sci. Adv.* **5**, eaaw2869 (2019).
9. N. J. Berry, O. L. Phillips, R. C. Ong, K. C. Hamer, *Landsc. Ecol.* **23**, 915–929 (2008).
10. G. P. Asner *et al.*, *Biol. Conserv.* **217**, 289–310 (2018).
11. M. V. Galante, M. A. Pinard, M. Mencuccini, *Int. For. Rev.* **20**, 58–78 (2018).
12. S. S. Saatchi *et al.*, *Proc. Natl. Acad. Sci. U.S.A.* **108**, 9899–9904 (2011).
13. K. Hamrick, M. Gallant, “Unlocking potential: State of the voluntary carbon markets 2017” (Report, Forest Trends’ Ecosystem Marketplace, Washington, DC, 2017).
14. K. Hamrick, M. Gallant, “Voluntary carbon market insights: 2018 Outlook and first-quarter trends” (Report, Forest Trends’ Ecosystem Marketplace, Washington, DC, 2018).
15. S. Donofrio, P. Maguire, W. Merry, S. Zwick, “Financing emissions reductions for the future: State of the voluntary carbon markets 2019” (Report, Forest Trends’ Ecosystem Marketplace, Washington, DC, 2019).
16. E. Rutishauser *et al.*, *Curr. Biol.* **25**, R787–R788 (2015).
17. L. Poorter *et al.*, *Nature* **530**, 211–214 (2016).
18. C. D. Philipson *et al.*, *Ecol. Evol.* **4**, 3675–3688 (2014).
19. A. Hector *et al.*, *Philos. Trans. R. Soc. London B Biol. Sci.* **366**, 3303–3315 (2011).
20. Materials and methods are available as supplementary materials.
21. T. Jucker *et al.*, *Biogeosciences* **15**, 3811–3830 (2018).
22. J. E. Stiglitz, N. Stern, M. Duan, O. Edenhofer, G. Giraud, “Report of the High-Level Commission on Carbon Prices” (Report, Carbon Pricing Leadership Coalition, 2017).
23. A. Ledo *et al.*, *J. Ecol.* **104**, 1819–1828 (2016).
24. G. M. F. van der Heijden, J. S. Powers, S. A. Schnitzer, *Proc. Natl. Acad. Sci. U.S.A.* **112**, 13267–13271 (2015).
25. S. Estrada-Villegas, S. A. Schnitzer, *Biotropica* **50**, 729–739 (2018).
26. L. Banin *et al.*, *J. Ecol.* **102**, 1025–1037 (2014).
27. C. Philipson *et al.*, *Biotropica* **44**, 627–636 (2012).
28. A. Shenkin *et al.*, *Front. For. Glob. Change* **2**, 32 (2019).
29. D. P. Edwards *et al.*, *Proc. Biol. Sci.* **278**, 82–90 (2011).
30. C. E. Wheeler *et al.*, *For. Ecol. Manage.* **373**, 44–55 (2016).
31. K. D. Holl, R. A. Zahawi, *For. Ecol. Manage.* **319**, 36–43 (2014).
32. K. D. Holl, R. A. Zahawi, R. J. Cole, R. Ostertag, S. Cordell, *Restor. Ecol.* **19**, 470–479 (2011).
33. C. J. Kettle *et al.*, *Science* **330**, 584 (2010).
34. D. Schimel *et al.*, *Glob. Chang. Biol.* **21**, 1762–1776 (2015).
35. J. M. B. Carreiras *et al.*, *Remote Sens. Environ.* **196**, 154–162 (2017).

36. R. Dubayah, J. B. Blair, S. Goetz, *Sci. Remote Sens.* **1**, 100002 (2020).
37. L. Gamfeldt *et al.*, *Nat. Commun.* **4**, 1340 (2013).
38. S. Budiharta *et al.*, *Environ. Res. Lett.* **9**, 114020 (2014).
39. M. E. J. Cutler *et al.*, NERC Environmental Information Data Centre (2020); <https://doi.org/10.5285/a75e6371-a931-4676-9199-d1f5af565ab2>.
40. C. D. Philipson, Code for manuscript – Active restoration accelerates the carbon recovery of human-modified tropical forests, Zenodo (2020); <https://doi.org/10.5281/zenodo.3899832>.

## ACKNOWLEDGMENTS

We thank the Sabah Biodiversity Council and the Danum Valley Management Committee for permission to conduct this work. INFAPRO field data were obtained by research assistants at Yayasan Sabah’s and Face the Future’s joint large-scale forest rehabilitation project INFAPRO. We acknowledge assistance and support from the South East Asia Rainforest Research Partnership (SEARRP) and Sabah Forestry. We also acknowledge J. Tay for assistance and advice for the original setup of the project. We are grateful to J. Alexander, N. Ocampo-Peñuela, E. Watts, and J. Bailey from mosaic media for help with graphics and cartography. Comments from four anonymous reviewers greatly improved previous versions of the manuscript. **Funding:** Field data were acquired for the EU-funded INDORSUS project (ER-BIC18T960102 to G.M.F.) and from projects funded by the Carnegie Trust for the Universities of Scotland (ref. 50076 to M.E.J.C. and D.F.R.P.B.) and the DfID and NERC Programme “Understanding the impact of the current El Niño event” (NE/P004806/1 to M.E.J.C., D.F.R.P.B., D.S.B., G.M.F., and G.M.F.v.d.H.). Airborne carbon mapping, processing, and analysis were funded by the UN Development Programme GEF, Avatar Alliance Foundation, Roundtable on Sustainable Palm Oil, Worldwide Fund for Nature, Morgan Family Foundation, and the Rainforest Trust (to G.P.A. and G.R.). **Author contributions:** M.E.J.C. and D.F.R.P.B. conceived the original idea for this study, building on work initiated by G.M.F., D.S.B., and M.E.J.C. C.D.P., D.F.R.P.B., and M.E.J.C. designed the field data collection for the 20-year resurvey of field plots, which was led by C.D.P. and undertaken by C.D.P., S.M., J.A.M., and SEARRP research assistants. Analysis of carbon accumulation was designed and performed by C.D.P., with input from A.L., P.G.B., D.F.R.P.B., and M.E.J.C. Additional inventory data were used from research designed by P.R.L. and M.A.P., P.M.C., C.E.W., M.S., and Y.S.W., with field data collected by P.R.L. and Y.S.W. The remotely sensed carbon map was produced by G.P.A. and staff, with analysis performed by C.D.P., P.G.B., G.P.A., J.A.M., J.F., and R.E.M. C.D.P., D.F.R.P.B., and M.E.J.C. conceived the paper, and all authors contributed to writing the manuscript. **Competing interests:** The authors declare no competing interests. **Data and materials availability:** Plot ACD data are available through the UK Environmental Information Data Centre (39). The carbon map data and code for all analysis are found at <https://github.com/PhilipsonChristopher/CarbonRecovery> (40).

## SUPPLEMENTARY MATERIALS

[science.sciencemag.org/content/369/6505/838/suppl/DC1](https://science.sciencemag.org/content/369/6505/838/suppl/DC1)  
Materials and Methods  
Figs. S1 to S3  
Table S1  
References (41–73)

21 June 2019; resubmitted 3 March 2020  
Accepted 19 June 2020  
10.1126/science.aay4490

## NEUROSCIENCE

# Importin $\alpha 3$ regulates chronic pain pathways in peripheral sensory neurons

Letizia Marvaldi<sup>1</sup>, Nicolas Panayotis<sup>1</sup>, Stefanie Alber<sup>1\*</sup>, Shachar Y. Dagan<sup>1\*</sup>, Nataliya Okladnikov<sup>1</sup>, Indrek Koppel<sup>1</sup>, Agostina Di Pizio<sup>1</sup>, Didi-Andreas Song<sup>1</sup>, Yarden Tzur<sup>1</sup>, Marco Terenzio<sup>1,2</sup>, Ida Rishai<sup>1</sup>, Dalia Gordon<sup>1</sup>, Franziska Rother<sup>3,4</sup>, Enno Hartmann<sup>4</sup>, Michael Bader<sup>3,4,5</sup>, Mike Fainzilber<sup>1†</sup>

How is neuropathic pain regulated in peripheral sensory neurons? Importins are key regulators of nucleocytoplasmic transport. In this study, we found that importin  $\alpha 3$  (also known as karyopherin subunit alpha 4) can control pain responsiveness in peripheral sensory neurons in mice. Importin  $\alpha 3$  knockout or sensory neuron-specific knockdown in mice reduced responsiveness to diverse noxious stimuli and increased tolerance to neuropathic pain. Importin  $\alpha 3$ -bound c-Fos and importin  $\alpha 3$ -deficient neurons were impaired in c-Fos nuclear import. Knockdown or dominant-negative inhibition of c-Fos or c-Jun in sensory neurons reduced neuropathic pain. In silico screens identified drugs that mimic importin  $\alpha 3$  deficiency. These drugs attenuated neuropathic pain and reduced c-Fos nuclear localization. Thus, perturbing c-Fos nuclear import by importin  $\alpha 3$  in peripheral neurons can promote analgesia.

**T**he importin  $\alpha$  subfamily of karyopherins is critical for nuclear import in eukaryotic cells (1, 2) and participates in cytoplasmic transport in large cells such as neurons (3, 4). Despite overlapping importin specificities (5, 6), differential expression profiles and varying cargo affinities enable regulation of specific functions by single importins (7–15). We sought to identify neuronal functions of importins by behavioral screens on importin  $\alpha$  knockout mice. Importin  $\alpha 3$  null animals uniquely exhibited an attenuated response to noxious heat (Fig. 1A and fig. S1, A to C), and these animals did not show overt coping behavior after capsaicin injection (fig. S1, D to F).

We corroborated these findings by intrathecal injection of adeno-associated virus 9 (AAV9) constructs for acute knockdown or overexpression of importin  $\alpha 3$  (fig. S2). Importin  $\alpha 3$  knockdown mice revealed delayed paw withdrawal latency to noxious heat in comparison with mice that received control short hairpin RNA (shRNA) (Fig. 1B), without any significant effects on exploratory behavior or motor coordination (fig. S3, A and B). Specificity of the effects was confirmed by reversal of the phenotype upon importin  $\alpha 3$  overexpression in importin  $\alpha 3$  knockout mice (Fig. 1C). Conversely, shRNA knockdown had no fur-

ther effect in the knockout background (fig. S3C). Thus, specific loss of importin  $\alpha 3$  attenuates responsiveness to diverse noxious stimuli.

We next evaluated importin  $\alpha 3$  in neuropathic pain using the spared nerve injury (SNI) model (16–18) (fig. S4, A and B), with periodic monitoring of mechanosensitivity in wild-type and importin  $\alpha 3$  SNI animals over 3 months. Initial responses were similar in both genotypes and diverged from day 60 onward. At this later stage, importin  $\alpha 3$  null animals exhibited increasing tolerance to SNI, with less hypersensitivity to touch (Fig. 1D) and reduced unevoked paw clenching (fig. S4C), whereas wild-type animals did not show any improvement. Similar results were obtained by knockdown of importin  $\alpha 3$  before induction of SNI (Fig. 1E and fig. S4, D and E). Starting 60 days after injury, control shRNA-treated SNI mice typically displayed a spontaneous clenched-paw phenotype associated with reduced paw print width in the CatWalk assay, while animals treated with anti-importin  $\alpha 3$  shRNA revealed improved gait parameters and reduced paw clenching (fig. S4, E and F). Mechanosensitivity assays showed that the neuropathic pain response developed in a similar manner in control and anti-importin  $\alpha 3$  shRNA treated mice up to 60 days after injury. From day 60 onward, importin  $\alpha 3$  knockdown animals exhibited a significant recovery of the paw withdrawal reflex, in contrast to controls (Fig. 1E). Thus, both knockout and acute knockdown of importin  $\alpha 3$  provides relief from chronic neuropathic pain in the SNI model.

Different cell types can participate in neuropathic pain circuits (19, 20). We therefore sought to determine whether importin  $\alpha 3$  effects on neuropathic pain arise specifically in

sensory neurons. To this end, we carried out viral transduction of shRNA using AAV-PHP.S, a capsid subtype developed for peripheral neuron specificity (21). We verified AAV-PHP.S selectivity by lumbar intrathecal injection, observing specific and efficient transduction of dorsal root ganglia (DRG) sensory neurons (fig. S5). We then tested the effects of importin  $\alpha 3$  knockdown by AAV-PHP.S delivery of shRNA after SNI induction (fig. S4D), monitoring both evoked (Fig. 1F) and unevoked (Fig. 1G, fig. S4G, and movie S1) responses to neuropathic pain. Both the evoked and spontaneous parameters revealed that sensory neuron-specific knockdown of importin  $\alpha 3$  provided relief from neuropathic pain, even when knockdown was initiated after establishment of the pain model.

To gain mechanistic insight on the effects of importin  $\alpha 3$  knockout in SNI, we compared DRG transcriptomes at 1 week versus 11 weeks after injury, when pain was significantly alleviated (Fig. 2A and table S1). The differentially expressed gene sets revealed signatures for a number of transcription factors affected by depletion of importin  $\alpha 3$  (Fig. 2B). Among these factors, the activator protein 1 (AP1) family was prioritized for further study because c-Fos is a well-documented marker for pain circuits (22–24). Quantitative analysis of four AP1 target genes after SNI revealed reduced expression of *Syngap1* and *RTL1* in importin  $\alpha 3$  null DRG compared with wild type (Fig. 2C). *Syngap1* has previously been implicated in tactile sensory processing (25).

c-Fos features both an importin  $\alpha$ -binding nuclear localization signal and a binding motif for transportin, a distinct nuclear import factor (26). Multiple members of both these nuclear import factor families are widely expressed in sensory neurons (27). We confirmed importin  $\alpha 3$  and c-Fos expression in DRG neurons (fig. S6, A to C) and verified that they interact by proximity biotinylation in transfected Neuro2a (N2a) cells (fig. S6D) and proximity ligation assay (PLA) of endogenous proteins in sensory neurons (Fig. 2, D and E). Basal c-Fos expression was not changed in importin  $\alpha 3$  knockout neurons (fig. S6, E and F). c-Fos immunostaining was mostly nuclear in wild-type DRG neurons, whereas, in contrast, there was little or no c-Fos nuclear accumulation in importin  $\alpha 3$  null neurons (Fig. 2, F to I, and fig. S6, A, B, and G). Thus, importin  $\alpha 3$  is required for c-Fos nuclear accumulation in adult sensory neurons.

The c-Fos inhibitor T-5224 is under investigation for analgesic efficacy (28, 29). We tested the effects of T-5224 by intraperitoneal injection in wild-type versus importin  $\alpha 3$  null mice. T-5224 treatment increased paw withdrawal latency in response to noxious heat in wild-type mice (fig. S7, A to D), but it had no additional effect beyond the already existing attenuation

<sup>1</sup>Department of Biomolecular Sciences, Weizmann Institute of Science, Rehovot 76100, Israel. <sup>2</sup>Molecular Neuroscience Unit, Okinawa Institute of Science and Technology, Kunigami-gun, Okinawa 904-0412, Japan. <sup>3</sup>Max Delbrück Center for Molecular Medicine, 13125 Berlin, Germany. <sup>4</sup>Center for Structural and Cellular Biology in Medicine, Institute of Biology, University of Lübeck, 23538 Lübeck, Germany. <sup>5</sup>Charité – Universitätsmedizin Berlin, 10117 Berlin, Germany.

\*These authors contributed equally to this work.

†Corresponding author. Email: mike.fainzilber@weizmann.ac.il



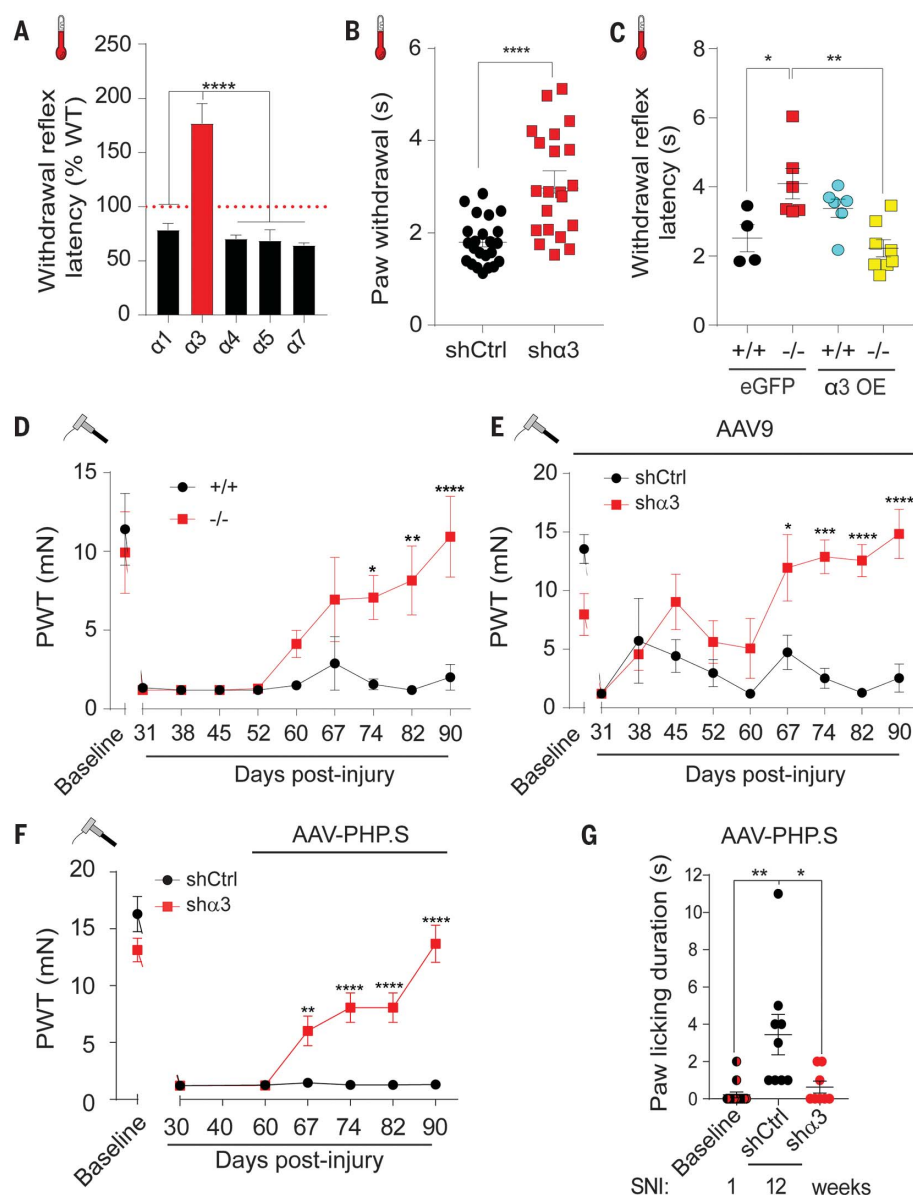


**Fig. 1. Attenuated pain responses in importin  $\alpha 3$  mice.** (A) Importin  $\alpha 3$  mice ( $\alpha 3$ ) are the only line of importin  $\alpha$  knockout mice with a higher latency of paw withdrawal in response to noxious heat stimulus (58°C) compared with wild-type littermates.  $n \geq 7$  mice, one-way analysis of variance (ANOVA) followed by Tukey's multiple comparison test. (B) Attenuated response to noxious heat after shRNA-mediated knockdown of importin  $\alpha 3$ .  $n = 20$  mice, two-tailed unpaired  $t$  test. (C) Overexpression of importin  $\alpha 3$  ( $\alpha 3$  OE) restored heat sensitivity in importin  $\alpha 3$  knockout animals, while enhanced green fluorescent protein (eGFP) overexpression had no such effect.  $n \geq 4$  mice, one-way ANOVA followed by Tukey's multiple comparison test. (D) Paw withdrawal threshold (PWT) assessed by the von Frey test in SNI animals shows alleviation of long-term neuropathic pain in importin  $\alpha 3$  knockout animals.  $n \geq 5$  mice, two-way ANOVA followed by Sidak's multiple comparison test. (E) PWT in SNI animals treated with AAV9 shRNA against importin  $\alpha 3$  (sha3) or scrambled control shRNA (shCtrl). The upper horizontal line indicates time frame from AAV9 injection.  $n = 7$  mice, two-way ANOVA followed by Sidak's multiple comparison test. (F) PWT in SNI animals treated with AAV-PHP.S shRNA against importin  $\alpha 3$  (sha3) or shCtrl. The upper horizontal line indicates time frame from AAV-PHP.S injection.  $n = 9$  mice, two-way ANOVA followed by Sidak's multiple comparison test. (G) Spontaneous (unevoked) paw licking duration measured at 1 week (baseline) and 12 weeks after SNI.  $n \geq 9$  mice per group, Kruskal-Wallis followed by Dunn's multiple comparison tests. All quantifications shown as mean  $\pm$  SEM. \* $P < 0.05$ , \*\* $P < 0.01$ , \*\*\* $P < 0.001$ , \*\*\*\* $P < 0.0001$ .

in importin  $\alpha 3$  null animals (fig. S7, C and D). However, T-5224 did ameliorate the paw withdrawal latency in von Frey tests of wild-type animals 1 week after induction of SNI (fig. S7E), a time point at which importin  $\alpha 3$  knock-out or knockdown still had no effect on SNI responses (Fig. 1). Thus c-Fos perturbation has analgesic effects, and importin  $\alpha 3$  may act mainly in the later maintenance stage of neuropathic pain.

To confirm that the AP1 pathway is required for late-stage neuropathic pain, we tested the effects of c-Fos or c-Jun knockdown in the SNI model (fig. S8). Similarly to the effects of importin  $\alpha 3$  depletion, c-Fos knockdown reduced sensitivity to noxious heat (Fig. 3A) without affecting basal mechanosensitivity (Fig. 3B). c-Jun knockdown reduced sensitivity

to both noxious heat and mechanical stimuli (Fig. 3, A and B). Comparison of c-Fos, c-Jun, and importin  $\alpha 3$  knockdowns in the SNI model showed that all three shRNAs significantly attenuated the neuropathic pain response 67 to 90 days after injury (Fig. 3C). Furthermore, neuron-specific expression of a dominant-negative form of AP1 called A-Fos (30) significantly attenuated noxious heat sensitivity without affecting basal mechanosensitivity (Fig. 3, D and E) and significantly reduced late-stage neuropathic pain in SNI (Fig. 3F). Thus, AP1 pathway inhibition attenuates neuropathic pain in the SNI model.

Finally, we carried out an in silico screen using the Connectivity Map (CMap) database (31, 32) to search for drugs that might target the importin  $\alpha 3$ -c-Fos pathway. The screen

identified ~50 compounds with high CMap scores, 35 of which were not known to affect pain (Fig. 4A and table S2). We selected three compounds for further analysis: ajmaline, an antiarrhythmic alkaloid; sulmazole, a cardiotonic agent; and sulfamethizole, an antibiotic. Ajmaline did not affect responses to noxious heat, but both sulmazole and sulfamethizole showed efficacy in this assay (Fig. 4B). Both of the latter drugs also provided time- and dose-dependent relief at both early and late stages of SNI (Fig. 4, C to E, and fig. S9, A and B) and were as effective as knockout or knockdown of importin  $\alpha 3$  in ameliorating response of SNI animals to a noxious mechanical stimulus (Fig. 4F). Additionally, both sulmazole and sulfamethizole significantly reduced c-Fos nuclear accumulation in wild-type neurons

but did not have any further effect on c-Fos nuclear accumulation in importin  $\alpha 3$  null neurons (fig. S9, C to E). Thus, drugs mimicking importin  $\alpha 3$  loss phenocopy both the analgesic and c-Fos localization effects observed in importin  $\alpha 3$  mutant animals.

Here, we have shown that perturbing c-Fos nuclear import by importin  $\alpha 3$  in sensory neurons reduces sensitivity to noxious stimuli and provides analgesia specifically in the maintenance phase of neuropathic pain. Direct c-Fos inhibition is effective at both early and main-

tenance stages of neuropathic pain, suggesting that other modes of c-Fos nuclear import or other transcription factors may control the early pain response, while importin  $\alpha 3$  has a key role for later chronic pain. Very recent studies have reported discrimination

**Fig. 2. Transcriptome analyses suggest that c-Fos nuclear import by importin  $\alpha 3$  mediates pain responses.** (A) Heatmap of z-score transformed normalized expression values for 530 differentially expressed genes (DEG) at the indicated times (weeks) after SNI in importin  $\alpha 3$  null mice ( $n \geq 3$  mice).

(B) FMatch (geneXplain) TRANSFAC analyses identify transcription factor (TF) families enriched in DEG promoters from the up-regulated (161) and down-regulated (369) genes at 11 weeks after SNI. The AP1 complex was identified as one of the top TF families for the down-regulated gene ensemble. (C) Reverse transcription quantitative polymerase chain reaction (RT-qPCR) analysis of four AP1-target genes, *Syngap1*, *Slc38*, *Gpr151*, and *RTL1*, comparing expression at 1 week versus 11 weeks after SNI in wild-type and importin  $\alpha 3$  null DRGs.  $n = 3$  mice, one-way ANOVA followed by Sidak's multiple comparison test. (D) Proximity ligation assay (PLA) for c-Fos and importin  $\alpha 3$  in calcitonin gene-related peptide-positive DRG neurons fixed after 24 hours in culture from both naïve and injury groups. PLA signals shown in red. Scale bar, 30  $\mu\text{m}$ .

(E) Quantification of PLA signals per neuron.  $n \geq 29$  neurons per group from three independent experiments, ANOVA followed by Tukey's multiple comparison test. (F) Reduced nuclear localization of c-Fos in cultured importin  $\alpha 3$  null DRG neurons versus wild type. Scale bar, 50  $\mu\text{m}$ . (G) Quantification of nuclear c-Fos intensity from the experiment shown in (F).  $n > 67$  neurons from three independent experiments, two-tailed unpaired  $t$  test. (H) Reduced nuclear localization of c-Fos in DRG neurons from sectioned ganglia of importin  $\alpha 3$  null compared with wild-type mice. Cell body and nucleus boundaries determined by TuJ-1 and 4',6-diamidino-2-phenylindole (DAPI) staining as indicated (see also fig. S6G). Scale bar, 10  $\mu\text{m}$ . (I) Quantification of c-Fos immunofluorescence along line scans as shown in (H),  $n > 206$  neurons from three independent experiments. All data are shown as mean  $\pm$  SEM. a.u., arbitrary units. \* $P < 0.05$ , \*\* $P < 0.01$ , \*\*\*\* $P < 0.0001$ .

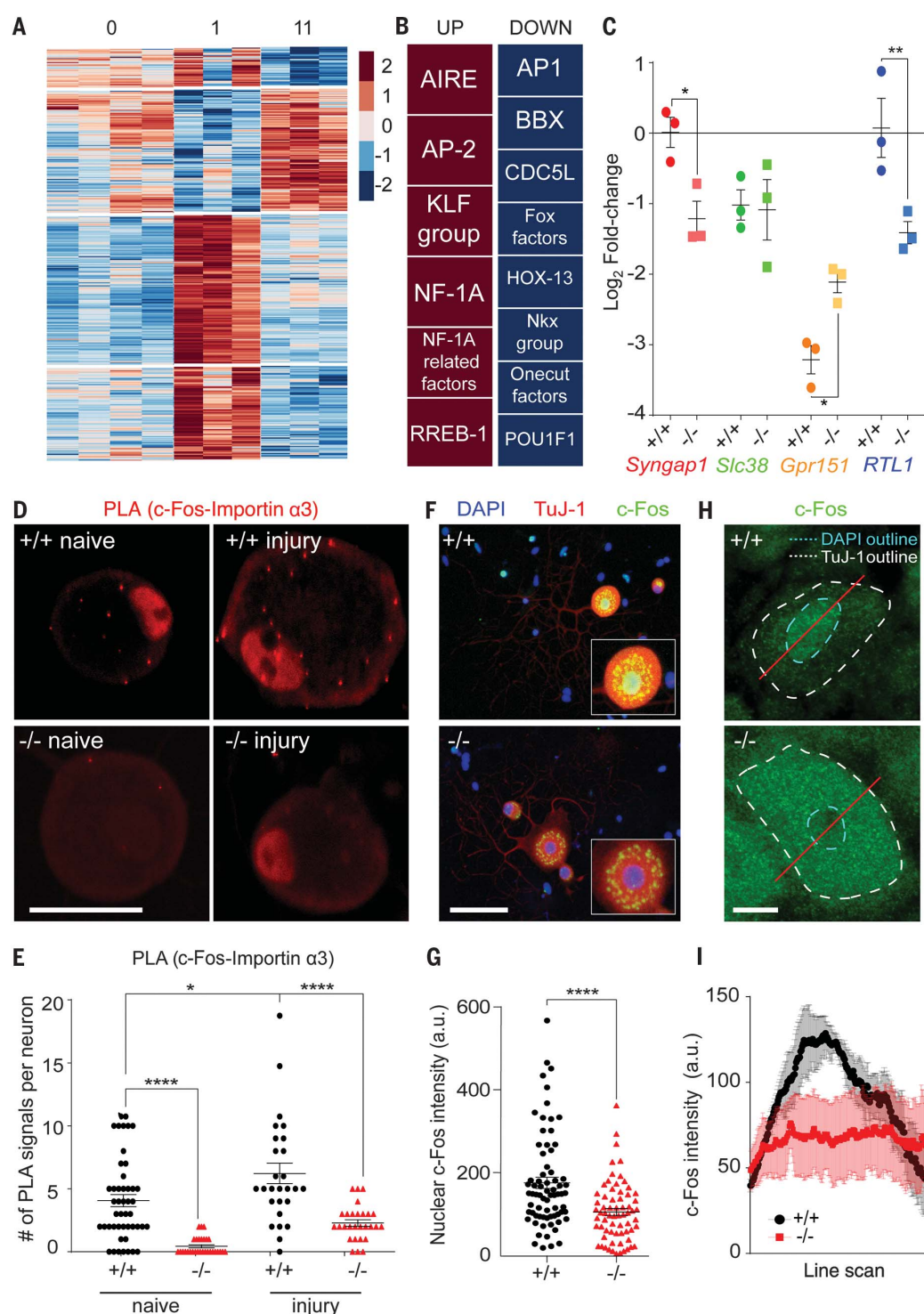




**Fig. 3. Acute knockdown or dominant-negative inhibition of AP1 transcription factors attenuates chronic pain after SNI.** (A) Reduced noxious heat responses in mice after intrathecal AAV9 delivery of shRNAs targeting c-Fos (shFOS1, shFOS2) or c-Jun (shJUN).  $n \geq 4$  mice, ANOVA followed by Dunnett's multiple comparison test.

(B) Reduced mechanosensitivity in shJUN, but not shFOS, treated animals.  $n \geq 4$  mice, ANOVA followed by Dunnett's multiple comparison test. (C) PWT assessed by the von Frey test in SNI animals treated with the indicated shRNAs (shFOS indicates a mixture of both).  $n \geq 5$  mice, two-way ANOVA. AAV IT, adeno-associated virus intrathecal injection. (D and E) AAV9 overexpression of the A-Fos dominant-negative (DN) under the neuron-specific human synapsin I promoter reduces noxious heat responses (D) without effects on basal mechanosensitivity (E).  $n \geq 6$  mice, two-tailed unpaired  $t$  test. (F) PWT in SNI animals treated with the A-Fos DN construct.  $n \geq 6$  mice, two-way ANOVA. Asterisks indicate significant treatment effects between the groups. All data shown as mean  $\pm$  SEM. \* $P < 0.05$ , \*\* $P < 0.01$ , \*\*\* $P < 0.001$ , \*\*\*\* $P < 0.0001$ .

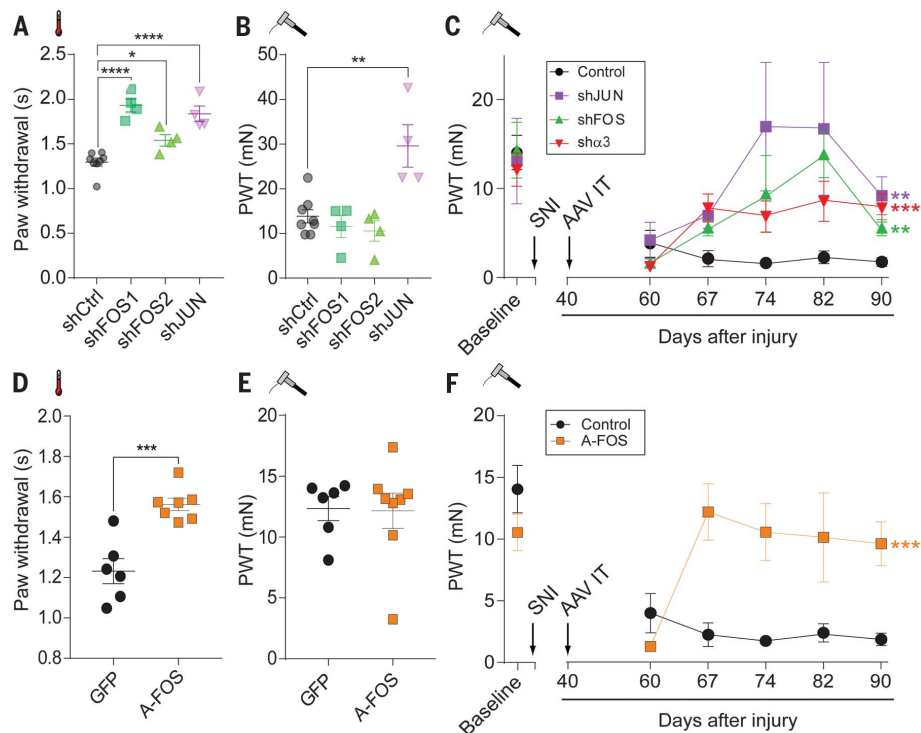
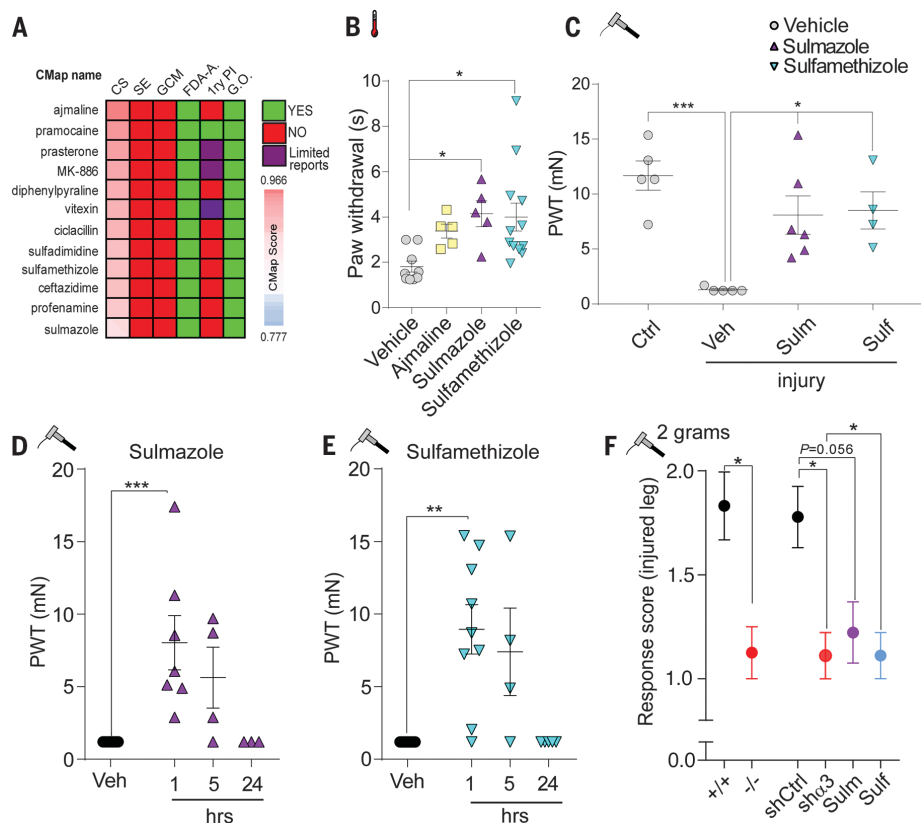


**Fig. 4. An in silico screen for mimics of transcriptional effects of importin  $\alpha 3$  loss reveals candidate analgesics.** (A) Imp $\alpha 3$  knockout DEG lists were used to query CMap for small molecules with similar effects on cell line transcriptomes.

Compounds with CMap scores (CS)  $> 0.85$  are shown. Compounds were further filtered for minimal predicted side effects (SE), lack of general cell-modifying effects (GCM), U.S. Food and Drug Administration approved status (FDA-A), whether their primary therapeutic indication (PI) is pain-related, and final go/no-go decision (G.O., general observation). (B) Three candidates meeting the desired criteria were tested in vivo for effects on response to noxious heat 1 hour after intraperitoneal injection. Sulmazole (0.5 mg/kg,  $n = 5$  mice) and sulfamethizole (1.25 mg/kg,  $n = 12$ ) showed significant effects as compared with vehicle [5% dimethyl sulfoxide (DMSO) in phosphate-buffered saline (PBS),  $n = 9$  mice], while ajmaline (1 mg/kg,  $n = 5$  mice) did not. (C) Significant effects of sulmazole (1.25 mg/kg,  $n = 6$  mice) and sulfamethizole (3.12 mg/kg,  $n = 4$  mice) compared with vehicle (5% DMSO in PBS,  $n = 5$  mice) in the SNI model of neuropathic pain. Drugs were tested 60 days after establishing the model by two intraperitoneal injections 1 week apart, followed by von Frey tests 1 hour after the second injection. Ctrl, control (i.e., the uninjured leg); Veh, vehicle; Sulf, sulfamethizole; Sulf, sulfamethizole. ANOVA followed by Sidak's multiple comparison test used for both (B) and (C). (D and E) Duration of drug effects 1 week after SNI, with von Frey tests performed 1, 5, and 24 hours after intraperitoneal injection.  $n \geq 4$  mice, Kruskal-Wallis test followed by Dunn's multiple comparison test. (F) Noxious mechanosensitivity testing of SNI mice treated as shown, using von Frey filaments of 2 gram-force. Scoring from 0 to 2, with 0 indicating no response, 1 indicating signs of discomfort, and 2 indicating withdrawal of the leg.  $n \geq 6$  mice, Kruskal-Wallis test followed by Dunn's multiple comparison test. Data shown as mean  $\pm$  SEM throughout. \* $P < 0.05$ , \*\* $P < 0.01$ , \*\*\* $P < 0.001$ .



at the spinal circuit level between rapid aversive behavior and sustained pain responses (33), as well as roles for different cell types in mechanosensitivity and nociception (19, 20). Our findings indicate that peripheral sensory neurons are the locus of the effects of importin  $\alpha 3$  on sustained neuropathic pain. The expression profiles and levels of both importin  $\alpha 3$  and c-Fos are conserved between mouse and human DRG (34), and a recent study reported marked up-regulation of AP1 family genes in the DRG of neuropathic pain patients (35), highlighting the potential of importin  $\alpha 3$  as a drug target for pain. Chronic pain is currently one of the most common unmet medical needs, owing to limited analgesic efficacy of existing drugs, coupled with adverse side effects (36, 37). Moreover, opioids, which are the most commonly used class of pain drugs, carry multiple risks of tolerance and dependence, which can lead to considerable levels of abuse (38). The vast majority of current targets for drug development in the pain field are ion channels and neurotransmitter receptors, localized at the plasma membrane and the synapse. Importin  $\alpha 3$  provides an alternative target both in terms of molecular identity and subcellular localization, offering opportunities for future analgesia development.

## REFERENCES AND NOTES

1. Y. Miyamoto, K. Yamada, Y. Yoneda, *J. Biochem.* **160**, 69–75 (2016).
2. M. Christie *et al.*, *J. Mol. Biol.* **428**, 2060–2090 (2016).
3. N. Panayotis, A. Karpova, M. R. Kreutz, M. Fainzilber, *Trends Neurosci.* **38**, 108–116 (2015).
4. M. Terenzio, G. Schiavo, M. Fainzilber, *Neuron* **96**, 667–679 (2017).
5. B. Friedrich, C. Quensel, T. Sommer, E. Hartmann, M. Köhler, *Mol. Cell. Biol.* **26**, 8697–8709 (2006).
6. M. T. Macknall *et al.*, *Mol. Syst. Biol.* **13**, 962 (2017).
7. T. Schmidt *et al.*, *Nat. Cell Biol.* **9**, 1337–1338 (2007).
8. F. Rother *et al.*, *PLOS ONE* **6**, e18310 (2011).
9. G. Gabriel *et al.*, *Nat. Commun.* **2**, 156 (2011).
10. T. Moriyama *et al.*, *FEBS J.* **278**, 1561–1572 (2011).
11. K. Ben-Yaakov *et al.*, *EMBO J.* **31**, 1350–1363 (2012).
12. N. Yasuhara *et al.*, *Dev. Cell* **26**, 123–135 (2013).
13. N. Panayotis *et al.*, *Cell Rep.* **25**, 3169–3179.e7 (2018).
14. A. S. Sowa *et al.*, *Proc. Natl. Acad. Sci. U.S.A.* **115**, E2624–E2633 (2018).
15. K. Döhner *et al.*, *PLOS Pathog.* **14**, e1006823 (2018).
16. I. Decosterd, C. J. Woolf, *Pain* **87**, 149–158 (2000).
17. M. Pertin, R. D. Gosselin, I. Decosterd, *Methods Mol. Biol.* **851**, 205–212 (2012).
18. S. Shiers *et al.*, *J. Neurosci.* **38**, 7337–7350 (2018).
19. H. Abdo *et al.*, *Science* **365**, 695–699 (2019).
20. X. Yu *et al.*, *Nat. Commun.* **11**, 264 (2020).
21. K. Y. Chan *et al.*, *Nat. Neurosci.* **20**, 1172–1179 (2017).
22. R. E. Coggeshall, *Prog. Neurobiol.* **77**, 299–352 (2005).
23. P. L. Santos, R. G. Brito, J. P. S. C. F. Matos, J. S. S. Quintans, L. J. Quintans-Júnior, *Mol. Neurobiol.* **55**, 4560–4579 (2018).
24. J. Lai *et al.*, *Nat. Neurosci.* **9**, 1534–1540 (2006).
25. S. D. Michaelson *et al.*, *Nat. Neurosci.* **21**, 1–13 (2018).
26. M. Arnold, A. Nath, D. Wohlwend, R. H. Kehlenbach, *J. Biol. Chem.* **281**, 5492–5499 (2006).
27. N. Sharma *et al.*, *Nature* **577**, 392–398 (2020).
28. Y. Aikawa *et al.*, *Nat. Biotechnol.* **26**, 817–823 (2008).
29. H. Makino *et al.*, *Sci. Rep.* **7**, 16983 (2017).
30. M. Olive *et al.*, *J. Biol. Chem.* **272**, 18586–18594 (1997).
31. J. Lamb *et al.*, *Science* **313**, 1929–1935 (2006).
32. A. J. Mears *et al.*, *NPJ Genom. Med.* **2**, 14 (2017).
33. T. Huang *et al.*, *Nature* **565**, 86–90 (2019).
34. P. Ray *et al.*, *Pain* **159**, 1325–1345 (2018).
35. R. Y. North *et al.*, *Brain* **142**, 1215–1226 (2019).
36. A. S. Yekkirala, D. P. Roberson, B. P. Bean, C. J. Woolf, *Nat. Rev. Drug Discov.* **16**, 545–564 (2017).
37. T. J. Price *et al.*, *Nat. Rev. Neurosci.* **19**, 383–384 (2018).
38. P. Skolnick, N. D. Volkow, *Neuron* **92**, 294–297 (2016).

## ACKNOWLEDGMENTS

We thank V. Kiss, T. Shalit, M. Tsoory, and C. Pritz for excellent professional expertise; N. Korem and Y. Levi for technical assistance; and H. Song, C. Vinson, and V. Gradinaru for generous gifts of essential plasmids via Addgene. **Funding:** Supported by research grants from the European Research Council (Advanced grant Neurogrowth, Proof of Concept grant ChronicPain), the Irwin Green Alzheimer's Research Fund, the Simon Family Foundation, and Mr. and Mrs. Lawrence Feis. N.P., I.K., and M.T. were partly supported by Koshland senior postdoctoral fellowships, and N.P. was also supported by the Israeli Ministry of Immigrant Absorption. M.F. is supported by the Chaya Professorial Chair in Molecular Neuroscience at the Weizmann Institute of Science. **Author contributions:** Conceptualization: M.F. and L.M.; behavior and pain models: L.M., N.P., S.Y.D., N.O., and S.A.; immunohistochemistry, biochemistry, and data analyses: L.M., N.P., S.A., I.K., A.D.P., D.-A.S., Y.T., M.T., I.R., and D.G.; mouse models: F.R., E.H., and M.B.; writing and revision: M.F. and L.M., with input from all authors; supervision and funding: M.F. **Competing interests:** L.M. and M.F. have patent applications related to this work [Israeli application 268111, pending; Patent Cooperation Treaty (PCT) PCT/IL2020/050801]. **Data and materials availability:** All data are available in the main text or the supplementary materials. RNA sequencing datasets are available in the GEO database online (accession no. GSE137515). The importin  $\alpha 3$  null mouse model is available upon request from M.B.'s laboratory.

## SUPPLEMENTARY MATERIALS

science.sciencemag.org/content/369/6505/842/suppl/DC1  
Materials and Methods  
Figs. S1 to S9  
Tables S1 and S2  
References (39–54)  
MDAR Reproducibility Checklist  
Movie S1

[View/request a protocol for this paper from Bio-protocol.](#)

21 September 2019; resubmitted 26 May 2020  
Accepted 30 June 2020  
10.1126/science.aaz5875



## CORONAVIRUS

# A mathematical model reveals the influence of population heterogeneity on herd immunity to SARS-CoV-2

Tom Britton<sup>1\*</sup>, Frank Ball<sup>2</sup>, Pieter Trapman<sup>1</sup>

Despite various levels of preventive measures, in 2020, many countries have suffered severely from the coronavirus 2019 (COVID-19) pandemic caused by the severe acute respiratory syndrome coronavirus 2 (SARS-CoV-2) virus. Using a model, we show that population heterogeneity can affect disease-induced immunity considerably because the proportion of infected individuals in groups with the highest contact rates is greater than that in groups with low contact rates. We estimate that if  $R_0 = 2.5$  in an age-structured community with mixing rates fitted to social activity, then the disease-induced herd immunity level can be ~43%, which is substantially less than the classical herd immunity level of 60% obtained through homogeneous immunization of the population. Our estimates should be interpreted as an illustration of how population heterogeneity affects herd immunity rather than as an exact value or even a best estimate.

Severe acute respiratory syndrome coronavirus 2 (SARS-CoV-2) has spread globally despite the many different preventive measures that have been put in place to reduce transmission. Some countries aimed for suppression by extreme quarantine measures (lockdown) and others aimed for mitigation by slowing the spread using certain preventive measures in combination with protection of the vulnerable (1). An important question for both policies has been when to lift some or all of the restrictions. A closely related question is if and when herd immunity can be achieved. Herd immunity is defined as a level of population immunity at which disease spreading will decline and stop even after all preventive measures have been relaxed. If all preventive measures are relaxed when the immunity level from infection is below the herd immunity level, then a second wave of infection may start once restrictions are lifted.

By 1 May 2020, some regions and countries reached high estimates for the population immunity level; for example, 26% of the population was infected (with a large confidence interval) in the metropolitan Stockholm region, as shown by a mathematical model (2). At the same time, population studies in Spain showed that in the second half of May 2020, >10% of the population of Madrid had antibodies for coronavirus disease 2019 (COVID-19) (3). It is debatable whether (classical) herd immunity for COVID-19, which is believed to lie between 50 and 75%, can be achieved without unacceptably high case fatality rates (4–6).

The definition of classical herd immunity originates from mathematical models for the impact of vaccination. The classical herd im-

munity level  $h_C$  is defined as  $h_C = 1 - 1/R_0$ , where  $R_0$  is the basic reproduction number, defined as the average number of new infections caused by a typical infected individual during the early stage of an outbreak in a fully susceptible population (7). Thus, if a fraction  $v$  is vaccinated (with a vaccine giving 100% immunity) and vaccinees are selected uniformly in the community, then the new reproduction number is  $R_v = (1 - v)R_0$ . From this, the critical vaccination coverage  $v_c = 1 - 1/R$ . So, if at least this fraction is vaccinated and hence immune, the community has reached herd immunity because  $R_v \leq 1$  and no outbreak can take place. If the vaccine is not perfect but instead reduces susceptibility by a fraction  $E$  (so  $E = 1$  corresponds to 100% efficacy), then the critical vaccination coverage is given by  $v_c = E^{-1}(1 - 1/R_0)$  (7), implying that a bigger fraction needs to be vaccinated if the vaccine is not perfect.

No realistic model will depict human populations as homogeneous; there are many heterogeneities in human societies that will influence virus transmission. Here, we use a model to illustrate how population heterogeneity can cause substantial heterogeneity among the people infected during the course of an infectious disease outbreak, with consequent impact on the herd immunity level and the performance of exit policies aimed at minimizing the risk of future infection spikes.

One of the simplest of all epidemic models is to assume a homogeneously mixing population in which all individuals are equally susceptible and equally infectious if they become infected. Before becoming infectious, infected individuals first go through a latent/exposed period, i.e., the susceptible-exposed-infected-recovered (SEIR) model (7). The basic reproduction number  $R_0$  de-

notes the average number of infectious contacts that an infected individual has before recovering and becoming immune (or dying). An infectious contact is defined as one close enough to infect the other individual if this individual is susceptible (contacts with already infected individuals have no effect).

To this simple model, we add two important features known to play an important role in disease spreading (the model is described in full detail in the supplementary materials). The first is to include age structure by dividing the community into different age cohorts with heterogeneous mixing between them. We categorized a community into six age groups and fit contact rates derived from an empirical study of social contacts (8) (see the supplementary materials for details on the community structure). The person-to-person infectious contact rate between two individuals depends on the age groups of both individuals. The average number of infectious contacts that an infected person in age group  $i$  has with individuals in (another or the same) age group  $j$  now equals  $a_{ij}\pi_j$ , where  $a_{ij}$  reflects both how much an  $i$  individual has contact with a specific  $j$  individual. It also reflects the typical infectivity of  $i$  individuals and susceptibility of  $j$  individuals. The population fraction of individuals belonging to age cohort  $j$  is denoted by  $\pi_j$ .

The second population structure element that we added to the simple model categorizes individuals according to their social activity level. A common way to do this is by means of network models [e.g., (9)]. Here, we take a simpler approach and categorize individuals into three different activity levels, which are arbitrary and chosen for illustration purposes: 50% of each age cohort have normal activity, 25% have low activity corresponding to half as many contacts compared with normal activity, and 25% have high activity corresponding to twice as many contacts as normal activity. By this we mean that, for example, a high-activity individual in age group  $i$  on average has  $2 \cdot a_{ij}\pi_j \cdot 0.5 \cdot 0.25$  infectious contacts with low-activity individuals of age group  $j$ . The factor 2 comes from the infective having high activity, the factor 0.5 from the contacted person having low activity, and the factor 0.25 from low-activity individuals making up 25% of each age cohort. The basic reproduction number  $R_0$  for this model is given by the dominant eigenvalue of the (next-generation) matrix  $M$  having these elements as its entries. (7).

The final fractions of the different groups in the population becoming infected in the epidemic are obtained by solving a set of equations (the final size equations are provided in the supplementary materials). To

<sup>1</sup>Department of Mathematics, Stockholm University, Stockholm, Sweden. <sup>2</sup>School of Mathematical Sciences, University of Nottingham, Nottingham, UK.

\*Corresponding author. Email: tom.britton@math.su.se

be able to say something about the time evolution of the epidemic, we assume a classical SEIR epidemic model. More precisely, we assume that individuals who get infected are initially latent for a mean of 3 days, followed by an infectious period of a mean of 4 days, thus approximately mimicking the situation for COVID-19 [e.g., (7)]. During the infectious period, an individual makes infectious contacts at rates such that the mean numbers of infectious contacts agree with those of the next-generation matrix  $M$ .

In the model, we assume that the basic reproduction number satisfies  $R_0 = 2.5$  (a few other values are also evaluated) and that the epidemic is initiated with a small fraction of infectious individuals on 15 February. On 15 March, when the fraction infected is still small, preventive measures are implemented such that all averages in the next-generation matrix are scaled by the same factor  $\alpha < 1$ , so the next-generation matrix becomes  $\alpha M$ . Consequently, the new reproduction number is  $\alpha R_0$ . These preventive measures are kept until the ongoing epidemic is nearly finished. That is, all preventive measures are relaxed thus setting  $\alpha$  back to 1 on 30 June. If herd immunity is not reached, then there will then be a second wave, whereas if herd immunity has been achieved, the epidemic continues to decline.

We used the model to investigate the effect of the preventive measures and, for two scenarios, we analyzed whether a given level of preventive measures yields disease-induced herd immunity. We did this for populations that are (i) homogeneous, (ii) categorized by age groups but not by activity levels, (iii) not categorized by age but assigned different activity levels, and (iv) have both age-related and activity structures.

For each of the four population structures described above, we show overall disease-induced herd immunity in Table 1. This was obtained by assuming that preventive measures having factor  $\alpha < 1$  are implemented at the start of an epidemic, running the resulting model epidemic to its conclusion and then exposing the population to a second epidemic with  $\alpha = 1$ . We obtain  $\alpha_c$ , the greatest value of  $\alpha$  such that a second epidemic cannot occur. The disease-induced herd immunity level  $h_D$  is given by the fraction of the population that is infected by the first epidemic. This approximates the situation in which preventive measures are implemented early and lifted late in an outbreak. Note that given the next-generation matrix,  $h_D$  is independent of the distributions of the latent and infectious periods.

As seen in Table 1, all three structured populations have lower disease-induced herd immunity  $h_D$  compared with the classical herd immunity  $h_C$ , which assumes that immunity

is uniformly distributed among the different types of individuals. From the table, it is clear that the different activity levels have a greater effect on reducing  $h_D$  than does age structure.

In Table 2, the final fractions infected in the different age activity groups for  $\alpha = \alpha_c$  just barely reaching disease-induced herd immunity are given. This is done for the age and activity group structure and assuming  $R_0 = 2.5$ . The overall fraction infected equals  $h_D = 43.0\%$ , in agreement with Table 1. Table S1 is a similar table in which only activity groups are considered.

We also illustrate the time evolution of the epidemic for  $R_0 = 2.5$ , assuming both age and activity structure and starting with a small fraction externally infected in mid-February. For this, we show the epidemic over time for four different levels of preventive measures put in place early in the epidemic outbreak (mid-March) and being relaxed once transmission has dropped to low levels (30 June).

In Fig. 1, the community proportion that is infectious during the course of the epidemic is plotted.

On 15 March, preventive measures (at four different levels for  $\alpha$ ) are put in place and in every case, the growth rate is reduced except when no preventative measures are applied (the blue curve;  $\alpha = 1$ ). Moreover, the preventive measures reduce the size of, and delay the time of, the peak. Sanctions are lifted on 30 June, putting transmission rates back to their original levels, but only in the curve with highest sanctions is there a clear second wave because the remaining curves have reached (close to) herd immunity. The yellow curve finishes at  $<50\%$  getting infected. The reason this exceeds the 43% infected shown in Table 1 is that preventive measures were not imposed from the start and were lifted before the epidemic was over. The corresponding cumulative fraction infected as a function of time is shown in Fig. 2. An interesting observation is that the purple curve results in a higher

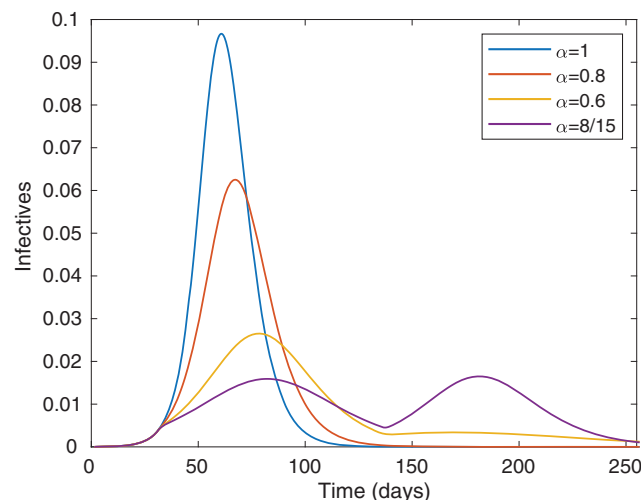


**Fig. 1. Overall fraction infected over time.** Shown is a plot of the overall fraction infected over time for the age and activity structured community with  $R_0 = 2.5$  for four different preventive levels inserted 15 March (day 30) and lifted 30 June (day 135). The blue, red, yellow, and purple curves correspond to no, light, moderate, and severe preventive measures, respectively.

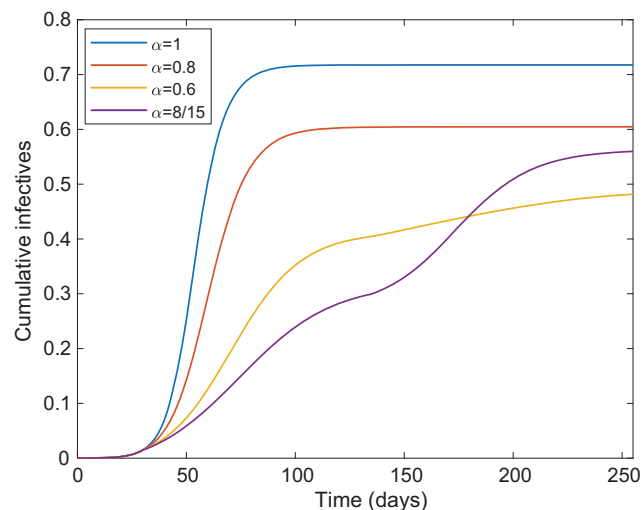


**Fig. 2. Cumulative fraction infected over time.** Shown is a plot of the cumulative fraction infected over time for the age and activity structured community and  $R_0 = 2.5$  for four different preventive levels inserted 15 March (day 30) and lifted 30 June (day 135). The blue, red, yellow, and purple curves correspond to no, light, moderate, and severe preventive measures, respectively.

overall fraction infected even though this scenario had more restrictions applied than the scenario of the yellow curve. This is because this epidemic was further from completion when sanctions were lifted.

Only the curve corresponding to greatest preventive measures shows a severe second wave when restrictions are lifted. In most cases, no (strong) second wave of outbreak occurs once preventive measures are lifted. Note also that the yellow curve, in which the overall fraction infected is well below the classical herd immunity level  $h_C = 60\%$ , is in fact protected by herd immunity because no second wave appears. See the supplementary materials for depictions of when restrictions are lifted continuously between 1 June and 31 August (figs. S1 and S2) and how the effective reproduction number evolves as a function of the time when restrictions are lifted (fig. S3).

Our simple model shows how the disease-induced herd immunity level may be substantially lower than the classical herd immunity level derived from mathematical models assuming homogeneous immunization. Our application to COVID-19 indicates a reduction of herd immunity from 60% under homogeneous immunization down to 43% (assuming  $R_0 = 2.5$ ) in a structured population, but this should be interpreted as an illustration rather than as an exact value or even a best estimate. Future efforts need to be made to quantify more precisely the size of this effect.

In our model, we have taken age cohorts and social activity levels into account. However, more complex and realistic models have many other types of heterogeneities; for instance, increased spreading within households (of different sizes) or within schools and workplaces. These activity levels and social structures are country or region specific and should be modeled as such. Further, spatial heterogeneity arises, with rural areas having lower contact rates than metropolitan regions. It seems reasonable to assume that most such additional heterogeneities will have the effect of reducing the disease-induced immunity level  $h_D$  even further. This is because in high-contact environments such as metropolitan regions, large households, and large workplaces, there will be a higher infected fraction and immunity will be concentrated even more among highly active and connected individuals. Some complex models [e.g., (1)] categorize by, for example, age and spatial location but omit individual variation within each category. The latter can be incorporated by including different activity levels or by adding a social network in which individuals have differing numbers of acquaintances. As we have illustrated, differences in social activity play a greater role in reducing the disease-induced herd immunity level than heterogeneous age-group mixing. Therefore, models excluding such features will see a smaller difference between  $h_D$  and  $h_C$ . Our choice of 50% having average activity,

25% having half activity, and 25% having double activity is of course arbitrary. An important future task is to determine the size of differences in social activity within age groups for different types of populations. The greater the social heterogeneity there is between groups, the greater the difference between  $h_D$  and  $h_C$ .

One assumption of our model is that preventive measures act proportionally on all contact rates, and this may not always hold. For example, most countries aim to protect elderly and other high-risk groups, which does not obey this assumption. Again, we expect that the effect of discriminatory protection would be to reduce the disease-induced immunity level because the oldest age group has the fewest contacts. For a model including schools and workplaces, it is not obvious what effect school closure and strong recommendations to work from home would have on the disease-induced herd immunity level. A different model extension would be to allow individuals to change their activity levels over time. The effect of such changes in activity levels, particularly whether they vary between different categories, remains unknown.

In our model, we assume that infection with and subsequent clearance of the virus leads to immunity against further infection for an extended period of time. If there is relatively quick loss of immunity, or if we want to consider a time scale in which the impact of demographic processes such as births and people changing age groups becomes substantial, then we need further models.

Different forms of immunity levels have been discussed previously in the literature, although, as far as we know, not when considering early-introduced preventions that are lifted toward the end of an epidemic outbreak. Anderson and May (10) concluded that immunity level may differ among uniformly distributed, disease-induced, and optimally located immunity [see also (11)], and vaccination policies selecting individuals to immunize in an optimal manner have been discussed in many previous studies [e.g., (12)]. A recent independent study by Gomes *et al.* (13) reported results similar to those of the present study but considers heterogeneities in terms of continuously varying susceptibilities. That model is solved numerically in a manner similar to our Fig. 1, but the analytical results for the final number of infected people and  $h_D$  are missing.

Rather than lifting all COVID-19 preventive measures simultaneously, most countries are lifting restrictions gradually. That strategy can prevent the type of overshoot illustrated by the purple curve in Fig. 2, which results in a greater fraction infected than if milder restrictions are enacted (yellow curve).

Table 1. Disease-induced herd immunity level $h_D$ and classical herd immunity level $h_C$ for different population structures. Numbers correspond to percentages.						
Population structure	$R_0 = 2.0$		$R_0 = 2.5$		$R_0 = 3.0$	
	$h_D$	$h_C$	$h_D$	$h_C$	$h_D$	$h_C$
Homogeneous	50.0	50.0	60.0	60.0	66.7	66.7
Age structure	46.0	50.0	55.8	60.0	62.5	66.7
Activity structure	37.7	50.0	46.3	60.0	52.5	66.7
Age and activity structure	34.6	50.0	43.0	60.0	49.1	66.7

Table 2. Final outcome fractions infected in different groups. These values assume that $R_0 = 2.5$ and preventive measures are put in place such that $\alpha = \alpha_c$ just barely reaching herd immunity for $R_0 = 2.5$ . Population structure includes both age and activity. Numbers correspond to percentages.			
Age group	Low activity	Average activity	High activity
0–5 years	17.6	32.1	53.9
6–12 years	25.8	44.9	69.7
13–19 years	31.4	52.9	77.8
20–39 years	27.4	47.2	72.1
40–59 years	22.8	40.3	64.4
≥60 years	14.6	27.0	46.7



## REFERENCES AND NOTES

1. S. Flaxman, S. Mishra, A. Gandy, H. J. T. Unwin, H. Coupland, T. A. Mellan, H. Zhu, T. Berah, J. W. Eaton, P. N. P. Guzman, N. Schmit, L. Cillon, K. E. C. Ainslie, M. Baguelin, I. Blake, A. Boonyasiri, O. Boyd, L. Cattarino, C. Ciavarella, L. Cooper, Z. Cucunubá, G. Cuomo-Dannenburg, A. Dighe, B. Djaafara, I. Dorigatti, S. van Elsland, R. FitzJohn, H. Fu, K. Gaythorpe, L. Geidelberg, N. Grassly, W. Green, T. Hallett, A. Hamlet, W. Hinsley, B. Jeffrey, D. Jorgensen, E. Knock, D. Laydon, G. Nedjati-Gilani, P. Nouvellet, K. Parag, I. Siveroni, H. Thompson, R. Verity, E. Volz, C. Walters, H. Wang, Y. Wang, O. Watson, P. Winskill, X. Xi, C. Whittaker, P. G. T. Walker, A. Ghani, C. A. Donnelly, S. Riley, L. C. Okell, M. A. C. Vollmer, N. M. Ferguson, S. Bhatt, Report 13: Estimating the number of infections and the impact of non-pharmaceutical interventions on COVID-19 in 11 European countries (Imperial College London, 2020); <https://doi.org/10.25561/77731>.
2. Public Health Institute of Sweden, Estimates of the peak-day and the number of infected individuals during the covid-19 outbreak in the Stockholm region, Sweden February–April 2020 [in Swedish] (2020); [www.folkhalsomyndigheten.se/contentassets/2da059f90b90458d8454a04955d1697f/skattning-peakdag-antal-infekterade-covid-19-utbrottet-stockholms-lan-februari-april-2020.pdf](http://www.folkhalsomyndigheten.se/contentassets/2da059f90b90458d8454a04955d1697f/skattning-peakdag-antal-infekterade-covid-19-utbrottet-stockholms-lan-februari-april-2020.pdf).
3. Instituto de Salud Carlos III, Second round national sero-epidemiology study of SARS-CoV-2 infection in Spain [in Spanish] (2020); [https://www.mscbs.gob.es/ciudadanos/ene-covid/docs/ESTUDIO\\_ENE-COVID19\\_SEGUNDA RONDA\\_INFORME\\_PRELIMINAR.pdf](https://www.mscbs.gob.es/ciudadanos/ene-covid/docs/ESTUDIO_ENE-COVID19_SEGUNDA RONDA_INFORME_PRELIMINAR.pdf).
4. N. M. Ferguson, D. Laydon, G. Nedjati-Gilani, N. Imai, K. Ainslie, M. Baguelin, S. Bhatia, A. Boonyasiri, Z. Cucunubá, G. Cuomo-Dannenburg, A. Dighe, I. Dorigatti, H. Fu, K. Gaythorpe, W. Green, A. Hamlet, W. Hinsley, L. C. Okell, S. van Elsland, H. Thompson, R. Verity, E. Volz, H. Wang, Y. Wang, P. G. T. Walker, C. Walters, P. Winskill, C. Whittaker, C. A. Donnelly, S. Riley, A. C. Ghani, Report 9: Impact of non-pharmaceutical interventions (NPIs) to reduce COVID-19 mortality and healthcare demand (Imperial College London, 2020); <https://doi.org/10.25561/77482>.
5. W. Bock, B. Adamik, M. Bawiec, V. Bezborodov, M. Bodych, J. P. Burgard, T. Goetz, T. Krueger, A. Migalska, B. Pabjan, T. Ozanski, E. Rafajłowicz, W. Rafajłowicz, E. Skubalska-Rafajłowicz, S. Ryfczynska, E. Szczurek, P. Szymanski, Mitigation and herd immunity strategy for COVID-19 is likely to fail. *medRxiv* 2020.03.25.20043109 [Preprint]. 5 May 2020; <https://doi.org/10.1101/2020.03.25.20043109>.
6. H. Salje, C. T. Kiem, N. Lefrancq, N. Courtejoie, P. Bosetti, J. Paireau, A. Andronico, N. Hozé, J. Richet, C.-L. Dubost, Y. Le Strat, J. Lessler, D. Levy-Bruhl, A. Fontanet, L. Opatowski, P.-Y. Boelle, S. Cauchemez, Estimating the burden of SARS-CoV-2 in France. *Science* 10.1126/science.abc3517 (2020).
7. O. Diekmann, H. Heesterbeek, T. Britton, *Mathematical Tools for Understanding Infectious Disease Dynamics* (Princeton Univ. Press, 2013).
8. J. Wallinga, P. Teunis, M. Kretzschmar, *Am. J. Epidemiol.* **164**, 936–944 (2006).
9. R. Pastor-Satorras, A. Vespignani, *Phys. Rev. Lett.* **86**, 3200–3203 (2001).
10. R. M. Anderson, R. M. May, *Infectious Diseases of Humans: Dynamics and Control* (Oxford Univ. Press, 1991).
11. M. J. Ferrari, S. Bansal, L. A. Meyers, O. N. Bjørnstad, *Proc. Biol. Sci.* **273**, 2743–2748 (2006).
12. F. Ball, T. Britton, O. Lyne, *Math. Biosci.* **191**, 19–40 (2004).
13. M. G. M. Gomes, R. M. Corder, J. G. King, K. E. Langwig, C. Souto-Maior, J. Carneiro, G. Goncalves, C. Penha-Goncalves, M. U. Ferreira, R. Aguas, Individual variation in susceptibility or exposure to SARS-CoV-2 lowers the herd immunity threshold. *medRxiv* 10.1101/2020.04.27.20081893 [Preprint]. 21 May 2020; <https://doi.org/10.1101/2020.04.27.20081893>.
14. F. Ball, T. Britton, P. Trapman, Code for: Population heterogeneity and consequences for herd immunity to SARS-CoV-2, Version 1, Zenodo (2020); <https://doi.org/10.1101/10.5281/zenodo.3899252>.

## ACKNOWLEDGMENTS

**Funding:** T.B. and P.T. acknowledge financial support from the Swedish Research Council (grant no. 2015-05015 to T.B. and grant no. 2016-04566 to P.T.). **Author contributions:** T.B. initiated and led the project. F.B. performed numerical computations and simulations. All authors developed the methodology and wrote and revised the manuscript.

**Competing interests:** The authors declare no competing interests. **Data and materials availability:** No data were used and all code for numerics and figure production, including a description of the different programs, is accessible through Zenodo (14). This work is licensed under a Creative Commons Attribution 4.0 International (CC BY 4.0) license, which permits unrestricted use, distribution, and reproduction in any medium, provided the original work is properly cited. To view a copy of this license, visit <https://creativecommons.org/licenses/by/4.0/>. This license does not apply to figures/photos/artwork or other content included in the article that is credited to a third party; obtain authorization from the rights holder before using such material

## SUPPLEMENTARY MATERIAL

[science.sciencemag.org/content/369/6505/846/suppl/DC1](https://science.sciencemag.org/content/369/6505/846/suppl/DC1)

Materials and Methods

Figs. S1 to S3

Table S1

References (15, 16)

MDAR Reproducibility Checklist

7 May 2020; accepted 18 June 2020

Published online 23 June 2020

10.1126/science.abc6810

## ELECTROCHEMISTRY

## A molecular mediator for reductive concerted proton-electron transfers via electrocatalysis

Matthew J. Chalkley<sup>\*†</sup>, Pablo Garrido-Barros<sup>\*</sup>, Jonas C. Peters<sup>‡</sup>

Electrocatalytic approaches to the activation of unsaturated substrates via reductive concerted proton-electron transfer (CPET) must overcome competing, often kinetically dominant hydrogen evolution. We introduce the design of a molecular mediator for electrochemically triggered reductive CPET through the synthetic integration of a Brønsted acid and a redox mediator. Cathodic reduction at the cobaltocenium redox mediator substantially weakens the homolytic nitrogen-hydrogen bond strength of a Brønsted acidic anilinium tethered to one of the cyclopentadienyl rings. The electrochemically generated molecular mediator is demonstrated to transform a model substrate, acetophenone, to its corresponding neutral  $\alpha$ -radical via a rate-determining CPET.

There has been a recent surge of interest in applying electrochemistry as a tool for synthetic organic chemistry (1), with the ultimate aim of harnessing renewably sourced electricity for the more sustainable synthesis of value-added organic products (2). Redox mediators, which enable indirect electrochemical transformations of organic substrates, may improve selectivity and prevent electrode passivation by avoiding the formation of reactive intermediates (e.g., radical anions or cations) directly at the electrode surface (3). Although electrochemical transformations that involve initial electron transfer (ET) and subsequent proton transfer (PT) are highly useful (e.g., electrochemical Birch reductions or electrochemical adiponitrile synthesis) (4, 5), the applied bias needed is substantially higher than that which would be required were the initial step a concerted proton-electron transfer (CPET). Illustrating this point is the fact that oxidative approaches to electrocatalytic CPET (eCPET) strategies based on nitroxyl radicals notably lower onset potentials compared with ET-PT approaches (6, 7).

Reductive (electro)catalytic CPET of an unsaturated substrate requires the formation of an X-H bond (where X is CR<sub>2</sub>, NR, or O) that is homolytically weak because of the concomitantly formed  $\alpha$ -radical [BDFE<sub>X-H</sub> = 20 to 40 kcal mol<sup>-1</sup> (BDFE, bond dissociation free energy); Fig. 1A]. An additional challenge is that the competing hydrogen evolution reaction (HER) is thermodynamically favorable ( $\Delta G_{\text{HER}} = -20$  to  $-60$  kcal mol<sup>-1</sup>, where  $\Delta G$  is Gibbs free energy). Thus, to be competent for CPET, the mediator must facilitate the rapid

colocalization of a proton and an electron that are sufficiently reactive to form the target X-H bond while kinetically suppressing the formation of H<sub>2</sub>. If this could be achieved, a CPET mediator would provide electrochemical means to access valuable, neutral radical intermediates. Such intermediates are synthetically versatile in the context of chemical and photochemical methodologies for reductive CPET transformations (8–10). Against this backdrop, we report a molecular mediator that is capable of facilitating reductive eCPET.

CPET donors that are sufficiently reactive to reduce unsaturated substrates can be generated through the coordination-induced weakening of an O-H bond—for example, by pairing SmI<sub>2</sub> with a polar protic solvent (Fig. 1B) (11). Relatedly, the formation of a homolytically weak and hence reactive Fe-H bond has been invoked to explain the CPET reactivity observed upon combining silanes (Si-H) with an iron alkoxide (Fe-OR) (12). An attractive photochemical approach to triggering a CPET step in challenging reductions has also been demonstrated by pairing an acid with a strong photoreductant (Fig. 1C) (13). Although these strategies are synthetically useful, each of them relies on the inclusion of a stoichiometric reductant (Sm<sup>II</sup>, a silane, and an amine, respectively); their adaptation to eCPET, in which the cathode is the ultimate source of reducing equivalents, has not proven straightforward. Thus, we set out to develop a method of forming strong CPET donors suited to electrochemical activation. Herein, we demonstrate that the synthetic integration of a Brønsted acid and a redox mediator facilitates reduction-induced bond weakening to enable controlled, reductive eCPET at a cathode in the presence of excess acid. Synthetic integration of the Brønsted acid, dimethylanilinium, and the redox mediator, cobaltocenium, proved key both to attenuating HER and to

facilitating CPET to a model acetophenone substrate.

Before pursuing synthetic integration of reductant and acid toward a CPET mediator, we explored the efficacy of pairing Cp<sub>2</sub>Co<sup>+0</sup> with an anilinium acid independently. Related approaches have proven effective in net oxidative eCPET reactions by pairing ferrocenium/ferrocene (Fc<sup>+0</sup>) as a one-electron oxidant and an alkoxide (e.g., MeO<sup>-</sup>) as a proton acceptor (14). Furthermore, we have recently established that a strong CPET donor can be generated in situ through the protonation of a Cp (or Cp<sup>\*</sup>) ligand of cobaltocenes (15, 16), and studies by our laboratory and others have suggested that cobaltocenes can act as redox mediators in the electrocatalytic reductive protonation of small molecules such as N<sub>2</sub> or CO<sub>2</sub> (17, 18). Nonetheless, with parent cobaltocenes, protonation at carbon is needed to generate the CPET reagent, a step that should be slow because of the substantial reorganization required (sp<sup>2</sup> to sp<sup>3</sup>) (19). Also, this protonation step transforms the Cp (or Cp<sup>\*</sup>) ligand, a  $\sigma$ - and  $\pi$ -donor, into a  $\pi$ -accepting diene ligand. This, in turn, anodically shifts the reduction potential ( $E^\circ$ ) (16, 20), thereby leading to rapid ET and, ultimately, facile and undesired HER.

To underscore these points, cyclic voltammograms (CVs) at 10 mV s<sup>-1</sup> of cobaltocenium ([Cp<sub>2</sub>Co]<sup>+</sup>) in the presence of 100 mM 4-cyanoanilinium ([<sup>4-CN</sup>PhNH<sub>3</sub>]<sup>+</sup>), in a 200 mM tetrabutylammonium hexafluorophosphate ([TBA][PF<sub>6</sub>]) solution of dimethoxyethane (DME), feature an irreversible wave consistent with electrocatalytic HER (see supplementary materials, section 8, for detailed discussion). An increase in current intensity upon increasing the [Cp<sub>2</sub>Co]<sup>+</sup> concentration, while maintaining constant acid concentration, demonstrates that the HER mechanism is first order in [Cp<sub>2</sub>Co]<sup>+</sup> (fig. S24). Alternatively, holding the [Cp<sub>2</sub>Co]<sup>+</sup> concentration constant and increasing that of the [<sup>4-CN</sup>PhNH<sub>3</sub>]<sup>+</sup> shows that HER is also first order in [<sup>4-CN</sup>PhNH<sub>3</sub>]<sup>+</sup> (fig. S25). CVs acquired at 100 mV s<sup>-1</sup> show partial reversibility at the Co<sup>III/II</sup> couple ( $-1.33$  V versus Fc<sup>+0</sup>), which suggests a buildup of Cp<sub>2</sub>Co during the electrocatalysis (fig. S22). These data are consistent with a rate-determining protonation of Cp<sub>2</sub>Co, which suggests that the ring-protonated species, [(Cp)Co( $\eta^4$ -C<sub>5</sub>H<sub>6</sub>)]<sup>+</sup>—which would be a strong CPET donor [BDFE<sub>C-H</sub> of 33.8 kcal mol<sup>-1</sup>; calculated by density functional theory (DFT); see supplementary materials]—is present only in low concentration. Thus, we anticipate that HER does not involve bimolecular combination of [(Cp)Co( $\eta^4$ -C<sub>5</sub>H<sub>6</sub>)]<sup>+</sup>, but likely proceeds through rapid reduction [ $\Delta G(\text{ET}) = -23$  kcal mol<sup>-1</sup>] to form (Cp)Co( $\eta^4$ -C<sub>5</sub>H<sub>6</sub>) and subsequent protonation to release H<sub>2</sub> and [Cp<sub>2</sub>Co]<sup>+</sup> (Fig. 2A). As [(Cp)Co( $\eta^4$ -C<sub>5</sub>H<sub>6</sub>)]<sup>+</sup> is both slow to form and rapid

Division of Chemistry and Chemical Engineering, California Institute of Technology, Pasadena, CA, USA.

<sup>\*</sup>These authors contributed equally to this work.

<sup>†</sup>Present address: Department of Pharmaceutical Chemistry, University of California, San Francisco, CA, USA.

<sup>‡</sup>Corresponding author. Email: jpeters@caltech.edu

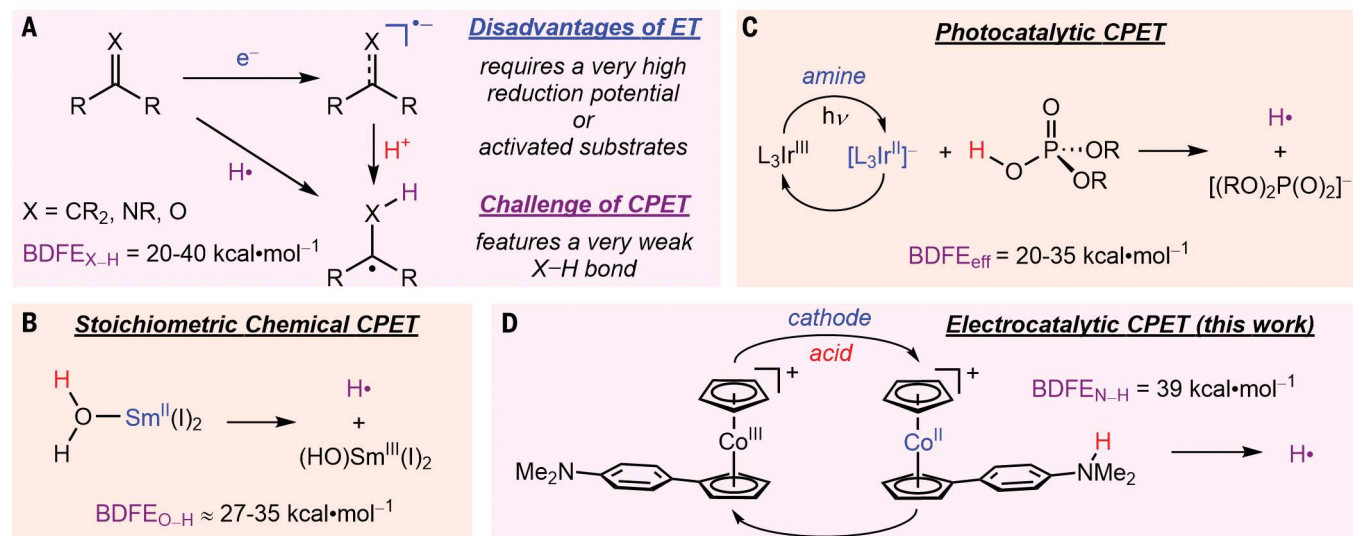


**Fig. 1. Strategies for reductive CPET reactions.** (A) Stepwise (ET-PT) and concerted (CPET) routes to the formation of a neutral  $\alpha$ -radical intermediate, featuring a homolytically weak X–H bond, from an unsaturated substrate (e.g., alkene, imine, or ketone). (B) Coordination-induced weakening of an O–H bond by SmII, activating H<sub>2</sub>O for reductive CPET transformations of unsaturated substrates (11). (C) Photocatalytic reductive

CPET via the pairing of an acid with a potent photoreductant (e.g., L = phenylpyridine) generated from a sacrificial amine reductant and light. eff. effective; hv, photons. (D) The approach introduced in this work, in which a redox mediator (cobaltocenium/cobaltocene) is synthetically integrated with a Brønsted acid/base (anilinium/aniline), so as to promote CPET to a substrate and disfavor H<sub>2</sub> evolution.

to consume, it is likely unsuitable as a CPET mediator under electrocatalytic conditions (vide infra).

Appending an aniline-derived Brønsted base to cobaltocenium can serve to accelerate the rate of protonation (due to minimal reorganization at nitrogen) and to insulate the Co<sup>III/II</sup> redox couple, as the immediate coordination sphere at cobalt remains unchanged. To accomplish this, we followed the synthetic protocol outlined in Fig. 2B. The target, aniline-modified cobaltocene, (Cp)Co(Cp<sup>N</sup>) (where Cp<sup>N</sup> is 4-*N,N*-dimethylanilincyclopentadienyl), can be isolated in pure form, as can its oxidized Co<sup>III</sup> salt, [(Cp)Co(Cp<sup>N</sup>)]<sup>+</sup>[OTf]<sup>–</sup>. The latter can be readily protonated to provide [(Cp)Co(Cp<sup>NH</sup>)]<sup>+</sup>[OTf]<sub>2</sub><sup>–</sup> (where Cp<sup>NH</sup> is 4-*N,N*-dimethylaniliniumcyclopentadienyl). The highly reactive CPET donor, [(Cp)Co(Cp<sup>NH</sup>)]<sup>+</sup>, can be generated in situ through either the low-temperature reduction of [(Cp)Co(Cp<sup>NH</sup>)]<sup>+</sup>[OTf]<sub>2</sub> or the low-temperature protonation of (Cp)Co(Cp<sup>N</sup>), as evidenced by optical spectroscopy and freeze-quench electron paramagnetic resonance spectroscopy (figs. S12 and S15). It can also be generated electrochemically (vide infra). The data are consistent with the conclusion that the Cp<sub>2</sub>Co core is maintained throughout, with the proton residing on the appended aniline (Fig. 2B).

The N–H BDFE of the CPET donor [(Cp)Co(Cp<sup>NH</sup>)]<sup>+</sup> is of central interest. To assess BDFEs, it is typical to measure the thermochemistry of the stepwise ET-PT or PT-ET pathways in a solvent (Eq. 1). Although DME is well suited

to the study of reductive protonations, it lacks a well-defined p*K*<sub>a</sub> scale (where *K*<sub>a</sub> is the acid dissociation constant) and *C*<sub>G</sub> value, a solvent-dependent thermodynamic constant to account for the energy required to form H• from H<sup>+</sup> and e<sup>–</sup>, both of which are required to assess Eq. 1. Thus, as is common in non-aqueous thermochemistry, we performed our thermochemical measurements in acetonitrile [*C*<sub>G</sub> in acetonitrile (MeCN) is 54.9 kcal mol<sup>–1</sup>]. The relevant BDFE values are likely similar to those in DME, as BDFEs typically vary little with solvent (21). The CV of [(Cp)Co(Cp<sup>N</sup>)]<sup>+</sup> in MeCN reveals both a reversible reduction at –1.35 V versus Fc<sup>+/0</sup> and a reversible oxidation at 0.52 V versus Fc<sup>+/0</sup>. The former is assigned to the Co<sup>III/II</sup> couple on the basis of its similarity to that of parent cobaltocenium, and the latter is assigned to an N-centered oxidation on the basis of its similarity to the oxidation of parent *N,N*-dimethylaniline (0.38 V versus Fc<sup>+/0</sup>) (22). An oxidation event for the aniline-protonated [(Cp)Co(Cp<sup>NH</sup>)]<sup>2+</sup> species is not observed; a reversible reduction (Co<sup>III/II</sup>) is observed at –1.21 V versus Fc<sup>+/0</sup>. The p*K*<sub>a</sub> of [(Cp)Co(Cp<sup>NH</sup>)]<sup>2+</sup> was assessed through equilibration experiments with aniline bases of known p*K*<sub>a</sub>'s probed by means of <sup>1</sup>H nuclear magnetic resonance (NMR) spectroscopy in MeCN-*d*<sub>3</sub>. The resultant p*K*<sub>a</sub> of 8.62 ± 0.02 can be compared with 11.4 for parent *N,N*-dimethylanilinium (23). This establishes that the [Cp<sub>2</sub>Co]<sup>+</sup> serves as an electron-withdrawing substituent on the aniline ring.

$$\text{BDFE} = 1.37 \times \text{p}K_a + 23.06 \times E^\circ + C_G \quad (1)$$

With these data and Eq. 1, the BDFE<sub>N–H</sub> of [(Cp)Co(Cp<sup>NH</sup>)]<sup>2+</sup> is predicted to be 79 kcal mol<sup>–1</sup>. This value agrees very well with the BDFE<sub>N–H</sub> of *N,N*-dimethylanilinium (79 kcal mol<sup>–1</sup>). However, reduction of Co<sup>III</sup> to the Co<sup>II</sup> state substantially lowers the strength of the remote N–H bond by 40 kcal mol<sup>–1</sup>. This reduction-induced bond weakening contrasts with previously studied examples, where a one-electron change in oxidation state lowered an X–H BDFE by ~10 to 15 kcal mol<sup>–1</sup> (24, 25). In these previous examples, the X–H bond was strongly electronically coupled to the redox site. By contrast, the remote redox effect that we observe with [(Cp)Co(Cp<sup>NH</sup>)]<sup>2+/+</sup> is in line with the effective BDFE postulate, which holds that Eq. 1 predicts the strength of a hypothetical H• donor formed by a separated acid and reductant. The effective BDFE predicted for the pairing of the two parent subunits, *N,N*-dimethylanilinium and Cp<sub>2</sub>Co, is 40 kcal mol<sup>–1</sup>, which is in good agreement with the experimentally determined BDFE<sub>N–H</sub> for our synthetically integrated system (39 kcal mol<sup>–1</sup>; Fig. 2C). Nevertheless, the thermodynamic equivalence between the independent reagent pair and the synthetically integrated construct does not imply kinetic equivalence. We next show that synthetic integration of the acid and reductant into a single molecule shifts the behavior of the system from undesired HER toward productive eCPET reactivity with substrate.



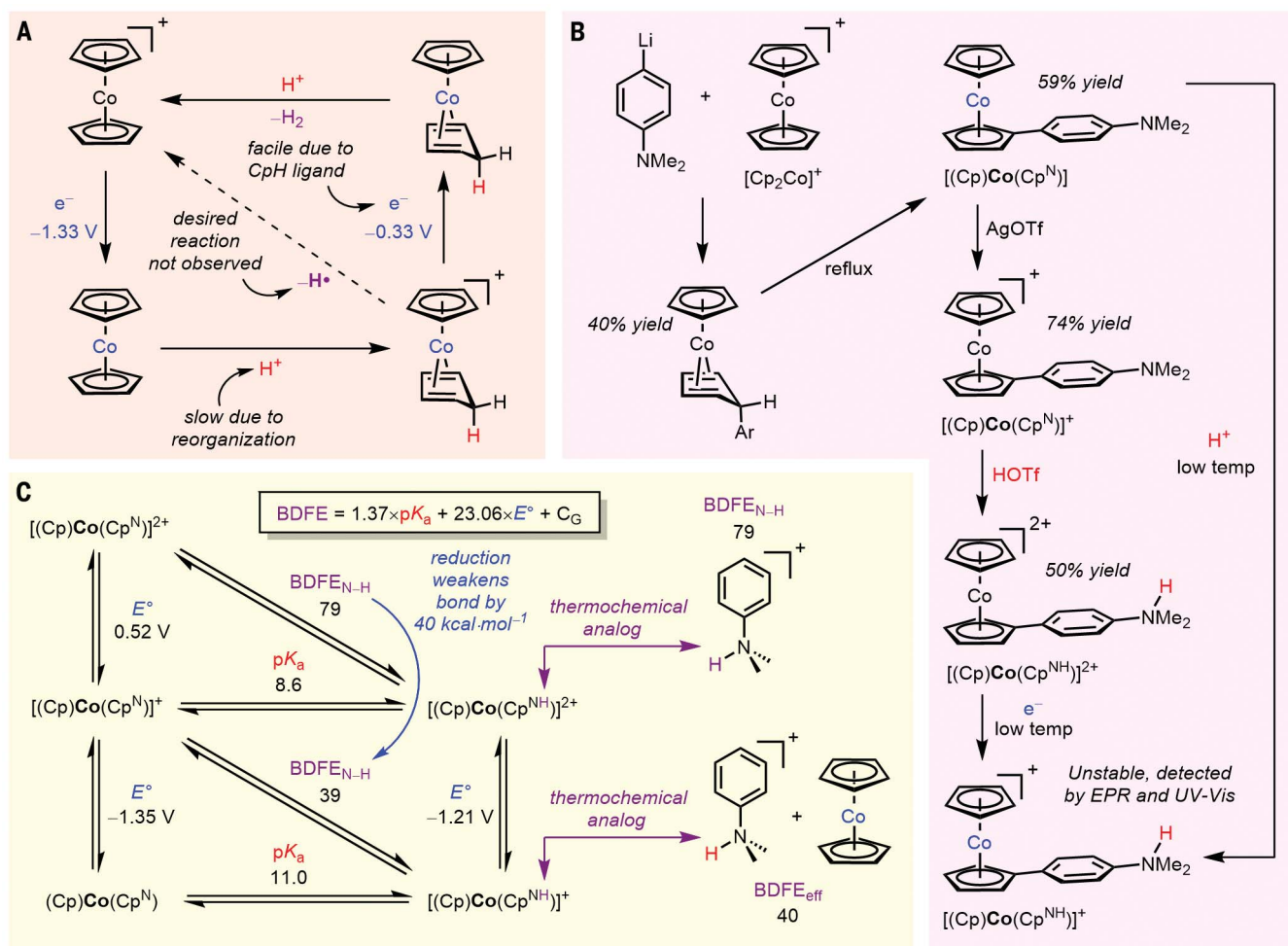


**Fig. 2. Mechanism, synthesis, and thermochemistry of relevance to cobaltocene-mediated CPET.** (A) The electrocatalytic HER pathway for  $[\text{Cp}_2\text{Co}]^+$  annotated with the challenges it presents for its utility in reductive eCPET. (B) Synthetic pathway for appending a Brønsted acidic anilinium unit onto the redox mediator, cobaltocenium, to generate the molecular CPET mediator [Ar = 4-(N,N-dimethylamino)phenyl]. EPR, electron paramagnetic

resonance; UV-Vis, ultraviolet-visible spectrophotometry. (C) Thermochemical properties ( $\text{pK}_a$ ,  $E^\circ$  versus  $\text{Fc}^{+/0}$ ) relevant to the determination of the homolytic N-H bond strengths for  $[(\text{Cp})\text{Co}(\text{Cp}^{\text{NH}})]^{2+}/^+$  (BDFE in kilocalories per mole) highlighting the unusual redox-induced bond weakening and thermochemical analogs. Both BDFE values and the  $\text{pK}_a$  of  $[(\text{Cp})\text{Co}(\text{Cp}^{\text{NH}})]^+$  were assessed with Eq. 1; all other values were measured.

CVs of 1 mM  $[(\text{Cp})\text{Co}(\text{Cp}^N)]^+$  in a 200 mM  $[\text{TBA}][\text{PF}_6]$  DME solution of excess acid (100 mM  $[\text{4-CNPhNH}_3]^+$ ) feature a wave at  $-1.21\text{ V}$  versus  $\text{Fc}^{+/0}$ ; this wave is reversible even at  $10\text{ mV s}^{-1}$ . This observation is consistent with protonation to form  $[(\text{Cp})\text{Co}(\text{Cp}^{\text{NH}})]^{2+}$  ( $\text{pK}_a = 8.6$ ) by  $[\text{4-CNPhNH}_3]^+$  ( $\text{pK}_a = 7.0$ ) and then reduction to  $[(\text{Cp})\text{Co}(\text{Cp}^{\text{NH}})]^+$ , and it is not consistent with catalytic HER. Although the thermodynamic driving force for HER remains substantial and essentially the same as in our aforementioned studies of  $\text{Cp}_2\text{Co}$  and  $[\text{4-CNPhNH}_2][\text{OTf}]$ , the rate of  $\text{H}_2$  release is markedly attenuated. This observation is despite the fact that a previously slow and rate-determining protonation step has now been made facile. We suggest that this is because further ET (and PT) steps are unfavorable, so the only feasible route to HER is a bimolecular coupling reaction between

two positively charged  $[(\text{Cp})\text{Co}(\text{Cp}^{\text{NH}})]^+$  species (fig. S19). Thus, with an appropriate unsaturated organic substrate, it should be possible to productively intercept the proton and electron equivalent that is stored on  $[(\text{Cp})\text{Co}(\text{Cp}^{\text{NH}})]^+$ .

To explore the feasibility of  $[(\text{Cp})\text{Co}(\text{Cp}^{\text{NH}})]^+$  as a CPET mediator, we chose acetophenone as a model substrate. DFT calculations predict a thermodynamic preference for it to react with  $[(\text{Cp})\text{Co}(\text{Cp}^{\text{NH}})]^+$  via CPET [ $\Delta G(\text{CPET})_{\text{calc}} = +0\text{ kcal mol}^{-1}$ ] instead of via initial PT [ $\Delta G(\text{PT})_{\text{calc}} = +19\text{ kcal mol}^{-1}$ ] or ET [ $\Delta G(\text{ET})_{\text{calc}} = +26\text{ kcal mol}^{-1}$ ; Fig. 3A]. In accord with this prediction, CVs at  $100\text{ mV s}^{-1}$  after the addition of 12 mM acetophenone to an electrochemical cell containing 1 mM  $[(\text{Cp})\text{Co}(\text{Cp}^N)]^+$  and 100 mM  $[\text{4-CNPhNH}_3]^+$  demonstrate an electrocatalytic wave at  $-1.21\text{ V}$  versus  $\text{Fc}^{+/0}$ . In the absence of

$[(\text{Cp})\text{Co}(\text{Cp}^N)]^+$ , there is only minimal current at this potential. Therefore, even though  $[(\text{Cp})\text{Co}(\text{Cp}^{\text{NH}})]^+$  is a weaker acid than the  $[\text{4-CNPhNH}_3]^+$ , colocalization of the proton and electron appears to substantially enhance the reaction rate.

To confirm that the observed wave corresponds to an eCPET reaction between  $[(\text{Cp})\text{Co}(\text{Cp}^{\text{NH}})]^+$  and acetophenone, we performed additional cyclic voltammetry experiments. These experiments were analyzed within the kinetic framework developed by Savéant and co-workers to extract information about the catalytic process [see (26) and supplementary materials, section 8, for additional details]. In brief, given a first order dependence of the rate-limiting chemical step on a species, the catalytic current should increase linearly with respect to a linear increase in catalyst

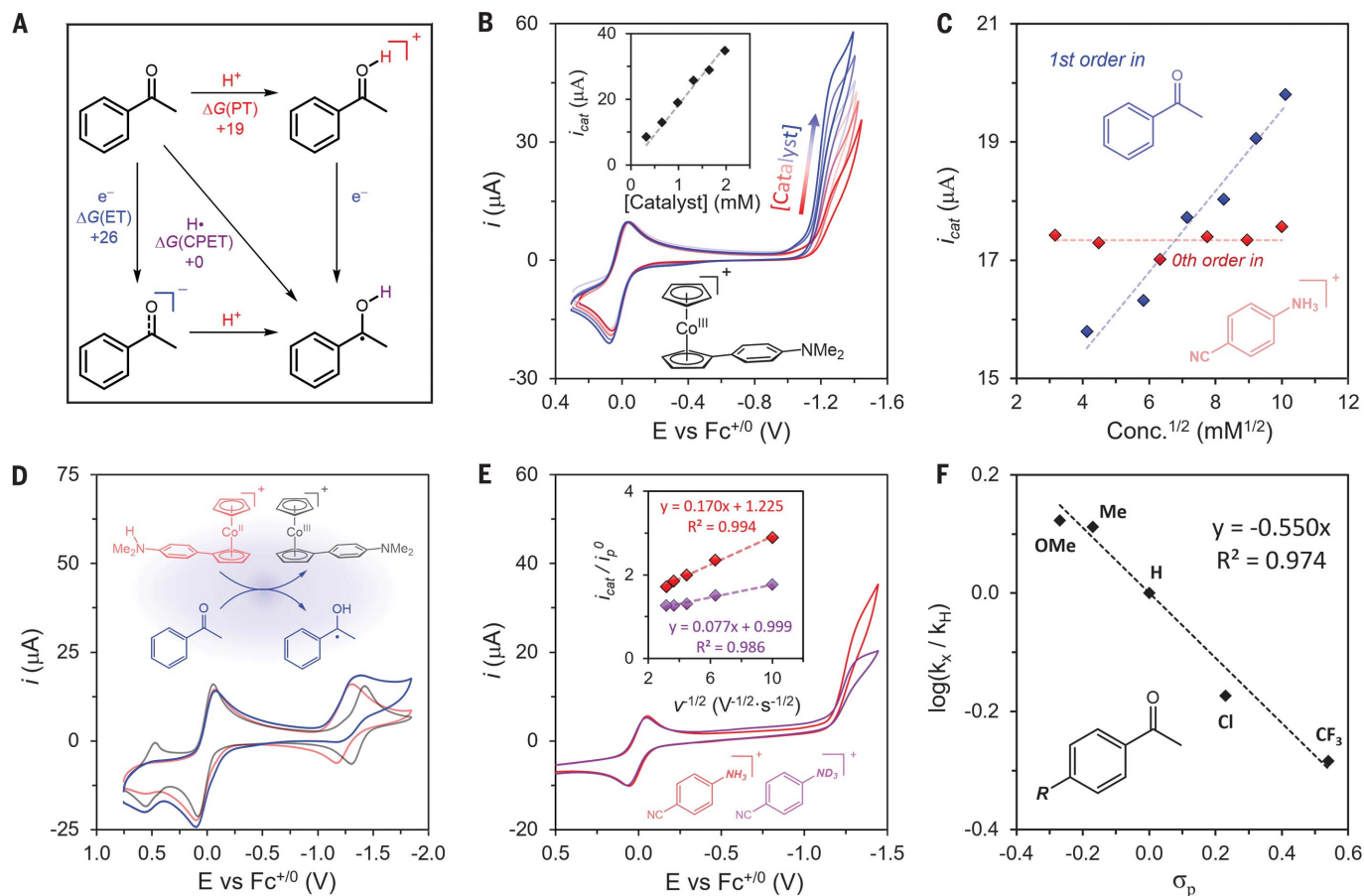


**Fig. 3. Mechanistic details of electrocatalytic reductive CPET.** (A) DFT calculated  $\Delta G$  (in kilocalories per mole) for initial ET, PT, and CPET from  $[(\text{Cp})\text{Co}(\text{Cp}^{\text{NH}})]^+$  to acetophenone. (B) CVs showing the increase in current with increasing concentration of  $[(\text{Cp})\text{Co}(\text{Cp}^{\text{N}})]^+$ , with an inset demonstrating the first order dependence of CPET on Co concentration. (C) Plot of the catalytic current ( $i_{\text{cat}}$ ) for CPET with respect to the square root of the concentration (Conc.) of acetophenone (blue) and  $[\text{4-CNPhNH}_3]^+$  (red) showing a first order and zeroth order dependence, respectively (eqs. S5 to

S7). (D) Demonstration of the redox couple of  $[(\text{Cp})\text{Co}(\text{Cp}^{\text{NH}})]^{2+/+}$  (red) and  $[(\text{Cp})\text{Co}(\text{Cp}^{\text{N}})]^{+/0}$  (gray), and a CV of  $[(\text{Cp})\text{Co}(\text{Cp}^{\text{NH}})]^{2+}$  in the presence of acetophenone (blue). (E) Comparison of CVs taken at 10 mV s<sup>-1</sup> with  $[\text{4-CNPhNH}_3]^+$  (red) and  $[\text{4-CNPhND}_3]^+$  (purple). The inset shows the plot used to determine the corresponding rates for evaluation of the KIE, where  $i_p^0$  is the current intensity of the one electron reduction for  $[(\text{Cp})\text{Co}(\text{Cp}^{\text{N}})]^{+/0}$  and  $v$  is the scan rate.  $R^2$ , coefficient of determination. (F) Hammett plot for the CPET reaction with 4-substituted acetophenones against the  $\sigma_p$  parameter.

concentration and a square root increase in the substrate concentration (i.e.,  $[\text{acetophenone}]^{1/2}$ ). Thus, by systematically varying the concentration of the reaction components, we can use the changes observed in the catalytic current to determine that the CPET reaction is first order in cobalt, first order in acetophenone, and zeroth order in acid (Fig. 3, B and C). To determine whether the acetophenone reacts with  $[(\text{Cp})\text{Co}(\text{Cp}^{\text{NH}})]^{2+/+}$  rather than  $[(\text{Cp})\text{Co}(\text{Cp}^{\text{N}})]^{+/0}$ , we studied the influence of acetophenone on the electrochemical behavior in the absence of acid (figs. S36 to S39). CVs of  $[(\text{Cp})\text{Co}(\text{Cp}^{\text{N}})]^+$  were unperturbed, whereas those of  $[(\text{Cp})\text{Co}(\text{Cp}^{\text{NH}})]^{2+}$  became irreversible with an additional reduction event observed at the  $[(\text{Cp})\text{Co}(\text{Cp}^{\text{N}})]^{+/0}$  redox couple. These data establish the consumption of  $[(\text{Cp})\text{Co}(\text{Cp}^{\text{NH}})]^+$  by a net proton and electron transfer to acetophenone, followed

by the reduction of the resulting  $[(\text{Cp})\text{Co}(\text{Cp}^{\text{N}})]^+$  product (Fig. 3D).

To establish the concerted nature of the proton-electron transfer in the rate-determining step, the kinetic isotope effect (KIE) of the catalysis was determined by comparing the catalytic current at different scan rates in experiments using either  $[\text{4-CNPhNH}_3]^+$  or  $[\text{4-CNPhND}_3]^+$  (Fig. 3E). The observed KIE of  $4.9 \pm 0.7$  is larger than that observed for both chemical and photochemical CPET reactions with ketones:  $\text{SmI}_2$  and  $\text{H}_2\text{O}$  have a KIE of  $\sim 2$  (27), and  $\text{Ir}(\text{phenylpyridine})_3$  and  $(\text{PhO})_2\text{P}(\text{O})\text{OH}$  have KIEs between 1.2 and 3 (13). Thus, the collective data are fully consistent with a rate-determining reductive CPET from  $[(\text{Cp})\text{Co}(\text{Cp}^{\text{NH}})]^+$  to acetophenone to form its neutral  $\alpha$ -radical.

The kinetics of eCPET for a series of para-substituted acetophenones  $[\text{4-RPhC(O)Me}]$ , where

R is  $\text{CF}_3$ , Cl, H, Me, or OMe) was also studied. A Hammett plot against  $\sigma_p$  (28) reveals a linear relationship with a modest negative slope ( $\rho = -0.50 \pm 0.04$ ; Fig. 3F). This observation suggests a slight buildup of positive charge on the acetophenone unit in the transition state (TS) and may be consistent with an asynchronous CPET reaction in which the TS involves slightly more proton-transfer than electron-transfer character (29, 30). Although these observations warrant further study, the relative rate of reactivity with 2-pentanone—which has a similar basicity to acetophenone ( $\Delta pK_a^{\text{calc}} = -0.6$ ) but forms an  $\alpha$ -radical with a homolytically much weaker O–H bond ( $\text{BDFE}_{\text{calc}} = 28 \text{ kcal mol}^{-1}$ ) than that formed by acetophenone—clearly illustrates the overall CPET nature of the transformation. Indeed, 2-pentanone reacts an order of magnitude more slowly than acetophenone ( $0.31 \pm 0.09 \text{ s}^{-1}$  versus  $4.6 \pm$

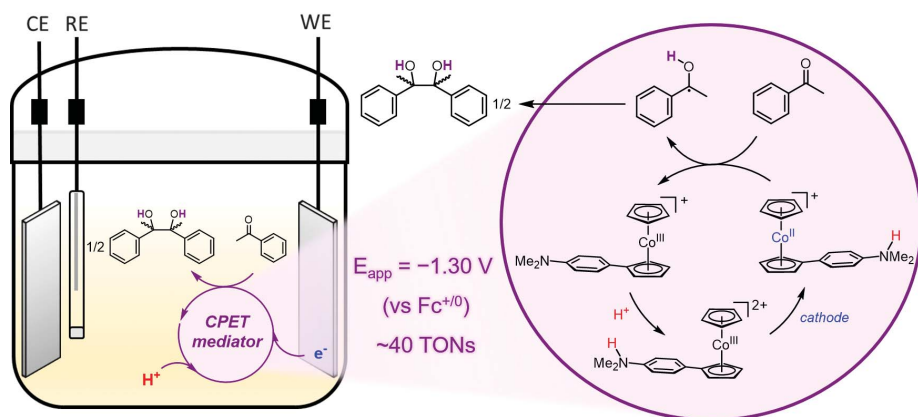


**Fig. 4. Overall reaction.** (Left) Schematic of an electrochemical setup for the reduction of acetophenone via eCPET. CE, counter electrode; RE, reference electrode; WE, working electrode. (Right) Atomistic mechanism for eCPET of acetophenone mediated by  $[(\text{Cp})\text{Co}(\text{Cp}^{\text{N}})]^+$ .  $E_{\text{app}}$ , applied potential.

$0.4 \text{ s}^{-1}$ , respectively). However, this result does suggest that thermally uphill CPET reactions [ $\Delta G(\text{CPET})_{\text{calc}} = +10 \text{ kcal mol}^{-1}$  for 2-pentanone] can proceed, in this case, likely driven by a subsequent irreversible step such as coupling of the  $\alpha$ -radical intermediates (vide infra).

Evidence for the generation of the neutral  $\alpha$ -radical intermediate is provided by controlled potential coulometry (CPC) experiments and subsequent product analysis. CPC at  $-1.30 \text{ V}$  versus  $\text{Fc}^{+/0}$  of  $1 \text{ mM } [(\text{Cp})\text{Co}(\text{Cp}^{\text{N}})][\text{OTf}]$ ,  $50 \text{ mM}$  acetophenone,  $100 \text{ mM}$  tosylic acid, and  $200 \text{ mM}$   $[\text{TBA}][\text{PF}_6]$  in DME with a glassy carbon counter electrode, a  $\text{Ag}/\text{AgOTf}$  ( $5 \text{ mM}$ ) reference electrode, and a boron doped diamond (BDD) working electrode afforded the pinacol-coupling product 2,3-diphenyl-2,3-butanediol in 83% yield with 11% recovery of remaining acetophenone. We presume that the 2,3-diphenyl-2,3-butanediol forms through the coupling of two neutral  $\alpha$ -radicals in a fast step that follows the rate-determining CPET reaction (Fig. 4). Related radical pinacol couplings have previously been observed to occur at essentially diffusion-controlled rates (31). A turnover number (TON) of  $\sim 40$  confirms the electrocatalytic nature of the CPET reaction and compares favorably to TONs demonstrated for oxidative eCPET reactions, which are typically between 5 and 10 (7, 32). The overall Faradaic efficiency (FE) for eCPET is 39%. Most of the remaining current is accounted for in the formation of  $\text{H}_2$  (FE = 45%) as a side product; the HER reaction likely begins to dominate at low ketone concentrations. The molecular CPET mediator appears to be stable during the CPC experiment; differential pulse voltammograms at the end of the experiment reveal the expected peaks for  $[(\text{Cp})\text{Co}(\text{Cp}^{\text{N}})]^+$  at 0.52 and  $-1.35 \text{ V}$ , and x-ray photoelectron spectroscopy does not indicate the deposition of Co on the BDD electrode (fig. S76).

Consistent with our cyclic voltammetry experiments, CPC in the absence of the CPET mediator,  $[(\text{Cp})\text{Co}(\text{Cp}^{\text{N}})]^+$ , also showed some pinacol product but at a much slower rate (10% yield over the same reaction time). Furthermore, none of the starting ketone was recovered in this case. This latter finding suggests that molecular eCPET mediators of the type described here, like redox mediators, may afford benefits compared with transformations that occur directly on the electrode, which can suffer from adsorption and passivation processes. Furthermore, the use of  $[\text{Cp}_2\text{Co}]^+$  in the CPC instead of  $[(\text{Cp})\text{Co}(\text{Cp}^{\text{N}})]^+$  was ineffective. In this case, the pinacol product yield was even lower than that of the background electrode (5%), and HER was enhanced (66% FE).

Synthetic integration of cobaltocenium and a Brønsted acid provides a molecular CPET mediator that operates via redox-induced bond weakening. This approach stores the chemical capacity of a reductant and an acid within a single molecule to facilitate a bimolecular transition state for CPET to an acceptor molecule. Site isolation of the proton and electron kinetically attenuates the thermally favorable HER reaction, thus allowing for reductive CPET in an electrocatalytic fashion.

## REFERENCES AND NOTES

1. M. Yan, Y. Kawamata, P. S. Baran, *Chem. Rev.* **117**, 13230–13319 (2017).
2. B. A. Frontana-Urbe, R. D. Little, J. G. Ibanez, A. Palma, R. Vasquez-Medrano, *Green Chem.* **12**, 2099–2119 (2010).
3. E. Steckhan, *Angew. Chem. Int. Ed.* **25**, 683–701 (1986).
4. B. K. Peters *et al.*, *Science* **363**, 838–845 (2019).
5. M. M. Baizer, *Chemtech* **10**, 161–164 (1980).
6. A. Badalyan, S. S. Stahl, *Nature* **535**, 406–410 (2016).
7. E. J. Horn *et al.*, *Nature* **533**, 77–81 (2016).
8. J. Hartung, J. R. Norton, in *Catalysis Without Precious Metals*, R. M. Bullock, Ed. (Wiley, 2010), pp. 1–24.

9. S. W. M. Crossley, C. Obradors, R. M. Martinez, R. A. Shenoi, *Chem. Rev.* **116**, 8912–9000 (2016).
10. D. C. Miller, K. T. Tarantino, R. R. Knowles, *Top. Curr. Chem.* **374**, 30 (2016).
11. T. V. Chciuk, R. A. Flowers 2nd, *J. Am. Chem. Soc.* **137**, 11526–11531 (2015).
12. D. Kim, S. M. W. Rahaman, B. Q. Mercado, R. Poli, P. L. Holland, *J. Am. Chem. Soc.* **141**, 7473–7485 (2019).
13. G. Qiu, R. R. Knowles, *J. Am. Chem. Soc.* **141**, 2721–2730 (2019).
14. Z.-W. Hou *et al.*, *Angew. Chem. Int. Ed.* **55**, 9168–9172 (2016).
15. M. J. Chalkley, T. J. Del Castillo, B. D. Matson, J. P. Roddy, J. C. Peters, *ACS Cent. Sci.* **3**, 217–223 (2017).
16. M. J. Chalkley, P. H. Oyala, J. C. Peters, *J. Am. Chem. Soc.* **141**, 4721–4729 (2019).
17. M. J. Chalkley, T. J. Del Castillo, B. D. Matson, J. C. Peters, *J. Am. Chem. Soc.* **140**, 6122–6129 (2018).
18. R. Cai *et al.*, *J. Am. Chem. Soc.* **140**, 5041–5044 (2018).
19. R. A. Henderson, *Angew. Chem. Int. Ed.* **35**, 946–967 (1996).
20. Y. Peng, M. V. Ramos-Garcés, D. Lionetti, J. D. Blakemore, *Inorg. Chem.* **56**, 10824–10831 (2017).
21. J. J. Warren, T. A. Tronic, J. M. Mayer, *Chem. Rev.* **110**, 6961–7001 (2010).
22. W.-Z. Liu, F. G. Bordwell, *J. Org. Chem.* **61**, 4778–4783 (1996).
23. I. Kaljurand *et al.*, *J. Org. Chem.* **70**, 1019–1028 (2005).
24. T. H. Parsell, M.-Y. Yang, A. S. Borovik, *J. Am. Chem. Soc.* **131**, 2762–2763 (2009).
25. S. Pattanayak *et al.*, *Inorg. Chem.* **56**, 6352–6361 (2017).
26. C. Costentin, S. Drouet, M. Robert, J.-M. Savéant, *J. Am. Chem. Soc.* **134**, 11235–11242 (2012).
27. T. V. Chciuk, W. R. Anderson Jr., R. A. Flowers 2nd, *J. Am. Chem. Soc.* **138**, 8738–8741 (2016).
28. C. Hansch, A. Leo, R. W. Taft, *Chem. Rev.* **91**, 165–195 (1991).
29. M. K. Goetz, J. S. Anderson, *J. Am. Chem. Soc.* **141**, 4051–4062 (2019).
30. D. Bim, M. Maldonado-Domínguez, L. Rulišek, M. Srnc, *Proc. Natl. Acad. Sci. U.S.A.* **115**, E10287–E10294 (2018).
31. M. P. J. Brennan, O. R. Brown, *J. Chem. Soc., Faraday Trans. 1* **69**, 132–142 (1973).
32. F. Wang, S. S. Stahl, *Acc. Chem. Res.* **53**, 561–574 (2020).

## ACKNOWLEDGMENTS

We thank the Dow Next Generation Educator Funds and Instrumentation Grants for their support of the NMR facility at Caltech and the X-ray Crystallography Facility in the Beckman Institute at Caltech. We also thank the Molecular Materials Research Center in the Beckman Institute at Caltech for use of the x-ray photoelectron spectrometer. **Funding:** This study was supported by funding from the U.S. Department of Energy (DOE-0235032). M.J.C. thanks the Resnick Sustainability Institute for a graduate fellowship, and P.G.-B. thanks the Ramón Areces Foundation for a postdoctoral fellowship. **Author contributions:** M.J.C. and P.G.-B. designed and executed experiments, and all authors analyzed and interpreted data and cowrote the manuscript. **Competing interests:** The authors declare no competing interests. **Data and materials availability:** X-ray structural data are available free of charge from the Cambridge Structural Database under CCDC 1985828 to 1985830. All other data are available in the main text or supplementary materials.

## SUPPLEMENTARY MATERIALS

science.sciencemag.org/content/369/6505/850/suppl/DC1  
Materials and Methods  
Supplementary Text  
Figs. S1 to S94  
Tables S1 to S44  
References (33–57)

9 April 2020; accepted 24 June 2020  
10.1126/science.abc1607



## METALLURGY

# Iron-based superelastic alloys with near-constant critical stress temperature dependence

Ji Xia<sup>1</sup>, Yuki Noguchi<sup>1</sup>, Xiao Xu<sup>1</sup>, Takumi Odaira<sup>1</sup>, Yuta Kimura<sup>1</sup>, Makoto Nagasako<sup>2</sup>, Toshihiro Omori<sup>1\*</sup>, Ryosuke Kainuma<sup>1</sup>

Shape memory alloys recover their original shape after deformation, making them useful for a variety of specialized applications. Superelastic behavior begins at the critical stress, which tends to increase with increasing temperature for metal shape memory alloys. Temperature dependence is a common feature that often restricts the use of metal shape memory alloys in applications. We discovered an iron-based superelastic alloy system in which the critical stress can be optimized. Our Fe-Mn-Al-Cr-Ni alloys have a controllable temperature dependence that goes from positive to negative, depending on the chromium content. This phenomenon includes a temperature-invariant stress dependence. This behavior is highly desirable for a range of outer space-based and other applications that involve large temperature fluctuations.

A shape memory alloy (SMA) is a type of smart material that exhibits a large recoverable strain due to a reversible martensitic transformation (*1*). SMAs have two particular properties of practical importance: the shape memory effect (SME) and superelasticity (SE). In the SME, a large strain can be recovered by heating the thermal-induced martensite. SE can be obtained by unloading associated with reverse transformation of the stress-induced martensite. Many SMA systems have been discovered since the first report of SME in an Au-Cd alloy (*2*). The Ti-Ni system is widely used for medical applications because of its attractive shape memory and mechanical properties, coupled with corrosion resistance. However, the high cost and poor cold-workability of Ti-Ni alloy limit its application to products in the form of thin wires or tubes. Low-cost, highly workable Fe-based SMAs could open up a wider range of applications. Iron-based superelastic alloys have been successfully synthesized in the Fe-Ni-Co-Al (*3*) and Fe-Mn-Al-Ni systems (*4*). However, the temperature range of these alloys still needs to be expanded for different types of applications.

The SMA alloy system Fe-Mn-Al-Ni is a promising candidate because of its lower cost and better cold-workability compared with the Ti-Ni system. Superelasticity, with recoverable strain up to 5% in polycrystalline alloy with a coarse grain structure (*4–8*) and 8% in a single crystal (*9*), associated with the martensitic transformation between the  $\alpha$  [body-centered cubic (BCC)] parent and the  $\gamma'$  [face-centered cubic (FCC)] martensite phases can be obtained in Fe-Mn-Al-Ni alloys containing nanoprecipitates (*10–13*). A very large single crystal ob-

tained by abnormal grain growth (*14–16*) in Fe-Mn-Al-Ni-Ti alloy has also been reported (*17*). Inexpensive Fe-Mn-Al-Ni-based SMAs are attractive not only for small applications but also large ones, for example, seismic applications in buildings and bridges (*18*).

Temperature changes are impossible to avoid, and material properties—including shape, owing to thermal expansion—generally change as well. The critical stress necessary to induce a martensitic transformation increases with increasing temperature because of the higher parent phase stability relative to the martensite phase. Therefore, the critical stress for martensitic transformation eventually becomes higher than the yield stress, which means that plastic deformation occurs instead of SE. This limits the temperature range for SE, which is smaller than 100 K at around room temperature for Ti-Ni alloys (*4*). Even in this temperature range, unstable performance resulting from temperature fluctuations can restrict applications. This temperature dependence has driven engineers and scientists to find materials that are insensitive to temperature or even temperature-invariant. A well-established example of a material that has a temperature-invariant property, namely an almost zero thermal expansion, is the Invar alloy Fe-36Ni (where 36 is the mass % of Ni) (*19*). Invar alloys are widely used in devices for applications such as precision metrology, where thermal expansion must be avoided. However, realizing an SMA that has a critical stress temperature invariance has proved challenging. We discovered an Fe-Mn-Al-Cr-Ni SMA that addresses this deficiency. The temperature dependence of critical stress can be tuned from a positive to a negative value by adding Cr with an almost zero temperature invariance from 10 to 400 K.

We evaluated the SE using compression tests of single crystals over a wide temperature range for Fe-Mn-Al-Cr-Ni alloys, where we

substituted Al and Fe with Cr (Fig. 1, A to D). We observed SE with complete shape recovery at all temperatures, because of the very small temperature dependence of the critical stress (Fig. 1, E to H). The temperature dependence of the critical stresses at temperatures higher than 50 K changes from positive to negative with increasing Cr substitution (Fig. 1I). The quaternary alloys without Cr also have positive temperature dependence of the critical stress (*4, 11, 20, 21*). The Co-Cr-Ga-Si (*22*) and Co-Cr-Al-Si (*23*) alloys have previously been reported to show negative temperature dependence of critical stress at low temperatures. However, because the magnetic entropy of the parent phase plays an important, direct role in the phenomenon, the negative dependence can be obtained only at temperatures lower than near Curie temperature, and the temperature dependence is not steady over a wide temperature range. More importantly, in the Fe-34Mn-13.5Al-3Cr-7.5Ni alloy, an almost zero temperature dependence of critical stress can be obtained. The average temperature dependence of 3Cr in the temperature range of 10 to 300 K is estimated to be 0.085 MPa/K, which is one order of magnitude smaller than that of the conventional Fe-Mn-Al-Ni alloy (0.514 MPa/K) and two orders of magnitude smaller than that of the practical Ti-Ni alloy (5.87 MPa/K). By changing the alloy composition, we can control the temperature dependence of the critical stress.

The transformation hysteresis ( $\sigma_{\text{hys}}$ ) is determined by subtracting the reverse martensitic transformation finishing stress ( $\sigma_{\text{Af}}$ ) from the forward martensitic transformation starting stress ( $\sigma_{\text{Ms}}$ ). The  $\sigma_{\text{hys}}$  sometimes has a temperature dependence, which may hinder SE in a wide temperature range. In Ti-Ni (*24*),  $\sigma_{\text{hys}}$  drastically increases below ~150 K, making SE hard to obtain at low temperatures. However, Cu-Al-Mn (*25*) shows an almost constant hysteresis independent of temperature, and SE occurs even at cryogenic temperatures. In Fe-Mn-Al-Cr-Ni alloys (fig. S3),  $\sigma_{\text{hys}}$  is almost independent of temperature for all Cr content, and the small hysteresis gives rise to a wide temperature range for SE.

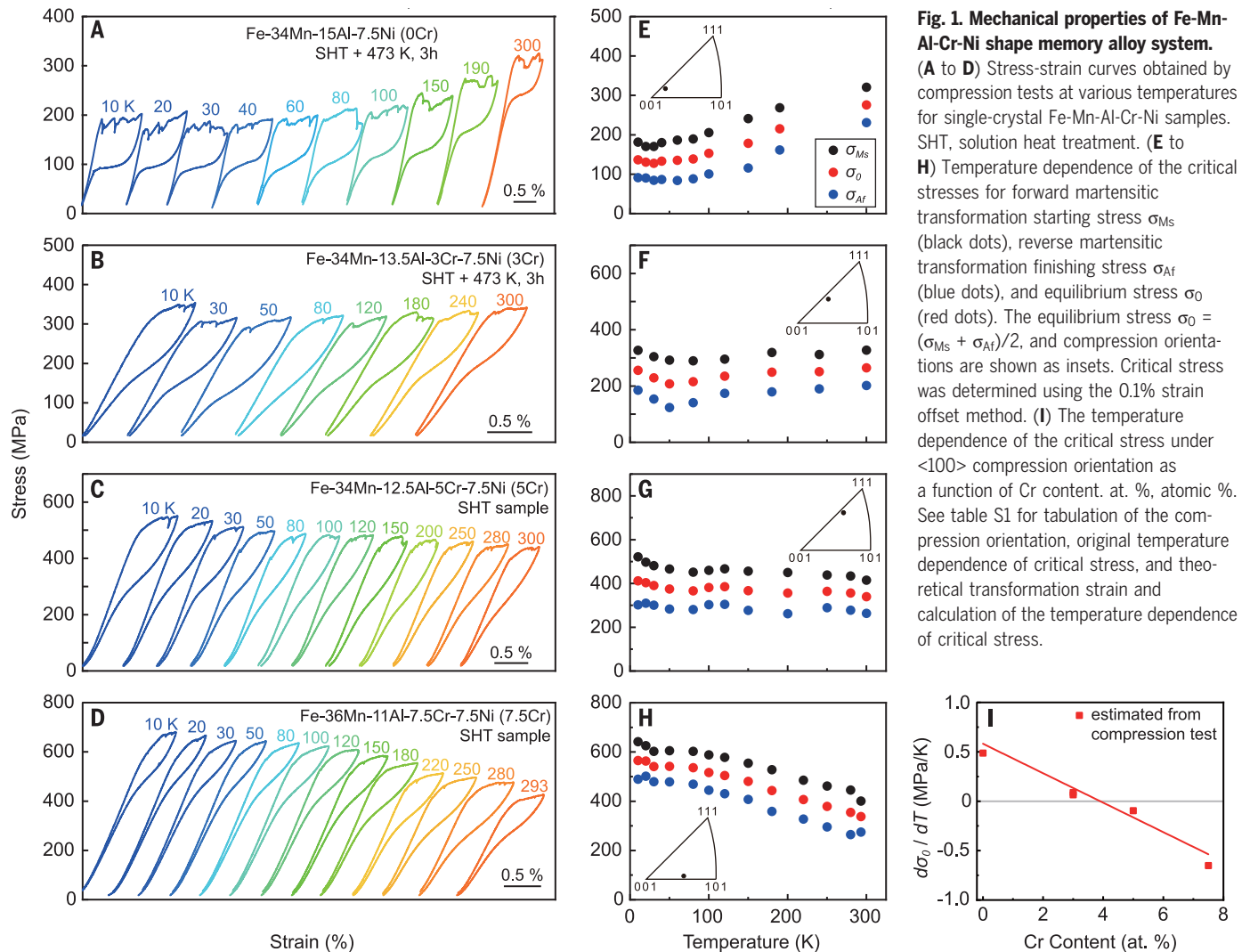
Nanoprecipitates play an important role in the thermoelastic martensitic transformation and SE in the Fe-Mn-Al-Ni alloy (*10*). Beta-NiAl particles (~20 nm in diameter) also precipitate in our Fe-Mn-Al-Cr-Ni alloys, but Cr is more strongly enriched in the matrix than beta-NiAl (fig. S1). The martensite phase has the FCC structure with nanotwins (fig. S2), similar to the quaternary alloy (*10*). These microstructural features, which are beneficial for SE, were also found in the Cr-doped alloys.

The samples we tested had different crystallographic orientations, making further analysis difficult, because the critical stress temperature dependence ( $d\sigma_0/dT$ ) depends on orientation.

<sup>1</sup>Department of Materials Science, Graduate School of Engineering, Tohoku University, Sendai 980-8579, Japan.

<sup>2</sup>Institute for Materials Research, Tohoku University, Sendai 980-8577, Japan.

\*Corresponding author. Email: omori@material.tohoku.ac.jp



This behavior is expressed through the Clausius-Clapeyron relationship

$$\frac{d\sigma_0}{dT} = -\frac{\Delta S}{\epsilon V_m} \quad (1)$$

where  $T$  is the temperature;  $\Delta S$  is the entropy change  $S_M - S_P$  (i.e., entropy of martensite phase minus entropy of parent phase) during martensitic transformation;  $\epsilon$  is the transformation strain, which depends on the orientation; and  $V_m$  is the molar volume. Because  $\Delta S$  during the martensitic transformation and  $V_m$  are independent of orientation,  $d\sigma_0/dT$  is inversely proportional to  $\epsilon$ . The theoretical  $\epsilon$  (table S1) for a given orientation is calculated from the shape strain (26) using the Wechsler-Lieberman-Read (WLR) phenomenological theory (27). The lattice parameter (fig. S6) and transformation strain (fig. S7) are hardly influenced by the Cr content. We estimated the

$d\sigma_0/dT$  for samples with different Cr content but the same orientation using the  $\epsilon$  we calculated. The temperature dependence of the critical stress changes from a positive to a negative variation with increasing Cr content for  $\langle 100 \rangle$  compression (Fig. 1I and table S1).

To verify this near-zero temperature dependence of the critical stress, we prepared another single-crystal Fe-34Mn-13.5Al-3Cr-7.5Ni sample for compression tests from 10 to 473 K (Fig. 2). We obtained a complete SE at all temperatures at which we measured the sample. The SE window is wider than for other SMAs, making the behavior very unusual. It took almost one hour to establish thermal stability and homogeneity at each temperature measurement. The critical stress increased in Fe-Mn-Al-Ni alloy by aging at 473 K (4, 11), which resulted in the noticeable increase of the critical stresses above 400 K. Changes in the critical stresses also occurred near both the Néel temperature of the martensite phase ( $T_N$ )

and the Curie temperature of the parent phase ( $T_C$ ) (fig. S9).

We determined the entropy change in 0Cr, 3Cr, and 7.5Cr alloys using specific heat measurements (fig. S10) (28). For the temperatures below  $\sim 300$  K,  $\Delta S$  increases with increasing Cr content, and its sign changes from negative to positive when the Cr content is 7.5 (Fig. 3A). Although the calculated  $\Delta S$  from Eq. 1 becomes close to zero at 3Cr or 4Cr, the measured  $\Delta S$  becomes close to zero at a higher Cr content. We do not know the reason for this difference. The negative  $d\sigma_0/dT$  at temperatures below 50 K (Fig. 1) also cannot be explained by the measured  $\Delta S$ . Nonetheless, we qualitatively show that the near-zero or negative temperature dependence of the critical stress in Fe-Mn-Al-Cr-Ni alloy is caused by the change in  $\Delta S$  (Fig. 3).

The martensite and parent phases undergo antiferromagnetic and ferromagnetic transitions, respectively, between 278 and 417 K (fig. S9).

These magnetic transitions increase the magnetic contribution of specific heat in each phase ( $c_p^{\text{mag}}$ ) (fig. S10) (28). Therefore,  $\Delta S$  increases and decreases as a result of the magnetic entropy  $S_i^{\text{mag}}$  of the martensite and parent phases, respectively (Fig. 3A), which corresponds to the change in  $\Delta S$  at temperatures mainly higher than 200 K. The  $\Delta S$  becomes close to zero as a result. This behavior is qualitatively the same as in the quaternary (4) and quinary alloys. In addition to the magnetic transitions at temperatures above 250 K, we found some spin glass-like magnetic transitions in the parent phase below 150 K (fig. S12). These magnetic transitions are crucial to the understanding of the complicated temperature dependence of  $\Delta S$ . We assumed that the combination of these magnetic transitions acts to prevent the entropy change  $\Delta S$  from deviating too far from zero. The anomalies in this alloy system, Invar alloy (29), Co-based alloys (22, 23, 30, 31), and Fe (32, 33) all have a deep relationship with magnetism.

Besides the magnetic effects, we found that  $\Delta S$  increases from negative to zero with the addition of Cr. The increasing part of entropy change through Cr substitution can be separated into the individual increases of the parent and martensite phases (28) (Fig. 3B). The entropies of the parent and martensite phases increase with the Cr addition, with the increasing amount being greater in the martensite phase below 350 K. We further separated the martensite phase entropy into lattice and nonlattice contributions (fig. S11). At temperatures below 250 K, entropy increase in the martensite phase is due to the difference in the lattice contribution between 0Cr and 7.5Cr. The difference in the nonlattice contribution visibly affects the alloy at higher temperatures.

An insensitive temperature dependence of stress is vital for practical applications of SE. The easily tunable temperature dependence of the critical stress allows engineers and scientists to design structures and components with desirable properties (Fig. 4). One example is the use of SMA for the treatment of ingrown nails, for which our Fe-36Mn-11Al-7.5Cr-7.5Ni alloy may be more suitable, because the strength of human nails has a negative temperature dependence (34). More importantly, the Fe-34Mn-13.5Al-3Cr-7.5Ni alloy has a very wide temperature window compared with other conventional SMAs (Fig. 4B). This property makes the superelastic alloy suitable for applications with wide temperature ranges, such as building damping or even space research.

A growing interest in space exploration by private companies and government agencies should drive demand for new materials. Exploration of a body such as the Moon or Mars requires materials that operate over large temperature ranges. The Moon has a day-to-night

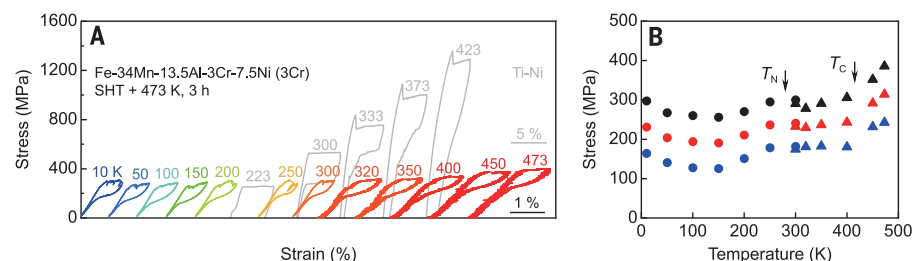


**Fig. 2. Mechanical properties of Fe-34Mn-13.5Al-3Cr-7.5Ni single-crystal sample.** (A) Stress-strain curves obtained by compression tests at various temperatures (compression orientation identical to that in Fig. 1B). (B) Temperature dependence of  $\sigma_{Ms}$ ,  $\sigma_{Af}$ , and  $\sigma_0$ . Arrows indicate the magnetic transition temperatures. The circles and triangles represent data obtained from different compression equipment (28).

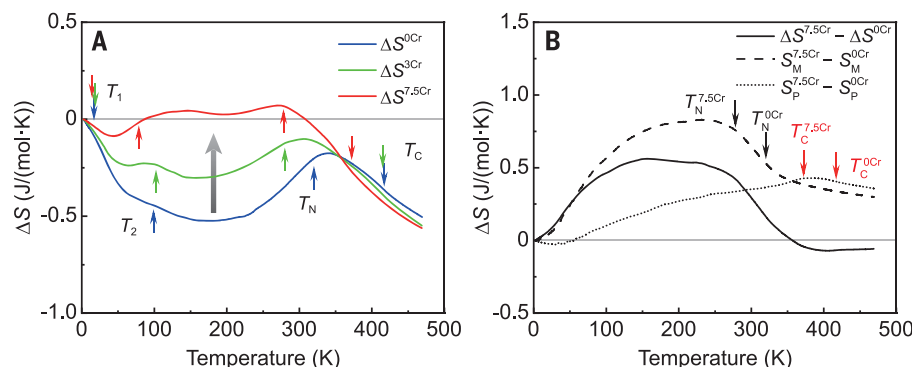


**Fig. 3. Thermodynamic analysis of the Fe-Mn-Al-Cr-Ni alloy system.** (A) The temperature dependence of the entropy change  $\Delta S$  between the parent and martensite phases from 2 to 473 K for samples with different Cr content. Arrows indicate the magnetic transition temperatures.  $T_1$  and  $T_2$  are possible spin glass-like magnetic transition temperatures observed in the parent phase (28). (B) Change of  $\Delta S$ ,  $S_p$ , and  $S_m$  by addition of 7.5 atomic % Cr.

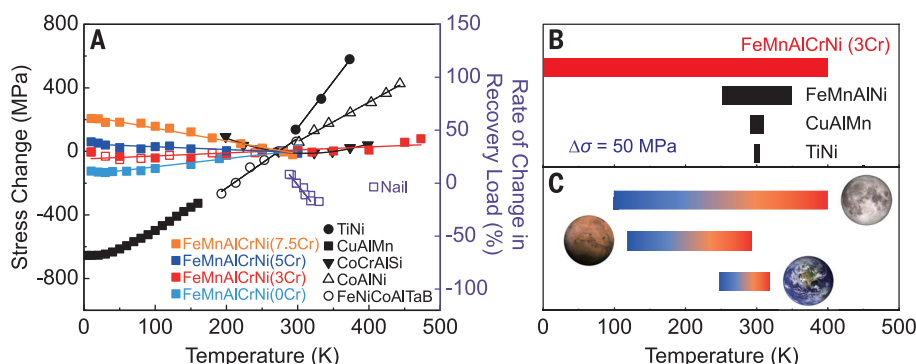


**Fig. 4. Comparisons between Fe-Mn-Al-Cr-Ni and other conventional shape memory alloys.** (A) Temperature dependence of the equilibrium stress change for martensitic transformation relative to the stress at 273 K in Fe-Mn-Al-Cr-Ni and other shape memory alloys. The rate of change in the recovery load for a human nail is plotted (34). (B) Temperature window around 300 K, when the critical stress change is 50 MPa in conventional SMAs and Fe-Mn-Al-Cr-Ni alloy, where average temperature dependence of critical stress is 0.514 MPa/K in Fe-Mn-Al-Ni (10 to 300 K), 2.87 MPa/K in Cu-Al-Mn (25), and 5.87 MPa/K in Ti-Ni (4). (C) The temperature change from day to night on the Moon, Mars, and Earth (38).

temperature change of 400 to 100 K, whereas Mars has a change of 290 to 120 K (Fig. 4C). Our iron-based superelastic alloys have small critical stress changes at lower temperatures (Fig. 2B), which means that alloys such as our

3Cr alloy have potential for use as springs for unfolding telescopes (35), exploration rover tires (36), and vibration control system of spacecraft, as well as applications in lunar infrastructure development (37).



## REFERENCES AND NOTES

1. K. Otsuka, C. M. Wayman, in *Shape Memory Materials*, K. Otsuka, C. M. Wayman, Eds. (Cambridge Univ. Press, 1998), pp. 1–48.
2. A. Ölander, *J. Am. Chem. Soc.* **54**, 3819–3833 (1932).
3. Y. Tanaka *et al.*, *Science* **327**, 1488–1490 (2010).
4. T. Omori *et al.*, *Science* **333**, 68–71 (2011).
5. T. Omori, M. Okano, R. Kainuma, *APL Mater.* **1**, 032103 (2013).
6. L. W. Tseng *et al.*, *Scr. Mater.* **125**, 68–72 (2016).
7. M. Vollmer *et al.*, *Scr. Mater.* **114**, 156–160 (2016).
8. M. Vollmer *et al.*, *Scr. Mater.* **108**, 23–26 (2015).
9. L. W. Tseng, J. Ma, S. J. Wang, I. Karaman, Y. I. Chumlyakov, *Scr. Mater.* **116**, 147–151 (2016).
10. T. Omori, M. Nagasako, M. Okano, K. Endo, R. Kainuma, *Appl. Phys. Lett.* **101**, 231907 (2012).
11. L. W. Tseng *et al.*, *Acta Mater.* **97**, 234–244 (2015).
12. P. La Roca, A. Baruj, C. E. Sobrero, J. A. Malarria, M. Sade, *J. Alloys Compd.* **708**, 422–427 (2017).
13. H. Ozcan *et al.*, *Scr. Mater.* **134**, 66–70 (2017).
14. T. Omori, H. Iwaizako, R. Kainuma, *Mater. Des.* **101**, 263–269 (2016).
15. T. Omori *et al.*, *Science* **341**, 1500–1502 (2013).
16. T. Kusama *et al.*, *Nat. Commun.* **8**, 354 (2017).
17. M. Vollmer *et al.*, *Nat. Commun.* **10**, 2337 (2019).
18. O. E. Ozbulut, S. Hurlbaeus, R. Desroches, *J. Intell. Mater. Syst. Struct.* **22**, 1531–1549 (2011).
19. C. E. Guillaume, *Compt. Rend.* **125**, 235–238 (1897).
20. L. W. Tseng *et al.*, *Acta Mater.* **89**, 374–383 (2015).
21. J. Xia *et al.*, *Shape Mem. Superelasticity* **3**, 467–475 (2017).
22. X. Xu *et al.*, *Appl. Phys. Lett.* **103**, 164104 (2013).
23. T. Odaira *et al.*, *Scr. Mater.* **153**, 35–39 (2018).
24. K. Niitsu, T. Omori, R. Kainuma, *Appl. Phys. Lett.* **102**, 231915 (2013).
25. K. Niitsu, Y. Kimura, T. Omori, R. Kainuma, *NPG Asia Mater.* **10**, e457 (2018).
26. K. Otsuka, C. M. Wayman, K. Nakai, H. Sakamoto, K. Shimizu, *Acta Metall.* **24**, 207–226 (1976).
27. M. S. Wechsler, D. S. Lieberman, T. A. Read, *Trans. Am. Inst. Min. Metall. Eng.* **197**, 1503–1515 (1953).
28. Materials and methods and supplementary text are available as supplementary materials.
29. Y. Nakamura, *IEEE Trans. Magn.* **12**, 278–291 (1976).
30. X. Xu, T. Omori, M. Nagasako, T. Kanomata, R. Kainuma, *Appl. Phys. Lett.* **107**, 181904 (2015).
31. X. Xu *et al.*, *Phys. Rev. B* **91**, 104434 (2015).
32. C. Zener, *JOM* **7**, 619–630 (1955).
33. R. J. Weiss, K. J. Tauer, *Phys. Rev.* **102**, 1490–1495 (1956).
34. T. Omori, Y. Sutou, N. Tabata, R. Kainuma, K. Ishida, *J. JRI/Cu* **50**, 86–91 (2011).
35. D. H. Lesser, L. Graves, C. K. Walker, *IEEE Trans. Terahertz Sci. Technol.* **9**, 409–416 (2019).
36. S. Padula II, “Utilizing Shape Memory Alloys for Novel, Non-Pneumatic Tire Design – Designing for the Best of Both Worlds” (GRC-E-DAA-TN67368, NASA Glenn Research Center, 2019).
37. A. S. Scott, B. Sherwood, *Out of This World: The New Field of Space Architecture* (American Institute of Aeronautics and Astronautics, 2009).
38. NASA Science, Solar System Exploration (2019); <http://solarsystem.nasa.gov/resources/925/solar-system-and-beyond-poster-set/>.

## ACKNOWLEDGMENTS

We thank K. R. A. Ziebeck for help with critical reading of the manuscript. Part of the experiments were conducted in the Center for Low Temperature Science, Tohoku University. J.X. thanks D. Lee, R. Y. Umetsu, and S. Takayama for their experimental help and acknowledges support from the Interdepartmental Doctoral Degree Program for Multi-dimensional Materials Science Leaders of Tohoku University. **Funding:** This study was supported by JSPS KAKENHI grant 15H05766. **Author contributions:** T.Om. and R.K. designed the study. J.X., Y.N., Y.K., and T.Od. carried out the mechanical tests. J.X. and X.X. conducted the magnetic and specific heat measurements. M.N. performed the transmission electron microscopy and scanning transmission electron microscopy observations. J.X., T.Om., X.X., and R.K. analyzed the data and wrote the draft of the paper. All authors discussed the results and commented on the manuscript. **Competing interests:** A portion of the authors are inventors on U.S. patent application no. US20190153571A1, filed by Tohoku University, Furukawa Techno Material Co., Ltd., and Furukawa Electric Co., Ltd., which covers the alloy compositions of the present work. **Data and materials availability:** All data are available in the main text or the supplementary materials.

## SUPPLEMENTARY MATERIALS

[science.sciencemag.org/content/369/6505/855/suppl/DC1](https://science.sciencemag.org/content/369/6505/855/suppl/DC1)  
Materials and Methods  
Supplementary Text  
Figs. S1 to S12  
Tables S1 and S2  
References (39–48)

8 April 2020; accepted 23 June 2020  
10.1126/science.abc1590

## NEURODEVELOPMENT

# Mitochondrial dynamics in postmitotic cells regulate neurogenesis

Ryohei Iwata<sup>1,2,3,4,5</sup>, Pierre Casimir<sup>1,2,3,4,5</sup>, Pierre Vanderhaeghen<sup>1,2,3,4,5\*</sup>

The conversion of neural stem cells into neurons is associated with the remodeling of organelles, but whether and how this is causally linked to fate change is poorly understood. We examined and manipulated mitochondrial dynamics during mouse and human cortical neurogenesis. We reveal that shortly after cortical stem cells have divided, daughter cells destined to self-renew undergo mitochondrial fusion, whereas those that retain high levels of mitochondria fission become neurons. Increased mitochondria fission promotes neuronal fate, whereas induction of mitochondria fusion after mitosis redirects daughter cells toward self-renewal. This occurs during a restricted time window that is doubled in human cells, in line with their increased self-renewal capacity. Our data reveal a postmitotic period of fate plasticity in which mitochondrial dynamics are linked with cell fate.

**W**ith neurogenesis, neural stem cells (NSCs) stop self-renewing and differentiate into postmitotic neurons. Mitochondrial dynamics, through fusion and fission, is associated with fate changes in various types of cells, including the conversion of NSCs into intermediate neural progenitors (1–6). We investigated whether and how mitochondria remodeling is coupled with neuronal fate commitment.

To examine mitochondrial dynamics during neurogenesis, we labeled mitochondria in radial glia cells (RGCs), the NSCs of the mouse embryonic cortex, through transduction of mito-GFP (green fluorescent protein fused to mitochondrial targeting sequence of COX8A) (7). Pax6<sup>+</sup> RGC displayed fused mitochondria, and T-box brain protein 2 (Tbr2)<sup>+</sup> intermediate neural progenitors displayed intermediate mitochondrial size (fig. S1A), as reported (3). Surprisingly, early-born  $\beta$ III-tubulin ( $\beta$ III-tub)<sup>+</sup> neurons' mitochondria were highly fragmented (Fig. 1A and fig. S1A), which was confirmed by means of immunostaining against endogenous translocase of the outer mitochondrial membrane 20 (TOMM20) (fig. S1C). Mitochondria remained fragmented for several days before gradually fusing in more mature neurons (fig. S1B).

On the other hand, mitochondria of RGCs during mitosis were fragmented (fig. S1D), which is typical of mitotic cells (8). We hypothesized that mitochondrial dynamics change in the daughter cells right after mitosis, depending on their prospective fate. We assessed mitochondrial dynamics of cortical progenitors through neurogenesis, from cell division

to fate acquisition (Fig. 1B). We expressed in cortical progenitors the mitochondrial label mito-mNep2 (mNeptune2 protein fused to mitochondrial targeting sequence of COX8A), together with the photactivatable fluorescent protein mEOS4b (9), which can be photoconverted from green to red, fused to histone protein H2B to target chromatin (H2B-mEOS4b). This enabled the identification of cells in mitotic metaphase/anaphase, based on labeling of chromatin with fluorescent mEOS proteins. Such cells were tagged by means of photoconversion, enabling the tracking of the daughter cells and their mitochondria 1 to 24 hours after mitosis. We used expression of  $\beta$ III-tub as a neuronal marker and Tbr2 for intermediate neural progenitors. Cells that expressed neither Tbr2 nor  $\beta$ III-tub corresponded mostly (95%) to Sox2<sup>+</sup> RGC (fig. S1E). The acquisition and stabilization of the identity of daughter cells could then be observed over the next 6 to 12 hours (fig. S1F), with similar timing as that reported in vivo (10). Mitochondrial dynamics in the first 3 hours after cell division were characterized either by increased mitochondrial length or by retaining shorter fragmented mitochondria (Fig. 1C). Presumptive RGC displayed long mitochondria, presumptive neurons retained short mitochondria, and intermediate progenitors displayed intermediate-sized mitochondria (Fig. 1C).

Could postmitotic alteration of mitochondrial dynamics influence neurogenesis? We tracked postmitotic cells, this time using compounds that promote mitochondria fusion [M1, (E)-4-chloro-2-(1-(2-(2,4,6-trichlorophenyl)hydrazono)ethyl)phenol (11)] or inhibit mitochondria fission [mitochondrial division inhibitor (Mdivi-1), 3-(2,4-dichloro-5-methoxyphenyl)-2-sulfany-4(3H)-quinazolinone (12)]. Compounds were added to the photoconverted cells right after mitosis (Fig. 1D), which resulted in an increase of mitochondrial size within 3 hours of postmitotic cell labeling (Fig. 1E). The iden-

tity of daughter cells was not significantly altered at 3 hours after treatment (Fig. 1F) but changed by 6 hours after treatment: The proportion of daughter cells that became RGCs increased, and the proportion that became neurons decreased, whereas the proportion of intermediate progenitors remained unchanged (Fig. 1, G and H). The number of cells was unchanged in either condition, excluding cell loss as a cause (fig. S2, A and B). The effect of M1 treatment on cell fate was maintained at 12 hours, with an increase in non-neurogenic divisions at the expense of neurogenic divisions (fig. S2, C and D), resulting in an increase in clonal size at 24 hours (fig. S2, E to G), indicating that RGCs generated under M1 treatment stably retained their self-renewal capacity. Morphogenesis of the neurons that could still be generated under M1 treatment also appeared to be normal at 24 hours (fig. S2H). To explore upstream mechanisms, we examined Drp1 that is activated during mitosis through CDK1 phosphorylation (13). We found high levels of pDrp1 in mitotic cells, followed by a dual pattern of phosphorylation, inversely correlated with mitochondrial size (fig. S3A). Postmitotic treatment with Roscovitine, an inhibitor of CDK activity, led to increased size of mitochondria, fewer neurons, and more RGCs, with no detectable cell loss (fig. S3, B to E).

Thus, in vitro with chemical intervention, increased fusion or decreased fission of mitochondria after mother RGC division biases fate acquisition of the daughter cells in favor of stem cell fate at the expense of neuronal fate. We next examined in vivo mouse corticogenesis with genetic manipulation of mitochondrial dynamics. We suppressed the expression of Drp1 by means of in utero electroporation and observed a decrease in the proportion of generated neurons and an increase in the proportion of intermediate progenitors and RGCs (Fig. 2, A and B). To test postmitotic manipulation of mitochondrial dynamics in vivo, we used the FlashTag method that enables in utero labeling of RGCs during mitosis (10). Injection of FlashTag, together with M1 to promote mitochondria fusion, resulted in increased mitochondrial size within 4 hours (Fig. 2C). FlashTag<sup>+</sup>-labeled cells 12 hours after M1 or Mdivi-1 treatment revealed an increase in the proportion of Sox2<sup>+</sup> RGCs and Tbr2<sup>+</sup> intermediate progenitors and a decrease of Neurod2<sup>+</sup> neurons (Fig. 2D). Thus, mitochondrial dynamics after mitosis affect mouse cortical neurogenesis in vivo, like in vitro.

We sought to examine whether the mitochondrial oxidation state could mediate these effects (3, 14) by testing the ionophore carbonyl cyanide *m*-chlorophenyl hydrazone (CCCP), which leads to hyperactivation of the electron transport chain, and thereby increased reactive oxygen species and oxidized nicotinamide

<sup>1</sup>VIB Center for Brain and Disease Research, 3000 Leuven, Belgium. <sup>2</sup>Department of Neurosciences, Katholieke Universiteit (KU) Leuven, 3000 Leuven, Belgium. <sup>3</sup>Leuven Brain Institute, KU Leuven, 3000 Leuven, Belgium. <sup>4</sup>Institut de Recherches en Biologie Humaine et Moléculaire (IRIBHM), Université Libre de Bruxelles (ULB), 1070 Brussels, Belgium. <sup>5</sup>ULB Neuroscience Institute (UNI), ULB, 1070 Brussels, Belgium.

\*Corresponding author. Email: pierre.vanderhaeghen@kuleuven.vib.be

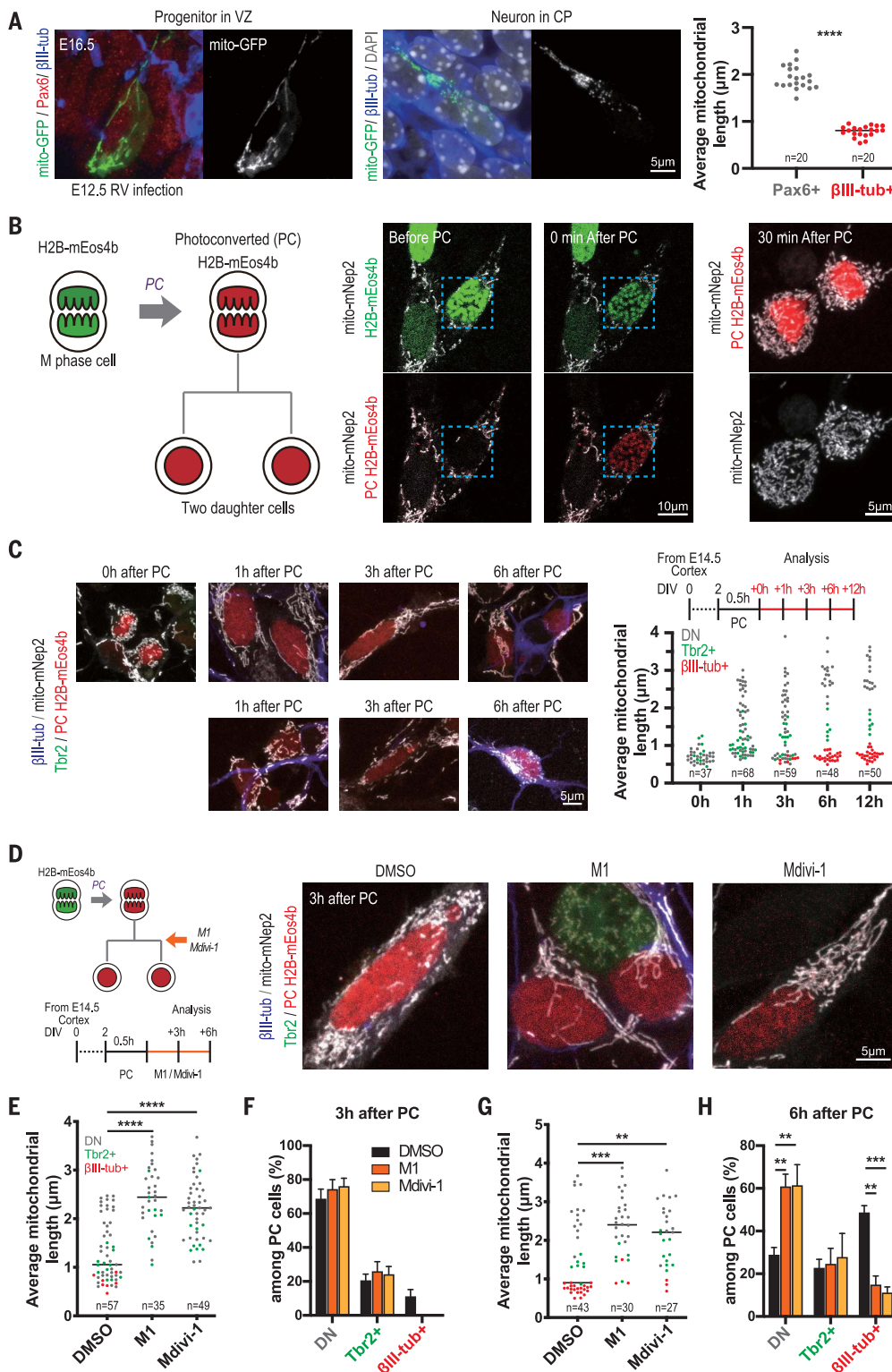


**Fig. 1. Mitochondrial dynamics influence fate decision in postmitotic cortical cells. (A)** Representative images of mitochondrial morphology (mito-GFP) in Pax6<sup>+</sup> RGCs in (left) ventricular zone (VZ) and (middle) βIII-tub<sup>+</sup> newborn neuron in cortical plate (CP) in embryonic day 16.5 (E16.5) mouse cortex, after in utero retroviral infection at E12.5. (Right) Quantified mitochondrial length from two biological replicate experiments. Each data point represents an individual cell average mitochondrial size. \*\*\*\**P* < 0.0001; unpaired Student's *t* test. **(B)** (Left) Schematic of the labeling strategy by using photoconverted (PC) histone H2B-mEos4b. (Right) Representative images of PC cell labeled with mito-Nep2. **(C)** (Left) Representative images and timeline of PC experiment to determine kinetics of mitochondrial dynamics after mitosis in mouse embryonic cortical cells. (Right) Quantified mitochondrial length from three biological replicate experiments. Each data point represents an individual cell average mitochondrial size, together with fate marker expression. Red, βIII-tub<sup>+</sup> neuron; green, Tbr2<sup>+</sup> intermediate progenitor; gray, double negative (DN) RGC. **(D)** Timeline and representative images of PC experiment by using M1 and Mdivi-1. DMSO, dimethyl sulfoxide. **(E and G)** Quantified mitochondrial length from three biological replicate experiments. (E) Three hours after label. (G) Six hours after PC. Each data point represents an individual cell average mitochondrial size. \*\**P* < 0.01, \*\*\**P* < 0.001, \*\*\*\**P* ≤ 0.0001; Dunn's multiple comparisons test. **(F and H)** Quantification of each cell fate marker<sup>+</sup> cells among PC cells from at least four biological replicate experiments. Data are shown as mean ± SEM. \*\**P* < 0.01, \*\*\**P* < 0.001; Dunn's multiple comparisons test.

adenine dinucleotide (NAD<sup>+</sup>)/reduced NAD<sup>+</sup> (NADH) ratio (15). This resulted in increased neurogenesis within 6 hours after mitosis, without change in mitochondria size (Fig. 3, A and B, and fig. S4A). We next tested the implication of Sirtuin-1 (Sirt1), which is acti-

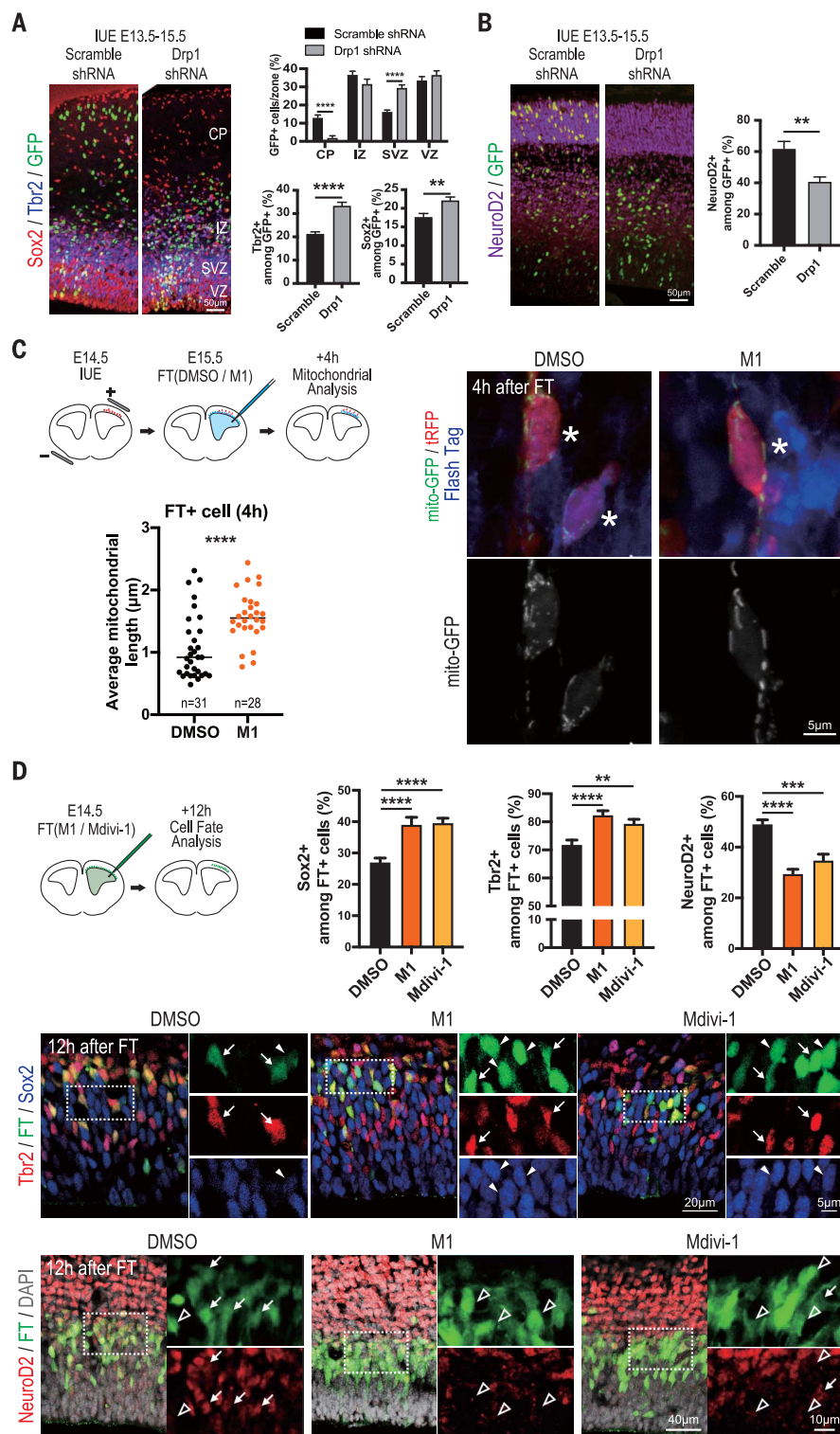
vated by increased NAD<sup>+</sup>/NADH ratio (16) and promotes cortical neurogenesis together with the BCL6 transcriptional repressor (17, 18). We found that Sirt1 inhibition through Ex-527 treatment in postmitotic cells blocked neurogenesis, also after CCCP treatment (Fig. 3C and fig. S4,

B to D). Sirt1 promotes neurogenesis through H4K16 histone deacetylation at BCL6 transcriptional targets (17, 19). We therefore examined H4K16 acetylation levels, which we found to be increased after Ex-527 treatment and decreased after CCCP treatment (Fig. 3D). We next



## Fig. 2. Mitochondrial dynamics in post-mitotic cells affect cortical neurogenesis in vivo.

(A and B) (Left) In utero electroporation (IUE) of scramble or Drp1 short hairpin RNA (shRNA) at E13.5, analyzed at E15.5. Histogram shows the percentage of H2B-GFP<sup>+</sup> cells in VZ, SVZ, IZ, and CP. (Right) Quantification of (A) Tbr2<sup>+</sup> or Sox2<sup>+</sup> and (B) NeuroD2<sup>+</sup> cells among electroporated cells from two biological replicate experiments. Data are shown as mean  $\pm$  SEM.  $**P < 0.01$ ,  $****P < 0.0001$ ; [(A), top] Bonferroni's multiple comparisons test, [(A), bottom] unpaired *t* test, (B) Mann-Whitney test. (C) (Top left) Timeline of in utero electroporation [Turbo red fluorescent protein (tRFP) and mito-GFP] and FlashTag (FT) labeling. (Right) Representative images of M1-treated tRFP and mito-GFP electroporated FT<sup>+</sup> cell (asterisks). (Bottom left) Quantification of mitochondrial length from two biological replicate experiments. Each data point represents an individual cell average mitochondrial size.  $****P < 0.0001$ ; Mann-Whitney test. (D) (Left) Schematic and representative images of in utero M1 treatment and FT labeling in the mouse embryonic cortex. (Right) Quantification of Sox2<sup>+</sup>, Tbr2<sup>+</sup>, and NeuroD2<sup>+</sup> cells among FT<sup>+</sup> cells from two biological replicate experiments. Data are shown as mean  $\pm$  SEM.  $**P < 0.01$ ,  $***P < 0.001$ ,  $****P < 0.0001$ ; Sox2 and Tbr2, Dunn's multiple comparisons test; NeuroD2, Dunn's multiple comparisons test. (Top) Arrows indicate Sox2<sup>+</sup>, and arrowheads indicate Tbr2<sup>+</sup>. (Bottom) Arrows indicate NeuroD2<sup>+</sup>, and open arrowheads indicate NeuroD2<sup>-</sup>.



explored potential links between mitochondrial dynamics and Sirtuins. We found that Sirtuin activation under SRT1720 treatment could abolish the effects of M1 on neurogenesis (fig. S4, E to G) and that H4K16 acetylation was increased after M1 or Mdivi-1 treatment (Fig. 3D). These data suggest that mitochond-

drial influence on neurogenesis may involve, at least in part, Sirt1.

Human cortical progenitors are characterized by intrinsic higher self-renewal potential that is thought to underlie the evolutionary increase in human cortical size (20, 21). We examined mitochondrial dynamics during

in vitro corticogenesis from human pluripotent stem cells. As in the mouse, human cortical RGCs were characterized by large mitochondria, whereas early-born neurons displayed fragmented mitochondria (Fig. 4A). Overexpression of mitochondrial fission-promoting Drp1 or mitochondrial fission factor (MFF) genes in

### Fig. 3. Mitochondria and Sirtuin activity influence cortical neurogenesis. (A) Timeline, representative images, and quantified mitochondrial length after CCCP postmitotic treatment. Each data point represents an individual cell average mitochondrial size from three biological replicate experiments. Mann-Whitney test. (B) Quantification of each cell fate marker<sup>+</sup> cells among PC cells (6 hours after label) from three biological replicate experiments after CCCP postmitotic treatment. Data are shown as mean ± SEM. \*\*\*\**P* < 0.0001; Bonferroni's multiple comparisons test. (C) Timeline and quantification of PC cells expressing cell fate markers by using Sirt1 inhibitor Ex-527 from three biological replicate experiments. Data are shown as mean ± SEM. \*\**P* < 0.01, \*\*\**P* < 0.001; Bonferroni's multiple comparisons test. (D) (Top right) Timeline and (left) representative images of H4K16ac signal in PC cells. (Bottom right) Quantified H4K16ac signal from two biological replicate experiments. Each data point represents an individual cell average H4K16ac signal. \*\**P* < 0.01, \*\*\*\**P* < 0.0001; Dunn's multiple comparisons test.

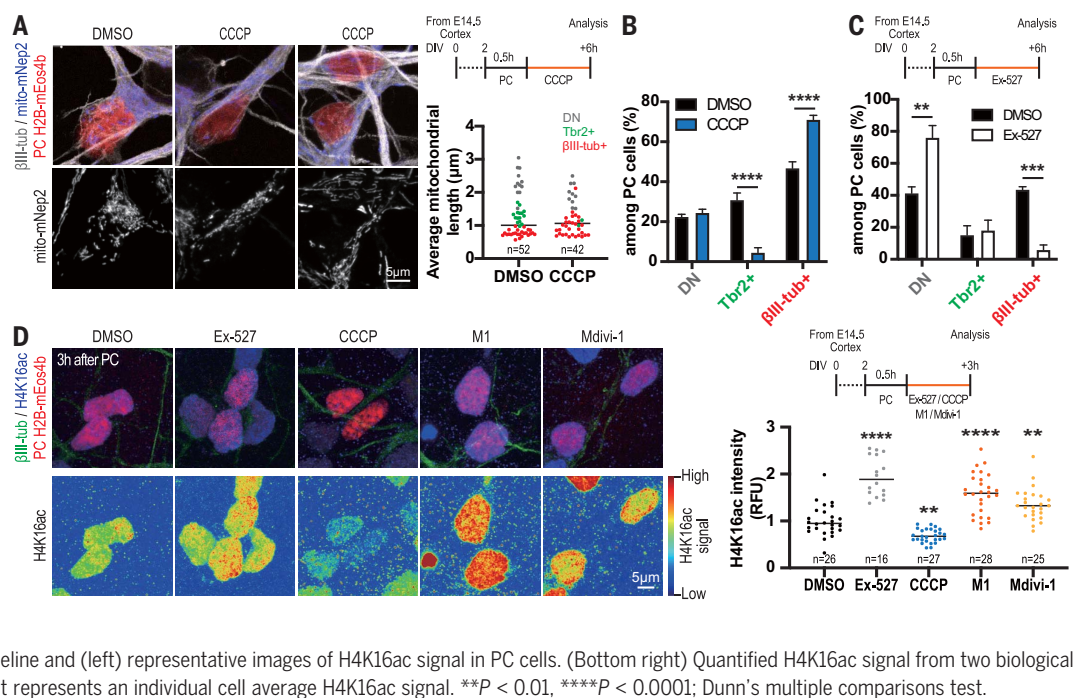
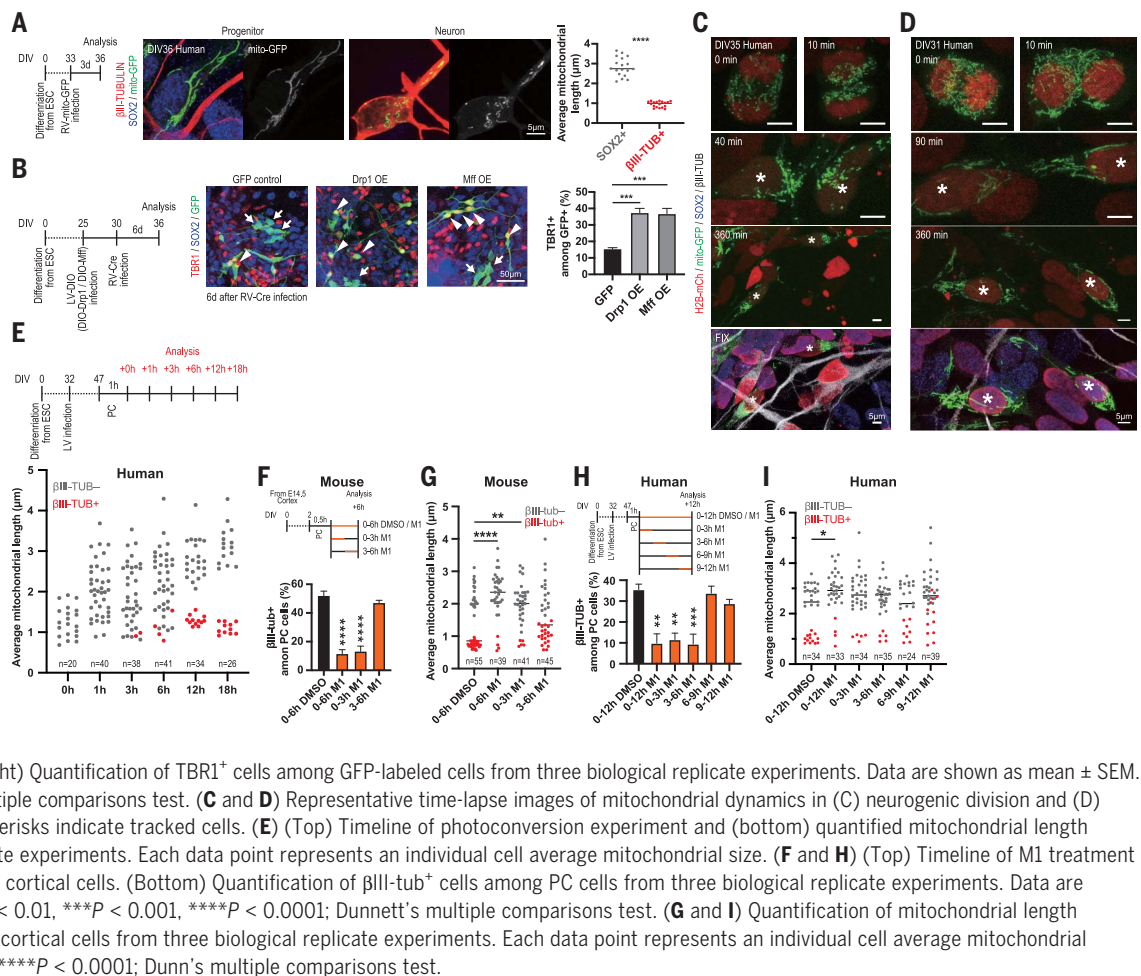


### Fig. 4. A species-specific postmitotic period of fate plasticity. (A) (Left and middle) Timeline and representative images of mitochondrial morphology in SOX2<sup>+</sup> (RGC) and βIII-tub<sup>+</sup> (Newborn neuron) human embryonic stem cell (ESC)-derived cortical cell 3 days after mito-GFP retroviral infection. (Right) Quantification of mitochondrial length from two biological replicate experiments. Each data point represents an individual cell average mitochondrial size. \*\*\*\**P* < 0.0001; Mann-Whitney test. (B) (Left and middle) Timeline and representative images of Drp1- and Mff-overexpressing human cortical cells (6 days after Cre-expressing retrovirus infection). Arrow-heads indicate Neuron (Tbr1<sup>+</sup>), and arrows indicate Progenitor (Sox2<sup>+</sup>). (Right) Quantification of TBR1<sup>+</sup> cells among GFP-labeled cells from three biological replicate experiments. Data are shown as mean ± SEM. \*\*\**P* < 0.001; Dunnett's multiple comparisons test. (C and D) Representative time-lapse images of mitochondrial dynamics in (C) neurogenic division and (D) non-neurogenic division. Asterisks indicate tracked cells. (E) (Top) Timeline of photoconversion experiment and (bottom) quantified mitochondrial length from three biological replicate experiments. Each data point represents an individual cell average mitochondrial size. (F and H) (Top) Timeline of M1 treatment in (F) mouse and (H) human cortical cells. (Bottom) Quantification of βIII-tub<sup>+</sup> cells among PC cells from three biological replicate experiments. Data are shown as mean ± SEM. \*\**P* < 0.01, \*\*\**P* < 0.001, \*\*\*\**P* < 0.0001; Dunnett's multiple comparisons test. (G and I) Quantification of mitochondrial length in (G) mouse and (I) human cortical cells from three biological replicate experiments. Each data point represents an individual cell average mitochondrial size. \**P* < 0.05, \*\**P* < 0.01, \*\*\*\**P* < 0.0001; Dunn's multiple comparisons test.



human RGCs resulted in increased neurogenesis (Fig. 4B).

We next performed time-lapse imaging of human cortical progenitors labeled with mito-GFP, followed by fate marker determination (Fig. 4, C and D). This revealed that at mitosis, the mitochondria were fragmented. After mitosis, as for mouse cells, human cells with large mitochondria remain progenitors, whereas those with fragmented mitochondria become neurons ( $n = 24$  cells). Similar data were obtained by using mEOS labeling of human mitotic RGC, like in the mouse (Fig. 4E and fig. S5A). M1 treatment after mitosis of human progenitors led to increased mitochondria size and decreased neuronal differentiation, as well as increased self-renewing division (Fig. 4I and fig. S5, B and C).

Thus, postmitotic control of cell fates through mitochondrial dynamics is conserved in mouse and human corticogenesis. We next used the mEOS system to determine the length of the susceptibility phase during which mitochondrial dynamics can affect neural cell fate. We speculated that given the higher self-renewal potential of human RGCs, the susceptibility phase might be longer in these cells. Human and mouse cells were treated in parallel over defined time periods after mitosis (Fig. 4, F to I). In the mouse, M1 treatment altered cell fate up to but not beyond 3 hours after mitosis (Fig. 4F). In human cells, M1 treatment altered cell fate up to 6 hours after mitosis (Fig. 4H), indicating that the susceptibility phase of postmitotic neural cell fate plasticity is doubled compared with mouse cells.

Our data suggest important mitochondria remodeling during postmitotic phases of neurogenesis, which will have to be characterized further with electron microscopy and metabolic analyses. Previous data emphasized fate decision of NSCs before mitosis (22–24). Our data reveal a fate plasticity period that extends much later, shortly after NSC mitosis. This period is longer in human than in mouse cortical progenitors, which could contribute to their increased self-renewal capacities (20, 21). High levels of mitochondria fission in newborn neurons themselves lead to irreversible fate commitment, in link with developmental neurogenic pathways, through mechanisms that remain to be elucidated.

## REFERENCES AND NOTES

1. K. Mitra, R. Rikhy, M. Lilly, J. Lippincott-Schwartz, *J. Cell Biol.* **197**, 487–497 (2012).
2. M. D. D. Buck *et al.*, *Cell* **166**, 63–76 (2016).
3. M. Khacho *et al.*, *Cell Stem Cell* **19**, 232–247 (2016).
4. A. Kasahara, S. Cipolat, Y. Chen, G. W. Dorn 2nd, L. Scorrano, *Science* **342**, 734–737 (2013).
5. A. Bahat, A. Gross, *J. Biol. Chem.* **294**, 13852–13863 (2019).
6. L. Pernas, L. Scorrano, *Annu. Rev. Physiol.* **78**, 505–531 (2016).
7. R. Rizzuto, M. Brini, P. Pizzo, M. Murgia, T. Pozzan, *Curr. Biol.* **5**, 635–642 (1995).
8. P. Mishra, D. C. Chan, *Nat. Rev. Mol. Cell Biol.* **15**, 634–646 (2014).
9. M. G. Paez-Segala *et al.*, *Nat. Methods* **12**, 215–218, 4, 218 (2015).
10. L. Telley *et al.*, *Science* **351**, 1443–1446 (2016).
11. D. Wang *et al.*, *Angew. Chem. Int. Ed.* **51**, 9302–9305 (2012).
12. A. Cassidy-Stone *et al.*, *Dev. Cell* **14**, 193–204 (2008).
13. N. Taguchi, N. Ishihara, A. Jofuku, T. Oka, K. Mihara, *J. Biol. Chem.* **282**, 11521–11529 (2007).
14. M. Liesa, O. S. Shirihai, *Cell Metab.* **17**, 491–506 (2013).

15. X. R. Bao *et al.*, *eLife* **5**, e10575 (2016).
16. C. Cantó, K. J. Menzies, J. Auwerx, *Cell Metab.* **22**, 31–53 (2015).
17. L. Tiberi *et al.*, *Nat. Neurosci.* **15**, 1627–1635 (2012).
18. S. Hisahara *et al.*, *Proc. Natl. Acad. Sci. U.S.A.* **105**, 15599–15604 (2008).
19. J. Bonnefont *et al.*, *Neuron* **103**, 1096–1108.e4 (2019).
20. I. K. I. K. Suzuki *et al.*, *Cell* **173**, 1370–1384.e16 (2018).
21. I. Espuny-Camacho *et al.*, *Neuron* **77**, 440–456 (2013).
22. C. Dehay, H. Kennedy, *Nat. Rev. Neurosci.* **8**, 438–450 (2007).
23. P. Salomoni, F. Calegari, *Trends Cell Biol.* **20**, 233–243 (2010).
24. T. Edlund, T. M. Jessell, *Cell* **96**, 211–224 (1999).

## ACKNOWLEDGMENTS

We thank members of the laboratory and CBD for helpful discussions and the ULB Light Microscopy Facility for support with imaging. **Funding:** This work was funded by Grants of the European Research Council (GENDEVOCORTEX), the Belgian FWO and FRS/FNRS, the AXA Research Fund, the Belgian Queen Elizabeth Foundation, and the Fondation ULB (to P.V.). Some of the images were acquired on a Zeiss LSM 880 system supported by Hercules AKUL/15/37\_GOH1816N and FWO G.0929.15 to P. Vanden Berghe, KU Leuven. R.I. was supported by a postdoctoral fellowship of the FRS/FNRS, and P.C. holds a Ph.D. fellowship of the FWO (file number 51989). **Author contributions:** Conceptualization and methodology, R.I. and P.V.; investigation, R.I., P.C., and P.V.; formal analysis, R.I., P.C., and P.V.; writing, R.I. and P.V.; funding acquisition, P.V.; resources, P.V.; supervision, P.V. **Competing interests:** The authors declare no competing interests. **Data and materials availability:** All data are available in the manuscript or the supplementary materials. All materials are available upon request from P.V.

## SUPPLEMENTARY MATERIALS

science.sciencemag.org/content/369/6505/858/suppl/DC1  
Materials and Methods  
Figs. S1 to S5  
Reference (25)  
MDAR Reproducibility Checklist

[View/request a protocol for this paper from Bio-protocol.](#)

7 February 2020; accepted 22 June 2020  
10.1126/science.aba9760



## PALEOANTHROPOLOGY

# Fire and grass-bedding construction 200 thousand years ago at Border Cave, South Africa

Lyn Wadley<sup>1\*</sup>, Irene Esteban<sup>1,2</sup>, Paloma de la Peña<sup>1</sup>, Marine Wojcieszak<sup>1,3</sup>, Dominic Stratford<sup>4</sup>, Sandra Lennox<sup>1</sup>, Francesco d'Errico<sup>5,6</sup>, Daniela Eugenia Rosso<sup>7,8</sup>, François Orange<sup>9</sup>, Lucinda Backwell<sup>1,10</sup>, Christine Sievers<sup>4</sup>

Early plant use is seldom described in the archaeological record because of poor preservation. We report the discovery of grass bedding used to create comfortable areas for sleeping and working by people who lived in Border Cave at least 200,000 years ago. Sheaves of grass belonging to the broad-leaved *Panicoidae* subfamily were placed near the back of the cave on ash layers that were often remnants of bedding burned for site maintenance. This strategy is one forerunner of more-complex behavior that is archaeologically discernible from ~100,000 years ago.

About 1 million years ago, an ephemeral fire was lit in Wonderwerk Cave, South Africa (1), and traces of fire have been dated to 1.5 million years ago at the open campsite FxJj20 in Koobi Fora, Kenya (2). Fire was used in the Spanish rock shelter Cueva Negra del Estrecho del Río Quípar 800,000 years (800 ky) ago (3), and it was used 780 ky ago at the open-air site Geshen Benot

Ya'akov, Israel (4). These rare early occurrences suggest the expedient harvesting of fire—for example, from lightning strikes—whereas stacked hearths and evidence for multiple uses of heat imply the ability to produce fire at will. After ~400 ky ago, fire appeared regularly in archaeological sites (5–8), where it was probably used for cooking, heating, light, socializing, and protection from predators.

In this work, we present evidence for other uses of fire, and its products, before 200 ky ago. People inhabiting Border Cave, South Africa, systematically placed floor coverings (bedding) of broad-leaved grass above ash layers, set hearths nearby, and occasionally burned their bedding. Before this discovery, the oldest-known plant bedding was 77 ky old from Sibudu, South Africa (9), and younger examples were found to occur in other archaeological sites (10–12). At Sibudu, layered sedge was garnished with medicinal plants, and stale bedding was sometimes burned (9). Border Cave data indicate that such practices began far earlier.

Border Cave is located in the Lebombo Mountains of KwaZulu-Natal, on the eSwatini border (fig. S1). Excavations between 2015 and 2019 (13) (Fig. 1A) have yielded archaeological data (14) not retrieved previously (15). The cave was occupied intermittently from before 227 ky ago until ~1000 CE (16) (table S1), and it is made up of alternating brown sand (BS) and white ash (WA) stratigraphic members (15). Member 6 Brown Sand (6 BS) rests on cave bedrock (Fig. 1B and fig. S2). Above this is Member 5 White Ash (5 WA), the base and top of which have ages of  $227 \pm 11$  and  $183 \pm 20$

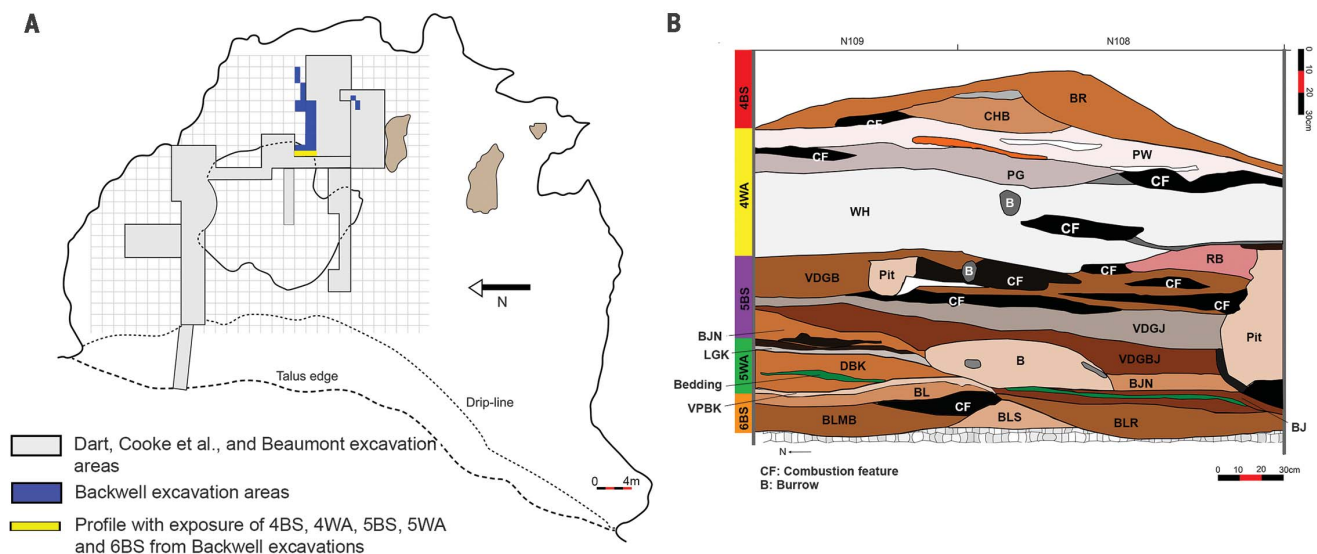


**Fig. 1. Border Cave plan and stratigraphy.** (A) Plan of Border Cave marking excavation areas. The profile featured in (B) (13) is shown in yellow. (B) East profile stratigraphy in squares N109, E113 and N108, E113. The thickest 5WA-DBK bedding is green, but the entire layer contains silicified grass fragments (see Fig. 4). Large combustion features (CFs), but not small ones (as shown in Fig. 4), are illustrated here. 4WA-WH comprises 12 superimposed layers of ash. Scale bar, 30 cm. For greater detail, see fig. S2; for profiles of more recent layers, see (13). B, burrow; BR, Brown; CHB, Chocolate Brown; PW, Pinkish White; PG, Pinkish Gray; WH, White; RB, Reddish Brown; VDGB, Very Dark Grayish Brown; VDGB, Very Dark Grayish Brown; VDGBJ, Very Dark Grayish Brown Jim; BJN, Brown John; LGK, Light Gray Kelly; DBK, Dark Brown Kevin; VPBK, Very Pale Brown Kim; BJ, Brown Jolly; BL, Brown Lad; BLR, Brown Larry; BLS, Brown Lassy; BLMB, Brown Lamb.

<sup>1</sup>Evolutionary Studies Institute, University of the Witwatersrand, 1 Jan Smuts Avenue, Braamfontein 2001, Johannesburg, South Africa. <sup>2</sup>African Centre for Coastal Palaeoscience, Nelson Mandela University, Port Elizabeth, Eastern Cape 6031, South Africa. <sup>3</sup>Royal Institute for Cultural Heritage, Jubelpark 1, 1000 Brussels, Belgium. <sup>4</sup>Archaeology Division, School of Geography, Archaeology and Environmental Studies, University of the Witwatersrand, 1 Jan Smuts Avenue, Braamfontein 2001, Johannesburg, South Africa. <sup>5</sup>PACEA UMR 5199, University of Bordeaux, CNRS, Allée Geoffroy Saint-Hilaire, 33600 Pessac, France. <sup>6</sup>SFF Centre for Early Sapiens Behaviour (SapienCE), University of Bergen, Øysteinsgate 3, 5020 Bergen, Norway. <sup>7</sup>CNRS - CEPAM UMR 7264, Université Côte d'Azur, 24, Avenue des Diables Bleus, 06300 Nice, France. <sup>8</sup>Università degli Studi di Ferrara, Dipartimento degli Studi Umanistici, Sezione di Scienze Preistoriche e Antropologiche, Corso Ercole I d'Este 32, 44121 Ferrara, Italy. <sup>9</sup>Université Côte d'Azur, Centre Commun de Microscopie Appliquée (CCMA), 28, Avenue Valrose, 06108 Nice, France. <sup>10</sup>Instituto Superior de Estudios Sociales (ISES-CONICET), San Lorenzo 429, San Miguel de Tucumán, CP4000, Tucumán, Argentina.

\*Corresponding author. Email: lyn.wadley@wits.ac.za

(means and standard error) ky ago, respectively (17). 6 BS is undated, so the start date of >300 ky ago for 5 WA that has been suggested by Bayesian modeling may be overestimated (18). Hearths, ash layers (fig. S2), and grass bedding (table S2) are visible throughout the Border Cave sequence (13). Stratigraphic profiles (13) show that bedding of all ages is generally located in the warm rear of the cave, and hearths often abut beds so that grass ends are scorched. Nonetheless, accidental incineration of beds was probably infrequent because most are desiccated, not burned (table S2). Thick ash in the cave center [for example, 4WA-WH (Member 4

White Ash, layer White) in Fig. 1B] confirms repeated fire making there by 170 ky ago, perhaps for protection from predators, but likely also for domestic uses, such as cooking and sharing *Hypoxis* rhizomes (14).

The oldest recovered bedding is from Member 5 WA, layer Dark Brown Kevin (5WA-DBK). In large-scale, rapid excavations of the past century, this material was largely removed but not recorded; therefore, site-wide spatial inferences must be made cautiously. Organic material degrades over time (19, 20), so 5WA-DBK bedding survives as visually ephemeral fragments of silicified plant (Fig. 2, A, B, and C,

and fig. S3). Its original appearance is exemplified by younger bedding features that are better preserved (Fig. 2D).

Grass in 5WA-DBK bedding was identified further by Fourier transform infrared (FTIR) spectroscopy, scanning electron microscopy (SEM), and phytolith analysis (16) (Fig. 3, figs. S4 to S14, and tables S3 to S6). Silicified plant fragments viewed at high magnification using SEM (16) reveal grass anatomy (Fig. 3, A and C). Phytolith analysis confirms the presence of prickles, stomata, and epidermal long and short cell bilobates that characterize the Panicoideae subfamily of grasses (Poaceae), especially *Melinis repens* (Willd.) Zizka, *Setaria pallide-fusca* (Schumacher) Stapf & C.E. Hubb., *Panicum maximum* Jacq., *Panicum deustum* Thunb., and *Themeda triandra* Forssk. (16) (Fig. 3, B and D, and fig. S14). The Border Cave phytolith concentration exceeds that from other archaeological sites (12, 16) (tables S5 and S7), and we infer intentional, intensive grass accumulation. Moreover, dicotyledonous epidermal leaf fragments, mostly lying on grass as articulated phytoliths, comprise at least three cell shapes, which implies the presence of several unidentifiable species. Charcoal in bedding (table S8) includes *Tarchonanthus trilobus* DC (broad-leaved camphor-bush) that has aromatic leaves like those from *T. camphoratus*, which is used as insect repellent in modern plant bedding in Africa (21). The identified grass and woody species still grow in woodland near the cave (supplementary text).

Thin sections made from 5WA-DBK sediment reveal details of the layered ash and plant material at millimeter scale (Fig. 4, C, D, E, and F, and fig. S15), which implies multiple phases of hearth and bed construction. Charred grass, charcoal, ash, and calcined bone fragments in some 5WA-DBK bedding phases (16) (Fig. 4, fig. S15, and supplementary text) imply that these beds were occasionally burned for site maintenance before being refreshed [as described in (22, 23)]. 5WA-DBK sediments are compressed against underlying ashy layer 5WA-VPBK (Member 5 WA, layer Very Pale Brown Kim). Both layers, especially 5WA-VPBK, are silicate- and apatite-rich (this includes carbonated hydroxyapatite) (figs. S5 to S7). The ash of *Panicum maximum*, one likely bedding grass at Border Cave, contains apatite among other minerals (16, 24) (fig. S9). The chemical content and high phytolith concentration in 5WA-VPBK (tables S3 to S5) imply burning of grass bedding there too (16). The chemistry might also signal the presence of bone, guano, or diagenetically altered calcite (16, 25, 26). Calcite is a better-known component of ash than apatite, and in bedding younger than that found in 5WA-DBK, layers of calcitic ash underlie desiccated grass bedding (16) (fig. S8). Although this is probably wood ash, we must be circumspect because ash studied

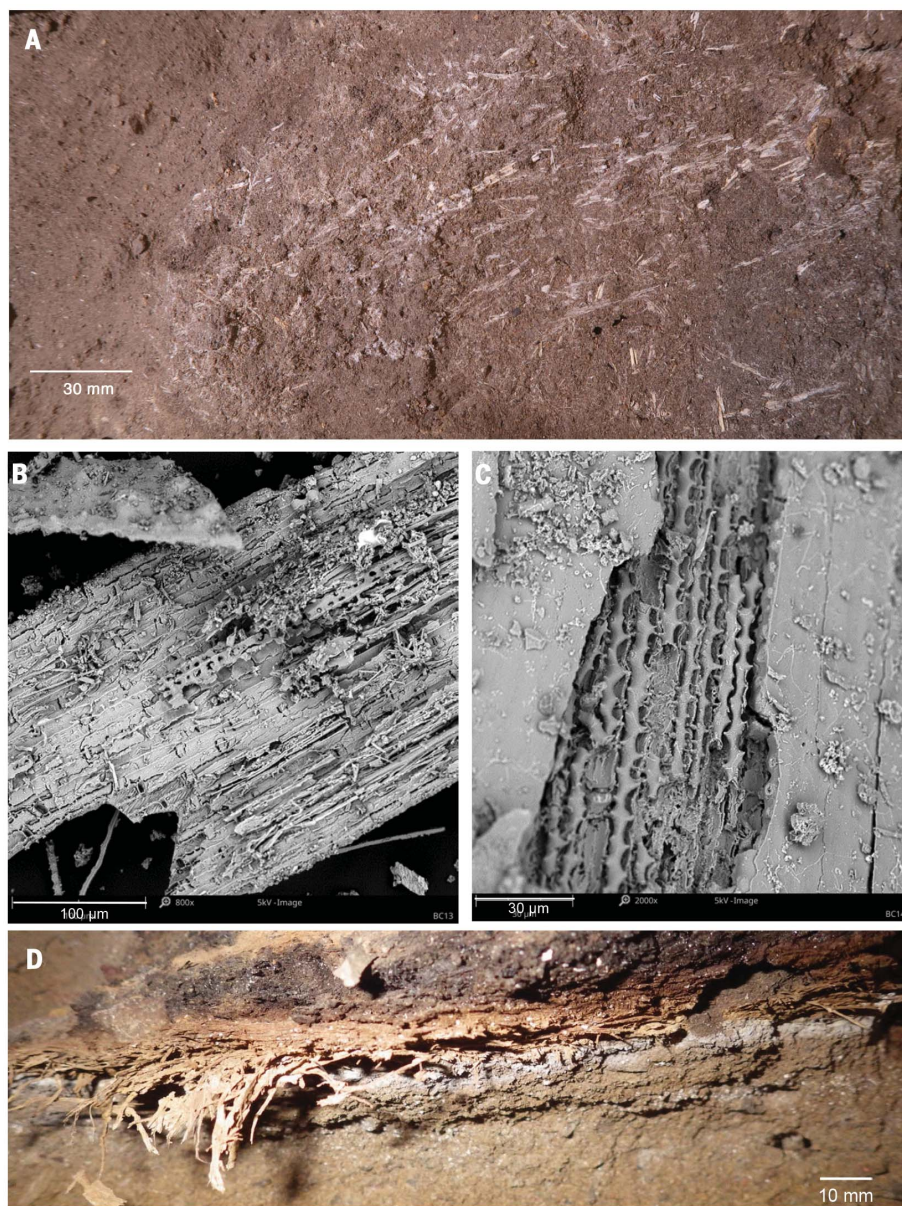


**Fig. 2. Border Cave plant bedding from 5WA-DBK and 1 WA.** (A) Horizontal field view of silicified bedding in 5WA-DBK. Scale bar, 30 mm. (B and C) SEM images of grass fragments from (A). Scale bar in (B), 100 µm. Scale bar in (C), 30 µm. (D) Vertical field section of desiccated bedding grass on Member 1 WA ash (~43 ky old). 5WA-DBK bedding may have looked like this 200 ky ago. Scale bar, 10 mm.



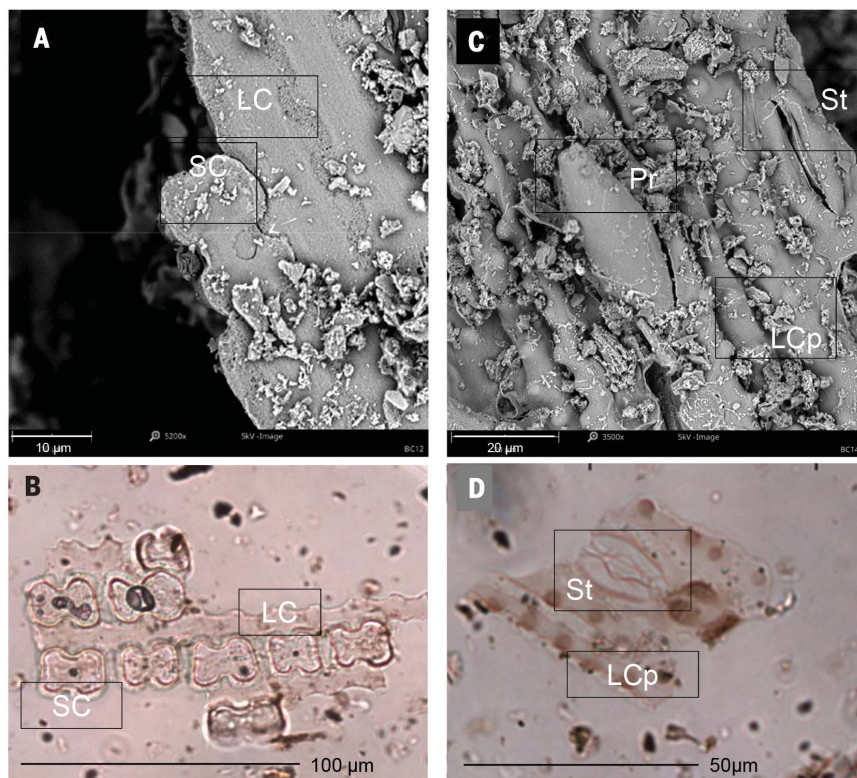


**Fig. 3. Silicified Panicoidae grass remains from plant bedding in 5WA-DBK.** (A) SEM image of silicified grass epidermis showing articulated short cell bilobate and epidermal long cells. Scale bar, 10 µm. (B) Microphotograph of silicified grass epidermis showing articulated short cell bilobate and epidermal long cells. Scale bar, 100 µm. (C) SEM image of silicified grass epidermis showing articulated epidermal long cells with papillate ornamentation, prickle, and stomata. Scale bar, 20 µm. (D) Microphotograph of silicified grass epidermis showing articulated epidermal long cells with papillate ornamentations and stomata. Scale bar, 50 µm. LC, long cell; LCp, long cell papillate; SC, short cell; Pr, prickle; St, stomata.

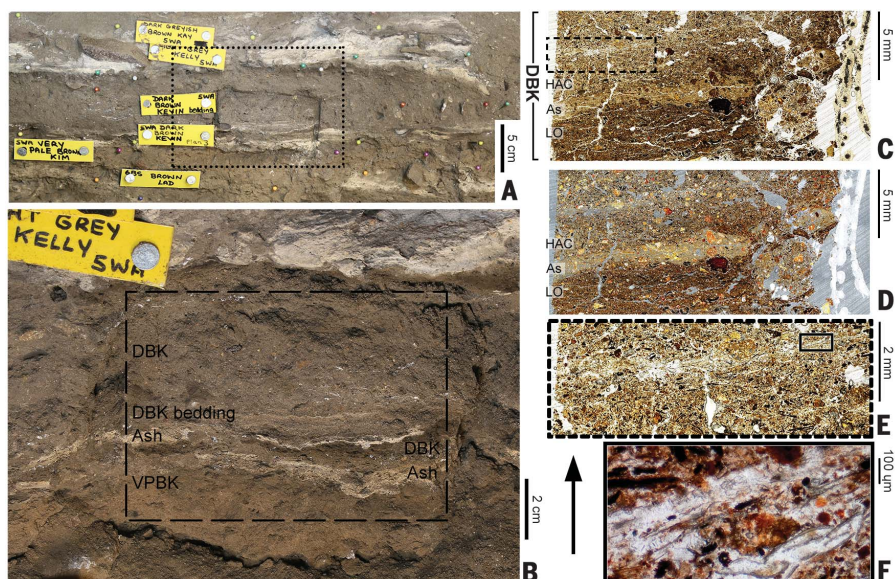


**Fig. 4. Border Cave plant bedding observed in the field and in thin sections of 5WA-DBK sediment.** (A) East profile of part of the stratigraphy from Fig. 1B. Scale bar, 5 cm. (B) Magnified image of 5WA-DBK stratigraphy showing the position of the micromorphological sample (black-dashed square). Scale bar, 2 cm. (C and D) Microphotographs of 5WA-DBK thin section 1/1. Microfacies include homogeneous anthropogenic components (HACs), ash (As), and dark brown laminar units rich in organic matter (LOs) (16). Image in (C) was taken with plane polarized light (PPL) and that in (D) with cross-polarized light (XPL) (16). Scale bars, 5 mm. (E) Magnified microphotograph of silicified, laminar bedding in black-dashed square in (C), taken with PPL. Scale bar, 2 mm. (F) Magnified image of plant remains in solid black square in (E), taken with PPL. Further detail is available in the supplementary text and fig. S15. Scale bar, 100 µm.

from 35 European plant species revealed diverse chemical compositions (27). Ash was possibly raked from hearths to create a clean, odor-controlling base for bedding. We speculate that such placement of bedding, as well as that on the ashes of previously burned bedding, was deliberate, because several ethnographies report that ash repels crawling insects, which cannot easily move through fine powder because it blocks their breathing and biting

apparatus and eventually leaves them dehydrated (28).

Stone flake and blade manufacture (tables S9 and S10 and figs. S16 and S17) on 5WA-DBK bedding surfaces demonstrate their occasional use as workspace. The lithics described here cannot be assigned to a specific industry, but they resemble those in the 1987 Member 5 WA collection, labeled MSA 1 (29), from which a few pieces of ochre were also recovered. In

5WA-DBK bedding, red and orange ochre grains are up to 37 times as frequent as in over- and underlying layers, and they are smaller and rounder than the dark red, angular fragments from cave roof detritus that provides an ochre source (figs. S18 and S20 and tables S11 to S13). This evidence, together with reports of regular ochre use in Africa from ~300 ky ago (30), supports the hypothesis that 5WA-DBK ochre particles were processed



anthropogenically and became detached from objects or human skin when people used the bedding. Elemental and mineralogical analyses cannot distinguish grains from bedding and those from over- and underlying layers (figs. S20 to S22 and tables S14 to S17), so either people collected and processed ochre from the cave rock or the 5WA-DBK grains have a natural origin that we cannot explain.

Modern hunter-gatherer camps have fires as focal points; people regularly sleep alongside them and perform domestic tasks in social contexts (31, 32). People at Border Cave also lit fires regularly, as seen throughout the sequence (13) and not only in the layered ash and grassy sediment of 5WA-DBK. Before 200 ky ago, close to the origin of our species, people could produce fire at will and used fire, ash, and medicinal plants to maintain clean, pest-free camps. Although hunter-gatherers are characteristically mobile, cleansing camps can extend their potential for occupancy. The simple strategies inferred from the Border Cave data not only broaden our knowledge of life-ways in the remote past, but they also suggest an early potential for the cognitive, behavioral, and social complexity that is more widely evident in innovative material culture from ~100 ky ago (33).

## REFERENCES AND NOTES

1. F. Berna et al., *Proc. Natl. Acad. Sci. U.S.A.* **109**, E1215–E1220 (2012).
2. S. Hlubik, F. Berna, C. Feibel, D. Braun, J. W. K. Harris, *Curr. Anthropol.* **58**, S243–S257 (2017).
3. M. J. Walker et al., *Antiquity* **90**, 571–589 (2016).
4. N. Goren-Inbar et al., *Science* **304**, 725–727 (2004).
5. W. Roebroeks, P. Villa, *Proc. Natl. Acad. Sci. U.S.A.* **108**, 5209–5214 (2011).
6. R. Shimelmitz et al., *J. Hum. Evol.* **77**, 196–203 (2014).
7. R. Barkai, J. Rosell, R. Blasco, A. Gopher, *Curr. Anthropol.* **58**, S314–S328 (2017).
8. P. Vidal-Matutano, R. Blasco, P. Sañudo, J. Fernández Peris, *Environ. Archaeol.* **24**, 269–284 (2019).
9. L. Wadley et al., *Science* **334**, 1388–1391 (2011).
10. A. M. Rosen, in *Neanderthals in the Levant: Behavioral Organization and the Beginnings of Human Modernity*, D. O. Henry, Ed. (Continuum, 2003), pp. 156–171.
11. D. Nadel et al., *Proc. Natl. Acad. Sci. U.S.A.* **101**, 6821–6826 (2004).
12. D. Cabanes, C. Mallol, I. Expósito, J. Baena, *J. Archaeol. Sci.* **37**, 2947–2957 (2010).
13. L. R. Backwell et al., *J. Field Archaeol.* **43**, 417–436 (2018).
14. L. Wadley, L. Backwell, F. d'Errico, C. Sievers, *Science* **367**, 87–91 (2020).
15. P. B. Beaumont, thesis, University of Cape Town, South Africa (1978).
16. Materials and methods are available as supplementary materials.
17. R. Grün, P. Beaumont, P. V. Tobias, S. Eggins, *J. Hum. Evol.* **45**, 155–167 (2003).
18. A. R. Millard, *Quat. Geochronol.* **1**, 159–166 (2006).
19. S. Schiegl, P. Goldberg, O. Bar-Yosef, S. Weiner, *J. Archaeol. Sci.* **23**, 763–781 (1996).
20. M. G. Canti, *Catena* **54**, 339–361 (2003).
21. H. J. Beentje, *Kew Bull.* **54**, 81–95 (1999).
22. P. Goldberg et al., *Archaeol. Anthropol. Sci.* **1**, 95–122 (2009).
23. S. M. Mentzer, *J. Archaeol. Method Theory* **21**, 616–668 (2014).
24. S. Schiegl, P. W. Stockhammer, C. Scott, L. Wadley, *S. Afr. J. Sci.* **100**, 185–194 (2004).
25. R. M. Albert, S. Weiner, O. Bar-Yosef, L. Meignen, *J. Archaeol. Sci.* **27**, 931–947 (2000).
26. P. Karkanas, O. Bar-Yosef, P. Goldberg, S. Weiner, *J. Archaeol. Sci.* **27**, 915–929 (2000).
27. G. Zajac, J. Szyszlak-Bargłowicz, W. Gołębowski, M. Szczepaniak, *Energies* **11**, 2885 (2018).
28. T. Hakbiji, *Environ. Archaeol.* **7**, 13–22 (2002).
29. I. Watts, thesis, University of London (1998).
30. A. S. Brooks et al., *Science* **360**, 90–94 (2018).
31. P. W. Wiessner, *Proc. Natl. Acad. Sci. U.S.A.* **111**, 14027–14035 (2014).
32. C. Mallol, A. Henry, *Curr. Anthropol.* **58**, S217–S229 (2017).
33. F. d'Errico et al., *Proc. Natl. Acad. Sci. U.S.A.* **114**, 7869–7876 (2017).

## ACKNOWLEDGMENTS

L.W. and C.S. thank the South African National Biodiversity Institute, and they thank J. van Rooy for the use of the Phenom Pure SEM. A. Millard provided numerical data from his 2006 Bayesian analysis of electron spin resonance dates. **Funding:** L.B. was funded by National Geographic (NGS-54810R-19) and the DSI-NRF (Department of Science and Innovation–National Research Foundation) Centre of Excellence in Palaeosciences (COEP2020-1). I.E. and P.d.I.P. acknowledge the DSI-NRF Centre of Excellence in Palaeosciences. D.E.R. was funded by the Fyssen Foundation, France, and the l'Oréal-UNESCO "Per le Donne e la Scienza" program (l'Oréal Italia and Italian National Commission for UNESCO, Italy). F.d'E. was funded by the Talents program of the Initiative d'Excellence of the University of Bordeaux, the Agence Nationale de la Recherche – LaScArBx Cluster of Excellence (ANR-10-LABX-52), and the Research Council of Norway through its Centre of Excellence funding scheme [SFF Centre for Early Sapiens Behavior (SapienCE) project number 262618]. **Author contributions:** Botanical investigation, formal analysis, and project conceptualization: L.W. and C.S. Site excavation: L.B., F.d'E., L.W., P.d.I.P., C.S., and D.S. 5WA-DBK bedding excavation: L.W. Phytolith study and some attenuated total reflectance (ATR)-FTIR: I.E. Lithic study and Fig. 1: P.d.I.P. ATR-FTIR and Raman analysis: M.W. Energy-dispersive x-ray fluorescence (EDXRF) and SEM–energy-dispersive x-ray spectroscopy (EDS): D.E.R. Micromorphology: D.S. Charcoal analysis: S.L. Ochre analysis: F.d'E., D.E.R., and F.O. Writing: L.W. with contributions from all other authors. All authors reviewed and edited the manuscript. **Competing interests:** The authors declare no competing interests. **Data and materials availability:** All data and materials are included in the text and supplementary materials. The Border Cave excavated material from 2015 to 2019 is housed in the Evolutionary Studies Institute, University of the Witwatersrand, Johannesburg, South Africa (Border Cave 2015/2019). See supplementary materials for additional acknowledgments.

## SUPPLEMENTARY MATERIALS

science.sciencemag.org/content/369/6505/863/suppl/DC1  
Materials and Methods  
Supplementary Text  
Figs. S1 to S22  
Tables S1 to S17  
References (34–96)

10 May 2020; accepted 22 June 2020  
10.1126/science.abc7239

## INTERGROUP RELATIONS

# Building social cohesion between Christians and Muslims through soccer in post-ISIS Iraq

Salma Mousa

Can intergroup contact build social cohesion after war? I randomly assigned Iraqi Christians displaced by the Islamic State of Iraq and Syria (ISIS) to an all-Christian soccer team or to a team mixed with Muslims. The intervention improved behaviors toward Muslim peers: Christians with Muslim teammates were more likely to vote for a Muslim (not on their team) to receive a sportsmanship award, register for a mixed team next season, and train with Muslims 6 months after the intervention. The intervention did not substantially affect behaviors in other social contexts, such as patronizing a restaurant in Muslim-dominated Mosul or attending a mixed social event, nor did it yield consistent effects on intergroup attitudes. Although contact can build tolerant behaviors toward peers within an intervention, building broader social cohesion outside of it is more challenging.

**O**n 10 June 2014, the Islamic State of Iraq and Syria (ISIS) captured the Iraqi city of Mosul. ISIS's offensive culminated in a genocide against Yazidis, Christians, Shi'a, and other minorities, displacing ~100,000 Christians to Iraqi Kurdistan overnight (1). Many Christians believe that their Muslim neighbors were complicit in these raids. These suspicions have discouraged Christians from returning to liberated areas, fueled support for self-defense militias, and heightened the potential for reprisal killings and future conflict (2). At the same time, Muslim communities from neighboring villages have been migrating into Christian enclaves, leading Iraq's Christians to fear the dilution of their culture and identity (3). Christian-Muslim relations in northern Iraq continue to be marked by mutual distrust and social segregation.

How can social cohesion between groups be rebuilt after war? Intergroup social cohesion, patterns of cooperation among individuals from different social groups who live and work in close proximity (4), is considered key for good governance (5) and economic development (6). However, countries recovering from war often backslide into violence and instability despite heavy international investment in state-building and peacekeeping (7). Sustainable peace requires a combination of policy interventions, such as power-sharing arrangements, and grassroots initiatives that aim to improve interactions between individuals (8). Meaningful intergroup contact represents one such grassroots approach.

Here, I provide causal evidence on whether meaningful contact between groups can build social cohesion after war. Using a field experiment among Iraqis displaced by ISIS, I randomly assigned amateur Christian soccer players to an all-Christian team or to a team mixed with three Muslims for a 2-month

league. The leagues largely met the conditions considered key for activating successful intergroup contact: Teammates had to cooperate to achieve their shared goal, players were subject to the equalizing effect of team sports, and local Christian leaders and organizations endorsed the leagues. This study thus serves as a proof of concept that near-optimal contact can build tolerant behaviors after violent conflict—at least toward those encountered in the intervention. The positive effects of contact among Christian study participants did not, however, generalize to Muslim strangers, highlighting a potentially important limitation of contact after war.

The “contact hypothesis” proposes that interpersonal contact across group lines can reduce prejudice if it is cooperative, places participants on equal footing, is endorsed by communal authorities, and is characterized by a common goal (9). Causal evidence shows that such contact reduces prejudice in several nonconflict settings by highlighting commonalities, forging friendships, lowering intergroup anxiety, and inducing empathy (10–12). On the other hand, wordless physical exposure has been found to exacerbate prejudice (13–16), and competitive contact has a similarly negative effect (17). These findings suggest that meaningful (positive and cooperative) contact might hold the potential to rebuild tolerance, at least in times of peace.

Should we expect contact to be similarly effective in conflict settings? Only a handful of contact studies involve groups in conflict (18, 19), in part because contact is more likely to be negative in these settings, which disproportionately shapes prejudice (20). The evidence we do have indicates that studies of ethnic prejudice generate “substantially weaker effects” relative to interventions aimed at reducing prejudice toward other stigmatized groups such as the elderly or the disabled, suggesting that the cleavages common to war are particularly rigid. Relatedly, ethnic violence

solidifies group identities, ethnic prejudices, and anxieties around being physically proximate to the outgroup, further tempering expectations around the impacts of contact after war (21–27).

Methodological constraints also limit our knowledge of intergroup contact. Contact is most effective if its effects can be generalized to an entire outgroup rather than just to individuals encountered in an intervention (28). However, most contact studies determine the generalization of contact effects using self-reported attitudes measured immediately after the intervention (29). Policy-makers have subsequently questioned whether contact can change actual behaviors toward the outgroup in lasting ways (19). In response to this concern, I tested the generalization hypothesis using real-world behaviors.

Despite the differences between Christians and Muslims in northern Iraq, amateur soccer is popular among both groups. Scholars and policy-makers consider cross-cutting civic associations such as amateur sports clubs to be engines for social capital (30–33). Intergroup sports in particular exemplify the “positive, energetic, community events...centered on non-political issues” (34) that facilitate the “sustained, meaningful interaction with members of different groups” recommended by policy-makers to integrate communities affected by ISIS (35).

Leveraging the social potential of team sports, the experiment comprised four soccer leagues spread across two waves and study sites (table S2 and fig. S5). Research staff invited Christian teams in two northern Iraqi cities to participate. Forty-two of the ~45 teams in the area were recruited on a first come, first served basis, resulting in a sample size that varied between 183 and 459 Christian players depending on the outcome (see the supplementary materials and methods). Captains were told that a local Christian community organization was working with a United States-based university to offer a soccer league for displaced people and to research their experiences. Participants were told that community-building was one of the leagues' aims and, as such, each team would be allocated an additional three players who may or may not be Christian in an effort to include diverse groups. Treated teams received additional Muslim players drawn from local Muslim teams, whereas control teams received fellow Christians. Christian and Muslim added players were indistinguishable in baseline skill (table S4), and league guidelines ensured that they played roughly the same number of minutes per game (see the supplementary text). A total of 91.8% of contacted participants were retained until the end of the study, whereas the remainder dropped out before treatment assignments were made or because of injuries sustained during games. Because Muslims were only

present in the treated group by design, they were excluded from the main analysis, although I measured changes in their attitudes over time.

Christians comprised the majority group in the study sites but remain an at-risk minority in Iraq, which has important implications for the dynamics of intergroup contact. To mitigate the power differentials between Muslims and Christians, and to increase the comfort of Christian participants, discussions between the research team and coaches concluded that Muslim players should remain a numeric minority (~25%) of each squad. This ethnic composition likely lowered perceived intergroup threat while preserving strong team identities (36). Further tempering intergroup anxieties, all Muslim participants had been displaced by ISIS regardless of denomination (45% Sunni Arab and 55% Shi’ite Shabak). This team composition likely biased in favor of a positive contact experience.

Limiting the study to internally displaced people also ensured that Christians would not come into contact with possible ISIS collaborators. It is important to note that Christians are marginalized (or persecuted outright) in many parts of the Arab world, where prejudice among some segments of the Muslim majority poses the larger challenge. The research team’s access to the Christian community, however, and the anticipated benefits of building social cohesion between displaced communities motivated the focus on Christian regard toward Muslims in this study. Other ethical considerations, and the steps taken to address them, are detailed in the supplementary text.

Participants were offered a baseline and end-line survey described as helping researchers understand the attitudes and experiences of displaced Iraqis. I used a baseline survey item capturing perceived commonalities with Muslims to conduct a block randomization. The item asked respondents to rate how much they had in common with Sunni Arabs on a four-point scale with no neutral option. I ranked each team based on their average response to this item and randomized within closely ranked pairs. Figure S1 and table S5 show the balance on baseline demographics and attitudes between the treatment and control groups.

In addition to these experimental leagues, I also created a comparison league without any Muslim players to explore the effects of no intergroup exposure at all. Assignment to this league was nonrandom, however, and these groups were not eligible to receive Muslim players. I used data from the comparison group for exploratory analyses.

This study investigated intergroup social cohesion as opposed to intragroup cohesion, which can be strengthened by war (4, 37). I focused on two core components of social

cohesion: interactions with outgroup peers (what I label “on-the-field outcomes”) and interactions with outgroup strangers (“off-the-field outcomes”) (38, 39).

On-the-field outcomes captured tolerant behaviors toward teammates or league-mates. First, at the end of the season, participants

voted for an added player to receive a “best newcomer” award based on sportsmanship. This player could not be on the respondent’s team. A positive treatment effect on this outcome signifies reduced ingroup bias (17). Second, the end-line survey asked players if they agreed to register for a mixed team next

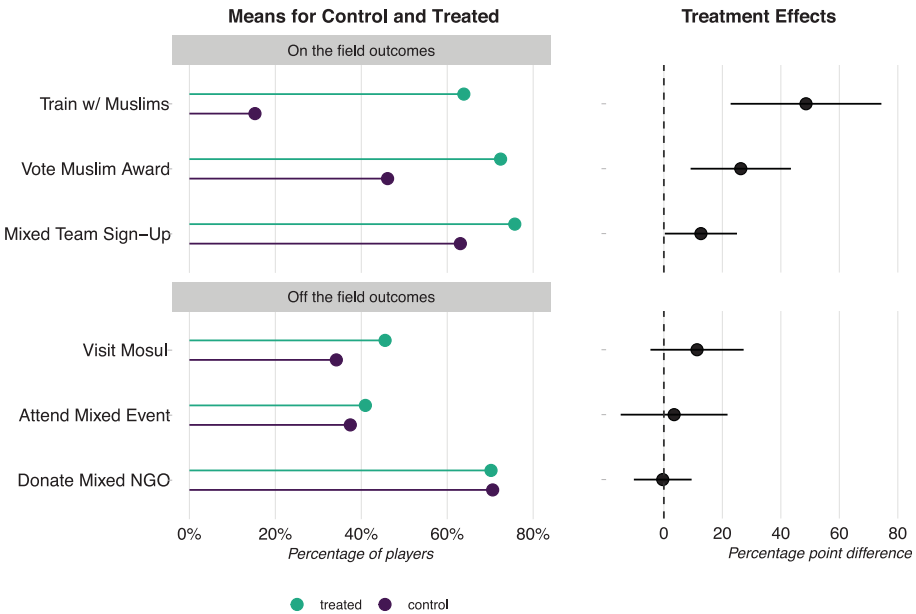


**Fig. 1. Behavioral results.** The intervention consistently improved on-the-field behavioral outcomes, with no detectable effects on off-the-field outcomes. The left panel shows covariate-adjusted mean outcomes for treated and control players, with covariates held at median or modal values. The right panel shows the difference between treated and control players, with 95% confidence intervals.

Table 1. Primary behavioral and attitudinal outcomes	
Behavioral outcomes	
1. Attend mixed dinner event (3 weeks to 5 months postintervention)	
2. Train with Muslims at least once a week (6 months postintervention)	
3. Patronize restaurant in Mosul (1 to 4 months postintervention)	
4. Donate \$1 survey compensation to church versus neutral nongovernmental organization (2 weeks to 5 months postintervention)	
5. Vote for Muslim player to receive sportsmanship prize (2 weeks to 5 months postintervention)	
6. Register for mixed team in the future (2 weeks to 5 months postintervention)	
Attitudinal indices (2 weeks to 5 months postintervention)	
1. National unity	
1.1 Believe that Iraq would be a better society if Iraqis treated each other as Iraqis first	
1.2 Believe that dividing Iraq into ethnic and religious groups is arbitrary	
2. Muslims as neighbors	
2.1 Comfortable with Shi’ite Shabak as neighbor	
2.2 Comfortable with Sunni Shabak as neighbor	
2.3 Comfortable with Shi’ite Arab as neighbor	
2.4 Comfortable with Sunni Arab as neighbor	
3. Blaming Muslims	
3.1 Believe that Shi’ite Shabak are responsible for Christian suffering	
3.2 Believe that Sunni Arabs are responsible for Christian suffering	



season. Third, the research staff contacted players 6 months after the league's end to record whether they regularly trained with Muslims.

Off-the-field outcomes focused on behaviors toward Muslims outside of the intervention, capturing the intervention's ability to overcome social segregation and build broader social cohesion. First, all players were invited to attend a neighborhood social event consisting of traditional dancing and dinner that took place up to 4 months after the intervention ended. Players were encouraged to bring their families and friends, meaning that Christians were confronted with the possibility of socializing not only with Muslim players, but also with Muslim players' family members and friends. The outcome of interest was whether a player attended and, conditional on attending, whether he brought his female family members. Second, I instituted a voucher system to track whether treated players were more likely to patronize businesses in Muslim neighborhoods. All players receive an \$8 (USD) voucher for a restaurant in Muslim-majority Mosul, a 40-min car ride away. Each voucher was stamped with the player's individual identification number, was valid for 4 months after the intervention ended, and was stored by the restaurant manager when availed. Third,

I recorded whether participants chose to donate their \$1 survey compensation to a Christian organization (most commonly, one's local church) or to a neutral non-governmental organization that benefits both Muslims and Christians (e.g., a cancer ward or orphanage).

I also recorded a set of outcomes that focused on intergroup attitudes rather than behaviors. I combined similar survey items into an index to reduce measurement error. I did this using an unsupervised hierarchical clustering algorithm, a data-driven method for identifying latent clusters in survey data (described in the supplementary materials and methods). I then conducted a factor analysis on these clusters. The Cronbach's alpha for each index was between 0.5 and 0.7, indicating strong internal consistency given the low number of items in each index. The resulting indices—now dependent variables—cover national unity, comfort with Muslims as neighbors, and blaming Muslim civilians for Christian suffering (Table 1).

For the main analysis, I estimated the average treatment effect on each behavioral outcome and attitudinal index, controlling for randomization block and other baseline covariates while clustering standard errors at the team level. Details about the statistical

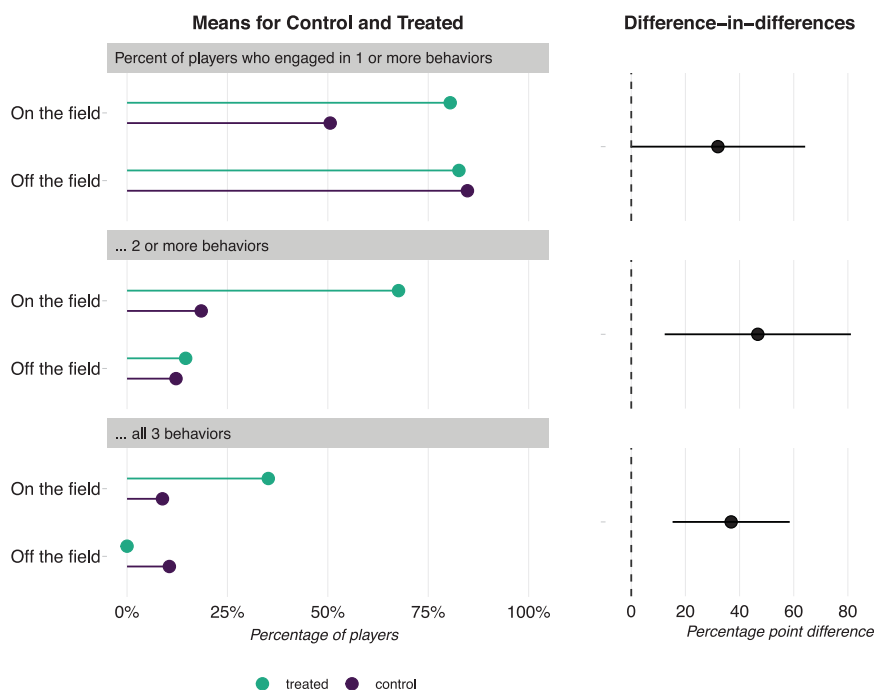
analysis are provided in the supplementary materials and methods. I prespecified all outcomes and analyses, except when otherwise noted as exploratory, in a preregistered analysis plan made available at the American Economics Association website under study ID AEARCTR-0003540.

Figure 1 summarizes the behavioral results. Looking first at tolerance on the field, treated players were 13 percentage points more likely to report that they would not mind being assigned to a mixed team next season ( $P = 0.044$ ), 26 percentage points more likely to vote for a Muslim player (not on their team) to receive a sportsmanship prize ( $P = 0.003$ ), and 49 percentage points more likely to train with Muslims 6 months after the intervention ended ( $P < 0.001$ ). The training outcome does not merely capture the inertia of continuing to play with teammates: 15% of treated teams recruited Muslim players from other teams in the league or from the neighborhood. Qualitative evidence described in the supplementary text provides further evidence of the interventions' positive effects on mixed teams, including newly forged friendships.

Moving to generalized tolerance off the field, estimated effects were smaller and not statistically distinguishable from zero. Treated players were not detectably more likely to attend a mixed social event or to patronize a Muslim-owned restaurant in Mosul up to 4 months after the intervention ended. Conditional on attending the social event, treated players brought their wives at almost identical rates as control players (fig. S6). Moreover, neither self-reported comfort in mixed neighborhoods nor trust in Muslims to receive a cash transfer on one's behalf improved, further suggesting little change with regard toward Muslim strangers (fig. S6).

Exploratory analyses revealed two factors that may have amplified the behavioral effects of contact. First, the treatment improved generalizable behaviors relative to the comparison league, suggesting a beneficial effect to simply having Muslim players in the league itself (figs. S7 to S9). Second, treatment effects were strongest among the most successful teams, operationalized by reaching the final (table S7). Success alone had little effect on tolerance, but playing on a successful, mixed team built tolerance toward Muslim strangers (table S7).

Like behaviors toward Muslim strangers, personal beliefs also proved difficult to change. I found no effect of the treatment on Christians' reported comfort with Muslim neighbors or blame directed at Muslim civilians for Christian suffering. I did observe a positive treatment effect for the national unity index of 0.43 standard deviations ( $P < 0.001$ ), driven by an item reflecting the view that ethnic and religious divisions are arbitrary (fig. S6). Relative to the other indices, the national unity index



**Fig. 2. On-the-field versus off-the-field behaviors.** The intervention shifted the probability of engaging in at least one on-the-field behavior more than it shifted the probability of engaging in at least one off-the-field behavior. The same was true of engaging in at least two behaviors or all three. The left panel shows covariate-adjusted means for the control and treatment groups separately for on-the-field and off-the-field outcomes. The right panel shows differences between on-the-field treatment effects and off-the-field treatment effects (i.e., difference-in-differences), with 95% confidence intervals generated using a block-bootstrapping approach (see the supplementary materials and methods).

mostly captures abstract attitudes rather than beliefs about specific outgroups. I found a similar pattern in an exploratory analysis of local residents ( $n = 121$ ): Exposure to the leagues correlated with a stronger belief in the arbitrariness of group-based divisions, pointing to potential spillover effects among fans (table S11). Among all main analyses, the effects on on-the-field behaviors and the national unity index survived the Benjamini-Hochberg multiple-comparisons correction at the 0.10 level (40) and remained broadly consistent under permutation tests (fig. S10), across study waves (fig. S11), and with block-bootstrapped standard errors (table S1).

As an exploratory analysis, I tested directly whether treatment effects were stronger for on-the-field behaviors relative to off-the-field behaviors. To do this, I estimated the average treatment effect on engaging in at least one, at least two, and all three on-the-field behaviors, and repeated this exercise for off-the-field behaviors. I then tested these treatment effects against each other. As shown in Fig. 2, treated players were consistently more likely to engage in on-the-field behaviors (however measured) relative to control players, whereas the two groups engaged in off-the-field behaviors at similar rates. The intervention's added boost for on-the-field outcomes relative to off-the-field outcomes is estimated at ~30 percentage points or more ( $P \leq 0.05$ ).

Naturalistic studies of contact, especially those that involve competition or take place in the aftermath of war, are likely to involve some amount of negative contact experiences that could negatively affect outcomes (17, 19). Proxying for aggression using yellow and red cards, I did not find evidence of increased hostility among those on all-Christian teams. Table S12 demonstrates that the prevalence of cards did not differ across match types: Matches that brought together all-Christian teams with mixed teams were not more hostile than matches between two treated or two control teams. Moreover, I did not detect differences in the number of cards based on the referee's religious identity (table S13). I also ruled out backlash effects among control participants and Muslim players. Analyzing changes in attitudes over time, neither control participants nor Muslim players became more prejudiced (figs. S12 and S13). These analyses suggest that competitive contact does not worsen prejudiced attitudes but does not alleviate them either.

Ongoing civil wars in the Middle East and Africa, persistent sectarianism across the Arab world, and a dearth of policies aimed at reintegrating communities hit by ISIS in particular have reinvigorated the question of how to build social cohesion in the wake of violence. Despite the potential of intergroup contact, we know little about whether it can build lasting,

real-world behavioral change, especially after war. This study provides causal evidence regarding both of these questions. I found that Christians assigned to compete on a soccer team with Muslim teammates were more likely to engage in tolerant behaviors toward Muslim peers encountered in the intervention up to 6 months after the intervention ended. These improvements did not come at the cost of exacerbating prejudice among the control group, as has been found in other studies of Muslim-Christian contact (21).

Contact was systematically weaker, however, at shifting generalized tolerance toward Muslim strangers. Several factors help to explain why contact effects did not generalize. This pattern could be symptomatic of how contact operates more broadly, compelling researchers to measure long-term, actual behaviors to understand the conditions under which contact effects extend to an entire outgroup [(41); for exceptions from nonconflict zones, see (42) and (43)]. The distrust, hostility, and trauma ingrained by war likely makes generalization all the more challenging. Groups recovering from violent conflict often continue to feel that their well-being, resources, and identity are under threat, conditions that run in stark contrast to the ideals of positive, cooperative contact (44). The quality of contact is particularly important in these settings (45, 46). In this vein, the data suggest that those on successful teams were able to unlock improved behaviors toward outgroup strangers, further indicating that an exceptionally positive experience may be needed to overturn the negative experiences instilled by war and pointing to a fruitful avenue for future work (47). Postconflict settings could also exacerbate the role of minority status, which is known to dilute contact effects (47, 48). Christians remain a targeted minority in Iraq, potentially making generalization of positive effects more difficult relative to members of advantaged groups.

Behaviors toward known contacts versus strangers also differ in costliness, shedding light on this pattern of results. Driving to Mosul entails higher psychological (e.g., intergroup anxiety) and economic (e.g., time and fuel) costs relative to measures such as voting for a peer to receive an award, for instance, possibly decreasing the sensitivity of this class of outcomes. Relatedly, some behaviors may be easier to shift relative to self-reported attitudes, a pattern echoed in other prejudice reduction studies, especially among victims of conflict (21, 45, 49).

Even if contact effects do not generalize to the entire outgroup, strengthening ties between peers could still build resilience and prevent future conflict. I found descriptive evidence of tolerant social norms among local residents most exposed to the leagues, pointing

to the potential for spillover effects. Future work should explore the extent to which localized cohesion can shield these communities from future shocks to tolerance, such as a resurgence in ethnic violence or prejudicial rhetoric by political entrepreneurs. Providing causal answers to these questions can inform the hundreds of millions of dollars allotted by the U.S. Agency for International Development (USAID) for civil society, conflict mitigation, and peace stabilization activities in 2020 (50) and the billions of dollars spent globally on peacebuilding programs (51).

## REFERENCES AND NOTES

1. "Iraq Christians flee as Islamic State takes Qaraqosh." *BBC News*, 7 August 2014; <https://www.bbc.com/news/world-middle-east-28686998>.
2. N. Kikoler, S. Langberg, *Communities at risk: Protecting civilians in the fight against the Islamic State* (Simon-Skjold Center for the Prevention of Genocide, 2016); <https://www.usihmm.org/m/pdfs/Protecting-Civilians-In-the-Fight-Against-ISIS.pdf>.
3. H. Johansen, K. Palani, D. Al'Aldeen, *Ninewa Plains and Western Ninewa barriers to return and community resilience: A meta-analysis of existing studies and literature* (U.S. Institute of Peace and Middle East Research Institute, 2020); [https://www.usip.org/sites/default/files/2020-04/20200429-ninewa-plains-and-western-ninewa-\\_barriers-to-return-and-community-resilience-report.pdf](https://www.usip.org/sites/default/files/2020-04/20200429-ninewa-plains-and-western-ninewa-_barriers-to-return-and-community-resilience-report.pdf).
4. M. J. Gilligan, B. J. Pasquale, C. Samii, *Am. J. Pol. Sci.* **58**, 604–619 (2014).
5. S. Bowles, H. Gintis, *Econ. J.* **112**, F419–F436 (2002).
6. S. Knack, P. Keefer, *Q. J. Econ.* **112**, 1251–1288 (1997).
7. K. Samuels, *Chic. J. Int. Law* **6**, 663 (2005); <https://chicagounbound.uchicago.edu/cjil/vol6/iss2/10>.
8. E. L. Paluck, "Interventions aimed at the reduction of prejudice and conflict," in *The Oxford Handbook of Intergroup Conflict*, L. R. Tropp, Ed. (Oxford Univ. Press, 2012), pp. 13–28.
9. G. W. Allport, K. Clark, T. Pettigrew, *The Nature of Prejudice* (Addison-Wesley, 1954).
10. J. Burns, L. Corno, E. La Ferrara, *Interaction, Stereotypes and Performance: Evidence from South Africa* (Working Paper, 2015); [https://pdfs.semanticscholar.org/45bb/98806ab8be2e4a5732e583edaf1c97de7eb8.pdf?\\_ga=2.224814298.1148653741.1595427502-2023252823.1595427502](https://pdfs.semanticscholar.org/45bb/98806ab8be2e4a5732e583edaf1c97de7eb8.pdf?_ga=2.224814298.1148653741.1595427502-2023252823.1595427502).
11. H. Finseraas, A. Kotsadam, *Eur. J. Polit. Res.* **56**, 703–722 (2017).
12. S. E. Carrell, M. Hoekstra, J. E. West, *The Impact of Intergroup Contact on Racial Attitudes and Revealed Preferences* (NBER Working Paper No. 20940, National Bureau of Economic Research, 2015); <https://www.nber.org/papers/w20940>.
13. L. N. Condra, S. Linardi, *J. Polit.* **81**, 1028–1042 (2019).
14. D. Hangartner, E. Dinas, M. Marbach, K. Matakos, D. Xefteris, *Am. Polit. Sci. Rev.* **113**, 442–455 (2019).
15. R. D. Enos, *Proc. Natl. Acad. Sci. U.S.A.* **111**, 3699–3704 (2014).
16. M. L. Sands, *Proc. Natl. Acad. Sci. U.S.A.* **114**, 663–668 (2017).
17. M. Lowe, *Types of contact: A field experiment on collaborative and adversarial caste integration* (CESifo Working Paper Series 8089, 2019); <https://osf.io/u2d9x/>.
18. T. F. Pettigrew, L. R. Tropp, *J. Pers. Soc. Psychol.* **90**, 751–783 (2006).
19. E. L. Paluck, S. A. Green, D. P. Green, *Behav. Pub. Policy* **3**, 129–158 (2019).
20. S. Paolini, J. Harwood, M. Rubin, *Pers. Soc. Psychol. Bull.* **36**, 1723–1738 (2010).
21. A. Scacco, S. S. Warren, *Am. Polit. Sci. Rev.* **112**, 654–677 (2018).
22. J. D. Fearon, D. D. Laitin, *Int. Organ.* **54**, 845–877 (2000).
23. B. Beber, P. Roessler, A. Scacco, *J. Polit.* **76**, 649–665 (2014).
24. R. D. Enos, N. Gidron, *J. Polit.* **78**, 851–867 (2016).
25. R. M. Kunovich, R. Hodson, *Sociol. Q.* **43**, 185–212 (2002).
26. K. Kasara, *Quart. J. Polit. Sci.* **11**, 441–470 (2017).
27. R. Bhavnani, K. Donnay, D. Miodownik, M. Mor, D. Helbing, *Am. J. Pol. Sci.* **58**, 226–245 (2014).
28. T. F. Pettigrew, L. R. Tropp, U. Wagner, O. Christ, *Int. J. Intercult. Relat.* **35**, 271–280 (2011).
29. A. Al Ramiyah, M. Hewstone, *Am. Psychol.* **68**, 527–542 (2013).

30. R. D. Putnam, R. Leonardi, R. Y. Nanetti, *Making Democracy Work: Civic Traditions in Modern Italy* (Princeton Univ. Press, 1994).
31. A. Varshney, *Ethnic conflict and civic life: Hindus and Muslims in India* (Yale Univ. Press, 2003).
32. B. Kidd, "A new social movement: Sport for development and peace," in *Sport and Foreign Policy in a Globalizing World*, S. J. Jackson, S. Haigh, Eds. (Routledge, 2013), pp. 36–46.
33. R. K. Dittmann, C. Samii, *Peace Conflict* **22**, 380–392 (2016).
34. B. Zupruk, A. Whelan, E. Brouch, "Social and political perspectives of Iraqi IDPs from Ninewa and their host communities," in *International Republican Institute Report* (IRI, 2018); [www.iri.org/sites/default/files/2018-09-05\\_iraq\\_fgd\\_report.pdf](http://www.iri.org/sites/default/files/2018-09-05_iraq_fgd_report.pdf).
35. N. Siddiqui, R. Guiu, A. A. Shwan, Reframing social fragility in areas of protracted displacement and emerging return in Iraq (International Organization for Migration, 2017); [https://iraq.iom.int/files/publications/IOM\\_Iraq\\_Reframing\\_Social\\_Fragility\\_in\\_Iraq.pdf](https://iraq.iom.int/files/publications/IOM_Iraq_Reframing_Social_Fragility_in_Iraq.pdf).
36. F. Boen, N. Vanbeselaere, L. Brebels, W. Huybens, K. Millet, *Eur. J. Soc. Psychol.* **37**, 380–389 (2007).
37. M. Bauer et al., *J. Econ. Perspect.* **30**, 249–274 (2016).
38. F. Tonnies, *Studien zu Gemeinschaft und Gesellschaft* (Springer, 2012).
39. M. S. Granovetter, *Am. J. Sociol.* **78**, 1360–1380 (1973).
40. Y. Benjamini, Y. Hochberg, *J. R. Stat. Soc. B* **57**, 289–300 (1995).
41. A. Al Ramiah, M. Hewstone, *The Oxford Handbook of Political Psychology* (Oxford Univ. Press, 2013).
42. G. Rao, *Am. Econ. Rev.* **109**, 774–809 (2019).
43. S. B. Billings, E. Chyn, K. Haggag, *The Long-Run Effects of School Racial Diversity on Political Identity* (National Bureau of Economic Research, no. w27302, 2020).
44. L. R. Tropp, "Dismantling an ethos of conflict: Strategies for improving intergroup relations," in *The Social Psychology of Intractable Conflicts*, E. Halperin, K. Sharvit, Eds. (Springer, 2015), pp. 159–171.
45. L. R. Tropp et al., *Peace Conflict* **23**, 239–249 (2017).
46. C. M. Weiss, Reducing prejudice through descriptive representation: Evidence from a natural experiment in Israeli medical clinics. APSA Preprints (2019); <https://doi.org/10.33774/apsa-2019-jzwtg-v2>.
47. L. R. Tropp, T. F. Pettigrew, *Psychol. Sci.* **16**, 951–957 (2005).
48. T. Saguy, L. R. Tropp, D. Hawi, "The role of group power in intergroup contact," in *Advances in Intergroup Contact*, G. Hodson, M. Hewstone, Eds. (Psychology Press, 2012), pp. 127–146.
49. E. L. Paluck, *J. Pers. Soc. Psychol.* **96**, 574–587 (2009).
50. U.S. Department of State, FY 2020 congressional budget justification: Department of State, Foreign Operations, and Related Programs (2020); <https://www.state.gov/fy-2020-congressional-budget-justification-department-of-state-foreign-operations-and-related-programs/>.
51. Institute for Economics & Peace, Measuring peacebuilding cost-effectiveness, IEP Report 46 (IEP, 2017); [http://visionofhumanity.org/app/uploads/2017/03/Measuring-Peacebuilding\\_WEB.pdf](http://visionofhumanity.org/app/uploads/2017/03/Measuring-Peacebuilding_WEB.pdf).
52. Replication code and deidentified data for: S. Mousa, Building social cohesion between Christians and Muslims through soccer in post-ISIS Iraq, Zenodo (2020).

#### ACKNOWLEDGMENTS

I thank K. Beal and R. Zakaria for excellent research assistance and project management and A. Alrababa'h, L. Blaydes, S. Chaskel,

S. Ejdemyr, S. Glazerman, J. Hain-mueller, D. Laitin, J. Mummolo, K. Kao, C. Parreira, P. Raffler, P. Sniderman, J. Weinstein, V. Yassenov, T. Zeitsoff, and conference participants for helpful advice. Previous versions of this paper were presented at Stanford University, Harvard University, Princeton University, Chapman University, WZB Berlin, UN City, New York University Abu Dhabi, APSA 2018, and APSA 2019. **Funding:** This research was funded by a grant from the UK Department for International Development, awarded through J-PAL's Crime and Violence Initiative and IPA's Peace & Recovery Program. I also gratefully acknowledge funding from the Program on Governance and Local Development, the United States Institute of Peace, the Stanford Center for International Conflict and Negotiation, Stanford's King Center for Global Development, and the Freeman Spogli Institute at Stanford University. **Data materials and availability:** Replication code and deidentified data will be made available at the time of publication on Zenodo (49). A preregistered analysis plan is available at the American Economics Association website under study ID AEARCTR-0003540. The institutional review board at Stanford University (protocol no. 39653) approved this research.

#### SUPPLEMENTARY MATERIALS

[science.sciencemag.org/content/369/6505/866/suppl/DC1](https://science.sciencemag.org/content/369/6505/866/suppl/DC1)

Materials and Methods

Supplementary Text

Figs. S1 to S14

Tables S1 to S13

References (53–56)

MDAR Reproducibility Checklist

19 February 2020; accepted 13 July 2020

10.1126/science.abb3153





### Refrigerated Microtube Homogenizer

The BeadBlaster 24R Refrigerated Microtube Homogenizer from Benchmark Scientific can grind, lyse, or homogenize up to 24 samples simultaneously. A wide range of sample types can be processed using the variety of bead materials and sizes offered. Samples can be processed wet or dry in 2-mL or 5-mL tubes. Tubes are placed in the stainless steel tube carrier where they are subjected

to an intense 3D motion causing high-energy impacts between the microbeads and sample, thus releasing cellular contents. To protect heat-labile samples, the unit is equipped with a powerful compressor to provide true refrigeration—no dry ice, liquid nitrogen, or compressed air is needed. Operation is programmable, allowing for short bursts of homogenizing with rests in between to protect sensitive samples and for setting of temperatures from  $-10^{\circ}\text{C}$  to ambient.

#### Benchmark Scientific

For info: 908-769-5555

[www.benchmarkscientific.com](http://www.benchmarkscientific.com)

### Glass Slide for Lung Models

The current COVID-19 pandemic places an extraordinarily high importance on SARS-CoV-2-related research using physiological lung models. ibidi's  $\mu$ -Slide Membrane ibiPore Flow has a porous glass membrane for transmigration and transport studies under both static and flow conditions. Various experimental approaches can be performed in 2D or 3D, such as endothelial barrier assays, cocultivation of two different cell types, or apical-basal cell polarity assays. The slide's horizontal porous glass membrane is inserted between two channels and has brilliant optical quality for high-resolution microscopy. To create a lung model with an air-liquid interface, a polarized cell monolayer (e.g., lung epithelial cells) is cultured on the upper side of the porous membrane, which is exposed to air. From the lower channel, the cells are supplied by culture medium under defined shear stress. Four different pore sizes are available for various cell types. Researchers can test the slide for their application with a trial pack containing two slides.

#### ibidi

For info: 844-276-6363

[ibidi.com](http://ibidi.com)

### Support System for Laboratory Scale Reactions

The ReactoMate DATUM from Asynt is a high-quality, dual-rod stainless steel and aluminum support system built to ensure the stability and safety of your lab reactor. Sturdy yet compact, the system can accommodate a wide range of reaction vessels from 100 mL up to 5,000 mL. The novel neck clamp allows fast changeover between reactor vessel sizes, enabling simple reaction scale-up, while the ingenious mounting mechanism promises excellent stability and alignment every time. The ReactoMate DATUM support system is fully compatible with all leading brands of overhead stirrers and circulator heating/cooling systems. Ideally suited for use within a benchtop fume hood, the DATUM's adjustable feet allow you to level the system, ensuring stability and security while you work. Each DATUM system is also supplied with a molded drip tray that fits perfectly within the base of the support, for safely catching any drips and spills from the reaction vessel during draining.

#### Asynt

For info: +44-(0)-1638-781709

[www.asynt.com/product/reactomate-datum](http://www.asynt.com/product/reactomate-datum)

### Differentiation of Human iPS and ES Cells

AMS Biotechnology (AMSBIO) introduces StemFit for Differentiation—a chemically defined formulation that enables differentiation of human induced pluripotent system cells (hiPSCs) and human embryonic stem cells (hESCs). The formulation's unique composition minimizes lot-to-lot variation, resulting in highly consistent cell differentiation. Free of animal- and human-derived components, StemFit for Differentiation can be used to eliminate the risk of immunogenic contamination. Applications proven to benefit from this preparation include lineage-specific (endodermal, mesodermal, and ectodermal) differentiation when it is used to replace serum-free supplements, as well as spontaneous differentiation of hiPSCs to organoids via embryoid body formation. Used in combination with StemFit Basic feeder-free medium with iMatrix-511 laminin as extracellular matrix, StemFit for Differentiation allows researchers to undertake clinical applications involving both expansion and differentiation of hiPSC-derived cells and tissues. Supplied as a 5X concentrate, StemFit for Differentiation has been formulated for use with basal-cell culture medium (e.g., DMEM, RPMI 1640, DMEM/F12) and a variety of different induction factors or cytokines (including Activin A and bFGF from AMSBIO).

#### AMS Biotechnology

For info: 617-945-5033

[www.amsbio.com/stemfit-for-differentiation](http://www.amsbio.com/stemfit-for-differentiation)

### RT-qPCR SARS-CoV-2 Detection

PCR Biosystems announces the launch of qPCR BIO Probe 1-Step Virus Detect, a high-concentration 4x reverse transcription quantitative PCR (RT-qPCR) kit designed specifically for ultrasensitive, high-throughput detection of viral RNA sequences, including SARS-CoV-2. The kit is ideally suited to high-throughput testing of COVID-19 clinical samples, either with laboratory-developed assays or as a component of diagnostic testing kits. It has been developed with the company's UltraScript Reverse Transcriptase enzyme. Reverse transcription can be performed in only 5 min and at temperatures up to  $55^{\circ}\text{C}$ , enhancing the detection of difficult viral RNA sequences. The PCR step is powered by PCR BIO HS Taq DNA Polymerase, which employs antibody-mediated, hot-start technology for specific amplification of virus-derived complementary DNA, with improved tolerance to the common PCR inhibitors found in clinical samples. Combined with a specially formulated buffer system developed using smart screen technology, qPCR BIO Probe 1-Step Virus Detect delivers accurate and precise RT-qPCR over a broad range of template concentrations.

#### PCR Biosystems

For info: 484-540-9108

[pcrbio.com/usa/products/qpcr/qpcrbio-probe-1-step-virus-detect](http://pcrbio.com/usa/products/qpcr/qpcrbio-probe-1-step-virus-detect)

### Xeno-Free Extracellular Matrix

CELLvo XF Matrix delivers efficient isolation of stem cells from primary cells while promoting expansion without loss of potency. Available from StemBioSys, it is the only commercially available substrate that recapitulates critical aspects of a cell's native niche by leaving its extracellular matrix intact. Composed of 150 proteins secreted and assembled by bone marrow cells, this extracellular matrix provides a 3D microenvironment in a culture dish with all the signals that cells expect to receive in vivo. It is xeno-free, allowing for easy translation to clinical studies. The substrate is available in six-well plates as well as 75-cm<sup>2</sup> or 150-cm<sup>2</sup> tissue culture flasks. CELLvo XF Matrix products are optically clear and cells grow in monolayer, allowing for beautiful brightfield images. Staining the cells for fluorescent imaging is also possible.

#### StemBioSys

For info: 210-877-9323

[www.stembiosys.com](http://www.stembiosys.com)

Electronically submit your new product description or product literature information! Go to [www.sciencemag.org/about/new-products-section](http://www.sciencemag.org/about/new-products-section) for more information.

Newly offered instrumentation, apparatus, and laboratory materials of interest to researchers in all disciplines in academic, industrial, and governmental organizations are featured in this space. Emphasis is given to purpose, chief characteristics, and availability of products and materials. Endorsement by *Science* or AAAS of any products or materials mentioned is not implied. Additional information may be obtained from the manufacturer or supplier.



International  
**Human Frontier  
Science Program**  
Organization

The Board of Trustees (Board) of the **International Human Frontier Science Program Organization (HFSP)** invites applications and nominations for the position of Secretary-General.

HFSP seeks to appoint a visionary scientist able to lead HFSP into the future through a rapidly changing scientific and research funding environment. The new Secretary-General will build further HFSP's prestigious reputation as the leading body in support of international collaboration in life sciences research.

HFSP takes a worldwide approach in the spirit of science without borders to promote and fund "basic research focused on the elucidation of the sophisticated and complex mechanisms of living organisms for the benefit of all humankind, through international cooperation". HFSP supports research grant and fellowship funding programs that enable international collaboration in innovative, cutting edge and high-risk research at the frontiers of the life sciences.

The Secretary-General should be an internationally recognized and respected scientist who: • supports the values of HFSP, including international collaboration • understands the value of basic life science research and its benefits for all humankind • is convinced of the distinctive value of frontier life science international collaboration • is able to make a compelling case to scientific and research leaders for the support and promotion of frontier research globally • is able to implement the Board's strategic vision to strengthen this prestigious Program and lead it into the next period of its development • demonstrates integrity and cultural sensitivity • has had senior-level scientific administrative experience • is an innovative researcher, qualified in a field relevant to the scientific priorities of the Program, who understands the importance of novel approaches for the development of life science research.

HFSP is an international organization supporting cultural diversity and gender equality. The position is fulltime and based in Strasbourg, France. The appointment begins in July 2021. The contract will be for 3 years, renewable once. Salary will be negotiated in accord with HFSP's salary policy. HFSP conducts all its work in English. The successful candidate may maintain a scientific appointment at a University or research institute, subject to the approval of the Board and in line with HFSP's policy on conflict of interest.

The Secretary-General may be a citizen of any HFSP Member, Australia, Canada, France, Germany, India, Israel, Italy, Japan, Republic of Korea, New Zealand, Singapore, Switzerland, UK, USA and other countries of the European Union.

Applications, accompanied by a CV, or enquiries should be sent to: [nderry@wittkiewer.com](mailto:nderry@wittkiewer.com) and [eyeckley@wittkiewer.com](mailto:eyeckley@wittkiewer.com)

**DEADLINE FOR SUBMISSIONS IS 30 SEPTEMBER.**



## **SUPERVISORY RESEARCH MOLECULAR BIOLOGIST/MICROBIOLOGIST/CHEMIST** **GS-0401/0430/1320-14/15**

Salary Range of \$107,807 to \$164,858

**Announcement Open: July 27, 2020 through August 27, 2020**

The USDA, ARS, Mycotoxin Prevention and Applied Microbiology Research Unit (MPM) in Peoria, IL is seeking a **Supervisory Research Molecular Biologist, Microbiologist or Chemist (Research Leader)**. The incumbent will lead a broad research program to limit mycotoxin contamination of food and feed, improve crop production and public health, and enhance economic development. As Research Leader, the incumbent will conduct and publish research, provide vision, establish an advisory stakeholder base, develop research programs to address stakeholder priorities, hire and supervise personnel, manage the fiscal and physical resources assigned to the unit, provide technical information and consultation both internal and external to the Agricultural Research Service and ensure the proper interpretation and reporting of scientific research results.

For further information and complete application instructions, search for announcement **ARS-D20MWA-10870108-JML** at <https://www.usa.jobs.gov/>

**U.S. Citizenship is required.** Applications must be received by the closing date of **August 27, 2020**.

USDA/ARS is an equal opportunity employer and provider

**myIDP: A career plan customized for you, by you.**

For your career in science, there's only one

Science

### **Features in myIDP include:**

- Exercises to help you examine your skills, interests, and values.
- A list of 20 scientific career paths with a prediction of which ones best fit your skills and interests.



Visit the website and start planning today!  
[myIDP.sciencecareers.org](https://myIDP.sciencecareers.org)

**Science Careers** | AAAS In partnership with:



# HANGZHOU INNOVATION RESEARCH INSTITUTE, BEIHANG UNIVERSITY



**H**angzhou Innovation Research Institute, Beihang University is a new high-level research institute jointly established by Beihang University, Zhejiang Province, Hangzhou City and Binjiang District. With the mission of “building a world-class technological innovation platform and innovative talent training platform in the field of information”, and focusing on the multidisciplinary intersection of information technology, life and health, cognitive science and new materials, Hangzhou Innovation Research Institute actively explores new mechanisms and gathers global innovative resources, and is committed to achieving a number of major original innovations and key technological breakthroughs and applications, striving to become a talent and innovation center that is rooted into Zhejiang Province while looking to the world’s first-class. The institute has been included in Hangzhou “Prestigious Schools, Universities, and Institutes” project, and has also been awarded the “2019 Hangzhou Most Influential New R&D Institution”.

## I. Open Positions

1. Principal Investigator
2. Senior research scientist, Senior Associate research scientist

## II. Research Areas

Computer science and technology, instrumentation science and technology, optical engineering, electronic science and technology, control science and engineering, material science and engineering, information and communication engineering, mechanical engineering, physics, mathematics, medical imaging and other related majors.

## III. How to Apply

This announcement is long-term effective. For details, please refer to the official website of Hangzhou Innovation Institute, Beihang University – recruitment (<http://hzii.buaa.edu.cn/zcyz/zpgz.htm>). Please send your resume to [buaa\\_hr@buaa.edu.cn](mailto:buaa_hr@buaa.edu.cn) (email: “intended position + name”)

**Contact:** Ms. Tian, Mr. Shi

**TEL:** +86-571-85367559 19957890995

**Email:** [buaahz\\_hr@buaa.edu.cn](mailto:buaahz_hr@buaa.edu.cn)



# HIGH-LEVEL GLOBAL TALENTS RECRUITMENT

## 2020 Global Online Job Fair ([www.edu.cn/cv](http://www.edu.cn/cv))

September 25, High-level Global Talents Recruitment  
00:30-14:30 GMT (08:30-22:30 Beijing time)

October 16, High-level Global Talents Recruitment  
00:30-14:30 GMT (08:30-22:30 Beijing time)

November 06, China High-level Talents Recruitment  
00:30-14:30 GMT (08:30-22:30 Beijing time)

November 27, High-level Global Talents Recruitment  
05:00-09:00 GMT (13:00-17:00 Beijing time)

December 18, High-level Global Talents Recruitment  
00:30-14:30 GMT (08:30-22:30 Beijing time)

## Qualification for Applicants

Global scholars, Doctor and Post-doctor, Doctoral Candidates

## Key Disciplines

Art & Science, Business, Economics, Computer Science and Information Technology, Chemistry, Agriculture, Fisheries and Food Science, Law, Life sciences, Mathematics, Medicine, Physics and Engineering, Psychology

## Participating Universities

Beijing Jiaotong University, Harbin Engineering University, Hebei University of Technology, Zhengzhou University, National University of Defense Technology, Northeastern University (continuously updating)

*Job Vacancies in China's Universities and Institutes*

Please visit [www.acabridge.edu.cn](http://www.acabridge.edu.cn)

Contact [consultant@acabridge.edu.cn](mailto:consultant@acabridge.edu.cn)



Scan to check the sessions

## EVEN SEPARATED BY MOUNTAINS AND RIVERS, WE HAVE OUR BLOOD TIGHTLY CONNECTED

The Coronavirus pandemic has forced many of us to consider different ways of working and communicating. Chinese universities and colleges are now holding online job fairs to help overseas scholars explore career options in China.



By Kathy Gillen

# Interrupted—again

**T**he two emails arrived the same early April day. One informed me that I had secured a \$3000 grant. Although the dollar value was small, it was a big step toward restarting my research career after a 22-year hiatus. The second email announced that my college had canceled in-person student research for the coming summer because of COVID-19. My newly relaunched research program had abruptly crashed back to Earth.

Two decades earlier, I had left my postdoc—and research—when my husband landed a tenure-track job at a small liberal arts college in a different state. A few years after our move, I was thrilled when an opportunity arose for me to teach at the college. When people asked whether I missed research, my pat response was that I was happy with my job. But that wasn't the full truth. I always felt an unpleasant pit in my stomach while celebrating my husband's grants and publication successes, sad that I couldn't claim the same achievements. And twinges of regret gnawed at me when students in my classes asked whether they could join my research lab and I had to tell them no—I didn't do research anymore.

A few years ago, those twinges grew stronger when a pair of talented students wanted to continue work they had started as an independent research project in one of my lab classes. I would have loved to work with these motivated students after the semester ended. Maybe it was time to explore whether that was possible.

I had always claimed I didn't have a research program because I wasn't a tenure-track professor, but was that really the barrier? Was it just easier to blame my status than to try to get a lab up and running? Was fear of failure holding me back?

Over the following months, the risks of not starting up research—boredom, depression, regret—began to outweigh the risk of trying and failing. I decided to give it a go.

When I reached out to the chair of the department, he said he would support my plan as long as I was mentoring students. Colleagues offered to share equipment, expertise, and space. I had enough money in a college-provided development fund to buy a few reagents. As for a research question, while teaching in the introductory lab I had learned that the worm *Lumbriculus variegatus* was



**“If I could ... return to research after a 22-year break, I won't let a slowdown stop me now.”**

inexpensive to work with, and it offered plenty of interesting avenues for investigation. I was ready to go.

In June of 2019, I nervously started to mentor my first group of research students, worried that my skills would be rusty or, worse, obsolete. Indeed, some bread-and-butter techniques from my past were no longer relevant. But I found that the core process of scientific inquiry—asking questions, designing experiments, interpreting data—hadn't changed. And my troubleshooting skills quickly kicked in. Our first western blot looked like a Rorschach test, but after weeks of fine-tuning, we had an interpretable blot—reason for a minor celebration. By the end of the summer, we had generated enough data to put together a poster to present at a conference in January. I left that

meeting feeling optimistic and energized about the future, wondering why I had waited so long to return to research.

Just 3 months after the conference my research was interrupted again—frustrating, to say the least. But despite the COVID-19 restrictions, I have found ways to carry on. I am currently collaborating remotely with a student who was slated for full-time lab research this summer. We hatched a plan: He designs experiments, and I do the hands-on work. From there, he interprets the data and plans the next steps. It's not ideal, but we are making progress.

Even in normal circumstances, research is hard. This summer, our results have been confusing, and at times I have felt like throwing in the towel. But I remember how much I enjoyed the summer of 2019, and that I chose this path. If I could overcome my fears and return to research after a 22-year break, I won't let a slowdown stop me now. ■

Kathy Gillen is an assistant professor of biology at Kenyon College in Gambier, Ohio. Do you have an interesting career story to share? Send it to [SciCareerEditor@aaas.org](mailto:SciCareerEditor@aaas.org).